Complexity

Advanced Control and Optimization for Complex Energy Systems 2022

Lead Guest Editor: Chun Wei
Guest Editors: Jing Na, Dan Lu, Xiaoqing Bai, Wenjie Lu, and Shubo Wang

Advanced Control and Optimization for Complex Energy Systems 2022

Complexity

Advanced Control and Optimization for Complex Energy Systems 2022

Lead Guest Editor: Chun Wei
Guest Editors: Jing Na, Dan Lu, Xiaoqing Bai, Wenjie Lu, and Shubo Wang

Contents

Electric Vehicle Charging Infrastructure Location Optimization with Mixed and Forecasted Charging Requirements
Dandan Hu, Shuxuan Cai, and Zhi-Wei Liu
Research Article (11 pages), Article ID 9567183, Volume 2023 (2023)

Optimal Calculation Method of Mean Equivalent Diameter of Floc Particles Based on MCC
Jun Liu, Siqi Peng, and Nan Zhou
Research Article (9 pages), Article ID 1862844, Volume 2022 (2022)

A Hybrid Deep Learning-Based Network for Photovoltaic Power Forecasting
Altaf Hussain, Zulfiqar Ahmad Khan, Tanveer Hussain, Fath U Min Ullah, Seungmin Rho, and Sung Wook Baik
Research Article (12 pages), Article ID 7040601, Volume 2022 (2022)

Design of a Small Quadruped Robot with Parallel Legs
Ming Lu, Baorui Jing, Hao Duan, and Guanbin Gao
Research Article (11 pages), Article ID 9663746, Volume 2022 (2022)

Optimization of Energy in Sustainable Architecture and Green Roofs in Construction: A Review of Challenges and Advantages
Sara ziaee, Zeynab Gholampour, Mina Soleymani, Parisa Doraj, Omid Hossein Eskandani, and Samireh Kadaei
Review Article (15 pages), Article ID 8534810, Volume 2022 (2022)

Integration and Modeling of Multi-Energy Network Based on Energy Hub
Min Mou, Yuhao Zhou, Wenguang Zheng, and Yurong Xie
Research Article (11 pages), Article ID 2698226, Volume 2022 (2022)

Evaluating and Identifying Climatic Design Features in Traditional Iranian Architecture for Energy Saving (Case Study of Residential Architecture in Northwest of Iran)
Amirmasood Nakhaee Sharif, Sanaz Keshavarz Saleh, Sadegh Afzal, Niloofar Shoja Razavi, Mozhdeh Fadaei Nasab, and Samireh Kadaei
Research Article (12 pages), Article ID 3522883, Volume 2022 (2022)

Deep Learning-Assisted Short-Term Power Load Forecasting Using Deep Convolutional LSTM and Stacked GRU
Fath U Min Ullah, Amin Ullah, Noman Khan, Mi Young Lee, Seungmin Rho, and Sung Wook Baik
Research Article (15 pages), Article ID 2993184, Volume 2022 (2022)

High-Voltage Topological Architecture-Based Energy Management Strategy of the Plug-In Hybrid Powertrain System
Ziliang Zhao, Jun Zhao, Bin Guo, and Rifei Lai
Research Article (8 pages), Article ID 3327722, Volume 2022 (2022)

Audio and Video Matching Zero-Watermarking Algorithm Based on NSCT
Di Fan, Wenxue Sun, Huiyuan Zhao, Wenshuo Kang, and Changzhi Lv
Research Article (14 pages), Article ID 3445583, Volume 2022 (2022)

Modeling the Thermal Performance for Different Types of Solar Chimney Power Plants
Ghassan F. Smaisim, Azher M. Abed, and Ali Shamel
Research Article (10 pages), Article ID 3656482, Volume 2022 (2022)

Insulator Semantic Segmentation in Aerial Images Based on Multiscale Feature Fusion
Zheng Cui, Chunxi Yang, and Sen Wang
Research Article (14 pages), Article ID 2468431, Volume 2022 (2022)

Advancements and Future Prospects of Electric Vehicle Technologies: A Comprehensive Review
M. S. Hossain, Laveet Kumar, Mamdouh El Haj Assad, and Reza Alayi
Review Article (21 pages), Article ID 3304796, Volume 2022 (2022)

Location Optimization Model of a Greenhouse Sensor Based on Multisource Data Fusion
DianJu Qiao, ZhenWei Zhang, FangHao Liu, and Bo Sun
Research Article (9 pages), Article ID 3258549, Volume 2022 (2022)

Incremental Adaptive Control of a Class of Nonlinear Nonaffine Systems
Yizhao Zhan, Shengxiang Zou, Xiongxiong He, and Mingxuan Sun
Research Article (19 pages), Article ID 2847785, Volume 2022 (2022)

Hindawi
Complexity
Volume 2023, Article ID 9567183, 11 pages
https://doi.org/10.1155/2023/9567183

Research Article

Electric Vehicle Charging Infrastructure Location Optimization with Mixed and Forecasted Charging Requirements

Dandan Hu,[1] **Shuxuan Cai**,[1] **and Zhi-Wei Liu**[2,3]

[1]*School of Management, South-Central Minzu University, Wuhan 430074, China*
[2]*School of Artificial Intelligence and Automation, Huazhong University of Science and Technology, Wuhan 430074, China*
[3]*Key Laboratory of Image Processing and Intelligent Control, Ministry of Education, Huazhong University of Science and Technology, Wuhan 430074, China*

Correspondence should be addressed to Zhi-Wei Liu; zwliu@hust.edu.cn

Received 18 July 2022; Revised 5 September 2022; Accepted 13 September 2022; Published 24 March 2023

Academic Editor: Wenjie Lu

Electric vehicles are not widely adopted without proper charging infrastructure, despite their environmental benefits and growing popularity in transportation. This paper focuses on the location problem of charging infrastructure to achieve a more optimized charging facility layout. The charging demands of electric vehicles can be divided into two categories. The first category is generated at network points such as shopping malls, office buildings, parking lots, and residential areas. The second category is generated along the flow of network paths, such as on the highway and on the way to and from work. The goal of this problem is to maximize both categories of charging demands using a nonlinear integer programming model. We introduce the spatial intersection model to obtain the data on path demand. The spatial intersection model is introduced to obtain data on path demand. In addition, future demand is taken into account in the optimization through data forecasting. Then, the greedy algorithm is designed to solve the optimization model. The effectiveness is proved by a lot of random experiments. Finally, the effects of parameters are analyzed by a case study. The location decision of charging stations for both demands is more reasonable than only one type of demand consideration. The proposed model ensures the coverage and appropriate extension of the charging network.

1. Introduction

In recent years, due to the energy crisis and serious environmental pollution, the Chinese government has vigorously promoted the development of new energy vehicles. National and local governments have adopted a series of incentive policies for the promotion of . With the support of these policies, the market size of EVs in China has increased rapidly, as shown in Figure 1. However, current EV penetration is far behind government planning. The new Energy Vehicle Industry Development Plan (2021–2035) puts forward the new goal that by 2025, the proportion of EV sales should reach about 20% of the total vehicle sales [1], but now the proportion is 5.4%. Among these reasons for the slow promotion, one of the major problems is the backward charging of infrastructure construction. On the one hand, the number of existing charging stations seriously lags behind the EV development plan. On the other hand, the of charging stations is unreasonable. In 2018, the utilization rate of public charging stations was less than 10%, which is difficult for operating enterprises to make a profit [2]. For example, Wuhan has more EV charging piles than the number of EVs, but the EV is still difficult to charge; the daily utilization rate of public charging piles in Beijing is only 6% to 7%, and they are idle most of the time; TELD, the new energy company, has suffered losses for four consecutive years, with a cumulative loss of 600 million yuan.

The purpose of this paper is to reasonably locate the charging stations to maximize the number of charging demands. The previous literature on the location of charging stations can be mainly divided into two categories [3]. One category assumes the charging demands generated in network points, such as in shopping malls, office buildings, parking lots, and residential areas. This kind of research is

usually based on the coverage location model, which sets the coverage radius of the charging station and aims to maximize the charging demands within the coverage radius [4–8]. The other research studies the charging demands as flows generated on the network paths, such as on the highway and on the way to and from work. This kind of research is often based on the flow interception location problem (FILP) [9–14].

However, in reality, the charging demands are not so clear to distinguish. One charging station intends to provide service to both demands. For example, the charging station on the main road serves lots of the charging demands on this path and its surrounding paths but also provides services for nearby communities, shopping malls, and office buildings around it. Similarly, charging piles built in office buildings and shopping malls can also charge EVs passing by. Therefore, this paper considers the charging demands from points and paths at the same time, through the weight factor, adjusting the influence of two types of demands on the location decision.

But actually, it is difficult to obtain the flow between origin-destination (O-D) pairs, which is assumed to be given in traditional FILP. However, in general, only transport with the given route can obtain the flow of O-D pairs, such as trains [15] and buses [16]. Moreover, in a large-scale complex network, it is almost impossible to obtain each O-D pair of traffic flow, even if the traffic on each network edge can be obtained through advanced technologies, such as monitoring and data crawling. In this paper, we introduce the spatial intersection model (SIM) to estimate the charging demands of each O-D pair. SIM is first applied to estimate the demand of the retail industry; the number of retail customers attracted from a town around the retail location is directly proportional to the population size of the town and inversely proportional to the distance between the two places [17]. Then, it is applied to measure the trade flows between two countries and traffic flows between two places [18].

In the existing empirical research or case analysis on the location of charging stations, the charging demand concerns the number of existing EVs [5–8, 11–14, 18, 19], assuming that charging demand is highly stochastic, with a scenario-based model to describe it; however, all scenarios are described on the current observation. Even scholars who study the expansion of multiperiod charging stations assume that the number of EVs will remain unchanged over each period [10, 16], which is seriously inconsistent with the current development of EVs. From Figure 1, the market size of EVs is increasing rapidly, so the design of charging stations must consider the operation in the future, or the charging station will be "outdated" after its establishment.

Compared with traditional vehicles, the most significant feature of is trip range restriction. Due to the limitations of battery technology, endurance cannot be compared with traditional vehicles, which causes range anxiety for drivers. Therefore, the distance between adjacent charging stations should not be too far. According to the data released by the National Energy Administration, the distance between adjacent public charging stations in China is no more than 50 km [20], which is adopted as one constraint in our model.

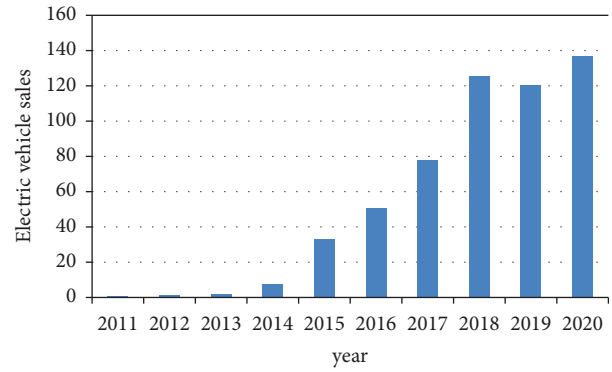

Figure 1: Annual sales volume of EVs in China from 2011 to 2020 (unit: 10,000).

Our model is an NP-hard problem, so an effective algorithm is necessary [21–24], and we design greedy heuristics to solve it.

For this paper, the main contributions are as follows:

(1) In reality, charging demands are generated from the points and paths, and the charging station intends to provide service to both demands. Therefore, we consider mixed charging demands in our location model.

(2) As EVs are increasing rapidly, we consider the future number of EVs as the basis for the design of charging stations. This paper proposed a prediction method for EV numbers with neural networks based on a government plan.

(3) As our model is an NP-hard problem, a heuristic algorithm for large-scale examples is proposed.

2. Model Establishment

2.1. Parameters and Decision Variables. First, the symbols are defined as follows:

Sets:

V: set of all points on the network
I: set of candidate locations of charging stations
P: set of all paths
H: set of all combinations of charging stations

Parameters:

θ: coefficient, $\theta \in [0, 1]$
w_j: the number of charging requirements at point j
f_ρ: the number of charging requirements on path ρ
m: the number of total charging stations to be built

Decision variables:

a_{ij}: if point j is within the coverage radius of charging station i, then $a_{ij} = 1$; otherwise, $a_{ij} = 0$, $i \in I$, $j \in V$
$b_{\rho h}$: if the charging station combination h can support an EV to complete the round trip of path ρ, $b_{\rho h} = 1$; otherwise, $b_{\rho h} = 0$, $h \in H$, $\rho \in P$
v_h: if all points in combination h establish charging stations, then $v_h = 1$; otherwise, $v_h = 0$, $h \in H$

v_{hi}: if charging station i is in combination h, then $v_{hi} = 1$; otherwise, $v_{hi} = 0$, $h \in H$, $i \in I$
z_j: if charging demands at point j can be served, then $z_j = 1$; otherwise, $z_j = 0$, $j \in V$
x_i: if a charging station is established at point i, then $x_i = 1$; otherwise, $x_i = 0$, $i \in I$
y_ρ: if EVs on path ρ can complete the round trip, then $y_\rho = 1$; otherwise, $y_\rho = 0$, $\rho \in P$

2.2. Mathematical Model. Through the above symbol definition, the charging station location model is established as follows:

$$\max Z = \theta \sum_{j \in V} w_j z_j + (1 - \theta) \sum_{\rho \in P} f_\rho y_\rho, \tag{1}$$

subject to

$$\sum_{i \in I} x_i = m, \tag{2}$$

$$\sum_{h \in H} b_{\rho h} v_h \geq y_\rho \quad \forall \rho \in P, \tag{3}$$

$$v_{hi} x_i \geq v_h \quad \forall h \in H; i | v_{hi} = 1, \tag{4}$$

$$\sum_{i \in I} a_{ij} x_i \geq z_j \quad \forall j \in V, \tag{5}$$

$$x_i, y_\rho, z_j, v_h \in \{0, 1\} \quad \forall i \in I,\ j \in V,\ \rho \in P,\ h \in H. \tag{6}$$

Objective function (1) represents maximizing of charging requirements from the covered points and paths by charging stations. Constraint (2) indicates that the number of charging stations to be established is m. Constraints (3) means that at least one combination that can support the EV to complete the round trip can be found, and all charging stations in the combination have been established, then the charging requirements on the path are covered. Constraints (4) mean v_h holds to zero unless all the charging stations in combination h are established. Constraints (5) indicate that charging requirements at a point j can be served only when the point j is within the coverage radius of the point i where the charging station has been established. Constraints (6) describe the binary restrictions.

2.3. The Relationship between f_ρ and w. Let $G(V, E)$ be a network where V is the set of demand points, E is the set of arcs, and I is the set of candidate locations of charging stations ($I \subseteq V$). It is assumed that the driver knows the shortest path ρ between O-D and selects it as the driving path. f_ρ represents the charging requirements on the path ρ. Berman et al. [9] and Hodgson [25] proposed. Assumes that the flow on the path between each O-D pair is known, and once a facility is built at a point, all flows passing through that point are covered.

However, in reality, the network is complex, and the acquisition of the flow of each O-D pair is difficult. The common method to obtain the data on O-D pairs and charging requirements is tracking the driving trajectory of electric taxis through GPS [26], but it is very difficult for the trajectory of other general EVs. Other methods are through technologies such as monitoring or data crawling to obtain the edge flow of the network [27], but it is not enough because monitoring cannot discriminate which flow belongs to which O-D pair. Still, the flows between O-D pairs cannot be made available. In this paper, SIM is introduced to obtain f_ρ from w by using the following formula [17]:

$$f_\rho = k \frac{(w_i w_j)^\alpha}{d_{ij}^\beta}. \tag{7}$$

From (7), the flow between the two points is directly proportional to the point demands but inversely proportional to the distance between the two points. In our model, ρ is assumed to be the path with the shortest distance between points i and j. There are a total of $C_{|V|}^2$ paths, in which $|V|$ represents the number of point generation charging demands. w_i and $w_j (i, j \in V)$ represent the charging demands generated at points i and j, and d_{ij} shows the shortest distance between points i and j. β indicates the sensitivity of distance to spatial interaction. The larger the value of β, the weaker the interaction between points i and j. The coefficients k, α, and β can be derived from the regression models based on historical data.

2.4. Determination of w Parameters. Due to the rapid development of EVs, the construction of charging stations must take into account the future number of EVs to be served. Therefore, the input parameter w in the model should be the future predicted value rather than the current value of the point charging requirement. In this paper, a nonlinear neural network tool is adopted for time series prediction [28–30] which is based on historical data. But, due to the short development time of EVs, there is less historical data collection. Furthermore, its development is mainly driven by government policies; therefore, prediction is unreasonable directly according to historical data like the previous research [31]. This paper proposes a prediction framework. This framework first predicts the number of vehicles in the future by the nonlinear neural network. Due to the long history of automobile development and the rich historical data of vehicles, the prediction of the number of vehicles is much more accurate than the direct prediction of the number of EVs. Then, combined with government planning, we can get the predicted number of EVs.

The model adopts a nonlinear autoregression with exogenous inputs (NAR) neural network, which can be described by the following formula:

$$y(t) = f(y(t-1), y(t-2), \ldots, y(t-p)), \tag{8}$$

where f is a nonlinear function, and the value of y at t time depends on the previous p values of y.

Assuming that the occupation ratio of the local EV is the same as the national average, the prediction framework is as follows:

Step 1: according to the historical data of national vehicle ownership, the NAR neural network is used to predict the future national vehicle ownership, VQ. According to the future national EV ownership EVQ planned by the government, the occupation ratio of national EVs in the future is obtained as $\theta = EVQ/VQ$.

Step 2: according to the historical data of vehicle ownership in a local area, the NAR neural network is used to predict the future local vehicle ownership VQ'. The future EV ownership in this region is $EVQ' = VQ'\theta$.

Step 3: allocate the number of EVs at each demand point according to the population proportion $w_i = EVQ'\,pi\%$, where $pi\%$ is the population ratio of point i.

2.5. Mileage Limit. Nowadays, the battery capacity of EVs is not enough to ignore the distance between adjacent charging stations, that is, the trip mileage limit. EV users are always afraid that the battery is out of power before they find the next charging station, which is called trip mileage anxiety. In order to reduce or even eliminate trip mileage anxiety, we set a reasonable trip mileage limit between adjacent charging stations before construction. If the distance between adjacent charging stations is more than the trip mileage limit, drivers will produce strong mileage anxiety. As mentioned above, the distance between charging stations established in China is no more than 50 km [20], so we set the trip mileage limit to 50 km.

In the mathematical model, we adopt the method in [32] to express the trip mileage limit. It is assumed that (1) when the distance between two adjacent charging stations exceeds the trip mileage limit, the charging stations cannot cover the path; (2) the covered path is a round-trip path; (3) the charging station can only be established at the point; (4) if there is no charging station at the starting point, the initial driving mileage of the EV is half of the trip mileage limit. Constraints (3) and (4) mean that at least one combination h that can support the EV to complete the round trip can be found, and all facilities in the combination h have been established, then the EV can complete the round trip. These constraints are obviously different from FILP in which as long as there is a facility on the O-D path, the flow can be intercepted.

3. Algorithm

As the charging station location model is an NP-hard problem, with the expansion of the model scale, the computing time of the accurate algorithm will be very long. It is necessary to find an effective algorithm for this kind of problem. In this paper, a greedy algorithm is used to solve the problem, and the solving steps are described as Algorithm 1.

4. Simulation Experiments

In this section, random examples are generated to verify the effectiveness of the greedy algorithm by comparing it with the exact solutions. The exact solutions are obtained by using the enumeration algorithm. A connected network is randomly generated, the point demand is randomly generated in the interval (0, 10), the distance between two adjacent points is distributed in the interval (0, 20), and the connection probability between points is 0.5. Because the calculation time of the enumeration algorithm is long, the number of points and charging stations cannot be large. In this paper, the number of network points is set to be 20, 25, 30, 50, 100, and 150, and the number of charging stations is set to be 3, 4, 5, 10, 15, and 20. When the point number of networks is 50 and the number of charging stations is 5, the computational time of enumeration exceeds 2 hours. We set the upper bound of the enumeration algorithm time to 2 hours. Different network points and charging stations constitute a group of examples, and 10 examples are generated randomly in each group. A total of 170 examples are generated in this section to verify the effectiveness of the greedy algorithm. The parameters of SIM are set as follows [25]: $k = 0.5$, $\alpha = 0.5$, and $\beta = 2$. Other parameters: $\theta = 0.5$, the point coverage is 8, and the trip mileage limit is 10. The calculation results of the greedy algorithm are shown in Table 1.

From Table 1, it can be found that the gap of the greedy algorithm is small, no more than 5.48%. Usually, the optimal solution can be found by using the greedy algorithm, and the lowest group is 70%. With the increasing number of points and charging stations, as computational time limitations of enumeration, the greedy algorithm shows more advantages in computational time and result accuracy than enumeration.

However, it is found that the trip mileage limit has a great impact on the accuracy of the greedy algorithm, as shown in Table 2. The trip mileage limit is set to be 0.5, 1, 1.5, 2, and 5, respectively, and 10 examples are randomly generated for each value of the trip mileage limit with 25 points and 5 charging stations. It is found that the smaller the trip mileage limit, the greater the gap. The performance of the greedy algorithm in our model is similar to that in the literature [32]. When the trip mileage limit is 0.5, the maximum gap reaches 75.25%, and only 4 of the 10 examples reach the optimal solution. When the trip mileage limit is too small, the greedy algorithm is difficult to find the optimal combination of charging stations to cover the round trip of a path because the greedy algorithm only adds one charging station each time.

Input: V, I, m, $w_j\,(j \in V)$, α, β, k, θ, coverage radius and trip mileage limit
Output: X
(1) adopt dijkstra algorithm to calculate the shortest distance d_{ij} between any two points $i\,(i \in I)$ and $j\,(j \in V)$ and the shortest path set P
(2) adopt SIM (fomular (7)) to obtain path demands f_ρ of all paths in P
(3) for $i \in I$
(4) for $j \in V$
(5) if d_{ij} is no more than the coverage radius
(6) $a_{ij} = 1$
(7) else
(8) $a_{ij} = 0$
(9) **endif**
(10) endfor
(11) **endfor**
(12) initialize $X = \Phi$
(13) for $n = 1$: m
(14) for $j \in V \backslash X$
(15) $W(j) = 0$
(16) **endfor**
(17) for $j \in V \backslash X$
(18) for $i \in I$
(19) $W(j) = W(j) + a_{ij} w_i$
(20) endfor
(21) endfor
(22) for $j \in V \backslash X$
(23) $F(j) = \sum_{\rho \in P(X \cup \{j\})} f_\rho$, $P(X)$ is the set of paths that is covered by charging station set X
(24) endfor
(25) for $j \in V \backslash X$
(26) $Z(j) = \theta W(j) + (1 - \theta) F(j)$
(27) endfor
(28) $j^* \leftarrow \text{argmax}_{j \in V \backslash X} \{Z(j)\}$
(29) $X = X \cup \{j^*\}$
(30) $V = V \backslash \{j^*\}$
(31) for $i \in I$
(32) if $a_{ij^*} = 1$
(33) $w_i = 0$
(34) endif
(35) endfor
(36) for $\rho \in P(X)$
(37) $f_\rho = 0$
(38) endfor
(39) endfor

Algorithm 1: The greedy algorithm for the charging station location model.

5. Case Analysis

Cixi City is located on the Bank of Hangzhou Bay, Zhejiang Province, with a population of 1,051,000. It is composed of 4 streets and 15 towns, as shown in Figure 2. In Figure 2, different sizes of points indicate different sizes of population. This case takes the predicted number of Cixi EV in 2030 as the demand parameter.

We adopt the GUI interface in MATLAB and Bayesian regularization back-propagation as the training functions. Through repeated experiments, a nonlinear autoregressive network with 1 : 5 feedback delay is created, the number of hidden layer neurons is 10, and the response of a delayed neural network is eliminated. According to the historical data of national vehicle ownership from 1940 to 2020, it is predicted that national car ownership will be 335.6 million in 2030. According to the historical data on vehicle ownership in Cixi from 1993 to 2020, it is predicted that the vehicle ownership in Cixi will be 0.57 million in 2030. Figure 3 shows the error between the national vehicle ownership forecast data and the actual data. The absolute error value is no more than 500. It can be seen that the error is very small, and the forecast data is reliable. Figure 4 shows the forecast trend of national car ownership. Figure 5 shows the error between the predicted car ownership data and the actual data in Cixi City. The relative error does not exceed 13%, and the predicted data are reliable. Figure 6 shows the forecast trend of vehicle ownership in Cixi City. According to the development of energy-saving and new energy vehicles plan, by 2030, the number of EVs in China will reach 80 million, and the percentage of EVs in the total number of vehicles will be 23.8%. Assuming that the percentage of EV ownership in

Table 1: Performance of the greedy algorithm.

Point number	m	Minimum gap (%)	Maximum gap (%)	Average gap (%)	Percentage of optimal solution (%)	Average computational time of the greedy algorithm (unit: s)	Average computational time of enumeration (unit: s)
20	3	0	5.84	0.72	70	2.08	27.16
	4	0	0.41	0.04	90	2.64	151.97
	5	0	0	0	100	2.89	413.25
25	3	0	0	0	100	4.05	119.05
	4	0	0	0	100	3.88	502.38
	5	0	0030	0	100	5.33	2003.40
30	3	0	0	0	100	6.95	221.58
	4	0	0	0	100	6.72	1492.20
	5	0	0.06	0.006	90	7.25	7585.80
50	5	−11.08	−0.09	−5.58	100	10.74	7200.00
	10	−21.89	−2.62	−10.34	100	31.10	7200.00
100	5	−11.17	−0.92	−16.06	100	113.19	7200.00
	10	−42.04	−4.33	−27.87	100	245.07	7200.00
150	10	−111.22	−1.56	−40.87	100	546.83	7200.00
	20	−9.79	−1.68	−4.76	100	2043.53	7200.00
200	10	−81.50	−1.00	−41.25	100	1698.80	7200.00
	20	−15.64	−4.23	−29.00	100	4377.60	7200.00

Table 2: Influence of the mileage limit on the accuracy of the greedy algorithm.

Mileage limit	Minimum gap (%)	Maximum gap (%)	Average gap (%)	Percentage of optimal solution (%)
0.5	0	75.25	13.35	40
1	0	22.78	3.07	70
1.5	0	3.47	0.35	90
2	0	1.08	0.13	80
5	0	0	0	100

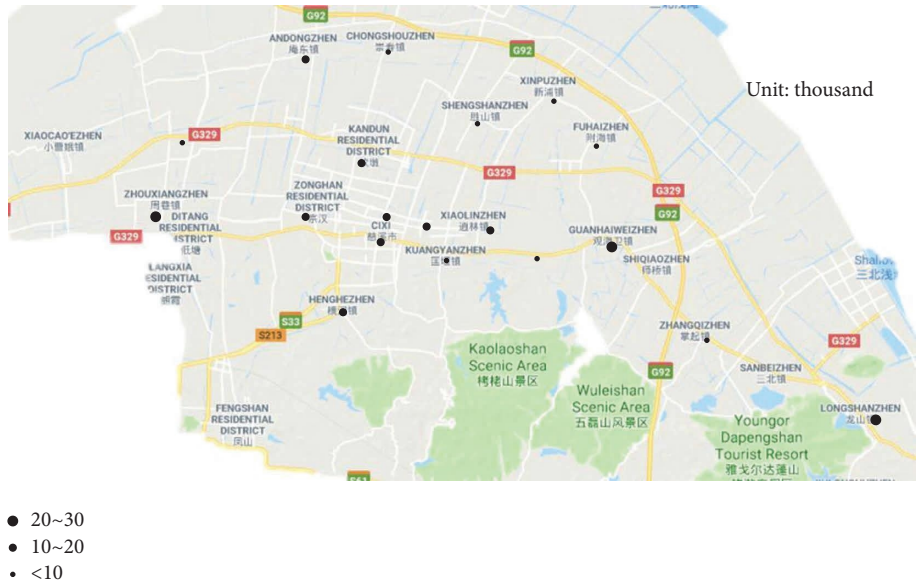

Figure 2: The map of Cixi.

Cixi City is consistent with the national average level, it is estimated that the number of EVs in Cixi City will be 0.136 million in 2030. According to the proportion of the population, the number of EVs in each region can be obtained, as shown in Table 3.

Take the forecast EV data of 2030 as the demand parameter. The coverage radius of the point demand is set to be 4 km. Figures 7–9 show the trends of covered point demands, covered path demands, and the objective values with the number of charging stations increasing under different θ.

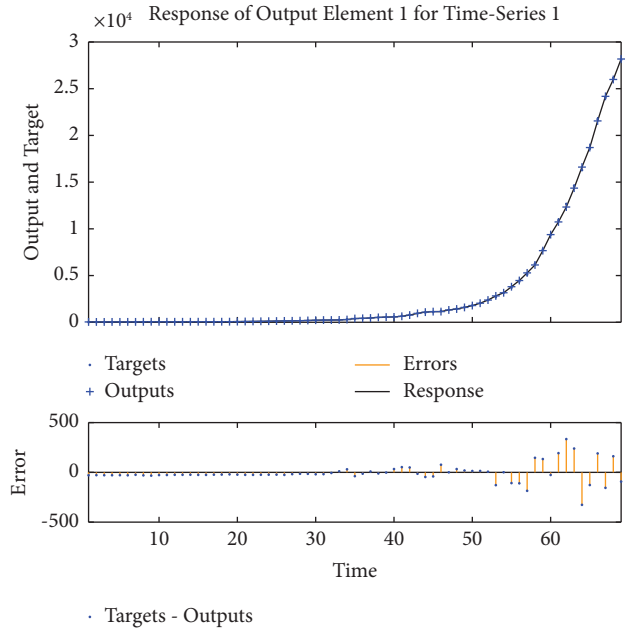

Figure 3: The error between the predicted national vehicle ownership data and the actual data.

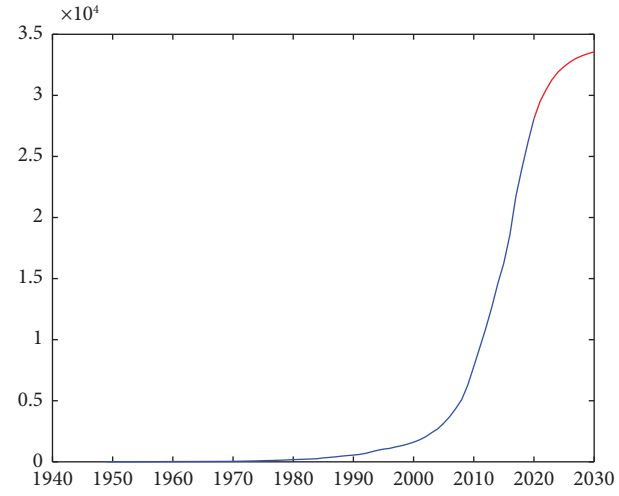

Figure 4: Forecast of vehicle ownership quantity in China.

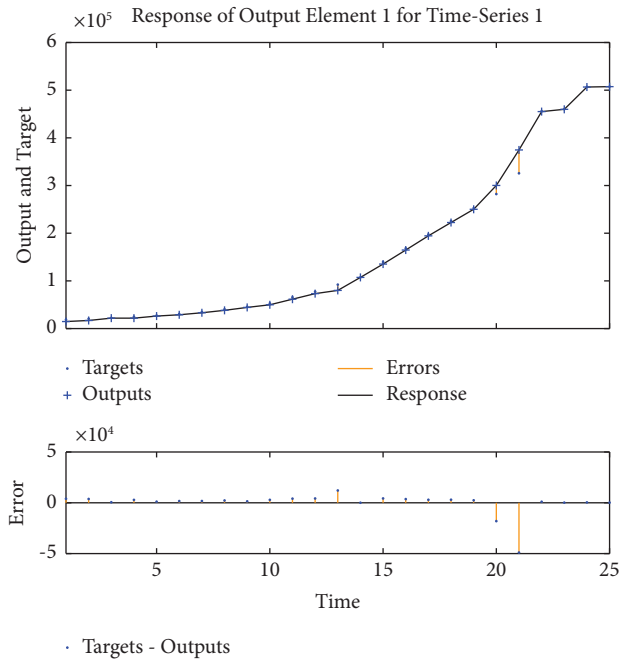

Figure 5: The error between the predicted car ownership data and the actual data in Cixi City.

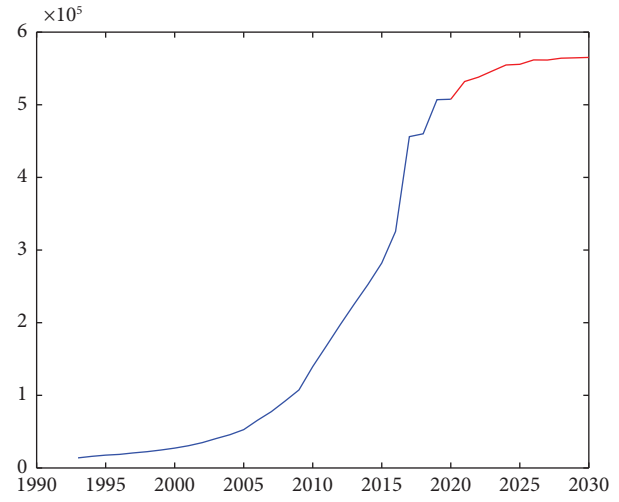

Figure 6: Forecast of vehicle ownership quantity in Cixi.

As we know, in traditional maximum coverage location problems and FILP, the objective is a convex function of the number of facilities. However, with the experiments of different θ, we find that the covered point and path demands have no convexity property with the number of charging stations in our model because of the trip mileage limit.

Figure 10 shows the impact of θ on the location decision. We considered two extreme cases, $\theta = 0$ and 1. When $\theta = 0$, the model is transformed into FILP with the trip mileage limit. When $\theta = 1$, the model is just the maximum coverage model. Compared with the only consideration being the point demand ($\theta = 1$) or flow demand ($\theta = 0$), what is the difference in charging station location when considering both demands? We set the number of charging stations at 5. Figure 10 shows the location decisions with consideration of only point demand, only flow demand, and both types of demands ($\theta = 0.1$). When only the point demand is considered, the layout of the charging station is relatively scattered. Although the demand for point 19 (Longshanzhen) is large, it is relatively remote and far away from other areas. Building the charging station at point 19 makes the station more isolated and unable to enter the effective mileage endurance network. When only the flow demand is considered, the charging stations are set up intensively, mainly in the urban area. Although it is convenient for residents to travel in the urban area, this setting is not ideal for properly expanding the service network, and it is inconvenient for rural areas. When set $\theta = 0.1$, we found that the solution balances the above contradictions. The charging

Table 3: Forecast of EV ownership quantity in each region.

Point	Region	Forecast quantity
1	Zhouxiangzhen	28216
2	Changhezhen	7979
3	Andongzhen	13533
4	Zhonghan district	13985
5	Hushan district	19279
6	Gutang district	13081
7	Baisha district	11705
8	Kandun district	11420
9	Congshouzhen	6342
10	Henghezhen	11641
11	Kuangyanzhen	5831
12	Qiaotouzhen	8567
13	Xiaolinzhen	10019
14	Shengshanzhen	6918
15	Xinpuzhen	8821
16	Fuhaizhen	5548
17	Guanhaiweizhen	24607
18	Zhangqizhen	9373
19	Longshanzhen	20136

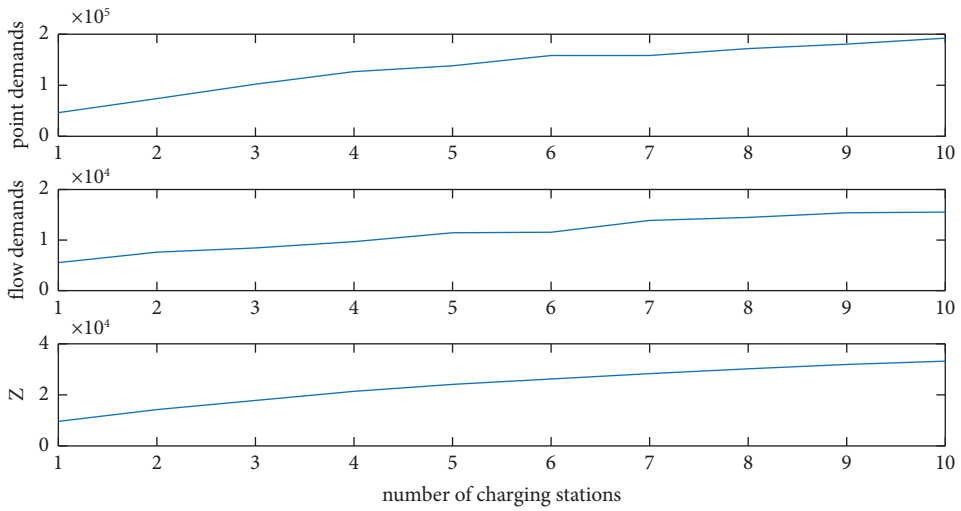

Figure 7: Covered point demands and covered path demands and the objective values with the number of charging stations increasing under $\theta = 0.1$.

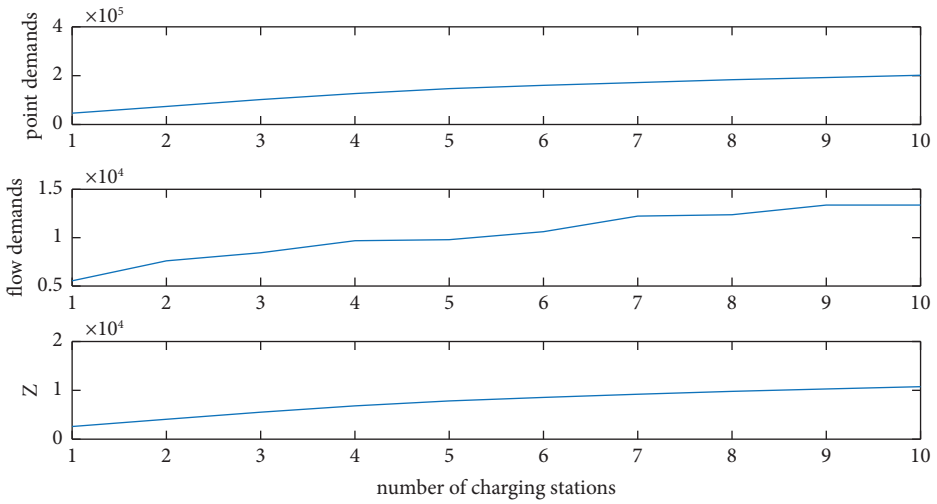

Figure 8: Covered point demands and covered path demands and the objective values with the number of charging stations increasing under $\theta = 0.5$.

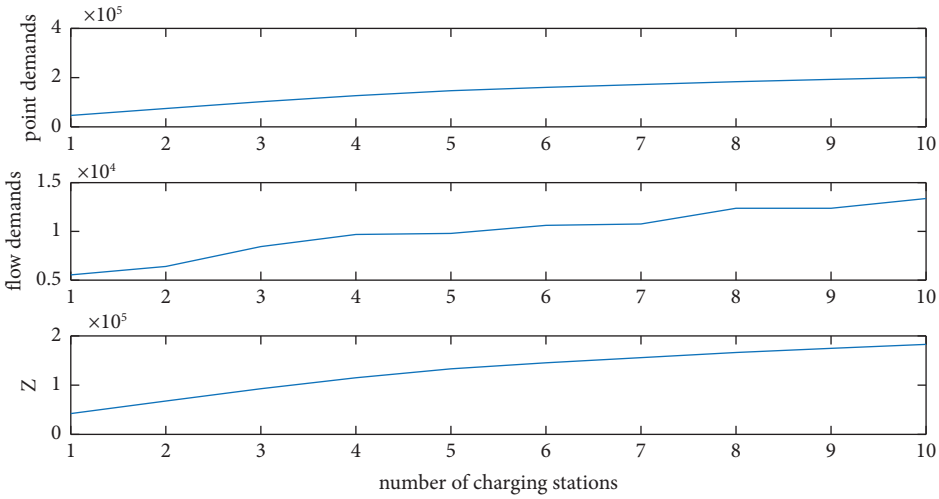

Figure 9: Covered point demands and covered path demands and the objective values with the number of charging stations increasing under $\theta = 0.9$.

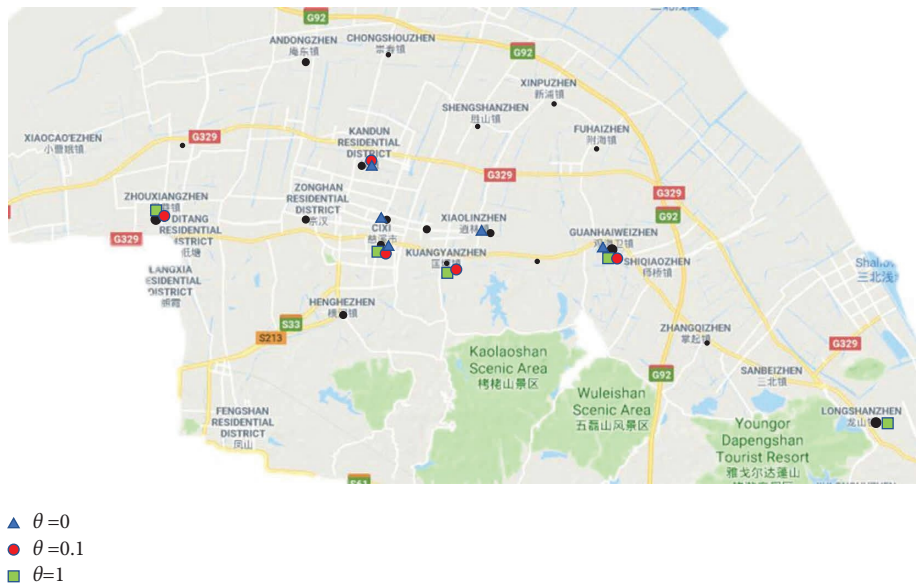

Figure 10: Influence of θ on location results.

station location is neither too centralized nor remote or isolated so as to ensure the coverage and appropriate extension of the charging network.

6. Conclusion

This paper studies the location of EV charging stations considering both point and path charging demands. Demands are closely related to the EV number. So, the location of the charging station largely depends on the data of EV numbers. As the fast expansion of EVs, the current number of EVs is not a solid basis for the design of charging stations because after the stations finish, the number of EVs has changed greatly. This paper proposes a prediction method for EV numbers with a neural network. Then, through SIM, we obtain the future path demand between each O-D pair. As range anxiety is one of the main concerns for consumers buying EVs, the trip mileage limit is considered in our model. Then we propose a greedy algorithm to solve our model. It is found that the solution accuracy of the algorithm is verified to be related to the value of the mileage limit by using random examples. The smaller the trip mileage limit, the greater the gap between the computational result and the precise solution. Finally, through a case study, we find that the location decision is shown to be more reasonable with our model than with the maximum coverage model or FILP. Our method ensures the coverage and appropriate extension of the charging network.

Data Availability

No data were used to support this study.

Conflicts of Interest

The authors declare that they have no conflicts of interest.

Acknowledgments

This work was supported in part by the Humanity and Social Science Youth Foundation of Ministry of Education of China under Grant 21YJA630030.

References

[1] Miit, "Notice of the General Office of the State Council on Printing and Distributing the Development Plan of New Energy Vehicle Industry," 2021, https://www.miit.gov.cn/xwdt/szyw/art/2020/art_4390362916324365a260ed97d7558f18.html.

[2] N R D C, "How Can Charging Service Market Develop Healthily in China," http://nrdc.cn/information/information-info?id=204cook=2.2019.

[3] M. O. Metais, O. Jouini, Y. Perez, J. Berrada, and E. Suomalainen, "Too much or not enough? planning electric vehicle charging infrastructure: a review of modeling options," *Renewable and Sustainable Energy Reviews*, vol. 153, Article ID 111719, 2022.

[4] R. Church and C. R. Velle, "The maximal covering location problem," *Papers in Regional Science*, vol. 32, no. 1, pp. 101–118, 2005.

[5] P. Fekete, S. Lim, S. Martin, K. Kuhn, and N. Wright, "Improved energy supply for non-road electric vehicles by occasional charging station location modelling," *Energy*, vol. 114, no. 1, pp. 1033–1040, 2016.

[6] J. Asamer, M. Reinthaler, M. Ruthmair, M. Straub, and J. Puchinger, "Optimizing charging station locations for urban taxi providers," *Transportation Research Part A Policy and Practice*, vol. 85, pp. 233–246, 2016.

[7] D. Hu, J. Zhang, and Q. Zhang, "Optimization design of electric vehicle charging stations based on the forecasting data with service balance consideration," *Applied Soft Computing*, vol. 75, 2018.

[8] X. Gan, H. Zhang, G. Hang, Z. Qin, and H. Jin, "Fast-charging station deployment considering elastic demand," *IEEE Transactions on Transportation Electrification*, vol. 6, no. 1, pp. 158–169, 2020.

[9] O. Berman, R. C. Larson, and N. Fouska, "Optimal location of discretionary service facilities," *Transportation Science*, vol. 26, no. 3, pp. 201–211, 1992.

[10] S. H. Chung and C. Kwon, "Multi-period planning for electric car charging station locations: a case of Korean expressways," *European Journal of Operational Research*, vol. 242, no. 2, pp. 677–687, 2015.

[11] J. Jung, J. Y. Chow, R. Jayakrishnan, and J. Y. Park, "Stochastic dynamic itinerary interception refueling location problem with queue delay for electric taxi charging stations," *Transportation Research Part C: Emerging Technologies*, vol. 40, pp. 123–142, 2014.

[12] Y. Wang, J. Shi, R. Wang, Z. Liu, and L. Wang, "Siting and sizing of fast charging stations in highway network with budget constraint," *Applied Energy*, vol. 228, pp. 1255–1271, 2018.

[13] P. Jochem, E. Szimba, and M. Reuter-Oppermann, "How many fast-charging stations do we need along european highways?" *Transportation Research Part D: Transport and Environment*, vol. 73, pp. 120–129, 2019.

[14] Ö. B. Kınay, F. Gzara, and S. A. Alumur, "Full cover charging station location problem with routing," *Transportation Research Part B: Methodological*, vol. 144, no. 4, pp. 1–22, 2021.

[15] K. i. Tanaka, T. Furuta, and S. Toriumi, "Railway flow interception location model: model development and case study of tokyo metropolitan railway network," *Operations Research Perspectives*, vol. 6, Article ID 100085, 2019.

[16] Y. Lin, K. Zhang, Z.-J. M. Shen, B. Ye, and L. Miao, "Multistage large-scale charging station planning for electric buses considering transportation network and power grid," *Transportation Research Part C: Emerging Technologies*, vol. 107, pp. 423–443, 2019.

[17] A. S. Fotheringham and M. E. O'Kelly, *Spatial Interaction Models: Formulations and Applications*, Kluwer Academic Publishers, Amsterdam, The Netherlands, 1989.

[18] J. Yang, F. Guo, and M. Zhang, "Optimal planning of swapping/charging station network with customer satisfaction," *Transportation Research Part E: Logistics and Transportation Review*, vol. 103, pp. 174–197, 2017.

[19] M. Hosseini, A. Rahmani, and F. Hooshmand, "A robust model for recharging station location problem," *Operational Research*, vol. 22.

[20] N E A, *Fostering New Kinetic Energy from the Perspective of New Energy Vehicles*, Beijing, ChinaNational Energy Administration.

[21] R. Xia, Y. Chen, and B. Ren, "Improved Anti-occlusion Object Tracking Algorithm Using Unscented Rauch-Tung-Striebel Smoother and Kernel Correlation Filter," *Journal of King Saud University - Computer and Information Sciences*, vol. 34, 2022.

[22] Y. Chen, H. Zhang, L. Liu et al., "Research on image inpainting algorithm of improved total variation minimization method," *Journal of Ambient Intelligence and Humanized Computing*, 2021.

[23] P. Li and Y. Chen, "Research into an image inpainting algorithm via multilevel attention progression mechanism," *Mathematical Problems in Engineering*, vol. 2022, Article ID 8508702, 12 pages, 2022.

[24] Y. Chen, L. Liu, V. Phonevilay et al., "Image super-resolution reconstruction based on feature map attention mechanism," *Applied Intelligence*, vol. 51, no. 7, pp. 4367–4380, JUL 2021.

[25] M. J. Hodgson, "A flow-capturing location-allocation model," *Geographical Analysis*, vol. 22, no. 3, pp. 270–279, 2010.

[26] W. Tu, K. Mai, Y. Zhang et al., "Real-time route recommendations for e-taxies leveraging gps trajectories," *IEEE Transactions on Industrial Informatics*, vol. 17, no. 5, pp. 3133–3142, 2021.

[27] V. Demianiuk, S. Gorinsky, S. I. Nikolenko, and K. Kogan, "Robust distributed monitoring of traffic flows," *IEEE/ACM Transactions on Networking*, vol. 29, no. 1, pp. 275–288, 2021.

[28] L. Ruiz, M. Cuéllar, M. Calvo-Flores, and M. Jiménez, "An application of non-linear autoregressive neural networks to predict energy consumption in public buildings," *Energies*, vol. 9, no. 9, p. 684, 2016.

[29] M. Ibrahim, S. Jemei, G. Wimmer, and D. Hissel, "Nonlinear autoregressive neural network in an energy management

strategy for battery/ultra-capacitor hybrid electrical vehicles," *Electric Power Systems Research*, vol. 136, pp. 262–269, 2016.

[30] L. Ruiz, R. Rueda, M. Cuéllar, M. Pegalajar, and Pegalajar, "Energy consumption forecasting based on elman neural networks with evolutive optimization," *Expert Systems with Applications*, vol. 92, pp. 380–389, 2018.

[31] H. Luo and F. Li, "A method for eletric vehicle ownership forecast considering different economic factors," *TELKOMNIKA Indonesian Journal of Electrical Engineering*, vol. 11, no. 4, 2013.

[32] M. Kuby and S. Lim, "The flow-refueling location problem for alternative-fuel vehicles," *Socio-Economic Planning Sciences*, vol. 39, no. 2, pp. 125–145, 2005.

Hindawi
Complexity
Volume 2022, Article ID 1862844, 9 pages
https://doi.org/10.1155/2022/1862844

Research Article

Optimal Calculation Method of Mean Equivalent Diameter of Floc Particles Based on MCC

Jun Liu[1], **Siqi Peng**[1] **and Nan Zhou**[2]

[1]*School of Automation, Chengdu University of Information Technology, Chengdu 610225, China*
[2]*School of Electronic Information and Electrical Engineering, Chengdu University, Chengdu 610106, China*

Correspondence should be addressed to Jun Liu; liujun@cuit.edu.cn and Nan Zhou; nzhouuestc@126.com

Received 30 May 2022; Accepted 22 August 2022; Published 8 October 2022

Academic Editor: Jing Na

In the process of water treatment, coagulation is an important process to remove minerals and organic particles from raw water, which has typical time delay and nonlinearity. The effect of coagulation directly affects the turbidity of the effluent. According to the good correlation between the mean equivalent diameter of floc particles and the turbidity of effluent water, the image processing method is used to preprocess the floc image, the parameters of floc particles are quantitatively analyzed, and the mean equivalent diameter of floc particles is obtained, which is used as one of the bases for the control of coagulant dosage. However, no matter whether the coagulation process in actual situations interferes with the outside world or not, the equivalent diameters of floc particles after coagulation may have abnormal and invalid values, which may lead to a problem that there is a large difference between the mean equivalent diameter of floc particles calculated by a least square method and the mean valid equivalent diameter of floc particles. In response to this problem, this article proposes an optimal calculation method of the mean equivalent diameter of floc particles based on the maximum correntropy criterion (MCC) to reduce the negative impact of the abnormal and invalid equivalent diameters of floc particles on the mean equivalent diameter and provide an important reference data for the precise dosing control of coagulants. Finally, the feasibility of the theoretical results is verified by several numerical experiments.

1. Introduction

The traditional water treatment process mainly includes steps such as coagulation, sedimentation, filtration, and disinfection. Coagulation is an important process to remove minerals and organic particles in raw water, and its effect directly affects the turbidity of the effluent. When the coagulant is added to the raw water for a period of intense mixing, the coagulant is evenly and rapidly distributed in the water so that these colloidal particles in the water lose their stability. The interaction force between the destabilized colloidal particles will change from repulsion to attraction, so they collide continuously and slowly aggregate and finally form floc particles with certain strength, size, and density. This process is called coagulation, which has typical time-delay and nonlinear characteristics [1–3]. With the development of computer technology, the method of using image processing technology to detect the shape of floc particles and extract the characteristic parameters of floc particles has gradually become a current research focus [4] to control the coagulant dosage. The camera can capture a large number of floc images in the coagulation tank. After image preprocessing and feature extraction of the floc images, the equivalent diameters of the floc particles can be calculated by formula. The weighted average calculation of the equivalent diameters of floc particles can obtain the mean equivalent diameter of floc particles, which can be used as one of the important parameters to characterize the overall situation of coagulation. When the coagulant dosage is within an appropriate range, the floc particles slowly aggregate and become denser, which leads to fast sedimentation of floc particles, clear water, and low turbidity. At this time, the mean equivalent diameter of the floc particles is also within a reasonable range. The mean equivalent diameter of floc particles is adjusted by controlling the dosage of the coagulant so that the mean equivalent diameter of floc particles

keeps approaching the set value of the mean equivalent diameter of floc particles and realizes the accurate control of the coagulant dosage and effluent turbidity [5]. Since there is a good correlation between the mean equivalent diameter of floc particles and the turbidity of effluent after flocculation and sedimentation, taking the mean equivalent diameter of floc particles as one of the control parameters for automatically controlling the dosage of coagulant can achieve better coagulation and sedimentation effect and obtain the expected effluent turbidity [6, 7].

Due to the important role of equivalent diameters of floc particles in modern water treatment automation control technology, scholars at home and abroad have carried out a lot of research on the extraction and application of the equivalent diameters of floc particles. To address the problem of hysteresis of obtaining water quality indicators in the water treatment process, Dai et al. [8] used micro-eddy current flocculation technology to detect floc particles. They combined the relationship between the equivalent diameter and the fractal dimension to determine the coagulant dosage and alleviate the time-delay problems in water treatment by analyzing and determining the coagulant dosage on the coagulation effect and the equivalent diameters of floc particles. Asensi et al. [9] developed a fully automatic activated sludge floc identification and morphological characterization toolbox based on digital image analysis and statistical processing. The toolbox could determine characteristic parameters such as the equivalent diameters of floc particles, which was mainly used to help study the characteristics of activated sludge flocs in urban sewage treatment plants. Khan et al. [10] used a microscope to collect floc images, used a state-of-the-art image segmentation algorithm to segment floc images with different equivalent diameters in different fluctuation ranges, and extracted morphological characteristic parameters for sludge volume index (SVI) and mixed liquor suspended solids (MLSS) modeling to explore the feasibility of applying the algorithm model to various plants in different regions. Chen et al. [11] used image acquisition system and data processing system to collect and process floc images in real time, took the mean equivalent diameter of floc particles calculated by the least square method as the target for controlling the coagulant dosage, and then automatically corrected the set system control parameters through flow and turbidity feedback so as to save the coagulant consumption and ensure the quality of the effluent from the sedimentation tank. Gao [12] used image processing technology to detect floc images, obtained various floc parameters that fluctuated within the correct range, and analyzed the effect of different flocculation time and coagulant dosage on the equivalent diameters of floc particles. It can provide a data reference for solving the problems of time delay and accuracy of dosing amount in the process of coagulation and dosing in water plants. Chen et al. [13] applied digital image processing technology to water treatment process control, improved the original water treatment experimental equipment, and used image processing algorithms to complete the extraction and analysis of the feature parameters of floc images in the coagulation process. The noncontact detection of floc properties in the flocculant addition control system provided an effective solution for water plants to improve the automation level of water treatment. Wang [14] used machine vision technology to explore the morphological change law of floc aggregation in the coagulation process and corresponded the characteristic parameters of floc particles such as porosity and equivalent diameters of floc particles with the factors that actually affected the flocculation process. Simulations were carried out to study the factors affecting the flocculation process and results, and the mean equivalent diameter of floc particles was determined as one of the key factors to regulate and control the flocculation process.

Although the above studies were only scattered and preliminary discussions on the application of the equivalent diameters of floc particles in the automatic process of water treatment, they have already demonstrated the importance of the equivalent diameter of floc particles in the automatic control technology of coagulant dosage. Researchers at home and abroad not only extracted the internal relationship between geometric parameters such as the equivalent diameters of floc particles and the coagulant dosage but also explored the internal relationship between other parameters of floc particles and the coagulant dosage, which alleviated the lag of water quality indicators in water treatment to a certain extent. However, the problem of accurate calculation of relevant parameters such as the mean equivalent diameter of floc particles still needs to be solved urgently in the application of precise control of coagulant dose. In the actual water treatment process of the water plant, the effect of coagulation is greatly affected by the actual environment. The influence of microorganisms, abnormal coagulant dosage, equipment leakage, and air temperature will lead to abnormal settlement in the floc particles after coagulation [15, 16]. For example, when the weather is hot, the microbes in the sludge will decompose and produce gas, which will cause trace bubbles in the sludge. The gas leakage in the equipment will cause the gas content in the water to be too high, and the low temperature will affect the reaction speed of the coagulant. These objective factors will affect the effect of the aggregation and sedimentation of floc particles so that the captured floc images can not reflect the actual situation of the sedimentation tank, and the equivalent diameters of floc particles calculated based on these images will have a small number of abnormal and invalid values. In addition, no matter how the coagulation effect is, there may also be a small number of abnormal and invalid values in the calculated equivalent diameters of floc particles without interference from the objective environment. The abnormal and invalid values will lead to a large deviation between the mean equivalent diameter obtained by the least square method and the mean valid equivalent diameter of floc particles so that the current coagulation effect cannot be accurately evaluated. Therefore, a new data processing optimization method of the mean equivalent diameter of floc particles is examined, which is of great significance to eliminate the negative effect of the abnormal and invalid equivalent diameters of a small number of floc particles on the mean equivalent diameter of floc particles.

In view of the abnormal and invalid values of the equivalent diameters of floc particles during the coagulation process, maximum correntropy criterion (MCC) [17–19] will be introduced in this article, and an optimal method will be proposed to calculate the mean equivalent diameter of floc particles based on MCC. This method optimizes the process of solving the mean equivalent diameter of floc particles, reduces the calculation error caused by abnormal and invalid equivalent diameters, and achieves the purpose of accurately calculating the mean equivalent diameter of floc particles, which provides an important reference data for the precise dosing control of subsequent coagulants.

2. Preliminaries

The equivalent diameter means that when a particle has the same or similar physical properties to a spherical particle, we can replace the diameter of the particle with the diameter of the spherical particle. In water treatment, the sedimentation characteristics of floc particles are complicated. The floc particles are in a discrete state during the sedimentation process; their mass, size, and characteristics do not change; and the sedimentation velocity of the floc particles is not disturbed. The mathematical expression to characterize the particle settling motion often adopts the Stokes formula [11, 20], whose specific form is as follows:

$$v = \frac{(\rho - \rho_0)g}{18\mu} d_s^2, \tag{1}$$

where v is the settling velocity of the floc particle, ρ is the floc density, ρ_0 refers to the density of water, g is the acceleration of gravity, μ is the viscosity coefficient of water, and d_s is the diameter of the floc particle.

Further studies show that as the diameter of the floc particle changes, the density of the floc particle changes according to the following formula:

$$\rho - \rho_0 = d_s^{-k_p}, \tag{2}$$

where k_p is a coefficient, whose value is generally $1.2 \sim 1.5$, depending on the coagulant filling rate and the quality of raw water. Combining the above formulas (1) and (2), it can be concluded that the relationship between the diameter and the sedimentation velocity of the floc particle can be obtained as

$$v = \frac{g d_s^{(2-k_p)}}{18\mu}. \tag{3}$$

The above analysis is based on the assumption that the floc particle is spherical, but we know that the actual floc particle is in an irregular state, and its sedimentation speed should indeed be slower than that of the spherical floc particle of the same volume. The size and shape of floc particles can be well reflected by the floc images collected by industrial cameras. Each floc region in the image reflects the state of floc particle movement during the coagulation process. The image of a floc particle in the 2D plane can be characterized by four parameters [11, 21]: the size-related area of the floc particle, the shape-related perimeter of the floc particle, the vacant area in the middle of the floc particle related to the degree of looseness, and the length to width ratio of the floc particle. These features represent the characteristics of the floc particle. The above four parameters can be converted into ϕ_i using the following formula:

$$\phi_i = 2\sqrt{\frac{s_i}{\pi}}\left[1 - \left(1 - \frac{2\sqrt{s_i\pi}}{l_i}\right)k_1\right] \times \left[1 - \left(1 - \frac{1}{m_i}\right)k_2\right] \times \left(1 - \frac{s_{i0}}{s_i}k_3\right), \tag{4}$$

where ϕ_i is the equivalent diameter of the ith floc particle; s_i is the area of the ith floc particle; l_i is the perimeter of the ith floc particle; s_{i0} is the hollow area of the ith floc particle; m_i is the length to width ratio of the ith floc particle; and k_1, k_2, and k_3 are the coefficients of the perimeter l_i, the length to width ratio m_i, and the hollow area s_{i0}, respectively. k_1, k_2, and k_3 are all decimals ranging from 0 to 1, which can be selected according to actual conditions.

By the above analysis and calculation, the equivalent diameter of a floc particle can be extracted from the image of the floc particle. The equivalent diameter of the floc particle is an important characteristic parameter of the floc particle and has a good correlation with the turbidity of water. It not only reflects the quality of the coagulation effect but also relates to whether the subsequent effluent turbidity meets the water supply requirements. Taking it as one of the target values to control the coagulant dosage can achieve a good control effect. It can be seen from the above formula (3) that the larger the equivalent diameter of the floc particle, the faster the settling velocity of the floc particle, that is, the better the integrity of floc particles, the more sufficient the sedimentation and the smaller the turbidity of the sedimented water. The change of the equivalent diameters of floc particles can not only reflect the quality of the coagulation effect but also relate to whether the utilization of the coagulant can achieve the maximum benefit.

However, the parameter ϕ_i still cannot fully characterize the overall effect of coagulation. In practical application, the equivalent diameter of each floc particle is calculated according to formula (4), and then the mean equivalent diameter Φ, which is regarded as a key parameter for the control of coagulant dosage, is calculated in real time according to the equivalent diameters of floc particles obtained within a certain time. The mean equivalent diameter Φ is expressed as follows:

$$\Phi = \frac{\sum_{i=1}^{N}(n_i\phi_i)}{\sum_{i=1}^{N}(n_i)}, \tag{5}$$

where N represents the number of floc particles with different equivalent diameters, and n_i represents the number of floc particles whose equivalent diameter is ϕ_i.

According to the above analysis, we can display the floc image collected in real time on the computer and calculate s_i, l_i, m_i, and s_{i0} of the ith floc particle in formula (4) by image preprocessing, image segmentation, and other image

processing technologies, which lead to obtain ϕ_i. Finally, we can obtain the mean equivalent diameter Φ of floc particles by substituting ϕ_i and n_i into formula (5).

3. Main Results

In the actual water treatment process of water plant, the influence of microorganisms, too much or too little coagulant dose, equipment leakage, and air temperature will lead to abnormal aggregation and settlement of floc particles. This will make the captured floc images cannot reflect the real state of the sedimentation tank, and the calculated floc equivalent diameters will have some abnormal and invalid values. In addition, no matter whether the coagulation effect is disturbed by the environment or not, the equivalent diameters of floc particles calculated from floc images will also have some abnormal and invalid values, so that the mean equivalent diameter of floc particles calculated by the traditional calculation method (the least square method) cannot accurately characterize the coagulation effect. To weaken the influence of the invalid equivalent diameters of floc particles on the mean equivalent diameter of floc particles, MCC will be introduced to optimize the calculation process of the mean equivalent diameter of floc particles so as to provide important reference data for accurately describing the actual coagulation effect. Because of its good robustness [22], MCC is widely used in many fields, such as computer vision [23], feature extraction [24, 25], and signal processing [26–28]. It is mainly used to deal with non-Gaussian noise and outliers [27, 29, 30]. MCC is based on entropy [31], which in turn derives from information theory. Correlation entropy is used to measure the similarity between two variables, which is expressed as follows:

$$V_\sigma(A,B) = E\left[k_\sigma(A-B)\right], \tag{6}$$

where $E(*)$ is the expectation of $*$, $k_\sigma(\cdot)$ represents the Gaussian kernel function, and σ represents the kernel width of $k_\sigma(\cdot)$. Usually, the joint probability distribution between variables A and B is unknown, and only a finite amount of data $A = (a_1, a_2, \ldots, a_N)$ and $B = (b_1, b_2, \ldots, b_N)$ can be available, which make the estimator of correlation entropy (6) can be represented as

$$\widehat{V}_\sigma(A,B) = \frac{1}{N}\sum_{i=1}^{N} k_\sigma(a_i - b_i), \tag{7}$$

where $k_\sigma(a_i - b_i) = e^{-(a_i-b_i)^2/2\sigma^2}$.

As we all know, the mean square error (MSE) is a measure that reflects the degree of difference between the estimator and the estimated value, and it is a global measure. Compared to the MSE, MCC is a local metric whose value mainly depends on the probability along the $A = B$ direction, and the local extent depends on the kernel size σ. The Gaussian kernel functions for various kernel widths are shown in Figure 1. As can be seen from Figure 1, the convergence rate of the function varies with the size of the kernel width. For large errors or outliers, the kernel function has better robustness. When the error between $A = B$ is large, the kernel function of $A = B$ gets a small value or even

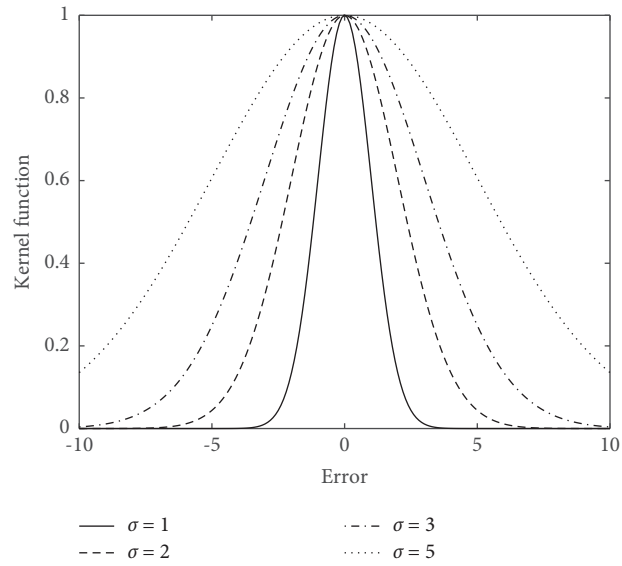

Figure 1: Gaussian kernel function with different kernel widths.

a value close to zero so that the calculation process can avoid the negative impact caused by outliers and has a good stable performance in the case of data anomalies caused by interference. Figures 2 and 3 illustrate the difference between the mean square error and the correlation entropy. In this article, an optimization model is constructed by MCC to eliminate the adverse effects of abnormal and invalid values (abnormal and invalid equivalent diameters of floc particles) on the mean equivalent diameter of floc particles.

The mean equivalent diameter of floc particles calculated by the least square method can be expressed as follows:

$$\Phi_c = \arg\min_{\Phi} \sum_{i=1}^{N} n_i(\phi_i - \Phi)^2, \tag{8}$$

which is an optimization problem whose solution of this optimization problem is

$$\Phi_c = \frac{\sum_{i=1}^{N}(n_i\phi_i)}{\sum_{i=1}^{N}(n_i)}. \tag{9}$$

According to formula (9), the mean equivalent diameter of floc particles calculated by the least square method is the mean of the sum of all equivalent diameters of floc particles, which cannot eliminate the abnormal and invalid equivalent diameter of floc particles. Considering the abnormal and invalid equivalent diameters of floc particles, we introduce maximum correntropy criterion [32] to weaken the influence of abnormal and invalid equivalent diameters of floc particles on the mean equivalent diameter of floc particles. Using MCC, the optimization problem is formulated as follows:

$$\Phi_{MCC} = \arg\max_{\Phi} \sum_{i=1}^{N} n_i \exp\left(-\frac{(\phi_i - \Phi)^2}{2\sigma^2}\right). \tag{10}$$

Assuming $f(z) = z - z\ln(-z)$, it can be obtained as follows:

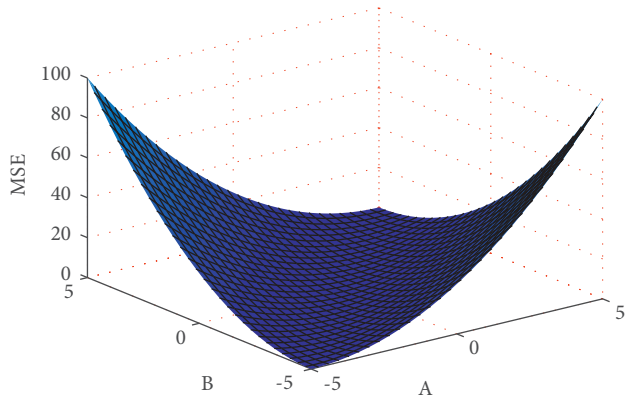

Figure 2: MSE in the joint space of variables A and B.

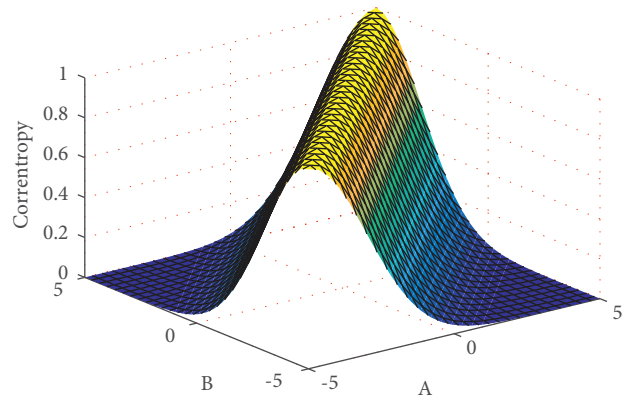

Figure 3: Correntropy in the joint space of variables A and B.

$$\exp(-x) = \sup_{z}(zx - f(z)). \tag{11}$$

By $\partial/\partial_z(zx - f(z)) = x + \ln(-z) = 0$, we can find that the maximum value of $(zx - f(z))$ can be obtained when $z = -\exp(-x)$.

The above derivation process is called the half-quadratic (HQ) strategy [33, 34].

If let

$$z = \rho_i, \tag{12}$$

and

$$x = \frac{(\phi_i - \Phi)^2}{2\sigma^2}, \tag{13}$$

then it is easy to get

$$\Phi_{MCC} = \arg\max_{\Phi} \sum_{i=1}^{N} n_i \left(\rho_i \frac{(\phi_i - \Phi)^2}{2\sigma^2} - f(\rho_i) \right), \tag{14}$$

and

$$\rho_i = -\exp\left(-\frac{(\phi_i - \Phi)^2}{2\sigma^2} \right), \tag{15}$$

where ρ_i is an auxiliary variable.

If we take the partial derivative of Φ of (14), then it is easy to obtain

$$\begin{aligned}
&\frac{\partial\left[\sum_{i=1}^{N} n_i\left(\rho_i\left((\phi_i - \Phi)^2/2\sigma^2\right) - f(\rho_i)\right)\right]}{\partial\Phi} \\
&= \frac{\partial\left[\sum_{i=1}^{N}\left(\rho_i n_i/2\sigma^2\right)(\phi_i - \Phi)^2 - \sum_{i=1}^{N} n_i f(\rho_i)\right]}{\partial\Phi} \\
&= \sum_{i=1}^{N}\left(\frac{\rho_i n_i}{2\sigma^2}\right)\frac{\partial\left[(\phi_i - \Phi)^2\right]}{\partial\Phi} \\
&= \sum_{i=1}^{N}\left(\frac{\rho_i n_i}{2\sigma^2}\right)\frac{\partial\left[\left(\phi_i^2 - 2\phi_i\Phi + \Phi^2\right)\right]}{\partial\Phi} \\
&= \sum_{i=1}^{N}\left(\frac{\rho_i n_i}{2\sigma^2}\right)(-2\phi_i + 2\Phi) \\
&= -\sum_{i=1}^{N}\frac{\rho_i n_i \phi_i}{\sigma^2} + \Phi\sum_{i=1}^{N}\frac{\rho_i n_i}{\sigma^2} = 0,
\end{aligned} \tag{16}$$

and it is easy to get

$$\begin{aligned}
\Phi_{MCC} &= \frac{\sum_{i=1}^{N}\rho_i n_i \phi_i/\sigma^2}{\sum_{i=1}^{N}\rho_i n_i/\sigma^2} \\
&= \frac{\sum_{i=1}^{N}\rho_i n_i \phi_i}{\sum_{i=1}^{N}\rho_i n_i}.
\end{aligned} \tag{17}$$

We can solve the problem (14) by alternative optimization.

Firstly, when Φ is fixed, the solution of ρ_i is derived as follows:

$$\rho_i^{(k+1)} = -\exp\left(-\frac{\left(\phi_i - \Phi^{(k)}\right)^2}{2\left(\sigma^{(k+1)}\right)^2} \right), \tag{18}$$

where $k \geq 0$ is the number of iterations.

Secondly, when ρ_i is fixed, the solution of Φ can be easily obtained as follows:

$$\Phi^{(k+1)} = \frac{1}{\sum_{i=1}^{N}\rho_i^{(k+1)} n_i}\sum_{i=1}^{N}\rho_i^{(k+1)} n_i \phi_i. \tag{19}$$

Furthermore, it is known from [23] that after each iteration σ^2 should be updated as follows:

$$\left(\sigma^{(k+1)}\right)^2 = \frac{1}{2\sum_{i=1}^{N} n_i}\sum_{i=1}^{N} n_i\left(\phi_i - \Phi^{(k)}\right)^2. \tag{20}$$

This update rule consists of the above three steps, which are repeated until the convergence condition is achieved. The procedure is summarized in Algorithm 1.

The proof is completed.

(1) **Input:** The equivalent diameter ϕ_i $(1 \le i \le N)$ of the ith floc particle, and the number n_i $(1 \le i \le N)$ of the ith floc particle whose equivalent diameter is ϕ_i.
(2) **Output:** The MCC-based samples' mean Φ_{MCC}.
(3) **Initialize:** $\Phi^{(0)} = \Phi_c$, $k = 0$.
(4) **while** Not convergent **do**
(5) Update $(\sigma^{(k+1)})^2 \leftarrow$ (20).
(6) Update $\rho_i^{(k+1)} \leftarrow$ (18).
(7) Update $\Phi^{(k+1)} \leftarrow$ (19).
(8) $k \leftarrow k + 1$.
(9) **end while**
(10) $\Phi_{MCC} = \Phi^{(k)}$ as the MCC-based samples' mean.

Algorithm 1: The MCC-based samples' mean Φ_{MCC} = MCC-Mean (ϕ_i, n_i).

4. Simulation Results

There are four sets of simulation data generated for us to verify the effectiveness of Algorithm 1, and n_i $(1 <= i <= N)$ is always equal to 1 for the convenience of simulation.

(1) The first set of simulation data is generated for us to verify the effectiveness of Algorithm 1. There are ninety points representing ninety valid equivalent diameters of floc particles randomly generated in 1D space by Gaussian distribution with mean $\Phi_v = 1.3$ mm and covariance $\sigma_v = 0.2$ and ten points representing ten abnormal and invalid equivalent diameters of floc particles by Gaussian distribution with mean $\Phi_a = 6$ mm and covariance $\sigma_a = 0.3$. Using these generated data, we can compute the conventional samples' mean Φ_c by (9), the MCC-based samples' mean Φ_{MCC} by Algorithm 1, and the valid samples' mean Φ_v by (9) with only considering the valid equivalent diameters. The positions of the three means are shown in Figure 4. It is obvious that the MCC-based samples' mean Φ_{MCC} and the valid samples' mean Φ_v are almost overlapped, whereas the conventional samples' mean Φ_c is seriously biased from the valid samples' mean Φ_v due to the existence of ten abnormal and valid equivalent diameters.

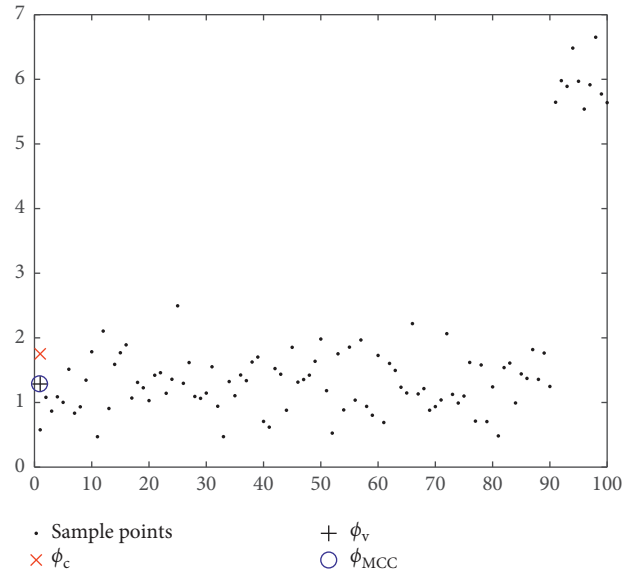

Figure 4: Toy problem with ninety inliers ranging from 0.3 mm to 2.6 mm and ten outliers ranging from 5.6 mm to 6.8 mm. The conventional samples' mean Φ_c, the valid samples' mean Φ_v, and MCC-based samples' mean Φ_{MCC}.

(2) The second set of simulation data is generated for us to verify the effectiveness of Algorithm 1. There are ten points representing ten abnormal and valid equivalent diameters of floc particles randomly generated in 1D space by Gaussian distribution with mean $\Phi_a = 1.3$ mm and covariance $\sigma_a = 0.2$ and ninety points representing ninety valid equivalent diameters of floc particles by Gaussian distribution with mean $\Phi_v = 6$ mm and covariance $\sigma_v = 0.3$. Using these generated data, we can compute the conventional samples' mean Φ_c by (9), the MCC-based samples' mean Φ_{MCC} by Algorithm 1, and the valid samples' mean Φ_v by (9) with only considering the valid equivalent diameters. The positions of the three means are shown in Figure 5. It is obvious that the MCC-based samples' mean Φ_{MCC} and the valid samples' mean Φ_v are almost overlapped, whereas the conventional samples' mean Φ_c is seriously biased from the valid samples' mean Φ_v due to the existence of ten abnormal and valid equivalent diameters.

(3) The third set of simulation data is generated for us to verify the effectiveness of Algorithm 1. Firstly, there are ninety points representing ninety valid equivalent diameters of floc particles randomly generated in 1D space by Gaussian distribution with mean $\Phi_v = 1.3$ mm and covariance $\sigma_v = 0.2$ and ten points representing ten abnormal and valid equivalent diameters of floc particles by Gaussian distribution with mean $\Phi_a = 6$ mm and covariance $\sigma_a = 0.3$. Secondly, the 100 points are randomly sorted. Finally, using these generated data, we can compute the conventional samples' mean Φ_c by (9), the MCC-based samples' mean Φ_{MCC} by Algorithm 1, and the valid samples' mean Φ_v by (9) with only considering

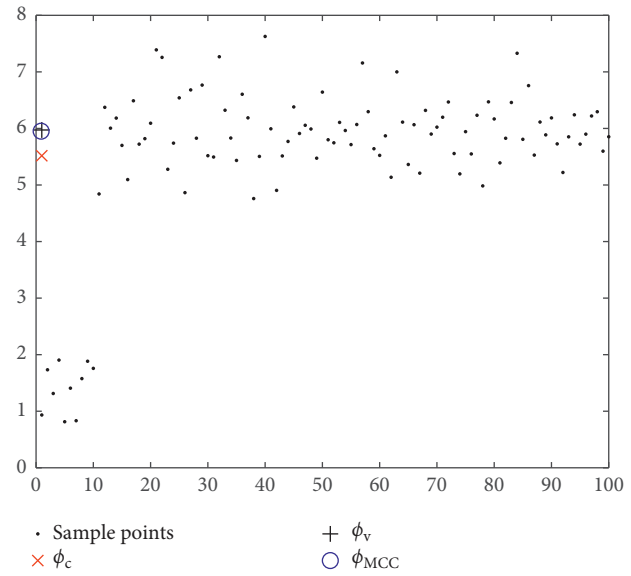

Figure 5: Toy problem with ninety inliers ranging from 4.6 mm to 7.7 mm and ten outliers ranging from 0.8 mm to 2 mm. The conventional samples' mean Φ_c, the valid samples' mean Φ_v, and MCC-based samples' mean Φ_{MCC}.

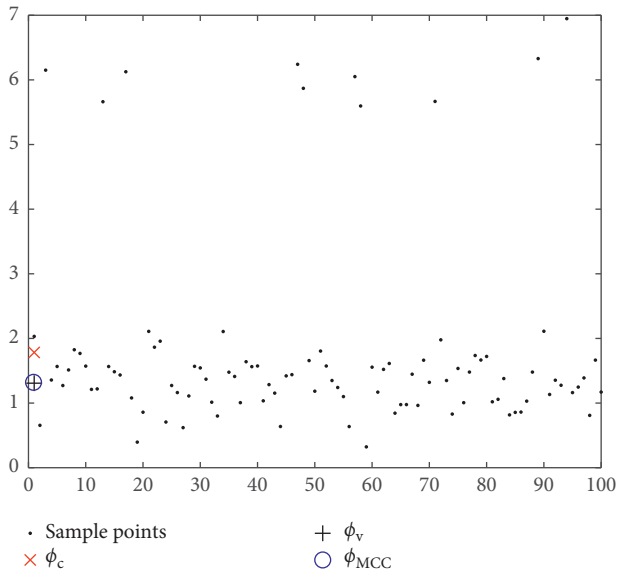

Figure 6: Toy problem with ninety inliers ranging from 0.3 mm to 2.3 mm and ten outliers ranging from 5.5 mm to 7 mm. The conventional samples' mean Φ_c, the valid samples' mean Φ_v, and MCC-based samples' mean Φ_{MCC}.

the valid equivalent diameters. The positions of the three means are shown in Figure 6. It is obvious that the MCC-based samples' mean Φ_{MCC} and the valid samples' mean Φ_v are almost overlapped, whereas the conventional samples' mean Φ_c is seriously biased from the valid samples' mean Φ_v due to the existence of ten abnormal and valid equivalent diameters.

(4) The last set of simulation data is generated for us to verify the effectiveness of Algorithm 1. Firstly, there are ten points representing ten abnormal and valid equivalent diameters of floc particles randomly generated in 1D space by Gaussian distribution with mean $\Phi_a = 1.3$ mm and covariance $\sigma_a = 0.2$ and ninety points representing ninety valid equivalent diameters of floc particles by Gaussian distribution with mean $\Phi_v = 6$ mm and covariance $\sigma_v = 0.3$. Secondly, the 100 points are randomly sorted. Finally, using these generated data, we can compute the conventional samples' mean Φ_c by (9), the MCC-based samples' mean Φ_{MCC} by Algorithm 1, and the valid samples' mean Φ_v by (9) with only considering the valid equivalent diameters. The positions of the three means are shown in Figure 7. It is obvious that the MCC-based samples' mean Φ_{MCC} and the valid samples' mean Φ_v are almost overlapped, whereas the conventional samples' mean Φ_c is seriously biased from the valid samples' mean Φ_v due to the existence of ten abnormal and valid equivalent diameters.

If the mean equivalent diameter of floc particles corresponding to the turbidity of the effluent within the normal range is about 1 mm-2 mm, then it can be seen from Figures 4 and 6 that the corresponding coagulation effect is

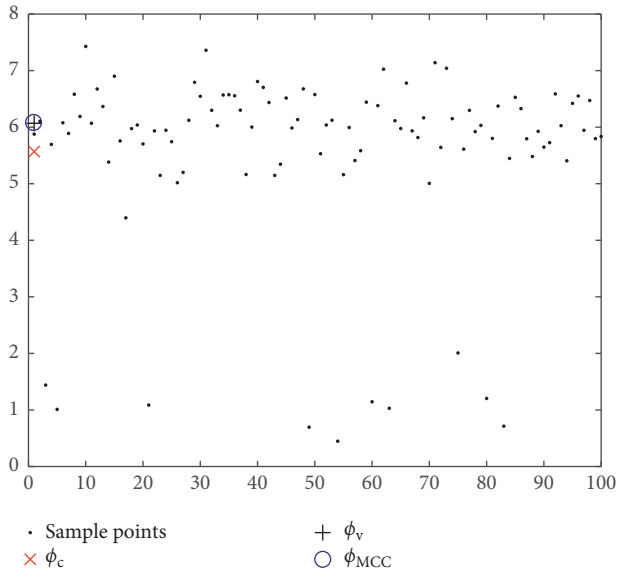

Figure 7: Toy problem with ninety inliers ranging from 4.3 mm to 7.5 mm and ten outliers ranging from 0.3 mm to 2.2 mm. The conventional samples' mean Φ_c, the valid samples' mean Φ_v, and MCC-based samples' mean Φ_{MCC}.

good, which indicates that the turbidity of the effluent is within the normal range, and then it can be seen from Figures 5 and 7 that the corresponding coagulation effect is not good, which indicates that the turbidity of the effluent is outside the normal range.

Several sets of mean equivalent diameters of floc particles calculated by the conventional method and the MCC-based optimization method are presented in Table 1, and the corresponding error rates are given. As can be seen from

Table 1: Calculation of the mean equivalent diameters of floc particles.

The number of images	The number of floc particles	Φ_v (mm)	Φ_c (mm)	Error rate 1 (%)	Φ_{MCC} (mm)	Error rate 2 (%)
1	30	0.8700	0.9317	7.09	0.8939	2.75
2	36	0.8400	0.8858	5.45	0.8492	1.10
3	29	1.0900	1.1540	5.87	1.1022	1.12
4	45	1.2100	1.2442	2.83	1.2205	0.87
5	52	0.7900	0.8289	4.92	0.7989	1.13

Table 1, the error rates of the mean equivalent diameters of the floc particles are reduced by means of the MCC algorithm.

5. Conclusion

According to the characteristics that the mean equivalent diameter of floc particles is closely related to the turbidity of the effluent, we use image processing technology to process and extract the characteristics of the collected floc images to obtain the relevant important parameters such as the mean equivalent diameter of floc particles and feed them back to the control system of coagulant dose. This can not only effectively improve the utilization rate of coagulants but also liberate human resources and reduce production costs. The mean equivalent diameter of floc particles is an important parameter used to describe the characteristics of floc precipitation after coagulation in the water treatment process. In the actual operation of the water plant, no matter whether the coagulation effect is good or bad, there will be abnormal and invalid values in the equivalent diameters of floc particles. To avoid the deviation of the mean equivalent diameter and the mean valid equivalent diameter caused by the abnormal and invalid equivalent diameters of floc particles, the MCC algorithm is introduced in this article. The MCC algorithm optimizes the solution of the mean equivalent diameter of floc particles to eliminate or reduce the influence of the abnormal and invalid values of equivalent diameters on the overall sedimentation in the actual situation and provides a reference method for water treatment fields such as tap water treatment and sewage treatment. Finally, the validity of the theoretical results is verified by numerical experiments.

Data Availability

The data used to support the findings of this study are available from the corresponding author upon request.

Conflicts of Interest

The authors declare that they have no conflicts of interest.

Acknowledgments

This work was supported in part by the Natural Science Foundation of Sichuan of China under Grant 2022NSFSC0462, the Major Industrial Projects of Sichuan Science and Technology Department of China under Grant 21ZDYF2965, and the National Natural Science Foundation of China under Grant 61802036.

References

[1] Y. S. Vadasarukkai and G. A. Gagnon, "Characterization, fate and transport of floc aggregates in full-scale flocculation tanks," *Environmental Sciences: Water Research & Technology*, vol. 2, no. 1, pp. 223–232, 2016.

[2] E. N. Banadda, I. Y. Smets, R. Jenne, and J. F. Van Impe, "Predicting the onset of filamentous bulking in biological wastewater treatment systems by exploiting image analysis information," *Bioprocess and Biosystems Engineering*, vol. 27, no. 5, pp. 339–348, 2005.

[3] R. K. Chakraborti and J. F. Atkinson, "Settling velocity analysis of natural suspended particles using fractal approach," *Journal of Environmental Engineering*, vol. 146, no. 12, Article ID 04020138, 2020.

[4] M. Lapointe and B. Barbeau, "Characterization of ballasted flocs in water treatment using microscopy," *Water Research*, vol. 90, pp. 119–127, 2016.

[5] Y. G. Perez, S. G. F. Leite, and M. A. Z. Coelho, "Activated sludge morphology characterization through an image analysis procedure," *Brazilian Journal of Chemical Engineering*, vol. 23, no. 3, pp. 319–330, 2006.

[6] K. Strom and A. Keyvani, "An explicit full-range settling velocity equation for mud flocs," *Journal of Sedimentary Research*, vol. 81, no. 12, pp. 921–934, 2011.

[7] A. Vahedi and B. Gorczyca, "Predicting the settling velocity of flocs formed in water treatment using multiple fractal dimensions," *Water Research*, vol. 46, no. 13, pp. 4188–4194, 2012.

[8] H. L. Dai, Z. M. Qiu, F. P. Hu, C. Gao, Y. F. Chen, and Z. Zhou, "Floc performance parameters during water treatment in a micro-vortex flocculation process determined by machine vision," *Environmental Technology*, vol. 40, no. 23, pp. 3062–3071, 2019.

[9] E. Asensi, D. Zambrano, E. Alemany, and D. Aguado, "Effect of the addition of precipitated ferric chloride on the morphology and settling characteristics of activated sludge flocs," *Separation and Purification Technology*, vol. 227, Article ID 115711, 2019.

[10] M. B. Khan, H. Nisar, and C. A. Ng, "Generalized modeling of the sludge volume index and suspended solids to monitor activated sludge bioflocculation using image analysis," *Environment Protection Engineering*, vol. 46, no. 3, pp. 17–37, 2020.

[11] F. Chen, H. Y. Ruan, and Q. Yang, "Technology of automatic control for coagulant dosing based on equivalent diameter of flocs," *Industrial Water and Wastewater*, vol. 36, no. 6, pp. 50–52, 2005.

[12] C. Gao, *The Study of Floc Measurement and Performance in the Flocculation Process of Water Treatment Based on Machine Vision*, East China Jiaotong University, China, 2016.

[13] K. G. Chen, X. J. Hang, and Y. Zhang, "Coagulation control method based on image processing," *Water Technology*, vol. 6, no. 1, pp. 40–42, 2012.
[14] Y. Wang, "Study on Treatment of Microplastics in Drinking Water by Coagulation-Sedimentation Process," Harbin Institute of Technology, China, 2020.
[15] Y. Rang, R. P. Liu, D. W. Zhang, and H. Xu, "Investigation of the coagulation process in the NingDong water treatment plant during abnormal water quality in spring," *Water Technology*, vol. 11, no. 5, pp. 11–16, 2017.
[16] Y. Q. Xu, H. J. Zhao, and Y. G. Kong, "Analysis and Solution of Abnormal Flocs in Precipitation Process," *Journal of Shijiazhuang Institute of Railway Technology*, vol. 11, no. 4, pp. 60–63, 2012.
[17] X. Q. Chen, Y. H. Hu, and Y. R. Huang, "Image thresholding segmentation based on two-dimensional mcc," *Journal of Infrared and Millimeter Waves*, vol. 24, no. 5, pp. 397–400, 2005.
[18] B. B. Wang and T. Hu, "Online gradient descent for kernel-based maximum correntropy criterion," *Entropy*, vol. 21, no. 7, p. 644, 2019.
[19] J. C. Yen, F. J. Chang, and S. Chang, "A new criterion for automatic multilevel thresholding," *IEEE Transactions on Image Processing*, vol. 4, no. 3, pp. 370–378, 1995.
[20] N. H. G. Rahmani, T. Dabros, and J. H. Masliyah, "Fractal structure of asphaltene aggregates," *Journal of Colloid and Interface Science*, vol. 285, no. 2, pp. 599–608, 2005.
[21] R. Y. Song, "Selection of automatic process mode for coagulant filling," *City and Town Water Supply*, no. 3, pp. 9–13, 1996.
[22] J. C. Principe, *Information Theoretic Learning: Renyi's Entropy and Kernel Perspectives*, Springer, New York, NY, USA, 2010.
[23] R. He, W. S. Zheng, and B. G. Hu, "Maximum correntropy criterion for robust face recognition," *IEEE Transactions on Pattern Analysis and Machine Intelligence*, vol. 33, no. 8, pp. 1561–1576, 2011.
[24] J. J. Y. Wang, X. L. Wang, and X. Gao, "Non-negative matrix factorization by maximizing correntropy for cancer clustering," *BMC Bioinformatics*, vol. 14, Article ID 107, 2013.
[25] L. Du, X. Li, and Y. D. Shen, "Robust nonnegative matrix factorization via half-quadratic minimization," in *Proceedings of the IEEE 12th International Conference on Data Mining*, Brussels, Belgium, December 2012.
[26] B. Chen, J. Wang, H. Zhao, N. Zheng, and J. C. Principe, "Convergence of a fixed-point algorithm under maximum correntropy criterion," *IEEE Signal Processing Letters*, vol. 22, no. 10, pp. 1723–1727, 2015.
[27] B. Chen, L. Xing, H. Zhao, N. Zheng, and J. C. Principe, "Generalized correntropy for robust adaptive filtering," *IEEE Transactions on Signal Processing*, vol. 64, no. 13, pp. 3376–3387, 2016.
[28] B. D. Chen, L. Xing, J. L. Liang, N. N. Zheng, and J. C. Principe, "Steady-state mean-square error analysis for adaptive filtering under the maximum correntropy criterion," *IEEE Signal Processing Letters*, vol. 21, no. 7, pp. 880–884, 2014.
[29] N. Zhou, B. D. Chen, Y. H. Du, T. Jiang, J. Liu, and Y. Y. Xu, "Maximum correntropy criterion-based robust semi-supervised concept factorization for image representation," *IEEE Transactions on Neural Networks and Learning Systems*, vol. 31, no. 10, pp. 3877–3891, 2020.
[30] W. Liu, P. P. Pokharel, and J. C. Principe, "Correntropy: properties and applications in non-Gaussian signal processing," *IEEE Transactions on Signal Processing*, vol. 55, no. 11, pp. 5286–5298, 2007.
[31] A. Renyi, *On Measures of Entropy and Information*, University of California Press, Berkeley, California, 1961.
[32] N. Zhou, H. Cheng, J. Qin, Y. H. Du, and B. D. Chen, "Robust high-order manifold constrained sparse principal component analysis for image representation," *IEEE Transactions on Circuits and Systems for Video Technology*, vol. 29, no. 7, pp. 1946–1961, 2019.
[33] J. C. Jiang, H. Tao, R. D. Fan, W. Z. Zhuge, and C. P. Hou, "Incomplete multi-view learning via half-quadratic minimization," *Neurocomputing*, vol. 443, pp. 106–116, 2021.
[34] P. P. Zhao and Y. M. Huang, "Conjugate gradient method preconditioned with modified block ssor iteration for multiplicative half-quadratic image restoration," *Calcolo*, vol. 57, no. 3, Article ID 31, 2020.

Hindawi
Complexity
Volume 2022, Article ID 7040601, 12 pages
https://doi.org/10.1155/2022/7040601

Research Article

A Hybrid Deep Learning-Based Network for Photovoltaic Power Forecasting

Altaf Hussain,[1] **Zulfiqar Ahmad Khan**,[1] **Tanveer Hussain**,[1] **Fath U Min Ullah**,[1] **Seungmin Rho**,[2] **and Sung Wook Baik**[1]

[1]*Sejong University, Seoul 143-747, Republic of Korea*
[2]*Department of Industrial Security, Chung-Ang University, Seoul 06974, Republic of Korea*

Correspondence should be addressed to Sung Wook Baik; sbaik@sejong.ac.kr

Received 13 May 2022; Revised 7 July 2022; Accepted 15 July 2022; Published 5 October 2022

Academic Editor: Chun Wei

For efficient energy distribution, microgrids (MG) provide significant assistance to main grids and act as a bridge between the power generation and consumption. Renewable energy generation resources, particularly photovoltaics (PVs), are considered as a clean source of energy but are highly complex, volatile, and intermittent in nature making their forecasting challenging. Thus, a reliable, optimized, and a robust forecasting method deployed at MG objectifies these challenges by providing accurate renewable energy production forecasting and establishing a precise power generation and consumption matching at MG. Furthermore, it ensures effective planning, operation, and acquisition from the main grid in the case of superior or inferior amounts of energy, respectively. Therefore, in this work, we develop an end-to-end hybrid network for automatic PV power forecasting, comprising three basic steps. Firstly, data preprocessing is performed to normalize, remove the outliers, and deal with the missing values prominently. Next, the temporal features are extracted using deep sequential modelling schemes, followed by the extraction of spatial features via convolutional neural networks. These features are then fed to fully connected layers for optimal PV power forecasting. In the third step, the proposed model is evaluated on publicly available PV power generation datasets, where its performance reveals lower error rates when compared to state-of-the-art methods.

1. Introduction

Photovoltaic (PV) power generation is one of the easiest-to-access, low-cost, and most promising sources of renewable energy. When the energy demands rise in the developing country, the PV power generation annually increases; therefore, it mitigates the global energy and climatic change crisis [1]. According to the Global Future Report, by 2050, the PV generation capacity will reach 8000 GW [2]. However, different atmospheric variables such as temperature, solar irradiance, humidity, and cloud properties cause significant uncertainty in integrating PVs to microgrid (MG) [3–7]. In contrast, an effective PV power forecasting model greatly improves solar power utilization [8–10]. Therefore, efficient forecasting models in the utility grid will operate the power grid economically and transfer the required energy to the end-users [11, 12]. Over the years, for efficient energy management and distribution, MG has played an important role in ensuring reliability, two-way power flow, self-healing, and demand response [6]. Although MG offers several advantages, due to the volatile and intermittent nature of PV power, integrating a larger portion of renewable energy into existing power generating systems creates several challenges, such as load and demand mismatch, poor scheduling, operation, penalties enforced by customers, and fluctuations in the load connected to the power systems. To tackle these challenges, integrating an intelligent forecasting model into the MG greatly reduces the aforementioned problems.

Forecasting PV power belongs to the time series (TS) forecasting problem which are divided into univariate and multivariate forecasting [13]. Based on the time horizon, these methods are divided into three types, such as long-

term, medium-term, and short-term power forecasting [14, 15]. For different scheduling and planning, each type has its own uses, for example, contributing to long-term planning and decision-making such as month or year, usually long-term forecasting is used. Similarly, for medium-term scheduling, such as looking ahead one week or less, medium-term forecasting is used. Finally, short-term forecasting is the most challenging since the target is to look ahead for a short period of time, such as hours, but it is the most reliable and accurate method for PV forecasting. The forecasting models are divided into three types, such as physical, statistical, and deep learning models [12]. Historical data is not needed in a physical model but they are used in the solar radiation and the interaction between physics laws [16], where it further consists of three sub-modules, such as numerical weather prediction [17], total sky image [18], and satellite image [19]. The modelling techniques of the physical model can be divided into regression model [20], autoregressive [21], grey theory [22], Markov chain [23], and fuzzy theory [24]. However, physical models poorly perform in ultra-short-term forecasting because it takes a long time and only produces six hours of meteorological data [16]. There are huge deviations and low precision in the results of the physical models; therefore, it is impractical to use them in PV forecasting [17] in the MG. The statistical forecasting modelling establishes a mapping relation between the historical data and the target forecasting data using the future prediction of PV power [16]. It is easy to use and possesses strong interregional versatility, but due to the complex and volatile nature of PV power generation, its TS is complex and nonperiodic [25]. The traditional statistical forecasting model provides limited performance on large-scale historical data due to long-range complex temporal information. Furthermore, due to shallow and simple processing methods, nonlinear PV power patterns are highly affecting the prediction of PV. Therefore, researchers investigated ANN-based approaches and significantly improved the performance of PV power due to their ability to learn the variational pattern of PV [26]. However, because of different atmospheric variables and complex patterns of the weather conditions, it is unable to extract the corresponding deep nonlinear characteristics and TS dynamics of PV power [27, 28]. The task of nonlinear mapping and feature extraction is extremely challenging; therefore, the best way to tackle these challenges is to employ deep learning models with the ability to extract the discriminative features end-to-end [29, 30]. In recent years, the application of deep learning models has significantly improved for image classification [31, 32], video classification [33–37], and power forecasting in TS data [38–42]. For instance, Khan et al. [43] proposed a hybrid model for electricity forecasting in residential and commercial buildings. They used the CNN model for spatial feature extraction and then applied a Bi-directional LSTM (Bi-LSTM) network for temporal feature extraction. Li et al. [44] proposed a hybrid model that integrated wavelet transform with CNN for PV power prediction in various horizons. Similarly, in [45], the authors predicted the day-ahead weather forecast data from the solar irradiance using LSTM and then established a mathematical model between irradiance and PV power to analyze the forecasting. Yona [46] proposed a novel method that uses atmospheric data and a deep neural network for the next day's PV generation.

However, to accurately forecast the PV power, numerous researchers investigate different techniques to map the association between the historical data and the target attributes. Their methods are mainly focused on only spatial or temporal features, but without focusing on different discriminative features extracting strategies to hold the long-range temporal dependencies among complex PV power patterns. Therefore, in this paper, we explore different feature extraction mechanisms and finally propose a hybrid model that prioritizes temporal features first followed by spatial features for PV power forecasting. Our proposed model was evaluated on four publicly available PV power generation datasets for an hour-ahead forecasting. The experiments concluded that the proposed feature extraction mechanism achieved the lowest error rates when compared with state-of-the-art techniques. The contributions of the proposed model are summarized as follows:

(1) A novel framework is proposed for the MG to accurately forecast an hour-ahead power generation to effectively manage the energy distribution between the consumers and suppliers. Next, a comparative study is conducted over different deep learning models for efficient feature extraction mechanisms, and finally, a hybrid GRU-CNN network is proposed.

(2) The mainstream methods first learn the spatial and then temporal features that degrade the overall performance for complex nonlinear PV power patterns. Herein, the temporal features are prioritized over spatial features to efficiently learn the long-range complex non-linear PV power patterns for an hour-ahead PV power forecasting. The proposed model learns temporal dependencies using a multilayered GRU sequential deep model and spatial patterns using convolutional features, thus making our proposed model robust and generalized for an hour-ahead PV power forecasting.

(3) To validate the performance of the proposed model, standard TS performance metrics such as mean square error, mean absolute error, root mean square error, and mean bias error are used to compared it with existing state-of-the-art methods over benchmark datasets. Our experimental results achieve the lowest error rates compared to other state-of-the-art methods.

2. Related Work

For efficient PV forecasting, different researchers have used different techniques, for example, in the early literature, researchers used shallow ANN, which achieved promising results when compared with the traditional techniques. For instance, Almonacid et al. [47] used multilayer perceptron (MLP) to predict the PV power generation. Similarly, Dahmani et al. [48] used the forward propagation MLP

model on the global solar radiation forecasting at a certain tilted angle for five-minute resolution. Another group of researchers [49] proposed a neural network with one hidden layer (extreme learning machine) for intermittent prediction. The authors claim that when there are large numbers of hidden layers in the network, it creates problems such as overfitting and gradient vanishing [50]. To solve these problems, researchers developed different techniques and finally, in 2006, introduced the Deep Belief Network (DBN) [51]. With the recent improvement of deep learning techniques in PV power forecasting, Kuremoto et al. [52] used DBN with a restricted Boltzmann machine (RBM) for TS forecasting. Similarly, Dalto et al. [53] investigated the performance of the deep and shallow networks for ultra-short-term wind prediction. The authors claimed that the computational complexity of the model is reduced by carefully selecting the input variables using their proposed variable selection algorithm. Wan et al. [54] used DBN with RBM for day-ahead wind speed prediction. They used 144 input and output nodes each in their regression model. The experimental results concluded that their model outperformed when compared with the support vector regression, single-hidden, and three-layer ANN. However, for efficient wind and PV power forecasting, their performance is affected by many variables; therefore, training DBN layers by layers requires extensive training and the model gets stuck in the local minimum. To tackle these problems, researchers introduced CNN architectures, which share features locally and globally to reduce the computational complexity and extract meaningful patterns from complex TS data. In this direction, different techniques are reported in the literature, for instance, Diaz-Vico et al. [55] used CNN for wind and solar irradiation prediction. Wang et al. [56] used ensemble techniques for wind power forecasting. Similarly, Wang et al. [29] used PV power forecasting using CNN. Sezer and Ozbayoglu [57] used the CNN model and changed the input format from 2D to 1-D for TS data. Usually, CNN is suitable to extract and learn spatial features from the input data; however, temporal features also play a key role in TS PV power prediction. Therefore, researchers used the LSTM model for long-range temporal dependencies, for example, Qing and Niu [58] used meteorological and weather data as input to the LSTM model for solar irradiance prediction. Recently, researchers concluded that integrating CNN with the LSTM model overcomes the shortcoming of a single model, as it utilizes the advantages of multiple models to jointly learn the spatial and temporal information for accurate and complex PV forecasting. Hybrid models are also introduced in the TS prediction domain, for example, Liu et al. [59] used wavelet transform followed by CNN to extract low-frequency information, while LSTM is used for high-frequency information extraction. Qin et al. [60] used the CNN model for spatial feature extraction while the temporal features were extracted by the LSTM model.

To reduce the energy crises and limit the harmfulness of climatic changes, researchers proposed different techniques as mentioned above to integrate PV power forecasting into their existing power generation systems. The existing traditional methods employ structural and parameter adjustments of the forecasting model. Their performance is better for traditional forecasting tasks. However, due to the extremely unsteady nature of the PV power, especially on cloudy and rainy days [61, 62], their performance is extremely degraded. In the literature, most researchers claim that for accurate PV power forecasting, both spatial and temporal features are important [63, 64]. The existing standalone network of deep learning paradigms is only capable of exploring spatial or temporal features. To address these challenges, researchers are developing hybrid networks that have the potential to learn spatial and temporal features at the same time. However, in the context of PV power forecasting, hybrid networks are developed in the literature without focusing on the discriminative features of spatial and temporal ordering. Therefore, in this paper, we have comprehensively analyzed different feature extraction mechanisms by using a hybrid model. Our experiments concluded that learning temporal features by GRU followed by spatial features by CNN has much more efficient and effective pattern representation and learning potential, thereby achieving the highest accuracy and greatly reducing the error rates as compared to state-of-the-art methods.

3. Proposed Methodology

This section briefly discusses the overall flow of the proposed framework, where power from the main grid flows through the MG towards the end users, as visualized in Figure 1. In this research, we have developed an intelligent and robust hybrid deep learning inspired model, which mainly consists of three steps: processing; model training; and its evaluation. In the preprocessing step, outliers and abnormalities are removed from the data, while in the second stage, a training procedure is applied on various machine and deep learning models. In the third stage, the final PV forecasting is computed and evaluated using different error metrics. All these steps of the proposed method are discussed in subsequent sections.

3.1. Preprocessing. A recent study shows that the performance of the deep learning model highly depends on the input data [45]. Therefore, the PV power data is refined in terms of filling missing values, removing outliers, standardization, and normalization, then the proposed deep learning model efficiently extracts the meaningful patterns more conveniently. The existing PV power data is obtained from the solar panel in a raw format that is incomplete and unorganized [42]. It contained abnormalities because of sensors' faults, bad weather conditions, and variable customer consumptions. Feeding these data directly to the deep learning model degraded the overall prediction [40]. Therefore, the input data is fed to the preprocessing stage to fill in missing values by taking the mean of the next and previous values. Then the data is normalized, and outliers are removed via the min-max and standard deviation methods, respectively.

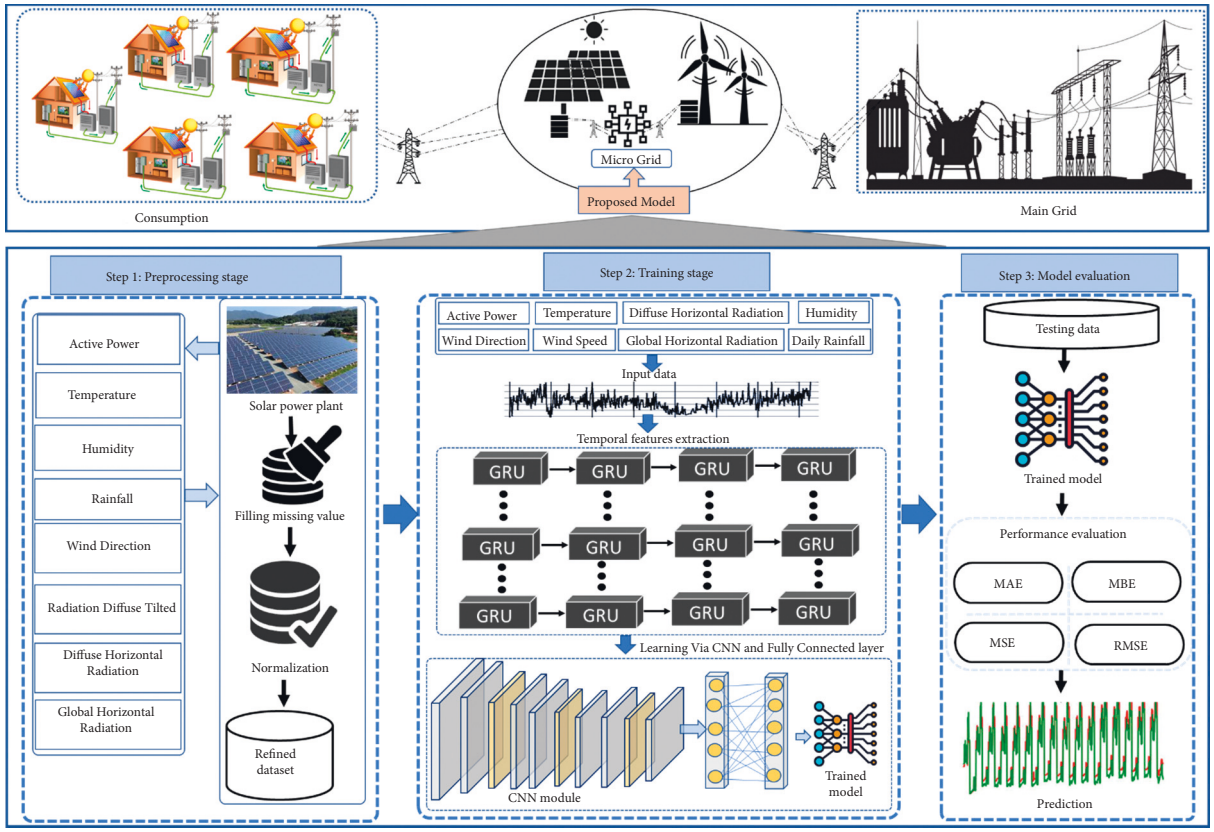

FIGURE 1: The proposed PV power forecasting framework comprises mainly three steps. Step 1: Preprocessing is applied to normalize the data, remove outliers, and fill in missing values. Step 2: Model selection with the refined data using the GRU and CNN networks. Step3: Evaluate the model via metrics, including MSE, MAE, RMSE, and MBE.

3.2. Temporal Feature Extraction. To capture long-range temporal dependencies in the complex PV power foresting data, most of the researchers used a recurrent neural network (RNN) that learns weights across the hidden layers of the network for long-range dependencies in TS data [65]. The intermediate layers of the RNN preserve meaningful information from the previous state. The visual representation of the internal structure of RNN is shown in Figure 2(a), where the input and output are represented by x^t and $\hat{y}^t$ at time t, similarly, the output of the single hidden layer at time t is represented by a^t, where w represents the weight metrics. Figure 2(a) can be mathematically represented as in equation (1).

$$a^t = g_1\left(w_{aa}a^{t-1} + w_{ax}x^{t-1} + b_a\right), \hat{y}^t = g_1\left(w_{ay}a^t + b_y\right). \quad (1)$$

In equation (1), the terms g_1, b_a, and b_y are used to represent the nonlinear activation and bias terms, while the term w refers to the learn weights when capturing temporal dependency in PV power forecasting. RNN suffers from the vanishing gradient problem when the time interval of the target output is long, therefore a special variant called GRU resolves the vanishing gradient problem, which has two structure-gated mechanisms such as reset and update. As a result, it is less complex than the LSTM model because it has fewer gates and require a small number of parameters during training [66]. Their visual representation is shown in Figure 2(b).

$$\Gamma_u = \sigma\left(w_u\left[c^{t-1}, x^t\right] + b_u\right), \quad (2)$$

$$\Gamma_r = \sigma\left(w_r\left[c^{t-1}, x^t\right] + b_r\right), \quad (3)$$

$$C^t = \tan h\left(w_c\left[\Gamma_r * c^{t-1}, x^t,\right] + b_c\right), \quad (4)$$

$$c^t = \left(1 - \Gamma_u\right) * c^{t-1} + \Gamma_u * \Gamma^t. \quad (5)$$

The mathematical representation of GRU is given in equations (2) to (5), the updated and reset gate is represented by w_u and w_r, similarly, the candidate activation and basis vectors are represented by C^t and b_u , b_r , b_c,, respectively. The c^t is the output of the current unit which is connected to the input of the next unit. Furthermore, c^{t-1} is the input of the current unit, which is also the output of the previous units. The σ and *tanh* represent the activation function while the input of the training data and their corresponding output are represented by x^t and $\hat{y}^t$ at a time stamp t. The reset gate and update gate are represented by Γ_r and Γ_u.

3.3. Spatial Features Extraction. CNN has two main properties, such as local connection and weight sharing to process high-dimensional data and extract meaningful discriminative features. CNN mainly consists of

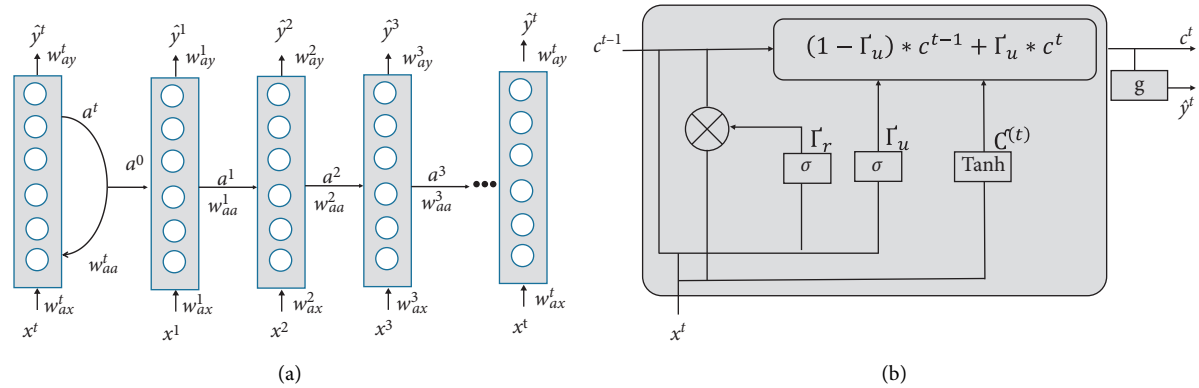

Figure 2: Visual representation of the (a) recurrent neural network, while (b) represents the gated recurrent unit.

convolutional layers, pooling layers, and fully connected layers. Convolution layers are the core layers that are responsible for extracting local features. The extracted features of the previous layer are multiplied with the convolutional kernel to form the output feature map j. It contains convolution with multiple input feature maps; their mathematical representation is given in equation (6).

$$y_j^{(l)} = \left(\sum_{i \epsilon C_j} t_i^{l-1} \otimes w_{ij}^{(l)} \right) + b_j^{(l)}, \quad t_j^{(l)} = f\left(y_j^{(l)}\right). \tag{6}$$

Here, the feature map of the input convolutional layers l and C_j are represented by $t_j^{(l)}$, while the bias, kernel, and output of the convolutional layer are represented by $b_j^{(l)}$, $y_j^{(l)}$, and $w_{ij}^{(l)}$, respectively. A Relu f activation function is used throughout the network and its mathematical representation is shown in equation (7)

$$f(x) = max(0, x). \tag{7}$$

The pooling layer is mainly responsible for reducing the dimensions of the features, also known as the downsampling layer. It has several variants, such as average, max-pooling, etc.

3.4. Network Architecture. The GRU module captures the long-range dependency, so it is capable of learning useful information from TS data using the memory cells. The nonsalient information is discarded by a memory gate called the forget gate. Their output is directly connected to the CNN module. In the proposed hybrid model, the GRU module consists of two layers. In the first and second layers, 32 and 64 cell sizes are used, followed by a two-layered CNN module having a kernel size of 3 and a filter size of 64 in each layer. For nonlinearity, a ReLU activation is used. A detailed summary of the proposed model is given in Table 1. The output features are then flattened and a fully connected layer with 16 numbers of neurons is applied. An MSE is used as a loss function when the model is successfully trained, and then we evaluated it on testing data.

Table 1: Detailed summary of the proposed model for short-term one-hour ahead solar power forecasting model.

Type of layer	Size of kernel	Size of filter	Params
GRU layer 1 (32)	—		4224
GRU layer 2 (64)	—		18816
CNN layer	3	64	12352
CNN layer	3	64	12352
Flatten	—	—	—
Dense (16)	—	—	8208
Dense (12)	—	—	204

4. Experimental Results and Discussion

In this section, we discussed the PV power datasets, evaluation metrics, and comparative analysis with state-of-the-art methods. The proposed model is implemented in the Python programming language and the Keras (2.3.1) with TensorFlow (1.14.0) deep learning framework. Windows 10 operating system with a GeForce RTX 2070 SUPER graphics card is used to speed up the training process and the complete details are given in Table 2.

4.1. Datasets Description. To assess the proposed method's performance, we use four publicly available real-world PV power datasets such as DKASC-AS-1A, DKASC-AS-1B, DKASC-AS-2Eco, and DKASC-Yulara-SITE-3A gathered in DKASC, Alice Springs (AS), Australia [67–69]. The DKASC-AS-1A dataset is taken from the 1A plant, which generates 10.5 kW from 2×30 solar panels, and their installation was completed on Thursday, January 8, 2009. Similarly, the DSKASC-ASA-1B dataset was collected from the 1B plant that generated 23.4 kW from 4×30 number of panels, and their installation was completed on Thursday, January 8, 2009. The overall details of each plant and collected data information are given in Table 3. All these datasets are recorded from active solar power generation plants at five-minute resolution with different power generation capabilities. It consists of different attributes, for example, power generation and meteorological elements such as wind speed, weather temperature, etc. For training purposes, these datasets are divided into 70% for training, 20% for validation, and 10% for testing.

Table 2: Training details required for the proposed model.

Parameters	Details
Programming language	Python 3.6
Operating system	Windows 10
Hardware	GeForce RTX 2070 SUPER GPU
Deep learning framework	Keras (TensorFlow backend)
Epochs	50
Batch size	20
Optimizer	Adam
Learning rate	0.001

4.2. Evaluation Metrics. The performance of the proposed model is evaluated on the four widely used forecasting metrics such as MSE, MAE, RMSE, and MBE, which are mathematically expressed in equations (8) to (11).

$$MSE = \frac{1}{n}\sum_{i=1}^{n}(y_i - \hat{y}_i)^2, \tag{8}$$

$$MAE = \frac{1}{n}\sum_{i=1}^{n}|y_i - \hat{y}_i|, \tag{9}$$

$$RMSE = \sqrt{\frac{1}{n}\sum_{i=1}^{n}(y_i - \hat{y}_i)^2}, \tag{10}$$

$$MBE = \frac{1}{n}\sum_{i=1}^{n}(y_i - \hat{y}_i). \tag{11}$$

5. Experimental Results and Discussions

The performance of the proposed model is evaluated with several deep learning models such as LSTM, GRU, CNN-LSTM, CNN-GRU, LSTM-CNN, and finally, the proposed GRU-CNN model.

5.1. Detailed Comparative Analysis. To analyze the performance of the proposed model, we have used four real-world PV power datasets, and their details are given in Table 3. In the literature, there are two types of feature extraction; one refers to spatial or temporal features extraction, and the second is a hybrid model where the spatial or temporal features are prioritized, respectively. Table 4 shows one-hour ahead PV power forecasting of the different standalone and hybrid models. Here, the error rate such as MSE, MAE, RMSE, and MBE of the proposed hybrid model is comparatively lower than standalone models. A graphical comparison of the forecasting results of naïve (SVR), state-of-the-art (LSTM-CNN), and the proposed model is given in Figure 3. While the visual representation of the proposed model on each dataset is given in Figure 4. The results reveal that the performance of naïve forecasting methods is much worse than the state-of-the-art and our proposed method. As given in Figure 4, there is a narrow gap between actual and forecasted values by the proposed model. This gap is higher in state-of-the-art models and much higher in naïve forecasting models.

Table 3: Technical details of each dataset and their corresponding details about the power generation plants.

Dataset	Technical specification	Value
DKASC-AS-1A [67]	Manufacturer	Trina
	PV technology	Mono-Si
	Array structure	Tracker: Dual axis
	Panel size	$2 \times 38.37\ m^2$
	Array tilt/azimuth	Variable. Dual axis tracking.
	Generation capacity of a panel	175 W
	Number of solar panels	2×30
	Power generation capacity	10.5 kW
	Duration	08-14-2013~07-01-2021
DKASC-AS-1B [68]	Manufacturer	Trina
	PV technology	Mono-Si
	Array structure	Tracker: Dual axis
	Panel size	$4 \times 38.37\ m^2$
	Array tilt/azimuth	Variable: Dual axis tracking
	Generation capacity of a panel	195 W
	Number of solar panels	4×30
	Power generation capacity	23.4 kW
	Duration	8-14-2013~7-1-2021
DKASC-AS-2Eco [69]	Manufacturer	Eco-kinetics
	PV technology	Mono-Si
	Array structure	Tracker: Dual axis
	Panel size	$199.16\ m^2$
	Array tilt/azimuth	Fixed. Tilt = 20′ azimuth = 0′
	Generation capacity of a panel	170 W
	Number of solar panels	156
	Power generation capacity	26.52 kW
	Duration	8-24-2010~8-22-2020
DKASC-Yulara-SITE-3A [70]	PV technology	Mono-Si
	Array structure	Fixed: Roof mount
	Panel type	SunPower SPR-327NE
	Array tilt/azimuth	Tilt = 10, azi = 0 (solar north)
	Generation capacity of a panel	327 W
	Number of solar panels	69
	Power generation capacity	22.56 kW
	Duration	4-1-2016~6-27-2022

Table 4: Comparative analysis of the proposed model with different existing deep learning models. Herein, DKASC-AS-1A, DKASC-AS-1B, DKASC-AS-2Eco, and DKASC-Yulara-SITE-3A represent the PV power datasets. The bold text shows the experimental result of the proposed models on one-hour ahead PV power forecasting.

Dataset	Model	RMSE	MSE	MAE	MBE
DKASC-AS-1A [67]	Decision Tree	0.4531	0.2053	0.2484	0.0684
	SVR	0.4309	0.1857	0.2373	0.0463
	LSTM	0.3118	0.0972	0.1578	−0.0283
	GRU	0.3004	0.0902	0.144	0.0322
	CNN-LSTM	0.2873	0.0825	0.117	−0.0054
	CNN-GRU	0.2606	0.0679	0.1535	0.082
	LSTM-CNN	0.2239	0.0501	0.1485	−0.1472
	GRU-CNN	**0.1468**	**0.0216**	**0.0742**	**0.0171**
DKASC-AS-1B [68]	Decision Tree	0.5344	0.2856	0.3365	−0.0824
	SVR	0.5087	0.2588	0.303	0.0709
	LSTM	0.3949	0.1559	0.2219	0.0287
	GRU	0.389	0.1514	0.2064	0.0089
	CNN-LSTM	0.2776	0.0771	0.1531	0.0172
	CNN-GRU	0.262	0.0686	0.1364	−0.0318
	LSTM-CNN	0.2496	0.0623	0.208	−0.187
	GRU-CNN	**0.1727**	**0.0298**	**0.0923**	**0.0235**
DKASC-AS-2Eco [69]	Decision Tree	0.4911	0.2412	0.1909	0.0709
	SVR	0.456	0.2079	0.2246	0.0187
	LSTM	0.3167	0.1003	0.157	−0.0158
	GRU	0.3302	0.109	0.1726	−0.0176
	CNN-LSTM	0.2959	0.0876	0.1449	−0.0143
	CNN-GRU	0.2801	0.0784	0.1467	0.0132
	LSTM-CNN	0.2274	0.0517	0.1599	−0.0155
	GRU-CNN	**0.1646**	**0.0271**	**0.1157**	**−0.0641**
DKASC-Yulara-SITE-3A [70]	Decision Tree	0.416	0.173	0.2566	0.0159
	SVR	0.4966	0.2466	0.2443	−0.0122
	LSTM	0.3627	0.1315	0.1735	0.0561
	GRU	0.3864	0.1493	0.2368	−0.0013
	CNN-LSTM	0.3056	0.0934	0.1388	−0.0153
	CNN-GRU	0.3063	0.0938	0.1506	0.0354
	LSTM-CNN	0.2465	0.0608	0.155	0.0919
	GRU-CNN	**0.1715**	**0.0294**	**0.1126**	**0.0099**

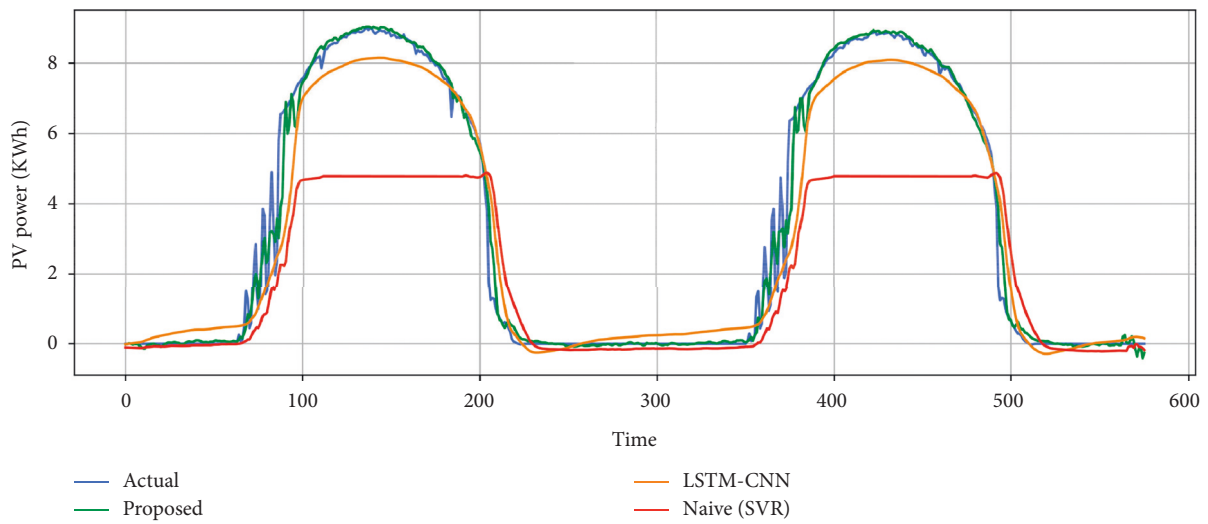

Figure 3: Visual representation to check the predictability of the proposed model with naïve and state-of-the-art model on two days ahead forecasting.

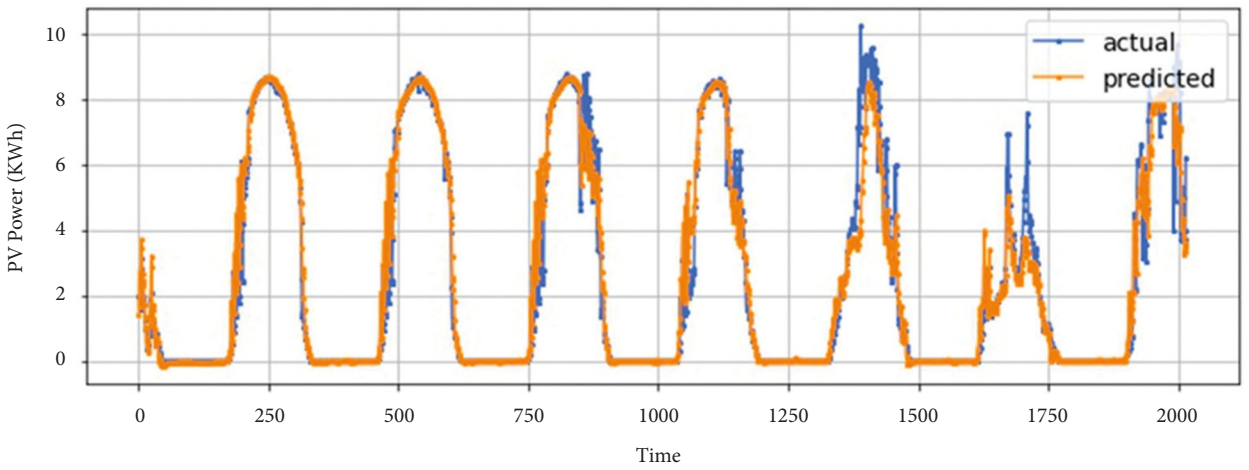

(a)

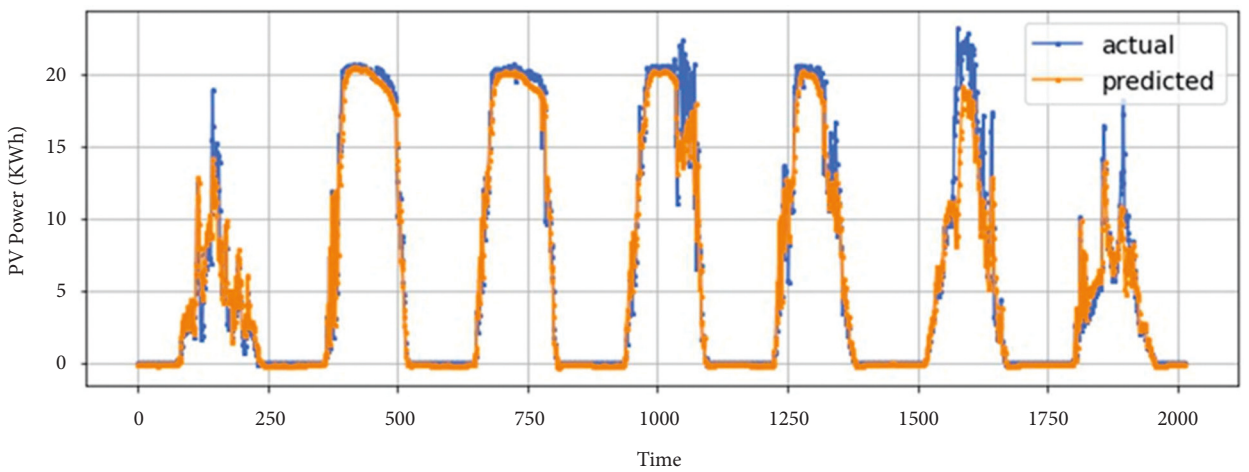

(b)

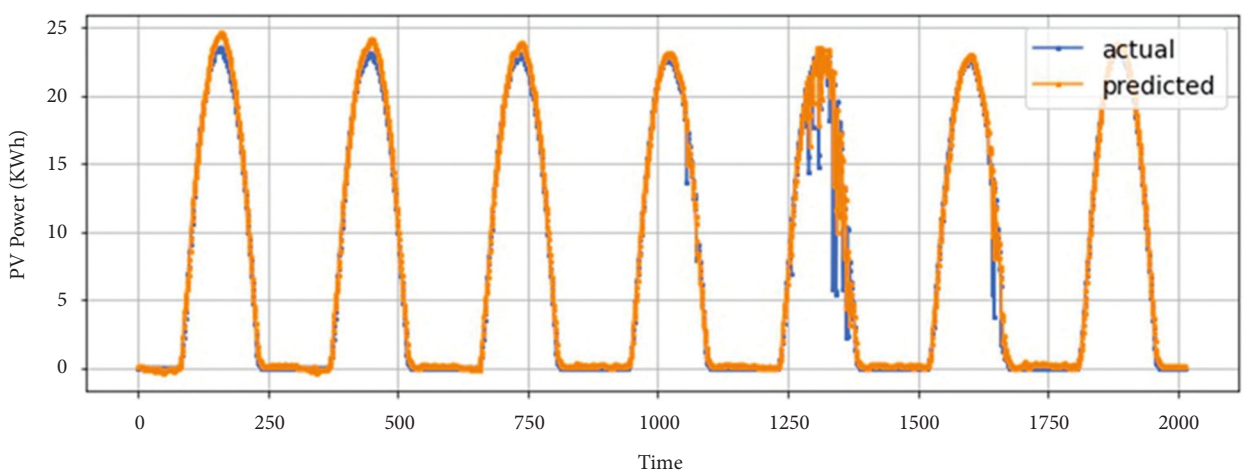

(c)

Figure 4: Continued.

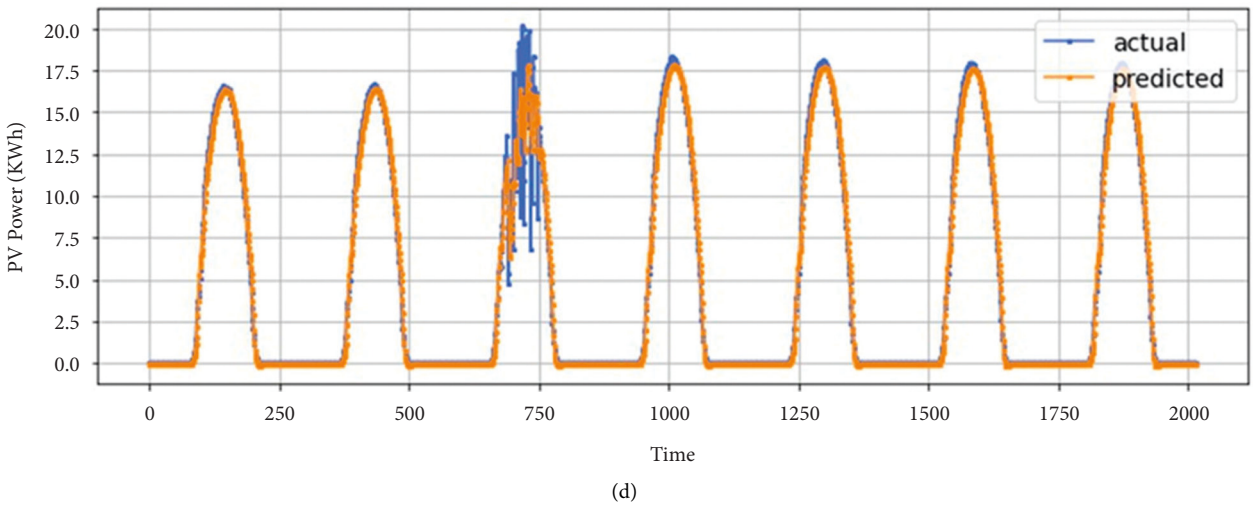

(d)

Figure 4: Visual representation of the proposed hybrid GRU-CNN forecasting model. (a) DKASC-AS-1A dataset, (b) DKASC-AS-1B dataset, (c) DKASC-AS-2Eco, and (d) DKASC-Yulara-SITE-3A datasets actual and forecasting values.

Table 5: The performance of the proposed model is compared with an existing state-of-the-art model for PV power forecasting. The best performance is shown in bold.

Dataset	Methods	RMSE	MSE	MAE	MBE
DKASC-AS-1B [68]	LSTM [45]	0.709	—	0.327	—
	CNN [45]	0.822	—	0.304	—
	CNN-LSTM [45]	0.693	—	0.294	—
	LSTM-CNN [45]	0.621	—	0.221	—
	GRU-CNN	**0.1727**	**0.0298**	**0.0923**	**0.0235**
DKASC-AS-2Eco [69]	LSTM [44]	1.0382	—	—	−0.084
	GRU [44]	1.0351	—	—	0.1206
	RNN [44]	1.0581	—	—	−0.1442
	MLP [44]	1.0861	—	—	0.1995
	WPD-LSTM [44]	0.2357	—	—	0.0067
	GRU-CNN	**0.1646**	**0.0271**	**0.1157**	**−0.0641**
DKASC-Yulara-SITE-3A [70]	RCC-BPNN [71]	1.173	—	—	—
	RCC-RBFNN [71]	1.37	—	—	—
	RCC-Elman [71]	1.158	—	—	—
	LSTM [71]	1.017	—	—	—
	RCC-LSTM [71]	0.94	—	0.587	—
	GRU-CNN	**0.1715**	**0.0294**	**0.1126**	**0.0099**

To summarize the Table 4 experiments, in the TS PV power forecasting, effective feature extraction highly correlates with the forecasting of the deep learning models. In our case, the temporal features are prioritized first and then reduced their dimensionality. Using 1D-CNN to extract spatial features is an effective approach for modelling complex PV power forecasting patterns. However, extracting temporal features using an LSTM model is not effective because it uses 3-layer structuring gates. Therefore, due to high-dimensional features, the final layers of LSTM are not able to recognize the complex patterns of PV power. While the GRU uses two layers of structure, its feature space is small as compared to LSTM; thereby, GRU requires fewer computations and achieves the highest accuracy. The performance of the GRU-CNN model on the four datasets concludes that the proposed model is more suitable to be deployed in real-world PV power forecasting at MG.

5.2. Quantitative Evaluation. In this section, the experimental results are discussed to compare the performance of our model with deep learning models. Table 5 shows the performance of the proposed model with existing state-of-the-art models, herein, the first part shows the results of the DKASC-AS-1B dataset when compared with existing state-of-the-art models. For instance, Wang et al. [45] used the 1D-CNN model and achieved 0.304 and 0.822 values for MAE and RMSE, respectively.

Similarly, a hybrid approach is also used where they extracted the spatial features with the help of CNN and then LSTM is used to learn the temporal information,

achieving 0.294 and 0.693 values for MAE and RMSE, respectively. Furthermore, when they first extracted temporal information via LSTM, followed by spatial information, it achieved 0.221 and 0.621 values for MAE and RMSE, respectively. Therefore, in this direction, we further proposed different feature extraction mechanisms, and finally, our proposed model achieved 0.1727, 0.0298, 0.0923, and 0.0235 values for RMSE, MSE, MAE, and MBE, respectively. The second row of Table 5 represents the performance of the DKASC-AS-2Eco dataset compared with existing techniques. In baseline research [44], the author's experiments on multilayer perceptron (MLP) achieved 1.0861 and 0.1995 values for RMSE and MBE, respectively. They also used RNN and reported 1.0581 RMSE and −0.1442 MBE. An LSTM and GRU network is also used for PV forecasting, and they have achieved 1.0382, −0.084, and 1.0351, 0.1206 values for RMSE and MBE, respectively. In the last model [44], the authors decomposed the power series task into subseries by employing wavelet packet decomposition and then used the LSTM model, achieving 0.2357 and 0.0067 values for RMSE and MBE, respectively. Our proposed model achieved superior performance of 0.1646, 0.0271, 0.1157, and −0.0641 for RMSE, MSE, MAE, and MBE, respectively, when compared to existing models. Finally, the performance of the proposed model is evaluated on the DKASC-Yulara-SITE-3A [70] dataset against state-of-the-art methods. Chen et al. [71] proposed a radiation coordinate classification called (RCC-LSTM) for solar forecasting. Their proposed method achieved 0.94 and 0.587 values for RMSE and MAE on the DKASC-Yulara-SITE-3A dataset, respectively. The proposed method achieved 0.1715, 0.0294, 0.1126, and 0.0099 values for RMSE, MSE, MAE, and MBE, respectively.

6. Conclusion

Accurate PV power forecasting plays an important role in avoiding penalties enforced by customers on various production companies, building trust in the energy markets, and is helpful in energy generation scheduling. Mainstream traditional and deep learning methods rely on simple features and only consider spatial or temporal features to inherent nonlinear patterns of PV power series. In the proposed framework, we have investigated different features extraction mechanisms and experimentally proved that the proposed temporal and spatial features extraction outperformed the existing state-of-the-art methods. Our proposed framework mainly consists of three steps. In the first step, preprocessing is applied to the input data to fill in the missing values and normalize the data. After normalization, the data is fed to the GRU-CNN model to first learn the temporal and then spatial features. Finally, the performance of the proposed model is evaluated against its rivals, advocating better prediction abilities with the lowest error rates and better generalization potential. In the future, we are planning to deploy the proposed model over resource-constrained devices of home appliances for energy management.

Data Availability

The codes and related materials can be downloaded from https://github.com/Altaf-hucn/Hybrid-Deep-Learning-Network-for-Photovoltaic-Power-Forecasting.

Conflicts of Interest

The authors declare that they have no conflicts of interest.

Acknowledgments

This work was supported by the National Research Foundation of Korea (NRF) grant funded by the Korean Government (MSIT) (No. 2019M3F2A1073179).

References

[1] E. Shagdar, Y. Shuai, B. G. Lougou, A. Mustafa, D. Choidorj, and H. Tan, "New integration mechanism of solar energy into 300 MW coal-fired power plant: performance and techno-economic analysis," *Energy*, vol. 238, p. 122005, 2022.

[2] A. M. Ismail, R. Ramirez-Iniguez, M. Asif, A. B. Munir, and F. Muhammad-Sukki, "Progress of solar photovoltaic in ASEAN countries: a review," *Renewable and Sustainable Energy Reviews*, vol. 48, pp. 399–412, 2015.

[3] S. Ferahtia, A. Djeroui, H. Rezk, A. Houari, S. Zeghlache, and M. Machmoum, "Optimal control and implementation of energy management strategy for a DC microgrid," *Energy*, vol. 238, p. 121777, 2022.

[4] W. Li, G. Zhang, and T. Zhang, "Knee point-guided multi-objective optimization algorithm for microgrid dynamic energy management," *Complexity*, vol. 2020, p. 8877007, 2020.

[5] N. Priyadarshi, S. Padmanaban, P. Kiran Maroti, and A. Sharma, "An extensive practical investigation of FPSO-based MPPT for grid integrated PV system under variable operating conditions with anti-islanding protection," *IEEE Systems Journal*, vol. 13, no. 2, pp. 1861–1871, 2019.

[6] K. V. G. Raghavendra, K. Zeb, A. Muthusamy et al., "A comprehensive review of DC–DC converter topologies and modulation strategies with recent advances in solar photovoltaic systems," *Electronics*, vol. 9, no. 1, p. 31, 2019.

[7] S. Padmanaban, N. Priyadarshi, M. Sagar Bhaskar, J. B. Holm-Nielsen, V. K. Ramachandaramurthy, and E. Hossain, "A hybrid ANFIS-ABC based MPPT controller for PV system with anti-islanding grid protection: experimental realization," *IEEE Access*, vol. 7, pp. 103377–103389, 2019.

[8] P. Ferreira, D. Almeida, A. Dionisio, E. Bouri, and D. Quintino, "Energy markets–Who are the influencers?" *Energy*, vol. 239, p. 121962, 2022.

[9] Y. Song, D. Wu, A. Wagdy Mohamed, X. Zhou, B. Zhang, and W. Deng, "Enhanced success history adaptive DE for parameter optimization of photovoltaic models," *Complexity*, pp. 2021-2022, 2021.

[10] N. Priyadarshi, S. Padmanaban, L. Mihet-Popa, F. Blaabjerg, and F. Azam, "Maximum power point tracking for brushless DC motor-driven photovoltaic pumping systems using a hybrid ANFIS-FLOWER pollination optimization algorithm," *Energies*, vol. 11, no. 5, p. 1067, 2018.

[11] M. Mou, Y. Zhou, W. Zheng, Z. Zhang, D. Lin, and D. Ke, "Real-time optimal control strategy for multienergy complementary microgrid system based on double-layer

nondominated sorting genetic algorithm," *Complexity*, pp. 1–12, 2020.

[12] S. Aslam, H. Herodotou, S. M. Mohsin, N. Javaid, N. Ashraf, and S. Aslam, "A survey on deep learning methods for power load and renewable energy forecasting in smart microgrids," *Renewable and Sustainable Energy Reviews*, vol. 144, p. 110992, 2021.

[13] S. Huang et al., "Dsanet: dual self-attention network for multivariate time series forecasting," in *Proceedings of the 28th ACM international conference on information and knowledge management*, New York, June 7 2019.

[14] C. Voyant, G. Notton, S. Kalogirou et al., "Machine learning methods for solar radiation forecasting: a review," *Renewable Energy*, vol. 105, pp. 569–582, 2017.

[15] P. Li, K. Zhou, and S. Yang, "Photovoltaic power forecasting: models and methods," in *Proceedings of the 2018 2nd IEEE Conference on Energy Internet and Energy System Integration (EI2)*, 20-22 October 2018.

[16] W. Gu, T. Ma, A. Song, M. Li, and L. Shen, "Mathematical modelling and performance evaluation of a hybrid photovoltaic-thermoelectric system," *Energy Conversion and Management*, vol. 198, p. 111800, 2019.

[17] F. M. Lopes, H. G. Silva, R. Salgado, A. Cavaco, P. Canhoto, and M. Collares-Pereira, "Short-term forecasts of GHI and DNI for solar energy systems operation: assessment of the ECMWF integrated forecasting system in southern Portugal," *Solar Energy*, vol. 170, pp. 14–30, 2018.

[18] J. Alonso-Montesinos, F. Batlles, and C. Portillo, "Solar irradiance forecasting at one-minute intervals for different sky conditions using sky camera images," *Energy Conversion and Management*, vol. 105, pp. 1166–1177, 2015.

[19] S. D. Miller, M. A. Rogers, J. M. Haynes, M. Sengupta, and A. K. Heidinger, "Short-term solar irradiance forecasting via satellite/model coupling," *Solar Energy*, vol. 168, pp. 102–117, 2018.

[20] L. Massidda and M. Marrocu, "Use of Multilinear Adaptive Regression Splines and numerical weather prediction to forecast the power output of a PV plant in Borkum, Germany," *Solar Energy*, vol. 146, pp. 141–149, 2017.

[21] X. G. Agoua, R. Girard, and G. Kariniotakis, "Short-term spatio-temporal forecasting of photovoltaic power production," *IEEE Transactions on Sustainable Energy*, vol. 9, no. 2, pp. 538–546, 2018.

[22] H. Wei, X. Jian, and N. Liyong, "Analysis of power genera-ti-on capacity of photovoltaic power generation sys-te-m in electric ve-hicle charging station [J]," *Electrical Technology*, vol. 32, no. 04, pp. 53–58, 2016.

[23] S. Miao, G. Ning, Y. Gu, J. Yan, and B. Ma, "Markov chain model for solar farm generation and its application to generation performance evaluation," *Journal of Cleaner Production*, vol. 186, pp. 905–917, 2018.

[24] L. M. Halabi, S. Mekhilef, and M. Hossain, "Performance evaluation of hybrid adaptive neuro-fuzzy inference system models for predicting monthly global solar radiation," *Applied Energy*, vol. 213, pp. 247–261, 2018.

[25] N. Priyadarshi, S. Padmanaban, J. B. Holm-Nielsen, F. Blaabjerg, and M. S. Bhaskar, "An experimental estimation of hybrid ANFIS–PSO-based MPPT for PV grid integration under fluctuating sun irradiance," *IEEE Systems Journal*, vol. 14, no. 1, pp. 1218–1229, 2020.

[26] G. Cervone, L. Clemente-Harding, S. Alessandrini, and L. Delle Monache, "Short-term photovoltaic power forecasting using artificial neural networks and an analog ensemble," *Renewable Energy*, vol. 108, pp. 274–286, 2017.

[27] W. Yu, G. Liu, L. Zhu, and W. Yu, "Convolutional neural network with feature reconstruction for monitoring mismatched photovoltaic systems," *Solar Energy*, vol. 212, pp. 169–177, 2020.

[28] H. Wang, Z. Lei, X. Zhang, B. Zhou, and J. Peng, "A review of deep learning for renewable energy forecasting," *Energy Conversion and Management*, vol. 198, p. 111799, 2019.

[29] H. Wang, H. Yi, J. Peng et al., "Deterministic and probabilistic forecasting of photovoltaic power based on deep convolutional neural network," *Energy Conversion and Management*, vol. 153, pp. 409–422, 2017.

[30] N. Priyadarshi, "An artificial fuzzy logic intelligent controller based MPPT for PV grid utility," in *Proceedings of the 2nd International Conference on Communication, Computing and Networking*, vol. 46, Springer, Chandigarh, India, September 2019.

[31] A. Hussain, "Automatic disease detection in wheat crop using convolution neural network," *The 4th International Conference on Next Generation Computing*, vol. 34, p. 22, 2018.

[32] A. Hussain, A. Khan, and H. Yar, "Efficient deep learning approach for classification of pneumonia using resources constraint devices in healthcare," in *Proceedings of the 5th International Conference on Next Generation Computing*, Bidholi Via-Prem Nagar, India, June 9 2019.

[33] A. Hussain, M. Khan, and U. Hayat, "Anomaly based camera prioritization in large scale surveillance networks," *Tech Science Press*, vol. 70, no. 2, pp. 2171–2190, 2021.

[34] A. Hussain, H. Tanveer, and U. Waseem, "Vision transformer and deep sequence learning for human activity recognition in surveillance videos," *Computational Intelligence and Neuroscience*, vol. 2022, p. 3454167, 2022.

[35] S. Habib, H. Altaf, M. Islam, and S. Khan, "Towards efficient detection and crowd management for law enforcing agencies," in *Proceedings of the 2021 1st International Conference on Artificial Intelligence and Data Analytics (CAIDA)*, 06-07 April 2021.

[36] F. U. M. Ullah, M. S. Obaidat, K. Muhammad et al., "An intelligent system for complex violence pattern analysis and detection," *International Journal of Intelligent Systems*, vol. 44, p. 224, 2021.

[37] F. U. M. Ullah, K. Muhammad, I. U. Haq et al., "AI-assisted edge vision for violence detection in IoT-based industrial surveillance networks," *IEEE Transactions on Industrial Informatics*, vol. 18, no. 8, pp. 5359–5370, 2022.

[38] Z. A. Khan, A. Ullah, I. Ul Haq et al., "Efficient short-term electricity load forecasting for effective energy management," *Sustainable Energy Technologies and Assessments*, vol. 53, p. 102337, 2022.

[39] S. U. Khan, I. U. Haq, Z. A. Khan, N. Khan, M. Y. Lee, and S. W. Baik, "Atrous convolutions and residual GRU based architecture for matching power demand with supply," *Sensors*, vol. 21, no. 21, p. 7191, 2021.

[40] N. Khan, S. U. Khan, S. Rho, M. Y. Lee, and S. W. Baik, "DB-Net: a novel dilated CNN based multi-step forecasting model for power consumption in integrated local energy systems," *International Journal of Electrical Power & Energy Systems*, vol. 133, p. 107023, 2021.

[41] N. Khan, F. U. M. Ullah, D. A. Afnan, M. Y. Lee, and S. W. Baik, "Batteries state of health estimation via efficient neural networks with multiple channel charging profiles," *IEEE Access*, vol. 9, pp. 7797–7813, 2021.

[42] N. Khan, F. U. M. Ullah, I. U. Haq, S. U. Khan, M. Y. Lee, and S. W. Baik, "AB-net: a novel deep learning assisted framework

for renewable energy generation forecasting," *Mathematics*, vol. 9, no. 19, p. 2456, 2021.

[43] Z. A. Khan, T. Hussain, A. Ullah, S. Rho, M. Lee, and S. Baik, "Towards efficient electricity forecasting in residential and commercial buildings: a novel hybrid CNN with a LSTM-AE based framework," *Sensors*, vol. 20, no. 5, p. 1399, 2020.

[44] P. Li, K. Zhou, X. Lu, and S. Yang, "A hybrid deep learning model for short-term PV power forecasting," *Applied Energy*, vol. 259, p. 114216, 2020.

[45] K. Wang, X. Qi, and H. Liu, "Photovoltaic power forecasting based LSTM-Convolutional Network," *Energy*, vol. 189, p. 116225, 2019.

[46] A. Yona, "Application of neural network to 24-hour-ahead generating power forecasting for PV system," in *Proceedings of the 2008 IEEE Power and Energy Society General Meeting-Conversion and Delivery of Electrical Energy in the 21st Century*, 20-24 July 2008.

[47] F. Almonacid, C. Rus, P. Perez-Higueras, and L. Hontoria, "Calculation of the energy provided by a PV generator. Comparative study: conventional methods vs. artificial neural networks," *Energy*, vol. 36, no. 1, pp. 375–384, 2011.

[48] K. Dahmani, R. Dizene, G. Notton, C. Paoli, C. Voyant, and M. L. Nivet, "Estimation of 5-min time-step data of tilted solar global irradiation using ANN (Artificial Neural Network) model," *Energy*, vol. 70, pp. 374–381, 2014.

[49] F. Lolli, R. Gamberini, A. Regattieri, E. Balugani, T. Gatos, and S. Gucci, "Single-hidden layer neural networks for forecasting intermittent demand," *International Journal of Production Economics*, vol. 183, pp. 116–128, 2017.

[50] Y. Zhang, J. Le, X. Liao, F. Zheng, and Y. Li, "A novel combination forecasting model for wind power integrating least square support vector machine, deep belief network, singular spectrum analysis and locality-sensitive hashing," *Energy*, vol. 168, pp. 558–572, 2019.

[51] G. E. Hinton, S. Osindero, and Y. W. Teh, "A fast learning algorithm for deep belief nets," *Neural Computation*, vol. 18, no. 7, pp. 1527–1554, 2006.

[52] T. Kuremoto, S. Kimura, K. Kobayashi, and M. Obayashi, "Time series forecasting using a deep belief network with restricted Boltzmann machines," *Neurocomputing*, vol. 137, pp. 47–56, 2014.

[53] M. Dalto, J. Matuško, and M. Vašak, "Deep neural networks for ultra-short-term wind forecasting," in *Proceedings of the 2015 IEEE international conference on industrial technology (ICIT)*, 17-19 March 2015.

[54] J. Wan, J. Liu, G. Ren, Y. Guo, D. Yu, and Q. Hu, "Day-ahead prediction of wind speed with deep feature learning," *International Journal of Pattern Recognition and Artificial Intelligence*, vol. 30, no. 05, p. 1650011, 2016.

[55] D. Díaz-Vico, A. Torres–Barran, A. Omari, and J. R. Dorronsoro, "Deep neural networks for wind and solar energy prediction," *Neural Processing Letters*, vol. 46, no. 3, pp. 829–844, 2017.

[56] H.-z. Wang, G. H. Li, and Y. Liu, "Deep learning based ensemble approach for probabilistic wind power forecasting," *Applied Energy*, vol. 188, pp. 56–70, 2017.

[57] O. B. Sezer and A. M. Ozbayoglu, "Algorithmic financial trading with deep convolutional neural networks: time series to image conversion approach," *Applied Soft Computing*, vol. 70, pp. 525–538, 2018.

[58] X. Qing and Y. Niu, "Hourly day-ahead solar irradiance prediction using weather forecasts by LSTM," *Energy*, vol. 148, pp. 461–468, 2018.

[59] H. Liu, X. Mi, and Y. Li, "Smart deep learning based wind speed prediction model using wavelet packet decomposition, convolutional neural network and convolutional long short term memory network," *Energy Conversion and Management*, vol. 166, pp. 120–131, 2018.

[60] Y. Qin, K. Li, Z. Liang et al., "Hybrid forecasting model based on long short term memory network and deep learning neural network for wind signal," *Applied Energy*, vol. 236, pp. 262–272, 2019.

[61] M. G. De Giorgi, M. Malvoni, and P. Congedo, "Comparison of strategies for multi-step ahead photovoltaic power forecasting models based on hybrid group method of data handling networks and least square support vector machine," *Energy*, vol. 107, pp. 360–373, 2016.

[62] A. Dolara, F. Grimaccia, S. Leva, M. Mussetta, and E. Ogliari, "A physical hybrid artificial neural network for short term forecasting of PV plant power output," *Energies*, vol. 8, no. 2, pp. 1138–1153, 2015.

[63] Z. A. Khan, A. Ullah, W. Ullah, S. Rho, M. Lee, and S. W. Baik, "Electrical energy prediction in residential buildings for short-term horizons using hybrid deep learning strategy," *Applied Sciences*, vol. 10, no. 23, p. 8634, 2020.

[64] Z. A. Khan, T. Hussain, and S. W. Baik, "Boosting energy harvesting via deep learning-based renewable power generation prediction," *Journal of King Saud University Science*, vol. 2022, p. 101815, 2022.

[65] N. Khan, I. U. Haq, F. U. M. Ullah, S. U. Khan, and M. Y. Lee, "CL-net: ConvLSTM-based hybrid architecture for batteries' state of health and power consumption forecasting," *Mathematics*, vol. 9, no. 24, p. 3326, 2021.

[66] X. Liu, "Short-term electricity load forecasting model based on EMD-GRU with feature selection," *Energies*, vol. 12, no. 6, p. 1140, 2019.

[67] Desert Knowledge Australia Solar Centre, https://dkasolarcentre.com.au/source/alice-springs/dka-m9-b-phase*DKASC-AS-1A*. 2009 25/6/2022]; Available from:, 2022.

[68] Desert Knowledge Australia Solar Centre, https://dkasolarcentre.com.au/source/alice-springs/dka-m9-a-c-phases*DKASC-AS-1B*. 2009 25/6/2022]; Available from:, 2022.

[69] Desert Knowledge Australia Solar Centre, https://dkasolarcentre.com.au/source/alice-springs/dka-m11-3-phase*DKASC-AS-2Eco* 2010 25/6/2022]; Available from:, 2022.

[70] Desert Knowledge Australia Solar Centre, https://dkasolarcentre.com.au/source/yulara/yulara-3-roof-sails-in-the-desert*DKASC-Yulara-SITE-3A* 2016 4/7/2022]; Available from:, 2022.

[71] B. Chen, P. Lin, Y. Lai, S. Cheng, Z. Chen, and L. Wu, "Very-short-term power prediction for PV power plants using a simple and effective RCC-LSTM model based on short term multivariate historical datasets," *Electronics*, vol. 9, no. 2, p. 289, 2020.

Hindawi
Complexity
Volume 2022, Article ID 9663746, 11 pages
https://doi.org/10.1155/2022/9663746

Research Article

Design of a Small Quadruped Robot with Parallel Legs

Ming Lu, Baorui Jing, Hao Duan, and Guanbin Gao

Faculty of Mechanical and Electrical Engineering, Kunming University of Science and Technology, Kunming 650500, China

Correspondence should be addressed to Baorui Jing; jingbarry@163.com

Received 14 June 2022; Revised 13 September 2022; Accepted 15 September 2022; Published 29 September 2022

Academic Editor: Wenjie Lu

In this paper, a lightweight and modular design of a quadruped robot with two-degree-of-freedom parallel legs is presented. To reduce the weight and enhance the transmission accuracy, the horizontal layout of the driving end is adopted for designing the legs of the quadruped robot. The rotation angle of each actuator for the quadruped robot is analyzed by the inverse kinematics algorithm. Moreover, the trajectory of the foot-end, including support and swing phases, is planned to reduce the impact between the foot-end and the ground. Furthermore, the gait of the four legs of the quadruped robot is designed by considering the conditions of trot, standing, take-off, and walking. Finally, the effectiveness of the foot-end trajectory and the stable gait is verified by conducting experiments on a prototype platform.

1. Introduction

Mobile robots have become a research hotspot in the field of robotics since they can perform dangerous tasks in place of humans in rescue and disaster relief, anti-terrorist and explosive ordnance disposal, and field exploration [1]. Mobile robots can be divided into wheeled, crawler-type, and legged [2]. Although wheeled robots and crawler robots can move efficiently on relatively flat ground, they cannot work normally in cluttered terrains such as mountains and hills. In contrast, legged robots can overcome almost all terrain obstacles and have broader application prospects [3]. According to the number of feet, legged robots can be divided into biped robots, quadruped robots, and multi-legged robots. Among them, quadruped robots are currently receiving more attention because they have better stability and higher load capacity than biped robots, more flexible motion performance, and higher motion efficiency than multi-legged robots [4].

Over the past few decades, many excellent quadruped robots have been developed. Among them, the large-scale quadruped robots mainly include BigDog [5], LS3 [6], Wildcat [7], and HyQserial [8, 9]. These quadruped robots are hydraulically driven and more than 100 kg such that they can perform large-load rugged terrain traversal tasks. However, due to their large weight, large size, and power source (hydraulics) limitations, the main obstacle to the wider commercial utilization of large-scale quadruped robots is complicated. Of the medium-sized quadruped robots, the outstanding ones are MIT Cheetah [10–12], ANYmal [13, 14], Spot [15], and Aliengo [16]. By using motor-based proprioceptive actuators and electrically powered actuators, medium-sized quadruped robots have shown excellent motion performance. However, the development difficulty and the cost of hardware are too high to be suitable for widespread rollout [17–20]. Therefore, it is of great practical significance to develop a quadruped robot that is suitable for robot beginners, that can be used in home entertainment and school teaching scenarios.

In this paper, a small quadruped robot with parallel legs is designed. The leg structure adopts a parallel configuration with the horizontal layout of the driving end so that the leg actuator can meet the installation requirements of the steering engine and have the performance of low self-weight and high transmission accuracy. The body adopts a lightweight and modular design, which not only improves the motion performance but also has the characteristics of convenient disassembly and assembly. For the designed new leg parallel configuration, the corresponding forward and inverse kinematic algorithm is proposed. Through foot-end

trajectory planning and gait planning, it can obtain stable walking ability. The prototype uses an STM32 microcontroller as the main controller, and the steering engine as the actuator, and is assembled by using 3D printed mechanical structural parts. The experimental results verify that the quadruped robot designed in this paper not only has excellent motion performance but also has the advantages of low power consumption, small size, low cost, simple operation, etc. Therefore, it has certain entertainment, teaching, and practical value.

This paper is organized as follows: the second section introduces the mechanical structure design of this quadruped robot. In Section three, an inverse kinematics algorithm for the novel parallel leg configurations is proposed. The fourth and fifth sections, respectively, introduce the methods of foot-end trajectory planning and gait planning applied to this robot. The implementation scheme of the prototype and its experimental results are illustrated in Section six. Finally, the conclusion is given in Section seven.

2. Mechanical Structure Design of Quadruped Robot

Inspired by the bionic principle of quadrupeds, the mechanical structure of quadruped robots is generally designed as two parts: torso and limbs. Most of the limbs are designed as a three-degree-of-freedom serial mechanism [2], and the structure is distributed from bottom to top as foot-ankle-calf-knee-thigh-hip- torso, respectively. After some simplification, the quadruped robot based on the serial leg configuration can be obtained as shown in Figure 1.

However, there are some problems with such serial legs in practical applications. Firstly, due to the load accumulation effect of the serial mechanism [21], the joint actuator needs to bear the additional load of other parts of the leg; thus, the overall carrying capacity of the quadruped robot is limited, which appears to be overwhelmed in the case of weight-bearing tasks. In particular, it will cause great weight-bearing pressure on the knee joint, affecting the motion stability and the life of the actuator. Secondly, the actuators are usually installed at the knee joints of the legs in a serial configuration [3], which not only increases the moment of inertia of the legs but also increases the load on the hip joint actuators, making the robot action cumbersome and affecting the control effect. To solve this problem, one type of solution is to place the actuator of the knee joint at the hip joint and transmit power through a transmission mechanism such as a synchronous belt. However, the use of the transmission mechanism will introduce transmission errors. Coupled with the cumulative error of the serial mechanism itself, it is difficult to guarantee the accuracy of the foot-end, thus reducing the motion performance of the robot.

Due to the natural disadvantages of the serial configuration, the parallel configuration is more suitable for small quadruped robots with limited actuator output power [22]. A typical quadruped robot with a parallel leg configuration is the Stanford Doggo [23], which utilizes a coaxial parallel mechanism and a quasi-direct drive actuator to achieve excellent vertical jumping agility. However, the cost of the quasi-direct drive actuator is too high, and the control is difficult, so it is not suitable for large-scale promotion, and the supporting coaxial mechanism does not match the installation of the lower-cost steering engine.

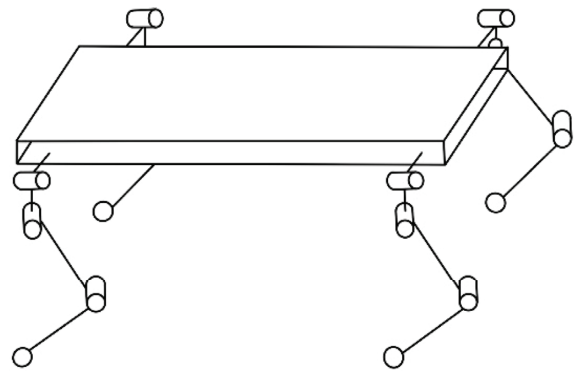

Figure 1: Quadruped robot based on serial leg configuration.

This paper refers to the parallel leg configuration of Stanford Doggo, splits the coaxial mechanism and arranges the actuators horizontally, and designs a 2-DOF parallel leg mechanism as shown in Figure 2. The mechanism has two active joints (hip joints) driven by steering engines, which are mounted horizontally at A and E on the side of the torso, and these two steering engines together control the movement of one leg. B, C, and D are passive joints without a power source, wherein B and D are the knee joints, and C is the foot end. The knee joints B and D change the position of the foot-end C with the rotation of the hip joints A and E.

The mechanism has the following advantages: First, the actuator can be installed in the torso to protect the actuator and reduce the moment of inertia of the legs. Second, the parallel leg mechanism has less transmission error and therefore has higher control accuracy. Compared with the 3-DOF series mechanism, this solution reduces the space and self-weight and increases the load capacity due to the subtraction of one hip joint transverse swing degree of freedom. In addition, the steering function responsible for the hip joint can be replaced by the differential method. Compared to the Stanford Doggo, our quadruped robot uses a small, low-cost steering engine as the actuator, eliminating the need for a separate gearbox and allowing the two actuators to be mounted horizontally with a direct drive output, thereby reducing the overall size of the robot and simplifying the structure.

Figure 3 illustrates the structure of the quadruped robot. The torso adopts a lightweight and modular design. It is 3D printed with PLA material, and the shape of which is a rectangular parallelepiped with four edges cut off, where the head and tail ends are connected by hollow brackets. This design can minimize weight reduction while maintaining strength, thereby improving athletic performance. The centre of the torso is the control module, which is used to place the controller and battery compartment, and its top is equipped with a boat-shaped power switch and a hinged battery compartment opening and closing cover for easy start-up and battery replacement. Eight steering engines are drive modules, which are symmetrically installed on both sides of the front and rear parts of the torso and extend out of

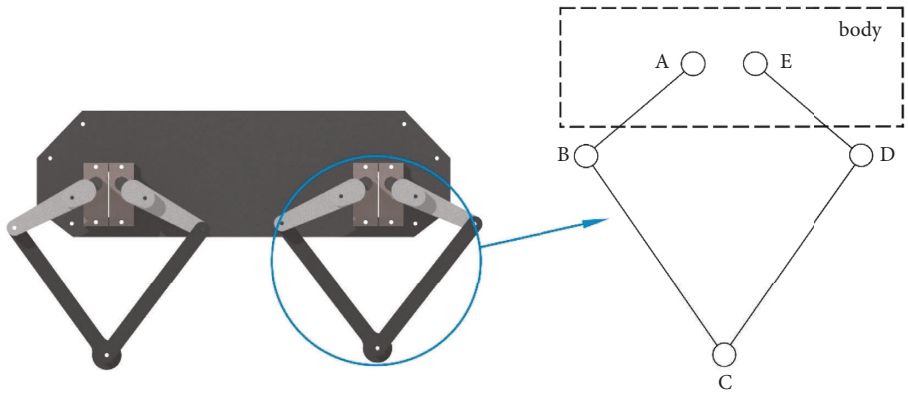

Figure 2: The 2-DOF parallel leg mechanism.

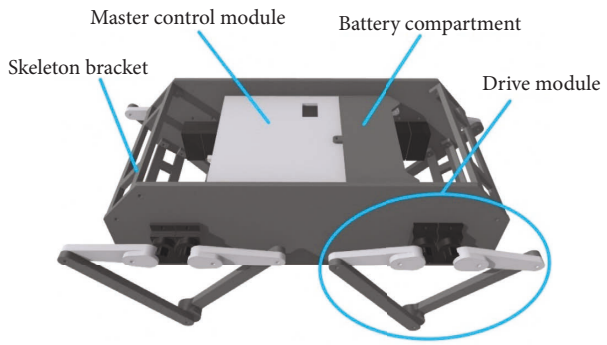

Figure 3: Small quadruped robot with a parallel leg mechanism.

the output shaft to connect the parallel leg mechanism. This layout makes the centre of gravity coincide with the centroid, ensuring control stability. Meanwhile, the modular design gives the quadruped robot the characteristics of quick assembly and easy replacement of parts.

The front and top views of the quadruped robot are shown in Figures 4 and 5, respectively, and its structural design parameters are listed in Table 1.

3. Kinematic Analysis of Legs

Kinematic analysis refers to the analysis of position, velocity, and acceleration changes of the mechanism without considering the force action, respectively. These three change analyses are also the pivot between the active input components and the passive output components of the mechanism. In this section, the forward and inverse kinematic analysis of the legs of the quadruped robot designed in this paper is performed separately.

By modeling the parallel leg mechanism, a Cartesian base coordinate system is established with the straight line where the two hip joints are located as the x-axis and the midpoint of the two hip joints as the origin, and the schematic diagram of the joint coordinates can be obtained as in Figure 6. Wherein, the definitions of joints A, B, C, D, and E are the same as in Figure 2, which make up a five-bar linkage. Define the lengths of AE, AB, DE, BC, and CD as l, l_1, l_1, l_2, l_2. The angles between each link and the x-axis are denoted as θ_1, θ_2, θ_3, θ_4 (range from 0 to 180 degrees) as shown in Figure 2. Moreover, the coordinate of the foot-end point C is represented by (x, y).

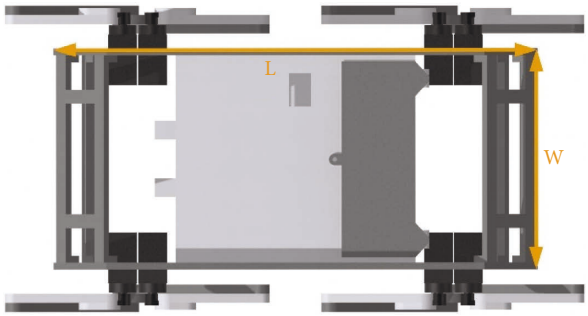

Figure 4: Top view of the quadruped robot.

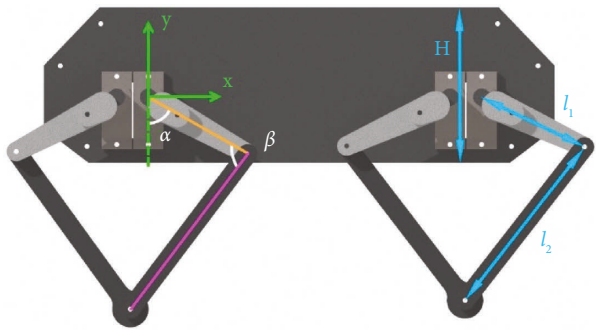

Figure 5: Side view of the quadruped robot.

Table 1: The structural design parameters.

Symbol	Description	Value
W	Torso width	96 mm
L	Torso length	210 mm
H	Torso high	64 mm
l	Interval of motor	15 mm
l_1	Length of thigh	50 mm
l_2	Length of calf	80 mm
α	Hip joint rotation range	−90°~+90°
β	Knee joint rotation range	15°~175°
M	Total mass	0.44 kg

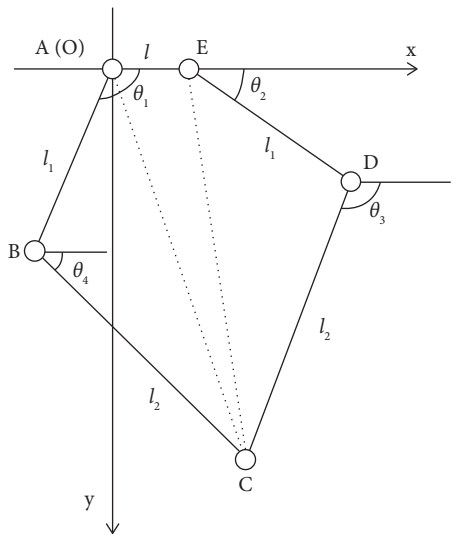

Figure 6: The schematic diagram of joint coordinates of parallel leg mechanism.

First, the matrix method is used for forwarding kinematics analysis. Calculating the projection lengths in the x and y directions, respectively, we can obtain the system of equations as

$$\begin{cases} l + l_1 \cos\theta_2 + l_2 \cos\theta_3 = l_2 \cos\theta_4 + l_1 \cos\theta_1, \\ l_1 \sin\theta_2 + l_2 \sin\theta_3 = l_2 \sin\theta_4 + l_1 \sin\theta_1. \end{cases} \tag{1}$$

According to Table 1, we have known the exact values of l, l_1 and l_2. In addition, the angles of θ_1 and θ_2 are active joints, thus the unknown variables are θ_3 and θ_4. By placing the unknown variable to the left of the equal sign, (1) becomes

$$\begin{cases} l_2 \cos\theta_3 - l_2 \cos\theta_4 = l_1 \cos\theta_1 - l_1 \cos\theta_2 - l, \\ l_2 \sin\theta_3 - l_2 \sin\theta_4 = l_1 \sin\theta_1 - l_1 \sin\theta_2. \end{cases} \tag{2}$$

Solving (2) by computer software, e.g., MATLAB, we can calculate the value of joints θ_3 and θ_4. Thereby, the coordinate of the foot-end point C can be solved as

$$\begin{aligned} &x\text{: } l + l_1 \cos\theta_2 + l_2 \cos\theta_3 \text{ or } l_2 \cos\theta_4 + l_1 \cos\theta_1, \\ &y\text{: } l_1 \sin\theta_2 + l_2 \sin\theta_3 \text{ or } l_2 \sin\theta_4 + l_1 \sin\theta_1. \end{aligned} \tag{3}$$

The relationship of joint angular velocity can be obtained by calculating the first derivative of (2) with respect to time as

$$l_2 \begin{bmatrix} -\sin\theta_3 & \sin\theta_4 \\ \cos\theta_3 & -\cos\theta_4 \end{bmatrix} \begin{bmatrix} \omega_3 \\ \omega_4 \end{bmatrix} = l_1 \begin{bmatrix} -\sin\theta_1 & \sin\theta_2 \\ \cos\theta_1 & -\cos\theta_2 \end{bmatrix} \begin{bmatrix} \omega_1 \\ \omega_2 \end{bmatrix}, \tag{4}$$

where the symbols $\omega_1 \sim \omega_4$ are the angular velocities of $\theta_1 \sim \theta_4$.

Based on the velocity function (4), the accelerate function can be further derived as

$$\begin{aligned} l_2 \begin{bmatrix} -\sin\theta_3 & \sin\theta_4 \\ \cos\theta_3 & -\cos\theta_4 \end{bmatrix} \begin{bmatrix} \alpha_3 \\ \alpha_4 \end{bmatrix} = &-l_2 \begin{bmatrix} -\omega_3 \cos\theta_3 & \omega_4 \cos\theta_4 \\ -\omega_3 \sin\theta_3 & \omega_4 \sin\theta_4 \end{bmatrix} \begin{bmatrix} \omega_3 \\ \omega_4 \end{bmatrix} + l_1 \begin{bmatrix} -\sin\theta_1 & \sin\theta_2 \\ \cos\theta_1 & -\cos\theta_2 \end{bmatrix} \begin{bmatrix} \alpha_1 \\ \alpha_2 \end{bmatrix} \\ &+ l_1 \begin{bmatrix} -\omega_1 \cos\theta_1 & \omega_2 \cos\theta_2 \\ -\omega_1 \sin\theta_1 & \omega_2 \sin\theta_2 \end{bmatrix} \begin{bmatrix} \omega_1 \\ \omega_2 \end{bmatrix}, \end{aligned} \tag{5}$$

where, the symbols $\alpha_1 \sim \alpha_4$ are the angular accelerations of $\theta_1 \sim \theta_4$. Therefore, by solving functions (4) and (5), we can obtain the angular velocities ω_3, ω_4 and the angular accelerations α_3, α_4.

Then, the inverse kinematic analysis of the legs is also conducted. The so-called inverse kinematics is to find the rotation angle of each actuator with the knowledge of the coordinates of the foot-end relative to the leg base coordinate system. Using the inverse kinematics algorithm, the mapping relationship between the position of the foot-end and the angles of the actuators can be determined, thus achieving the purpose of foot-end position control. In this section, the inverse kinematics analysis is performed for the novel parallel leg mechanism designed in this paper to obtain the leg inverse kinematics algorithm applicable to our quadruped robot. According to the algebraic method, the angle of each joint is solved as follows:

$$l_{AC} = \sqrt{x^2 + y^2}, \tag{6}$$

$$l_{EC} = \sqrt{(x - l)^2 + y^2}. \tag{7}$$

Then according to the cosine theorem, we can infer the value of $\angle CAE$, $\angle CEA$, $\angle BAC$, $\angle CED$, namely,

$$\begin{aligned} \angle CAE &= \cos^{-1} \frac{l^2 + l_{AC}^2 - l_{EC}^2}{4 l_{AC} l}, \\ \angle CEA &= \cos^{-1} \frac{l^2 + l_{EC}^2 - l_{AC}^2}{4 l_{EC} l}, \end{aligned} \tag{8}$$

$$\begin{aligned} \angle BAC &= \cos^{-1} \frac{l_1^2 + l_{AC}^2 - l_2^2}{2 l_1 l_{AC}}, \\ \angle CED &= \cos^{-1} \frac{l_1^2 + l_{EC}^2 - l_2^2}{2 l_1 l_{EC}}. \end{aligned} \tag{9}$$

Finally, by combining (7), (9), we can derive θ_1 and θ_2 as:

$$\theta_1 = \angle CAE + \angle BAC, \tag{10}$$

$$\theta_2 = \pi - \angle CEA - \angle CED. \tag{11}$$

Equations (10)~(11) are the inverse kinematics algorithm of the novel parallel leg mechanism designed in this paper.

4. Trajectory Planning of Foot-End

Although the inverse kinematics solution can be used in positioning control for the foot-end of the quadruped robot, to make the foot-end move according to the preset trajectory, it is necessary to plan a reasonably foot-end trajectory. The planned trajectory can be discrete into a sequence of foot-end trajectory points to be sent to the controller, thereby achieving foot-end trajectory control.

To illustrate the trajectory of the foot-end, we need first to introduce some concepts as follows [24].

(i) Gait Cycle: The duration of the robot's leg from the moment it hits the ground to the next moment it hits the ground, represented by T_s

(ii) Support Phase: The state when one leg is supported on the ground

(iii) Swing Phase: The state when one leg is off the ground

(iv) Duty Ratio: The ratio of the time occupied by the swing phase of one leg to the whole gait cycle

It was found that the cycloid trajectory can reduce the impact of the foot landing so that the quadruped robot has better stability in motion. Therefore, this paper adopts the cycloid method to plan the foot-end trajectory. By setting the gait parameters of the quadruped robot such as the step length, step height, and cycle, the foot trajectory is obtained as

$$\begin{cases} x_{\exp} = \left(x_f - x_s\right)\dfrac{\sigma - \sin\sigma}{2\pi} + x_s, \\ y_{\exp} = h\dfrac{1 - \cos\sigma}{2} + y_s, \end{cases} \tag{12}$$

where $(x_{\exp}, y_{\exp})$ is the coordinates of the desired foot-end point, (x_s, y_s) is the coordinate of the foot-end starting point, h is the step height, which is the maximum height of the foot-end from the ground, $x_f - x_s$ is the step size, i.e., the distance between the landing point x_f and the starting point x_s. parameter $\sigma = 2\pi t/\lambda T_s$, where $0 < t < T_s$, T_s the cycle time of the whole foot-end trajectory, λ is the duty ratio of the swing phase.

The whole trajectory is divided into the support phase and swing phase, the duty ratio of the swing phase in the whole cycle time T_s can be adjusted by the duty ratio parameter λ. Also, the cycle time T_s, the step height h, and the step size $x_f - x_s$ can be changed according to different environments and speed requirements. For example, when $\lambda = 0.5$, $T_s = 1s$, $h = 10mm$ and $x_f - x_s = 20mm$, the trajectory and speed curve of the foot-end are depicted in Figures 7 and 8.

Through the analysis of the speed curve of the foot-end (Figure 8), it can be seen that the speed curve of the robot remains continuous in one motion cycle, and the velocity in the x-direction and y-direction is zero at the moment when the foot-end touches the ground and leaves the ground, which can effectively reduce the impact between the foot-end and the ground and helps to maintain the motion stability of the quadruped robot.

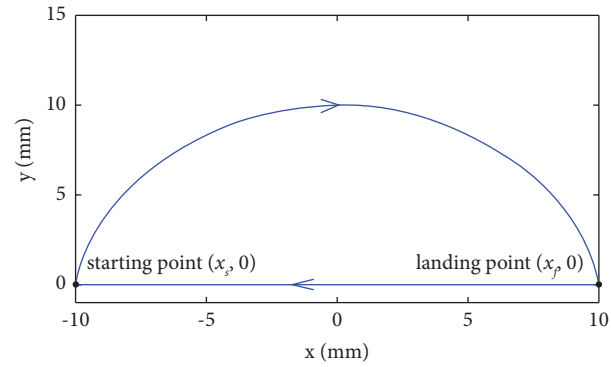

Figure 7: The cycloid trajectory of foot-end.

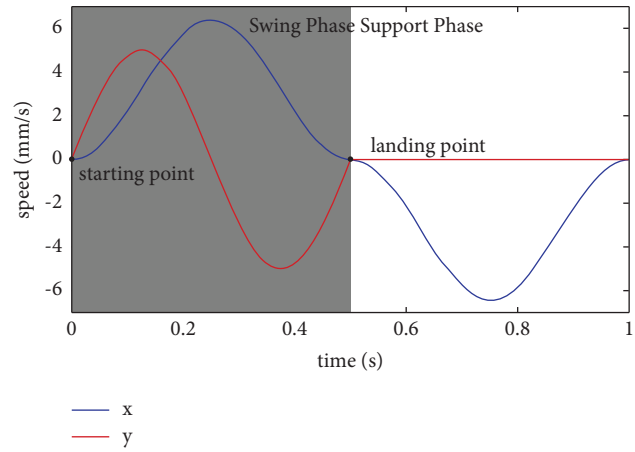

Figure 8: The speed curve of the foot-end.

5. Gait Planning

The foot-end trajectory only specifies the action of one leg. To make the quadruped robot move, it is necessary to reasonably distribute the action rhythm of the four legs, that is, gait planning. In bionics, gait refers to the movement pattern of a footed animal, that is, the fixed positional relationship between the individual legs. The quadruped robot designed in this paper adopts the mainstream trot gait and walking gait to obtain the corresponding behavioral capabilities. To describe gait, the four legs are labeled in Figure 9, where RF, LF, LH, and RH represent the right front leg, the left front leg, the left hind leg, and the right hind leg.

The trotting gait is suitable for the fast walking of the quadruped robot, which means that the two legs on the diagonal move in the same way. Currently, the legs on the two diagonals move in the opposite direction, and the support phase and the swing phase of the foot-end trajectory of one leg each account for half of the cycle time. Figure 10 displays the timing diagram of the trot gait, where a couple

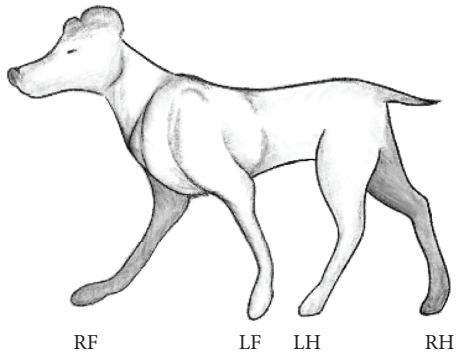

Figure 9: The label has four legs.

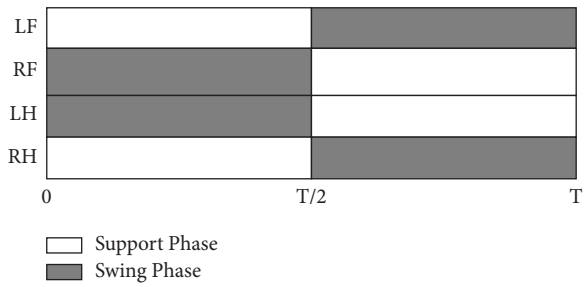

Figure 10: The timing diagram of the trot gait.

of legs in one diagonal are in the state of support phase while another couple of legs are in the state of swing phase. Since the trot gait has high energy efficiency, it can be adapted to a large speed range [24]. Furthermore, this kind of symmetrical gait is also conducive to maintaining the stability of quadruped robots and has become the most used gait for quadruped robots.

The differential steering gait is the most common gait used for the steering of an 8-DOF quadruped robot. Based on the trot gait, the differential steering gait changes the foot-end step length or the leg swing direction on both sides of the robot, where a displacement difference is generated to rotate the robot body.

The walking gait is also a widely used gait, which is suitable for the slow walking of quadruped robots. When a quadruped robot is performing the walking gait, there are always three legs on the ground. At this time, the support phase of each leg occupies 3/4 of the cycle, and the swing phase occupies 1/4 of the cycle. The positions of the four legs in a cycle are different from each other, differing by 1/4 of a cycle in turn, as shown in Figure 11.

6. Prototype and Experiments

The prototype uses SolidWorks software to design the mechanical structure, and the mechanical parts are produced by 3D printing. The control system of the prototype is shown in Figure 12, in which the controller is the STM32f103c8t6 minimum core board, and the control program is written through Keil software. The actuator used in the quadruped robot is the mg90s steering engine, which is driven by the PCA9685 driver board. In terms of power supply, a 7.4 V rechargeable lithium battery is used to power the control system and steering engine after it is stepped down to 5 V by the LM2596 step-down module. The control system is also equipped with a PS2 signal receiver, which is responsible for receiving the remote-control signal from the PS2 handle. The major functions of the controller STM32 are calculation and communication. The calculation function is responsible for planning the gait of the robot and executing the inverse kinematics solution. The communication function is in charge of communicating with the PS2 receiver and the PCA9685 driver board.

By receiving the remote-control signal from the PS2 handle, STM32 transmits the calculated motor position signal to the PCA9685 driver board to realize the motion control. The rotation angle of the steering engine is controlled by the PWM signal, which is output through PCA9685. Note that the corresponding relationships between the rotation angle and the PWM signal are illustrated in Figure 13.

It can be seen from Figure 13 that the rotation angle can be controlled by adjusting the duty cycle of the PWM signal. Note that the duty cycle refers to the proportion of high-level duration in one signal period. Then, according to the relationship, we can calculate the duty cycle ω as

$$\omega = \frac{0.5 + (\varphi/180) \times (2.5 - 0.5)}{20}, \tag{13}$$

where φ is the rotation angle of the steering engine.

By using (13), we can achieve angle control of a steering engine by sending PWM signals from the controller to the driver board.

Figure 14 is the picture of the prototype. It has been verified by experiments that the prototype can perform the trot gait and walk gait well. In addition, based on the trot gait, the in-situ stepping gait, the in-situ take-off gait, and the lateral gait relying on the offset of the centre of gravity are developed.

Compared with similar quadruped robots, the design cost of our robot is extremely low. Table 2 lists the cost of each component required to build the robot.

We conducted experiments on the motion of the robot's legs on a motion capture system (Figure 15). In this experiment, four calibration balls were installed on one leg of the robot, and the robot was controlled to walk forward, then the foot-end trajectory of the robot in the world coordinate system could then be obtained. Use Matlab to draw the velocity curve of the trajectory as shown in Figure 16. Compared with Figure 8, the actual speed curve obtained in the experiment is consistent with the design curve, and it can be clearly seen that the swing phase and the support phase account for half of each gait cycle.

To evaluate the performance of our quadruped robot, we introduce the concept of "Normalized Work Capability" (NWC) [25]. NWC represents the proportional relationship between Normalized Speed (NS) and Payload Capacity (PLC). Where NS is the ratio of maximum speed to body length, reflecting the performance of speed per unit body

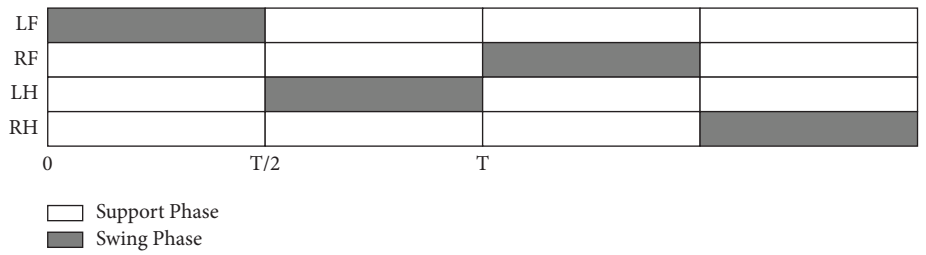

Figure 11: The timing diagram of the walking gait.

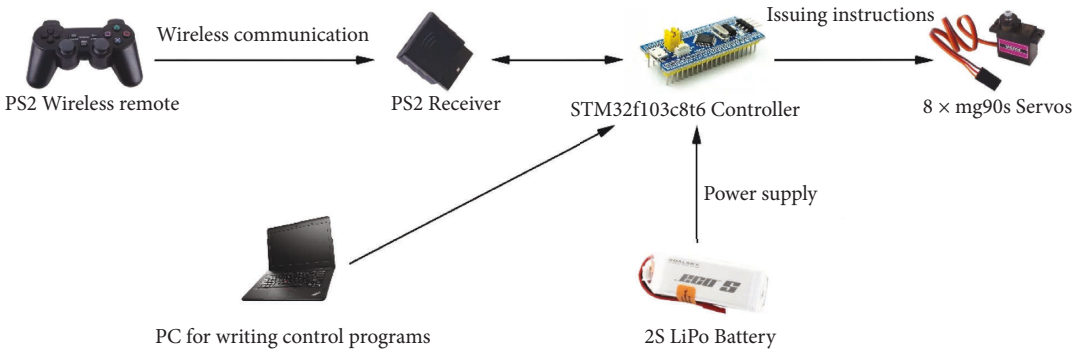

Figure 12: The control system of the prototype.

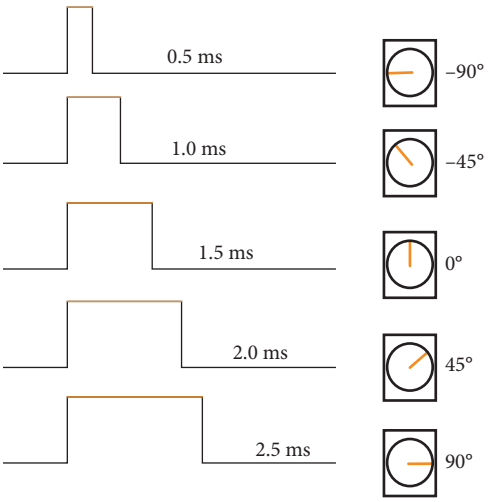

Figure 13: The corresponding relationship between the rotation angle and the PWM signal.

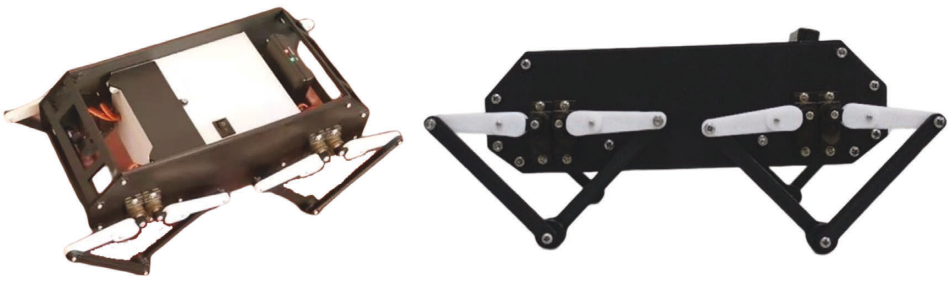

Figure 14: The prototype.

Table 2: The prototype BOM.

Item	Price	Quantity	Cost
MG90S steering engines	6.85	8	54.80
3D print parts	53.00 (RMB/kg)	0.21 (kg)	11.13
STM32f103c8t6 controller	36.88	1	36.88
PCA9685 driver board	23.00	1	23.00
2S 800 mAh lithium battery	26.13	1	26.13
PS2 handle	45.00	1	45.00
LM2596 step-down module	3.60	1	3.6
		Total:	200.54 RMB

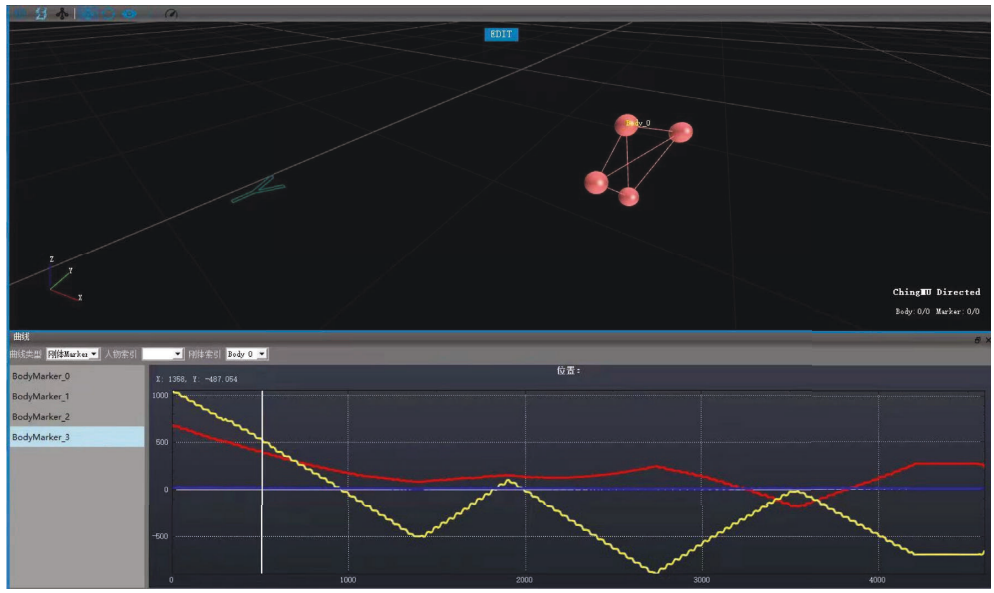

Figure 15: The experiment in the motion capture system.

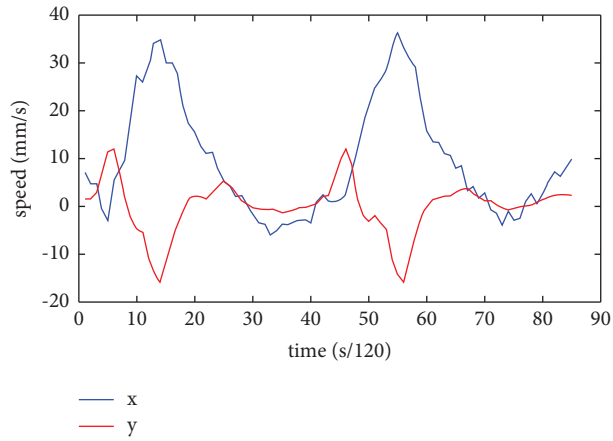

Figure 16: The actual speed curves.

length, the greater the value, the better. The PLC refers to the ratio of the robot's weight to the payload, reflecting the required self-weight per unit load, the smaller the value, the better. Therefore, NWC is the integrated performance of NS and PLC. The larger the value, the better. For the small parallel-legged quadruped robot designed in this paper, the NS, PLC, and NWC are 1.36%, 55.31%, and 75.22%, respectively. Compared with the data of other famous quadruped robots provided in reference [3], we can conclude that the performance of the mechanical dog designed in this paper is at roughly average level [3]. The comparison results are shown in Figures 17~19. Because the new

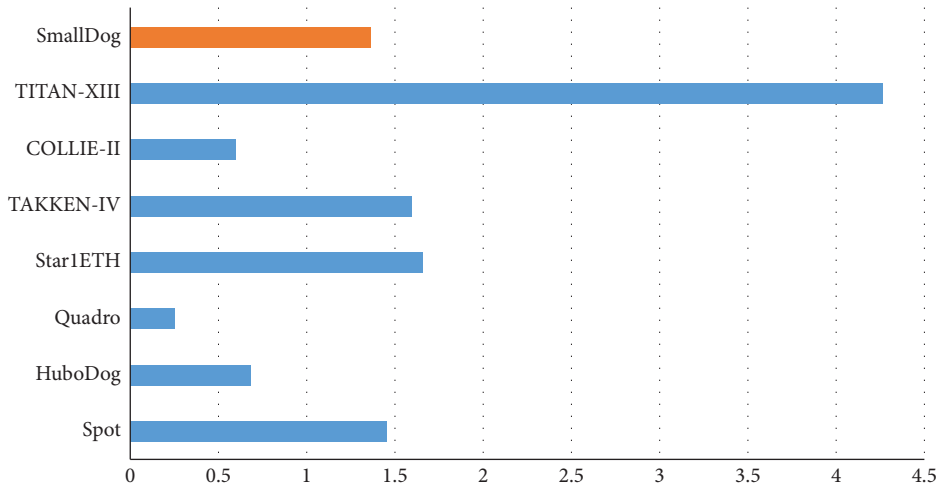

Figure 17: Normalized speed.

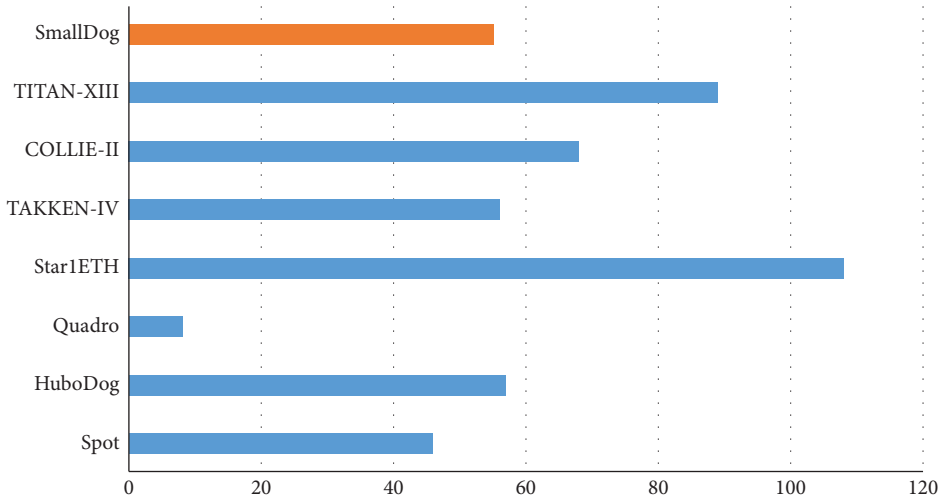

Figure 18: Payload capacity.

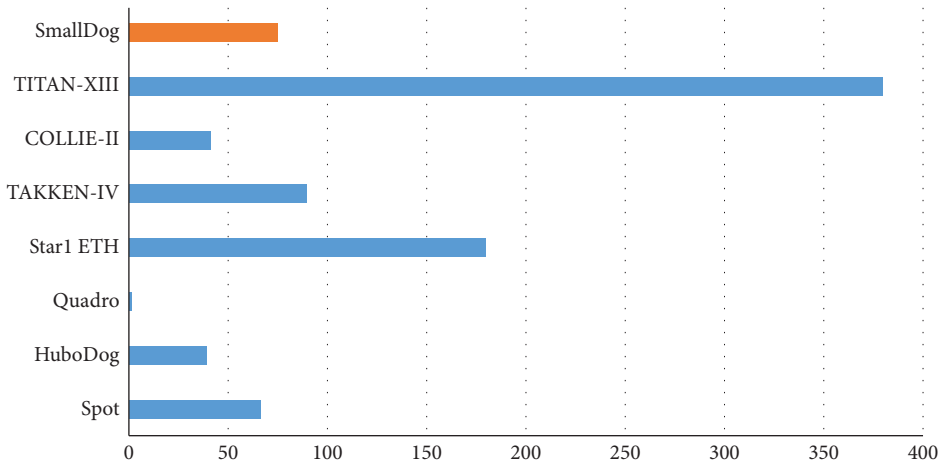

Figure 19: Normalized work capacity.

quadruped robot has lower cost and thus higher cost performance, it is more suitable for promotion to the entertainment and teaching market.

7. Conclusion

In this paper, a small, low-cost, and simple-to-operate two-degree-of-freedom parallel leg configuration is designed and realized. Besides, the structure, kinematics analyses, foot trajectory, and gait planning of the designed quadruped robot are studied. First, from the perspective of bionics and mechanics, this paper adopts the parallel scheme of the horizontal layout of the driving end and the concepts of lightweight and modularization and designs a quadruped robot with low self-weight, simple structure, and high transmission performance. In the quadruped robot structure, the actuator is installed in the fuselage, which protects the actuator and reduces the moment of inertia of the legs. Second, the paper analyses the two-degree-of-freedom parallel leg configuration. By using the matrix method, we performed a kinematic analysis of the legs and used the inverse kinematics algorithm to determine the mapping relationship between the position of the foot end of each leg and the angle of the leg actuator, to achieve the purpose of position control. Furthermore, the paper verifies the effectiveness of the cycloid trajectory and the stability of the mainstream gait by planning the trajectory and gait of the quadruped robot. Finally, this paper builds a quadruped whole machine experiment platform with two degrees of freedom in parallel leg configuration and conducts related experiments on trot gait and walking gait. Based on the trot gait, the experiment extended the gait in situ, gait in- situ jumping, and lateral movement gait relying on the offset of the centre of gravity, which verifies the correctness of the prototype design method and control algorithm. Compared with commercial products, the mechanical dog designed in this paper is made by 3D printing, so the structure of the legs can be arbitrarily changed, and the corresponding kinematics algorithm can also be adapted to the modifications by adjusting the parameters of the legs. In addition, the controller is completely open source so that any desired functionality can be added. Based on the above advantages, people can customize a mechanical dog that is different in structure and program on the basis of the prototype, thus meeting the needs of teaching and entertainment. Moreover, the cost of this robot has been compressed to 200 RMB, and its performance is no less than that of other well-known quadruped robots, which greatly reduces the development threshold of quadruped robots.

Data Availability

Data were curated by the authors and are available upon request.

Conflicts of Interest

The authors declare that there are no conflicts of interest regarding the publication of this paper.

Acknowledgments

This work was supported by the National Natural Science Foundation of China (Grant no. 51865020).

References

[1] L. Yao, H. Yu, and Z. Lu, "Design and driving model for the quadruped robot: an elucidating draft," *Advances in Mechanical Engineering*, vol. 13, no. 4, 2021.

[2] X. Meng, S. Wang, Z. Cao, and L. Zhang, "A review of quadruped robots and environment perception," in *Proceedings of the 2016 35th Chinese Control Conference (CCC)*, pp. 6350–6356, Chengdu, China, July 2016.

[3] P. Biswal and P. K. Mohanty, "Development of quadruped walking robots: a review," *Ain Shams Engineering Journal*, vol. 12, no. 2, pp. 2017–2031, 2021.

[4] D. J. Todd, *Walking Machines: An Introduction to Legged Robots*, Springer Science & Business Media, Germany, 2013.

[5] M. Raibert, K. Blankespoor, G. Nelson, and R. Playter, "BigDog, the rough-terrain quadruped robot," *IFAC Proceedings Volumes*, vol. 41, no. 2, pp. 10822–10825, 2008.

[6] B. Dynamics, "LS3 - Legged Squad Support System," 2012, https://www.youtube.com/watch?v=R7ezXBEBE6U.

[7] "Boston Dynamics, Introducing WildCat," 2013, https://www.youtube.com/watch?v=wE3fmFTtP9g.

[8] C. Semini, V. Barasuol, J. Goldsmith et al., "Design of the hydraulically actuated, torque-controlled quadruped robot HyQ2Max," *IEEE*, vol. 22, no. 2, pp. 635–646, 2017.

[9] C. Semini, N. G. Tsagarakis, E. Guglielmino, M. Focchi, F. Cannella, and D. G. Caldwell, "Design of HyQ – a hydraulically and electrically actuated quadruped robot," *Proceedings of the Institution of Mechanical Engineers - Part I: Journal of Systems & Control Engineering*, vol. 225, no. 6, pp. 831–849, 2011.

[10] G. Bledt, M. J. Powell, B. Katz, J. Di Carlo, P. M. Wensing, and S. Kim, "MIT Cheetah 3: Design and Control of a Robust, Dynamic Quadruped Robot," in *Proceedings of the 2018 IEEE/RSJ International Conference on Intelligent Robots and Systems (IROS)*, pp. 2245–2252, Madrid, Spain, October 2018.

[11] P. M. Wensing, A. Wang, S. Seok, D. Otten, J. Lang, and S. Kim, "Proprioceptive actuator design in the MIT Cheetah: impact mitigation and high-bandwidth physical interaction for dynamic legged robots," *IEEE Transactions on Robotics*, vol. 33, no. 3, pp. 509–522, 2017.

[12] S. Seok, A. Wang, M. Y. Chuah, D. Otten, J. Lang, and S. Kim, "Design Principles for Highly Efficient Quadrupeds and Implementation on the MIT Cheetah Robot," in *Proceedings of the 2013 IEEE International Conference on Robotics and Automation*, pp. 3307–3312, Karlsruhe, Germany, May 2013.

[13] P. Fankhauser and M. Hutter, "ANYmal: A Unique Quadruped Robot Conquering Harsh Environments," *Research Features*, vol. 126, pp. 54–57, 2018.

[14] M. Hutter, C. Gehring, D. Jud et al., "ANYmal - a Highly mobile and Dynamic Quadrupedal Robot," in *Proceedings of the 2016 IEEE/RSJ International Conference on Intelligent Robots and Systems (IROS)*, pp. 38–44, Daejeon, Korea, October 2016.

[15] *Spot® - the Agile Mobile Robot*, Boston Dynamics, Waltham, Massachusetts, USA, 2022.

[16] Z. Chen, "Aliengo—versatility and industry applications," *Unitree*, https://www.unitree.com/aliengo/, 2022.

[17] S. Xie and Q. Chen, "Adaptive nonsingular predefined-time control for attitude stabilization of rigid spacecrafts," *IEEE Transactions on Circuits and Systems II: Express Briefs*, vol. 69, no. 1, pp. 189–193, 2022.

[18] M. Tao, Q. Chen, X. He, and S. Xie, "Fixed-time filtered adaptive parameter estimation and attitude control for quadrotor UAVs," *IEEE Transactions on Aerospace and Electronic Systems*, p. 1, 2022.

[19] D. Xiao, H. Chen, C. Wei, and X. Bai, "Statistical measure for risk-seeking stochastic wind power offering strategies in electricity markets," *J. Mod. Power Syst. Clean Energy*, 2021.

[20] C. Wei, Y. Zhao, Y. Zheng, L. Xie, and K. Smedley, "Analysis and Design of a Non-isolated High Step-Down Converter with Coupled Inductor and ZVS Operation," *IEEE Trans. Ind. Electron*, vol. 69, pp. 9007–9018, 2021.

[21] K.-H. Grote and E. K. Antonsson, *Springer handbook of mechanical engineering*, Vol. 10, Springer, Berlin, Germany, 2009.

[22] L. Li, Y. Fang, S. Guo, H. Qu, and L. Wang, "Type synthesis of a class of novel 3-DOF single-loop parallel leg mechanisms for walking robots," *Mechanism and Machine Theory*, vol. 145, Article ID 103695, 2020.

[23] N. Kau, A. Schultz, N. Ferrante, and P. Slade, "Stanford Doggo: An Open-Source, Quasi-Direct-Drive Quadruped," 2019, http://arxiv.org/abs/1905.04254.

[24] A. Spröwitz, A. Tuleu, M. Vespignani, M. Ajallooeian, E. Badri, and A. J. Ijspeert, "Towards dynamic trot gait locomotion: design, control, and experiments with Cheetah-cub, a compliant quadruped robot," *The International Journal of Robotics Research*, vol. 32, no. 8, pp. 932–950, 2013.

[25] M. B. Binnard, *Design of a Small Pneumatic Walking Robot*, Massachusetts Institute of Technology, Cambridge, Massachusetts, USA, 1995.

Hindawi
Complexity
Volume 2022, Article ID 8534810, 15 pages
https://doi.org/10.1155/2022/8534810

Review Article

Optimization of Energy in Sustainable Architecture and Green Roofs in Construction: A Review of Challenges and Advantages

Sara ziaee,[1] Zeynab Gholampour,[2] Mina Soleymani,[3] Parisa Doraj,[4] Omid Hossein Eskandani,[4] and Samireh Kadaei[5]

[1]*Department of Architecture, Islamic Azad University West Tehran Branch, Bachelor of Architecture Engineering, Tehran, Iran*
[2]*Department of Art and Architecture, Payame Noor University, Shiraz, Iran*
[3]*Urban Development Department, Fine Arts School, University of Tehran, Tehran, Iran*
[4]*Department of Architecture, Faculty of Architecture and Design, Ataturk University, Erzurum, Turkey*
[5]*Department of Architecture, Faculty of Art and Architecture, Central Tehran Branch, Islamic Azad University, Iran*

Correspondence should be addressed to Samireh Kadaei; samira.kadaei@gmail.com

Received 26 June 2022; Revised 23 July 2022; Accepted 4 August 2022; Published 17 September 2022

Academic Editor: Chun Wei

Sustainability has been one of architecture's most significant trends over the last twenty years. The environmental consciousness of professionals has put sustainability at the heart of the architectural profession and has contributed to adopting and implementing sustainable designs on the scale of urban landscapes. A green roof or living roof, which is a sustainable solution in architecture, is a roof on the surface of which plants are grown. The roof is covered by plants, covering the waterproof layer beneath the vegetation. However, various types of plants can be used in this scheme. Understanding the influencing factors in choosing the right plant species and the impact that utilizing green roofs has on the overall energy consumption of the building can tremendously help scientists and clarify the possible future research topics in this field. Hence, this article investigates energy optimization in the construction process of a green roof in sustainable architecture and its advantages and challenges. The results of this study show that budget limitations, managerial and organizational policies, legal issues, technical and scientific infrastructure, and cultural and geographical aspects are all affecting the widespread use of green roofs currently and need to be considered in future studies.

1. Introduction

The geographical expansion of cities has led to the destruction of natural environments and agricultural lands. Some anthropogenic activities may result in deleterious effects on environmental elements. Issues such as air and water pollution and depletion of natural resources are deteriorating the earth's ecosystem [1]. The urban system and its correlation with varying environmental needs may lead to catastrophic consequences such as reshaped societies and environment [2]. The degradation of the land leads to biodiversity loss and decreases public animal and human health. For sustainable wildlife, the conservation technique needs new strategies and innovation including analyses on the carbon and greenhouse gas emissions as well as ecological monitoring, which is carried out to evaluate climate change effects [3]. Some solutions have been proposed to reduce these destructive effects. These solutions are known as green property development which includes passive design methods such as wall insulation, low E-window, and solar heating systems. Such solutions have evolved as a potential choice for different types of environments [4]. Additionally, many new technologies and activities have been developed to reduce the human impact on the earth, including alternative energy resources, efficient use of natural resources, sustainable agriculture, and green spaces [5–7].

The creation and development of green spaces play an essential role in human life and are considered a substitute for the natural environment that is lost during construction [8]. Roofs can be utilized as hosts for green spaces [9]. In urban buildings, flat roofs are designed at a high cost to

protect the building from rain and snow and store mechanical equipment [10]. Flat roofs usually lack architectural aesthetics and, therefore, cannot enrich the aesthetic and architectural value of the building. These rough surfaces give the building area and the city, as a whole, an unpleasant look. Today's apartment dwellers try to return the spirit of the nature to the rough residential blocks by connecting the living and green nature with the modern technology and create beautiful and original landscapes [11]. Also, the land is scarce and very expensive to create green spaces in cities. Hence, green roofs are part of the efforts of city managers to stabilize the urban space by expanding the green space to buildings and are among the modern strategies for addressing urban environmental issues [12, 13]. Many countries have considered using a vegetation layer on the roof of residential units, office buildings, educational, medical, pilgrimage, recreational, and sports spaces in urban areas [14].

Modern green roofs, which are essentially prefabricated layered systems, are relatively new. They were developed in Germany in the 1960s and have been common in some other European countries as well [15]. Although these roofs are quite common in northern Europe, such as the Scandinavian countries, the Netherlands, and Scotland, their modern, urban form was born in Germany. Today, it is estimated that about 10% of all German roofs are green [16]. Developed countries have long been at the forefront of utilizing green roofs, which serve the development of green spaces in metropolitan areas [17]. A green roof is an interconnected complex system of the following items: a waterproof insulation covering the roof, a well-proportioned vegetation layer, and a proper drainage layer.

One of the main concerns regarding the sustainability of cities is the increasing trend of domestic and industrial energy consumption and its adverse effects and irreparable damage to the natural environment. Utilizing green roofs has been one of the choices for reducing building energy usage [18]. If properly designed and implemented by taking climate considerations into account, green roofs can greatly help reduce energy consumption [19]. Creating greenery in the roof space has a positive effect on cooling the city's climate and the indoor air of the building on which they are located by blocking sunlight and reducing surface evaporation and transpiration [20]. The cooling is carried out by reducing heat fluctuations on the roof's outer surface and increasing the roof's heat capacity, which keeps the space under the roof cool in summer and maintains a moderate temperature during winter [21]. Other benefits of utilizing a green roof include noise and air pollution reduction, urban heat island mitigation, support of biodiversity, and management of stormwater. Furthermore, they may lead to an increase in the lifespan of roof materials [22]. Additionally, these roofs are a good alternative for enjoying the green space in the environment [23–25].

Green roof execution knowledge does not vary much from ordinary roofs and includes thermal insulation, thermal waterproofing, sand, and sealant [10]. Under the requirements specified in the house, green roof projects include materials and elements that could provide moist maintenance/drainage and plant maintenance. However, a green roof is partly or entirely filled by biomass or a growing medium [12, 15, 17], which makes its design and maintenance more complicated than normal flat roofs. Green roofs require plants that can withstand the harsh and lifeless environment of the roof in conditions of dehydration, frost, storms, etc. The type of plant selected varies depending on the climate and climatic conditions [26, 27]. Conducting a comprehensive investigation into green roofs can tremendously help researchers identify possible research and experimental topics as well as future trends in this field.

Table 1: The number of selected studies for each journal.

Journal	#
Current Opinion in Environmental Sustainability	24
Sustainability	53
International Journal of Sustainability in Higher Education	42
Environmental Advances	2
Environmental Challenges	1
Environmental Development	8
Energy	11
Energy and Buildings	73
Urban Forestry & Urban Greening	65
Science of the Total Environment	38
Journal of Environmental Management	22
Urban Forestry & Urban Greening	66
Hellion	1
Building and Environment	57
Construction and Building Materials	5
Sustainable Cities and Society	12
Renewable and Sustainable Energy Reviews	11
Journal of Cleaner Production	21

Accordingly, this paper investigates the concept of green roofs and sustainable construction and their advantages and challenges. The primary purpose of this study is to investigate the environmental benefits of green roofs and their effects on urban residents as well as the challenges of their construction using a descriptive-analytical method. To comprehend green roof technology, the analysis in this research offers the general consumer an informative overview of green roof technology. This analysis also describes in depth each part of the green roof, its advantages, and the challenges in utilizing it.

The rest of this article is structured as follows. The next section reviews the most prominent studies on green roofs. Section 3 focuses on the benefits of green roofs and how they contribute to the sustainability of the building as well as the whole urban area. Section 4 discusses the challenges of using green roofs and their current downsides, which need to be addressed in further studies. Finally, the conclusion is presented in Section 5.

2. Literature Review

To gain a comprehensive understanding of the studies that have been conducted on green roofs and sustainable architecture as a whole, this section reviews the most prominent research that has been conducted in this field. First, the review materials and methods are discussed in the next

Table 2: Keywords of some research used in the current research in the field of green roof.

	Keywords	N
1	Green roof technology	15
2	Green roof structure	17
3	Green roof components	11
4	Green roof benefits	8
5	Roof garden	6
6	Green roof and energy consumption	27
7	Green roof policies	3
8	Green roof advantages	28
9	Green roof challenges	31
10	Green roof implementation	12

section. Then, the types of green roofs and the general classification of green roof components in the literature are discussed in detail in the following two sections.

2.1. Materials and Methods. There have been more than 28,000 scholarly research studies on green roofs since before the 19th century. In this section, international research articles from different sources, i.e., scientific studies, books, case studies, and reports, are reviewed. First, the indexes of journals were searched to identify some related journals, such as Science Direct, Scimagojr, and Scopus. Then, we searched for the desired keyword (green roof) on the sites of each journal to determine the number of articles in each journal separately. Table 1 reports the results of this search.

Then, article search platforms such as Scopus, Web of Science, Google Scholar, and Science Direct were searched for a list of relevant keywords which are tabulated in Table 2. Several articles are stored in the library. Similar or non-accessible articles were then removed from the library.

Figure 1 shows the percentage of studies for different green roof-related keywords. The statistics from the Science Direct site show that the amount of research studies in the field of green roofs is increasing. Table 3 reports the number of articles and research studies about green roofs. Also, Figure 2 reports the number of research studies on green roofs every seven years starting from 1998. This chart indicates a steady increase in the total number of publications in this field.

2.2. Types of Green Roofs. Green gardens or roof gardens are divided into three main categories based on the executive system and depending on the average planting depth and the number of facilities required, namely, 1- extensive system, 2- intensive centralized system, and 3- modular system or planter box.

2.2.1. Extensive System. This system is also known as the low height or low thickness system. This type of green roof includes only one or two types of plants and a shallow growing environment [28, 29]. The term "green roof" is mostly applied to this class of roofs. Sedum is the most common plant that is used in this type of roof because it grows easily in harsh environments, has a low cost, and is relatively lightweight. However, other plants that are resistant to a wide range of weather and drought conditions and plants that contribute to biodiversity can also be used with this type of roof [30–34].

Due to the wider roof area, extensive roofs are light and thin structures that usually have a 6 to 20 cm deep growing medium. However, small roofs usually require heavier and thicker green roofs. The thickness of the growing medium ranges from 15 cm to 1 meters. Semicompact green roofs are a mixture of the two styles mentioned above, as their title indicates. They also have a thinner growing layer than a small roof but are thicker than a large roof, and the entire structure is 120 mm to 250 mm. The weight of the large roof is between 60 and 125 kg per square meter while the weight of the semidense roof is between 120 and 180 kg per square meter, and the weight of the compact roofs is greater than 180 kg per square meter and up to 500 kg per square meter. Compact roofs are the most expensive of the three systems, and wide roofs are the least expensive [16, 35–38]. Table 4 shows the advantages and limitations of this system.

2.2.2. Intensive Centralized System. Followed by aforementioned extensive systems, the intensive centralized system is the second class of green roofs. This type of green roof includes different kinds of plants and is designed similar to a park. This system often requires new structural requirements for the roof, especially for public access roofs [39–42]. For the centralized system, the term Roof Garden is mostly used. Plants used in this type of roof include shrubs, native and nonnative herbaceous plants, grass, and large tropical perennials [25].

Intensive green roofs could allow the growth of a wide variety of plants, such as trees and grass. In contrast, a small collection of drought-resistant plants, mostly with poor root systems, can usually only tolerate large green roofs. Most low-growing plants and grasses are viable options for wide roofs [23, 24]. Hence, wide roofs require less maintenance and do not require irrigation except in heat waves. On the other hand, intensive green roofs require a lot of maintenance and should be watered regularly [14, 26, 27]. Table 5 examines the advantages and limitations of this system. Furthermore, Table 6 compares intensive and extensive systems based on multiple factors.

2.2.3. Modular System or Planter Box. After the evolution of extensive and intensive systems, modular systems/planter boxes have emerged. In this framework, the plant and its planting medium are stored in special boxes covering most or all of the green roofs. The growing layer is continuous on the green roof within a nonmodular structure [16].

In Figure 3, the growing layer is a continuous sheet on the green roof within a nonmodular structure [8, 37]. No data were found regarding the limitations and advantages of a modular system in the literature background, and no more details could be provided accordingly.

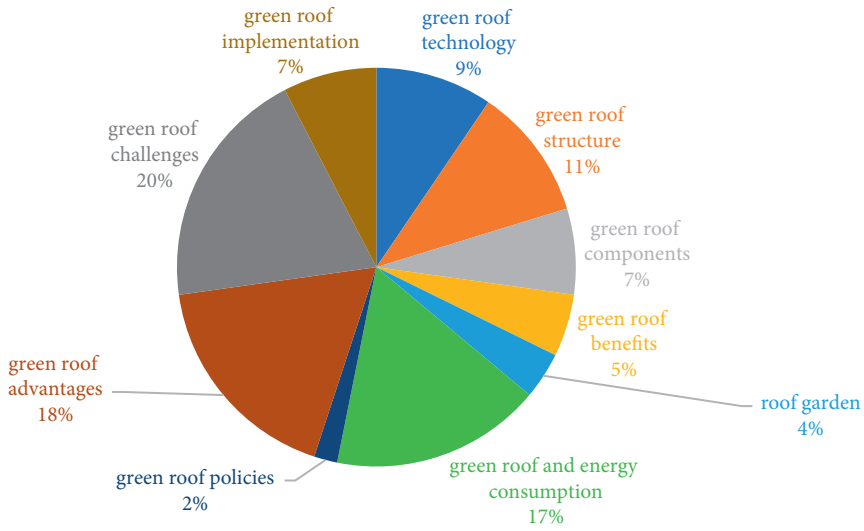

Figure 1: Keywords of some research were used in the current research in green roof.

Table 3: The number of articles and research in the field of the green roof by year of publication.

Year	#
1998	377
1999	333
2000	372
2001	426
2002	450
2003	519
2004	561
2005	651
2006	697
2007	837
2008	948
2009	1020
2010	1042
2011	1354
2012	1648
2013	1787
2014	2103
2015	2346
2016	2752
2017	3198
2018	3194
2019	3482
2020	3943
2021	1514

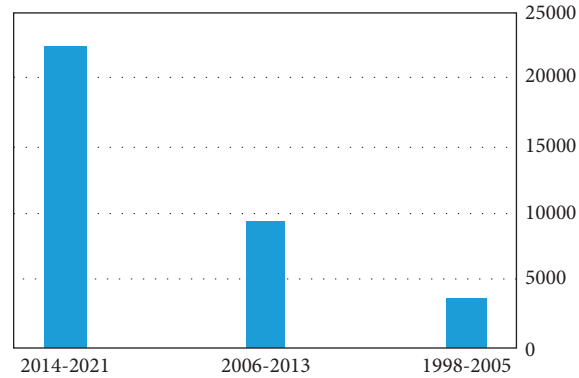

Figure 2: The number of articles and research on green roofs every seven years from 1998.

2.3. General Classification of Green Roof Components

2.3.1. Green Roof Structure. Creating different types of green roofs requires special planning and knowledge. Green roofs need technology beyond the usual roof engineering systems in terms of maintaining and controlling the weight of soil, rain, and snow and installing sidewalks [46]. A green roof consists of the following three parts [6, 47–49]:

(1) The roof of the building on which a layer of insulation such as gypsum or any other insulation is stretched, and sometimes it is mosaic, asphalt, or paving.

(2) A protective layer that separates the roof and waterproofing from the soil and plant layer.

(3) Soil, fertilizer, and garden irrigation system, each of which is carefully placed. Green roofs are designed to last more than 30 years. Hence, the materials used in constructing a green roof need to be replaced periodically. Generally, equipment manufacturers consider two scales for roof gardens: dense/compact roofs and wide roofs [47]. The application of each of these types depends on the definition of the use of the roof garden, the plant variety considered, and the amount of construction and maintenance budget [50]. Lightweight green roof systems require less maintenance and are more durable. Materials used can absorb rainwater and reduce the risk of flooding by slowing down the flow of water during sudden and torrential rains [51].

New roof garden irrigation methods minimize water consumption and maintain soil moisture to prevent rapid evaporation [52–54]. First, a layer of waterproofing and then a suitable drainage network is installed on the roof during

Table 4: Advantages and limitations of the extensive system.

Limitations	Advantages
Less energy saving and retention of water	Lightweight: normally, the roof does not need reinforcing
Extremely limited plant variety	Appropriate for spacious areas
Commonly, no links to recreation with other uses	Suitable for roofs with a 0–3 degree celsius slope
Unattractive to others, in fall in particular	Low upkeep and high durability
	No need for specialized irrigation and drainage systems
	The need for fewer technological skills
	Reasonable for retrofit projects as well
	Vegetation may grow on its own
	Relatively inexpensive
	More common
	Easier to request a planning reference for approval

Table 5: Advantages and limitations of intensive systems.

Limitations	Advantages
Heavier load on the building structure	Much more plant to produce and habitat diversity
Requires irrigation and drainage systems with resources, water, and materials	Properties of good insulation
Lower cost of capital and repairs	A park on the earth will simulate
More complicated processes and experience	Visually appealing
	Using a more varied range of ceilings for recreation
	Better quality of energy and capacity for water storage
	Longer lifespan on membranes

Table 6: The comparison between intensive and extensive systems.

Features	Intensive	Extensive	Source
Diversity	High	Low	[28, 43]
Maintenance	Complex	Easy	[28, 43, 44]
Cost	High	Low	[13, 28, 43, 45]
The thickness of growing media	>200 mm	<200 mm	[19, 28, 40, 43]
Construction	Complex	Easy	[28, 43]
Weight	>300 kg/m^2	50–150 kg/m^2	[28, 34, 43]

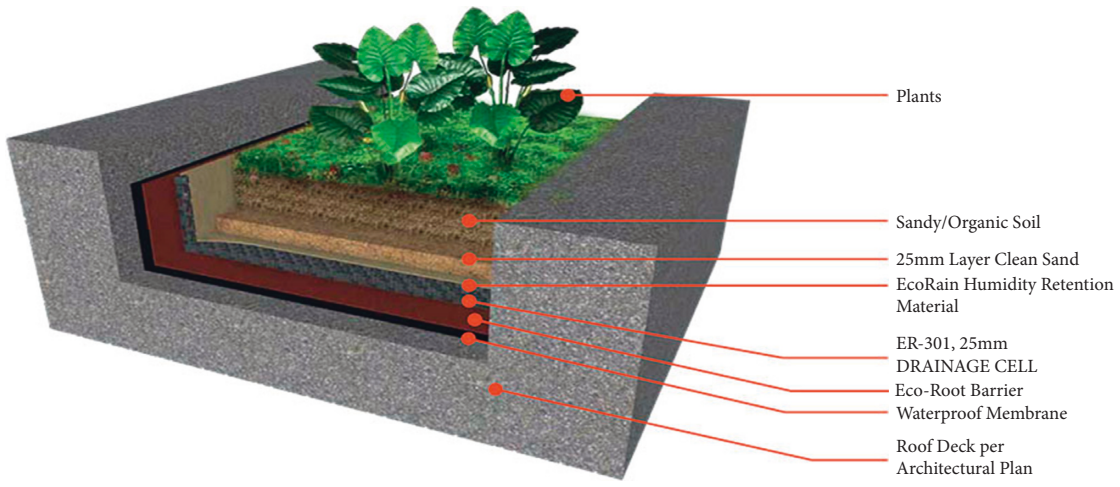

Figure 3: Green roof system [38].

construction. Creating the perfect growing environment is essential for green roof success. Unlike natural arable soil, this system is perfectly designed to fit the environment and does not become too heavy when wet. Eventually, the plants are planted. Cold and heat-resistant vegetation is used. Plants used for this purpose usually include herbaceous perennials, flowers, wild grasses, and mosses [29, 32–35].

2.3.2. Green Roof Components

(i) Plant layer:

While any plant could be planted mainly on the roof, barriers such as climate, building systems, maintenance costs, and ideas of green roof designers impact the final decision. As green roofs are built to be as light as possible, they also include plants that can grow in shallow soil [10, 19–21].

(ii) Growing medium:

The growing medium is the space in which plants begin to grow. Due to special structural requirements, the growing medium should have a lower weight than ordinary soil. In this case, the growing medium should be used as light as possible and weigh about 900 kg per cubic meter when it is wet. A typical mixture of one-third sand, one-third porous rock, and one-third artificial soil (a combination of rotten wood and vegetable manure) forms a suitable environment [23–25, 39–42].

(iii) Drainage layer:

Roofs usually hold a large amount of rainwater, which reduces the pressure imposed on the drainage system. However, there is always some excess water that must be drained. The drainage layer is applied between the growing medium and the protective layer for the rain and snow water to flow to the drainage system anywhere on the green roof [13, 55, 56]. The excess water can be disposed of in the following ways: 1- by the roof itself, 2- through gutters connected to slopes, and 3- waterways and water canals.

As a precaution, two outlet ducts or an outlet and a place for overflow should be installed. The outlets should be free of any plants, which is carried out by installing a valve on top of them for inspection. A terrace grid can be used in terraces [12].

The suitable drainage layer should be chosen based on the maximum water flow determined using precipitation details. The compressive strength, including its drainage layer, should be appropriate as it supports the plant and the growing medium [39–41]. A dense layer of extended soil is used for specific structures. But most green roofing companies use a corrugated plastic drainage mat with a structural pattern. The lowest possible drainage layer thickness is equivalent to standard 20 mm cardboard, but thicker mats will include an extra insulation layer [25, 39]. The drainage layer itself can be a complex collection of other layers.

(iv) Filter layer:

A filter between the growing medium and the drainage layer removes moisture from the root environment and prevents root rot. This filter can contain a fabric texture used in the nonwoven system. Even modern geo-textile filters can usually be a layer of sand in one or two layers, which may be combined with the drainage layer [43].

(v) Root barrier:

It keeps the insulation and roof membrane from entering and destroying the roots. This layer is mostly used in the centralized system, placed under the final seal or waterproof thermal insulation or directly above it. This layer is generally made of a polyethylene shell and is often used in public projects where plants with strong and aggressive roots are grown and in which there is a lot of extra load [57–59].

(vi) Drainboard:

The top layer is filtered by a three-layer plate that extracts excess water from the roots. This layer serves as a defensive layer against the root as well. The middle layer, a conical cup, receives and retains excess water from the roots. Rainwater tends to minimize the rate of environmental emissions, causes air circulation, and avoids runoff from this layer. The bottom layer is a fabric filter that prevents damage to the membrane and insulation [30, 37].

(vii) Protection layer:

This layer includes coatings that protect the roof and insulation system from leakage and water penetration directly into the membrane. The protection layer covers the shield plate during operation. Based on the size and use of the green roof, this plate may be a strip of lightweight concrete, a sheet of solid insulation, a thick plastic sheet, a copper sheet, or a mixture of those. Most green roof structures do not generally need a shield and instead use a root barrier [17, 28, 60].

(viii) Roofing membrane or waterproofing layer:

This layer safeguards the roof against leakage and dripping. The membrane has been used both within an articulated waterproof layer and in the form of interconnected sheets. Selecting a proper membrane depends on the situation of the roof, price, and ease of installation and maintenance. In recent years, a product that combines a layer of root and membrane major barrier into one layer has been produced by some factories [17].

To avoid losing its effectiveness over time, a refining coefficient is entered in the calculations when calculating the required soil volume, which is carried out by adding a percentage of the soil.

3. The Benefits of Green Roofing

The quick urbanization and densification led to the reduction of green spaces. Sometimes, urban zones' natural resources and environmental values have been ignored. Among the suggestions to decrease the vitality loss in expansive cities, using adequately designed and implemented green rooftops with due regard to the natural environment is one of the most effective technologies [61]. Installing green roofs could aid in recovering the green areas in urban regions. Hence, green roofs can be viewed as an instance of environmental stewardship. It is usually implemented to depict environmental development activities and attempts that significantly guarantee perfect environmental resources necessary for current and next generations' lives. Green roof inventive plans are a collaborative attempt of the public and private sectors, including different stakeholders, like municipal managers, policy-makers, building designers, and builders, to improve the sustainability of cities [88]. In addition to their numerous benefits, green roofs can help reduce urban vitality loss, increase urban competitiveness, decorate the city, decrease urban pollution, and diminish urban pressures. It is possible to classify the contrast between green and traditional rooftops into two quantity and quality categories [61–63]. On green rooftops, the process of heat exchange is very distinct. Plants assimilate an incredible amount of sunshine through their natural processes, including photosynthesis, sweat, breath, and dissipation. When moving through to the roof of building materials, the rest of the sun's beams are converted into warm loads and affect the indoor conversation. Plants disappear and return water to the atmosphere, effectively regulating temperatures around them [16, 37].

Much research has been conducted to examine the benefits of green roofs in specific countries. Table 7 reports the number of studies in this field from 2006 to 2021 for twenty countries. Based on Table 7, about 40% of research has been conducted in Asia. Almost all of these studies conclude that green roofs are effective in reducing pollution and advancing the living environment, offering opportunities for inventiveness and improving social interactions [37, 50, 64].

Psychologists' research into the effects of flowers and plants on social behavior indicates that contact with nature and enjoying its beautiful scenery is an easy yet essential way to relax and soften the human spirit. Additionally, the calming effect that plants have on humans reduces society's psychological burden [63]. Besides, its comprehensive development of collective biological complexes can help reduce aggression, depression, and suicide and create spaces for human beings, especially the elderly, to relax and relieve themselves [50]. Some of the other benefits of green space can be listed as follows [37, 50, 61–66]:

Table 7: Green roof research by country from 2006 to 2021.

Country	#
China	10
Italy	6
Australia	4
Poland	4
Korea	4
Spain	3
Canada	2
Egypt	2
Japan	2
Iran	2
Taiwan	2
UK	2
Austria	1
Belgium	1
Chile	1
Colombia	1
France	1
Germany	1
Indonesia	1
Israel	1
Jordan	1
Lithuania	1
Malaysia	1
The Netherlands	1
Norway	1
Portugal	1
Saudi Arabia	1
Slovakia	1
Turkey	1
USA	1

(i) Adjustment to climate change: green space changes natural conditions and influences climate change.

(ii) Acting as a protective cover: green roofs cover and preserve the roof of the building while reducing the need for repairs. They prevent extreme temperature changes and fires due to grass and soil insulation layers by extending the roof's lifespan by shielding the building from natural or human-made destructive factors.

(iii) Providing wildlife habitat: green roofs contribute to the beauty of the residential unit and the surrounding area and give children happy and safe recreational spaces to play and older people to exercise.

(iv) Reducing the impact of urban heat islands: turning housing roofs into green spaces increases the exchange of air between high building density areas and free spaces between suburbs and the city center. This regulates the air temperature in the city center. In the city center, density increases the temperature and warms the air. The city center's air temperature is 2 to 3 degrees colder than in the suburbs.

(v) Improving the city's drainage system as a whole and balancing water levels outside the city.

(vi) The potential for sound insulation and thermal energy storage while minimizing energy consumption.

(vii) Roof gardens, especially in densely populated areas, help to improve air quality. In addition to absorbing dust, generating oxygen, and cooling the city during the hot summer months, plants, whether planted on the ground, on the walls, or on the roof of a house, will extend the green landscape and natural space.

Green roofs have several consequences for the city's ecology, the regional economy, and other facets of the urban climate. [37, 50, 64]. Overall, these effects can be summarized into the following six advantage groups:

(1) Soundproofing: in urban areas, streets are a big concern. Even though the façade covering helps reduce sound penetration, that is, reduce the amount of commotion from the outside to the inside of the house, the type of roof also impacts the overall noise pollution entering the house. Within the roof system, green rooftops maximize sound coverage. These rooftops diminish commotion by storing, reflecting, and transmitting sound waves. Soils and plants absorb and trap acoustic frequencies, which prevent their proliferation.

(2) Reducing heat effects: large cities rapidly absorb the sun's radiant heat and act as sources of heat emission due to their high levels of hard impermeability and lack of vegetation. The "urban heat island" phenomenon is one such condition. In this situation, there is a significant temperature difference between asphalt and bitumen-covered urban areas and vegetation-covered areas. Asphalt and concrete surfaces create a heat island. The ceilings and streets represent heat and light and establish a temperature bubble over the towns at dusk. However, according to research, the area's climate is influenced by the urban heat phenomenon, thus increasing the use of climate control and cooling equipment, which raises energy consumption, and the greenhouse gas phenomenon, which is the critical factor in ozone depletion. In terms of the region's surface energy and climate characteristics, a deeper understanding of the landscape and how the changes in the cover that are associated with urbanization happen over time can be very useful.

(3) Reducing air pollution: trees have a remarkable contribution in urban areas to decreasing the urban air toxic pollutants. By lowering the surface temperature, they decrease the photochemical responses of toxic pollutants such as ozone in the air.

(4) Reducing carbon dioxide: global warming is normally caused by the natural climate cycle. However, excessive use of fossil fuels has also contributed significantly to this phenomenon. Carbon dioxide is produced as a by-product of the combustion of fossil fuels. This compound prevents the infrared wave that is radiated back from Earth during a sunny day from leaving the atmosphere, which increases the average temperature. The vegetation on green rooftops absorbs carbon dioxide and reduces the overall temperature by allowing the radiation to leave the atmosphere in the absence of this compound.

(5) Reducing the load of sewage systems: green roofs decrease the flow of surface water, which improves the efficiency of the water flow and reduces the overflow of wastewater. Green roofs will carry 80–70 percent water in summer and 25–40 percent in winter. Eventually, water stored in the soil may evaporate or return to outer space. Furthermore, water flow is delayed due to soil saturation, which retains moisture and urban surface water, especially during seasonal rainfall, and storing it prevents runoff and overflow. Green roof vegetation can consume and remove more than 95 percent of cadmium, copper, lead, and 16 percent of "zinc" from the rainwater and significantly reduce nitrogen levels.

(6) Reducing heat transfer through building energy storage: during summer, green roofs help cool the roof space and keep it warm in winter by minimizing temperature fluctuations on the outside of the roof. In the winter, foliage reduces freezing, raising the roof's insulation.

Overall, the benefits of a green roof can be categorized into four classes as represented in Table 8.

3.1. Impact of Green Roofs on Climate Resilience Enhancement in Buildings. As a sustainable building element, the impact of green roofs is to improve the new and current buildings' resilience according to climate change conditions, energy demand, and indoor comfort. Despite the slightly increasing deterioration of indoor comfort conditions over time, it is noteworthy to mention that a green roof decreases the effects of external temperature fluctuations due to climate change. Green roofs are effective in improving the buildings' climate resilience. It should be noted that the impact made on indoor comfort is not the mere consequence of green roofs. Green roofs play a major role in mitigating the impact of urban heat islands and thus improving outdoor comfort condition. According to the relevant research background, such an impact depends considerably on the climatic region and the extent of the green roof dryness. This leads to a high and low level of mitigation, which is commonly achieved in the evenings and on cloudy winter days, respectively [67]. Nevertheless, while temperature mitigation may be still achieved at the rooftop level, such an effect on urban heat islands at the pedestrian level is minor in all climate conditions. In such a scenario, additional greening interventions such as planting trees and urban vegetation at the street level are considered a more effective mitigation strategy [68], which may be combined with an urban green roof deployment [69–71].

Table 8: Summary of the benefits of green roofs.

Class	Function
Ecological	Conservation of biodiversity, habitat creation and improving the ecological-biological quality of the city
Eclipse	Reducing the effect of heat islands and cold winds through thermal insulation
Environmental	Improving air quality by purifying airborne particles, exchanging oxygen and carbon dioxide, reducing noise through sound insulation, reducing the volume of rainwater runoff by preserving surface sewage, increasing water quality and preventing pollution, reducing the negative effects of electromagnetic radiation up to 99%
Economic and cultural	Reducing the cost of artificial ventilation, increasing the lifespan of roof insulation, increasing the value of the property, increasing the sense of belonging, saving energy by insulation in winter)

3.2. The Role of Green Roofs in Optimizing Energy Consumption. Green roofs reduce energy consumption for heating and cooling. Of the total solar radiation received by the green roof, 27% is reflected, the plant absorbs 60%, and 13% penetrates the soil [78–80, 101–105]. Studies have shown that green roofing can reduce the heat flow on the roof by 70% to 90% in summer and 10% to 30% in winter. This would also lead to a 75% decrease in the amount of energy consumption as well, because heat transfer is always from the body and space of the building [9, 17, 24, 28, 34, 81]. Therefore, the heat transfer from the roof is from inside to outside in winter and from outside to inside in summer. Still, this percentage varies according to the seasons and the amount of humidity. Green roofs reduce the cumulative electrical energy compared to the cumulative electrical energy consumed by conventional flat roofs during representative similar cooling demand periods. Therefore, extensive green roofs, especially with rubber crumbs as a drainage layer, can be a good tool for passive energy saving during summer in dry climates [82]:

(i) Heat transfer in summer:

Green roof layers help cool the roof space during the summer by reducing the heat fluctuations on the outer surface of the roof. They also increase the heat capacity of the roof by shading, moisture retention, and photosynthesis. The combination of soil reactions, photosynthetic reactions, and plant perspiration reduces the amount of solar energy absorbed by the roof layer. Green roof research suggests that most of the benefits of cooling in the summer are related to green roof sweating [9, 17, 20, 28, 48, 83, 84].

(ii) Heat transfer in winter:

In addition to increasing the heat capacity of the building by raising the roof layers, the green roof insulates the building against cold weather. It reduces energy consumption for heating the rooms by protecting the building with vegetation and soil and reducing wind speed [50, 77–79, 85, 86].

(iii) Roof insulation:

Plants continuously retain some air around their roots, which acts as a thermal insulation layer. The efficiency of this layer of thermal insulation in green roofs depends on the amount of moisture it retains. The higher the humidity of the roof, the lower its efficiency and the more heat it loses [47, 62, 81, 87].

(iv) Reducing the wind speed:

A study at the University of Toronto shows that green roofs in cold climates also have the necessary function to keep spaces warm. This study shows that the effect of green roofs in reducing the intensity of wind is greater than the effect of shading. Vegetation prevents the environment from freezing in winter, which increases the roof's insulation. It provides energy storage in winter [33, 36, 50, 78, 79, 85].

The temperature of flat roof and green roof spaces in winter shows that if the average daily temperature on a winter day is 0°C, the temperature of flat roof space is 0.2°C, and the temperature of green roof space is 4.7°C. This indicates that these roofs reduce heat transfer [9, 17, 24, 28, 34, 37, 48, 62, 83].

3.3. Green Roof and Economic Savings. The main portion of the roof has the role of a preservative wall that decreases the sun's direct radiation on the external wall, having a role in shadowing. This leads to the reduction of artificial ventilation expenses (cooling in summer) and an increase in property value. The environment temperature is disseminated vertically. Because of the perfect heat dissolution of the roof, the vertical air temperature does not alter considerably at night while it changes remarkably at noon. Because of suitable heat buffer, the front porch temperature is not too high, and as a result, the construction could be more efficient in the summer. Simultaneously, the roof equipped with shoulder eaves keeps the bamboo and wood elements safe against rainwater floods and extends the possible usage of building elements [91].

The cities of arid or semiarid zones may take advantage of preservative or no drainage and demand further water resources. Moreover, the evaporation forecast applications can complement precipitation forecasts to confine drainage while high evaporation demands are predicted. Cities do not have a similar number of flat roofs, and also, in some cities, the roofs do not have enough toughness to tolerate a blue layer to attenuate stormwater. It is necessary for roofs with adequate toughness to consider the extremes of future weather in their design by applying regional climate forecasts. Identifying the extremes of the upcoming weather could improve the decision process regarding the depth of

Table 9: Challenges and downsides of using green roofs.

Challenge	Main barriers
Budget	Compared to traditional roofs, the cost of building green roofs depends on the type, materials, climate, and the aesthetic decisions by customers
	Cheap electricity in some countries, which leads to the residents' unwillingness to install green roofs
	Lack of financial support from governmental or nongovernmental sources
	Different maintenance costs compared to traditional roofs
	Failure to provide public and private developers with financial facilities
	Lack of economically justified projects for developers from the public and private sectors
	Excess plant maintenance costs
	Lack of private-sector information on the benefits of investing in and supporting this sector
Managerial aspects and organizational policies	Nonconsideration of the green roof, along with other planning policies and urban green space architecture, as part of the sustainable green space scheme
	Failure to educate and inform municipality authorities, experts, and managers about the advantages of green roofs
	Lack of programs and technologies built-in municipalities and green space commissions to address the needs and challenges of green roofing
	Lack of symbolic public or private green roof projects
	Not using the successful experiences of other nations in this field
	Lack of consultants and contractors' persuasion concerning operations and researches
	Lack of local standards and a system for ongoing assessment to address challenges over time
Legal aspects	Lack of a legal basis for encouraging investment in this sector
	Lack of compulsory rules to build a green roof
Technical and scientific infrastructure aspects	Quick construction and fitting of ordinary roofs and easy access to their accessories and equipment
	Lack of awareness, practice, and relation with the green roofing industry
	Lack of the native green roofing contractors
	Lack of green roofing systems for residential houses, homes, etc.
	Lack of a robust framework of software and hardware to access information and equipment in the consultation and implementation phases
	The ability of traditional roofs to cover any type of building
	Lack of applied research for metropolitan areas to extend and justify green roofs and to assess different types of plant species
	Low scientific knowledge level for realistic evaluation in various local situations
	Inability to use mobile irrigation systems
Cultural aspects	Culturally normative compatibility with ordinary roofs
	Lack of participation and management space between individuals due to the growth and maintenance of green roofs in residential and commercial areas
	Lack of human capital and human staff preparation to construct, standardize and maintain green roofs
	Lack of nongovernmental bodies
	Lack of people's culture regarding the sensitivity and significance of environmental and climate issues and the need to improve the situation
	Lack of understanding of green roofs and their benefits by the public society
Geographical aspects	Lack of community awareness about green roofs and their benefits
	No green roofs in some metropolises or specific geographical areas within urban areas

the water preservation layer. Future research could explore factors that originated in the social and financial aspects of green roofs [43, 92–96].

3.4. The Performance of Green Roofs. The essential criteria to assess the performance of a green roof consist of aesthetic attraction, environmental contexts involving different types of climates, surface texture and depth, plant choice, methods of deployment, and preservation. The purpose of the design, easy deployment, and preservation asset allocation are the main criteria in specifying surface depth and plant choice that could affect aesthetics as well. Aesthetic goals should be considered before plant species selection since most species have their slumbering periods, such as native prairie grasses and perennials, in which the roof might not seem very "green" [90, 97–100].

Aesthetic attraction is more significant on small roofs developed for public services than on low-depth large roofs to manage stormwater. Some large roofs might not be easily seen from outside the building, and they could be viewed just from the air. Mixtures of evergreens and long-blooming flowering plants present a breathtaking sight while growing together. However, the dry weather of summer could change

flowering perennials into a pile of browned-out, dead-looking flowers that might become a fire danger as well. Likewise, grass can be difficult to keep green during the summer, specifically on large roofs [75]. Irrigation is necessary and surface depths should be deeper to bring up perennial flowering herbaceous plants and grasses on large roofs. If proper irrigation is not accessible, tender species, like Sedum, Sempervivum, and Delosperma, are suitable selections due to their ability to resist long-term drought situations and other harmful environmental factors that often exist on a roof.

The aforementioned criteria are mostly subjective factors. As for mathematically objective measures, the three important physical parameters governing the green roofs' energy performance are as follows: 1- coverage ratio (σf), 2- leaf area index (LAI), and 3- foliage temperature (Tf). LAI provides information on the depth that the solar radiation has to go through before reaching the roof, indicating the level of its attenuation by the vegetation. The coverage ratio, σf, identifies parts of the roof that are directly hit by solar radiation, which is then characterized by a different energy model [70]. On the other hand, the foliage temperature, Tf, is clearly an important parameter of the vegetation's energy model and, in turn, of the green roof's energy model.

4. Challenges

There are many obstacles to designing green spaces, especially green roofs. Moreover, there are some drawbacks to using green roofs as well. First and foremost, the roof of the building needs to be reinforced in order to build a green roof. Also, most of these roofs are not intended for human presence. However, with alternative structures being planned and introduced, this defect can also be eliminated [44]. Reasonable structural requirements often include green roofs. Many existing roofs are not ideal for green roofs due to the extra weight that the soil and plants force upon the structure of the building [45]. For example, a concrete structure transforms into a green roof much more effectively than a wooden or metal structure.

The vegetation options for green roofs depend on the climatic conditions, the amount of shade, and the quality of the region's water to preserve vegetation for all seasons [72]. It should be noted that plants with deep roots can harm the roof water insulation performance and create problems due to the difficulty of repair [73–75]. Hence, experts should be consulted when choosing the vegetation of such gardens. Disregarding the impact of aesthetics, climate and microclimate could significantly affect plant preference. Notably, different levels of temperatures, sweltering and freezing temperatures, the levels of irradiance, wind speed, and the volume of rainfall during the year could specify which types of plants can be used in a specific region. The drought tolerance can be significant since high solar radiation levels and low media moisture could be typically the standard, specifically in large shallow systems [89].

Similarly, microclimates on the roof are affected by some parameters. Roof angle and direction might impact the power of the sun that reaches the building and surface moisture content. The nearby constructions might make the shadow a part of the roof, chimneys, and air-conditioning facilities might dry the surface, and industrial constructions' chemical smoke might affect the growth of the plant. Environmental contexts such as the volume of rainfall and temperature levels could limit the possibility of using specific types of plants or could necessitate irrigation. Though aesthetic attraction is a significant factor on many roofs, the selected plants should first have the ability to survive the harsh environment of the rooftop of an urban building [66].

Another downside of green roofs is their initial cost of implementation, which is higher than ordinary roofs. However, this expense is paid only once in the long run and is minimal due to the benefits above. To summarize, the overall challenges and downsides of green roofs are tabulated in Table 9 [45, 72–74, 76, 77].

5. Conclusion

Sustainable architecture is one of the new trends and approaches in architecture that many contemporary designers and architects have considered in recent years. This architecture, which is one of the solutions in the field of sustainable development and seeks to adapt to the environment, is one of the basic human needs in today's world. Creating green buildings aims to improve the climate, prevent the loss of energy used for cooling and heating, and prevent the harmful effects of construction on the environment. One of the most important technologies in sustainable architecture is the green roof, which, if properly implemented, will reduce energy loss and improve the aesthetics of the building. This technology aims at slowing down the growing trend of energy consumption, its adverse effects, and irreparable damage to the natural environment. If properly designed and implemented with climatic considerations in mind, a roof garden or green roof can significantly help reduce energy consumption. Creating greenery in the backyard space leads to the blocking of sunlight and reduces surface evaporation and transpiration. These changes have a positive effect on cooling the city's climate and the region and the indoor air of the building on which they are located. This cooling is done by reducing heat fluctuations on the roof's outer surface and increasing the roof's heat capacity. This keeps the space under the roof cool in the summer and regulates the temperature during the winter. Due to the improvement of social, economic, and environmental conditions, green roofs have been included in the planning of most developed cities in the world. This is promising, especially while heat loss through the roof is considered high in the nineteenth article of the national building and housing regulations regarding energy consumption. The green roof acts as a thermal insulator by increasing the roof layers and controlling the heat exchange between the inside and outside of the building. This study aimed to review the green roof and the issues of green and sustainable buildings and their advantages and challenges. Recent research on green roofing has grown significantly. Green roofs represent an increasingly important passive component in urban buildings due to the many benefits that can be attributed to them, such as reducing air pollution. For a

future research project, we suggest that the obstacles to green roof implementation in developing countries be identified and ranked. Then, appropriate strategies can be adopted to address these challenges.

Data Availability

No data were used to support this study.

Conflicts of Interest

The authors declare that they have no conflicts of interest.

References

[1] P. D. Tortell, "Earth 2020: science, society, and sustainability in the anthropocene," *Proceedings of the National Academy of Sciences*, vol. 117, no. 16, pp. 8683–8691, 2020.

[2] L. Stephen, "75% of Earth's land areas are degraded. National Geographic website," 2018, https://news. nationalgeographic. com/2018/03/ipbes-land-degradation-environmental-damage-report-spd.

[3] M. Bedinger, L. Beevers, G. Walker, A. Visser Quinn, and K. McClymont, "Urban systems: mapping interdependencies and outcomes to support systems thinking," *Earth's Future*, vol. 8, no. 3, Article ID e2019EF001389, 2020.

[4] S. Pandey, S. Jain, and R. Gupta, "Review paper on forest conservation model and modern techniques for sustainable wilderness," *International Journal of Research*, vol. 2, no. 9, pp. 233–238, 2015.

[5] Y. Dusza, S. Barot, Y. Kraepiel, J. C. Lata, L. Abbadie, and X. Raynaud, "Multifunctionality is affected by interactions between green roof plant species, substrate depth, and substrate type," *Ecology and Evolution*, vol. 7, no. 7, pp. 2357–2369, 2017.

[6] S. Kratschmer, M. Kriechbaum, and B. Pachinger, "Buzzing on top: linking wild bee diversity, abundance and traits with green roof qualities," *Urban Ecosystems*, vol. 21, no. 3, pp. 429–446, 2018.

[7] H. Chen, J. Ma, J. Wei et al., "Biochar increases plant growth and alters microbial communities via regulating the moisture and temperature of green roof substrates," *Science of the Total Environment*, vol. 635, pp. 333–342, 2018.

[8] J. C. Lata, Y. Dusza, L. Abbadie et al., "Role of substrate properties in the provision of multifunctional green roof ecosystem services," *Applied Soil Ecology*, vol. 123, pp. 464–468, 2018.

[9] Y. He, H. Yu, A. Ozaki, N. Dong, and S. Zheng, "Influence of plant and soil layer on energy balance and thermal performance of green roof system," *Energy*, vol. 141, pp. 1285–1299, 2017.

[10] G. Krebs, K. Kuoppamaki, T. Kokkonen, and H. Koivusalo, "Simulation of green roof test bed runoff," *Hydrological Processes*, vol. 30, no. 2, pp. 250–262, 2016.

[11] W. Yu, S. Cheng, C. Miao, and G. Perng, "Green innovation of green roof technology-a case study: umweltverträgliche Dachtechnologieeine Fallstudie," *Materialwissenschaft und Werkstofftechnik*, vol. 48, no. 5, pp. 420–429, 2017.

[12] P. Bevilacqua, D. Mazzeo, and N. Arcuri, "Thermal inertia assessment of an experimental extensive green roof in summer conditions," *Building and Environment*, vol. 131, pp. 264–276, 2018.

[13] M. Maglionico and I. Stojkov, "A long-term hydrological modelling of an extensive green roof by means of SWMM," *Ecological Engineering*, vol. 95, pp. 876–887, 2016.

[14] Z. Peng and V. Stovin, "Independent validation of the SWMM green roof module," *Journal of Hydrologic Engineering*, vol. 22, no. 9, Article ID 04017037, 2017.

[15] V. Azeñas, J. Cuxart, R. Picos et al., "Thermal regulation capacity of a green roof system in the mediterranean region: the effects of vegetation and irrigation level," *Energy and Buildings*, vol. 164, pp. 226–238, 2018.

[16] M. Shafique, R. Kim, and K. Kyung-Ho, "Green roof for stormwater management in a highly urbanized area: the case of seoul, korea," *Sustainability*, vol. 10, no. 3, p. 584, 2018.

[17] Y. He, H. Yu, N. Dong, and H. Ye, "Thermal and energy performance assessment of extensive green roof in summer: a case study of a lightweight building in Shanghai," *Energy and Buildings*, vol. 127, pp. 762–773, 2016.

[18] A. Ávila-Hernández, E. Sima, J. Xaman, I. Hernandez-Perez, E. Tellez-Velazquez, and M. Chagolla-Aranda, "Test box experiment and simulations of a green-roof: thermal and energy performance of a residential building standard for Mexico," *Energy and Buildings*, vol. 209, Article ID 109709, 2020.

[19] S. De-Ville, M. Menon, and V. Stovin, "Temporal variations in the potential hydrological performance of extensive green roof systems," *Journal of Hydrology*, vol. 558, pp. 564–578, 2018.

[20] P. Bevilacqua, D. Mazzeo, R. Bruno, and N. Arcuri, "Surface temperature analysis of an extensive green roof for the mitigation of urban heat island in southern mediterranean climate," *Energy and Buildings*, vol. 150, pp. 318–327, 2017.

[21] C. Catalano, V. A. Laudicina, L. Badalucco, and R. Guarino, "Some European green roof norms and guidelines through the lens of biodiversity: do ecoregions and plant traits also matter?" *Ecological Engineering*, vol. 115, pp. 15–26, 2018.

[22] B. Hailemariam, "Suitable site selection for urban green space development using geographic information system and remote sensing based on multi criterion analysis," *International Journal of Human Capital in Urban Management*, vol. 6, no. 1, pp. 97–110, 2021.

[23] S. De-Ville, M. Menon, X. Jia, G. Reed, and V. Stovin, "The impact of green roof ageing on substrate characteristics and hydrological performance," *Journal of Hydrology*, vol. 547, pp. 332–344, 2017.

[24] C. L. Tan, P. Y. Tan, N. H. Wong et al., "Impact of soil and water retention characteristics on green roof thermal performance," *Energy and Buildings*, vol. 152, pp. 830–842, 2017.

[25] A. Mahdiyar, S. Tabatabaee, A. Abdullah, and A. Marto, "Identifying and assessing the critical criteria affecting decision-making for green roof type selection," *Sustainable Cities and Society*, vol. 39, pp. 772–783, 2018.

[26] T. M. Young, D. D. Cameron, and G. K. Phoenix, "Increasing green roof plant drought tolerance through substrate modification and the use of water retention gels," *Urban Water Journal*, vol. 14, no. 6, pp. 551–560, 2017.

[27] I. Ziogou, A. Michopoulos, V. Voulgari, and T. Zachariadis, "Implementation of green roof technology in residential buildings and neighborhoods of Cyprus," *Sustainable Cities and Society*, vol. 40, pp. 233–243, 2018.

[28] P. Karachaliou, M. Santamouris, and H. Pangalou, "Experimental and numerical analysis of the energy performance of a large scale intensive green roof system installed on an office building in Athens," *Energy and Buildings*, vol. 114, pp. 256–264, 2016.

[29] M. Köhler and D. Kaiser, "Evidence of the climate mitigation effect of green roofs A 20-year weather study on an extensive green roof (egr) in northeast Germany," *Buildings*, vol. 9, no. 7, p. 157, 2019.

[30] W.-D. Yu, S. Cheng, C. Miao, and G. Perng, "Green innovation of green roof technology - a case study," *Materialwissenschaft und Werkstofftechnik*, vol. 48, no. 5, pp. 420–429, 2017.

[31] L. Grunwald, J. Heusinger, and S. Weber, "A GIS-based mapping methodology of urban green roof ecosystem services applied to a Central European city," *Urban Forestry and Urban Greening*, vol. 22, pp. 54–63, 2017.

[32] P. A. Versini, A. Gires, I. Tchiguirinskaia, and D. Schertzer, "Fractal analysis of green roof spatial implementation in European cities," *Urban Forestry and Urban Greening*, vol. 49, Article ID 126629, 2020.

[33] M. Tang and X. Zheng, "Experimental study of the thermal performance of an extensive green roof on sunny summer days," *Applied Energy*, vol. 242, pp. 1010–1021, 2019.

[34] P. Bevilacqua, D. Mazzeo, R. Bruno, and N. Arcuri, "Experimental investigation of the thermal performances of an extensive green roof in the Mediterranean area," *Energy and Buildings*, vol. 122, pp. 63–79, 2016.

[35] S. Cascone, "Green roof design: state of the art on technology and materials," *Sustainability*, vol. 11, p. 3020, 2019.

[36] J. Cao, S. Hu, Q. Dong, L. Liu, and Z. Wang, "Green roof cooling contributed by plant species with different photosynthetic strategies," *Energy and Buildings*, vol. 195, pp. 45–50, 2019.

[37] M. Shafique, R. Kim, and M. Rafiq, "Green roof benefits, opportunities and challenges A review," *Renewable and Sustainable Energy Reviews*, vol. 90, pp. 757–773, 2018.

[38] B. Y. Schindler, L. Blaustein, R. Lotan, H. Shalom, G. J. Kadas, and M. Seifan, "Green roof and photovoltaic panel integration: effects on plant and arthropod diversity and electricity production," *Journal of Environmental Management*, vol. 225, pp. 288–299, 2018.

[39] C. Loiola, W. Mary, and L. Pimentel da Silva, "Hydrological performance of modular-tray green roof systems for increasing the resilience of mega-cities to climate change," *Journal of Hydrology*, vol. 573, pp. 1057–1066, 2019.

[40] S. A. Palermo, M. Turco, F. Principato, and P. Piro, "Hydrological effectiveness of an extensive green roof in mediterranean climate," *Water*, vol. 11, no. 7, p. 1378, 2019.

[41] Z. Zhang, C. Szota, T. D. Fletcher, N. S. Williams, and C. Farrell, "Green roof storage capacity can be more important than evapotranspiration for retention performance," *Journal of Environmental Management*, vol. 232, pp. 404–412, 2019.

[42] B. G. Johannessen, H. M. Hanslin, and T. M. Muthanna, "Green roof performance potential in cold and wet regions," *Ecological Engineering*, vol. 106, pp. 436–447, 2017.

[43] W. Gu, L. Wei, W. Zhang, and X. Yan, "Evolutionary game analysis of cooperation between natural resource- and energy-intensive companies in reverse logistics operations," *International Journal of Production Economics*, vol. 218, pp. 159–169, 2019.

[44] R. Berto, C. A. Stival, and P. Rosato, "Enhancing the environmental performance of industrial settlements: an economic evaluation of extensive green roof competitiveness," *Building and Environment*, vol. 127, pp. 58–68, 2018.

[45] X. Zhang, L. Shen, V. W. Tam, and W. W. Y. Lee, "Barriers to implement extensive green roof systems: a Hong Kong study," *Renewable and Sustainable Energy Reviews*, vol. 16, no. 1, pp. 314–319, 2012.

[46] T. Carson, M. Keeley, D. E. Marasco, W. McGillis, and P. Culligan, "Assessing methods for predicting green roof rainfall capture: a comparison between full-scale observations and four hydrologic models," *Urban Water Journal*, vol. 14, no. 6, pp. 589–603, 2017.

[47] M. Santamouris, "Cooling the cities – a review of reflective and green roof mitigation technologies to fight heat island and improve comfort in urban environments," *Solar Energy*, vol. 103, pp. 682–703, 2014.

[48] B. Scharf and I. Zluwa, "Case study investigation of the building physical properties of seven different green roof systems," *Energy and Buildings*, vol. 151, pp. 564–573, 2017.

[49] S. Cascone, F. Catania, A. Gagliano, and G. Sciuto, "A comprehensive study on green roof performance for retrofitting existing buildings," *Building and Environment*, vol. 136, pp. 227–239, 2018.

[50] S. H. van der Meulen, "Costs and benefits of green roof types for cities and building owners," *Journal of Sustainable Development of Energy, Water and Environment Systems*, vol. 7, no. 1, pp. 57–71, 2019.

[51] V. Stovin, G. Vesuviano, and S. De-Ville, "Defining green roof detention performance," *Urban Water Journal*, vol. 14, no. 6, pp. 574–588, 2017.

[52] M. A. Chagolla-Aranda, E. Sima, J. Xaman, G. Alvarez, I. Hernandez-Perez, and E. Tellez-Velazquez, "Effect of irrigation on the experimental thermal performance of a green roof in a semi-warm climate in Mexico," *Energy and Buildings*, vol. 154, pp. 232–243, 2017.

[53] R. Baraldi, L. Neri, F. Costa, O. Facini, F. Rapparini, and G. Carriero, "Ecophysiological and micromorphological characterization of green roof vegetation for urban mitigation," *Urban Forestry and Urban Greening*, vol. 37, pp. 24–32, 2019.

[54] A. Karczmarczyk, A. Baryla, and P. Kozuchowski, "Design and development of low P-emission substrate for the protection of urban water bodies collecting green roof runoff," *Sustainability*, vol. 9, no. 10, p. 1795, 2017.

[55] Y. Dusza, S. Barot, Y. Kraepiel, J. C. Lata, L. Abbadie, and X. Raynaud, "Multifunctionality is affected by interactions between green roof plant species, substrate depth, and substrate type," *Ecology and Evolution*, vol. 7, pp. 2357–2369, 2017.

[56] D. Yeom and P. La Roche, "Investigation on the cooling performance of a green roof with a radiant cooling system," *Energy and Buildings*, vol. 149, pp. 26–37, 2017.

[57] M. Maiolo, "Life cycle assessment of a bitumen anti-root barrier on a green roof in the mediterranean area," *Energy*, p. 23, 2018.

[58] D. H. Jang, H. S. Kim, and S. K. Choi, "Greenhouse test results for two years of sheet shaped root barrier materials apply to green roof system for sustainable building construction," *Journal of the Korea Institute of Building Construction*, vol. 11, no. 6, pp. 634–644, 2011.

[59] C. Oh, "Adhesion performance of electromagnetic induction heating pixture for the integration with a waterproof & root barrier sheet and a roof green unit system," *Journal of the Korean Institute of Building Construction*, vol. 18, pp. 463–469, 2018.

[60] I. Au, *Root Barrier Sheet for green Roof System*, 2010.

[61] J. Lamond, S. Wilkinson, and C. Rose, "Conceptualising the benefits of green roof technology for commercial real estate owners and occupiers," in *Proceedings of the Pacific Rim Real*

Estate Society, p. 1321, Christchurch, New Zealand, January 2014.

[62] J. Goussous, H. Siam, and H. Alzoubi, "Prospects of green roof technology for energy and thermal benefits in buildings: case of Jordan," *Sustainable Cities and Society*, vol. 14, pp. 425–440, 2015.

[63] B. Y. Alfred and C. G. Ofonedum, "Thermal benefits of green roof in the tropical region. Case study of Malaysia," *International Journal of Engineering Research and Technology*, vol. 5, 2016.

[64] M. F. Chow and M. A. Bakar, *Environmental Benefits of Green Roof to the Sustainable Urban Development: A Review*, Monash University, Australia, 2017.

[65] S. Tabatabaee, A. Mahdiyar, S. Durdyev, S. R. Mohandes, and S. Ismail, "An assessment model of benefits, opportunities, costs, and risks of green roof installation: a multi criteria decision making approach," *Journal of Cleaner Production*, vol. 238, Article ID 117956, 2019.

[66] R. Berto, C. Stival, and P. Rosato, "The valuation of public and private benefits of green roof retrofit in different climate conditions," *Values and Functions for Future Cities*, pp. 145–166, 2020.

[67] T. Susca, "Green roofs to reduce building energy use? A review on key structural factors of green roofs and their effects on urban climate," *Building and Environment*, vol. 162, Article ID 106273, 2019.

[68] G. Evola, G. Evola, F. Nocera et al., "Greenery systems for the mitigation of the urban heat island: a simulation experience for southern Italy," in *Innovation in Urban and Regional Planning*Springer, Neywork, NY, USA, 2021.

[69] T. Elliot, J. Babí Almenar, and B. Rugani, "Modelling the relationships between urban land cover change and local climate regulation to estimate urban heat island effect," *Urban Forestry and Urban Greening*, vol. 50, Article ID 126650, 2020.

[70] C. Gohr, J. S. Blumroder, D. Sheil, and P. L. Ibisch, "Quantifying the mitigation of temperature extremes by forests and wetlands in a temperate landscape," *Ecological Informatics*, vol. 66, Article ID 101442, 2021.

[71] M.-M. Fernandez-Antolin, J. M. del-Rio, F. del Ama Gonzalo, and R. A. Gonzalez-Lezcano, "The relationship between the use of building performance simulation tools by recent graduate architects and the deficiencies in architectural education," *Energies*, vol. 13, no. 5, p. 1134, 2020.

[72] I. Ezema, O. Ediae, and E. N. Ekhae, *Prospects, Barriers and Development Control Implications in the Use of Green Roofs in Lagos State*, Domestic, Nigeria, 2016.

[73] A. Mahdiyar, S. R. Mohandes, S. Durdyev, S. Tabatabaee, and S. Ismail, "Barriers to green roof installation: an integrated fuzzy-based MCDM approach," *Journal of Cleaner Production*, vol. 269, Article ID 122365, 2020.

[74] Z. Tong, *The Barriers of Green Roof Systems Implementation in Malaysia*, 2018.

[75] K. E. Lee, K. J. Williams, L. D. Sargent, C. Farrell, and N. S. Williams, "Living roof preference is influenced by plant characteristics and diversity," *Landscape and Urban Planning*, vol. 122, pp. 152–159, 2014.

[76] N. S. Williams, J. P. Rayner, and K. J. Raynor, "Green roofs for a wide brown land: opportunities and barriers for rooftop greening in Australia," *Urban Forestry and Urban Greening*, vol. 9, no. 3, pp. 245–251, 2010.

[77] A. Agbonyin and S. Zoras, *Techno-economic Inquiry into Implementation Barriers in Green Roof Adoption as an Energy Retrofit Measure in Temperate Climates: UK Study*, IOP Science, Bristol, England, 2020.

[78] M. J. Mirzababaie and M. Karrabi, "Implementing green roof technology: an investigation of the effects on energy demand, fuel consumption, and pollutant emission," *Clean Technologies and Environmental Policy*, vol. 21, no. 9, pp. 1873–1881, 2019.

[79] Y. Movahhed, A. Safari, S. Motamedi, and R. H. Khoshkhoo, "Simultaneous use of PV system and green roof: a techno-economic study on power generation and energy consumption," *Energy Procedia*, vol. 159, pp. 478–483, 2019.

[80] J. A. Pinzon, P. P. Vergara, L. C. P. da Silva, and M. J. Rider, "Optimal management of energy consumption and comfort for smart buildings operating in a microgrid," *IEEE Transactions on Smart Grid*, vol. 10, no. 3, pp. 3236–3247, 2019.

[81] M. Ebadati and M. A. Ehyaei, *Thermal Analysis Model Building with a green Roof and Energy Efficiency Management*, 2012.

[82] J. Coma, G. Perez, C. Sole, A. Castell, and L. F. Cabeza, "Thermal assessment of extensive green roofs as passive tool for energy savings in buildings," *Renewable Energy*, vol. 85, pp. 1106–1115, 2016.

[83] F. E. Boafo, J. T. Kim, and J.-H. Kim, "Evaluating the impact of green roof evapotranspiration on annual building energy performance," *International Journal of Green Energy*, vol. 14, no. 5, pp. 479–489, 2017.

[84] M. Eksi, D. B. Rowe, I. S. Wichman, and J. A. Andresen, "Effect of substrate depth, vegetation type, and season on green roof thermal properties," *Energy and Buildings*, vol. 145, pp. 174–187, 2017.

[85] S. S. Ab Azis, I. Sipan, M. Sapri, N. S. Mohd Yusoff, and H. Abdullah Hashim, "Comparison on energy saving: green roof and green wall," *Planning Malaysia Journal*, vol. 17, no. 9, 2019.

[86] A. Ávila-Hernández, E. Sima, J. Xaman, I. Hernandez-Perez, E. Tellez-Velazquez, and M. Chagolla-Aranda, "Test box experiment and simulations of a green-roof: thermal and energy performance of a residential building standard for Mexico," *Energy and Buildings*, vol. 209, Article ID 109709, 2020.

[87] T. Hong, C. Koo, J. Kim, M. Lee, and K. Jeong, "A review on sustainable construction management strategies for monitoring, diagnosing, and retrofitting the building's dynamic energy performance: focused on the operation and maintenance phase," *Applied Energy*, vol. 155, pp. 671–707, 2015.

[88] E. Shin and H. Kim, "Benefit–cost analysis of green roof initiative projects: the case of Jung-gu, Seoul," *Sustainability*, vol. 11, no. 12, p. 3319, 2019.

[89] J. Vanstockem, L. Vranken, B. Bleys, B. Somers, and M. Hermy, "Do looks matter? A case study on extensive green roofs using discrete choice experiments," *Sustainability*, vol. 10, no. 2, p. 309, 2018.

[90] L. F. M. Francis and M. B. Jensen, "Benefits of green roofs: a systematic review of the evidence for three ecosystem services," *Urban Forestry and Urban Greening*, vol. 28, pp. 167–176, 2017.

[91] H.-f. Wang and S.-c. Chiou, "Research on the sustainable development of traditional dwellings," *Sustainability*, vol. 11, no. 19, p. 5333, 2019.

[92] T. Busker, H. de Moel, T. Haer et al., "Blue-green roofs with forecast-based operation to reduce the impact of weather extremes," *Journal of Environmental Management*, vol. 301, Article ID 113750, 2022.

[93] M. M. Fernandez-Antolin, J.-M. del-Río, and R. A. Gonzalez-Lezcano, "Influence of solar reflectance and renewable energies on residential heating and cooling demand in sustainable architecture: a case study in different climate zones in Spain considering their urban contexts," *Sustainability*, vol. 11, no. 23, p. 6782, 2019.

[94] B. Bathaei, "Change Is of the Essence, Regenerating of Brown Fields (Landscape Revitalization of Tehran's Brick Kilns)," in *Proceedings of the 2nd International Conference on Architecture, Structure and Civil Engineering (ICASCE'16)*, UK, London, March 2016.

[95] W. Wu, X. Li, and S. Kadaei, "An experimental study on the lateral stress of composite steel wall structure by using self-compacting concrete," *Advances in Civil Engineering*, vol. 2022, Article ID 7772556, 9 pages, 2022.

[96] C. Gao, M. Hao, J. Chen, and C. Gu, "Simulation and design of joint distribution of rainfall and tide level in Wuchengxiyu Region, China," *Urban Climate*, vol. 40, Article ID 101005, 2021.

[97] Q. Quan, S. Gao, Y. Shang, and B. Wang, "Assessment of the sustainability of Gymnocypris eckloni habitat under river damming in the source region of the Yellow River," *Science of the Total Environment*, vol. 778, Article ID 146312, 2021.

[98] L. Xu, X. Liu, D. Tong, Z. Liu, L. Yin, and W. Zheng, "Forecasting urban land use change based on cellular automata and the PLUS model," *Land*, vol. 11, no. 5, p. 652, 2022.

[99] B. Bathaei and M. Abdel-Raheem, "Assessment of the relative importance of the main parameters used in the selection of the urban heat island mitigation strategies," *Construction Research Congress*, pp. 627–636, 2022.

[100] X. Xu, D. Niu, B. Xiao, X. Guo, L. Zhang, and K. Wang, "Policy analysis for grid parity of wind power generation in China," *Energy Policy*, vol. 138, Article ID 111225, 2020.

[101] X. Xu, D. Niu, L. Peng, S. Zheng, and J. Qiu, "Hierarchical multi-objective optimal planning model of active distribution network considering distributed generation and demand-side response," *Sustainable Energy Technologies and Assessments*, vol. 53, Article ID 102438, 2022.

[102] J. Yang, H. Liu, K. Ma, B. Yang, and J. M. Guerrero, "An optimization strategy of price and conversion factor considering the coupling of electricity and gas based on three-stage game," *IEEE Transactions on Automation Science and Engineering*, pp. 1–14, 2022.

[103] B. Bathaei, "special issue– international conference- architecture technology and the city workshop questions," vol. 61, no. 3, 2018.

[104] J. Fang, G. Kong, and Q. Yang, "Group performance of energy piles under cyclic and variable thermal loading," *Journal of Geotechnical and Geoenvironmental Engineering*, vol. 148, no. 8, 2022.

[105] S. Kadaei, S. M. Shayesteh Sadeghian, M. Majidi, Q. Asaee, and H. H. Mehr, "Hotel construction management considering sustainability architecture and environmental issues," *Shock and Vibration*, vol. 2021, Article ID 6363571, 13 pages, 2021.

Hindawi
Complexity
Volume 2022, Article ID 2698226, 11 pages
https://doi.org/10.1155/2022/2698226

WILEY | Hindawi

Research Article

Integration and Modeling of Multi-Energy Network Based on Energy Hub

Min Mou, Yuhao Zhou, Wenguang Zheng, and Yurong Xie

Huadian Electric Power Research Institute Co, Ltd., Hangzhou, Zhejiang 310000, China

Correspondence should be addressed to Min Mou; min-mou@chder.com

Received 24 June 2022; Revised 9 August 2022; Accepted 11 August 2022; Published 5 September 2022

Academic Editor: Xiaoqing Bai

The energy conversion units and energy storage equipment connected to the multi-energy system are becoming diversified, and the uncertain factors brought by distributed wind power and photovoltaic power generation make the system energy flow structure more complex, which brings great difficulties to the modeling and application of traditional energy hub modeling methods. This study deeply analyzes the multi-energy flow coupling structure and operation mechanism of multi-energy systems, and carries out the power flow calculation and analysis of multi-energy systems based on an energy hub, so as to ensure the safe and stable operation of regional energy. Based on the physical characteristics of energy systems such as power systems, thermal systems, and gas systems, this article studies the comprehensive power flow model including the electric-gas-thermal multi-energy coupling network and proposes the power flow decomposition of the energy supply subsystem and its applicable equation based on Newton–Raphson method. The effectiveness of the proposed method under different operation modes is verified by case studies. The calculation results show that under constant load, the energy hub running in fixing thermal by electricity (FEL) and fixing electricity by thermal (FTL) mode has little influence on the voltage of each node in the power sub-network. Within the constraint range, the natural gas flow obtained from the natural gas subsystem is coupled with the power subsystem to meet the load demand. The influence on the power flow at each node of the heat network is not obvious.

1. Introduction

With the popularization and development of multi-energy and low-carbon technologies, such as combined heat and power generation (CHP), heat pump, electric boiler and absorption refrigerator, the interaction between power network, heat pipe network and natural gas network in various links is closer, and the coordination between networks is stronger. Therefore, a new energy system with multiple types of energy such as natural gas, comes into being. Its main feature is multi-energy complementary coordination [1], unified planning, and unified scheduling of various energy sources such as electricity, gas, and heat. At the same time, based on the idea of interconnection, many energy supply systems can realize the dual interaction of energy and information for different individuals and regions like the internet [2]. This coordinated interconnection can not only improve the flexibility, security and economy of the system but also change the energy supply mode. The complementary advantages and synergistic benefits brought by this change can make up for the shortcomings of the separate operation of the traditional sub-energy system, which is of great significance to improve the energy utilization efficiency of the whole system. Therefore, it is highly praised by various countries [3].

In the integrated energy system, the energy is no longer a relatively independent relationship, but a coupling relationship. Obviously, the traditional energy network analysis methods can not reflect the real nature of the coupling network. Therefore, it is necessary to study the modeling of multi-energy systems to tap the energy supply advantages and potential of different energy systems [4]. The concept of power flow is not only limited to the AC/DC hybrid power flow algorithm of micro-grid [5], but also refers to a multi-energy flow calculation method that satisfies the analysis of coupled energy demand under the framework of an

integrated energy system. It can effectively evaluate the network operation state and is of great significance to realize safe and stable operation.

In the power flow analysis and optimization research of electric-gas combined energy systems, a study [3] proposes the optimal power flow calculation method of the electric-gas coupled energy system, in which the dual interior point method is used to calculate the optimal power flow. Although this method has the advantage of fast calculation speed, it is not suitable for solving non-convex optimization problems. In the power flow analysis and optimization research of electric-thermal combined energy systems, a study [6] proposes the power flow decomposition and comprehensive solution method for electric-thermal coupling systems. On this basis, one study [7] establishes the power flow model of the CHP energy supply system and analyzes its economic and social benefits.

In the power flow analysis and optimization research of the system considering the interaction and combination of multiple energy sources, the coupling relationship between electricity, gas, and heat is considered in detail in [8], and the corresponding power flow solution method is proposed. The study [9] uses the power flow decoupling method to transform the integrated energy system into an independent solution problem similar to the traditional form and puts forward a calculation method suitable for large-scale multi-energy power flow distribution. The study [10] comprehensively considers the actual operation constraints of each energy sub-network in the multi-energy system and realizes the multi-objective optimization calculation of comprehensive economy and emission. The study [11] coordinates the interests of all parties in the integrated energy system, constructs an optimization model with energy efficiency, economy, and environmental protection as indicators, and sets the Pareto frontier to obtain the optimal solution. Load demand will affect the operation of the integrated energy system with climate change. Therefore, the study [12] establishes the supply and demand power balance model of regionally integrated energy system under different scenarios according to different seasons and climate, selects the economy and environmental protection of the objective function, and considers the multiple operating conditions of the equipment, so as to solve the global optimal energy flow. Overall, there is still a lack of intuitive, easy, and general modeling methods for regional integrated energy networks.

This study proposes a multi-energy network integration and modeling method based on energy hub, which is not only the basis for studying the scheduling and planning of an integrated energy system, but also the basis of ensuring the reliability and safe operation of the multi-energy coupling system. Through power flow calculation, the value of each state quantity in the system can be obtained. The operation state of the equipment and various equipment parameters in the system can be adjusted during operation, which provides help for the dispatching organization to formulate a reasonable energy supply scheme and ensure the safe and optimal operation of the system.

2. Power Flow Modeling of Multi-Energy System

Various forms of energy can be divided into electricity, gas, heat, etc. they are connected to the multi-energy system as energy supply subsystems. In addition, there are various energy hub models and coupling equipment to realize the interaction and transformation between a variety of energy sources. Therefore, when solving the power flow state of the multi-energy system, it is necessary to consider that this interaction and transformation will make the sub-power flow of a single system affected by other systems. It can also be understood that the power flow equation of an energy subsystem contains the state variables of other subsystems. This study mainly studies the multi-energy system for electricity-gas-heat interaction [13]. Therefore, the comprehensive power flow model of the regional comprehensive energy system can be described as

$$\begin{cases} F_e\left(x_e, x_h, x_g, x_{eh}\right) = 0 \\ F_h\left(x_e, x_h, x_g, x_{eh}\right) = 0 \\ F_g\left(x_e, x_h, x_g, x_{eh}\right) = 0 \\ F_{eh}\left(x_e, x_h, x_g, x_{eh}\right) = 0 \end{cases}, \tag{1}$$

where F_e, F_h, F_g, and F_{eh}, respectively, represent the power equations of the electric, thermal, and gas energy supply subsystems and their energy hubs in the multi-energy system; x_e represents the variables related to the operation of the power subsystem [14]; x_h represents the variables related to the operation of thermal subsystem; x_g represents variables related to the operation of natural gas subsystem; x_{eh} represents the variables related to the operation of the coupling elements in the energy hub.

Due to the complex coupling relationship between each part of the energy network, the complexity of the coupled system is higher than that of the single energy system, and the solution method becomes more complex. For the coupling relationship, the electric-thermal-gas interaction part can be decoupled, and then the iterative solution results of each energy network can be coupled through the energy hub. When the iteration termination conditions are met, the power flow calculation results of each energy network can be output to realize the power flow solution of the multi-energy system. For this decomposition solution method, there is a more mature method, which is called the alternating decomposition method [15].

3. Power Flow Solution of Energy Supply Subsystem

When solving the multi-energy power flow distribution, the extended Newton–Raphson method is usually used as the iterative method for power flow solution [16]. The deviation of the power flow equation in the power flow iterative process of multi-energy system can be expressed by (2), and the iterative correction equation is shown in (3):

$$\left[\begin{array}{cccccccc}\Delta P & \Delta Q & \Delta\Phi & \Delta h & \Delta T_s & \Delta T_r & \Delta f\end{array}\right]^T, \tag{2}$$

$$\begin{cases}\Delta x^{(k)} = -\left[J^{(k)}\right]^{-1} F\left(x^{(k)}\right) \\ x^{(k+1)} = x^{(k)} + \Delta x^{(k)}\end{cases} \quad k = 0, 1, 2, \cdots n, \tag{3}$$

where ΔP is the active power deviation in the iterative process; ΔQ is reactive power deviation; $\Delta\Phi$ is the thermal power deviation of the thermal system; Δh is the head pressure deviation of the thermal system; ΔT_s, ΔT_r respectively represents the deviation of heating water temperature and return water temperature of thermal system; Δf is the natural gas flow deviation vector of the natural gas system. $x^{(k)}$ is the vector composed of state variables at the k^{th} iteration; $\Delta x^{(k)}$ is the correction vector for the state variable at the k^{th} iteration; $J^{(k)}$ is the Jacobian correction matrix at the k^{th} iteration; $F(x)$ is the power flow equation.

3.1. Power Subsystem. During the operation of multi-energy system, each node of the power subsystem can be numbered, as shown in Table 1.

The state variables in the iterative correction equation can be expressed by (4)–(6):

$$x_E^{(k)} = \left[\begin{array}{cc}U^{(k)} & \theta^{(k)}\end{array}\right]^T, \tag{4}$$

$$U^{(k)} = \left[\begin{array}{cccc}\dfrac{\Delta U_1^{(k)}}{U_1^{(k)}} & \dfrac{\Delta U_2^{(k)}}{U_2^{(k)}} & \cdots & \dfrac{\Delta U_m^{(k)}}{U_m^{(k)}}\end{array}\right]^T, \tag{5}$$

$$\theta^{(k)} = \left[\begin{array}{cccc}\theta_1^{(k)} & \theta_2^{(k)} & \cdots & \theta_{n-1}^{(k)}\end{array}\right]^T, \tag{6}$$

where $U^{(k)}$ and $\theta^{(k)}$ respectively represents the substitution vector of the voltage amplitude and the voltage phase at the k^{th} iteration.

The Jacobian matrix and its elements in the corresponding iterative correction process are shown in (7)–(11):

$$J_E^{(k)} = \left[\begin{array}{cc}H^{(k)} & N^{(k)} \\ M^{(k)} & L^{(k)}\end{array}\right], \tag{7}$$

$$H_{ij} = \frac{\partial \Delta P_i}{\partial \theta_j} = \begin{cases}-U_i U_j\left(G_{ij}\sin\theta_{ij} - B_{ij}\cos\theta_{ij}\right), & i \neq j \\ U_i^2 B_{ii} + Q_i, & i = j\end{cases}, \tag{8}$$

$$N_{ij} = \frac{\partial \Delta P_i}{\partial U_j} U_j = \begin{cases}-U_i U_j\left(G_{ij}\cos\theta_{ij} + B_{ij}\sin\theta_{ij}\right), & i \neq j \\ -U_i^2 G_{ii} - P_i, & i = j\end{cases}, \tag{9}$$

$$M_{ij} = \frac{\partial \Delta Q_i}{\partial \theta_j} = \begin{cases}U_i U_j\left(G_{ij}\cos\theta_{ij} + B_{ij}\sin\theta_{ij}\right), & i \neq j \\ U_i^2 G_{ii} - P_i, & i = j\end{cases}, \tag{10}$$

$$H_{ij} = \frac{\partial \Delta Q_i}{\partial U_j} U_j = \begin{cases}-U_i U_j\left(G_{ij}\sin\theta_{ij} - B_{ij}\cos\theta_{ij}\right), & i \neq j \\ U_i^2 B_{ii} - Q_i, & i = j\end{cases}. \tag{11}$$

3.2. Natural Gas Subsystem. When calculating the power flow of natural gas subsystem, the natural gas system can be compared with the power system, and the nodes can be numbered, as shown in Table 2.

When solving the power flow of natural gas subsystem, Newton–Raphson completes the power flow iteration process. According to the network modeling of natural gas subsystem, the node branch incidence matrix meets the node

$$A_{g,ij} = \begin{cases}1 & \text{flows into node } i \text{ from pipeline } j \\ -1 & \text{flows out of node } i \text{ from pipeline } _j \\ 0 & \text{no natural gas connection between pipeline } j \text{ and node } i\end{cases}. \tag{12}$$

The Weymouth equation can be replaced by (13), where $\pi_i = p_i^2$, $\pi_j = p_j^2$. And the branch pressure drop can be expressed by the node branch matrix as (14).

$$f_{ij} = K_{ij} s_{ij} \sqrt{\left|\pi_i - \pi_j\right|} = K_{ij} s_{ij} \sqrt{\left|\Delta\pi_{ij}\right|}, \tag{13}$$

$$\Delta\pi = -A_g^T \pi. \tag{14}$$

Table 1: Node number of power subsystem.

Node type	PQ node	PV node	Balance node
Node number	1, 2, ..., m	$m+1$, $m+2$, ..., $n-1$	n
Number of nodes	m	$n-m-1$	1

Table 2: Node number of natural gas subsystem.

Node type	Unbalanced node	Balance node
Node number	1, 2, ..., m	$m+1$, $m+2$, ..., n
Number of nodes	m	$n-m$

Combining (12)–(14), the unbalance deviation when using the Newton–Raphson method to solve the natural gas network power flow can be expressed as (15), the correction equation can be expressed as (16), and the elements of the Jacobian matrix are shown in (17).

$$M(\pi) = \begin{bmatrix} \sigma_1(\pi) \\ \cdots \\ \sigma_n(\pi) \end{bmatrix} = A_g K s \sqrt{\left| -A_g^T \pi \right|} - f, \tag{15}$$

$$\begin{cases} \varphi\pi^{(i)} = -\left[J^{(i)}\right]^{-1} M\left(\pi^{(i)}\right) \\ \pi^{(i+1)} = \pi^{(i)} + \varphi\pi^{(i)} \end{cases}, \tag{16}$$

$$\begin{cases} J_{ii} = \dfrac{1}{2} \displaystyle\sum_{j \in i} k_{ij} s_{ij} \left| \Delta\pi_{ij} \right|^{-\frac{1}{2}}, i = m \\ J_{ij} = -\dfrac{1}{2} k_{ij} s_{ij} \left| \Delta\pi_{ij} \right|^{-\frac{1}{2}} \text{Node } i \text{ is connected to node } j \\ J_{ij} = 0, \text{Node } i \text{ and node } j \text{ are not connected} \end{cases}. \tag{17}$$

To sum up, after analogy with the power flow of the power subsystem, the power flow calculation process of the natural gas subsystem shall be solved uniformly and iteratively according to the following steps:

(1) Input the original data of the natural gas system, such as network topology and node parameters; classify and number the nodes;

(2) The initial pressure value of each non-equilibrium node is given, and the number of iterations is zero;

(3) After each iteration, calculate the deviation and check each component of the unbalance; if the maximum value of each component after iteration is less than the given accuracy, stop the iteration; the pressure of the non-equilibrium node, the natural gas flow of the equilibrium node and the flow of each branch pipeline are calculated.

(4) Calculate the Jacobian matrix and modify the state variables;

(5) Add one to the number of iterations and return to step (3).

3.3. Thermal Network Subsystem. Similar to the natural gas system, the thermal subsystem can also be classified and numbered by a method similar to the power subsystem, as shown in Table 3.

The hydraulic model and thermal model can be obtained from the thermal system model. Combined with these two models, they can be transformed into the general power flow model of the thermal subsystem [17], as shown in (18):

$$\begin{cases} F_1\left(m_l, T_i^{in}, T_i^{out}\right) = C_l A_s m_l \left(T_i^{in} - T_i^{out}\right) - q_i \\ F_2\left(m_l\right) = B_h s m_l^2 \\ F_3\left(m_l, T_i^{in}\right) = C_s T_i^{in} - a_s \\ F_4\left(m_l, T_i^{out}\right) = C_r T_i^{out} - a_r \end{cases}. \tag{18}$$

When the Newton–Raphson method is used for unified iterative calculation of power flow in a thermal system, the selected state variable is (19), the correction equation is (20), and the Jacobian matrix and its elements are (21)–(24). The subscript of each matrix is the number of rows and columns of the matrix, m_{mix} is the number of nodes with pipeline crossing in the load node, $m_{non-mix}$ is the node without pipeline crossing in the heat supply network load node.

$$x = \left[\left(m_l\right)_{n_{pipe}} \left(T_i^{in}\right)_{n-m-1} \left(T_i^{out}\right)_{n-m-1} \right], \tag{19}$$

$$\begin{cases} \Delta x^{(i)} = -\left[J^{(i)}\right]^{-1} F\left(x^{(i)}\right) \\ x^{(i+1)} = x^{(i)} + \Delta x^{(i)} \end{cases}, \tag{20}$$

$$J = \begin{bmatrix} J_{11} & J_{12} & J_{13} \\ J_{21} & J_{22} & J_{23} \\ J_{31} & J_{32} & J_{33} \end{bmatrix}, \tag{21}$$

Table 3: Node number of the thermal subsystem.

Node type	Load node	Heat source node	Balance node
Node number	1, 2, ..., m	$m+1$, $m+2$, ..., $n-1$	n
Number of nodes	m	$n-m-1$	1

$$\begin{cases} J_{11} = \dfrac{\partial [F_1; F_2]}{\partial m_l} = \begin{bmatrix} \left(2B_h s |m_l|\right)_{n_{loop} \times n_{pipe}} \\ \left(C_l A_s \left(T_i^{in} - T_{oi}\right)\right)_{(n-1) \times n_{pipe}} \end{bmatrix} \\ J_{12} = \dfrac{\partial [F_1; F_2]}{\partial T_i^{in}} = \begin{bmatrix} (0)_{n_{loop} \times n} \\ (diag[C_l A_s m_l])_{(n-1) \times (n-1)} \end{bmatrix} \\ J_{13} = \dfrac{\partial [F_1; F_2]}{\partial T_i^{out}} = \begin{bmatrix} (0)_{n_{loop} \times n} \\ (diag[-C_l A_s m_l])_{(n-1) \times (n-1)} \begin{bmatrix} 0_m \\ E_{n-m-1} \end{bmatrix} \end{bmatrix} \end{cases}, \tag{22}$$

$$\begin{cases} J_{21} = \dfrac{\partial F_3}{\partial m_l} = \begin{bmatrix} (0)_{m \times m_{non-mix}} & \begin{bmatrix} (0)_{m_{non-mix} \times (n - m_{non-mix})} \\ \left(\left(-T_{i,j}^{in} \psi_k + T_{i,i}^{in}\right) \& 0\right)_{m_{mix} \times (n - m_{non-mix})} \end{bmatrix} \end{bmatrix} \\ J_{22} = \dfrac{\partial F_3}{\partial T_i^{in}} = (C_s)_{m \times m} \\ J_{23} = \dfrac{\partial F_3}{\partial T_i^{out}} = (0)_{m \times m} \end{cases}, \tag{23}$$

$$\begin{cases} J_{31} = \dfrac{\partial F_4}{\partial m_l} = \begin{bmatrix} \begin{bmatrix} \left(T_{i,i}^{out} - T_{oi}\right) \& \left(-T_{i,i}^{out} \psi_k + T_{oi}\right) \& 0 \\ (0)_{m_{non-mix} \times m} \end{bmatrix} & (0)_{m \times (n-m)} \end{bmatrix} \\ J_{32} = \dfrac{\partial F_4}{\partial T_i^{in}} = (0)_{m \times m} \\ J_{33} = \dfrac{\partial F_4}{\partial T_i^{out}} = (C_r)_{m \times m} \end{cases}. \tag{24}$$

Similar to the power flow calculation of the natural gas subsystem, the specific steps in the power flow calculation of thermal subsystem can be summarized as follows:

(1) Input the original data of the thermal system, including network topology and node parameters; classify and number the nodes, and select the balance node of the heating network [18, 19];

(2) The initial values of heating temperature and return water temperature of each pipeline flow and load node are given, and the number of iterations is zero;

(3) Calculate the unbalance after each iteration and check each component of the unbalance; if the maximum value of each component after iteration is less than the given accuracy, stop the iteration; calculate the balance node power and return water temperature;

(4) Calculate the Jacobian matrix and modify the state variables, and calculate the return water temperature of each node;

(5) Add one to the number of iterations and return to step (3).

4. Multi-Energy Network Power Flow Calculation

4.1. Power Calculation of Coupling Part Energy Hub. Multi-energy systems generally work in the grid connection mode, that is, they are directly connected with the power grid and other energy equipment through the tie line and obtain the energy transmitted by them [20]. Under the grid connection mode, the active and reactive powers of each equipment have been given, and the frequency of the power

subsystem is controlled by the large power grid [21]. In the process of power flow iteration, the calculation methods after coupling are different due to different operation modes. When the electric heating load is known, the interaction value between the energy hub and each network can be obtained. When the PQ node of the power system is taken as the balance node, its voltage and parameter values can be obtained, as shown in (25) and (26); Thus, the pressure and flow value of the equipment in the natural gas network coupled with the electric and thermal network can be obtained, as shown in (27).

$$\begin{cases} P_{e,i}^{MT} = v_{MT}\eta_{ge,i}^{MT}P_{g,i} \\ P_{g,i}^{MT} = v_{MT}P_{g,i} = P_{e,i}^{MT}/\eta_{ge,i}^{MT} \end{cases}, \tag{25}$$

$$\begin{cases} P_{e,i}^{AC} = v_{AC}P_{e,i} \\ P_{h,i}^{MT} = \eta_{gh,i}^{MT} * P_{e,i}^{MT}/\eta_{ge,i}^{MT} \\ P_{h,i}^{AC} = v_{AC}P_{e,i}\eta_{i}^{AC} = P_{e,i}^{AC} \\ P_{g,i}^{GB} = (1 - v_{MT})\eta^{GB} = \left(L_{h,i} - P_{h,i}^{MT} - P_{h,i}^{AC}\right)/\eta^{GB} \end{cases}, \tag{26}$$

$$\begin{cases} f_{MT} = P_{g,i}^{MT}/LHV \\ f_{GB} = P_{g,i}^{GB}/LHV \end{cases}, \tag{27}$$

where LHV is the low calorific value of fuel, also known as net thermal efficiency. Similarly, when the natural gas balance node is selected to be solved first, the electrical network parameters of the coupling equipment can be obtained by using (25) to (27) through the known quantity of the coupling matrix of the joint energy hub.

4.2. Power Flow Decomposition Algorithm for Multi-Energy Network. Combined with the modeling and power flow calculation methods in the above sections, this section introduces the power flow decomposition algorithm of multi-energy system. The multi-energy system power flow decomposition algorithm takes into account the interactive coupling of electricity, heat, gas, and other energy sources, realizes power flow calculation by decoupling them, and can adjust the correlation value between the hub and the energy network, so as to obtain a more accurate multi-energy flow distribution based on the interaction between electricity, heat, and gas [22]. Figure 1 shows the method of solving multi-energy system power flow and the specific steps can be expressed as follows:

(1) Input the network parameters of each energy subnetwork, node type, node injection energy, and the electric heating load demand of the system;

(2) Select the energy hub model and its operating parameters, generate the conversion matrix, and convert it into the corresponding network node parameters;

(3) According to the known quantity of electric heating load, the electrical demand is converted by using the conversion matrix;

(4) The power flow distribution is solved independently by using the energy supply subsystem model and its balance node parameters [23]; if the result converges, go to step (5); if not, correct the power exchange between the energy hub and the network and return to step (3);

(5) According to the power flow calculation results of each subsystem, the joint coupling equipment model pushes back and forth to calculate the parameters of the coupling network; if the constraints are met, go to step (6); if the results do not meet the constraints, adjust the parameter setting of the network coupling node and return to step (2);

(6) Output the result and end the operation.

5. Case Study

5.1. Basic Data. IEEE14 node, 9-node natural gas system, and 12 node thermal system are used as examples. In the coupling equipment part, CHP unit, gas boiler GB and central air conditioning AC are selected as the energy hub for coupling each energy system, and the grid-connected working mode is used for the system. The schematic diagram of the calculation example is shown in Figure 2. In the figure, EB, GB, and Hb are used to represent the electrical system bus, natural gas system bus and thermal bus, and the numbers represent the number of nodes. The following describes the configuration of network parameters and node configuration.

(1) In IEEE 14 node power system, node parameter setting is shown in Table 4 and node classification is shown in Table 5.

Among them, node 1 is the public connection point between the multi-energy system and the large power grid; Other PV nodes 2, 6, and 8 can be used as access points for new energy power generation equipment or coal-fired units and other power generation units; Node 3 is the connection point between the power system and the gas turbine to realize the coupling interaction with node 8 of the natural gas subsystem; Node 14 serves as the power load node connected to the air conditioning AC to realize the coupling with the heating network and the gas network; The remaining nodes except node 7 are regarded as load nodes.

(2) In the 9-node natural gas system, the node classification is shown in Table 6, and the network node parameter setting of the natural gas system is shown in Table 7.

Among them, GB1 is the constant pressure node of the system, GB8 and GB9 are constant pressure and constant current nodes, and other gas distribution nodes can be simplified to be expressed only by the flow. At the same time, as an output node of the natural gas network, GB8 is connected with the gas turbine (MT) to generate electric energy, which realizes the coupling and interaction between the two

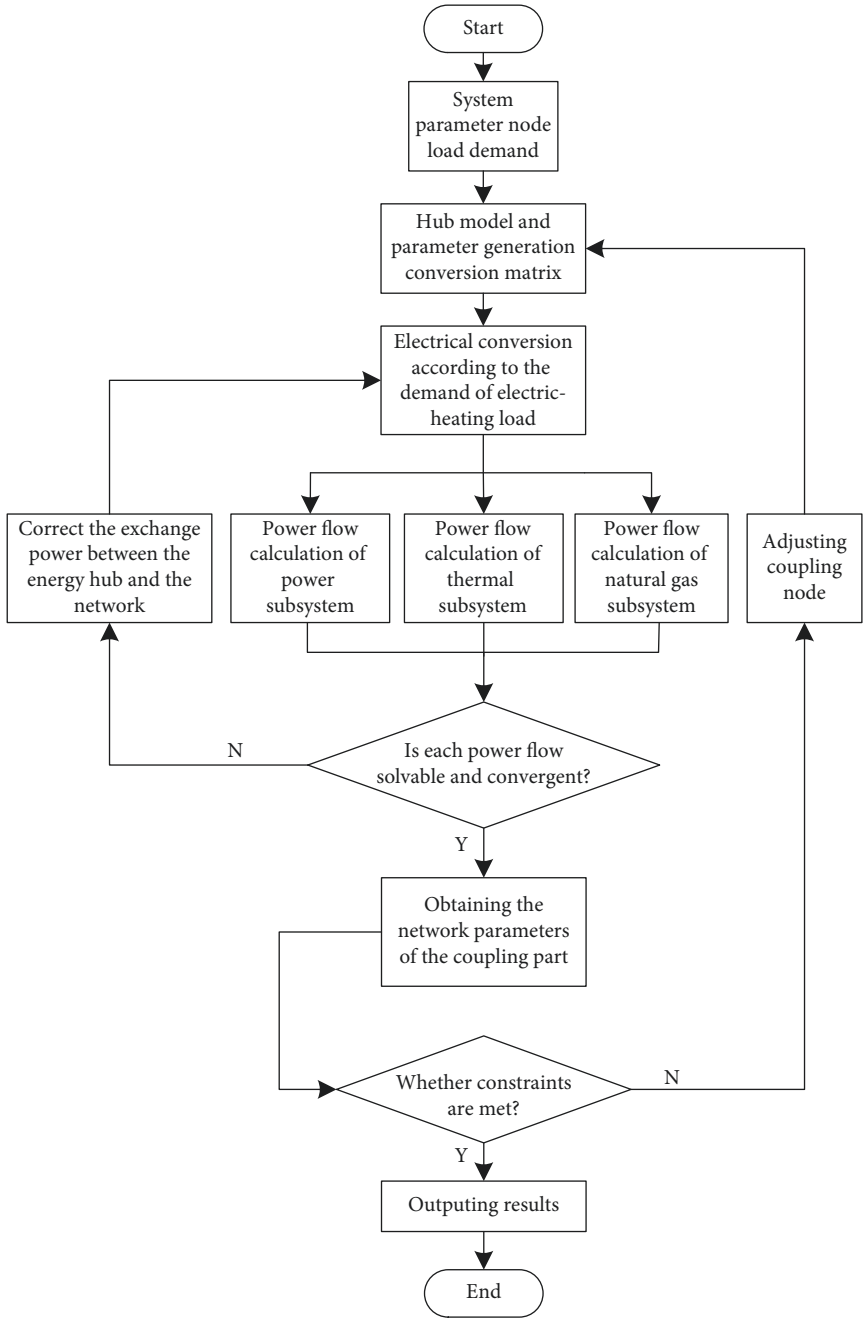

Figure 1: Flow chart of power flow decomposition algorithm.

electrical energy sources. The gas turbine generates heat, which realizes the coupling and interaction with the thermal system; as the access point of the gas-fired boiler (GB), GB9 realizes the coupling of the natural gas system and thermal network.

(3) In the 12-node thermal system, the load of each node is shown in Table 8, and the pipeline parameters and heating distance are shown in Table 9.

.In the thermal system, only node 12 is the heat source node, and the other nodes are the heating load nodes. The heat source nodes are connected with the energy hub, and are associated and coupled with the power grid and gas network through the air conditioning AC, gas turbine MT and gas boiler GB in the energy hub.

5.2. Energy Hub Parameters. The load parameters in the energy hub are taken respectively, and the electrical load L_e is 180 kW, the thermal load L_h is 300 kW and other loads L_o are 100 kW; the performance and parameters of the energy hub of the coupling part, such as gas turbine, transformer, distributed energy, and central air conditioning, are shown in Table 10.

The energy distribution coefficient shown in (28) can be coupled with other energy conversion parameters of the

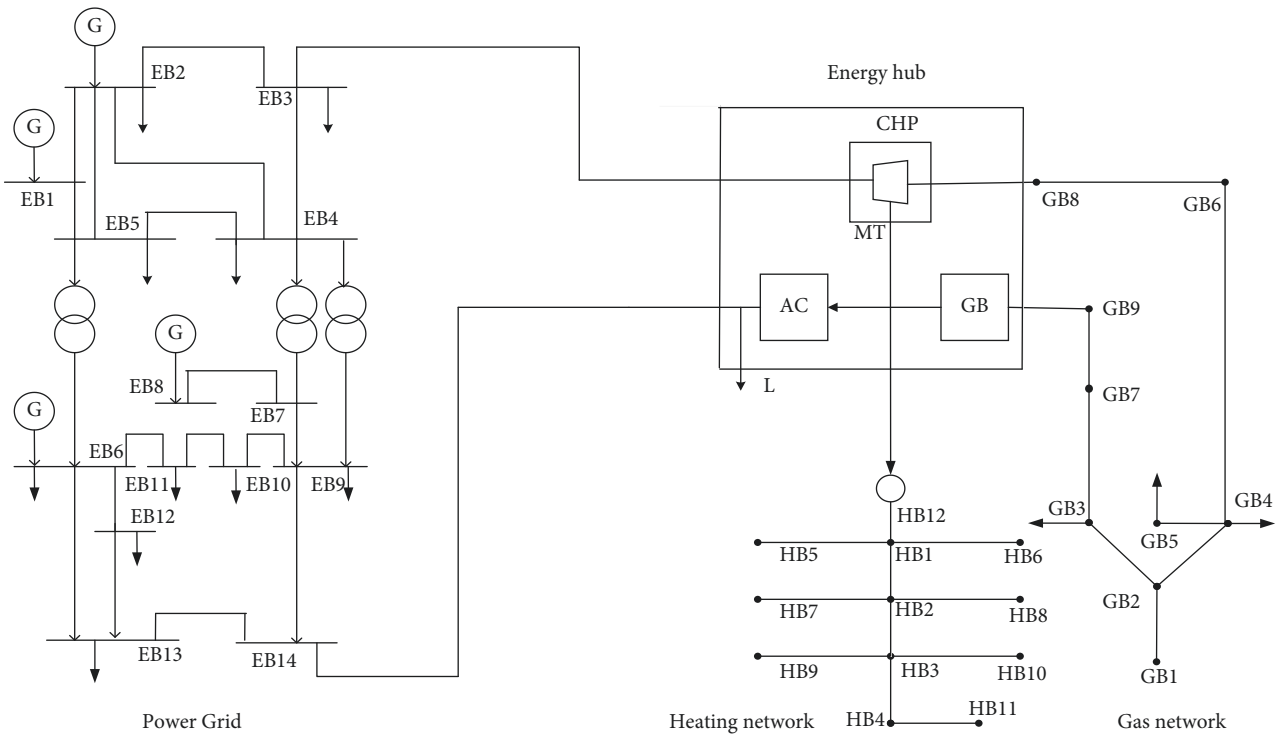

Figure 2: Schematic diagram of calculation example of the multi-energy system.

Table 4: Power system node parameters.

Node number	Generating power (MW)	Load power (MW)	Initial value of voltage (V)	Voltage setting value at PV node (V)
1	60	0	1	1.06
2	$65 + 42.4i$	21.7 + 12.7i	1	1.045
3	Pmt	$94.2 + 19i$	1	1.01
4	0	47.8 − 3.9i	1	0
5	0	7.6 − 1.6i	1	0
6	$85 + 12.24i$	$11.2 + 7.5i$	1	1.07
7	0	0	1	0
8	$17.36i$	0	1	1.09
9	0	$29.5 + 16.6i$	1	0
10	0	$9 + 5.8i$	1	0
11	0	$3.5 + 1.8i$	1	0
12	0	$6.1 + 1.6i$	1	0
13	0	$13.5 + 5.8i$	1	0
14	0	P_{ac}	1	0

Table 5: Power system node classification.

Node classification	Node number
Balance node	1
PV node	2, 3, 6, 8
PQ node	4, 5, 9, 10, 11, 12, 13, 14

Table 6: Node classification of natural gas subsystem.

Node number	Node classification
1	Gas source node
3, 4, 5, 8, 9	Gas distribution node

distributed device, and the energy distribution coefficient can be reduced.

$$\begin{bmatrix} 180 \\ 300 \\ 100 \end{bmatrix} = \begin{bmatrix} 0.95 \times (1 - v_{AC} - v_{oe}) & 0.35 \times v_{MT} & 0.1 \\ 0.62 \times v_{AC} & 0.43 \times v_{MT} + 0.81 \times (1 - v_{MT} - v_{og}) & 0.1 \\ v_{oe} & v_{og} & 0.98 \end{bmatrix} \begin{bmatrix} P_e \\ P_g \\ P_o \end{bmatrix}, \tag{28}$$

Table 7: Node parameter values of the natural gas subsystem.

Node number	Set value
1	$\pi_1 = 5$ MPa
2	$f_2 = 0$
3	$f_3 = 200\,m^3/h$
4	$f_4 = 150m^3/h$
5	$f_5 = 250\,m^3/h$
8	$\pi_8 = 5.5$ MPa, $f_8 = f_{MT}$
9	$\pi_9 = 6$ MPa, $f_9 = f_{GB}$

Table 8: Load of each node of the thermal subsystem.

Node number	Heat load power	Output temperature	Node number	Heat load power	Output temperature
1	0.15	40	7	0.1	40
2	0.15	40	8	0.1	40
3	0.15	40	9	0.25	40
4	0.15	40	10	0.15	40
5	0.15	40	11	0.2	40
6	0.15	40	12	—	—

Table 9: Thermal pipe network parameters.

Pipeline direction	Length	Diameter
12-1	500	200
1-2	400	200
2-3	600	200
4-3	400	200
1-5	200	200
1-6	150	200
2–7	180	200
2–8	150	200
3–9	100	200
3–10	110	200
4–11	90	200

Table 10: Equipment parameters in heat supply network.

Parameter variable	Type	Value
Micro gas turbine (MT)	Upper power limit	150
	Generating power	0.35
	Thermal power	0.43
Gas-fired boiler (GB)	Upper power limit	500
	Efficiency	0.81
Central air-conditioning (AC)	Upper power limit	200
	Efficiency	0.62
Transformer (T)	Efficiency Nt	0.95
	Efficiency Noe	0.1
Distributed energy	Efficiency Nog	0.1
	Efficiency No	0.98

where the distribution coefficient v_{oe} and v_{og} are almost zero. When the power flow is calculated first, the f_{MT} and f_{GB} can be solved by P_e^{MT} and P_e^{AC}, so as to solve the coupled natural gas network power flow; when the natural gas power flow is calculated first, the initial value can be set first, and then the corresponding electrical interaction value can be calculated, so as to solve the coupled power network power flow. After each interaction, the value of the coupling network is obtained, and the constraints of the integrated power flow network of the multi-energy system can be verified through back calculation, so as to adjust the distribution coefficient and stabilize the power flow distribution.

5.3. Result Analysis. The impact of different operation modes on the system power flow is analyzed to determine the power flow distribution of multi-energy systems. For more intuitive analysis, it is assumed that in the whole multi-energy system, only the input and output of the coupling node and balance node change, and the electric, gas, and heat energy input and load demand of other nodes are constant. The two operation modes of the energy hub are fixing thermal by electricity (FEL) and fixing electricity by thermal (FTL). In the electric heating mode, the natural gas can be obtained from the electrical quantity, and in the thermal heating mode, the electrical quantity can be obtained from the natural gas. By comparing the two modes, the initial solution of the power flow calculation of the system can be obtained, as shown in Table 11.

5.3.1. Power Subsystem. From the above data, we can get the voltage value of each node in the power subsystem under FEL and FTL modes. The results are shown in Figure 3.

Through the voltage results of each node shown in Figure 3, it can be found that the voltage amplitude of each node of the power subsystem in FEL mode is slightly higher than that in FTL mode, but the difference is extremely small and remains within the stable range. This shows that under the condition of constant load, the operation of the energy hub in FEL and FTL modes has little effect on the voltage of each node of power sub-network.

5.3.2. Natural Gas Subsystem. The pressure change at each node of the natural gas system under the two different operation modes is shown in Figure 4.

Table 11: Initial solution of power flow in multi-energy systems.

Operation mode	Power subsystem			Natural gas subsystem	
	P_{mt}	P_{ac}		f_{mt}	f_{gb}
FEL	90	50	⟶	27.65	18.51
FTL	97.65	43.37	←	30	20

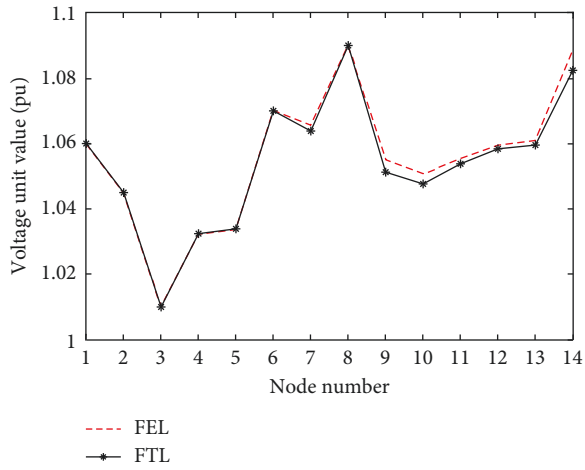

Figure 3: Voltage of each node in different modes.

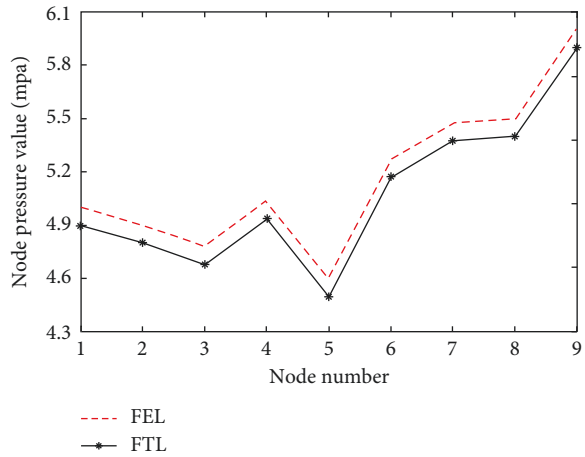

Figure 4: Pressure of each node in different modes.

From the node pressure results of the natural gas subsystem under different operation modes shown in Figure 4, it is not difficult to see that under the assumption that the load of the branch node does not change, the air pressure value of each node is stable within the rated working pressure. Here, the energy hub plays a regulating role, coupling and interconnecting the natural gas flow obtained in the natural gas subsystem with the power subsystem within the constraint range, and jointly output to meet the load demand.

5.3.3. Thermal Subsystem. The supply and return water temperature of each node of the thermal system under the above two operation modes are shown in Figures 5 and 6.

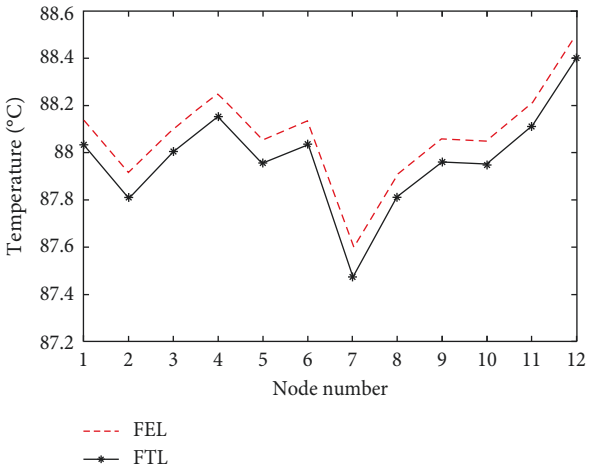

Figure 5: Water supply temperature at each node.

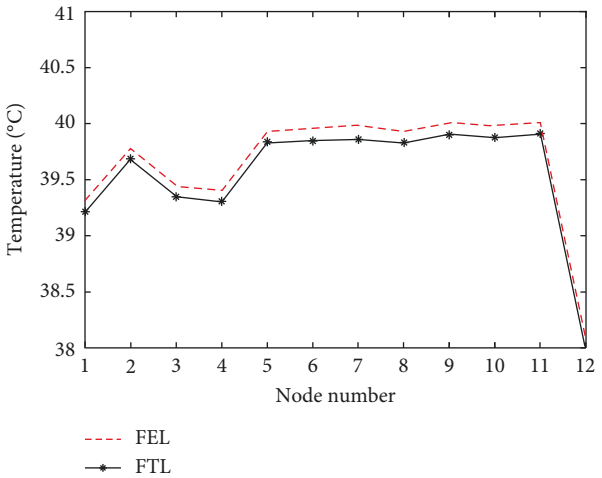

Figure 6: Return water temperature of each node.

It can be seen from Figures 5 and 6 that when the energy hub operates in two different modes, the variation range of heating water temperature and return water temperature at each node of the heat supply network is small, i.e., the impact of power flow at each node of the heat supply network is not obvious, which is related to the selection of the scale of the heat supply network system, and also because the delay change of the heat supply network is not reflected in time. Node 12 is a heat source node, and its heating temperature is the highest. Because it provides heat to other nodes, its temperature change is the largest.

6. Conclusion

This study models and analyzes the integrated network power flow when the multi-energy system is operating and analyzes the energy conversion relationship of the energy hub model. The Newton–Raphson method is used to calculate the power flow of each energy supply subsystem. At the same time, for the electrical-thermal interaction coupling unit, the electric heating load is decoupled in the multi-energy network. When the power flow is solvable, the cross-back derivation algorithm is used to adjust the interaction value between the hub and the network, so as to obtain an accurate multi-energy power flow distribution. Finally, according to the comprehensive power flow calculation method of multi-energy systems, the simulation examples and analysis of the corresponding electrical-thermal interaction system are given, and the power flow calculation results under different operating modes are compared and analyzed.

Data Availability

The data used to support the findings of this study are included within the article.

Conflicts of Interest

The authors declare no conflicts of interest.

Acknowledgments

This work was supported in part by the Key R&D Program of Zhejiang Province under Grants no. 2022C01206 and the S&T Major Project of Inner Mongolia Autonomous Region in China (2020ZD0018).

References

[1] E. J. Coster, J. M. A. Myrzik, B. Kruimer, and W. L. Kling, "Integration issues of distributed generation in distribution Grids," *Proceedings of the IEEE*, vol. 99, no. 1, pp. 28–39, 2011.

[2] W. Wang, D. Wang, and H. Jia, "Review of steady-state analysis of typical regional integrated energy system under the background of energy internet," *Proceedings of the CSEE*, vol. 36, no. 12, pp. 3292–3306, 2016.

[3] T. Li, *Model Research and Evaluation Analysis of User-Based Building Distributed Energy Supply System*, Shanghai Jiao Tong University, 2013.

[4] G. Zhang, *Research on Modeling and Optimization of Distributed Energy Network Based on Energy Hub*, North China Electric Power University, 2021.

[5] L. Chen and X. Lin, "Modeling and multi-objective optimal dispatch of micro energy grid based on energy hub," *Power System Protection and Control*, vol. 47, no. 6, pp. 9–16, 2019.

[6] X. Liu, N. Jenkins, J. Wu, and A. Bagdanavicius, "Combined analysis of electricity and heat networks," *Energy Procedia*, vol. 61, pp. 155–159, 2014.

[7] R. Lund and B. V. Mathiesen, "Large combined heat and power plants in sustainable energy systems," *Applied Energy*, vol. 142, no. 1, pp. 389–395, 2015.

[8] X. Xu and H. Jia, "Research on hybrid power flow algorithm of electricity/gas/heat in regional integrated energy system," *Proceedings of the Chinese Society for Electrical Engineering*, vol. 35, no. 14, pp. 3634–3642, 2015.

[9] M. Moeini-Aghtaie, A. Abbaspour, M. Fotuhi-Firuzabad, and E. Hajipour, "A decomposed solution to multiple-energy carriers optimal power flow," *IEEE Transactions on Power Systems*, vol. 29, no. 2, pp. 707–716, 2014.

[10] W. Lin, "Xiaolong Jin, et al. Multi-objective optimal hybrid power flow algorithm for regional integrated energy system," *Proceedings of the Chinese Society for Electrical Engineering*, vol. 37, no. 20, pp. 5829–5839, 2017.

[11] C. Chen and X. Shen, "Multi-objective optimal scheduling method for integrated energy system considering exergy efficiency," *Power system automation*, vol. 658, no. 12, pp. 78–86, 2019.

[12] Bo Yu and L. Wu, "Optimization scheduling method for regional integrated energy system," *Electric power construction*, vol. 37, no. 1, pp. 70–76, 2016.

[13] T. Ma, J. Wu, and H. A. O. Liangliang, "The energy flow modeling and optimal operation analysis of micro energy grid based on energy hub," *Power System Technology*, vol. 42, no. 1, pp. 179–186, 2018.

[14] C. Wei, Y. Zhao, Y. Zheng, L. Xie, and K. M. Smedley, "Analysis and design of a non-isolated high step-down converter with coupled inductor and ZVS operation," *IEEE Transactions on Industrial Electronics*, vol. 69, no. 9, pp. 9007–9018, 2022.

[15] Y. Shang, *Multi-energy System Modeling and Power Flow Optimization Analysis*, Northeastern University, 2018.

[16] Y. Wang, J. Zhao, and F. Wen, "Market equilibrium of multi-energy system with power- to-gas functions," *Automation of Electric Power Systems*, vol. 39, no. 21, pp. 1–10, 2015.

[17] Y. Zhang, X. Wang, and J. He, "Optimal energy flow calculation method of integrated energy system considering thermal system modeling," *Transactions of China Electrotechnical Society*, vol. 34, no. 3, pp. 562–570, 2019.

[18] M. Mou, D. Lin, Y. Zhou, W. Zheng, J. Ruan, and D. Ke, "An optimal allocation strategy for multi-energy networks based on double-layer non-dominated sorting genetic algorithms," *Complexity*, vol. 2019, pp. 1–11, 2019.

[19] M. Mou, Y. Zhou, W. Zheng, Z. Zhang, D. Lin, and D. Ke, "Real-time optimal control strategy for multi-energy complementary microgrid system based on double-layer non-dominated sorting genetic algorithm," *Complexity*, vol. 2020, pp. 1–12, 2020.

[20] X. Zhao, L. Yang, and X. Qu, "An improved energy flow calculation method for integrated electricity and natural gas system," *Transactions of China Electrotechnical Society*, vol. 33, no. 3, pp. 467–477, 2018.

[21] D. Xiao, H. Chen, C. Wei, and X. Bai, "Statistical measure for risk-seeking stochastic wind power offering strategies in electricity markets," *Journal of Modern Power Systems and Clean Energy*, 2021.

[22] G. Chicco and P. Mancarella, "Matrix modelling of small-scale trigeneration systems and application to operational optimization," *Energy*, vol. 34, no. 3, pp. 261–273, 2009.

[23] C. Wei, J. Xu, Q. Chen, C. Song, and W. Qiao, "Full-order sliding-mode current control of permanent magnet synchronous generator with disturbance rejection," *IEEE J. Emerging Sel. Top. Ind. Electron., early access*, 2022.

Hindawi
Complexity
Volume 2022, Article ID 3522883, 12 pages
https://doi.org/10.1155/2022/3522883

Research Article

Evaluating and Identifying Climatic Design Features in Traditional Iranian Architecture for Energy Saving (Case Study of Residential Architecture in Northwest of Iran)

Amirmasood Nakhaee Sharif,[1] Sanaz Keshavarz Saleh,[2] Sadegh Afzal,[3] Niloofar Shoja Razavi,[4] Mozhdeh Fadaei Nasab,[5] and Samireh Kadaei[6]

[1]*Faculty of Art and Architecture, Department of Architecture, Islamic Azad University of Mashhad, Mashhad, Iran*
[2]*Department of Architecture, Zanjan Branch, Islamic Azad University, Zanjan, Iran*
[3]*Department of Mechanical Engineering, University of Mohaghegh Ardabili, Ardabil, Iran*
[4]*Department of Architecture and Urbanism, M.A. Graduated of Urban Development, Imam Khomeini International University (IKIU), Qazvin, Iran*
[5]*Faculty of Payame Noor University of Sirjan, Sirjan, Kerman, Iran*
[6]*Department of Architecture, Faculty of Art and Architecture, Bushehr University, Bushehr, Iran*

Correspondence should be addressed to Samireh Kadaei; samira.kadaei@gmail.com

Received 30 March 2022; Revised 28 June 2022; Accepted 22 July 2022; Published 5 September 2022

Academic Editor: Chun Wei

In the last decades, researchers have been considering some fundamental issues such as energy saving, global warming, greenhouse emissions, and non-renewable energy to make models of house environmental standards to achieve a suitable consumption pattern for saving energy. In architecture, using natural energy is one of the essential pillars of design because it was one of the criteria of designing, which was considered on climate and geography, and it has been a high performance of climate adaptation in the modeling of traditional houses. In this research, Azerbaijan (located in northwestern Iran) is selected to evaluate the practical features of traditional Iranian houses designed in the cold climate, and criteria for developing sensible solutions to achieve a suitable design model for energy saving are provided. The primary purpose of this paper is to evaluate and identify the features of climate design in traditional houses in a cold climate, which are suitable residential buildings for energy management, and to identify the components affecting energy saving. The data collection method is based on checklists, observation, considering the orientation, density, solar radiation angle in the region, documentary, analysis of maps, and adaptation of the architectural plan of the studied houses with the pattern of solar radiation in the area. This research discusses the design criteria for future structures and their adaptable measures based on the obtained results. Finally, it is declared that the traditional architectural design model follows the region's climatic conditions, and considering the current climate and energies, traditional houses were designed; therefore, the best model for maximum use of available energy is climatic design. As a result, suggestions are made regarding residential architecture design to save energy.

1. Introduction

Increasing fossil fuel consumption and carbon dioxide production levels need no further stress globally, and maximum energy saving is a universal goal. Statistics show that the construction sector is one of the largest energy consumers worldwide [1]. As the number of people living in urban areas is expected to grow to almost 70% by 2050, the energy consumption in cities is likely to follow that trend. Therefore, urban energy efficiency will be critical [2].

Due to the rate of economic development and growing population densities in the world, the majority of these cities are dominated by high-rise apartment buildings [3]. The improvement of building services and comfort level and

growth in population has increased energy consumption to the level of transport and industry [4]. The research undertaken by Ref. [5] specified that buildings consume 40% of world energy. The massive magnitude of energy consumption in buildings for cooling and heating by heaters and air-conditioner systems portrays a considerable problem for the system. Available statistics state that the Heat, Ventilation, and Air Conditioning (HVAC) systems in standard buildings account for more than 50% of annual energy consumption globally [6]. This state, coupled with the threat of increasing global temperature and energy cost, induces the need to regulate the temperatures in these buildings [7–10].

In the construction sector of Iran, this issue's importance has been raised, and initial measures in this regard have begun. Currently, according to fuel consumption statistics, energy optimization is vital, especially in the construction sector and in the layout of spaces and the orientation of the building to the natural energies of the sun and wind, etc. The average energy consumption in Iranian buildings per square meter is about 310 kWh per year, which in the same situation in European countries is about 120 kWh per square meter. Therefore, energy consumption in Iranian buildings is about 2.5 times that of European countries. Implementing appropriate methods in designing buildings that coordinate with the place's climate has always been the focus of architects.

The crisis in the relationship between humans and nature, as well as the population density and congestion of information in the current age, is leading to a tense atmosphere in life [11–13].

The various forms existing in our nature have special meanings, which all come from the proper orientation and climate of the area. The region's climate is like the law of nature and the maximum use of natural energy. Considering the four prevailing climates in Iran, a significant amount of energy is consumed to balance cold and hot climates with nature. This research considers the cold climate covering the west to the northwest. Existing buildings in cold climates show significant energy-saving potential, and retrofitting the building stock is essential to targets. Retrofitting measures should reduce energy consumption and improve the indoor climate while being affordable. These can be challenging in cold climates. This paper discusses energy performance requirements and challenges in the retrofitting process. It also presents an overview of the retrofitting status and relevant energy-saving retrofitting measures with their potential for residential buildings [14–17].

One should look at environmental and natural phenomena from a new and different perspective to find these meanings. Hence, for the various climatic regions of Iran, the beautiful and famous form of traditional Iranian houses is suggested, which has been repeated since prehistoric times not only in the internal regions of Iran but also in the regions of the Middle East. Building designers, considering climatology, use the maximum climatic facilities of each region and natural energies to save fossil fuel consumption in buildings, which increases the quality of comfort, tranquility, and physical and mental health of the residents. Therefore, the world is looking to renewable resources, especially solar energy, and to evolve and develop productivity technology, exploiting them is rapidly advancing. The incompatibility of buildings with their bed climate and for getting past experiences have caused damage, including the increase in energy consumption. Moreover, the production of materials and the countless building construction have taken much energy and led to much environmental pollution. Accordingly, it is necessary to orient design strategies in new buildings to reduce energy consumption and environmental pollution.

In addition, some studies in different fields are trying to reduce energy consumption in buildings. Researchers are trying to optimize to reduce energy consumption. Summaries of recent publications on vernacular architectures in the energy-saving field are presented in Table 1.

The design of buildings with maximum usage of renewable energy is proposed to achieve this goal. This research aims to find the relationship between energy-saving and architecture and provide information to achieve logical architectural designs that are in harmony with the desired climate. The purpose of this study is to study and identify cold climatic conditions and explain a suitable model for architectural design with an appropriate climatic approach in modern Iranian architecture.

Among all neglected states, Azerbaijan is one of the most critical states of Iran, is located in the northwest of the county, and shares the same name with the neighboring northern country, Azerbaijan. Despite the distinctive architectural characteristics of the buildings, there is only a little literature published reflecting how the people of this area adapted their buildings to the harsh environment [13, 24–28]. This study aimed to identify the main differences between the architectural characteristics of buildings of Azerbaijan state with those of the central areas of Iran for climatic design issues. The traditional architectural values of this country have been used for centuries and have met the needs of residents in the best way possible.

Therefore, the present research evaluates the spatial features of traditional houses to increase natural energy, then identifies the components affecting the design of contemporary houses, and seeks to answer these questions: which features and models of traditional architecture are effective in designing the architecture for cold climates? what effect does climatic design have on the use of natural energy in the architecture of contemporary houses? how can we achieve solutions to design houses in cold climates? and what are the architectural models to meet these demands? In Figure 1, the overall framework of the current study is illustrated.

2. Methodology

2.1. Definition of the Problem. Azerbaijan could be considered one of the highest geographical places in Iran. The whole state is bounded by other highlands from all sides, which has led to numerous plateaus, e.g., Moghan, Tabriz, Saraband Maragheh. Sahand peak (3722 meters) is the highest place in the state, which is only 50 kilometers far

Table 1: A summary of newly published works with the aim of energy saving in domestic buildings.

References	Description
Ref. [18]	This work is purposed on the impact of building orientation on energy consumption in a domestic building using emerging BIM
Ref. [19]	In this paper, the climate-responsive solutions in the vernacular architecture of Bushehr city are investigated
Ref. [20]	Studies on sustainable features of vernacular architecture in different regions across the world
Ref. [21]	The simultaneous effects of building orientation and thermal insulation on heating and cooling loads in different climate zones are evaluated
Ref. [22]	This research investigates the relationship between optimum building forms in decreasing the cooling load
Ref. [22]	This paper reviews examples of vernacular architecture and its building elements in Nepal and analyses them in a qualitative manner in which bioclimatic design strategies were applied
Ref. [23]	This paper aims to classify almost all climatic strategies into different levels of space in Iranian vernacular architecture strategies

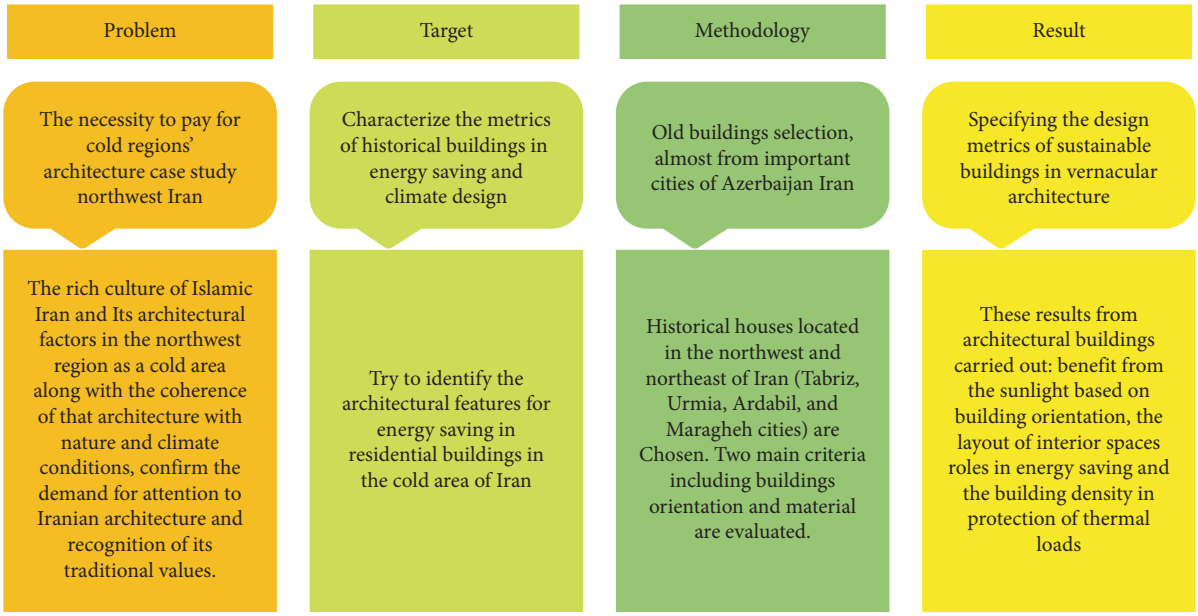

Figure 1: A overall framework of the current study.

from Tabriz, while Urmia Lake (1220 meters) is not more than 100 kilometers far from Tabriz city [29]. Such a geographical position and altitude lead to cold, dry, raining, and snowing weather in certain seasons, with a massive difference between the conditions in the cold and hot seasons. In essence, this part of the country significantly differs from the central arid zones in terms of temperature and weather.

2.2. Main Contributions and Novelties. Reviewing the previous studies confirms that investigating the vernacular buildings of northwest Iran did not observe based on their climate features. Hence, this paper tried to identify the architectural features for energy saving in residential buildings in the cold area of Iran. The study area is Iran's cold climate around West and East Azerbaijan. The current paper focuses on sustainable vernacular buildings according to their orientation and material. Therefore, this matter motivates this paper to investigate the energy in Iranian architectures based on climate design and energy saving, in which thermal comfort in architecture based on cold weather and the optimum use of solar energy without any mechanical systems are evaluated. In addition, the relation between the architecture of the old building in the proposed area and this building's orientation and density are investigated. For exact statistical analysis, the collected data include all buildings in the cold climate that have followed the climatic model and indigenous architecture. Library and field studies and case studies are selected as data collection tools according to the environmental features of the territory. Hence, based on the aim of vernacular architecture, sustainable buildings were built as environmental-friendly buildings, which tried to have a minimum negative effect on the environment. The following novelties are considered to clarify the current paper's advantages:

(i) Selection of 29 old buildings almost from important cities of Azerbaijan and Iran as shown in Table 2.

(ii) The collected data are employed to investigate the climate influence on the orientation of the studied old domestic building.

(iii) The using materials and their effects on energy saving are specified.

Table 2: The studied houses were separately sorted by each city (Source: Author).

Maragheh	Urmia	Tabriz	Ardabil
House of Ashraf Al-Muluk Nabi Vand	Ansari House Urmia)	Sharbat Oghli House	Mobasheri residential complex in the center of the Uch Dokan neighborhood
Nosrati Azar House	Dizaj Siavash House	Heidarzadeh House	Sadeghi House
Shahabian House	General houses	House of Dr. Yahya Zaka (Laleei)	Ershadi House
—	Majidi Afshar House	Ghadaki House	Vakil-or-Roaya House
—	Hadidi House	House of Amir Nezam	Moravej House
—	Moayeri Nia House	Mojtahedi House	Manafzadeh House
—		Behnam House	Marathi House
—	—	Sarraflar House (alavi)	Asef House
—	—	Salmasi House	Mobasheri House

(iv) The specific partitioning of the studied areas is identified.

(v) The zone with the most application is located on the south front, such as the family living room.

3. Main Discussion

3.1. Architectural Climatology. According to the scientific definition of climate, climate is the temporal combination of the physical state of the atmosphere, which is a characteristic of a specific geographical location. Since the weather is the current atmospheric condition of a specific location, we can define climate as the temporal combination of weather conditions [30]. Today, paying attention to climatic conditions in the design and construction of all buildings, especially buildings directly used by humans and living creatures, is vital in two ways. On the one hand, buildings in harmony with climate or with a climatic design have a better quality in terms of human thermal comfort. The environmental conditions of such buildings are better, and the daily and seasonal change and variety, light, heat, and airflow create various and pleasant spaces. On the other hand, the harmony of the building with the climate saves energy consumption required to control the environmental conditions of such buildings. In this building, the interior conditions of buildings in harmony with the climate can be adjusted to human comfort naturally throughout the year without the need for mechanical HVAC systems. To achieve a comfortable condition, using ways to provide comfort in buildings is essential. The following conditions must be observed to continue the fight against the environment in the construction of buildings:

(a) designing a building suitable for the environment;

(b) selecting materials suitable for the environment.

3.1.1. Energy in Architecture. Each city and region consumes different energy based on the types of existing buildings. In residential buildings, space heating, water heating, lighting, and cooking shape energy consumption. Among the mentioned activities, energy consumption for heating the house's interior accounts for about 60% of the total energy consumption in these buildings and has the most significant proportion [31]. In architecture, energy is divided into two components: light energy and thermal energy. A) Light energy is for sighting, seeing, studying, walking, and living. This type of energy is controllable and adjustable, but it is wasted without planning. B) Thermal energy is to make the environment favorable for work and life by heating or cooling inside the house, work environment, and other spaces for a better life. Such energies, like other energies, can be wasted. One of the most important parameters in architecture is the use of light, especially natural light such as the sun. In ancient times, the use of light and thermal energy in architecture was common, including inhibition of heating by thick walls and cooling production by proper orientation of the building. Necessary and sufficient light can turn the environment of the created architectural space into an artistic, familiar, livable and useable environment [32]. Regarding the temperature inside the complex and its usability and usefulness, like the optimal use of outside temperature, it is necessary to make the necessary controls in the design regarding the optimal use of thermal energy. In summer, thermal energy is radiated by the sun on the building's body and makes inside the building warmer. In this case, architects must control this case by thinking together and seeking the opinion of experts (engineers and installation experts) [33].

In summer, thermal energy is transferred from outside to inside. In winter, thermal energy is transferred from inside to outside; this change and exchange of energy cause architects and designers to consider the necessary design arrangements.To achieve the above goals to control and use energy optimally, according to current knowledge, experts have developed guidelines and criteria for the optimal use of energy in the design of buildings known as Article [34]. Therefore, the world should focus on how to save energy in their operations and environmental impacts and improve resource efficiency [35].

3.1.2. Climatic Design and Energy Saving. The degradability and limitation of energy resources, especially fossil fuel

sources, have led countries to research and study other energy sources, especially renewable energy such as solar, wind, geothermal, and sea and ocean waves, and on the other hand, to put the optimal, appropriate, and correct use of fossil fuels on the agenda.

Governments have committed themselves to various climate change agreements and policies. Trends are highlighted, and motivations for specific trends are explored and investigated, distinguishing between the world's developed and developing economies. Despite the efforts and resolutions of many countries, the cursory penetration of energy efficiency and the adoption of environmentally sustainable energy sources highlight the fundamental challenge of the need for a solution that will entrench a culture of energy efficiency and sustainable energy in our way of life [36–41].

Throughout the history of architecture and construction, designers have always sought to respond to climatic conditions; so-called traditional architects' climatic design has had an accurate and orderly expression. In this method of climatic design, no mechanical and installation means are used. In other words, this method has no cost, and the building receives and maintains this energy with its elements and components. Only knowledge and awareness about buildings of climatic design are needed. Whether in the form of the direction of buildings located in mountainous cities that are protected from the wind and facing south or in the form of traditional central courtyard house plans designed to maintain the cold of night in hot and dry climates. For example, the design of the buildings (Pavilion) is based on the ancient architecture of Iran using renewable energy such as solar and wind energy [16, 17, 34, 42].

Indigenous buildings and local styles, climate, and weather were considered the primary basis of human life and activities, ultimately leading to a beautiful form. This method is called building climatic design, and climate design is a method to reduce the energy of a building. The building design is the first line of defense against external climatic factors. In all climates, buildings built according to design principles minimize the need for mechanical heating and cooling and instead use the natural energy around the building. The climatic design causes the buildings to have the best comfort conditions. Instead of putting much pressure on the heating and cooling systems, the building provides comfortable conditions without equipment and devices. The use of central generating devices reduces the environmental effects and the consumption of fossil fuels, which we see in this model of climatic design in the architectural design of traditional houses. Factors such as heat, humidity, wind, etc., are effective in the type and style of buildings in a city [43] (Figure 2).

3.1.3. Typology of Architecture and Climate. Designing is the attempt to see beyond. It is an attempt to control a space's quality and make it appropriate for humans. We have the perception that in many cases, the visual quality was the main element considered by architects. However—at the same time—the missing control of "other" qualities in the building was precise. The result was an unbalanced feeling of pleasant and unpleasantness that is difficult to decode and understand [34].

The function of the building envelope is to physically separate the interior of the building from the exterior environment. Therefore, it serves as external protection to the indoor environment while facilitating climate control at the same time [43–45]. Environmental control installations must be considered with the external conditions [43]. Because building envelopes separate indoor and outdoor environments, they are exposed to temperature fluctuations, humidity, air movement, rain, solar radiation, and other natural factors [46]. The climatic thermal design of the building envelope affects thermal performance, which also affects energy consumption [47].

There are five methods of heat and mass transfer in the buildings: conduction through opaque elements, including external walls, ceilings, floor slabs, roofs, and partitions; solar radiation and conduction through window glazing; infiltration of outdoor air and air from adjacent rooms; and heat and moisture dissipation from the room's lighting, equipment, occupants, and other materials. The HVAC system provides heating or cooling and humidification or dehumidification [48]. A study by Ref. [49] shows that the building envelope contributes 73% of the total heat/gain loss. The choice of construction materials is dependent on thermal, moisture, and sound considerations. Walls, doors, windows, ventilators, roofs, etc., are components that are directly exposed to the sun.

3.2. Building Density. Building density is one of (Figure 3) the most critical factors affecting the amount of energy consumption in the building. The higher the building density, the lower the covered area of the land and the better the area's climate will become. It should be noted that in case of an excessive increase in building density in the city, the height of buildings will increase. Then, it will cause wind draft around the building and thus reduce the temperature. Therefore, more energy is spent on heating the house space in the building [50].

3.2.1. Plan and Layout of the Building. The layout form of residential buildings is referred to how they are placed, which has various types. Such as attached and separate, linear, central courtyard, and high-rise blocks. Each of them has its characteristics and changes the amount of energy consumption of the building considering the difference between each point of view of access to sunlight and exposure to wind. For example, suppose residential buildings are attached. In that case, the free surface of the buildings is reduced. As a result, the heat exchange of the building with the surrounding environment is reduced. Less energy is needed to heat the building [50].

3.3. Orientation of Traditional Houses in the Cold Climate of Azerbaijan. The orientation of buildings (particularly houses) is one of the most influencing factors in determining the characteristics of Iranian architecture and urban

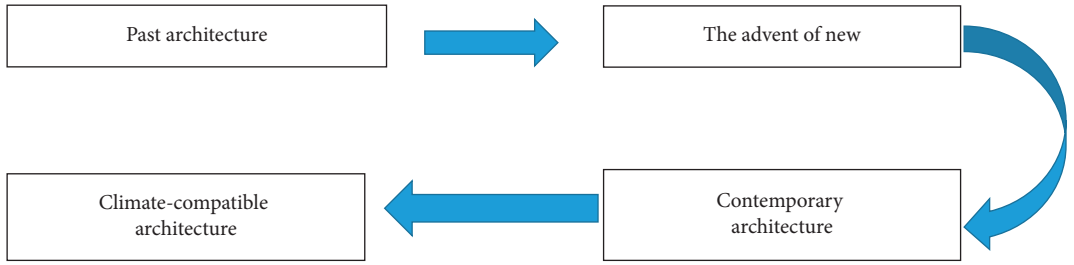

Figure 2: The trend of climatic design from the past to the present [30].

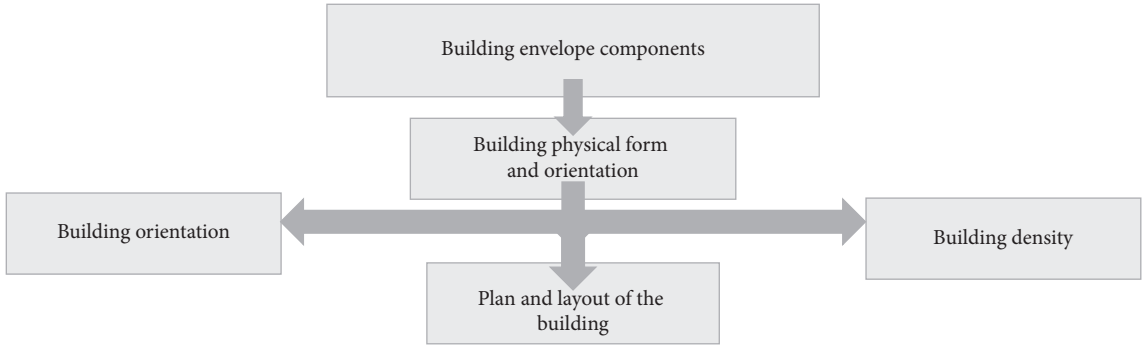

Figure 3: Effective characteristics in climatic design (Source: Author).

structures. The term "Ron" was the dominant traditional term that Iranian architects used to orient buildings. In terms of the classification of the building based on their orientation, Iranian vernacular architectures have three Rons: Raster Ron, Isfahani Ron, and Kermani or Shirazi Ron. Pirnia (1995) asserted that vernacularly in Iran, climate, ground conditions, topography, and slope significantly contribute to the formation of these Rons. Based on their tacit knowledge, traditional Iranian architects were aware of the direction of the prevailing winds, and they knew that giving enough credit to this factor could significantly affect environmental comfort. For instance, although the plateau of Tabriz, which is located among high mountains, naturally has various strong winds throughout the year, some prevailing winds strongly affect the direction of houses in this region, e.g., the East wind throughout the year and the North-East wind, which is very strong in winters [51]. As such, the vernacular houses of Tabriz mainly face south (varying from 15 degrees towards East to 10 degrees towards West), and all main spaces, including Tanabe (reception), study rooms, and lounge area are located at this site [18]. Mosques are also not excluded from this rule. Unlike those in the central parts of Iran, most mosques in Tabriz have multiple openings. This Ron order is the only Iranian Ron that coincides with the Kiblah direction as the direction for the prayer of Muslims, hence the natural.

The religious beliefs further lead to the orientation of buildings in the Azerbaijan area. In traditional complexes, using natural resources and energies is one of the principles of their construction and spatial organization. The direction of the house followed the angle of sunlight and the Kiblah. In the vast majority of traditional houses, the main axis of the buildings was the north-south axis. They had the best position to receive sunlight, so they could have shade on hot summer days and warm sun in winter. The main living spaces were built on the north and south sides, and the less important spaces, especially the service spaces, were built on the east and west sides. Considering the difficult climate and environmental and natural elements, the traditional architect has paid attention to the suitable climatic direction. The direction of buildings in villages and cities with cold climates is generally on the foothills' southern slopes (positive slopes). With this type of placement and extension of buildings in the east and west axis, the lowest surface is exposed to adverse winds, which often blow from the west. In addition, the construction of buildings on negative slopes (behind the sun) should be avoided, and positive slopes (slopes facing south and up to +60 degrees of deviation to the east and west) should be selected for the location of buildings [52].

3.3.1. Building Materials in the Cold Climate. What should be examined more carefully in this climate are the materials used in the body of walls and the body of buildings. In most areas and climates, using vernacular materials favorably meets the climatic needs of the region. For example, clay and mud are obtained from the region's clay in hot and dry climates. In temperate and humid climates, wood, found in abundance in temperate and humid areas, meets the climatic demands of the regions. However, in cold climates, such as mountainous areas, the body and walls are often made of stone, which due to the high heat transfer property of the stone causes the heat exchange of the indoor and outdoor

spaces to increase. The cold outside enters the interior spaces in the cold areas, and the inside heat is transferred to the outside environment. Therefore, it is recommended to use materials with low density and high heat capacity in cold climates. In ancient times, a Cobb covering was used on the stone wall to prevent this heat exchange. However, the appropriate materials for this climate and materials with low thermal conductivity should be used due to the great variety of building materials in all climates and, most notably, in cold and mountainous climates. This climate has high energy consumption, and in fact, a lot of heat energy is required to heat different parts of a building and stabilize the temperature of various interior spaces. Considering this issue, materials with low heat capacity (porous and lightweight concrete) are among the suitable materials that can be very practical and useful in this climate. However, it should be noted that these materials are more desirable to be used in parts of the building that are used for insulation and are not suitable in parts of the building that require dense materials (such as Trombe walls on the south). In the other parts of the building, where thermal insulation is important, mineral wool (glass wool and rock wool with thermal conductivity of 0.039–0.047 and expanded polystyrene plastics with thermal conductivity of 0.047–0.057) can be used. The proper use of materials such as thermal insulation (felt layers and soft coatings impregnated with bitumen as well as rubbles at the foot of the walls) is another critical factor in removing moisture around the building. The proper use of these materials is a good solution for preventing the infiltration of rising dampness into the walls of the building [53].

3.3.2. Evaluation of Energy-Saving Criteria in Residential Architecture in the Cold Climate. As we know, the number of residential buildings in a city is much higher than office-commercial; in this article, the main emphasis is on residential buildings and their energy consumption. Based on the reviewed sources, factors such as orientation, the layout of the building plan (using the direction of sunlight), and building density are introduced as physical features of the building, which affect energy consumption and are affected by the traditional design model of residential houses [54–56]. Qualitative criteria in case research samples are evaluated using the tools that in this research are energy management indicators in the design of residential architecture in cold climates. Two groups of data are obtained in this study, which is related to the indicators obtained from the two main factors of the research. The first group is the parameters derived from the indicators about the first factor—the characteristics and needs of users—in traditional houses, the information provided by various methods of library studies, document reviews, and interviews with experts. The second group is the parameters obtained about the second factor—the characteristics and needs of the residential environment—in each of these houses, the information obtained by the literature review, interviews with experts, observation, analysis of maps, and investigations of spatial features. In this way, the necessary background for recognizing the criteria related to each indicator, developing a model for each of them, and then evaluating the priority of the indicators in defining the climatic design of traditional houses is provided.

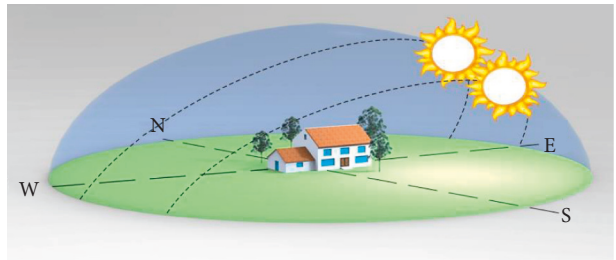

Figure 4: Positions of solar radiation at latitude 37° north in summer and winter seasons [53].

4. Findings and Analysis of the Research

The architecture requires special design measures that, in addition to saving energy consumption, provide very favorable conditions for residents in terms of cooling and heating in a cold and dry climate.

Concerning issues, with the proper design of residential buildings and considering the critical factors suitable for the climatic conditions of this region, efforts are made to create a favorable condition for the comfort of residents in this region. In the history of modern architecture, the achievements of environmental adjustment have significantly affected the visual appearance of many architectural masterpieces. Moreover, the climatic design is an obvious reaction to the visible and hidden forces. In traditional architectural design, instead of relying on HVAC equipment and energy consumption, efforts are made to use the form and orientation of a building so that the necessary comfort is provided by using natural energy flows. Thermal comfort is a state that includes both physical and mental comfort, and designers are obliged to create weather conditions.

Revitalization in this approach: The effort is to minimize the intervention with the structure, and the emphasis is on application change to eliminate functional exhaustion. The primary purpose is to keep the main structure of the old structure and framework unchanged while introducing positive social and economic functions to it.

Now, given the cold weather in this climate in winter, it is tried to create solar space in the building to heat and balance the temperature of the building at night by storing heat during the day. In fact, by the maximum use of thermal energy in winter and creating a temperature draft in summer, it is possible to provide an ideal condition without the intervention of any electrical system. Used sunlight is directly related to the geographical direction of the opening and the building skin relative to the south. At the design stage, only the volumetric orientation of the building in the face of wind and radiation is usually considered, and the composition of the spaces based on the solar cycle is marginalized. We reach the following results by determining the peak hours of receiving solar energy and the position and

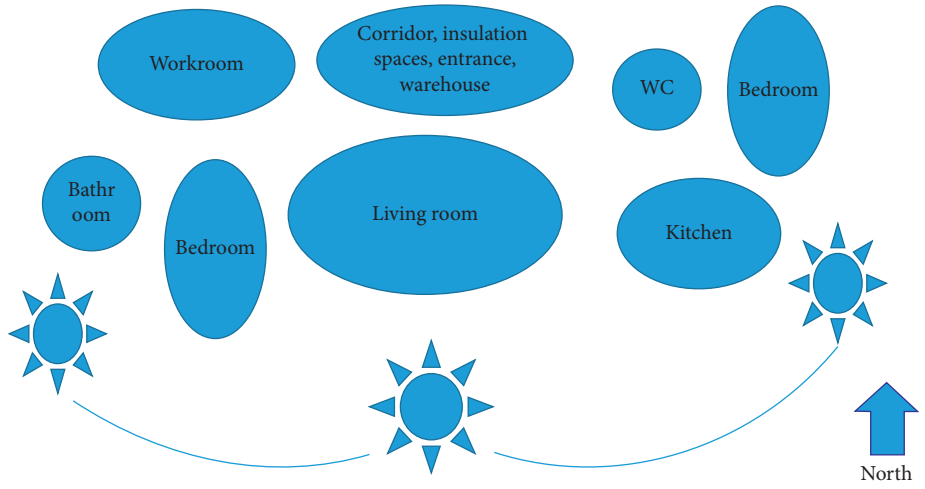

Figure 5: Dominant building partitioning of northwest Iran [57].

angles of solar radiation at latitude 37 degrees north. Since the position of the sun and its radiation is known, the spaces can be designed and laid out to make the most of the beneficial heat of the sun.

The main goal is to find a solution for a more outstanding balance between natural and artificial to achieve a higher level of quality of life and energy storage in residential architecture.

4.1. Solar Altitude Angle. Due to the cold climate in northwest Iran, the main goal of traditional architecture is utilizing solar energy and temperature fluctuations and avoiding cold winter wind to provide thermal comfort. In these areas, extreme cold is the main factor in forming urban and village contexts. The compact cities with central courtyards, flat roofs, low heights of rooms, the good-sized windows facing to the south, and thick walls are the features of northwest buildings. Generally, traditional architecture tries to minimize the building surface's connection with the cold outside in cold areas. As above-mentioned, the northwest of Iran is located about 37° north latitude, so the position of buildings in the purposed area and solar radiation angels in the winter and summer seasons is shown in Figure 4. As can be seen from Figure 4, the buildings are south facing to get the maximum solar energy in winter; the old architects funded it. In addition, building partitioning in the intended area is discussed in the next section.

In the design based on the sun circulation, the space occupancy model by residents during the day and night is the most important factor in the layout of zones (Figure 5).

According to the above figure, the warm and daily used spaces are placed on the south face of the building, the spaces used in the morning are placed on the east section, the spaces used at night are placed on the north section, and the warm spaces are placed on the west front of the building. The cold and dry climate where the spaces are arranged next to each other is dense to store more energy and prevent energy loss. The neighborhoods should be east-westward, and the lighting should be provided from the south-north.

The results of studies conducted for four sample cities and residential buildings in the cold weather context are investigated to achieve the optimal orientation for the location of buildings in cold climates. In the present research, historical houses located in the northwest and northeast of Iran (Tabriz, Urmia, Ardabil, and Maragheh cities) are evaluated, which are located in cold climates. After studies, it was found that the construction of buildings was based on the region's climatic conditions and the direction of sunlight and light. The following table and results are obtained from the review of 29 samples.

Table 3 shows the plan of selected residential buildings. Based on the plan analysis and considering the solar energy role in the cold climates, the following reasons can be derived:

(i) The family living room is located on the south front, and the rooms use southwest light.

(ii) Retaining spaces such as stairs and entrance warehouses should be located between the main zone and the undesirable front.

(iii) The kitchen is located on the east side of the building to enjoy the morning sun.

4.2. Interpretation of Results. Table 3 shows the results of the analysis of 29 case studies that discussed and studied the plans of historical buildings using solar plans. Based on the 29 samples studied, four models of buildings are given in Table 3. According to this study, it is found that historical buildings received the maximum natural energy by following the orientation of sunlight in all months of the year and other climatic factors.

In Figure 6, 19% of the buildings were constructed in the north, 17% of the buildings were constructed in the northeast, 16% of the buildings were constructed in the northwest of the land (52% in the north in total), 6.7% of the buildings were constructed in the south, 12% of the buildings were constructed in the southeast, 12% of the buildings were constructed in the southwest (30.7% in the

Table 3: Evaluation of the studied architectural plan (Source: Author).

	Plan		Explanation
Tabriz (Sharbat Oghli House)	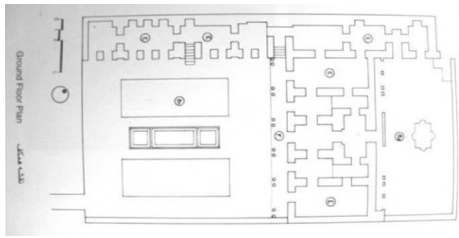	The lighting direction of north and east	Complies with the solar plan
Urmia (Ansari House)		The lighting direction of north, east, and south	Complies with the solar plan
Mobasheri House		The lighting direction of north and east	Complies with the solar plan
Maragheh (Shahabian House)	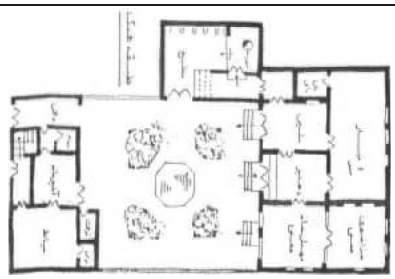	The lighting direction of north and east, west	Complies with the solar plan

south in total), 6.7% of the buildings were constructed in the east, and 10.6% of the buildings were constructed in the west.

In Figure 7, the density of the studied buildings was analyzed. 3 units had a density of up to 50%, 22 units had a density of up to 100%, 3 units had a density of up to 150%, one unit had a density of more than 150%, and the percentages are 20% to 50%, 68% to 100%, 9% to 150%, and 2% more than 150%.

The general plan forms in various periods and their changes; most of the plans followed the module of room and atrium, and now all the plans are affected by the region's cold climate. As mentioned, all plans are dense and the close connection of heat-creating spaces such as the kitchen with the living area, the relatively proper use of solar energy, double-glazed windows, and the small size of doors and windows that minimize the connection with the outside space and thick walls can be considered as reasons for the effect of climate on the architecture of this region.

4.3. Limits of the Research. Because this research is a kind of historical study with all case studies aligned accordingly, it is evident that neither time nor limited resource access allowed the deep ancient archeological study to obtain new data. As a result, the best practice was to go through as many available books and documents as possible. Furthermore, due to a lack of sufficient observations or information, studying the shreds of evidence belonging to specific eras became inevitable. In addition, any literature similar to the present study did not do previously to validate this work.

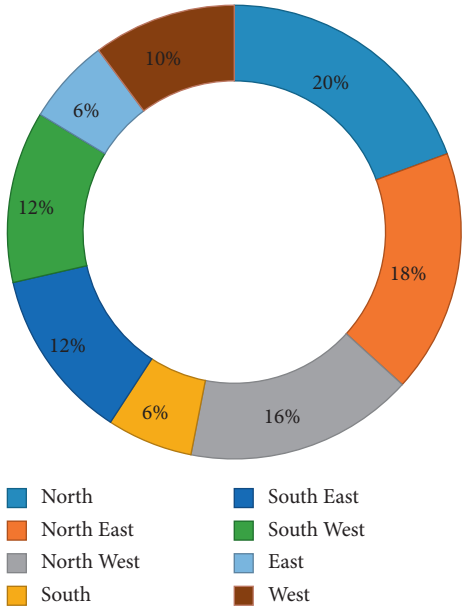

Figure 6: Orientation of the studied buildings (Source: authors based on the research findings).

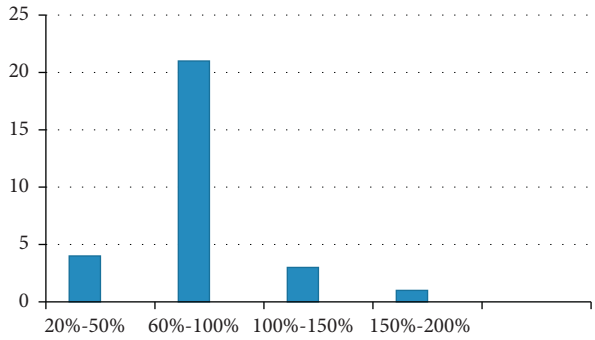

Figure 7: The density of studied buildings (Source: authors based on the research findings).

5. Conclusion

Today, reduction in the consumption of non-renewable energy and maximum use of sustainable and green energy, including solar thermal energy, is considered by architects and building designers. Hence, paying attention to each region's climate and climatic conditions and designing based on climatic conditions, especially in cold and dry climates, is very important. Due to Iran's geographical and climatic location can reach the energy-saving model in contemporary houses by considering other factors such as economy, independence, using natural (non-fossil) energy such as the sun and wind for energy saving, using past experiences, and the help of traditional architectural methods. Therefore, harmonizing the environment with the prevailing climatic conditions is the first step to using natural energy. In other words, the necessary condition for using natural conditions is the coordination and adaptation of buildings to climatic conditions. The optimal orientation of a building has a significant effect on reducing energy demand. Hence, in cold weather, the orientation of a building plays a vital role in its energy demand. Consequently, it is more important to pay attention to the orientation in cold weather conditions. Optimal orientation always reduces the total annual energy consumption. Buildings with optimal orientation need less insulation than those built with other orientations. It can be inferred that orientation plays a more prominent role.

On the other hand, architecture often ignores sufficient attention to the building orientation, which can be important for urban planners and decision-makers. The above analysis and comparison of the structure and unique features of the space in traditional Iranian houses in cold climates and case studies is the main objective of the present research, and various results can be yielded. These results in the similar buildings studied are as follows: In the historical buildings in the cold climate, to reduce the thermal load of the houses, the points necessary to benefit from the sunlight are taken into account. In addition to the orientation of buildings, the layout of interior spaces is very effective in the amount of thermal load of the buildings. By modeling traditional buildings in cold climates, it can be seen that these buildings significantly decrease the thermal load of the building and thus the energy consumption of houses. For architecture to be able to orient toward energy-saving goals and the construction industry to minimize environmental pollution, it is necessary to observe two principles in it: First, the architecture should be flexible, compatible, and adaptable to the environmental conditions and needs of the residents of that region, and measures should be taken so that it can accept future developments at any time and can be updated. Second, the plan should be designed using the surrounding environment and climate in the area, and the materials used in it should be vernacular and returnable to the environmental cycle. Thus, it can be inferred that the designer of such a structure should also be its main planner.

Moreover, as it turned out from the historical documents and traditional houses, the designer must design the building entirely, aware of the environment's information. In other words, the design should be local and indigenous. Finally, it can be concluded that in contemporary houses, according to the climatic conditions of the region, using renewable energy in the main aspect of the building, proper orientation, the layout of spaces next to each other, and choosing the suitable form and volume for the building and building components should be considered.

All of the above solutions seek to make the most of the available and appropriate renewable energy in the region and greater coordination and consistency with the environment and climate of the region. Since this study depends on climatic factors, the same can be repeated in any climatic condition. Further analysis of the results showed that the type of building in the cold climate of Azerbaijan to confirm whether it is compatible with the climate, and further research is needed. Orientation is the best choice for all types of buildings.

Data Availability

There are no available data for this paper.

Conflicts of Interest

The authors declare that they have no conflicts of interest.

References

[1] B. M. Ziapour, M. Saadat, V. Palideh, and S Afzal, "Power generation enhancement in a salinity-gradient solar pond power plant using thermoelectric generator," *Energy Conversion and Management*, vol. 136, pp. 283–293, 2017.

[2] Y. C. Aydin, P. A. Mirzaei, and S. Akhavannasab, "On the relationship between building energy efficiency, aesthetic features, and marketability: toward a novel policy for energy demand reduction," *Energy Policy*, vol. 128, pp. 593–606, 2019.

[3] C. Cheung, R. Fuller, and M. Luther, "Energy-efficient envelope design for high-rise apartments," *Energy and Buildings*, vol. 37, no. 1, pp. 37–48, 2005.

[4] L. Pérez-Lombard, J. Ortiz, and C. Pout, "A review of building's energy consumption information," *Energy and Buildings*, vol. 40, no. 3, pp. 394–398, 2008.

[5] C. C. Siew, A. Che-Ani, N. Tawil, N. Abdullah, and M. Mohd-Tahir, "Classification of natural ventilation strategies in optimizing energy consumption in Malaysian Office buildings," *Procedia Engineering*, vol. 20, no. 0, pp. 363–371, 2011.

[6] A. Bastide, P. Lauret, F. Garde, and H. Boyer, "Building energy efficiency and thermal comfort in tropical climates: presentation of a numerical approach for predicting the percentage of well-ventilated living spaces in buildings using natural ventilation," *Energy and Buildings*, vol. 38, no. 9, pp. 1093–1103, 2006.

[7] R. V. Ralegaonkar and R. Gupta, "Review of intelligent building construction: a passive solar architecture approach," *Renewable and Sustainable Energy Reviews*, vol. 14, no. 8, pp. 2238–2242, 2010.

[8] C. Zhang, A. A. Mousavi, S. F. Masri, G. Gholipour, K. Yan, and X. Li, "Vibration feature extraction using signal processing techniques for structural health monitoring: a review," *Mechanical Systems and Signal Processing*, vol. 177, Article ID 109175, 2022.

[9] X. Chen, Q. Quan, K. Zhang, and J. Wei, "Spatiotemporal characteristics and attribution of dry/wet conditions in the Weihe River Basin within a typical monsoon transition zone of East Asia over the recent 547 years," *Environmental Modelling & Software*, vol. 143, Article ID 105116, 2021.

[10] C. Guo, C. Ye, Y. Ding, and P. Wang, "A multi-state model for transmission system resilience enhancement against short-circuit faults caused by extreme weather events," *IEEE Transactions on Power Delivery*, vol. 36, no. 4, pp. 2374–2385, 2021.

[11] B. Bathaei, *Process Analysis of environmental perception of Persian garden based on psychological theory of environment*, Vol. 124, EDITURA UNIVERSITAR, ION MINCU, 2016.

[12] L. Qiu, L. He, H. Lu, and D. Liang, "Systematic potential analysis on renewable energy centralized co-development at high altitude: a case study in Qinghai-Tibet plateau," *Energy Conversion and Management*, vol. 267, Article ID 115879, 2022.

[13] S. Kadaei, *Human Presence in the Architectural Environment (From a Phenomenological Perspective)*, p. 144, Bid Publishing, Tehran, 2020.

[14] L. C. Felius, F. Dessen, and B. D. Hrynyszyn, "Retrofitting towards energy-efficient homes in European cold climates: a review," *Energy Efficiency*, vol. 13, no. 1, pp. 101–125, 2020.

[15] Y. Shan, J. Zhao, H. Tong, J. Yuan, D. Lei, and Y. Li, "Effects of activated carbon on liquefaction resistance of calcareous sand treated with microbially induced calcium carbonate precipitation," *Soil Dynamics and Earthquake Engineering*, vol. 161, Article ID 107419, 2022.

[16] O. Hossein Eskandani, S. Yılmaz, and P. Doraj, "Role of nature in the formation of organik architecture," *International Journal of Social Humanities Sciences Research (JSHSR)*, vol. 8, no. 69, pp. 1114–1122, 2021.

[17] B. Bathaei and M. Abdel-Raheem, "Assessment of the relative importance of the main parameters used in the selection of the urban heat island mitigation strategies," *Construction Research Congress*, pp. 627–636, 2022.

[18] F. H. Abanda and L. Byers, "An investigation of the impact of building orientation on energy consumption in a domestic buildiqng using emerging BIM (Building Information Modelling)," *Energy*, vol. 97, pp. 517–527, 2016.

[19] P. Motealleh, M. Zolfaghari, and M. Parsaee, "Investigating climate responsive solutions in vernacular architecture of Bushehr city," *HBRC journal*, vol. 14, no. 2, pp. 215–223, 2018.

[20] M. E. Kohansal, H. R. Akaf, J. Gholami, and S. Moshari, "Investigating the simultaneous effects of building orientation and thermal insulation on heating and cooling loads in different climate zones," *Architectural Engineering and Design Management*, vol. 18, no. 4, pp. 410–433, 2021.

[21] W. S. S. W. Rashdi and M. R. Embi, "Analysing optimum building form in relation to lower cooling load," *Procedia-Social and Behavioral Sciences*, vol. 222, pp. 782–790, 2016.

[22] S. Bodach, W. Lang, and J. Hamhaber, "Climate responsive building design strategies of vernacular architecture in Nepal," *Energy and Buildings*, vol. 81, pp. 227–242, 2014.

[23] S. Saljoughinejad and S. Rashidi Sharifabad, "Classification of climatic strategies, used in Iranian vernacular residences based on spatial constituent elements," *Building and Environment*, vol. 92, pp. 475–493, 2015.

[24] M. A. Keynejad and M. R. Shirazi, *Historical houses of Tabriz*, Vol. 1, Tabriz Islamic Art University Press, Tabriz, Iran, 2010.

[25] S. Kheyri, *Architecture and Decoration of Wooden Verandas in Safavid Ear in Azerbaijan*, vol. 1, Mahdi Azadi's Publications, Tabriz, Iran, 2006.

[26] L. Guo, C. Ye, Y. Ding, and P. Wang, "Allocation of centrally switched fault current limiters enabled by 5G in transmission system," *IEEE Transactions on Power Delivery*, vol. 36, no. 5, pp. 3231–3241, 2021.

[27] X. Xu and M. Nieto-Vesperinas, "Azimuthal imaginary poynting momentum density," *Physical Review Letters*, vol. 123, no. 23, Article ID 233902, 2019.

[28] S. Huang, M. Huang, and Y. Lyu, "Seismic performance analysis of a wind turbine with a monopile foundation affected by sea ice based on a simple numerical method," *Engineering applications of computational fluid mechanics*, vol. 15, no. 1, pp. 1113–1133, 2021.

[29] R. Shaterian, *Climate and Architecture*, Simaye Danesh Publications, Tehran, Iran, 2009.

[30] E. Iranmanesh, N. Darya, M. D. Maryam, and H. Marzieh, "Provide local housing design patterns with emphasis on design elements climatology; case: Kerman," *Urban Management*, vol. 14, no. 38, pp. 347–370, 2015.

[31] K. Steemers, "Energy and the city: density, buildings, and transport," *Energy and Buildings*, vol. 35, no. 1, pp. 3–14, 2003.

[32] R. Gurabi and Bahman, "The relationship between sustainable development of environmental architecture and climate design in mountainous areas Case study," *Geographical*

Quarterly Journal of Environmental Management, vol. 4, no. 14, pp. 21–38, 2011.

[33] A. Heidari, A. Qasemian Asl, and M. Kiai, "Analysis of spatial structure of traditional Iranian homes using spatial method case study: comparison of yazd, kashan, and isfahan houses," *Iranian Islamic City Quarterly*, vol. 7, no. 28, pp. 21–33, 2017.

[34] B. Bathaei, "Achieving sustainable city by the concept of Persian garden," *Acta Technica Napocensis: Civil Engineering & Architecture*, vol. 61, no. 3, 2018.

[35] M. Nhleko and L. Professor Freddie, "Inambao, energy audit on primary municipal facilities: reflection of municipality's energy consumption as a direct consumer of the energy utility (eskom)," *International Journal of Engineering Research and Technology*, vol. 13, no. 12, pp. 4033–4047, 2020.

[36] J. Jerusha and F. L. Inambao, "Trends: energy efficiency and energy security," *International Journal of Engineering Research and Technology*, vol. 13, no. 12, pp. 4084–4117, 2020.

[37] C. Lu, H. Zhou, L. Li et al., "Split-core magnetoelectric current sensor and wireless current measurement application," *Measurement*, vol. 188, Article ID 110527, 2022.

[38] S. Liu, C. Liu, Z. Song, Z. Dong, and Y. Huang, "Candidate modulation patterns solution for five-phase PMSM drive system," *IEEE transactions on transportation electrification*, vol. 8, pp. 1194–1208, 2022.

[39] H. Tian, J. Pei, J. Huang et al., "Garlic and winter wheat identification based on active and passive satellite imagery and the google earth engine in northern China," *Remote Sensing*, vol. 12, no. 21, p. 3539, 2020.

[40] P. Doraj, M. Baran, and O. Hossein Eskandani, "Using thermal potential of the earth to optimize energy consumption in architectural structures," *Natural Volatiles & Essentional Oils (NVEO) Journal*, vol. 9, no. 1, pp. 7–20, 2022.

[41] J. Yuan, D. Lei, Y. Shan, H. Tong, X. Fang, and J. Zhao, "Direct shear creep characteristics of sand treated with microbial-induced calcite precipitation," *International Journal of Civil Engineering*, vol. 20, no. 7, pp. 763–777, 2022.

[42] L. Qiu, L. He, H. Lu, and D. Liang, "Pumped hydropower storage potential and its contribution to hybrid renewable energy co-development: a case study in the Qinghai-Tibet Plateau," *Journal of Energy Storage*, vol. 51, Article ID 104447, 2022.

[43] M. Shams and M. Khodakarami, "Study of traditional architecture in harmony with the cold climate," *Geographical Preparation of the Quarterly*, vol. 3, no. 10, pp. 91–114.

[44] A. Rogora, "Simplified methods and tools for the representation of energy in the project of architecture," in *Bioclimatic Approaches in Urban and Building Design*, G. Chiesa, Ed., PoliTO Springer Series. Springer, Cham, 2021.

[45] G. K. Oral, A. K. Yener, and N. T. Bayazit, "Building envelope design with the objective to ensure thermal, visual, and acoustic comfort conditions," *Building and Environment*, vol. 39, no. 3, pp. 281–287, 2004.

[46] S. B. Sadineni, S. Madala, and R. F. Boehm, "Passive building energy savings: a review of building envelope components," *Renewable and Sustainable Energy Reviews*, vol. 15, no. 8, pp. 3617–3631, 2011.

[47] S. Al-Saadi and I. Budaiwi, "Performance-based envelope design for residential buildings in hot climates," in *Proceedings of Building Simulation*, Beijing city, January 2007.

[48] S. Sabouri, *Optimization of Architectural Properties of a Tropical Bungalow House with Respect to Energy Consumption*, Universiti Kebagnsaan Malaysia, Malaysia, 2012.

[49] U. DoE, *Buildings Energy Databook*, Energy Efficiency & Renewable Energy Department, 2011.

[50] M. Biddulph, *Introduction to Residential Layout*, Elsevier, Oxford, 2007.

[51] Department of Housing and Urban Development, *An Experience for Documentation of Iranian Bazaars, Iran's Bazaar*, Jahad Daneshgahi Press, Tehran, Iran, 2010.

[52] C. Binggeli, *Building Systems for interior Designers*, John Wiley & Sons, 2003.

[53] T. Iran, *The 19th Issue of Iran National Building Regulations, Deputy of Housing and Building*, Tehran, Iran, 2010.

[54] V. Ghobadian, *Traditional Buildings*, Tehran University Press, Tehran, 2015.

[55] Khalil and Allah, "Energy Efficiency Strategies in Urban Planning of Cites," in *Proceedings of the 7th International Energy Conversion Engineering Conference*, Reston, US, August 2009.

[56] B. Bathaei, "Persian enclosed garden: recognition & recreation of the Persian garden," *Revista Şcolii Doctorale de Urbanism*, vol. 1, no. 1, pp. 53–56, 2016.

[57] S. Kadaei, M. Majidi, Q. Asaee, and H. H. Mehr, "Hotel construction management considering sustainability architecture and environmental issues," *Shock and Vibration*, vol. 2021, Article ID 6363571, 13 pages, 2021.

Hindawi
Complexity
Volume 2022, Article ID 2993184, 15 pages
https://doi.org/10.1155/2022/2993184

Research Article

Deep Learning-Assisted Short-Term Power Load Forecasting Using Deep Convolutional LSTM and Stacked GRU

Fath U Min Ullah,[1] **Amin Ullah**,[2] **Noman Khan**,[1] **Mi Young Lee**,[1] **Seungmin Rho**,[3] **and Sung Wook Baik**[1]

[1]*Sejong University, Seoul 143-747, Republic of Korea*
[2]*Collaborative Robotics and Intelligent Systems (CoRIS) Institute, Oregon State University, Corvallis, OR, USA*
[3]*Department of Industrial Security, Chung-Ang University, Seoul 06974, Republic of Korea*

Correspondence should be addressed to Sung Wook Baik; sbaik@sejong.ac.kr

Received 10 June 2022; Accepted 19 July 2022; Published 26 August 2022

Academic Editor: Xiaoqing Bai

Over the decades, a rapid upsurge in electricity demand has been observed due to overpopulation and technological growth. The optimum production of energy is mandatory to preserve it and improve the energy infrastructure using the power load forecasting (PLF) method. However, the complex energy systems' transition towards more robust and intelligent system will ensure its momentous role in the industrial and economical world. The extraction of deep knowledge from complex energy data patterns requires an efficient and computationally intelligent deep learning-based method to examine the future electricity demand. Stand by this, we propose an intelligent deep learning-based PLF method where at first the data collected from the house through meters are fed into the pre-assessment step. Next, the sequence of refined data is passed into a modified convolutional long short-term memory (ConvLSTM) network that captures the spatiotemporal correlations from the sequence and generates the feature maps. The generated feature map is forward propagated into a deep gated recurrent unit (GRU) network for learning, which provides the final PLF. We experimentally proved that the proposed method revealed promising results using mean square error (MSE) and root mean square error (RMSE) and outperformed state of the art using the competitive power load dataset.(Github Code). (Github code: https://github.com/FathUMinUllah3797/ConvLSTM-Deep_GRU).

1. Introduction

Over the decade, the global energy consumption by the large-scale machinery in factories, buildings, and transport has remarkably increased due to population growth and economic development [1, 2]. This phenomenon rapidly shifted the energy resource demands towards clean power generation and its system improvement through intelligent methods for its efficiency [3]. These days, different renewable energy resources such as solar, wind, etc., are becoming the most optimal and significant resources aiming towards green technology; therefore, an extra layer of PLF will further assist the smart grid operation and its smooth maintenance [4]. Still, there exist some challenges for energy scientists to precisely establish an accurate and smart cooperative platform between the smart grids and the consumer side. A large amount of power energy is consumed and wasted due to improper infrastructure. Therefore, forecasting this power energy is an essential and imperative step towards optimal usage to overcome its dissipation. This will also enhance its future demand through smart grid and renewable energy production [5]. Researchers and data scientists are developing efficient ways to handle energy wastage and improve its optimal usage through different machine learning and time-series modeling techniques. However, a large amount of work has been done so far, with accurate results or with some uncertainties yielding erroneous forecasting that raised the need of establishing a highly precise, generalized ability, and robust energy forecasting model. According to [6], the scenario of generating

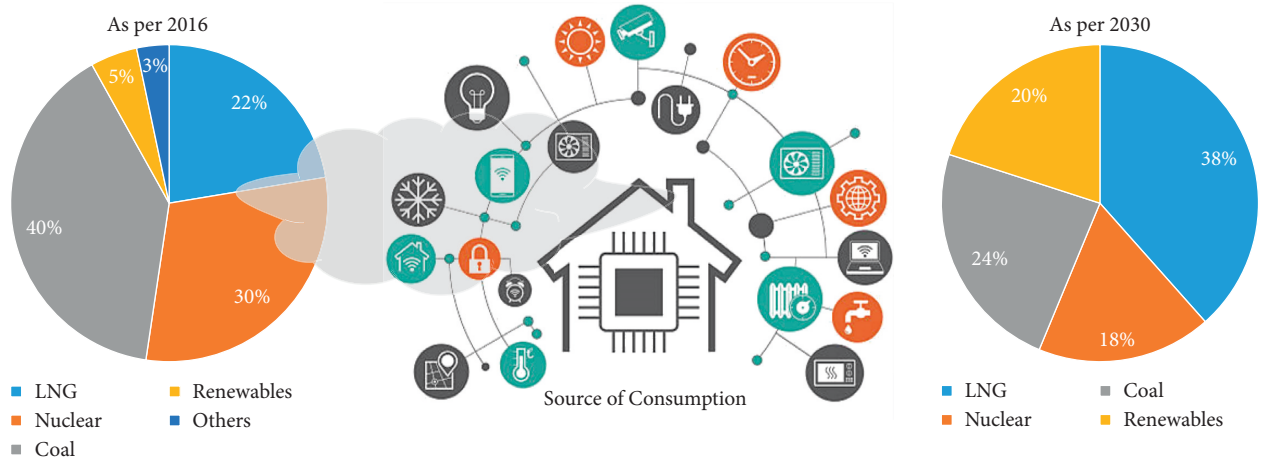

Figure 1: Statistics of power energy generation [6] as of 2016 and 2030. Also, different sources of power energy consumption are stepped.

the power energy from 2016 is 40%, 30%, 22%, 5%, and 3% for coal, nuclear, liquefied natural gas (LNG), renewables, and other resources, respectively. This statistic is illustrated in Figure 1, which shows the percentage of power energy generation and the consumption of resources.

Energy consumption via machinery in factories, buildings, and transport has remarkably increased over the last decades in the world due to population growth and the development in the economy. The prediction of this energy consumption is essential to reserve it for optimal use to overcome its dissipation and enhance its future demand, which is especially the current need of several countries. Researchers and scientists are developing efficient ways to handle energy wastage and improve its optimal usage in industries and residential areas. However, a large amount of work has been done so far, with accurate results or with some uncertainties. A challenge was raised to establish a highly precise, generalized ability, and robust energy prediction model. Mainly three kinds of building energy consumption models are used such as data-driven models, physical models, and hybrid models [7, 8]. Among these models, the most provocative is the data-driven model that became a popular method owning lower time in consumption with good performance. Several data-driven approaches are appropriate to cluster the buildings (residential [9] and nonresidential buildings [10]) with different timescales such as short term [11] or long term [12]. A majority of prediction methods have been proposed over the past years in building ECP. Therefore, it is important to predict the future energy consumption and manage the energy usage accordingly. This method is a step towards efficient energy consumption. Also, it is an emerging field where the future world is widely based on energy and its utilization in industries, companies, government organizations, etc.

The utmost goal of the proposed method is the reduction of energy consumption and to ensure its efficient usage that is a prominent factor influencing the economy growth in the country. However, there exist numerous challenges in power load forecasting in buildings such as accuracy, efficient data processing, model evaluation, errors calculation, etc. Therefore, it is important to develop a method that can achieve a fast performance to forecast and assess power energy infrastructure with a reasonable accuracy and least error. The tactics used for PLF heavily depend on the available data gained from the meters that are the foci of various problems. The mainstream methods that are mostly based on lack of preprocessing of power load data and fail in noisy condition when the data are noisy and have outliers or effects of user's behavior. This problem is handled via the refinement layer. Similarly, they provide a coarse way to collect the features for PLF, practicing low-level methods that widely skip the most discriminative features of the power data sequence. They are based on traditional feature extraction such as clustering, ensemble learning, or hand-feature engineering techniques which fail in terms of amassing the most advanced knowledge and deep characteristic from the data. In addition, the practiced approaches use a single RNN layer and passed via single hidden state that ignore the capturing of (hierarchical/think) temporal structure of the sequence. Furthermore, existing PLF techniques hands on complex architecture resulting into a large number of parameters and become computational. We handle these problems by proposing a deep learning-assisted short-term PLF method, which investigate the ConvLSTM layers giving its latter to GRU. Applying such procedure, the proposed method achieved the accurate and fast calculation results.

The key contributions of the proposed method are highlighted as follows:

(1) Existing PLF strategies practice traditional filters to overcome noisiness in data which remove the noisy disordering only. To tackle this problem, an acquisition and refinement layer is employed that refines the data through past value substitution, normalization, and organizing the data into a rolling window sequence.

(2) Employed works apply conventional learning and hand-feature engineering strategies making the load forecasting stiffer and tedious. However, for the first

time, we propose a novel ConvLSTM network for PLF that extracts the most discriminative spatiotemporal features from the power load sequence and generate a block of feature map.

(3) We employ a deep GRU for sequence learning that obtains the spatiotemporal features (feature map) from the ConvLSTM network. The deep GRU network is more suitable for learning the sequence patterns and provides effective PLF demonstrated through visual and tabular results.

(4) We experimentally prove that the proposed method shows outstanding results and outperforms state of the art through recording the least value of MSE and RMSE on the most challenging dataset. The demonstration of the proposed method's results depicts the method suitability for efficient management of energy infrastructure and ensuring saving of vast amount of energy wastage.

The rest of the article is organized as follows: Section 2 covers the literature review while the proposed PLF method and experimental analysis are discussed in Section 3 and Section 4, respectively. Finally, Section 5 describes the comparative analysis while Section 6 concludes the article.

2. Literature Review

Several techniques have been developed with the aim to efficiently forecast the energy consumption for buildings, industries, institutes, or residential areas. These methods are broadly based on conventional and deep learning-based techniques. The details are covered in the following sections.

2.1. Conventional Learning-Based PLF Methods. PLF methods remained popular for their promising results to forecast the power load consumption in residential buildings [13, 14], subways [15], industries [16], and households [17, 18]. Majority of the methods are based on traditional approaches. For instance, Guo et al. [19] composed a machine learning-based model to forecast the building thermal energy using extreme learning machine (ELM), multiple linear regression, and support vector machine. They analyzed the performance of each model for the heating system. Next, Peng et al. [20] used a framework that worked with multiprocessing learning based on certain defined rules to control cooling. They applied a method to adapt user scenarios with no prior knowledge. Similarly, Ngo [21] proposed an ensemble machine learning-based method to estimate the inside building cooling loads and analytically proven the ensemble learning as best performance. Hygh et al. [22] employed the Monte Carlo framework to develop multivariate linear regression model for 27 buildings that are relevant to early design, as the energy performance is sensitive to the size and building geometry. Another researcher, Wang and Ding [23], proposed an occupant-based PLF model for equipment by applying the polynomial and Markov Chain Monte method to investigate the time-varying occupancy rate. Considering time accumulation, they calculated the consumption of equipment in the office. Furthermore, Zhong et al. [24] defined a vector field based on support vector regression for PLF in building. They transformed the model nonlinearity into linearity using these vectors. Another research in [25] performed daily and hourly analysis with the use of quadratic regression such as simple and multiple linear regression. They proved that the time interval is the relevant factor that defines the model quality. Furthermore, the researchers also proposed clustering-based energy consumption to categorize electricity usage into different levels. Hence, a majority of these methods failed and remained limited to obtain accurate forecasting and least error.

2.2. Deep Learning-Based PLF Methods. Deep learning is gaining overwhelming growth in solving different computer vision tasks such as video analytics [26] or time-series problem [27, 28]. It deeply inspires the field of energy consumption and getting involved due to model robustness and performance. For instance, Muralitharan et al. [29] proposed an optimization approach based on a neural network to analyze the energy demand through PLF. They used neural network-based genetic algorithm and particle swarm optimization methodologies. A research carried out in [30] proposed a hybrid forecasting model based on evolutionary deep learning which combined the genetic algorithm with LSTM and optimized it with the objective function. Inspired by LSTM performance, a method presented in [31] applied deep recurrent neural network (DRNN) with LSTM for PLF and photovoltaic power in a microgrid. They proved that the DRNN with LSTM performs better than multilayer perceptron and optimized the load dispatch using the particle swarm algorithm. Next, Rahman et al. [32] developed two DRNNs to forecast the electricity and applied them over medium to long horizon. They further used these models to compute the missing data scheme. Several researchers proposed hybrid approaches of combining convolutional neural network (CNN) with LSTM autoencoder to forecast future energy in residential building. Similarly, Shi et al. [33] used pooling-based DRNN that batches the group comprise customer's profiles where they addressed the problem of overfitting by increasing the data volume and its diversity. An approach presented in [34] combined the stacked autoencoders with ELM as a hybrid connection. They used ELM as a predictor and used autocorrelation analysis to determine the ELM variables.

3. Proposed Power Load Forecasting Method

The energy consumption from small buildings infrastructure to global level has greater consequences. Worldwide development and rise in technology increased energy consumption. Its management by the users is greatly impacted, bringing drastic variations in economies and different sectors. In this view, the industries and smart grids have energy deficits due to wastage of large amount of energy, improper infrastructure, inefficient supply system, and the consumption building are not synchronized to efficiently

manage it. So far, the researchers apply several techniques to manage and synchronize the energy usage through its future forecasting. However, their improper spatial and temporal structure has made it more difficult to build the most robust forecasting model. The existing state of the arts have presented several sets of procedure but failed due to misleading features tools, metering procedure, etc. Based on these assumptions, we propose a proficient deep learning-assisted intelligent PLF method that provides a useful way to overcome the energy dissipation. The proposed method reduces the error rates with a high margin and obtains the most promising results. The visuals of each steps performed in the proposed method are presented in Figure 2, while the details are covered in the following sections.

3.1. Power Data Acquisition. This section delivers a detailed explanation of data gathering from its sources such as meter and installed sensors, and the data preprocessing is explained. To collect the data, wires across the building floors are articulated into a single edge with the main board and the meter with few sensors is installed to read and measure the energy consumed over the building setup where the data are normally collected with minute resolutions. Usually, the data collected through sensors and meter are greatly affected by the climate condition, occupant's behavior, redundancy, wire break or short circuit that brings abnormalities, outlier, and noise in the variable values. Tackling this issue is necessary for accurate forecasting; therefore, we refine the data prior to actual processing. For cleansing the data, we apply several smoothing filters such as LOESS or LOWESS that are used by numerous researchers [35, 36] for reasonable results. We remove the noise and considered the previous values on that position and remove data redundancy. In addition, we found the data attributes with different scale that are handled by applying the normalization.

3.2. Sequence Modeling via Long Short-Term Memory. Long-term dependencies with distant characteristics are not sufficiently captured through RNN because of the vanishing gradient effect. Therefore, the gating mechanisms are introduced where the classical activation is replaced. To model the sequential data, a type of recurrent neural networks (RNNs) such as LSTM has been proven to be the most stable and powerful network which understands and deals the long-range information [37]. LSTM has the capability of learning the long-term sequence information. The most interesting fact about the LSTM is their memory cells C_t that significantly act as accumulator for the state information. These cells are accessed, controlled, and written through numerous self-parameterized gates. The cells are accumulated by keeping the input gates active I_t with the arrival of a new information as an input. The controlled information flow inside the cell allows the network to memorize long-term dependencies. Similarly, if the forget gate F_t is active, the status of past cell C_{t-1} will be forgotten. Next, the latest information that will be controlled by the final gate F_t is managed by an output gate O_t. The most significant and vital role of the memory cells and gates for the information flow is such that the gradient will be trapped into the cell which is known to be constant error [38], is prevented from vanishing, and acts as a critical problem for vanilla RNN model [38]. The fully connected LSTM is considered to be LSTM multivariate version where the input, output, and forget gates are briefly given in Figure 3(a). The sigmoid activation determines what kind of information needs to be updated, as certain information might be ignored. The mechanism followed in an LSTM is defined by equations (1) to (6).

$$i_t = \sigma_g\left(W_i * x_t + W_i * h_{t-1} + b_i\right), \tag{1}$$

$$f_t = \sigma_g\left(W_f * x_t + W_f * h_{t-1} + b_f\right), \tag{2}$$

$$o_t = \sigma_g\left(W_o * x_t + W_o * h_{t-1} + b_o\right), \tag{3}$$

$$C_t = \sigma_c\left(W_c * x_t + W_c * h_{t-1} + b_c\right), \tag{4}$$

$$c_t = f_t * c_{t-1} + i_t * C_t, \tag{5}$$

$$h_t = o_t * \sigma_c\left(c_t\right), \tag{6}$$

where i_t, f_t, and o_t are the input, forget, and output gate, respectively, while c_t and h_t are the cell state and hidden state, respectively. Similarly, C_t is the vector value constructed for tanh at t represented by σ_c while σ_g is sigmoid function. $*$ is the elementwise multiplication. W_f, W_i, and W_{xo} are weight matrices representing forget, input, and output cell, respectively.

3.3. ConvLSTM Network. Input data that have to be collected in a longer time horizon can be reduced and filtered based on the convolution operations incorporated in LSTM networks or LSTM cell directly. Such approaches intend in the improvement of prediction accuracy of long-term sequence based on additional input data processing through projecting the data into lower dimensional space. Approaches to incorporate the convolution operations in LSTM are present in [39]. In the previous cases, the network is capable to model locally distributed relations and extract the corresponding features. LSTM, on the other hand, is useful to learn the temporal dependencies, so that the composition of the networks in the stacked form shows the best prediction results. Using convolutional LSTM, features can capture long-term horizon which makes them able of incorporating a larger amount of past information in the prediction. Fully connected LSTM is powerful in handling the temporal correlation and face redundancy in the spatial data. Tackling such an issue needs an extension of an entirely connected LSTM that has a convolutional' structure with both input and state-to-state transition. To form an encoding forecasting mechanism, multiple ConvLSTM layers are stacked together which not only build the model for precipitation forecasting but also build the model for spatiotemporal sequencing forecasting procedure. In fully connected LSTM, the inputs are unfolded into 1D vectors before actual processing to handle the spatiotemporal data; as result of this, the important information is lost. This

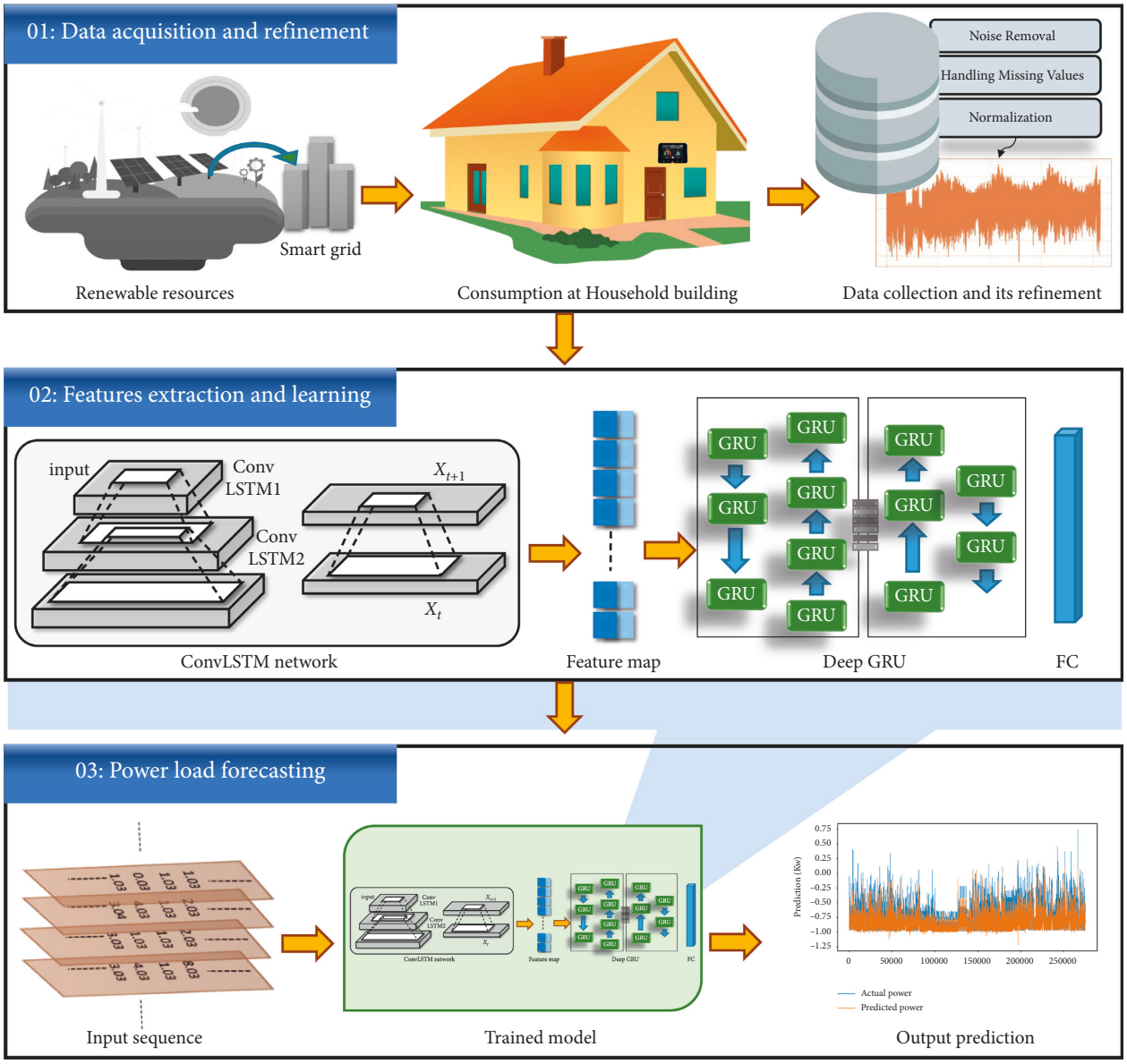

FIGURE 2: Overview of the proposed framework. Step 1: Data acquisition from sensors and the smart meters that contain the user behavior for data management and response to energy usage. Also, its refinement is performed to stabilize and remove the user behavior. Step 2: Detailed feature extraction from the energy data through ConvLSTM. Step 3: The prediction of future energy consumption based on the input data resolution.

problem can be overcome such that all the inputs into ConvLSTM are likely to be 3D tensors where the last dimensions are spatial row and column. ConvLSTM defines next state of some cells into a grid through inputs and previous states around its neighbor sides. This strategy can be achieved through convolution operation from the input-to-state and also state-to-state transitions. Furthermore, the deep mechanism along with the key equations of the process is given in equations (7) to (11).

$$i_t = \sigma\left(W_{xi} * x_t + W_{hi} * \mathcal{H}_{h-1} + W_{ci} o C_{t-1} + b_i\right), \quad (7)$$

$$f_t = \sigma\left(W_{xf} * x_t + W_{hf} * \mathcal{H}_{T-1} + W_{cf} o C_{t-1} + b_f\right), \quad (8)$$

$$C_t = F_t o C_{t-1} + i_t o \tanh\left(W_{xc} * X_t + W_{hc} * \mathcal{H}_{t-1} + b_C\right), \quad (9)$$

$$o_t = \sigma\left(W_{xo} * x_t + W_{ho} * \mathcal{H}_{t-1} + W_{co} o C_t + b_o\right), \quad (10)$$

$$H_t = o_t o \tanh\left(C_t\right). \quad (11)$$

Similar to simple LSTM, the ConvLSTM can also be adopted which is the building block for the complex type of structure. The structure presented in Figure 3(c) solves the forecasting problem of our spatiotemporal sequence. The structure of this building block consists of an encoding and a forecasting network. To form such a

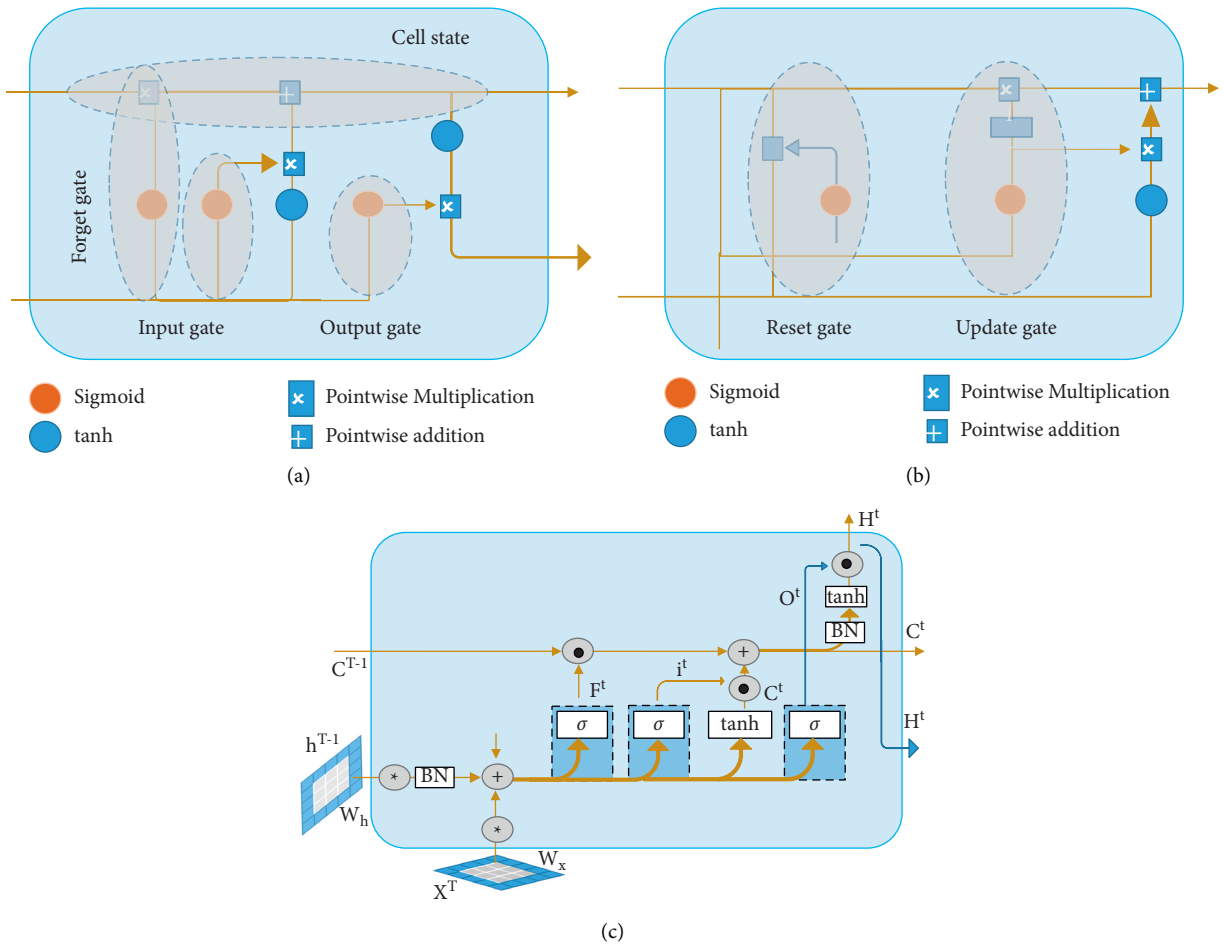

Figure 3: Internal structure of each sequential network. (a) LSTM has three main gates such as input, output, and forget. (b) GRU has two gates including reset and update. (c) Internal mechanism of ConvLSTM.

network, multiple ConvLSTM layers are stacked together, where the states in forecasting network are concatenated and fed into a 1×1 convolutional layer to generate final forecasting. This strategy is performed, as the input has the same dimensionality to target the prediction. This structure is considered with a similar viewpoint as in [37]. The encoding LSTM compresses the given sequence into state of hidden tensor where the forecasting LSTM unfolds the hidden state that gives the final prediction. The structure of this network is similar to LSTM as a future prediction model [40], but the input and output elements in our model are 3D tensors where the spatial information is preserved. As multiple ConvLSTM layers are stacked together, they give a strong representation and empower to give a fine prediction for a complex sequence such as PLF.

3.4. Deep GRU Network. GRU is an improved form of RNN which uses the time-series data sample for forecasting purposes. Traditional neural networks are characterized via the interconnection established between the input towards the hidden layer and then towards the input layer where a direct node in every layer is connected [41]. Consequently, RNN memorizes the previously passed information that is applied to compute and find the current output. Several improvements are made in LSTM that solve the common errors and the shortcomings in the long-term sequential application of RNN. For instance, LSTM holds three gates such as input, output, and forget. Here, the forget gate is used to control the information and its rate of forgotten, while the output gate is applied to control the status of current unit condition that is strained out. The GRU overcomes the deficiencies present in RNN which is unable to handle the long-term dependencies in an effective manner; however, GRU on the other hand, makes the structure simpler and brings efficiency by preserving the effectiveness of LSTM [42]. The GRU network is well visualized in Figure 3(b). The GRU contains two gate functions, namely update and reset. The update gate function is to control the state information of the previous moment that is brought to current state (rate of updating state information). The greater the value of the update function, the more information will be brought in the previous moment. Similarly, the reset gate controls to avoid the information obtained from the previous moment (rate of forgetting information). The minute value of the reset gate indicates more information will be forgotten.

Subsequently, the unit state and output are combined into a single state H where the input is X_t, the state previously passed by the hidden layer is H_{t-1}, and similarly the information from the previous node is included via X_t and H_{t-1}. The GRU gets the output from the hidden state with the control gate while the information is passed into the next hidden layer. Two gates with states are obtained that are based on information Z_t and R_t, which are given in the following equations.

$$p_t = f\left(w_p\left[x_t, h_{t-1}\right] + b_p\right), \tag{12}$$

$$q_t = f\left(w_q\left[x_t, h_{t-1}\right] + b_q\right), \tag{13}$$

where W_p and W_q are weights of neurons, f shows the sigmoid function controlling the values between 1 and 0, which are used to obtain the gating signal. After getting the signal, first, the reset gate is used and then the data are obtained from the reset function that is combined with tanh activation function that give $\sim H_t$.

4. Experimental Results

This section discusses the experiments performed over the competitive energy dataset such as the household power dataset [43]. We comprehensively inspect the energy consumption and discuss the details of the dataset in the subsequent sections. Similarly, we visualize the results of energy consumption and its forecasting. The comparison of forecasting results on the existing dataset with state of the art is also covered which prove the effectiveness of the proposed method.

4.1. Implementation Settings. We verify and analyze the results of the proposed method using different kinds of experiments to check and evaluate the method's performance. The proposed method is implemented in Python (Version 3.5) with Keras (Deep Learning Framework) supported by the TensorFlow at the backend and ADAM-prop optimizer is used. Next, as we are dealing with regression problem, we apply four basic evaluation metrics such as MSE, RMSE, mean absolute error (MAE), and mean absolute percentage error (MAPE). These metrics are abundantly used for performance evaluation in regression problems throughout the energy forecasting-related literature. MSE is the basic error metric used in the PLF, renewable energy generation forecasting, weather prediction, humidity, etc. The formulation of each metric is described below:

Suppose $y_i^{\sim}$ indicates the variable values for n number of predictions for energy consumption and y_i indicates the observed values, so equations (14) to (16) show the MSE, RMSE, and MAE formulation where the RMSE is the square root of MSE values. Similarly, to measure the performance of forecasting that compute the correctness of the proposed method, MAPE is used, which gives the absolute error in percentage and compute the mean of the error and is given in equation 17.

$$MSE = \frac{1}{n}\sum_{i}^{n}\left(y_i - y_i^{\sim}\right)^2, \tag{14}$$

$$RMSE = \sqrt{MSE} = \sqrt{\frac{1}{n}\sum_{i}^{n}\left(y_i - y_i^{\sim}\right)^2}, \tag{15}$$

$$MAE = \frac{1}{n}\sum_{i}^{n}\left|y_i - y_i^{\sim}\right|, \tag{16}$$

$$MAPE = \frac{100\%}{n}\sum_{i}^{n}\left|\frac{y_i - y_i^{\sim}}{y_i}\right|. \tag{17}$$

4.2. Dataset. Standard and publicly available dataset is used to verify and evaluate the proposed method. The dataset is publicly available at [43] and its further details are covered in the following sections.

4.2.1. House Power Dataset. We evaluate and analyze the proposed ConvLSTM-GRU network using several kinds of experiments to gauge its performance on the household power dataset [43] that is available on the UCI official (deep learning) repository. This dataset is collected between 2006 and 2010—4 years of data. It contains 2075259 instances, where 25979 instances contain missing values making 1.25% of total data. Usually, the use of missing values creates problems in incorrect forecasting of energy consumption. Researchers use various techniques to overcome this problem. To tackle this problem, we pass the data from the refinement step that is previously explained in the proposed method. Next, this dataset is covered with 1 minute's time horizons of electric power consumption over the building located in France. In this dataset, the global active power indicates the total power consumed by submetering 1, 2, and 3 over single minutes provided in watt-hours. Testing the proposed method, we use different time steps that explain the PLF for each time horizon. The variables used in this dataset are given in Table 1 with their detailed remarks. Furthermore, we provide the quantitative details of the household power dataset in Table 2, where 11.12 is the maximum value for active power given in kilowatts and 0.076 is the minimum value. If we analyze the attribute values, the maximum energy is consumed over submetering 1 such as 88.000 that is dissipated over the daily usage devices such as microwave oven, dishwasher, etc.

4.3. Result Analysis and Discussion. This section describes the detailed experimental evaluation of the proposed method on the household power dataset [43].

We perform an ablation study where each model is implemented and trained on the given dataset to inspect the performance of the proposed method. These models include GRU and its variants such as encoder-decoder GRU (ED-GRU) and CNN-GRU. Each deep learning network is

Table 1: Household power dataset [43] with its attribute description.

#	Given attributes	Given symbol	Used units	Description
1	Date	D	Days/months/years	1~30/1~12/2006~2010
2	Timing	T	Hours/minutes/seconds	1~24/1~60/1~60.
3	Active power	AP	Kilowatts	Total power consumed in each minute
4	Reactive power	RP	---	Total reactive power consumed in each minute
5	Voltage	V	Volts	Total voltage in each minute
6	Intensity	I	Ampere	Current consumed in each minute.
7	Submetering-1	$S(1)$	Watts per hour	Energy consumed for dishwasher and microwave oven.
8	Submetering-2	$S(2)$	---	Energy consumed in living room over washing machines, drier, and refrigerator
9	Submetering-3	$S(3)$	---	Energy consumed for air conditioner and water heater

Table 2: Detailed description of the household power dataset [43] with its attributes and quantitative analysis.

Attribute	D	AP	RP	V	I	$S1$	$S2$	$S3$
Average	/	1.089	0.124	240.844	4.618	1.117	1.289	6.453
Min	16.12.2006	0.076	0	223.200	0.200	0	0	0
Max	26.11.2010	11.12	1.390	254.150	48.400	88.000	80.000	31.000
Std. Dev	/	0.055	0.113	3.239	4.435	6.139	5.794	8.436

compared with the proposed method for every time horizon such as minute, hour, day, and week. The deep learning networks are trained up to 100 epochs. Originally, the data in the household power dataset are given in minutes' resolution. For experiments, we convert the data into hour, day, and weekly horizons. After conversion, the number of instances become smaller which can be easily identified from the patterns given in Figure 4 showing the representation of the data.

4.3.1. Performance Evaluation of the GRU Network. Conducting the experiments, the deep GRU is initially evaluated to check its performance over the household power dataset [43]. Basically, the GRU network tries to solve the vanishing gradient problem which is originated with the standard RNN. This network is also considered to be a variation of LSTM because both have similarities and sometimes produce equally excellent results. A simple GRU network uses update and reset gates which are basically two vectors that control the information which need to be passed as an input. Its internal details are covered in the previous section while its internal structure is given in Figure 3(b).

For experiments, two GRU layers are stacked together followed by the dense layer. The total obtained parameters for this network are 382607. Furthermore, the values obtained for MSE, RMSE, MAE, and MAPE for GRU on minutes' horizons are 0.3569, 0.5974, 0.4012, and 0.4083, respectively. The other error values obtained for the household power dataset on each time horizon such as minute, hour, day, and weekly are provided in Table 3. The forecasting obtained for energy consumption over minute and hour time horizons using the GRU network is graphically presented in Figure 5, while the daily and weekly based results are given in Figure 6.

4.3.2. Performance Evaluation of the ED-GRU Network. Subsequently, we also use the ED-GRU network to identify its results and performance in the forecasting of energy consumption over the buildings. Setting the internal structure of ED-GRU, the encoder is set to stack several layers of GRU in such a way that each unit accepts a single input element sequence and collects the most important information from it and forward propagate it. Internally, the encoder vector is produced from the encoder which is known to be final hidden state. This state encapsulates the information of all the input elements to make an accurate load forecasting of power energy. It acts to be the hidden state of the model decoder part. Next, the decoder stacks several units which predict the output y at time t. Each of the decoder unit accepts the hidden state from the previous and produce its own hidden state. The hidden state h_i can be calculated using the formula given in (18) while the output y_t at time t is calculated through the formula given in (19). The layered GRU is followed by the time distributed layer. The number of obtained parameters for ED-GRU is 154,051. The values obtained on each time resolution for the household power dataset are given in Table 3. Next, the forecasting for the energy consumed considering minute and hour resolution is visually presented in Figure 7 while the daily and weekly based forecasting is given in Figure 8. The MSE obtained for ED-GRU on the household power dataset considering minute horizon is 0.3246 while RMSE, MAE, and MAPE are 0.5697, 0.3635, and 0.3485, respectively. Similarly, its performance is somehow improved on hour resolution with the least MSE which is 0.3134. Similar to its performance on the household power dataset, its performance becomes better when daily resolution is considered, where the value becomes 0.3054 while the RMSE, MAE, and MAPE are 0.5526, 0.3519, and 0.3401, respectively. Hence, this analysis clearly exhibits the good performance of ED-GRU after CNN-GRU and the proposed method.

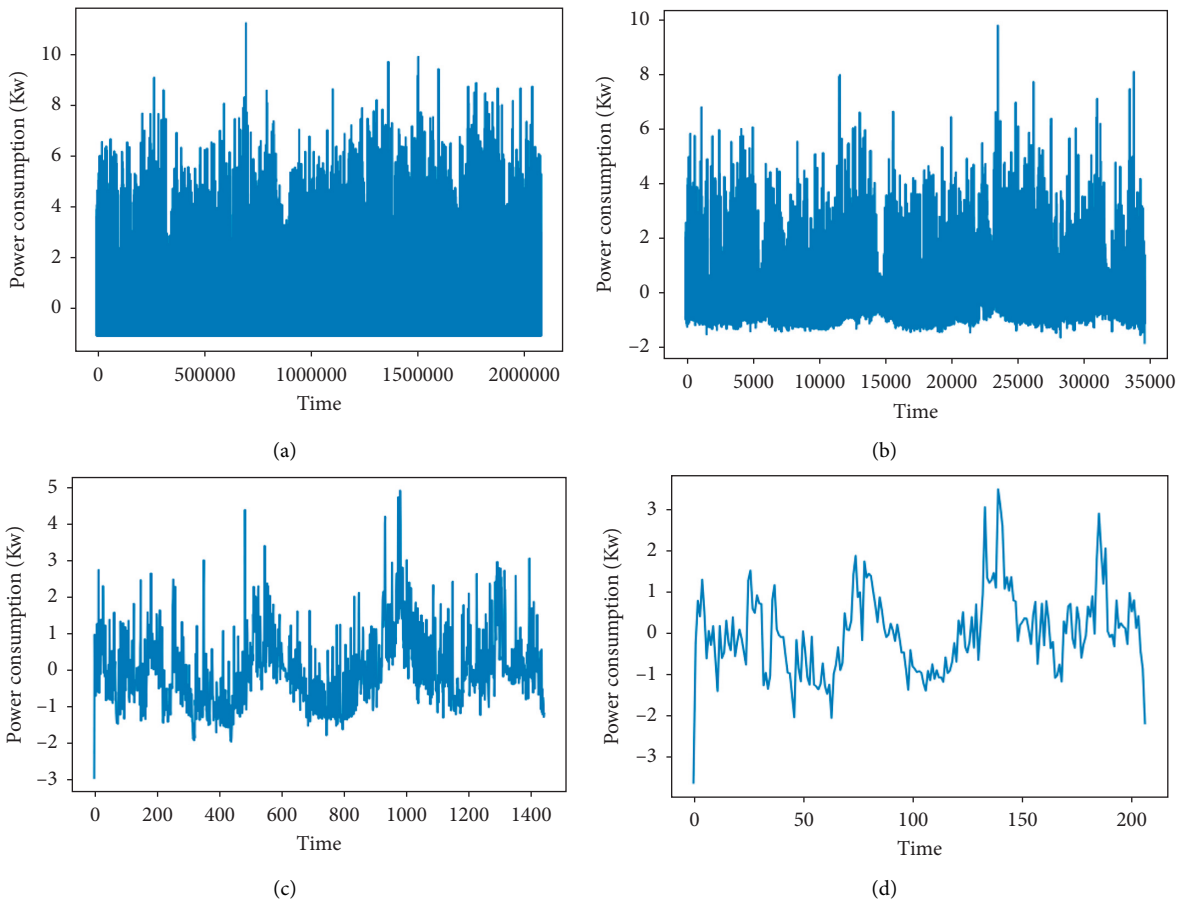

Figure 4: Data representation of the publicly available household power dataset [43] with different horizons. (a) Minutely data. (b) Hourly data. (c) Daily data. (d) Weekly data.

Table 3: Performance results of the proposed method and its comparison with other competitive deep learning models on the household power dataset for all time horizons such as minute, hour, daily, and week.

Methods	MSE	RMSE	MAE	MAPE
		Minutely		
GRU	0.3569	0.5974	0.4012	0.4083
ED-GRU	0.3246	0.5697	0.3635	0.3485
CNN-GRU	0.3215	0.5670	0.3618	0.3064
Proposed method	**0.3101**	**0.5568**	**0.3467**	**0.2902**
		Hourly		
GRU	0.3251	0.5701	0.3814	0.3962
ED-GRU	0.3134	0.5598	0.3585	0.3415
CNN-GRU	0.2897	0.5382	0.3607	0.3042
Proposed method	**0.2384**	**0.4882**	**0.3435**	**0.2897**
		Daily		
GRU	0.3099	0.5566	0.3691	0.3586
ED-GRU	0.3054	0.5526	0.3519	0.3401
CNN-GRU	0.2821	0.5311	0.3524	0.3021
Proposed method	**0.2315**	**0.4811**	**0.3419**	**0.2879**
		Weekly		
GRU	0.3198	0.5655	0.3796	0.3697
ED-GRU	0.3157	0.5618	0.3627	0.3591
CNN-GRU	0.2981	0.5459	0.3619	0.3032
Proposed method	**0.2497**	**0.4996**	**0.3517**	**0.2882**

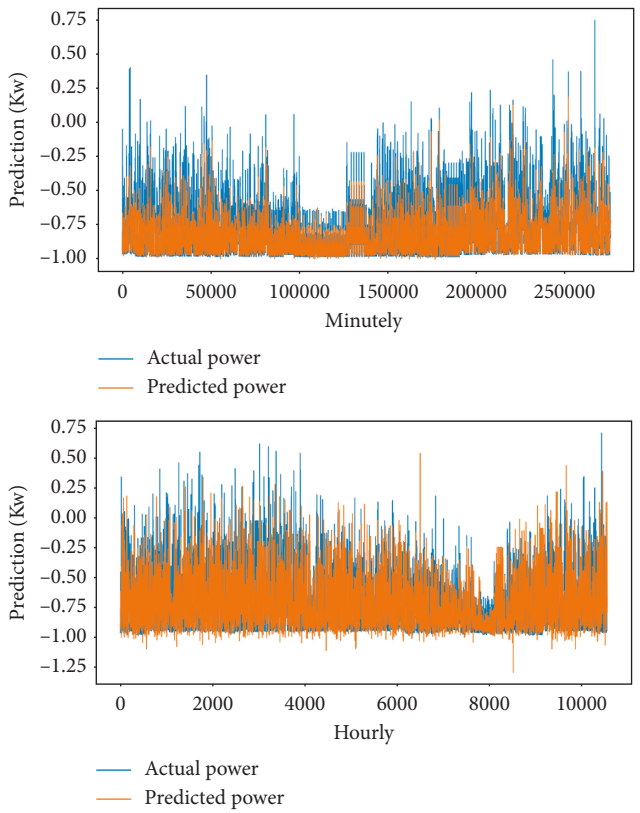

Figure 5: Visual representation of GRU-based forecasting results considering minute and hour horizons on the household power dataset.

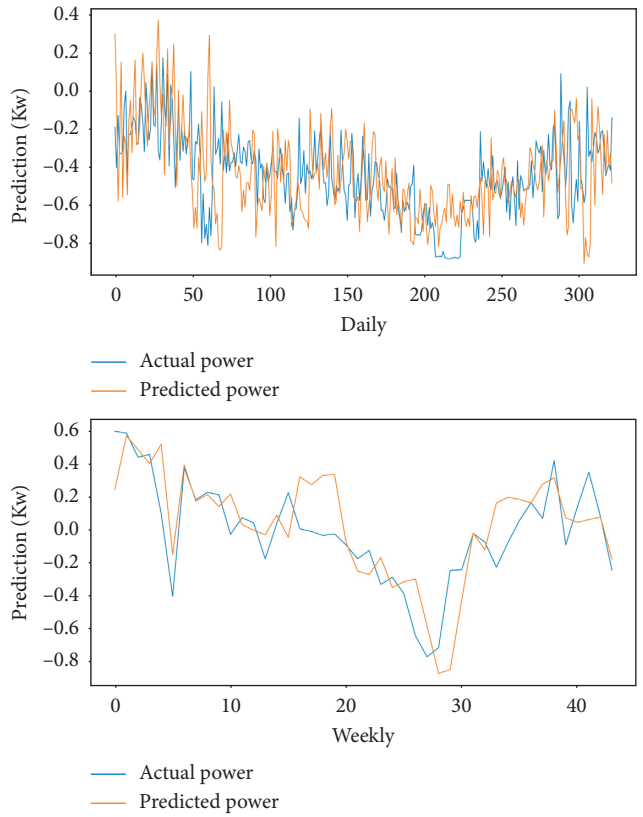

Figure 6: Visual representation of GRU-based forecasting results considering daily and weekly horizons on the household power dataset.

$$hs_t = f\left(W^{(hh)} hs_{t-1}\right),$$
$$y_t = \text{software}\left(W^s hs_t\right). \tag{18}$$

4.3.3. Performance Evaluation of the CNN-GRU Network. Recently, CNNs have shown the most promising results in different fields such as computer vision, time-series analysis, energy informatics, and energy monitoring system. To evaluate and analyze its performance, we incorporate its several layers for PLF problem. We combine it as hybrid connection with deep GRU and add three convolutional layers followed by the max pooling and flatten layer. The features obtained from these layers are given to deep GRU where two GRU layers are connected and followed by the time distributed layer. Furthermore, the error values obtained for each time horizon on the CNN-GRU network for the household power dataset are given in Table 3. Moreover, the forecasting of energy consumption on this network considering minute and hour resolution is graphically illustrated in Figure 9, while the daily and weekly based consumption forecasting is given in Figure 10. The CNN-GRU network has better performance than other deep learning models for consumption forecasting in terms of MAPE and MAE metrics.

Furthermore, CNN-GRU has better performance over all the methods and become a runner up. CNN-GRU shows the same response as ED-GRU in terms of its performance for resolution. For instance, CNN-GRU achieves an MSE of 0.3215 value considering the minute horizon; however, its results become better in hour resolution where MSE obtained is 0.2897. The value of RMSE, MAE, and MAPE obtained for CNN-GRU considering minutes resolution is 0.5670, 0.3618, and 0.3964, respectively. After deep analysis, we realize that CNN-GRU reflects its better results on the household power dataset rather than in terms of considering the minute resolution. In the final phase, we pose the results obtained for the proposed ConvLSTM with the GRU network. The values obtained by the proposed method on the household power dataset for metrics of MSE, RMSE, MAE, and MAPE for the minute horizon are 0.3101, 0.5568, 0.3467, and 0.2902, respectively, and are given in Table 3. Next, the visual representation of forecasting results considering minute and hour resolution is given in Figure 11, while the daily and weekly based resolution results are depicted in Figure 12.

5. Comparison with State of the Art

In this section, we analyze and compare the results of the proposed method with existing competitive state of the art in terms of performance considering the basic metric using the household power dataset. For a fair comparison, we consider and evaluate the minute horizon of the proposed method as

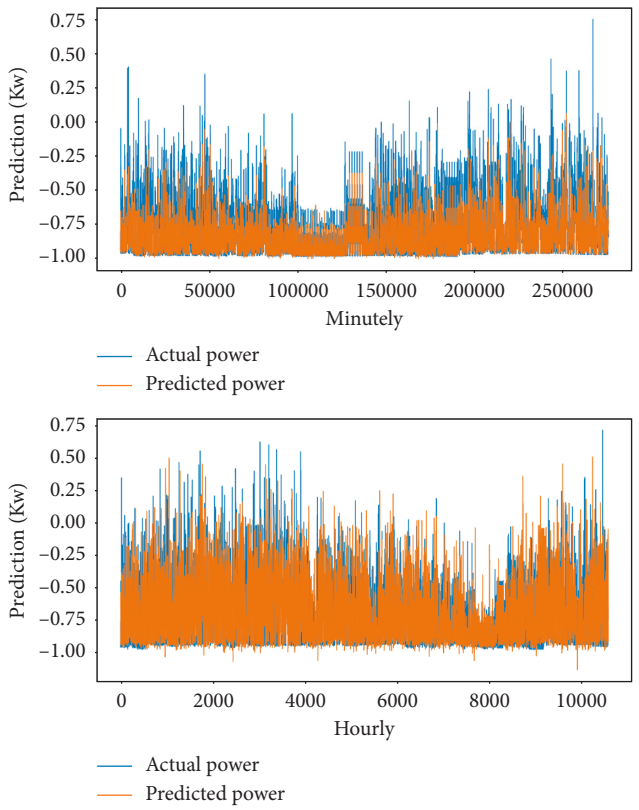

Figure 7: Visual representation of ED-GRU-based forecasting results considering minute and hour horizons on the household power dataset.

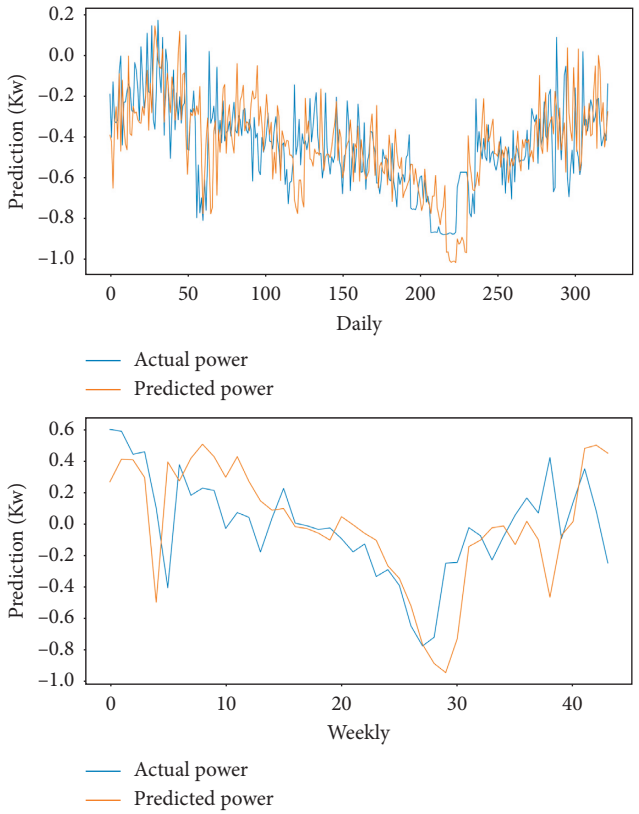

Figure 8: Visual representation of ED-GRU-based forecasting results considering daily and weekly horizons on the household power dataset.

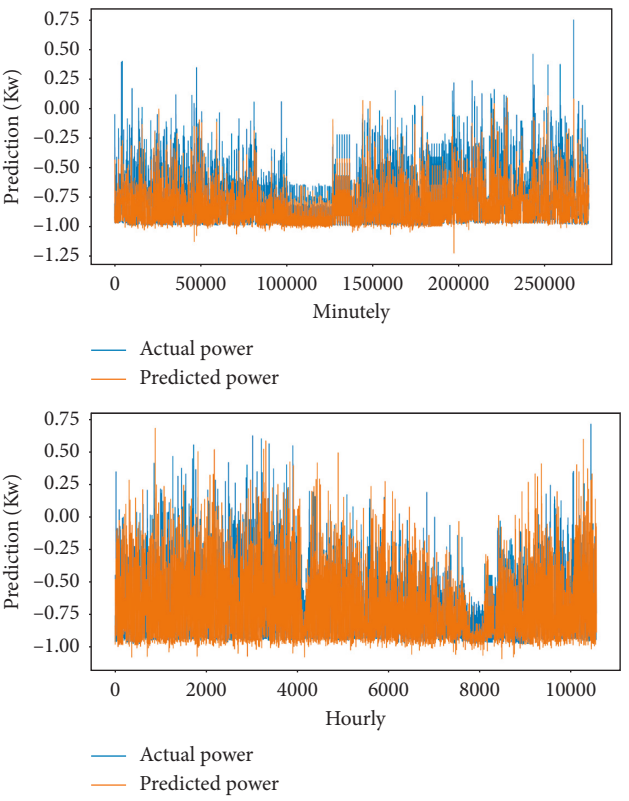

Figure 9: Visual representation of CNN-GRU-based forecasting results considering minute and hour horizons on the household power dataset.

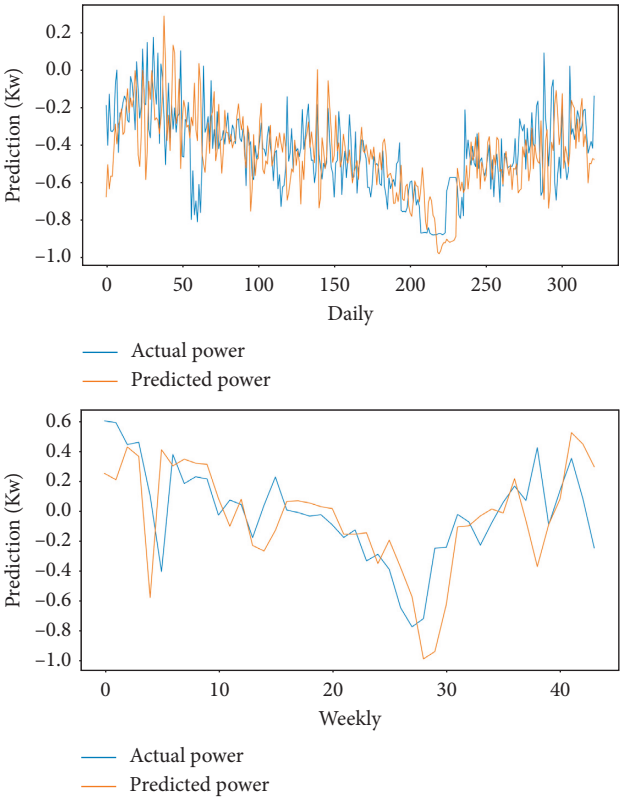

Figure 10: Visual representation of CNN-GRU-based forecasting results considering daily and weekly horizons on the household power dataset.

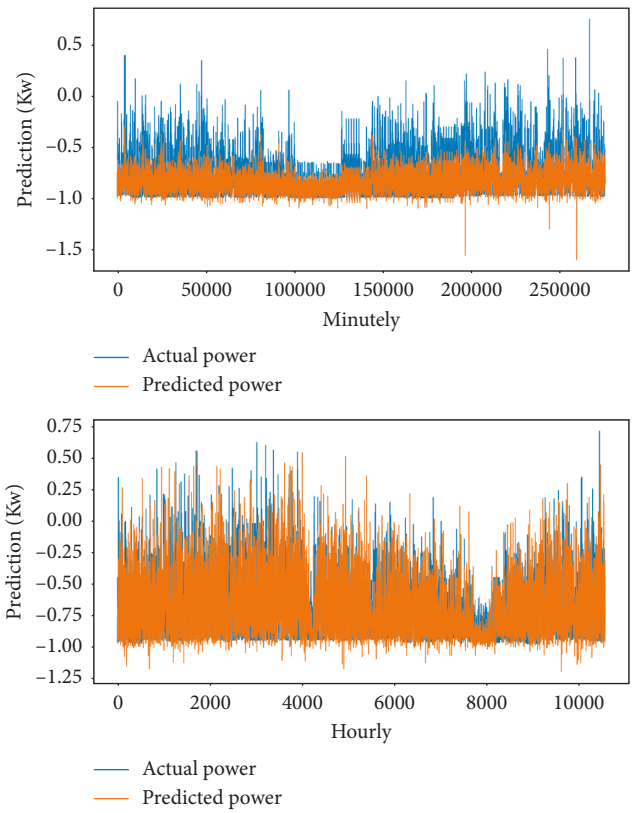

Figure 11: Forecasting results obtained using the proposed method for the household power dataset considering minute and hour time horizons.

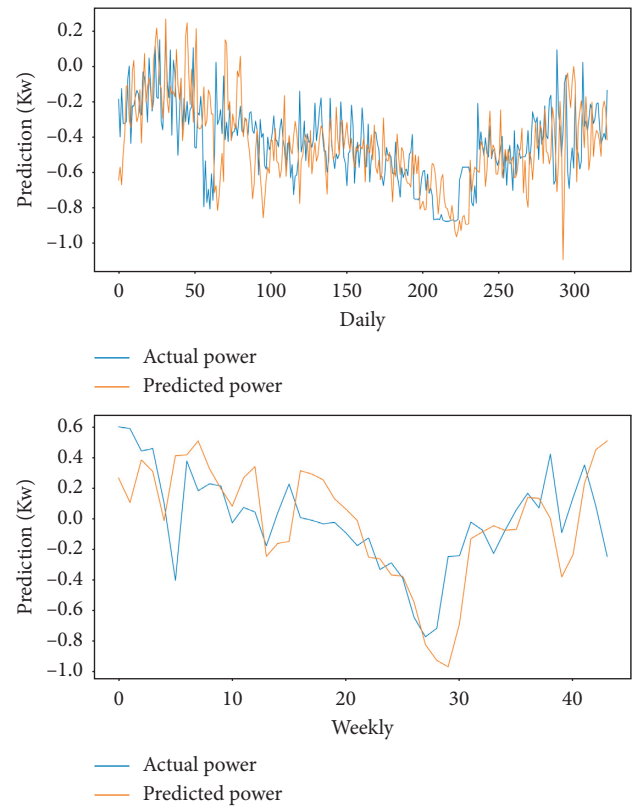

Figure 12: Forecasting results obtained through the proposed method for the household power dataset over day and week time horizons.

considered by other works. Similarly, we consider the same metrics for comparison. A method presented in [47] proposed a three-stage hybrid network of CNN with a multilayer BLSTM network to forecast the power load. They first practiced LSTM and then BLSTM to assess their performance by obtaining 0.3446 and 0.3295 MSE values, respectively. However, their proposed method's outcomes obtained for MSE, RMSE, MAE, and MAPE on this method are 0.3193, 0.5650, 0.3469, and 0.2910, respectively. Next, Mocanu et al. [44] investigated two main models to estimate the energy consumption in buildings such as the conditional restricted Boltzmann machine and the factored conditional restricted Boltzmann machine. They further considered the support vector machine and RNN to investigate their method. Their method used a single layer of factored conditional restricted Boltzmann machine to fit the needs for representing different useful parameters. They used RMSE as an evaluation metric and obtained 0.6663 value for it. They also computed correlation coefficient (R) and p-value achieving 0.4552 and 0.0070, respectively. Furthermore, Kim and Cho [45] proposed a deep learning-based method to forecast the energy demand. For this purpose, they used a state explainable autoencoder-based model and obtained 0.3840 value for the RMSE metric. A research presented in [46] used the hybrid approach of CNN with LSTM and reported 0.3738, 0.6114, 0.3493, and 0.3484 values for MSE, RMSE, MAE, and MAPE, respectively. The comparative results are summarized in Table 4.

Table 4: Detailed comparative analysis with competitive state of the arts with the proposed method on the household power dataset.

Techniques	Evaluation metrics			
	MSE	RMSE	MAE	MAPE
FCBRM [44]	—	0.6663	—	—
BPTT [45]	0.3840	0.6196	0.3953	—
CNN-LSTM [46]	0.3738	0.6114	0.3493	0.3484
CNN-M-BLSTM [47]	0.3193	0.5650	0.3469	0.2910
Proposed method	0.3101	0.5568	0.3467	0.2902

Primarily, the aforementioned methods apply the traditional way of collecting the feature information from the sequence, which are old machine learning practices yielding lower correctness in prediction problem. Similarly, in the case of deep learning usage by these methods, their networks apply complex architectures where the training consumes more time. Next, if overview, the PLF methods are heading towards convolutional networks and sequential learning mechanisms such as RNN, LSTM, or BLSTM, which are the recent state-of-the-art learning methods [48]. These methods highly rely on the input model parameters and mostly hunt towards error reduction for the precise prediction. After thorough exploration, these methods have high error rates considering the minute horizon and have complex architecture. We improved our method by reducing the

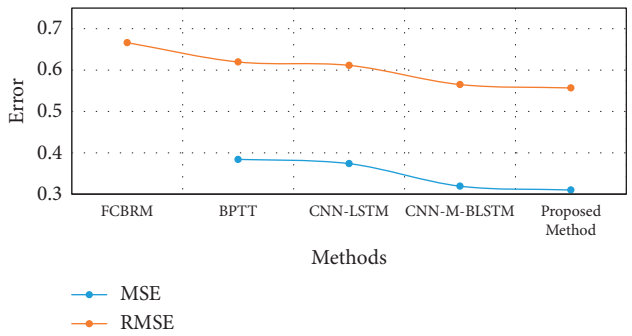

Figure 13: Comparative analysis of the proposed method with state of the arts. The blank area for FCBRM shows that there is no MSE value provided by them.

error to 0.3101 while the runner up method is our previously published work with an error rate of 0.3193. The comparison of our method with other PLF methods is visually presented in Figure 13.

6. Conclusions

Over the decades, the energy demand is growing throughout the world due to an increase in technology, industrial machinery, and population. This results in the wastage of a large amount of energy due to a lack of efficient usage and its storage from the grid or renewable energy resources. Therefore, energy generation companies and smart grid authorities are investigating new ways to tackle this issue. To this end, we proposed an intelligent deep learning-based architecture for energy to boost the PLF for the proper establishment of energy infrastructure. To carry out, initially, the data collected through various installed sensors and meters are fed into the acquisition layer for refinement purposes. Next, the refined data are passed into the ConvLSTM network to extract the deep features and generate the final feature map. Further, the feature map is passed into deep GRU to learn the series which gives us final forecasting of the energy. In addition, we proved that the proposed method outperforms the existing state of the art using different error metrics that are applied for regression model evaluation. The proposed method is verified and tested on a publicly available household power dataset.

In the future, we intend to enhance the method by the involvement of the Internet of things (IoT) [49], that is the deployment over resource-constrained devices, which will reduce the complexity in terms of computational power and resources as performed in [50]. This will help to reduce the bandwidth and easethe transmission of information. Furthermore, we aim to include the forecasting for years and decade-wise consumption and generation of power energy by considering various characteristics. The characteristic involves weather condition, energy consumption over industries, public transport, and occupants' behavior in response to these disruptions. We will incorporate these kinds of datasets to further confirm and verify their impact on load forecasting.

Data Availability

The data that are used to support the findings of this study are included at https://archive.ics.uci.edu/ml/datasets/individual+household+electric+power+consumption.

Conflicts of Interest

The authors declare that they have no conflicts of interest.

Acknowledgments

This work was supported by the National Research Foundation of Korea (NRF) grant funded by the Korea government (MSIT) (No. 2019M3F2A1073179).

References

[1] P. Zhang, X. Ma, and K. She, "A novel power-driven grey model with whale optimization algorithm and its application in forecasting the residential energy consumption in China," *Complexity*, vol. 2019, pp. 1–22, Article ID 1510257, 2019.

[2] H. Luo, H. Zhang, and J. Wang, "Ensemble power load forecasting based on competitive-inhibition selection strategy and deep learning," *Sustainable Energy Technologies and Assessments*, vol. 51, Article ID 101940, 2022.

[3] B. Wang, L. Zhang, H. Ma, H. Wang, and S. Wan, "Parallel LSTM-based regional integrated energy system multienergy source-load information interactive energy prediction," *Complexity*, vol. 2019, pp. 1–13, Article ID 7414318, 2019.

[4] X. Guo, Q. Zhao, S. Wang, D. Shan, and W. Gong, "A short-term load forecasting model of LSTM neural network considering demand response," *Complexity*, vol. 2021, Article ID 5571539, 2027 pages, 2021.

[5] A. Yang, W. Li, and X. Yang, "Short-term electricity load forecasting based on feature selection and Least Squares Support Vector Machines," *Knowledge-Based Systems*, vol. 163, pp. 159–173, 2019.

[6] S. Woo-hyun, "Moon's nuclear-free policy lauded but face technical hurdles," 2017, http://www.koreaherald.com/view.php?ud=20170623000670.

[7] Z. Wang and R. S. Srinivasan, "A review of artificial intelligence based building energy use prediction: contrasting the capabilities of single and ensemble prediction models," *Renewable and Sustainable Energy Reviews*, vol. 75, pp. 796–808, 2017.

[8] Y. Chen, Z. Dong, Y. Wang et al., "Short-term wind speed predicting framework based on EEMD-GA-LSTM method under large scaled wind history," *Energy Conversion and Management*, vol. 227, Article ID 113559, 2021.

[9] J. Massana, C. Pous, L. Burgas, J. Melendez, and J. Colomer, "Short-term load forecasting for non-residential buildings contrasting artificial occupancy attributes," *Energy and Buildings*, vol. 130, pp. 519–531, 2016.

[10] A. Tascikaraoglu and B. M. Sanandaji, "Short-term residential electric load forecasting: a compressive spatio-temporal approach," *Energy and Buildings*, vol. 111, pp. 380–392, 2016.

[11] M. H. Alobaidi, F. Chebana, and M. A. Meguid, "Robust ensemble learning framework for day-ahead forecasting of household based energy consumption," *Applied Energy*, vol. 212, pp. 997–1012, 2018.

[12] P. Lusis, K. R. Khalilpour, L. Andrew, and A. Liebman, "Short-term residential load forecasting: impact of calendar effects

and forecast granularity," *Applied Energy*, vol. 205, pp. 654–669, 2017.

[13] F. U. M. Ullah, N. Khan, T. Hussain, M. Y. Lee, and S. W. Baik, "Diving deep into short-term electricity load forecasting: comparative analysis and a novel framework," *Mathematics*, vol. 9, no. 6, p. 611, 2021.

[14] N. Khan, I. U. Haq, F. U. M. Ullah, S. U. Khan, and M. Y. Lee, "CL-net: ConvLSTM-based hybrid architecture for batteries' state of health and power consumption forecasting," *Mathematics*, vol. 9, no. 24, p. 3326, 2021.

[15] I. Koprinska, M. Rana, and V. G. Agelidis, "Correlation and instance based feature selection for electricity load forecasting," *Knowledge-Based Systems*, vol. 82, pp. 29–40, 2015.

[16] A. Abdoos, M. Hemmati, and A. A. Abdoos, "Short term load forecasting using a hybrid intelligent method," *Knowledge-Based Systems*, vol. 76, pp. 139–147, 2015.

[17] R. Talavera-Llames, R. Pérez-Chacón, A. Troncoso, and F. Martínez-Álvarez, "Big data time series forecasting based on nearest neighbours distributed computing with Spark," *Knowledge-Based Systems*, vol. 161, pp. 12–25, 2018.

[18] L. Harrington, L. Aye, and B. Fuller, "Impact of room temperature on energy consumption of household refrigerators: lessons from analysis of field and laboratory data," *Applied Energy*, vol. 211, pp. 346–357, 2018.

[19] Y. Guo, J. Wang, H. Chen et al., "Machine learning-based thermal response time ahead energy demand prediction for building heating systems," *Applied Energy*, vol. 221, pp. 16–27, 2018.

[20] Y. Peng, A. Rysanek, Z. Nagy, and A. Schlüter, "Using machine learning techniques for occupancy-prediction-based cooling control in office buildings," *Applied Energy*, vol. 211, pp. 1343–1358, 2018.

[21] N.-T. Ngo, "Early predicting cooling loads for energy-efficient design in office buildings by machine learning," *Energy and Buildings*, vol. 182, pp. 264–273, 2019.

[22] J. S. Hygh, J. F. DeCarolis, D. B. Hill, and S. Ranji Ranjithan, "Multivariate regression as an energy assessment tool in early building design," *Building and Environment*, vol. 57, pp. 165–175, 2012.

[23] Z. Wang and Y. Ding, "An occupant-based energy consumption prediction model for office equipment," *Energy and Buildings*, vol. 109, pp. 12–22, 2015.

[24] H. Zhong, J. Wang, H. Jia, Y. Mu, and S. Lv, "Vector field-based support vector regression for building energy consumption prediction," *Applied Energy*, vol. 242, pp. 403–414, 2019.

[25] N. Fumo and M. Rafe Biswas, "Regression analysis for prediction of residential energy consumption," *Renewable and Sustainable Energy Reviews*, vol. 47, pp. 332–343, 2015.

[26] F. U. M. Ullah, M. S. Obaidat, K. Muhammad et al., "An intelligent system for complex violence pattern analysis and detection," *International Journal of Intelligent Systems*, vol. 12, 2021.

[27] C. Fan, Y. Sun, Y. Zhao, M. Song, and J. Wang, "Deep learning-based feature engineering methods for improved building energy prediction," *Applied Energy*, vol. 240, pp. 35–45, 2019.

[28] N. Khan, F. U. M. Ullah, A. Ullah, A. Ullah, M. Y. Lee, and S. W. Baik, "Batteries state of health estimation via efficient neural networks with multiple channel charging profiles," *IEEE Access*, vol. 9, pp. 7797–7813, 2021.

[29] K. Muralitharan, R. Sakthivel, and R. Vishnuvarthan, "Neural network based optimization approach for energy demand prediction in smart grid," *Neurocomputing*, vol. 273, pp. 199–208, 2018.

[30] A. Almalaq and J. J. Zhang, "Evolutionary deep learning-based energy consumption prediction for buildings," *IEEE Access*, vol. 7, pp. 1520–1531, 2019.

[31] L. Wen, K. Zhou, S. Yang, and X. Lu, "Optimal load dispatch of community microgrid with deep learning based solar power and load forecasting," *Energy*, vol. 171, pp. 1053–1065, 2019.

[32] A. Rahman, V. Srikumar, and A. D. Smith, "Predicting electricity consumption for commercial and residential buildings using deep recurrent neural networks," *Applied Energy*, vol. 212, pp. 372–385, 2018.

[33] H. Shi, M. Xu, and R. Li, "Deep learning for household load forecasting—a novel pooling deep RNN," *IEEE Transactions on Smart Grid*, vol. 9, no. 5, pp. 5271–5280, 2018.

[34] C. Li, Z. Ding, D. Zhao, J. Yi, and G. Zhang, "Building energy consumption prediction: an extreme deep learning approach," *Energies*, vol. 10, p. 1525, 2017.

[35] I. Ullah, R. Ahmad, and D. Kim, "A prediction mechanism of energy consumption in residential buildings using hidden Markov model," *Energies*, vol. 11, no. 2, p. 358, 2018.

[36] M. Fayaz and D. Kim, "A prediction methodology of energy consumption based on deep extreme learning machine and comparative analysis in residential buildings," *Electronics*, vol. 7, no. 10, p. 222, 2018.

[37] I. Sutskever, O. Vinyals, and Q. V. Le, "Sequence to sequence learning with neural networks," *Advances in Neural Information Processing Systems*, vol. 1, pp. 3104–3112, 2014.

[38] S. Hochreiter and J. Schmidhuber, "Long short-term memory," *Neural Computation*, vol. 9, no. 8, pp. 1735–1780, 1997.

[39] C.-J. Huang and P.-H. Kuo, "A deep CNN-LSTM model for particulate matter (PM2. 5) forecasting in smart cities," *Sensors*, vol. 18, no. 7, p. 2220, 2018.

[40] N. Srivastava, E. Mansimov, and R. Salakhudinov, "Unsupervised learning of video representations using LSTMs," *International conference on machine learning*, pp. 843–852, 2015.

[41] A. Graves and J. Schmidhuber, "Framewise phoneme classification with bidirectional LSTM and other neural network architectures," *Neural Networks*, vol. 18, no. 5-6, pp. 602–610, 2005.

[42] K. Greff, R. K. Srivastava, J. Koutník, B. R. Steunebrink, and J. Schmidhuber, "LSTM: a search space odyssey," *IEEE Transactions on Neural Networks and Learning Systems*, vol. 28, no. 10, pp. 2222–2232, 2017.

[43] A. B. Georges Hebrail, "Individual household electric power consumption Data Set," 2012, https://archive.ics.uci.edu/ml/datasets/individual+household+electric+power+consumption.

[44] E. Mocanu, P. H. Nguyen, M. Gibescu, and W. L. Kling, "Deep learning for estimating building energy consumption," *Sustainable Energy, Grids and Networks*, vol. 6, pp. 91–99, 2016.

[45] J.-Y. Kim and S.-B. Cho, "Electric energy consumption prediction by deep learning with state explainable autoencoder," *Energies*, vol. 12, no. 4, p. 739, 2019.

[46] T.-Y. Kim and S.-B. Cho, "Predicting residential energy consumption using CNN-LSTM neural networks," *Energy*, vol. 182, pp. 72–81, 2019.

[47] F. U. M. Ullah, A. Ullah, I. U. Haq, S. Rho, and S. W. Baik, "Short-term prediction of residential power energy consumption via CNN and multilayer Bi-directional LSTM networks," *IEEE Access*, vol. 8, Article ID 123380, 2020.

[48] T. Hussain, F. U. Min Ullah, K. Muhammad et al., "Smart and intelligent energy monitoring systems: a comprehensive literature survey and future research guidelines," *International Journal of Energy Research*, vol. 45, no. 3, pp. 3590–3614, 2021.

[49] F. U. M. Ullah, K. Muhammad, I. U. Haq et al., "AI-assisted edge vision for violence detection in IoT-based industrial surveillance networks," *IEEE Transactions on Industrial Informatics*, vol. 18, no. 8, pp. 5359–5370, 2022.

[50] M. Babar, M. U. Tariq, and M. A. Jan, "Secure and resilient demand side management engine using machine learning for IoT-enabled smart grid," *Sustainable Cities and Society*, vol. 62, Article ID 102370, 2020.

Hindawi
Complexity
Volume 2022, Article ID 3327722, 8 pages
https://doi.org/10.1155/2022/3327722

Research Article

High-Voltage Topological Architecture-Based Energy Management Strategy of the Plug-In Hybrid Powertrain System

Ziliang Zhao[1,2] **Jun Zhao**[3] **Bin Guo**[1] **and Rifei Lai**[4]

[1]*College of Transportation, Shandong University of Science and Technology, Qingdao 266590, China*
[2]*China FAW Group Corporation, Changchun 130000, China*
[3]*College of Mechanical and Electronic Engineering, Shandong University of Science and Technology, Qingdao 266590, China*
[4]*Xiaopeng Automobile Technology Limited Company, Guangzhou 510640, China*

Correspondence should be addressed to Jun Zhao; junzhao1993@163.com

Received 13 June 2022; Revised 24 July 2022; Accepted 2 August 2022; Published 25 August 2022

Academic Editor: Chun Wei

Hybrid technology (including plug-in hybrid) integrates the advantages of traditional automobile technology and pure electric technology, which can greatly reduce fuel consumption and improve emissions. It has become one of the main technologies developed at present and in the next 15~20 years. Energy management is the core algorithm of hybrid electric vehicle control strategy, and it is the focus of current research. However, these studies mainly focus on the high efficiency of control assembly, optimal management of power system energy, and maximum recovery of renewable energy but have not considered energy distribution management and optimization between the power battery and the low-voltage battery. Hence, based on the high-voltage topology of the plug-in hybrid system, this paper proposes the optimal energy management strategy between the power battery and the low-voltage battery under different working conditions. The charging and discharging characteristics of the power battery under different electric quantities are also combined. The experimental results show that based on the optimized energy management strategy, the pure electric driving range is increased by 6% under NEDC condition for a C-class plug-in hybrid car, and the energy-saving effect of the vehicle is further improved.

1. Introduction

The power unit of plug-in hybrid electric vehicle (PHEV) is a hybrid system composed of engine and electric drive system. Through the advanced vehicle control system, the two work together to distribute the driving force reasonably between engine and motor, so as to achieve high efficiency, energy saving, and low pollutant emission [1].

The real-time optimal distribution of driving force is realized through the whole vehicle energy management strategy. Energy management is the core algorithm of hybrid electric vehicle control strategy and the focus of current research results [2]. Yang et al. proposed a new type of an electromechanical-electrohydraulic coupling power vehicle model that combines the traditional motor and the piston pump into a unit and achieves the torque of electric and hydraulic torque. It ensures the reasonable use of vehicle energy [3]. You et al. used Matlab/Simulink to establish the IEEE 13 bus test feeder model with a cross-feedback end and conducted experimental testing on the hardware in the loop platform and proposed a control strategy for comprehensive voltage imbalance compensation to use standard operation procedures to alleviate the adjacent unbalanced voltage between feed lines [4]. Zhang et al. selected typical four types of urban conditions and applied the K average clustering algorithm to identify the working conditions and established the relationship between fuel coefficient and fuel consumption and proposed the minimum energy management strategy based on equivalent fuel [5]. Hofman et al. analyzed and evaluated the concept of IMA and Prius's transmission system, in order to reveal the potential limitations of fuel economy and performance, and the design and cost involved in the quantitative implementation (limited) fuel economy and performance trade off [6]. Torres et al. designed a rules-

based controller to ensure that the vehicle manages the power system in accordance with the standards of maximizing efficiency and autonomy [7]. Noyori et al. have developed a regenerative braking system. The regenerative braking energy obtained through the speed of vehicle deceleration or coast-down, through efficient power generation and charging, realized the improvement of fuel economy [8]. Masjosthusmann et al. carried out research on electric vehicle energy management, a type of electric vehicle energy management system proposed by testing on a test bench, and established a vehicle simulation model for the electric vehicle [9].

The study of the abovementioned hybrid vehicle energy management strategies mainly focuses on the energy distribution between power systems. At the same time, it is considered that the SOC of the power battery is maintained in a reasonable range, so that the entire system consumes the smallest energy, and the above work is considered during the design stage of the vehicle power system solution. However, by optimizing the power distribution between the power battery and the low-voltage battery, it can also improve the economic performance of the vehicle. No relevant research has been seen in this field.

The major contributions of this paper include the following:

(1) A special energy management strategy and optimization idea are proposed, namely, the optimized energy management strategy between the power battery and the low-voltage battery is considered.

(2) We construct a high-voltage topology of the plug-in hybrid system, while the special operation conditions are classified into charging conditions, electric driving conditions, and energy regenerating conditions.

(3) The energy management strategies under different operation conditions are carried out and verified as energy saving based on the charging and discharging characteristics of the power battery in different power.

This paper is organized as follows: in Section 2, we introduce the system overview of high-voltage system topology and vehicle and main components specifications. In Section 3, the energy management strategy and optimization solution are proposed under different operation conditions. Section 4 gives the experimental results to illustrate the effectiveness of the proposed control strategy. Some conclusions are stated in Section 5.

2. Problem Formulation

2.1. High-Voltage System Topology. The P2 configuration of a C-class car hybrid system is shown as Figure 1, which consists of a high-efficiency 4-cylinder gasoline direct injection boost engine, clutch coupling motor module, motor inverter, 7-speed dual clutch transmission, lithium-ion power battery, DC/DC converter, and on-board charger. The C-class vehicle and components main technical parameters are given in Table 1.

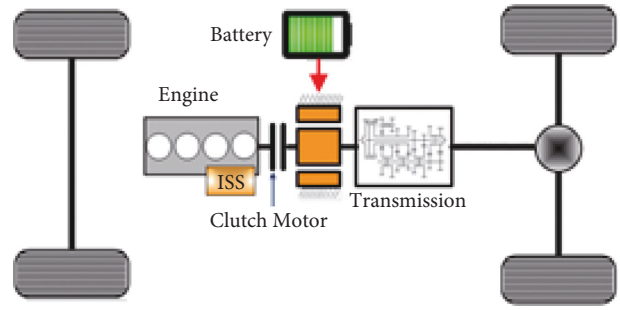

Figure 1: A certain C class plug-in hybrid system configuration.

The high-voltage system topology of the plug-in hybrid car is as shown in Figure 2, where the power battery high-voltage end is connected to the motor inverter, the on-board charger high-voltage output terminal and the DC/DC high-voltage input are connected together, and DC/DC low-voltage output and the low-voltage battery and the low-voltage load are connected. Based on the high-voltage system topology, the charging and discharge state of the power battery and the low-voltage battery can be managed to achieve optimize energy management purposes by adjusting the operating state of the motor, DC/DC, and on-board charger.

2.2. High-Voltage System Operation Conditions. Based on high-voltage system topology, several basic operation conditions of high-voltage systems can be determined.

2.2.1. Charging Conditions. The input 220 V AC electrically converted to the high-voltage of the power battery charged the power battery by on-board charger under the charging operation. DC/DC converts a portion of the charge output of on-board charger to the low-voltage output and supply charge to the power battery and the low-voltage load.

2.2.2. Electrical Drive Conditions. The power battery in the driving condition is in the discharge state. The motor inverter converts the DC power output from the power battery to the electricity of the motor, providing driving power for the motor, while DC/DC converts the power battery electrical energy to the low-voltage output terminal, which provides power to the power battery and the low voltage load. The DC/DC output can also be unpermitted to provide an energy source to a low-voltage load in the case of sufficient low-voltage battery power.

2.2.3. Energy Recovery Conditions. Under the energy recovery condition, the motor is in the energy feedback state of negative torque, and the inverter can transfer the feedback energy of the motor to the power battery and DC/DC [2]. When the power battery can recover energy, a part of the recovered energy transmitted by the inverter will charge the power battery and the other part will supply power to DC/DC. When the power battery cannot recover energy, all the recovered energy transmitted by the inverter can be stored in the battery and consumed by the low voltage load through DC/DC.

Table 1: Main technical parameters of the C-class vehicle and components.

Items	Technical indicator	Value
Vehicle parameters	$L \times W \times H$/axis/mm	5095 × 1875 × 1485/2970
	Curb weight/kg	2000
Powertrain configuration	P2	
Vehicle performance	Max. Speed/km	≥210
	0–100 acceleration time/s	≤8.6
	NEDC driving cycle fuel consumption L/100 km	≤2.4
	Pure electric driving range/km	≥50
Engine	Type	4-Cylinder GDI
	Power kW/torque Nm	145/280
Transmission	Type	DCT-7gears
Driving motor	Type	PM
	Peak power/kW	55
	Peak torque/Nm	280
Battery	Type	Lithium
	Energy/kWh	13
DCDC	Input voltage/V	200~400@DC
	Rated output voltage/V	14.5 ± 0.2@DC
	Rated output current/A	120
On-board charger	Rated power/kW	3.6
	Input voltage/V	180~260V@AC
	Output voltage/V	200~400
	Input current/A	≤16

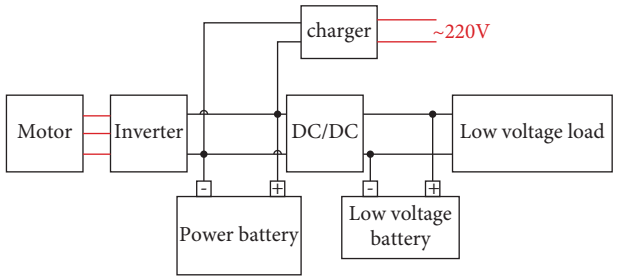

Figure 2: High-voltage system topology.

3. Energy Management Strategy

3.1. Power Battery Charge and Discharge Power Characteristics. Ternary lithium-ion batteries are often used as power batteries. Figure 3 shows the characteristic curve of the allowable charge and discharge power of the power battery. It can be seen from Figure 3 that the higher the battery temperature within the normal non-limit operating temperature range, the higher the allowable charge power and allowable discharge power of the battery. However, as battery power is higher than a certain value a%, the allowable charge power of the battery drops rapidly to close to zero, when battery power is lower than a certain value b%, the allowable discharge power of the battery drops rapidly to close to zero. The power battery power range in which the vehicle can run purely electric is between b% and 100%. Therefore, in terms of improving the driving range of purely electric, it is necessary to focus on solving the charging recovery problem in the power battery power range from a% to 100%.

3.2. Energy Optimization Solution. In the later stage of vehicle performance achievement, improving the pure electric driving range of the vehicle needs to be realized by optimizing the energy management strategy. The optimization work can be performed in the following two aspects, as described below.

3.2.1. Energy Recovery Optimization When the Low Permitted Charging Power of the Power Battery. According to the charging and discharging characteristics of the power battery, in order to solve the problem that the energy cannot be recovered when the allowable charging power of the power battery is low, an energy recovery scheme as shown in Figure 4(a) can be formulated. The recovered electric energy is absorbed through the low voltage load and the battery, and the recovered electric energy is used for the low voltage load part, which can reduce electric energy consumption of the power battery at the current time, while a small part of the recovered electric energy can be stored in the battery for later use.

3.2.2. Optimization of Low Voltage Battery Power. To make full use of the electric energy of the battery, the electric energy stored in the battery during charging and energy recovery can be released to the low voltage load under the electric driving condition, so as to further reduce the electric energy consumption when the power battery is driven, as shown in Figure 4(b).

3.3. Energy Management Strategies under Different Conditions. Figure 5 shows a complete energy management process, the period is a charging condition from t_0 to t_2, and

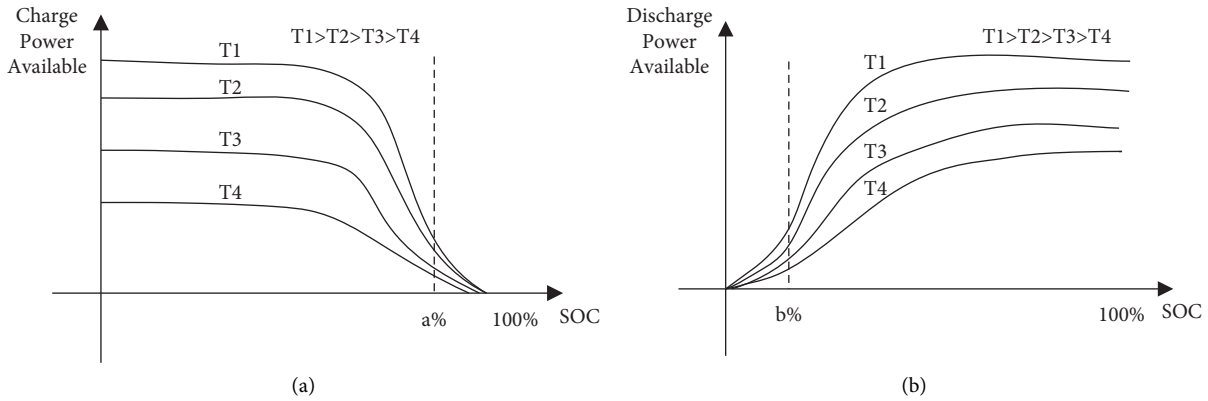

Figure 3: Power battery charging/discharging power characteristics. (a) Power battery charging power characteristics. (b) Power battery discharging power characteristics.

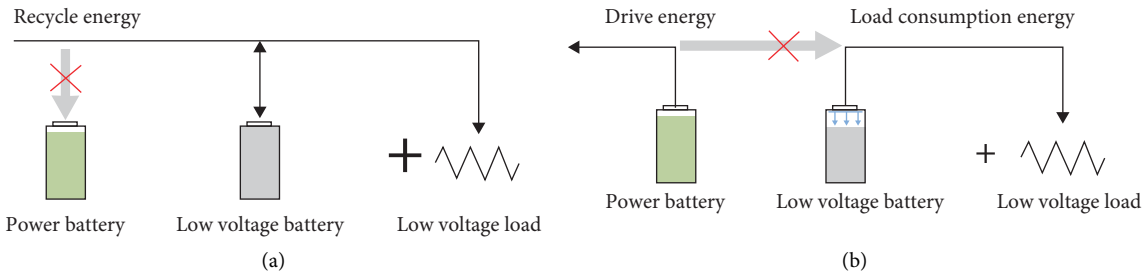

Figure 4: Energy management policy optimization scheme. (a) Energy recovery when the low permitted charge power of power battery. (b) Optimization of low-voltage battery power.

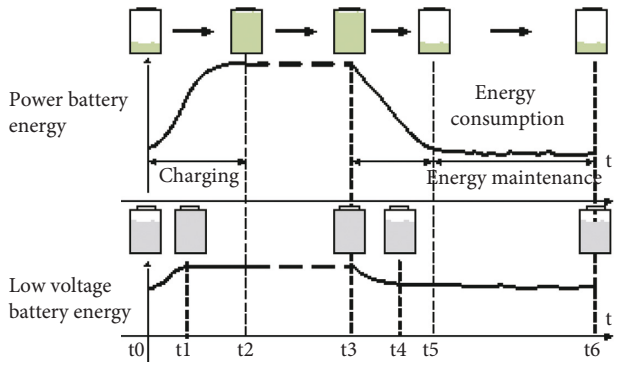

Figure 5: Energy management process.

power in the grid is stored in the power battery and the low-voltage battery. The period is a power consumption process from t_3 to t_5, stored power in the power battery and the low-voltage battery is converted to the kinetic energy of the vehicle by motor driving. The period is the power retention process from t_5 to t_6, the power battery and the low-voltage battery are maintained at a certain level.

The following is description for energy management strategies under different conditions of different conditions:

3.3.1. Charging Conditions. Since the power of the power battery is at a lower level due to the use of the power battery, meanwhile, low-voltage battery power has a certain lifting space, so the electric energy in the grid can be stored in the power battery and the low-voltage battery when the battery is charged, as shown in Figure 6. The power battery and the low-voltage battery can be filled in the full power state, which can increase the electric energy reserves stored in the low-voltage battery, and this stored electrical energy can be lately used for motor drive and low-voltage load consumption. The relation of input and out energy shown in (1) and (2).

$$E_{\text{grid}} = \frac{E_{\text{chargeout}}}{\eta_{\text{charger}}}. \tag{1}$$

$$E_{chargerout} = E_{batteryin} + \frac{(E_{lvbin} + E_{lvlin})}{\eta_{DC\ DC}}. \tag{2}$$

$E_{chargerout}$ is the energy output of charger; $E_{gri\ d}$ is the energy of grid; $\eta_{charger}$ is the efficiency of charger; $E_{batteryin}$ is the energy input of power battery; E_{lvbin} is the energy input of low-voltage battery; E_{lvlin} is the energy input of low-voltage load; and $\eta_{DC\ DC}$ is the efficiency of DCDC.

3.3.2. Electric Drive Conditions When Sufficient Low Voltage Battery Power. Under the electric drive, the power battery needs to provide driving power to the motor. The power

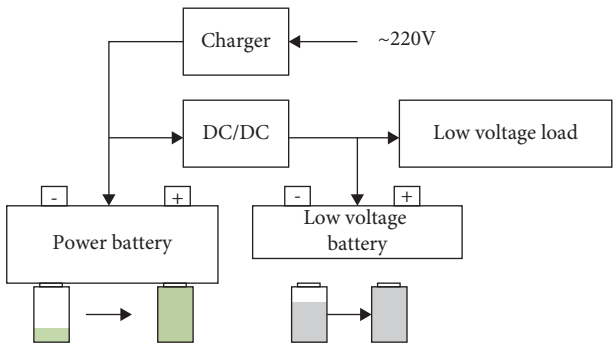

Figure 6: Energy management under charging conditions.

consumption of the low voltage load can be provided from the low-voltage battery in sufficient low-voltage battery power, as shown in Figure 7(a), i.e., during the electric driving process, stored power in the low-voltage battery can be released to a low-voltage load at this time, reducing the power consumption of the power battery.

The relation of input and output energy are shown in (3) and (4).

$$E_{batteryout} = \frac{E_{motorin}}{\eta_{inverter}}. \tag{3}$$

$$E_{lvbout} = E_{lvlin} \tag{4}$$

$E_{batteryout}$ is the energy output of power battery; $E_{motorin}$ is the energy input of drive motor; $\eta_{inverter}$ is the efficiency of inverter; E_{lvbout} is the energy output of low-voltage battery; and E_{lvlin} is the energy input of low-voltage load.

3.3.3. Electrical Drive Conditions When the Low Voltage Battery Power Balance. When the low-voltage battery is released to a better operating point, the low-voltage battery power balance mode is entered. In this mode, the target load of DC/DC is set to zero; that is, the zero with the target output current of DC/DC is closed-loop controlled, so that it can be protected to prolong the low-voltage battery life [9]. At this time, the power battery is not only supplied to the motor but also provides power consumption to the low-voltage load by DC/DC, as shown in Figure 7(b).

Because of the low-voltage battery in an electric quantity balancing control mode, the low-voltage battery is no longer acquired from the power battery, which can reduce the power consumption of the power battery.

The relation of input and out energy are shown in (5)–(7).

$$E_{batteryout} = E_{inverterin} + E_{DCDCin} \tag{5}$$

$$E_{motorin} = E_{inverterin} \times \eta_{inverter} \tag{6}$$

$$E_{DCDCout} = E_{lvbin} + E_{lvlin} \tag{7}$$

$E_{batteryout}$ is the energy output of power battery; $E_{inverterin}$ is the energy input of inverter; E_{DCDCin} is the energy input of DCDC; $E_{motorin}$ is the energy input of drive motor; $E_{inverterin}$ is the energy input of inverter; $\eta_{inverter}$ is the efficiency of inverter; $E_{DCDCout}$ is the energy output of DCDC; E_{lvbin} is the energy input low-voltage battery; and E_{lvlin} is the energy input low-voltage load.

3.3.4. Energy Recovery Conditions When Low Permitted Charging Power of the Power Battery. When the allowable charging power of the power battery is very low or even close to zero, if the power battery is charged through energy recovery, the battery cell voltage may be too high, resulting in cell failure. Hence, the power battery absorbed the energy recovery replacement of DC/DC, as shown in Figure 8(a). DC/DC passes the recovered energy to a low voltage load and the low-voltage battery, and the battery can store partially recovered energy and release it to the low-voltage load under electric drive conditions.

The relation of input and output energy are shown in (8)–(10).

$$E_{motorout} = \frac{E_{inverterout}}{\eta_{inverter}}. \tag{8}$$

$$E_{inverterin} = \frac{E_{DCDCout}}{\eta_{DCDC}}. \tag{9}$$

$$E_{DCDCout} = E_{lvbin} + E_{lvlin} \tag{10}$$

$E_{motorout}$ is the energy output of drive motor; $E_{inverterout}$ is the energy output of inverter; $\eta_{inverter}$ is the efficiency of inverter; $E_{inverterin}$ is the energy input of inverter; $E_{DCDCout}$ is the energy output of DCDC; η_{DCDC} is the efficiency of DCDC; E_{lvbin} is the energy input low-voltage battery; and E_{lvlin} is the energy input low-voltage load.

3.3.5. Energy Recovery Conditions When the High Permitted Charging Power of the Power Battery. When the power battery is in the normal power range, and the battery temperature is in the normal temperature range, the power battery has a higher charging power, and the energy of the sliding or braking can be recovered, as shown in Figure 8(b). The power battery stores most of the energy recovered by the motor, and a small portion is supplied to a low-voltage load through DC/DC, and the low-voltage battery is in a power balance. Thus, when the power battery is in the normal power range, it is possible to store most of the electric energy recovered by the sliding or braking.

The relation of input and output energy are shown in (11)–(13).

$$E_{motorout} = \frac{E_{inverterout}}{\eta_{inverter}}. \tag{11}$$

$$E_{inverterout} = \frac{E_{batteryin} + E_{DC\ DCout}}{\eta_{DC\ DC}}. \tag{12}$$

$$E_{DCDCout} = E_{lvbin} + E_{lvlin} \tag{13}$$

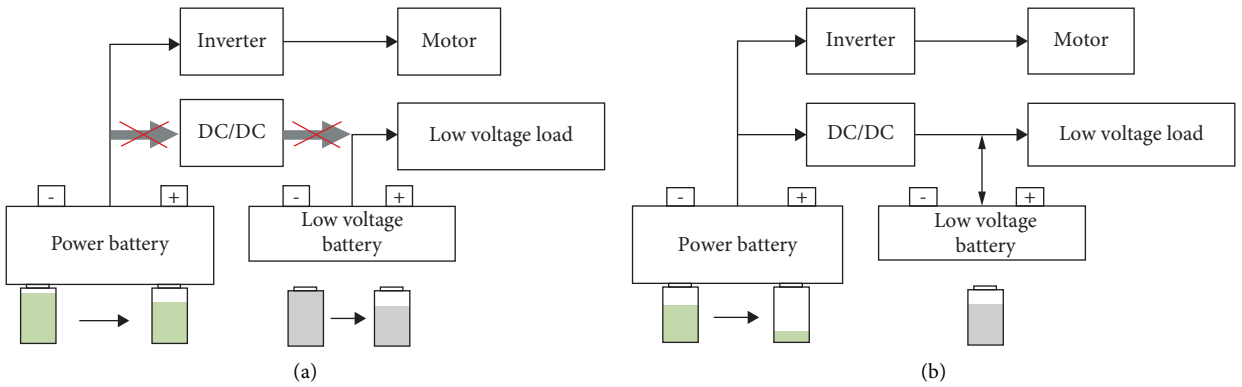

Figure 7: Energy management of electric drive conditions. (a) Energy management under sufficient power of the low-voltage battery. (b) Energy management under power balance of the low-voltage battery.

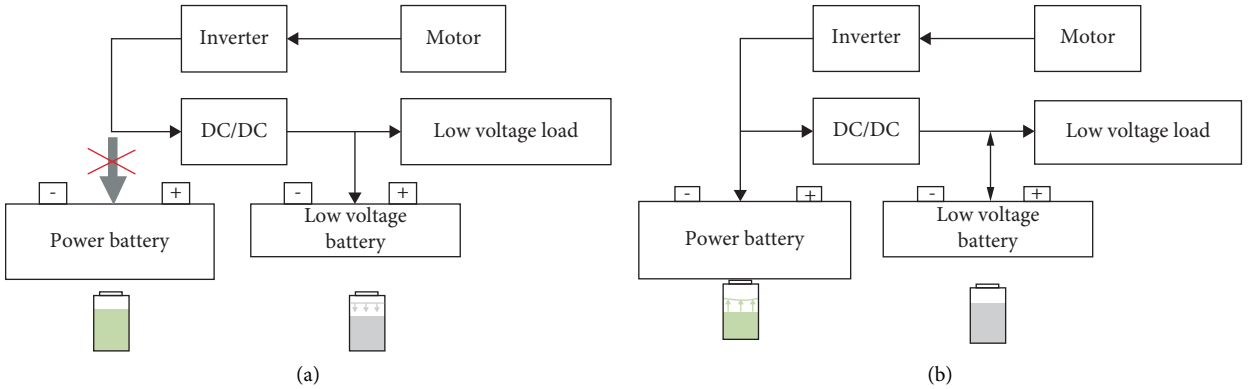

Figure 8: Energy management of energy recovery. (a) Energy management when the low power of the power battery permitted charge power of the power battery. (b) Energy management when the sufficient power of the power battery permitted charge power of the power battery.

$E_{motorout}$ is the energy output of drive motor; $E_{inverterout}$ is the energy out of inverter; $\eta_{inverter}$ is the efficiency of inverter; $E_{batteryin}$ is the energy input of power battery; $E_{DCDCout}$ is the energy output of DCDC; η_{DCDC} is the efficiency of DCDC; E_{lvbin} is the energy input low-voltage battery; and E_{lvlin} is the energy input low-voltage load.

3.4. Energy Management Strategy Implementation. According to the abovementioned energy management policy and optimization, the key of implementation is to adjust the energy of the DC/DC output. Based on the situation, it can be achieved by controlling the output voltage of DC/DC at different operation conditions, as shown in Table 2. The current conditions should be identified through the vehicle state, the state of the power battery, and the state of the low-voltage battery, and then the corresponding DC/DC target output voltage command is output according to the identified operation condition and finally implements the energy management policy and optimization.

4. Test Verification

In order to verify the effect of the optimized energy management strategy, a comparative test of two groups of pure electric driving range tests was carried out on the vehicle. One group used the original strategy that was not optimized and the other group used the optimized strategy. The final test results are shown in Table 3. It can be seen from the table that the total electric energy consumption after the strategy optimization is 0.642kWh lower than that of the non-optimization when driving the same 50 km.

Figure 9 shows the curve comparison of two groups of tests in the first NEDC cycle. It can be seen from the figure that in this cycle, compared with the nonoptimized strategy, the optimized strategy can discharge the battery when driving and charge when recovering, realizing the optimal management of energy.

Table 4 shows the comparison results of the pure electric driving range of the two groups of tests when the power consumption of the power battery is the same. It can be seen from the table that the optimized energy management

Table 2: Target output voltage of DC/DC.

Num.	Conditions	Target output voltage before optimization of DC/DC (V)	Target output voltage after optimization of DC/DC (V)
1	Charging condition	14.5	14.5
2	Electric driving condition under sufficient power of low-voltage battery power	14.5	12.0
3	Electric driving condition under balance power of low-voltage battery power	14.5	12.0
4	Energy recovery condition when low permitted charging power of the power battery	14.5	14.5
5	Energy recovery condition when sufficient permitted charging power of the power battery	14.5	14.5

Table 3: Energy management comparison test data.

Num.	Electric driving range (km)	Energy consumption of low-voltage battery (kWh)	Energy consumption of power battery (kWh)	Total energy consumption (kWh)
Before optimization	50	0.637	10.297	10.934
After optimization	50	0.289	10.009	10.298

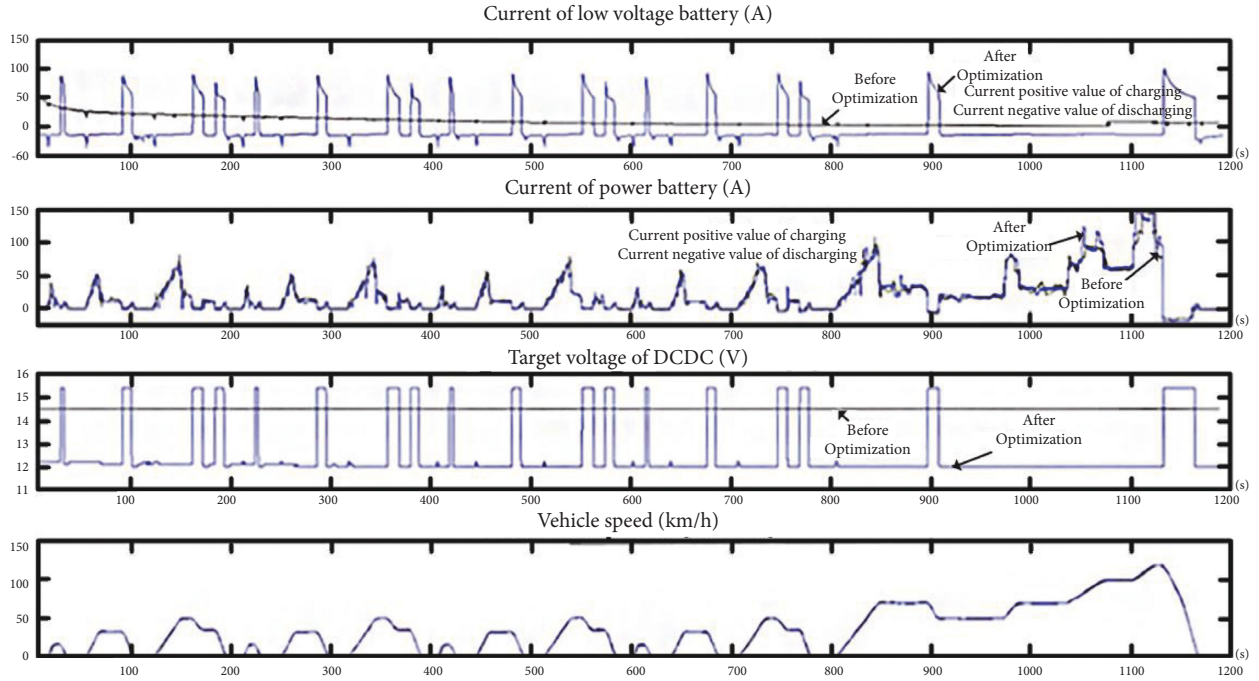

Figure 9: Comparison of two sets of tests under the first NEDC cycle.

Table 4: Comparison of electric range.

Test num.	Window range SOC of power battery (%)	Pure electric range (km)
Before optimization	80	50
After optimization	80	53

strategy can increase the pure electric driving range of the vehicle from 50 km to 53 km; that is, the driving range is increased by 6%, and the expected goal is achieved.

5. Conclusion

In the later stage of the vehicle performance, in order to further improve the pure electric driving range of the vehicle, the strategy of energy management optimization between the power battery and the battery under different working conditions is proposed. The strategy fully considers the allowable charge discharge power characteristics of the power battery and summarizes five service conditions for optimizing energy management, namely, charging condition, electric driving condition when the battery is full, electric driving condition when the battery is balanced, energy recovery condition when the allowable charging power of the power battery is low, and energy recovery condition when the allowable charging power of the power battery is high.

Then the corresponding energy management optimization strategy is formulated for each working condition. Finally, based on the energy management optimization strategy under different working conditions, the corresponding target output voltage of DC/DC is controlled to achieve the expected results. Through the NEDC pure electric driving range test results of C-class plug-in hybrid power, it can be seen that when the optimized energy management strategy is used for control, the pure electric driving range of the vehicle is increased by 6%, and the purpose of improving the pure electric driving range is achieved.

Data Availability

The data are available upon request.

Conflicts of Interest

The authors declare that there are no conflict of interest regarding the publication of this paper.

References

[1] H. Peter and Y. Geng, *Hybrid Electric Vehicle*, Mechanical Industry Press, South Norwalk, Connecticut, 2017.

[2] S. Onori, L. Serrao, and G. Rizzoni, *Hybrid Electric Vehicles Energy Management Strategies*, pp. P31–P101, China Machine Press, Baiwanzhuang Ave, 2020.

[3] J. Yang, T. Zhang, J. Hong, H. Zhang, Q. Zhao, and Z. Meng, "Research on driving control strategy and Fuzzy logic optimization of a novel mechatronics-electro-hydraulic power coupling electric vehicle," *Energy*, vol. 233, Article ID 121221, 2021.

[4] R. You and X. Lu, "Voltage unbalance compensation in distribution feeders using soft open points," *Journal of Modern Power Systems and Clean Energy*, vol. 10, no. 4, pp. 1000–1008, 2022.

[5] Z. Zhang, D. Qin, and Y. Zeng, "Hybrid electric motor energy management strategy based on genetic optimization K mean clustering algorithm [J]," *Chinese Journal of Highways*, vol. 29, no. 4, pp. 130–137, 2016.

[6] T. Hofman, R. Van Druten, and A. Serrarens, *A fundamental case study on the Prius and IMA drivetrain concepts[J]. EVS*, vol. 21, Monaco, 2005.

[7] J. Torres, R. Gonzalez, A. Gimenez, and J. Lopez, "Energy management strategy for plug-in hybrid electric vehicles. A comparative study," *Applied Energy*, vol. 113, pp. 816–824, 2014.

[8] T. Noyori, S. Komada, and H. Awakawa, "Development of a new regenerative braking system," *SAE Technical Paper*, vol. 32, 2013.

[9] C. Masjosthusmann, U. Bueker, U. Köhler, and N. Decius, "A Load Balancing Strategy for Increasing Battery Lifetime in Electric Vehicles," *SAE Technical Paper*, vol. 01, Article ID 0499, 2013.

Hindawi
Complexity
Volume 2022, Article ID 3445583, 14 pages
https://doi.org/10.1155/2022/3445583

Research Article

Audio and Video Matching Zero-Watermarking Algorithm Based on NSCT

Di Fan, Wenxue Sun, Huiyuan Zhao, Wenshuo Kang, and Changzhi Lv

Shandong University of Science and Technology, Qingdao, Shandong 266590, China

Correspondence should be addressed to Changzhi Lv; lvchangzhi@126.com

Received 2 April 2022; Revised 15 June 2022; Accepted 29 July 2022; Published 24 August 2022

Academic Editor: Wenjie Lu

In the Internet age, information security is threatened anytime and anywhere and the copyright protection of audio and video as well as the need for matching detection is increasingly strong. In view of this need, this paper proposes a zero-watermarking algorithm for audio and video matching based on NSCT. The algorithm uses NSCT, DCT, SVD, and Schur decomposition to extract video features and audio features and generates zero-watermark stream through synthesis, which is stored in a third-party organization for detection and identification. The detection algorithm can obtain zero watermark from the audio and video to be tested and judge and locate tampering by comparing with the zero watermark of the third party. From the experimental results, this algorithm can not only detect whether the audio and video are mismatched due to tampering attacks but also locate the mismatched audio and video segments and protect the copyright.

1. Introduction

With the development of global networking, digital media is fast and convenient. While bringing convenience, security issues are increasingly prominent. Digital watermarking technology can protect the copyright of audio or video to a certain extent and is a hot research field of data security. But at present, the matching of audio and video cannot be detected and located by digital watermarking technology, which is a blind area of security protection and detection. Therefore, the research on audio and video matching detection and location is urgent.

At present, there are very few watermarking algorithms for audio and video matching detection. Most of the digital watermarking algorithms are image watermarking, audio watermarking, video watermarking, etc. The media attached to the algorithm are single. Image digital watermarking mainly includes spatial domain method [1], transform domain method [2–6], and deep learning-based method [7]. Transform domain method commonly uses DCT (Discrete Cosine Transform), NSCT (Nonsubsampled Contourlet Transform) [4, 5], DWT (Discrete Wavelet Transform) [6], and so on. As a new direction, watermarking algorithm based on deep learning appears on the way of watermarking technology, but it still needs to be improved in terms of watermark capacity and algorithm complexity. Video watermarking can be divided into original video watermarking algorithm and video watermarking algorithm based on compression domain. The former can refer to the existing image watermarking algorithm [8–10]. The latter is a watermarking technology combined with specific video encoding methods, such as MPEG [11], H.264 [12], and H.265 [13] video watermarking algorithms. Audio watermarking algorithms mainly include time domain and transform domain algorithms, and time domain audio algorithms include least significant bit algorithm [14], echo hiding algorithm [15], and phase coding algorithm. In order to improve the robustness of watermarking algorithm, more scholars begin to pay attention to the research of watermarking algorithm in transform domain and transfer the embedding position of watermark from time domain to transform domain. For example, [16] proposed the audio watermarking technology based on DWT, [17] proposed the audio watermarking technology based on SVD (singular value decomposition) and fractional Fourier transform, and [18] proposed the audio watermarking technology based on

DWT and SVD. At present, most of the watermarking algorithms of audio and video are designed separately, but multimedia data is composed of audio and video together, so it is not enough to protect only one of them. Tamper protection or even matching protection is needed for both audio and video. Dittmann et al. [19] proposed the earliest cross-watermarking algorithm in 1999, which can verify the synchronization between audio and video. Although this cross-watermarking algorithm can be easily implemented, the watermark cannot resist various attacks [19]. In order to improve the robustness of watermarking, Wang and Pan [20] proposed an audio-video cross-watermarking algorithm combined with a visual saliency model, which embedded the watermark into the DC coefficient of DCT through quantitative index modulation [20]. Esmaeilbeig and Ghaemmaghami [21] proposed an audio and video watermarking algorithm based on compressed domain. The algorithm generates hash bits in the audio part and embeds them as watermarks in the QDCT coefficients of video Immc1 frames [21]. The above audio and video cross-watermarking does not provide copyright protection for audio and video at the same time but only generates watermarks based on the whole multimedia stream, which can only judge whether the whole audio and video match and cannot locate the tampering of small segments in audio and video streams. Sun et al. [22] proposed a video zero-watermarking algorithm based on NSCT, DCT, DWT, and SVD. The algorithm generates zero-watermarking frame by combining audio watermark with video frame feature matrix, which can be utilized locating the attacks for the video besides verifying its copyright [22].

This paper presents an audio and video matching digital watermarking algorithm based on NSCT transform. The algorithm extracts video features and audio features of each segment, respectively, and generates a zero-watermark stream through synthesis. Experiments show that this algorithm can not only detect whether the audio and video are mismatched due to tampering attacks and locate the mismatched audio and video segments but also protect the copyright.

2. General Framework of Audio and Video Matching Zero-Watermarking Algorithm

The difference between zero watermarking and traditional digital watermarking is that it is not really embedded into the carrier, but it is obtained by extracting the stable features of the carrier to construct the feature moment and performing XOR operation with the watermark information. This paper can not only generate zero watermark but also realize the matching detection of audio and video, and its generation and detection framework is shown in Figure 1. The generation algorithm first preprocesses the audio and video and segments them by 1s, and the audio and video segments are synchronized and corresponding in time. Then, the audio stable features are extracted from the audio segment to construct the audio feature matrix, and the key frames and their features are extracted from the visual frequency band to generate the encrypted video watermark. XOR is performed between the encrypted video watermark and the audio feature matrix to obtain the zero watermark of the segment. The zero watermark generated by each segment is integrated with its audio and video features. When the whole audio and video performs the same operation, a zero-watermark stream is formed, which is saved together with the key frame number and other information to a third party such as the copyright center. The matching detection process is to generate zero watermark for audio and video segments in the same way as that of the copyright center and detect the matching of audio and video by comparing with the zero watermark of the copyright center. In addition to detecting audio and video matching, this zero watermark can also be used for traditional copyright recognition.

3. Zero-Watermarking Generation Algorithm for Audio and Video Matching

The zero-watermark generation algorithm for audio and video matching is shown in Figure 2. The audio and video are decoded and segmented in 1s to obtain several short audio and video pairs composed of video and audio segments. Each audio and video pair are matched and detected so as to realize audio and video tampering judgment and positioning in a small time period. Video watermarking is generated by NSCT, DCT, Schur decomposition, and other algorithms. DWT and SVD algorithms are used to extract audio features. The encrypted video watermarking is XOR operated with the extracted sound feature matrix to obtain the audio and video matching zero watermark. Zero watermark will be registered by the third-party copyright organization to save, when the audio and video need to be authenticated and detected out of the use.

3.1. Generation of Encrypted Video Watermark. Video watermark is composed of key frame features of video segment. First, the key frame image is extracted based on frame difference Euclide distance method, and the extracted key frame number is saved as the key, and the video frame image as the watermark is found by the key in the zero-watermarking detection of audio and video matching. Based on the key frame image, it is converted from RGB space to YCoCg color space. The Co component was decomposed by NSCT, DCT, Schur decomposition, and other methods to generate the video feature matrix, which was binarized and encrypted to obtain the encrypted video watermark. The detailed steps of generating encrypted video watermarks are shown in Figure 3.

3.1.1. Key Frame Extraction Algorithm Based on Euclidean Distance between Frames. This algorithm uses the method based on the Euclidean distance between frames to extract key frames [23]. The main idea of this method is to calculate the Euclidean distance of two consecutive frames of images and select the key nodes through the Euclidean distance of images. This method is simple and easy to operate. The definition of interframe Euclidean distance is shown in the following equations:

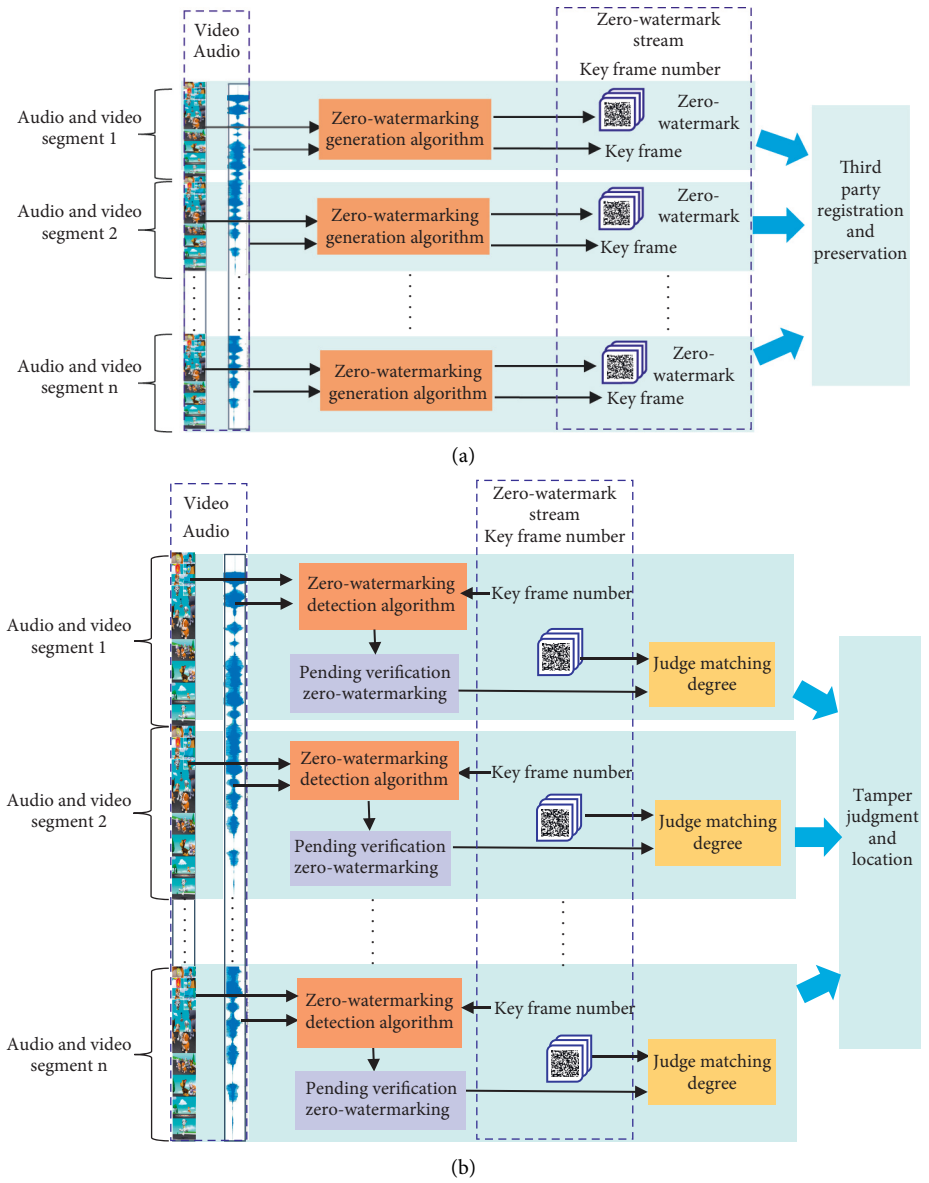

FIGURE 1: Total frame of zero-watermarking generation and detection based on the audio and video. (a) The overall framework of zero-watermarking generation algorithm for audio and video segments. (b) The overall framework of zero-watermarking detection algorithm.

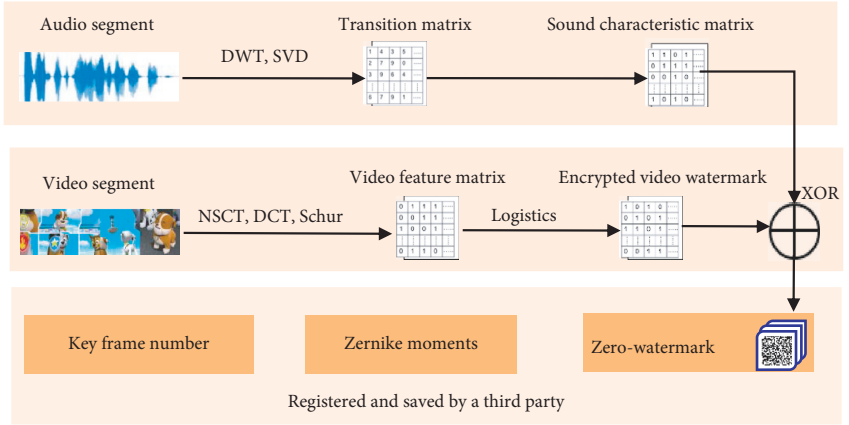

FIGURE 2: Zero-watermark generation process based on audio and video features.

Algorithm 1 name:	Generation of encrypted video watermark
Input:	Keyframe image I
Initialize:	D=zeros (32,32)
Begin:	calculate B_{nm} = Zernike (l) /*Calculate the Zernike moment B_{nm} of I*/ Convert I from RGB to YCocg and extract Co component L=NSCT2 (Co) /*The low-frequency subband L is obtained by two-layer NSCT transformation of Co*/ L is divided into non overlapping blocks, and block (i,j) is remarked as $n_{i,j}$ (i,j = 1,2,...,32) $N_{i,j}$ = *DCT2 (ni,j)* /*2-D DCT transformation of ni,j*/ for i=1:32 for j=1:32 $[U_{i,j}, T_{i,j}]$ = Schur ($N_{i,j,}$) /*Schur decomposition of $N_{i,j}$*/ λ = diag ($T_{i,j}$) d (i,j)=max (λ) end for end for calculate M=mean (d) a=find (d>M) /*Look for points greater than M in the matrix D*/ D (a)=1 W=logistics (D) /*Encrypt D with logistics to obtain the encrypted video watermark W*/
Output:	Encrypted video watermark W

Figure 3: Pseudocode of generating algorithm of encrypted video watermark.

$$t_k(i,j) = \left(g_{k+2}(i,j) - g_{k+1}(i,j)\right) - \left(g_{k+1}(i,j) - g_k(i,j)\right), \tag{1}$$

$$S_k = \sqrt{\sum_{i=0}^{M-1}\sum_{j=0}^{N-1} t_k^2(i,j)}, \tag{2}$$

where $g_k(i,j)$, $g_{k+1}(i,j)$, and $g_{k+2}(i,j)$ represent the gray value of the k frame image, $k+1$ frame image, and $k+2$ frame image at pixel point (i,j), respectively, k represents the number of frames of the video, and $k = 1, 2, 3, \ldots, J$. $t_k(i,j)$ represents the gray difference between the $k+2$ frame image and the $k+1$ frame image minus the gray difference between the $k+1$ frame image and the k frame image. The image size is $M \times N$.

The steps of extracting key frames based on the Euclidean distance between frames are as follows:

(1) Use (1) and (2) to calculate the Euclidean distance of each frame of image. If there are J frames of images, there are $J-2$ Euclidean distances.

(2) Calculate the extreme value of $J-2$ Euclidean distances.

(3) Find the maximum and minimum values of these extreme points and calculate their mean values.

(4) Compare each extreme point and the mean value. The image corresponding to the extreme point greater than the mean value is the key frame image.

3.1.2. NSCT Transform. NSCT has multiscale property and good anisotropy and translational invariance. NSCT transform is composed of NSP (Nonsubsampled Pyramid) and NSDFB (Nonsubsampled Directional Filter Bank). The nonsampling tower filter performs multiscale decomposition on the image first and then removes the low-frequency part. The nonsampling direction filter bank performs directional decomposition on the high-frequency part, making the NSCT transform multiscale and multidirectional anisotropy. The principle of three-stage NSCT transformation is shown in Figure 4. Its output is low-frequency $y1$ and three-stage high-frequency $y2$, $y3$, and $y4$, and its direction numbers are 2, 4, and 8, respectively.

After NSCT, the low-frequency part gathers the energy of the image and represents the contour information of the image, while the high-frequency part contains less energy of the image. The algorithm in this paper can ensure the embedding strength of watermark by taking advantage of the large energy value of the low-frequency part transformed by NSCT and the same size of the image as the original image, so the transformed low-frequency subband is selected as the object to construct zero watermark.

3.1.3. DCT Transform. DCT is a kind of orthogonal real transform, which has strong information concentration ability and is widely used in digital watermarking technology because of its strong robustness and good concealment [24]. For the two-dimensional image $f(x, y)$, its DCT and its inverse transform are shown as follows:

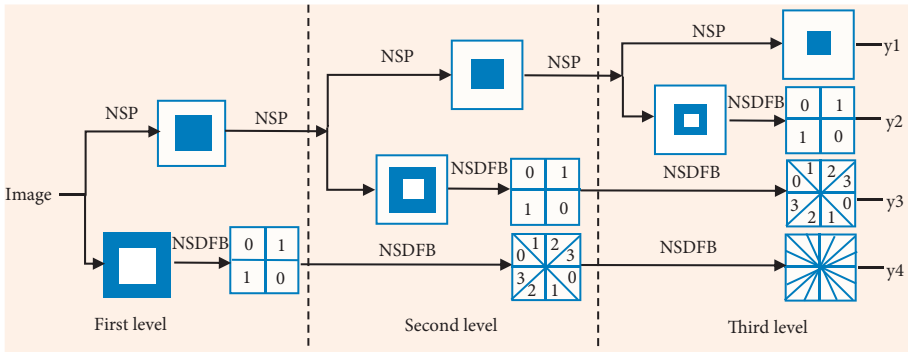

Figure 4: NSCT decomposition block diagram.

$$F(u,v) = \frac{2}{\sqrt{MN}} c(u)c(v) \sum_{x=0}^{M-1} \sum_{y=0}^{N-1} f(x,y) \cos\frac{(2x+1)u\pi}{2M} \cos\frac{(2y+1)\pi}{2N},$$
$$f(x,y) = \frac{2}{\sqrt{MN}} \sum_{u=0}^{M-1} \sum_{v=0}^{N-1} c(u)c(v)F(u,v) \cos\frac{(2x+1)u\pi}{2M} \cos\frac{(2y+1)v\pi}{2N}, \tag{3}$$

where $c(u) = c(v) = \begin{Bmatrix} 1/\sqrt{2}\,\mathrm{y}u & v = 0 \\ 1 & \text{others} \end{Bmatrix}$, u and v are the horizontal and vertical frequency, respectively, x, y are the pixel coordinates, $x, u = 0, 1, 2, \cdots, M-1$,and $y, v = 0, 1, 2, \cdots, N-1$.

3.1.4. Schur Decomposition. Schur decomposition decomposes a matrix X into the unit orthogonal matrix Y and the upper triangular matrix U such as $X = YUY^H$, and Y^H is the conjugate transpose of Y [25]. Then, the Schur of any n-order square matrix X can be decomposed into

$$X = YUY^H = \begin{bmatrix} \lambda_1 & r_{12} & \cdots & r_{1n} \\ & \lambda_2 & \ldots & r_{2n} \\ & & \ddots & \vdots \\ & & & \lambda_n \end{bmatrix}. \tag{4}$$

Schur decomposition is widely used in digital watermarking because of its scaling invariance and low computational complexity. When the matrix is scaled by a certain multiple, only the eigenvalues change by a multiple. The scaling invariance of Schur decomposition can deal with scaling attack well and improve the robustness of watermarking. In addition, Schur decomposition is a step of singular value decomposition; it does not need to transform the upper triangular matrix into diagonal matrix, so the calculation is less.

3.2. Generation of the Sound Feature Matrix. The sound feature matrix is generated from the features of the audio segment. The algorithm performs DWT and SVD on the segmented decoded audio to obtain stable audio features. Based on this, the feature matrix is formed and binarization is carried out. After that, XOR generates zero watermark for the encrypted video watermarking. The detailed steps of sound feature matrix generation are shown in Figure 5.

4. Audio and Video Matching Detection Algorithm

The video matching detection algorithm and the audio-video matching zero-watermark generation algorithm are inverse processes to each other, as shown in Figure 6. Supported by the key frame number, Zernike moment, and other information saved by the third party, the zero-watermarking generation algorithm is used to obtain the zero watermark of the audio and video to be tested. The similarity between the zero watermark to be detected and the zero-watermark stream saved by the third party is judged, and whether the audio and video segment has been tampered is determined according to the similarity threshold. The Zernike moment can better resist rotation attack. The detailed steps of audio and video matching detection algorithm are shown in Figure 7.

5. Experimental Results and Analysis

The experiment is carried out on MATLAB R2018b. The watermark is encrypted by logistic chaos, and its initial value x_0 and parameter u are used as the key. Only by knowing the zero-watermark algorithm, encryption method, and its key can the watermark information be decrypted correctly. Considering the security of the algorithm and watermark, the parameter of Logistic chaotic encryption is set as $x_0 = 0.1, u = 4$. For the length of audio and video segments, this paper determines that the audio and video segmentation unit is 1s through comprehensive analysis and experiments from the aspects of the stability of audio and video features, the rapidity of generating zero watermark, the minimization of occupied resources, the

Algorithm 2 name:	Generation of sound characteristic matrix
Input: Initialize:	Audio segment Q, Vector length of each segment n F=zeros (32,32)

Begin:	[Ca2,L]=wavedec (Q,2,'haar') /*Extract the approximate component Ca2 of wavelet transform of audio Q*/
	l=floor (sqrt (n))
	for k=1:1024 do
	A=Ca2 ((k-1)n+1 :kn) /*Divide Ca2 into 1024 segments, each with a length of n*/
	J=reshape (A, *l*, *l*) /*Upgrade A dimension to a matrix of 32*32 size*/
	[U,S,V]=SVD (J) /*The diagonal matrix s is obtained by SVD decomposition of J*/
	e (k)=S (1,1)
	end for
	e1 = reshape (e,32,32) /* Upgrade e dimension to a matrix of 32 * 32 size*/
	calculate m=mean (e1)
	b=find (e1>m) /* Look for the point in E1 greater than m*/
	F (b)=1

Output:	Sound characteristic matrix F

Figure 5: Pseudocode of sound feature matrix generation algorithm.

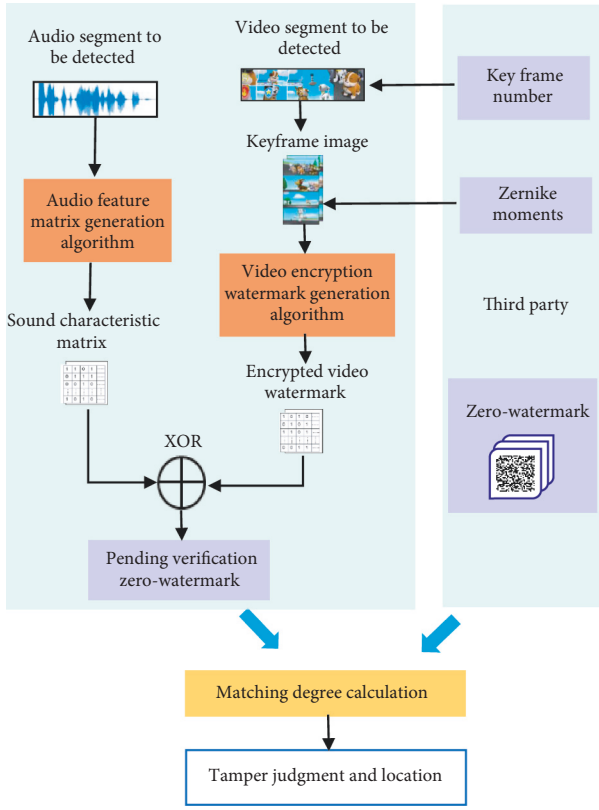

Figure 6: Audio and video matching detection and location process.

accuracy of matching detection, and so on. In this way, on the one hand, it can effectively extract the stable features of audio and video segments and quickly build an optimized zero watermark. On the other hand, it can also detect the tampering of small audio or video segments in the entire audio and video stream more accurately [22]. The following experiments use the video (including audio) in H.264 coding format, which is divided into 30 audio and video segments in the experiment. The video frame size is 1080×1920, the duration is 30 seconds, the frame rate is 27 fps, the audio stream sampling rate is 44.1 KHz, 16-bit quantization bits, and two channels.

Algorithm 3 name:	Zero-watermark detection algorithm
Input:	Audio and video streaming V, Zernike moment A_{nm}, Key frame number, Zero-watermark W, Tamper judgement threshold T

Begin:	Decode the V segment top obtain the audio segment and video segment to be verified
	Extract key frame image G according to frame number
	$\alpha = \frac{\arg(A'_{nm} - A_{nm})}{m}$ /* The Angle that the keyframe needs to be adjusted, where *m* is the multiplicity of Zernike moments *n* is the order of Zernike moment*/
	The adjusted image *G* is obtained by rotating *G* angle *a*
	Produce w for *G* using Algorithm 1
	/*Generate encrypted video watermark*/
	Produce F' for audio segment using Algorithm2
	/*Generate sound characteristic matrix*/
	W=w' F'
	calculate NC /*$NC(W',W)=\frac{\sum_i^N \sum_i^N W'(i,j)W(i,j)}{\sum_i^N \sum_i^N W(i,j))^2 \times \sum_i^N \sum_i^N W(i,j))^2}$*/
	ifNC>T then /* T is the initial set tamper judgement threshold*/
	Flag=0 /* V is not tampered with and remarked as 0*/
	else
	Flag=1 /* V is tampered with and marked as 1*/
	end if

Output:	Normalized correlation NC, Flag

Figure 7: Audio and video matching detection algorithm pseudocode.

In the experiment, the NC (Normalized Correlation) and BER (Bit Error Ratio) are used as the objective evaluation standard of watermark robustness. The NC experiment and analysis of the watermark image show that when the NC value is above 0.8, the correlation between the two watermark images is high [24]. Therefore, the tamper-proof threshold of audio and video is set as 0.8 in this paper for audio and video matching detection and identification; that is, when NC is greater than or equal to 0.8, audio and video are matched. When the value is less than 0.8, the audio or video is tampered with [22]. BER refers to the percentage of the extracted watermark error bits in the total bits. The PSNR (Peak Signal-to-Noise Ratio) is used as the difference measurement index of two images. The larger the value of PSNR, the better the invisibility of the watermark algorithm.

5.1. Audio and Video Matching and Tamper-Proof Test. For the above experimental audio and video, we replaced the video frames and audio segments in different time periods and then carried out the audio and video matching detection and positioning experiment. The experimental results are shown in Figure 8. The NC values of the zero watermark detected in Figure 8(a) are all less than the set threshold value of 0.8, so it is determined that they do not match. Therefore, segments 2, 5, 8, 11, 13, 16, 20, 23, 25, and 27 of the video are tampered with. The NC values in Figure 8(b) are all lower than the initially set threshold value, so it is determined that they do not match. Therefore, audio segments 2, 6, 8, 12, 15, 18, 21, 24, 26, 28, and 30 are tampered with. Experiments show that this method can detect whether the audio and video are mismatched due to tampering attacks and can locate the mismatched audio and video segments.

5.2. Algorithm Robustness Testing

5.2.1. Video Robustness Testing. In order to verify the robustness of this algorithm, common attacks such as Gaussian noise, salt and pepper noise, clipping, scaling, rotation, Gaussian filtering, median filtering, and frame attack are carried out on the video, as well as the combination of several one-way attacks, and the experimental results are shown in Table 1. From the whole experimental results, after the attack, even if some PSNR has reached below 10 dB, the NC value of the watermark of this algorithm is still above 0.9, indicating that the algorithm has good robustness:

(1) *Noise Attack*. Noise attack is one of the most common types of attacks. The algorithm in this paper has carried out Gaussian noise and salt and pepper noise attack experiments on the video. The results are shown in Figure 9. The range of noise attack intensity is 0.01–0.1, with 0.01 as an interval. The figure demonstrates that as noise level increases, the signal-to-noise ratio of the video key frame image is decreasing, but the NC mean of the watermark remains above 0.95, which shows that the algorithm in this paper has good robustness to noise attacks.

(2) *JPEG Compression Attack*. In this paper, the robustness of the algorithm is tested for JPEG

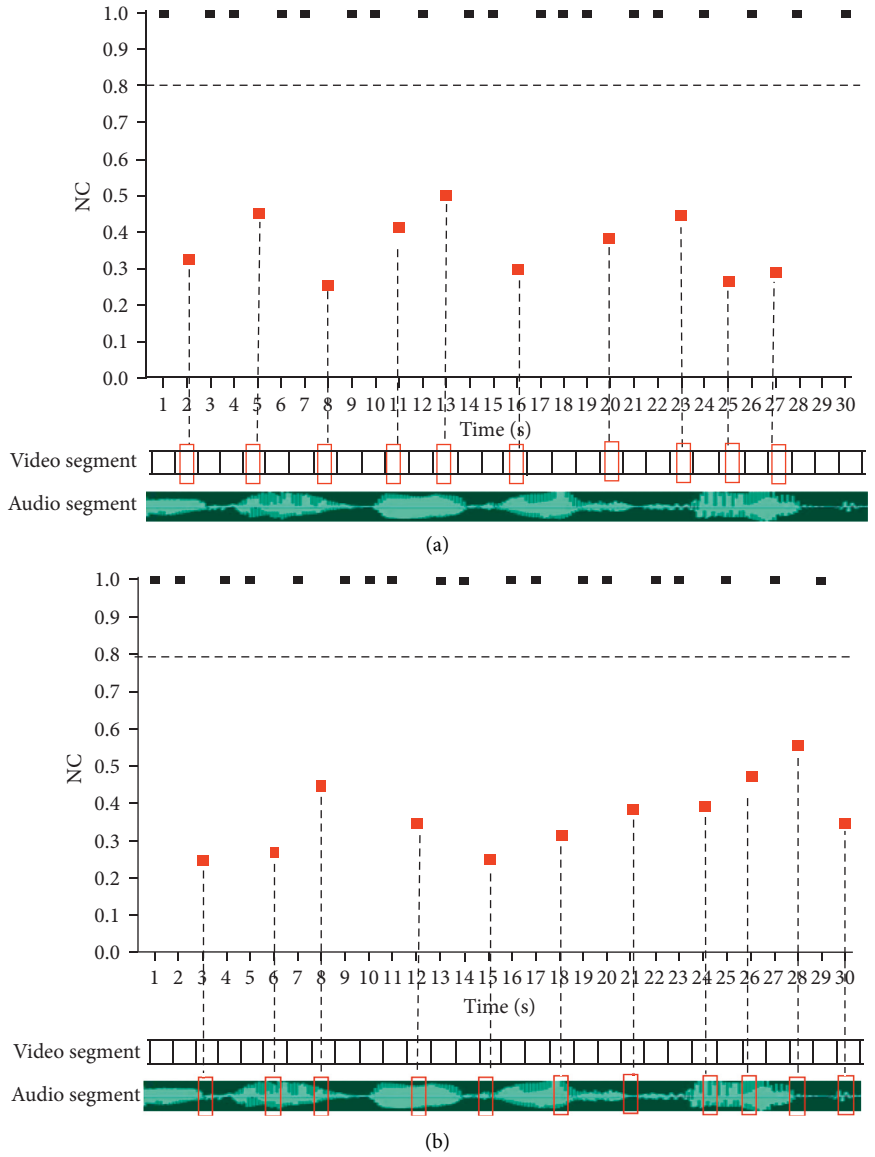

Figure 8: Experimental results of matching detection and location of audio and video. (a) Experimental results of matching detection after video tampering. (b) Experimental results of matching detection after audio tampering.

compression in the range of quality factor 10–90 with increments of 10 intervals, which is shown in Figure 10. According to experiment results shown in the figure, when the quality factor improves, the NC values which were extracted from key frames steadily rise and the distribution becomes more concentrated, and the NC values also increase with the improvement of quality factor. Within the experimental range, the NC values are greater than 0.96, indicating that the algorithm in this paper has good robustness in resisting JPEG compression.

(3) *Filter Attack*. In the research of image and video, image filtering is one of the most common operations. In this section, it is a Gaussian filtering attack that is applied on the video. As shown in Figure 11, when facing the Gaussian filtering attack, with the increase of the filter window size and the surrounding scale, the NC value of the watermark decreases, but it is still greater than 0.94, which shows that the robustness of the Gaussian filtering is better.

(4) *Shear Attack*. The algorithm in this paper conducts an attack experiment of cutting 1/20, 1/16, and 1/8 of the video on the upper left, lower left, upper right, and lower right, and the results are illustrated in Figure 12. The results demonstrate that because the algorithm extracts the features of the key frames when generating the watermark, even if the clipping attack will lead to the loss of a large number of features of the key frame image, the mean value of NC in the experiment is still above the matching detection threshold, which ensures the accuracy of the matching detection.

Table 1: Experimental results of video robustness.

Attack type	Attack parameter	PSNR	NC	BER (%)
Gaussian noise	0.01	20.7781	0.9947	0.1558
	0.05	14.3098	0.9853	0.4748
Salt and pepper noise	0.01	21.3424	0.9948	0.1646
	0.05	16.7343	0.9892	0.4720
Shear attack	Upper left 1/16	13.2199	0.9821	0.4759
	Lower right 1/20	14.8016	0.9930	0.1546
Scaling	1/2	33.5737	0.9985	0.1498
	2	45.3691	0.9994	0.1454
Frame attack	Frame average	28.8532	0.9932	0.15
	Frame reorganization	34.7721	0.9972	0.1499
Recompression	Mpeg4	32.2128	0.9853	0.4819
	H.264	33.2266	0.9875	0.4812
Rotate attack	15°	18.3589	0.98	0.4823
	90°	19.1075	0.9807	0.4817
	180°	19.9432	0.9914	0.1745
JPEG compression	90	45.8949	0.9984	0.1440
	50	35.4672	0.9917	0.1599
	20	30.9995	0.9841	0.4798
Combined attack	JPEG60 + rotate 30°	8.803	0.9523	1.7499
	JPEG30 + rotate 45°	8.2203	0.9340	2.2831
	JPEG10 + rotate 90°	6.2247	0.9120	3.4837
	Gaussian filtering 3*3 + upper left shear 1/20	14.1580	0.9835	0.4827
	Gaussian filtering 5*5+ upper left shear 1/20	14.0569	0.9815	0.4850
	Gaussian filtering 7*7 + upper right shear 1/20	14.4891	0.9841	0.4814

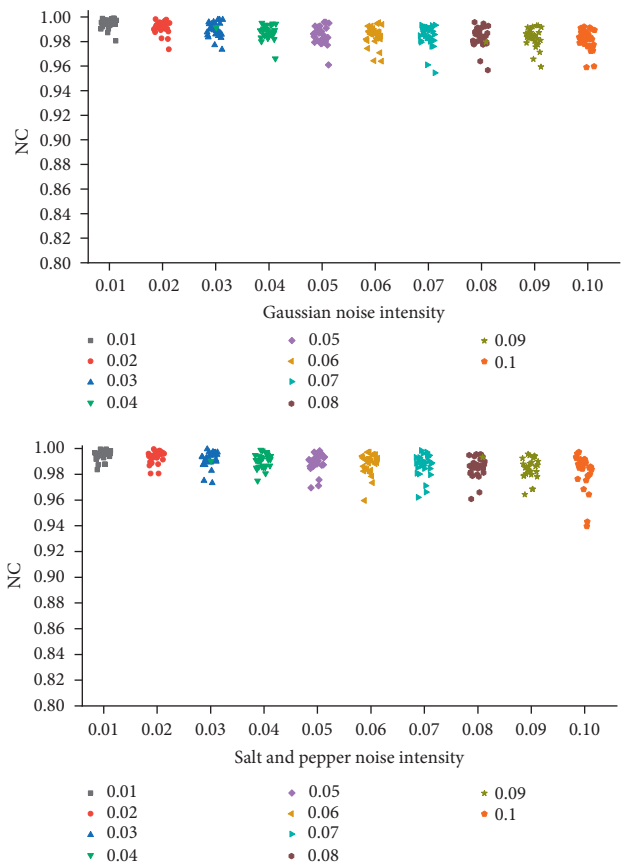

Figure 9: NC value under noise attack.

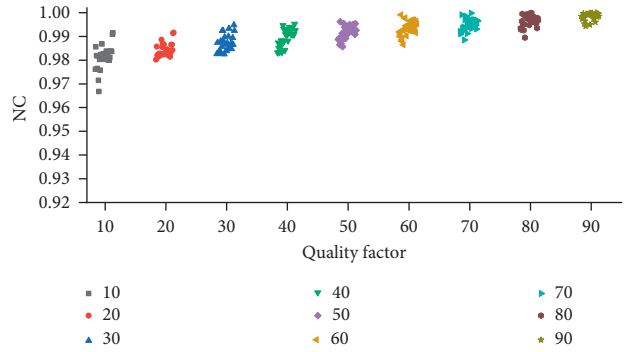

Figure 10: NC value under JPEG compression attack.

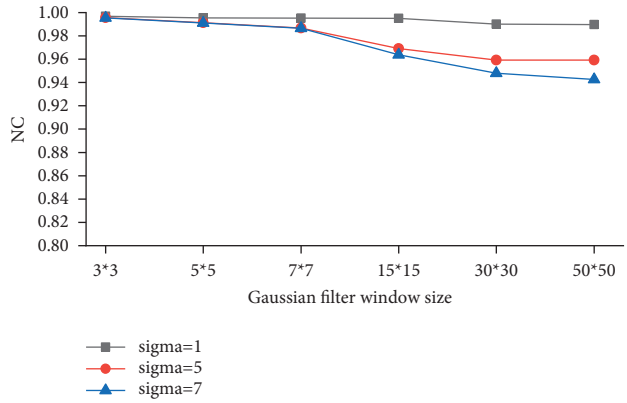

Figure 11: NC value under Gaussian filter attack.

(5) *Rotate Attack*. The algorithm in this paper carries out rotation attack from 0° to 180° on the video. It can be seen from Figure 13 that, with the increase of rotation angle, the NC value is gradually decreasing, but all of them are above 0.96, indicating that the algorithm can resist rotation attack well.

(6) *Scaling Attack*. The algorithm in this paper uses different scaling multiples to attack the video key frame images, respectively. As can be seen from Figure 14, the NC values are above 0.96, indicating that the algorithm in this paper has good robustness to scaling attacks.

(7) *Combined Attack*. In actual audio and video transmission, video often suffers from more than one attack, and there may be multiple attacks acting at the same time. Robustness under combined attack is also an important aspect of algorithm performance. The algorithm in this paper selects three combined attack methods of rotation and JPEG compression attack, shearing and Gaussian filtering attack, and H.264+ other attacks to conduct experiments. The results are shown in Figures 15–17, respectively. In general, for the three combined attacks, the NC value of the watermark is above 0.9, and there is still a large margin space from the threshold of 0.8, indicating that the algorithm can well resist the combined attack.

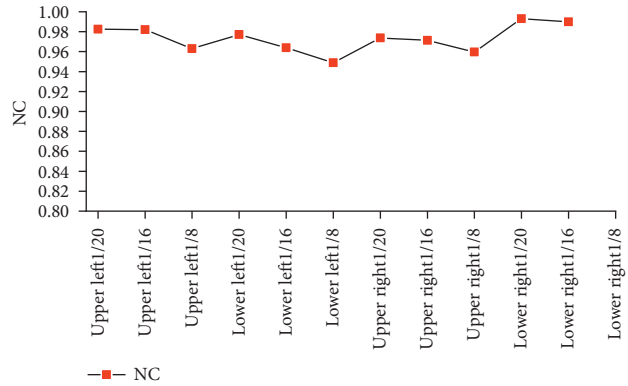

Figure 12: NC mean under shear attack.

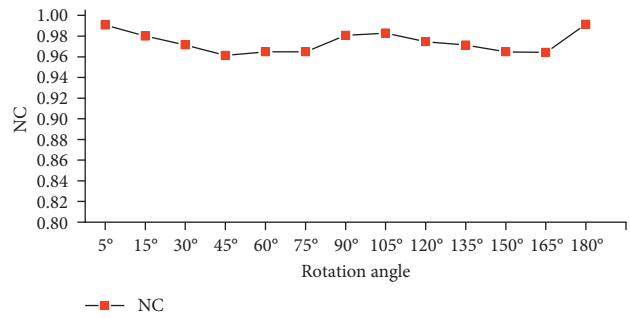

Figure 13: NC mean under rotation attack.

For Figure 15, the NC value of the watermark extracted by the algorithm under small-scale cropping and Gaussian filtering attacks can reach more than 0.96, which has strong robustness. Compared with the two attacks, the NC value of the algorithm is lower under the large-scale cropping attack, and the sensitivity to the cropping attack is slightly higher than that of the Gaussian filter.

For Figure 16, the experimental results show that the algorithm has good antiattack ability against the combined attack of rotation + JPEG compression. Most of the extracted watermark NC values are about 0.94, and it can be seen that the sensitivity of the algorithm to rotation attack is higher than that of JPEG compression attack.

For Figure 17, under the combined attack of format conversion and other attacks, the NC value of the extracted watermark is relatively high, which can be used for matching detection. Further analysis will find that the sensitivity of different video frames to the attack is different, and the ability to resist the combined attack has a certain relationship with the image content.

5.2.2. Audio Robustness Test. Audio with watermark may encounter attacks in the process of transmission. Some attacks may be unintentional, such as noise. Although they may not affect the visual perception, they also affect the reliability of watermark; some attacks may be intentional, such as cutting, filtering, and compression. The algorithm needs to have sufficient attack ability to resist various attacks and ensure the reliability and security of the watermark. In

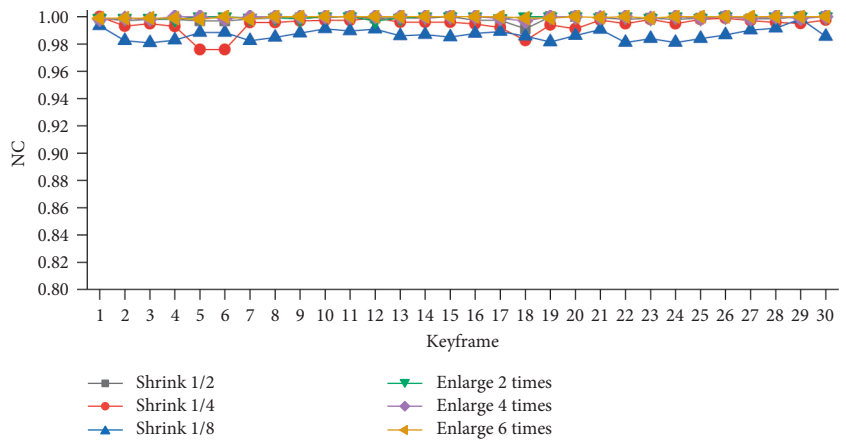

Figure 14: NC value under scaling attack.

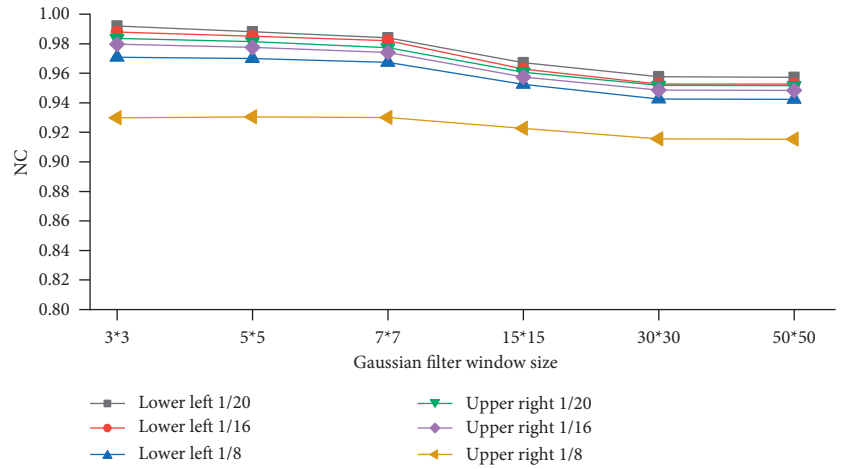

Figure 15: NC mean under combined attack of shear and Gaussian filter.

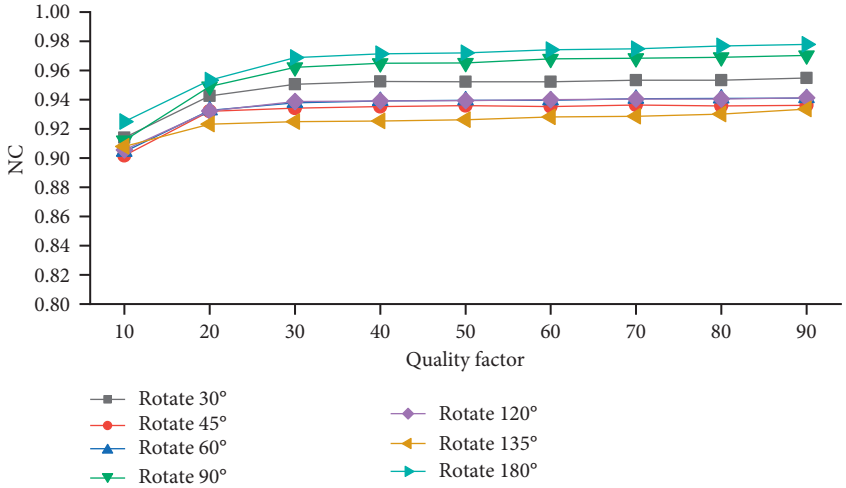

Figure 16: NC mean under combined attack of rotation and JPEG compression.

this paper, noise, weight, resampling, MP3 compression, and other attacks on audio are carried out, and the audio robustness experiments are carried out. The results are shown in Table 2. It can be seen from the data in the table that, under several attacks on the experiment, the watermark NC value obtained by the algorithm in this paper is more than 0.91, most of which are more than 0.99, and the robustness of the algorithm is good.

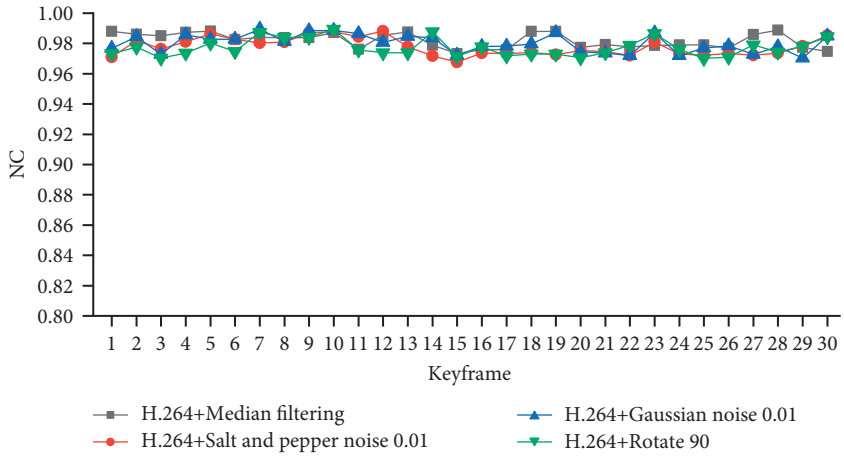

Figure 17: NC mean under H.264 and other attacks.

Table 2: Experimental results of audio robustness.

Attack type	Attack parameter	NC mean	PSNR mean	BER mean (%)
White Gaussian noise	20 dB	0.9191	28.8435	3.4829
	25 dB	0.9954	32.4838	0.1482
	30 dB	1	32.5631	0
Requantization	Up quantization	0.9995	31.6278	0.1473
	Down quantization	0.9962	32.0576	0.1492
Resampling	Upsampling	0.9939	31.5582	0.1495
	Downsampling	0.9879	33.5632	0.4796
Low-pass filtering	4 kHz	0.9954	32.9113	0.1489
	8 kHz	0.9938	32.9013	0.1496
MP3 compression	128 kbps	0.9917	31.4401	0.1507
	64 kbps	0.9938	31.9790	0.1495

Table 3: The experimental results of the proposed algorithm are compared with those of literature algorithms (NC value).

Experiment audio	Attack type	Literature [26] algorithm	Literature [27] algorithm	Proposed algorithm
Classical	Requantization	0.9910	0.9963	0.9978
	Resampling	0.9874	0.9899	0.9914
	Gaussian noise (20 dB)	0.9158	0.9467	0.9235
	Gaussian noise (30 dB)	0.9756	0.9999	1
	Low-pass filtering	0.9845	0.9913	0.9946
	MP3 compression	0.9389	0.9864	0.9969
Pop	Gaussian noise (20 dB)	0.9295	0.9665	0.9451
	Gaussian noise (30 dB)	0.9819	0.9993	1
	Low-pass filtering	0.9876	0.9911	0.9985
	MP3 compression	0.9539	0.9899	0.9984
	Requantization	0.9945	0.9985	0.9992
	Resampling	0.9956	0.9918	0.9996

5.3. Comparison Experiment with Similar Algorithms. This paper makes relevant experiments on similar algorithms in literature [26, 27] and compares and investigates them with the algorithms in this paper. Literature [26] selects the audio segment according to the local time domain characteristics of the audio signal and uses DWT and SVD algorithms to construct a zero watermark for the selected audio segment. Reference [27] is a zero-watermarking method based on DWT-DCT-SVD. Compared with the two algorithms, the algorithm in this paper is different in feature extraction and decomposition methods.

In the experiment, two different styles of audio signals, classical and pop, are selected as the original audio carrier. They are mono audio signals with the sampling frequency of 44.1 kHz and quantization accuracy of 16 bits; [26, 27] adopt 32×32 fixed binary watermark image, and the algorithm in these papers adopts 32×32 binary video watermark image generated from video. The attack experimental results of this algorithm and two comparative literature algorithms are shown in Table 3. It clearly shows that the proposed algorithm has excellent robustness against Gaussian noise, weighting, resampling, and low-pass filtering attacks. These

attacks are better than the comparison algorithm, and the advantage is more prominent under MP3 compression attack.

6. Conclusion

In this paper, a zero-watermarking algorithm for audio and video matching based on NSCT transform is proposed, which can detect whether the audio and video are mismatched due to tampering attacks, locate the mismatched audio and video segments, and play a role in protecting and identifying digital media information security. The algorithm uses NSCT, DCT, SVD, and Schur decomposition to extract video features and audio features and generate zero watermarking after synthesis. From the experimental results, the algorithm not only has strong robustness to common single-item attacks but also has high antiattack ability to combined attacks. Information security is a subject of constant development and change.

With the advancement of technology, the forms and types of attacks are also changing and improving, further improving antiattack capabilities, anti-new attack capabilities, robustness, and positioning speed and accuracy. It needs continuous research and continuous improvement.

Data Availability

The data used to support the findings of this study are available from the corresponding author upon request.

Conflicts of Interest

The authors declare that they have no conflicts of interest.

Acknowledgments

The research was supported by the Scientific Research Project of National Language Commission (YB135-125) and Key Research and Development Project of Shandong Province (2019GGX101008 and 2016GGX105013).

References

[1] J. Abraham and V. Paul, "An imperceptible spatial domain color image watermarking scheme," *Journal of King Saud University-Computer and Information Sciences*, vol. 31, no. 1, pp. 125–133, 2019.

[2] D. Fan, Y. Li, and S. Gao, "A novel zero watermark optimization algorithm based on Gabor transform and discrete cosine transform," *Concurrency and Computation: Practice and Experience*, vol. 2020, no. 2, 13 pages, 2020.

[3] M. Moosazadeh and G. Ekbatanifard, "An improved robust image watermarking method using DCT and YCoCg-R color space," *Optik*, vol. 140, pp. 975–988, 2017.

[4] C. Kumar, A. K. Singh, P. Kumar, and S. Siddharth, "SPHIT-based multiple image watermarking in NSCT domain," *Concurrency and Computation: Practice and Experience*, vol. 32, no. 1, pp. e4912.1–e4912.9, 2020.

[5] C. V. Narasimhulu, "A robust hybrid video watermarking algorithm using NSCT and SVD," in *Proceedings of the IEEE International Conference on Power, Control, Signals and Instrumentation Engineering*, pp. 1495–1501, New York, NY, USA, September 2017.

[6] N. N. Zermi, A. Khaldi, R. Kafi, F. Kahlessenane, and S. Euschi, "A DWT-SVD based robust digital watermarking for medical image security," *Forensic Science International*, vol. 320, no. 3.20, Article ID 110691, 2021.

[7] Yu Yang, M. Lei, X. Liu, Z. Qu, and C. Wang, "Novel zero-watermarking scheme based on DWT-DCT," *China Communications*, vol. 13, no. 7, pp. 122–126, 2016.

[8] S. B. Latha, D. V. Reddy, and A. Damodaram, "Video watermarking using neural networks," *International Journal of Information and Computer Security*, vol. 14, no. 1, pp. 40–59, 2021.

[9] C. Priya and C. Ramya, "Robust and secure video watermarking based on cellular automata and singular value decomposition for copyright protection," *Circuits, Systems, and Signal Processing*, vol. 40, no. 5, pp. 2464–2493, 2020.

[10] A. Bhardwaj, V. S. Verma, and R. K. Jha, "Robust video watermarking using significant frame selection based on coefficient difference of lifting wavelet transform," *Multimedia Tools and Applications*, vol. 77, no. 15, pp. 19659–19678, 2018.

[11] R. Ahuja and S. S. Bedi, "Video watermarking scheme based on IDR frames using MPEG-2 structure," *International Journal of Information and Computer Security*, vol. 11, no. 6, pp. 585–603, 2019.

[12] Li Chen, Yi Yang, K. Liu, L. Tian, and H. Lu, "A semi-fragile video watermarking algorithm based on H.264/AVC," *Wireless Communications and Mobile Computing*, vol. 2020, Article ID 8848553, 11 pages, 2020.

[13] F. Madine, M. A. Akhaee, and N. Zarmehi, "A multiplicative video watermarking robust to H.264/AVC compression standard," *Signal Processing: Image Communication*, vol. 68, pp. 229–240, 2018.

[14] S. Anguraj, S. P. Shantharajah, and E. J. Jeba, "A steganographic method based on optimized audio embedding technique for secure data communication in the Internet of Things," *Computational Intelligence*, vol. 36, no. 2, pp. 557–573, 2019.

[15] P. Hu, D. Z. Peng, Z. Yi, and Y. Xiang, "Robust time-spread echo watermarking using characteristics of host signals," *Electronics Letters*, vol. 52, no. 1, pp. 5-6, 2016.

[16] S. M. Pourhashemi, M. Mosleh, and Y. Erfani, "A novel audio watermarking scheme using ensemble-based watermark detector and discrete wavelet transform," *Neural Computing & Applications*, vol. 33, no. 11, pp. 6161–6181, 2020.

[17] M. Abdelwahab Khaled, M. Abd El-atty Saied, Wi El-Shafa, S. El-Rabaie, and F. Abd El-Samie, "Efficient SVD-based audio watermarking technique in FRT domain," *Multimedia Tools and Applications: International Journal*, vol. 79, no. 9-10, pp. 5617–5648, 2020.

[18] A. R. Elshazly, M. E. Nasr, M. M. Fouad, and F. E Abdel-Samie, "Intelligent high payload audio watermarking algorithm using colour image in DWT-SVD domain," *Journal of Physics: Conference Series*, vol. 2128, no. 1, Article ID 012019, 2021.

[19] J. Dittmann, A. Steinmetz, and R. Steinmetz, "Content-based digital signature for motion pictures authentication and content-fragile watermarking," in *Proceedings of the IEEE International Conference of the Multimedia Systems Multimedia Computing and Systems*, pp. 574–579, Florence, Italy, June 1999.

[20] X. Wang and Y. Pan, "Audio and video cross watermarking algorithm based on visual saliency model," *Electronic Measuremeent Technology*, vol. 40, no. 8, pp. 112–115, 2017.

[21] Z. Esmaeilbeig and S. Ghaemmaghami, "Compressed video watermarking for authentication and reconstruction of the audio part," in *Proceedings of the 2018 15th International ISC (Iranian Society of Cryptology) Conference on Information Security and Cryptology (ISCISC)*, pp. 1–6, IEEE, Tehran, Iran, August 2018.

[22] W. Sun, H. Zhao, X. Zhang et al., "Zero-watermarking algorithm for audio and video matching verification," *AIMS Mathematics*, vol. 7, no. 5, pp. 8390–8407, 2022.

[23] M. Bao, G. Lu-yang, L. Xiao-dong, and J. Tian, "A study on optimum classification character based on the distributive entropy of euclidian distance," *Journal of Optoelectronics - Laser*, vol. 2, no. 3, pp. 469–473, 2007.

[24] K. Huda and M. Mahmoud, "An imperceptible, robust, and high payload capacity audio watermarking scheme based on the DCT transformation and Schur decomposition," *Analog Integrated Circuits and Signal Processing*, vol. 99, no. 3, pp. 571–583, 2019.

[25] W. Liu, S. Sun, and H. Qu, "Fast zero-watermarking algorithm based on Schur decomposition," *Journal of Frontiers of Computer Science and Technology*, vol. 13, no. 3, pp. 494–504, 2019.

[26] X. Feng, G. Feng Naiguang, and Y. Wang, "Watermarking algorithm of audio signal based on discrete wavelet transform and singular value decomposition," *Journal of Huaqiao University*, vol. 37, no. 6, pp. 770–773, 2016.

[27] S. Liu, Q. Du, H. Long, Y. Shao, and Y. Peng, "A robust audio watermarking algorithm based on DWT-DCT-SVD," *Journal of Optoelectronics - Laser*, vol. 32, no. 9, pp. 1015–1022, 2021.

Hindawi
Complexity
Volume 2022, Article ID 3656482, 10 pages
https://doi.org/10.1155/2022/3656482

Research Article

Modeling the Thermal Performance for Different Types of Solar Chimney Power Plants

Ghassan F. Smaisim,[1,2] **Azher M. Abed**,[3] **and Ali Shamel**[4]

[1]*Department of Mechanical Engineering, Faculty of Engineering, University of Kufa, Kufa 54001, Iraq*
[2]*Nanotechnology and Advanced Materials Research Unit (NAMRU), Faculty of Engineering, University of Kufa, Kufa 54001, Iraq*
[3]*Air Conditioning and Refrigeration Techniques Engineering Department, Al-Mustaqbal University College, Babylon 51001, Iraq*
[4]*Department of Chemistry, Ardebil Branch, Islamic Azad University, Ardebil, Iran*

Correspondence should be addressed to Ghassan F. Smaisim; ghassan.smaisim@uokufa.edu.iq and Ali Shamel; ali.shamel8020@yahoo.com

Received 26 May 2022; Revised 28 June 2022; Accepted 30 June 2022; Published 18 July 2022

Academic Editor: Wenjie Lu

Nowadays, due to restrictions on fossil fuels, the use of renewable energies is increasing day by day. Among renewable energies, solar energy has received more attraction due to its availability in all places. Among solar energy technologies, the solar tower has been welcomed due to its high power generation of electrical energy. For accurate modeling of the studied system, each component of the system has been evaluated and modeling has been done. Therefore, in this research, solar tower modeling has been conducted to achieve high electrical energy production, and to better compare the production rate, 5 cities in Iran with different weather conditions have been considered. According to the results, it can be mentioned that the highest production power by the studied system is related to Shiraz city with an average production of 20 kW/m^2, and among the cities studied, the lowest rate is related to Mashhad with a production power of 15 kW/m^2.

1. Introduction

Nowadays, the importance of using clean energy and replacing it with fossil fuels is not covered as a basic solution for protecting the environment. Also, the advantages of consuming solar energy as a clean energy source, especially in Iran, are clear [1, 2]. A simple technology that uses solar energy to generate electricity is the solar chimney power plant. In addition to using a simple technology, this type of power plant has special advantages such as no need for water and the possibility of generating electricity during the day and night [3, 4].

Figure 1 shows a solar chimney power plant in the form of a schema. The power plant consists of a transparent collector and a cylinder chimney at its center. One or more turbines are also installed near the chimney base, which is connected to a generator. The function of this power plant is that the sun's radiation after passing through the ceiling of the collector (which is a transparent layer like a glass) mainly absorbs the surface of the earth, leading to the warming of the earth's surface and, consequently, the air adjacent to the earth, the higher temperature of the air inside the chimney column than the outside air, causing the effect of the chimney, which leads to the suction of the ambient air into the collector and then the chimney. Inside the chimney, it moves turbines and generates electricity [5–7].

The beginning of the most important studies on this subject dates back to 1931 when the basic principles and description of the solar chimney power plant were reported by Günter [8]. The original example of the solar chimney power plant with an output power of 50 kilowatts was designed by Cuce in 2020, 150 kilometers south of Madrid, Manzanares, Spain [2, 3]. Cuce et al. presented a brief discussion of energy balance, design rules, production power, and power plant cost analysis [9]. In the next study, Cuce reported the preliminary results of testing the power

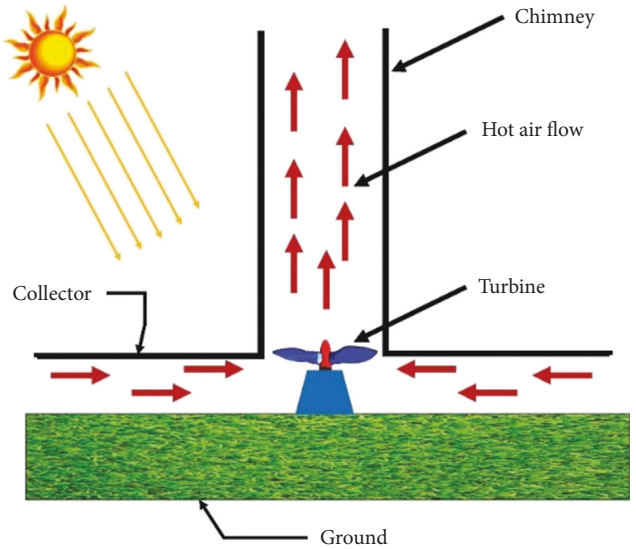

Figure 1: Schema of a solar chimney power plant.

plant built in Spain [10]. In 2021, Malta provided an analysis to determine the total efficiency of the power plant. He found that even though a solar chimney has little efficiency, building a large-scale power plant is the only economically viable option [11]. Belkhode et al. presented an evaluation of the experimental data to determine the performance of a solar chimney power plant [12].

Khidhir considered the airflow inside the collector as an extended radial flow between the two parallel disks in order to obtain the heat transfer coefficient of the solar chimney collector. In this study, the required analytical equations were presented to estimate the coefficients of heat transfer and pressure drop obtained from friction [13]. Galia studied the performance of the turbine used in the solar chimney power plant [14].

To predict the performance of solar chimney power plants, many researchers have used computational fluid dynamics (CFD). As an illustration, Torabi et al. presented a two-dimensional numerical model to estimate the air temperature distribution within the power plant collector [15]. In the following sections, Arzpeyma et al. simulated the solar chimney power plant and its correlation with the ambient wind effect [16]. In Reference [17], the authors presented the developed mathematical model CFD analysis for solar chimney efficiency evaluation with height variation.

Habibollahzade et al. developed a comprehensive theoretical model considering hourly changes in solar radiation and investigated the effect of different geometric parameters of the power plant on the output power [18]. Moreover, Aligholami et al. studied the feasibility of implementing solar chimney power plants in the Mediterranean regions [19].

Many researchers investigated the performance of solar chimney power plants and the quantity of electrical energy production in Iran [20, 21]. However, in most studies, transmission phenomena in the power plant have been modeled in a reliable state [22–24]. While the constraints of accumulation, especially the accumulation of heat in the surface layers of the earth and the chimney wall, can cause a significant error in the simulation results [25].

In Reference [4], the authors presented the effects of geometric parameters on the performance of solar chimney power plants. Torabi et al. studied the investigation the performance of the solar chimney power plant for improving the efficiency and increasing the outlet power of turbines using computational fluid dynamics [15]. In Reference [26], the authors presented the solar chimney power plants—dimension matching for optimum performance. Cuce et al. studied the performance assessment of solar chimney power plants with the impacts of divergent and convergent chimney geometry [27].

In this study, the modeling of all parts of the power plant has been done seamlessly and in unstable conditions. The use of the discontinuous model allows, along with considering the changes in the ambient temperature and the amount of sunlight during the day and night, heat reserves in different power plant environments, including in the surface layers of the earth and the chimney wall, are included in the calculations. In addition, the instantaneous solar radiation for Iranian cities is calculated using associate professors' equations, which have been developed based on Iran's climatic conditions. In addition, the information about ambient temperature during the day and night has been extracted from meteorological data and used.

After verifying the accuracy of the proposed model by comparing its results with the existing empirical data, a simulation of the power plant with dimensions and same-sex power plants constructed in Manzanares, Spain (capacity of 50 kW) has been carried out in 5 different cities of Iran (Shiraz, Bushehr, Kerman, Tehran, and Mashhad) and its average year-long power has been calculated. The results of the modeling, while emphasizing on higher efficiency of this power plant in Iran compared to Spain, indicate a significant difference in the performance of solar chimney power plants in different cities of Iran. Accordingly, the construction of power plants in Shiraz will have the highest efficiency among the five selected cities.

2. Materials and Methods

In this section, the governing equations of transmission phenomena are presented in different parts of the power plant which include the collector, turbine, and chimney tower. In order to be more accurate in calculations, in modeling all parts of the collector and chimney, accumulation expression is considered for continuity, motion, and energy equations.

2.1. Collector. The governing equations in the collector, assuming that the radial current is fully developed, are as follows.

2.1.1. Equation of Continuity.

$$-\frac{1}{r}\frac{\partial}{\partial r}(r\rho u) = \frac{\partial \rho}{\partial t}, \tag{1}$$

where ρ and u better is the density and speed of airflow within the collector, r is the radius of the collector, and t is the time.

2.1.2. Equation of Motion. This equation is derived from the momentum balance as follows:

$$-\frac{\partial P}{\partial r} - \rho u \frac{\partial u}{\partial r} - \frac{\tau_r}{H_r} - \frac{\tau_g}{H_r} = \rho \frac{\partial u}{\partial t}. \tag{2}$$

Here, P and H_r are better indications of the air pressure inside the collector and the height of the collector's cover from the ground up. Also, τr and τg are better shear stress in the ceiling of the collector and the ground surface.

By condoning the roughness of the collector's ceiling, during the fully developed turbulence, the value τr can be obtained from the following equation:

$$\tau_r = 0.023 \frac{\rho u^2}{\mathrm{Re}^{0.2}}. \tag{3}$$

The Reynolds number is defined and calculated as follows:

$$Re = \frac{\rho u d_h}{\mu}, \tag{4}$$

where μ is the dynamic viscosity and d_h is the hydraulic diameter. This quantity for flowing between parallel pages is twice the distance between pages. Shear stress caused by the radial flow on the earth's surface can be calculated by the Kruger–Bayes equation (6).

$$\tau_g = \frac{1}{2} f \rho u^2, \tag{5}$$

where f is the friction coefficient and can be calculated as follows:

$$f = 0.02975 \left(\frac{\varepsilon_g}{d_h}\right)^{0.254} \left[1.75 \left(\frac{\mu}{\rho u \varepsilon_g}\right)^{0.51} + 1\right]. \tag{6}$$

Here, ε_g is earth roughness. The combination of the above two equations can be expressed as follows:

$$\tau_g = 0.014875 \rho u_r^2 \left(\frac{\varepsilon_g}{2H_r}\right)^{0.254} \left[1.75 \left(\frac{\mu}{\rho u_r \varepsilon_g}\right)^{0.51} + 1\right]. \tag{7}$$

2.1.3. The Equation of Air Energy inside the Collector. Energy balance on a fluid element that is in contact from below with the ground and from above is in contact with the collector, as expressed in the following form:

$$-\rho C_p H_r u_r \frac{\partial T_f}{\partial r} + h_{gf}\left(T_g - T_f\right) + h_{rf}\left(T_r - T_f\right) = \rho C_p H_r \frac{\partial T_f}{\partial t}. \tag{8}$$

In this equation, C_p is special thermal capacity, and T_g, T_f, and T_r are ground surface temperature, airflow temperature inside the collector, and ceiling temperature of collector cover, respectively.

Due to low airspeed, the displacement mechanism is a combination of free and compulsory displacement. In this case, the displacement coefficient between the air f and the ground (h_{gf}) can be calculated from the following relationship [8]:

$$h_{gf} = \left(\left(Nu_{force} \frac{k_f}{2H_r}\right)^4 + \left(Nu_{free} \frac{k_f}{H_r}\right)^4\right)^{1/4}. \tag{9}$$

That k_f is the thermal conductivity of the air inside the collector. Also, Nusselt no-dimension numbers are obtained based on the following equations:

$$\begin{aligned} Nu_{free} &= 0.15\,(Gr\mathrm{Pr})^{1/3}, \\ Gr &= \frac{g\beta\left(T_{g,1} - T_f\right)H^3}{\upsilon^2}, \\ Nu_{force} &= 0.024\mathrm{Re}^{0.8}\mathrm{Pr}^{0.4}, \end{aligned} \tag{10}$$

where Gr and Pr are better than numbers without the Grashof dimension and Prandtl, g is the acceleration of earth's gravity, β volumetric expansion coefficient, υ cinematic viscosity, and $T_{g,1}$ ground surface temperature.

$$Re = \frac{2uH_r}{\upsilon}. \tag{11}$$

The heat transfer coefficient of the displacement between the inner airflow and the cover of the collector (h_{rf}) is similar to the method of calculating the heat transfer coefficient of the displacement between the airflow and the ground, of course, with this method.

The difference in the Grashof equation should be the temperature of the collector's surface instead of the temperature of the earth's surface.

2.1.4. Equation of Collector Ceiling Energy. The energy balance on the roof of the collector is as follows:

$$\begin{aligned} &I_b\alpha_b + I_d\alpha_d + h_{gr}\left(T_g - T_r\right) - h_{ra}\left(T_r - T_a\right) \\ &\quad - h_{rs}\left(T_r - T_s\right) + h_{rs}\left(T_r - T_s\right) = \rho_r C_{pr} \delta_r \frac{\partial T_r}{\partial t}. \end{aligned} \tag{12}$$

In this equation, I_b and I_d are direct solar radiation intensity and scattered solar radiation intensity, respectively, which are calculated by associate professors' equations (17). α_b is the direct effective absorption coefficient, α_d is the effective absorption coefficient of dispersion, and T_a is the ambient air temperature. Also, ρ_r, C_{pr}, and δ_r are better density, special thermal capacity, and thickness of collector coating. The heat transfer coefficient of the displacement between the cover surface of the collector and the outer air (h_{ra}), which is affected by the wind on the flat surface, is calculated as follows [18]:

$$h_{ra} = 2.8 + 3u_w. \tag{13}$$

Here, u_w is the ambient wind speed. Also, h_{gr} and h_{rs}, which are the radiation heat transfer coefficient between the

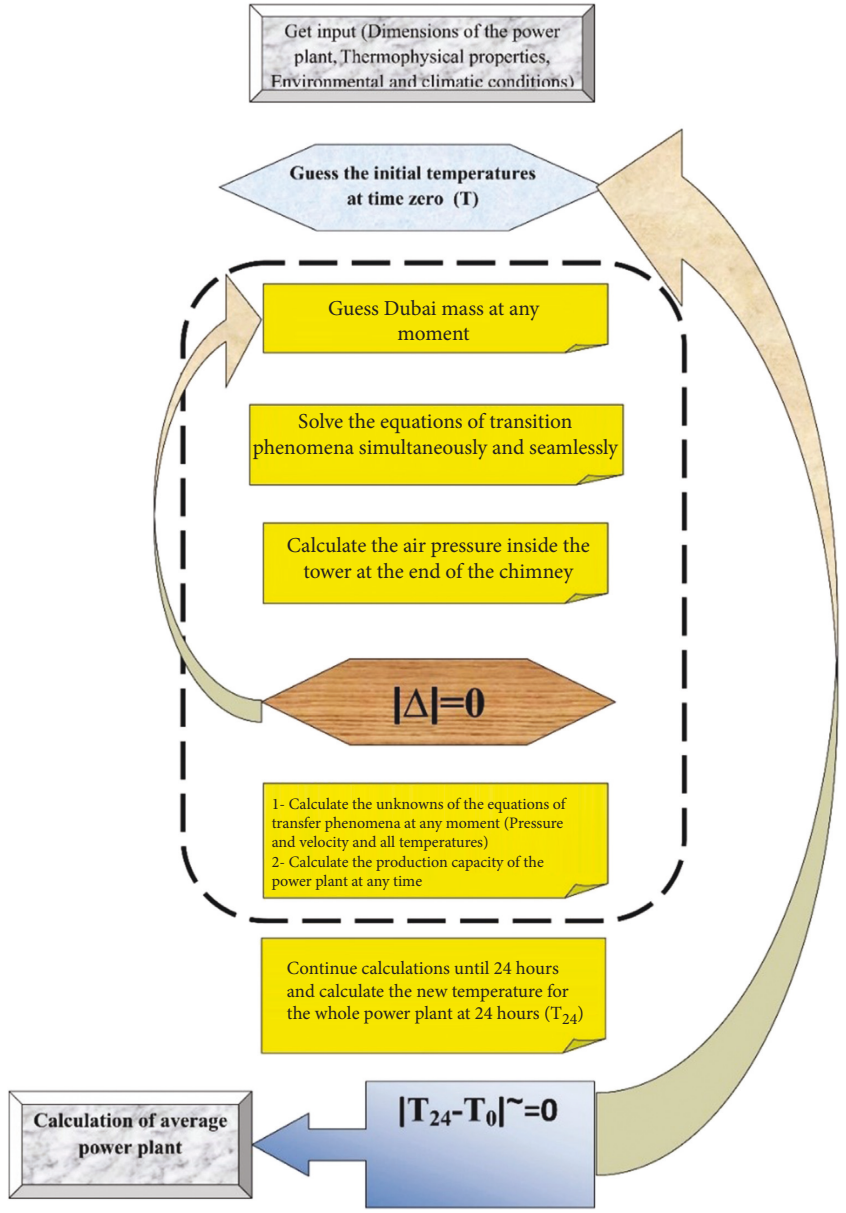

Figure 2: Layout of calculations.

earth's two surfaces and the coating, respectively, as well as the radiation heat transfer coefficient between the earth and the sky, can be calculated from the following equations (19):

$$h_{gr} = \frac{\sigma}{1/\varepsilon_g + 1/\varepsilon_r - 1}\left(T_g^2 + T_r^2\right)\left(T_g + T_r\right),$$
$$h_{rs} = \sigma\varepsilon_r\left(T_s^2 + T_r^2\right)\left(T_s + T_r\right), \tag{14}$$

where σ, ε_g and ε_r are Stephen Boltzmann's constant, land propagation coefficient, and collector cover dike coefficient, respectively, and T_s is sky temperature, the amount of which is estimated in terms of Kelvin as follows [20]:

$$T_s = 0.0552T_a^{1.5}. \tag{15}$$

2.1.5. Equation of Earth's Energy. In this section, the Earth can be considered as a semiunlimited body. Therefore, the Earth's temperature equation is as follows:

$$\frac{\partial^2 T_g}{\partial Z^2} = \frac{\rho_g c_{pg}}{k_g}\frac{\partial T_g}{\partial t}, \tag{16}$$

where ρ_g, c_{pg}, and k_g are density, special thermal capacity, and thermal conductivity coefficient of the earth, respectively.

The first boundary condition of this equation is obtained using the energy balance at the ground level as follows:

$$I_b\left(\tau_r\alpha_g\right)_b + I_d\left(\tau_r\alpha_g\right)_d = h_{gr}\left(T_g - T_r\right) + h_{gf}\left(T_g - T_f\right) - k_g\frac{\partial T_g}{\partial Z}. \tag{17}$$

Table 1: Thermophysics properties and power plant dimensions.

The ceiling of the collector (glass)	
Glass emission coefficient	0.85
The roughness of glass	0
Thickness of glass	0/004
External radius	112
Internal radius	12
Average elevation from the ground level	1/85
Earth (soil)	
Emission coefficient	0/9
Absorb coefficient	0/91
Density	1900 Kg/m^3
Special thermal capacity	840 Jules per kilogram degree celsius
Roughness	0/05
Turbine	
Output	0/83
Chimney (cement)	
Height	200
Inner diameter	10
Thickness	0/1
Roughness on the surface	0/002
Publication coefficient	0/84

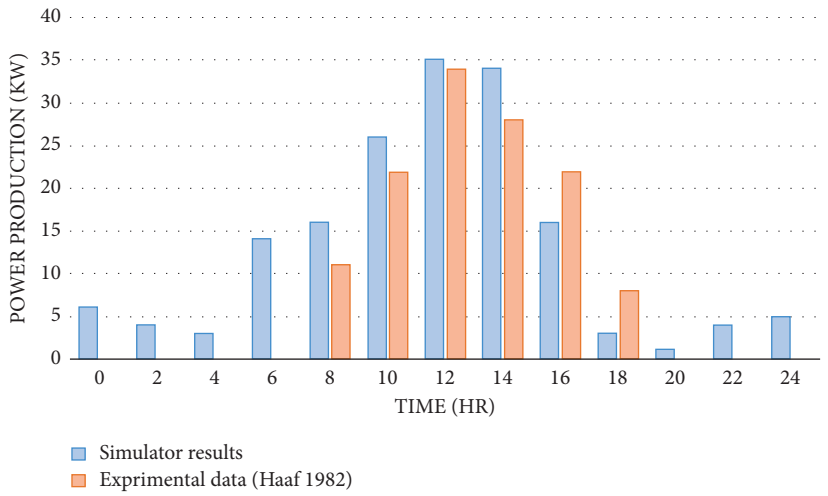

Figure 3: The output of Manzanares power plant in Spain and its comparison with experimental data.

Due to the inseparability of the Earth's radius and its low thermal conductivity, the second boundary condition is as follows.

$$Z \longrightarrow \infty: \frac{\partial T_g}{\partial Z} = 0. \tag{18}$$

2.2. Turbine. Turbine pressure drop can be calculated using the Betz power rule [8]:

$$\Delta p_t = \frac{8}{27}\rho u_t^2, \tag{19}$$

where u_t is the airspeed at the turbine's output. The power output power of the power plant is also calculated as follows [12]:

$$Power = \frac{m\eta_t \Delta p_t}{\rho}, \tag{20}$$

Table 2: Comparison of production power and energy production in September.

	Daily generated energy (MJ)	Average production (kW/day)
Shiraz	2671/49	30/92
Spain	1390/18	16/09

where η_t is the turbine efficiency, considering the experimental results obtained in the Spanish laboratories, this parameter is considered to be 0.83. [2].

2.3. Chimney. By condoning the changes in air velocity in line with the radius of the governing equations in the chimney, it is expressed as follows.

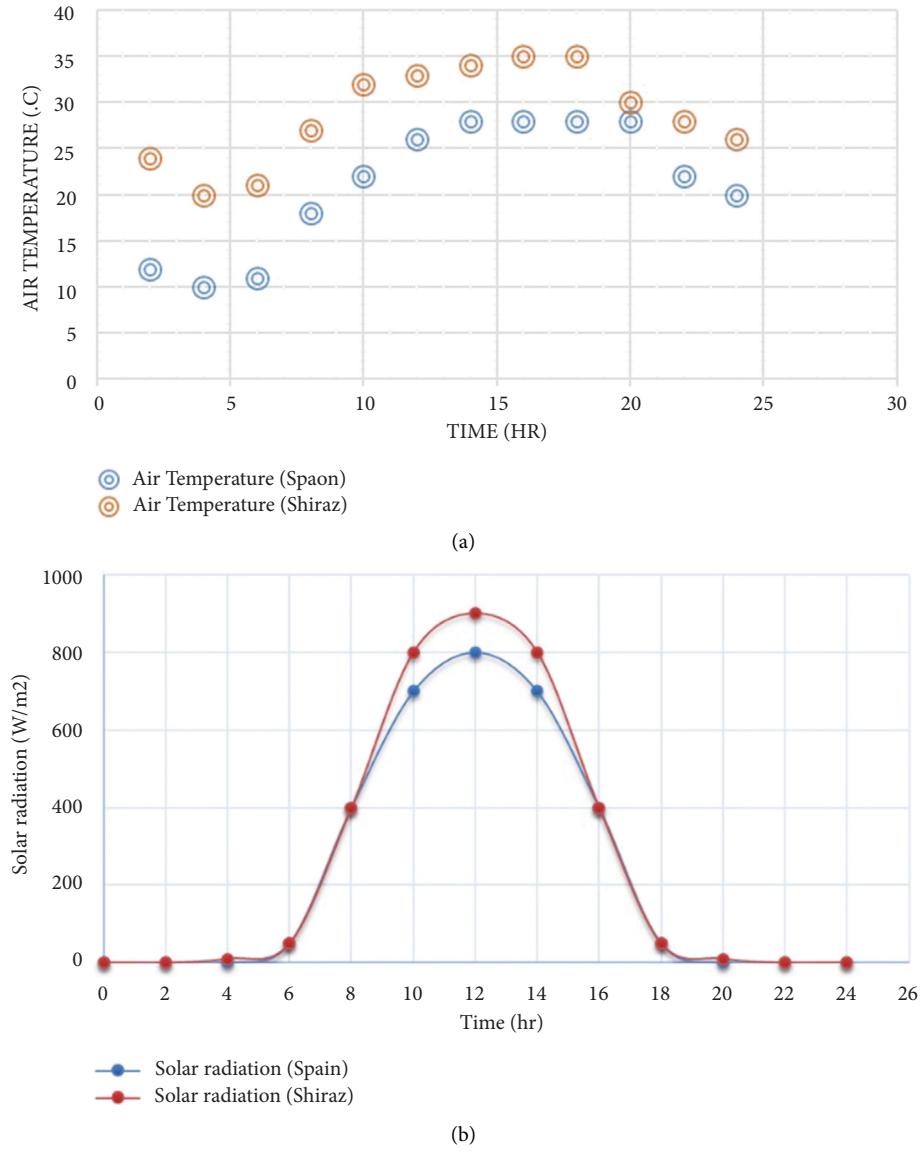

Figure 4: Comparison of (a) ambient temperature and (b) solar radiation between Shiraz and Manzanares on September 2.

2.3.1. Equation of Continuity.

$$-\frac{\partial}{\partial Z}(\rho u_z) = \frac{\partial \rho}{\partial t}. \tag{21}$$

2.3.2. Equation of Motion.

$$-\frac{\partial P}{\partial Z} - \rho u_z \frac{\partial u_z}{\partial Z} - \frac{2\tau_{ch}}{R_{ch}} - \rho g = \rho \frac{\partial u_z}{\partial t}. \tag{22}$$

Shear stress on the chimney wall can be calculated from the following equation:

$$\tau_{ch} = \frac{1}{8} f \rho u_z^2. \tag{23}$$

Due to the magnitude of the chimney diameter, the roughness effect of its surface is negligent and the friction coefficient of the (f) chimney wall is obtained from the following equation (22):

$$f = (1.82\log \mathrm{Re} - 1.64)^{-2}. \tag{24}$$

2.3.3. The Equation of Air Energy inside the Chimney. By condoning the changes in air temperature in the direction of radius and in addition to giving up thermal conductivity in comparison with displacement, the equation of air temperature distribution inside the chimney is written as follows.

$$-\rho u_z C_p \frac{\partial T_z}{\partial Z} - \frac{2h_f}{R_{ch}}(T_z - T_{wi}) = \rho C_p \frac{\partial T_z}{\partial t}. \tag{25}$$

The required boundary condition of this part is obtained from equal to the temperature of the entrance to the

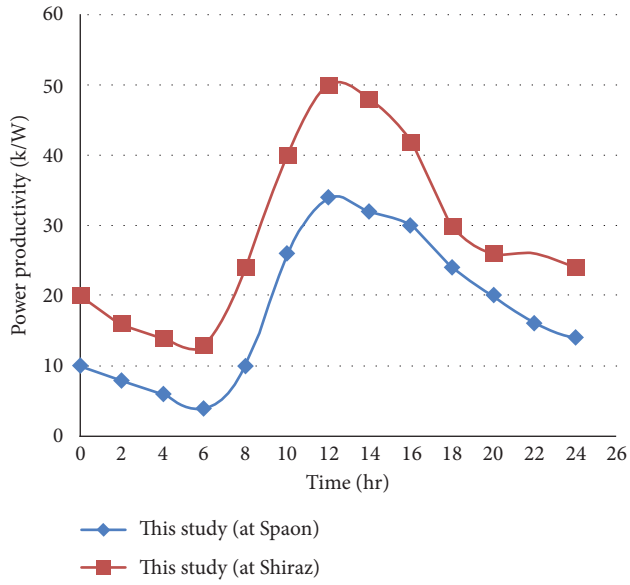

Figure 5: Comparison of power production in Shiraz and Manzanares cities on September 2.

chimney with the air temperature of the output from the collector. The heat transfer coefficient between the air inside the tower and the inner wall of the tower is calculated from the following equations:

$$h_f = \frac{Nu_f k_{air}}{d_{ch}},$$

$$Nu_f = 0.023\mathrm{Re}^{0.8}\mathrm{Pr}^{1/3}, \tag{26}$$

$$Re = \frac{\rho u d_{ch}}{\mu}.$$

2.3.4. Equation of Chimney Wall Energy. Since the thickness of the chimney is insignificant compared to its height, heat conductivity can be assumed to be one-dimensional and unstable.

$$\frac{1}{r}\frac{\partial}{\partial r}\left(rk_w\frac{\partial T_w}{\partial r}\right) = \frac{\partial}{\partial t}\left(\rho_w C_{\rho_w} T_w\right). \tag{27}$$

Boundary conditions at the internal and external levels of energy balance on those surfaces are obtained as follows:

The equation for the internal surface is as follows:

$$k_w\frac{\partial T_w}{\partial r}|r = R_i = h_f\left(T_w|r = R_i - T\right). \tag{28}$$

The equation for the external surface is as follows:

$$g_T - k_w\frac{\partial T_w}{\partial r}|r = R_{\text{out}} + h_a\left(T_a\, r = R_{\text{out}} - T\right) = 0. \tag{29}$$

In this regard, q_t is the total direct and solar intrusive radiation absorbed by the external surface of the chimney.

The heat transfer coefficient between the ambient air and the external wall of the tower can also be calculated from the following equation (19):

$$h_a = 11.4 + 1.4u_{\text{wind}}. \tag{30}$$

2.4. Method of Performance Calculations. To simulate the performance of a solar chimney power plant, it is necessary to solve all the governing equations seamlessly. In the prepared simulation, these equations are solved using the finite difference numerical method.

Simulation calculations are performed in two circles of trial and error. In the external circle, the early temperature values of the fluid and power plant components (including the air inside the collector and the chimney, the surface layers of the earth, the cover surface, and the temperature of the chimney wall) are guessed at zero time; all of these temperatures must be equal to the computational values for the temperature at the end of the day at 24 o'clock.

In the inner circle at each time stage, the mass discharge of the air inside the power plant is guessed. The correct condition of this guess is the equal value calculated for the air pressure reached at the end of the chimney with the outside air pressure at that altitude. Figure 2 shows the design of the calculations in the prepared simulator.

3. Results and Discussion

To validate the prepared model and numerical method of solving the simulation results equations are compared with the experimental data of The Manzanares Solar Chimney Power Plant in Spain. The power plant is built from a collector with a diameter of 224 meters and a tower with a diameter of 10 meters and a height of 200 meters. Also, the average height of the collector from the ground level is 85.1 meters. Other thermophysics dimensions and properties of different parts of the power plant are listed in Table 1 [28].

Figure 3, the output results of the Manzanars power plant can be compared with the results of this research. As

Table 3: Climate and climatic conditions of selected cities.

City	Latitude	Average annual relative humidity (%)	The average yearly temperature difference	Annual solar radiation (MJ/m)
Shiraz	29/53	28/4	14/58	7675/51
Bushehr	28/29	62/7	8/49	7337/18
Kerman	30/25	12/5	18/55	7071/19
Tehran	35/68	23/4	8/54	6678/48
Mashhad	36/26	24/3	11/02	6571/66

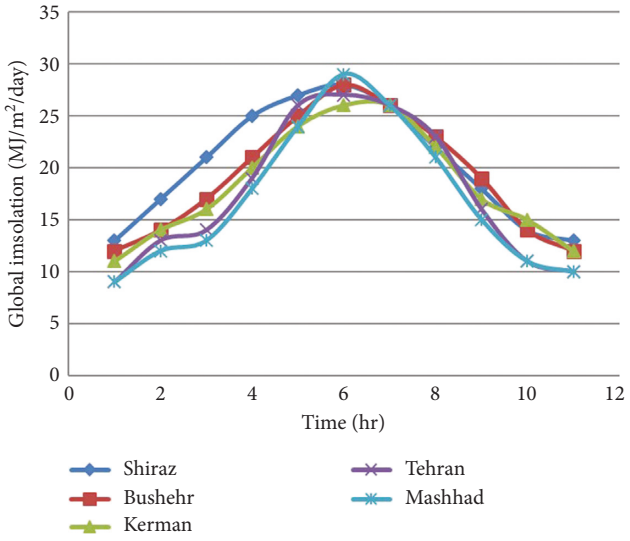

Figure 6: Average monthly total solar radiation per day in different months of the Gregorian year in selected cities.

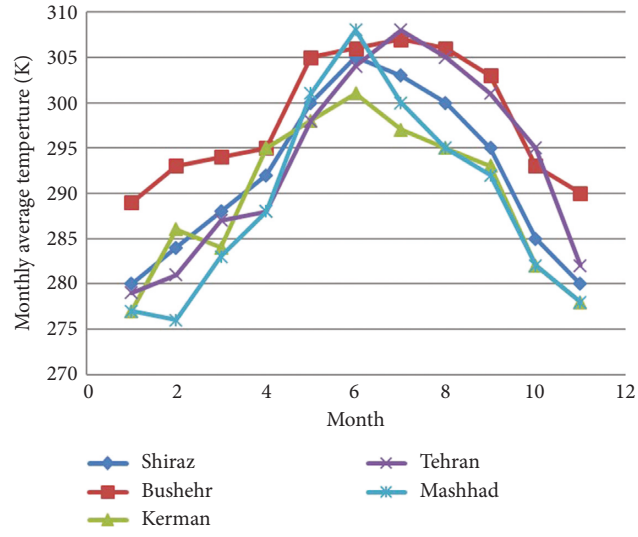

Figure 7: Monthly average temperature changes in different months of the year for selected cities in Iran.

can be seen, the simulation results are in very good agreement with the experimental data, which confirms the accuracy of the calculations. Table 2 shows the average daily power and energy generated on September 2 for two power plants. As can be seen, this power plant in Shiraz has approximately 92% more production capacity than the Spanish pilot. This indicates the importance of investigating and the possibility of building such power plants in Iran, especially in Shiraz.

Figure 4 shows changes in ambient temperature and solar radiation in Shiraz and Manzanares cities. A comparison of the power output of the Shiraz power plant compared to the Spanish pilot is shown in Figure 5.

In this research, to investigate the effect of geographical location and environmental factors on the performance of solar chimney power plants and to optimize their construction location in Iran, 5 cities in Iran (Shiraz, Bushehr, Kerman, Tehran, and Mashhad) with different climatic and environmental conditions and a high amount of solar radiation, have been selected. In Table 3, the climate and climatic conditions of the selected cities can be seen [17].

Figure 6 shows the solar energy radiated per unit area of the horizon on the middle of the moon in 5 selected cities, fulfilled using the associate's equations (17). As can be seen, Shiraz has the highest MJ/m^2/year (51.7675) and Mashhad has the lowest solar/year MJ/m (66.6571), and the average monthly temperature in the 5 selected cities is shown in Figure 7.

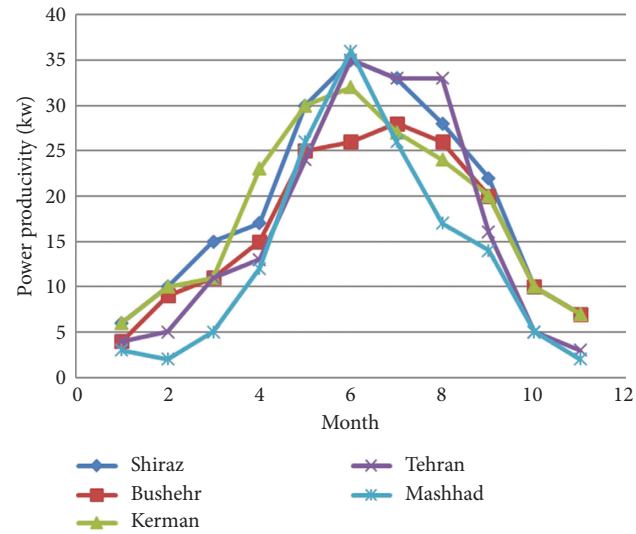

Figure 8: Average changes in power plant production power in different months of the year for selected cities.

Figure 8 shows the average monthly production power of the modeled power plant in 5 cities in Iran (Shiraz, Bushehr, Kerman, Tehran, and Mashhad).

As can be seen in Figure 8, among these five selected cities, the construction of power plants in Shiraz has the highest efficiency and is better than Mashhad, Tehran,

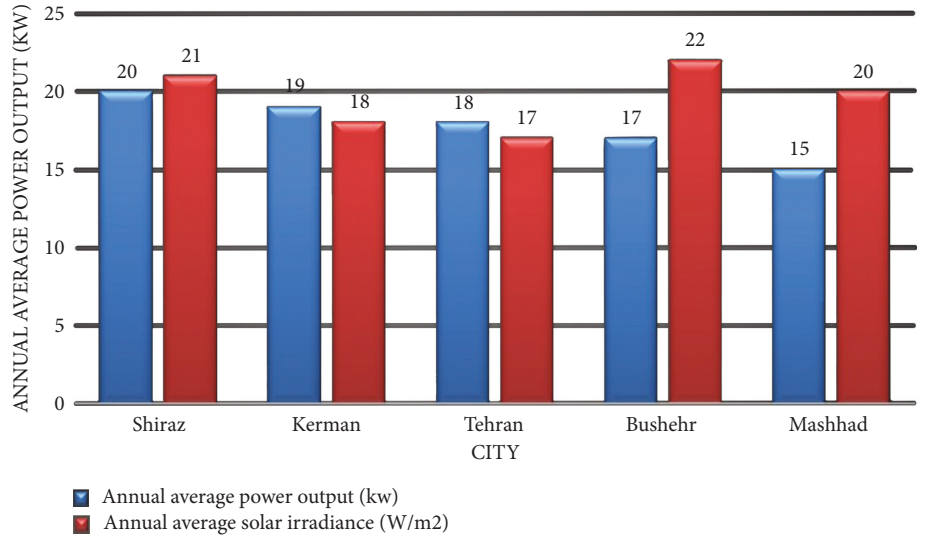

Figure 9: Comparison of average year-on-year power production in different cities of Iran.

Kerman, and Bushehr has better 40%, 13%, 3%, and 16% more production capacity than Mashhad and Tehran, comparing average year power and average year radiation for 5 cities of Iran (Shiraz, Bushehr, Kerman, Tehran). In Figure 9, we can see the results of Mashhad city, which includes the average production power.

Bushehr, despite having the stronger radiation, has less efficiency than Shiraz; the humidity of the air as well as the amplitude of temperature changes during the day.

4. Conclusion

In this paper, the governing equations of the solar chimney simulator were presented and it was illustrated that the prepared household simulator has good accuracy. Using a simulator of a solar power plant in the dimensions of a Spain power plant, for five different cities of Iran (Shiraz, Bushehr, Kerman, Tehran, and Mashhad), the model and the following results were observed.

(1) If this power plant is constructed in Shiraz, the energy produced per month in September is 92% higher than the same amount in Spain.

(2) Among the 5 selected cities, Shiraz has the highest efficiency, and power plants in Shiraz are 7.14% more than the average power in four cities (Bushehr, Kerman, Tehran, and Mashhad) estimated.

(3) Among the five cities studied, after Shiraz, the priority of constructing power plants is in Kerman, Tehran, Bushehr, and Mashhad, respectively.

(4) The reason for the lower efficiency of the power plant in the coastal city of Bushehr seems to be the high humidity of the city's air, as well as the lower scope of the daily temperature changes in this city.

Data Availability

All data used to support the findings of this study are included within the article.

Conflicts of Interest

The authors declare that they have no conflicts of interest.

References

[1] R. Alayi and H. Rouhi, "Techno-economic analysis of electrical energy generation from urban waste in Hamadan, Iran," *International Journal of Design & Nature and Ecodynamics*, vol. 15, no. 3, pp. 337–341, 2020.

[2] R. Alayi, F. Zishan, S. R. Seyednouri, R. Kumar, M. H. Ahmadi, and M. Sharifpur, "Optimal load frequency control of island microgrids via a PID controller in the presence of wind turbine and PV," *Sustainability*, vol. 13, no. 19, p. 10728, 2021.

[3] R. Alayi, M. Jahangiri, and A. Najafi, "Energy analysis of vacuum tube collector system to supply the required heat gas pressure reduction station," *International Journal of Low Carbon Technologies*, vol. 16, no. 4, pp. 1391–1396, 2021.

[4] D. Toghraie, A. Karami, M. Afrand, and A. Karimipour, "Effects of geometric parameters on the performance of solar chimney power plants," *Energy*, vol. 162, pp. 1052–1061, 2018.

[5] A. Abdeen, A. A. Serageldin, M. G. Ibrahim, A. El-Zafarany, S. Ookawara, and R. Murata, "Solar chimney optimization for enhancing thermal comfort in Egypt: an experimental and numerical study," *Solar Energy*, vol. 180, pp. 524–536, 2019.

[6] R. Alayi, M. Jahangiri, J. W. G. Guerrero, R. Akhmadeev, R. A. Shichiyakh, and S. A. Zanghaneh, "Modelling and reviewing the reliability and multi-objective optimization of wind-turbine system and photovoltaic panel with intelligent algorithms," *Clean Energy*, vol. 5, no. 4, pp. 713–730, 2021.

[7] O. K. Ahmed and A. S. Hussein, "New design of solar chimney (case study)," *Case Studies in Thermal Engineering*, vol. 11, pp. 105–112, 2018.

[8] H. Günther, *Hundred Years-Future Energy Supply of the World*, Kosmos, Franckh'sche Verlagshandlung, 1931.

[9] E. Cuce, P. M. Cuce, and H. Sen, "A thorough performance assessment of solar chimney power plants: case study for Manzanares," *Cleaner Engineering and Technology*, vol. 1, p. 100026, 2020.

[10] E. Cuce, H. Sen, and P. M. Cuce, "Numerical performance modelling of solar chimney power plants: influence of chimney height for a pilot plant in Manzanares, Spain," *Sustainable Energy Technologies and Assessments*, vol. 39, p. 100704, 2020.

[11] S. Pradhan, R. Chakraborty, D. K. Mandal, A. Barman, and P. Bose, "Design and performance analysis of solar chimney power plant (SCPP): a review," *Sustainable Energy Technologies and Assessments*, vol. 47, p. 101411, 2021.

[12] P. Belkhode, C. Sakhale, and A. Bejalwar, "Evaluation of the experimental data to determine the performance of a solar chimney power plant," *Materials Today Proceedings*, vol. 27, pp. 102–106, 2020.

[13] D. K. Khidhir and S. A. Atrooshi, "Investigation of thermal concentration effect in a modified solar chimney," *Solar Energy*, vol. 206, pp. 799–815, 2020.

[14] R. A. Galia, "Study effect of chimney height on the power output of the solar chimney system," 2021.

[15] M. R. Torabi, M. Hosseini, O. A. Akbari et al., "Investigation the performance of solar chimney power plant for improving the efficiency and increasing the outlet power of turbines using computational fluid dynamics," *Energy Reports*, vol. 7, pp. 4555–4565, 2021.

[16] M. Arzpeyma, S. Mekhilef, K. M. S. NewazNewaz et al., "Solar chimney power plant and its correlation with ambient wind effect," *Journal of Thermal Analysis and Calorimetry*, vol. 141, no. 2, pp. 649–668, 2020.

[17] G. Goswami and N. Yadav, "CFD analysis for solar chimney efficiency evaluation with height variation," *Research Journal of Engineering Technology and Medical Sciences*, vol. 5, no. 1, pp. 2582–6212, 2022.

[18] A. Habibollahzade, E. Houshfar, M. Ashjaee, A. Behzadi, E. Gholamian, and H. Mehdizadeh, "Enhanced power generation through integrated renewable energy plants: solar chimney and waste-to-energy," *Energy Conversion and Management*, vol. 166, pp. 48–63, 2018.

[19] M. Aligholami, S. Khosroshahi, and A. Khosroshahi, "Hydrodynamic and thermodynamic enhancement of a solar chimney power plant," *Solar Energy*, vol. 191, pp. 180–192, 2019.

[20] A. Kasaeian, M. Ghalamchi, and M. Ghalamchi, "Simulation and optimization of geometric parameters of a solar chimney in Tehran," *Energy Conversion and Management*, vol. 83, pp. 28–34, 2014.

[21] A. Asnaghi, S. M. Ladjevardi, A. H. Kashani, and P. S. Izadkhast, "Solar chimney power plant performance analysis in the central regions of Iran," *Journal of Solar Energy Engineering*, vol. 135, no. 1, p. 011011, 2013.

[22] H. H. AlKayiem, M. A. Aurybi, and S. I. Gilani, "Influence of canopy condensate film on the performance of solar chimney power plant," *Renewable Energy*, vol. 136, pp. 1012–1021, 2019.

[23] P. H. Guo, J. Y. Li, and Y. Wang, "Annual performance analysis of the solar chimney power plant in Sinkiang, China," *Energy Conversion and Management*, vol. 87, pp. 392–399, 2014.

[24] H. Kebabsa, M. Lounici, and A. Daimallah, "Numerical investigation of a novel tower solar chimney concept," *Energy*, vol. 214, p. 119048, 2021.

[25] P. M. Cuce, E. Cuce, H. Sen, Improving electricity production in solar chimney power plants with sloping ground design: an extensive CFD research," *Journal of Solar Energy Research Updates*, vol. 7, no. 1, pp. 122–131, 2020.

[26] P. J. Cottam, P. Duffour, P. Lindstrand, and P. Fromme, "Solar chimney power plants - dimension matching for optimum performance," *Energy Conversion and Management*, vol. 194, pp. 112–123, 2019.

[27] E. Cuce, A. Saxena, P. M. Cuce, H. Sen, S. Guo, and K. Sudhakar, "Performance assessment of solar chimney power plants with the impacts of divergent and convergent chimney geometry," *International Journal of Low Carbon Technologies*, vol. 16, no. 3, pp. 704–714, 2021.

[28] W. Haaf, K. Friedrich, G. Mayr, and J. Schlaich, "Solar chimneys part I: principle and construction of the pilot plant in Manzanares," *International Journal of Solar Energy*, vol. 2, no. 1, pp. 3–20, 1983.

Hindawi
Complexity
Volume 2022, Article ID 2468431, 14 pages
https://doi.org/10.1155/2022/2468431

Research Article

Insulator Semantic Segmentation in Aerial Images Based on Multiscale Feature Fusion

Zheng Cui, Chunxi Yang, and Sen Wang

Faculty of Mechanical and Electrical Engineering, Kunming University of Science and Technology, Kunming 650500, China

Correspondence should be addressed to Chunxi Yang; ycx2003@163.com

Received 18 April 2022; Revised 15 May 2022; Accepted 26 May 2022; Published 1 July 2022

Academic Editor: Chun Wei

As one of the important components in the transmission line, the insulator is related to the safe and reliable operation of the entire transmission line. Aerial images are characterized by complex backgrounds, multiple pseudotargets, and low signal-to-noise ratios. Rapid and accurate localization of insulators in aerial images is a critical and challenging task in automatic inspection of transmission lines. Most insulator localization methods suffer from the loss of target edge detail information and large amount of model parameters. To solve these problems, this paper adopts an Encoder-Decoder architecture, called ED-Net, to realize end-to-end intelligent and accurate identification of insulators in aerial images. Firstly, Initial Module and CA-Bottleneck which are used to extract features from images to generate finer feature maps are proposed in the Encoder path. Meanwhile, global average pooling is used to preserve the maximum receptive field. Secondly, in the Decoder path, Refinement Boundary Module and Asymmetric Convolution Module are given to perform boundary optimization on the feature map, which are generated by the Encoder path. Finally, the Attention Feature Fusion Module is introduced into the Decoder path to combine high-level features with low-level features better and reduce the gap between features of different levels. The proposed model architecture keeps a suitable balance between the model parameters and insulator segmentation performance on insulator test datasets. Specifically, for a 512×512 input image, 95.12% mean intersection over union is achieved on the insulator test datasets with different environments and model parameters size being only 13.61 M. Compared with the current state-of-the-art semantic segmentation methods, the results show that the proposed method has higher efficient and accuracy.

1. Introduction

As an important part of transmission line, the integrity of insulator directly affects the safety and reliability of transmission line. According to statistics, the trip accident of the transmission lines due to insulator fault in Figure 1 accounts for 81.3% [1]. Since insulators are exposed to the natural environment for a long time, they will be affected inevitably by different climate and environmental factors, resulting in defects such as filthiness, corrosion, breakage, and so on, which threaten the safe operation of transmission lines. Therefore, it is necessary to inspect the insulators regularly to eliminate hidden dangers in time to ensure the stable operation of the entire transmission line.

In the early days, the regular inspection of transmission lines was carried out manually, and the insulators on the transmission lines were observed, inspected, and measured manually through eyes or telescopes. This inspection method requires personnel to have rich prior knowledge, which is inefficient and dangerous. In recent years, with the advancement of computer vision and Unmanned Aerial Vehicle (UAV) multimodal information fusion, UAV-based aerial solutions are widely used in the transmission line inspection [2]. Camera is the main way for UAV to perceive external information; technicians use the image information collected by UAV and image processing technology to complete the regular detection of insulators in transmission lines. However, as transmission lines are usually located in different natural environments, aerial images obtained by UAV camera have characteristics of complex background, multiple pseudotargets, and low signal-to-noise ratio, which make it difficult for image

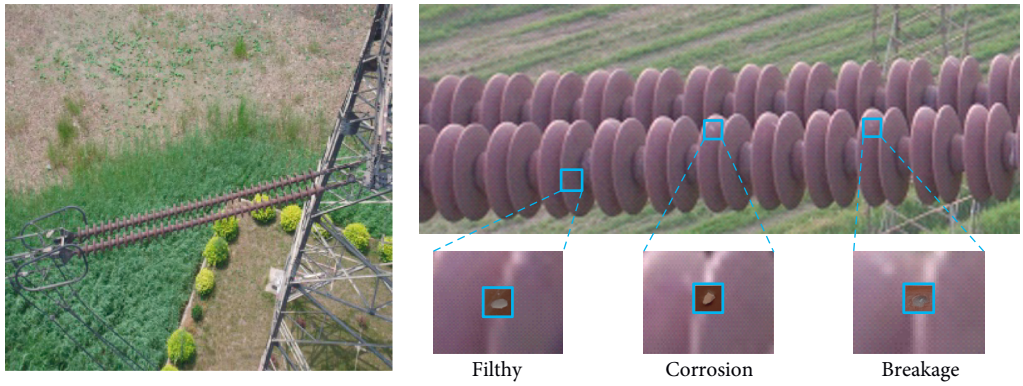

Figure 1: Insulator image. (a) Original aerial image. (b) Common insulator defects.

processing technology to identify insulators from aerial images [3].

In traditional image processing, artificial feature engineering is used to design and extract the feature information (e.g., color, texture, and edge) of the insulator to distinguish the insulator from the background in the aerial image [3]. Reddy et al. [4] first transformed the insulator image into the LAB color space and used the k-means clustering algorithm to fuse similar pixels in the image and then calculated the pixel intensity to draw a bounding box based on a preset threshold. The bounding box features are extracted as the input of the adaptive neurofuzzy inference system (ANFIS), and finally the ANFIS model is trained to detect insulators in the image. The disadvantage of this method is that the model relies on the bounding box generated by the clustering results, which is suitable for the segmentation of insulators with less background interference. Murthy et al. used Hough transform and support vector machines (SVM) to segment the insulators in aerial images and used multiresolution wavelet changes to extract the features of the extracted insulators and then used SVM to judge the state [5]. This method is suitable for aerial images where the background texture and intensity information are quite different from those of insulators. In [6], a method based on orientation angle detection and binary shape prior knowledge (OAD-BSPK) was proposed to realize the localization of insulators with different azimuths in complex aerial survey images. The algorithm first uses the binarization and multicascade morphological methods to obtain the edge of the insulator in the image to initially detect the possible azimuth of the insulator. For possible azimuths, binary shape priors are used to precisely locate the insulators in the image. However, this method needs to set a large number of thresholds to segment the insulators, and the thresholds for different environmental changes need to be reset, which greatly weakens the detection of insulators in the natural environment. In [7], a method was proposed to identify insulators in aerial images by fusing shape, color, and texture information. The line segments in different directions in different images are extracted; thus, the candidate regions are obtained by clustering according to the characteristics of the insulators. Moreover, the insulator regions are obtained based on the saliency features of the color and the prior knowledge model; the texture features are used to detect the insulator shedding defects. In [8], saliency detection was used to determine the position of insulators based on color and gradient features. Furthermore, adaptive morphological methods were used to detect insulator defects. This method is only suitable for the identification of glass insulators. Traditional image processing algorithms are limited to scenes with single background and fixed objects. Although all the above methods can solve some problems in object recognition, the design of artificial features requires more a priori knowledge and makes it difficult to be highly robust in natural environment image of insulators.

In recent years, with the development of deep learning, many models based on convolutional neural networks (CNN) have achieved excellent results in semantic segmentation tasks, such as FCN [9], SegNet [10], U-Net [11], and so on. Pixel-level segmentation can obtain targets in the image and the location of the targets precisely; these models have been widely used in the field of autonomous driving, industry, and embedded devices, solving problems in computer vision and promoting industrial automation. Compared with traditional methods, CNN can automatically extract features from images, which reduces the subjectivity of artificially designed features and provides more flexible solutions. It makes the insulator segmentation and identification process more robust to light, background, material, and other changes. At present, many researchers have studied semantic segmentation network models to perform pixel-level segmentation of insulator images. Gao et al. [12] used the two-stage target detection Faster-RCNN network to detect the insulators in the aerial images, input the detected insulators into the fully convolutional network (FCN) to complete the segmentation, and completed the defect detection of the insulators. But the network is divided into two convolutional neural networks: object detection and semantic segmentation. This method reduces the computational complexity of the semantic segmentation algorithm and improves the segmentation speed. Ling et al. [13] used the object detection network to identify insulators in aerial images and cropped the identified insulators from

the images, which were input into the U-Net semantic segmentation network to complete the detection of the insulator defects. The object detection would be unable to satisfy demands for the detection of small defects (e.g., flashover and corrosion). However, semantic segmentation is pixel-level detection, which would improve the accuracy of model detection. It was noted that Up-Net network is given to achieve semantic segmentation of insulator images in [14]. This method does not require an object detection network in advance and directly uses the semantic segmentation method to complete the identification and segmentation of insulators. Alahyari et al. [15] proposed a two-stage convolutional neural network model consisting of segmentation and classification units for fault classification of insulators. Aerial insulator images have the characteristics of complex backgrounds, many pseudotargets, and low signal-to-noise ratios, which bring difficulties for segment insulators. Semantic segmentation networks based on deep convolutional neural networks are general algorithms. Consequently, it is necessary to fine-tune the algorithm to improve its accurate and efficiency for the enhancement of insulator segmentation performance in complex background.

Since the premise of insulator fault detection is to accurately identify the insulator target in the image, it is radical to develop a better insulator identification algorithm. This paper focuses on the identification and segmentation of insulators in complex background, aiming to improve the identification efficiency and segmentation accuracy of insulators in aerial images. In this paper, an insulator semantic segmentation network is proposed, called ED-Net, which is constructed based on an end-to-end Encoder-Decoder structure, which realizes pixel-level segmentation of insulators. The network consists of two parts: Encoder path and Decoder path. In the Encoder path, Initial Module (IM) and CA-Bottleneck Module are proposed to extract the feature of the original image. The Coordinate Attention (CA) mechanism [16] and the depth-wise separable convolution are used in the CA-Bottleneck module to make the network pay more attention to the region of interest in the image and reduce the amount of model parameters and make the network more effective, respectively. The global average pooling layer (GP) is added in the tail of the Encoder path to retain the maximum receptive field. In the Decoder path, we proposed Asymmetric Convolution Module (ASM) and Refinement Boundary Module (RBM) to optimize the insulator boundary information. For reducing the diversity of features, the attention feature fusion module (AFFM) is proposed to fuse the features better in each stage.

Our contributions are summarized as follows:

(1) In the Encoder path, the proposed IM is used to quickly downsample the original image and then add coordinate attention mechanism in the original Bottleneck module, named CA-Bottleneck Module. The module is stacked in the Encoder path to enhance the feature extraction ability of the network. Ultimately, the GP is added at the end of the encoder path to retain the maximum receptive field.

(2) In the Decoder path, this paper introduces ASM and RBM modules for optimizing edge detail information of feature maps. AFFM is thus used to fuse high-level features and low-level features and reduce the diversity of them. In this case, the effectiveness of feature fusion can be ensured.

(3) The impressive results are achieved on the insulator dataset. More specifically, 95.18% mean IOU on the insulator test dataset and the parameter amount of the network of only 13.61 M are obtained.

The rest of this paper is organized as follows: Section 2 reviews the semantic segmentation network model and the work of attention mechanism. Section 3 introduces the proposed semantic segmentation network model based on the encoder-decoder structure and the details of each part of the network. Section 4 introduces the insulator segmentation dataset and discusses the impact of each module in the network model proposed in Section 3 on the overall segmentation accuracy. The experimental results of mainstream semantic segmentation models in the insulator test dataset are compared and analyzed. Section 5 provides the conclusions.

2. Related Work

In recent years, researchers have made a lot of progress on insulator defect detection and state classification. However, in most of these tasks, deep learning-based object detection algorithms are used to obtain the region of the insulator in the image and crop it into the region of interest. The segmentation method is used to obtain the segmentation map of the insulator in the region of interest (RoI), and finally the insulator defect detection is carried out. These algorithms usually require two CNN models, resulting in a large number of model parameters, which cannot be applied to devices with limited computing resources. With the development of semantic segmentation algorithms in deep learning, more and more semantic segmentation models can be used to solve the problems of complex backgrounds and many pseudotargets when segmenting insulator images and have achieved state-of-the-art performance. Most of the current insulator segmentation methods are based on FCN [9] variants or U-Net [11] variants to achieve high performance. However, these methods do not consider applying the CNN model to mobile devices. In semantic segmentation tasks, most networks are designed based on encoder-decoder structures, and to achieve a balance between network speed and accuracy, some methods will be used, such as depth-wise separable convolution and attention mechanisms.

2.1. Encoder-Decoder Structure. The encoder part inherent in the FCN [9] model encodes the feature of different scales. Naturally, some methods combine features of different scales to optimize the final prediction map. These methods mainly

consider the loss of target spatial information due to the decrease of spatial resolution caused by continuous pooling and convolution with stride equal to 2 and restore the resolution of the feature map by feature fusion. For example, SegNet [10] restores the resolution of the feature map by saving the index at the time of the maximum pooling operation to reduce the loss of image spatial information, U-Net [11] uses skip joins to fuse high-level semantic information with low-level spatial information to improve the result of the segmentation, GCN [17] uses a large convolution kernel to obtain a larger receptive field and extract more image context information when fusing the feature map in the encoding and decoding structure. However, spatial information lost during image downsampling is difficult to be restored by directly fusing feature maps of different scales [18].

2.2. Feature Fusion in Semantic Segmentation. Feature fusion is a common method in the semantic segmentation task, which is used to fuse feature images extracted at different stages. In DeepLab series [19–22], ASPP modules are proposed to extract multiscale features with different dilation rates and combine them to process targets of different scales. The pyramid pooling module in PSPNet [23] achieves the goal of coding different scales through the feature map of different stages. ParseNet [24] adds global pooling branches to extract multiscale feature.

2.3. Context Information. Semantic segmentation requires more image context information to generate more accurate segmentation results. Recently, most methods use the fusion of different scale feature maps or large receptive fields to obtain the context information of the image. DeepLab v2/v3 uses hole convolution with different dilation rates in parallel to extract multiscale context information from the feature map extracted from the backbone network. It is proposed that ASPP module can change the receptive field of convolution kernel by controlling the dilation rate so as to capture richer multiscale features. PSPNet [23] proposed a PSP module using multiscale pooling to captures multiscale information. However, atrous convolution will lose the continuity of image information while increasing the receptive field, which is not conducive to the pixel-level dense prediction task [25].

2.4. Attention Mechanism. The attention module can make the model pay more attention to the region of interest. Attention mechanism is a powerful tool for depth convolution neural network [26]. At present, the most popular attention mechanism is the SE Attention proposed by SENet [27]. It calculates channel attention through 2D global pooling, providing significant performance improvements at a relatively low computational cost. However, the SE module only considers the encoding of information between channels and ignores the importance of location information, which is crucial for semantic segmentation. CBAM [28] combines the spatial attention module and the channel attention module to refine the extracted features and improve the expressive force of the model.

3. Methodology

In daily inspections, UAV can collect hundreds of thousands of aerial images. The network should have less complexity and less parameters while ensuring the segmentation accuracy. Traditional convolutional neural networks (e.g., GoogLeNet [29] and ResNet [30]) have a large number of network model parameters and high computational complexity, making it difficult to run on mobile devices (e.g., UAV). Aiming at the characteristics of the complex background of aerial images, the traditional CNNs is complicated calculation, and the number of model parameters is large. In this section, an alternative network is proposed to solve the above problems, called ED-Net; Figure 2(a) shows the overall framework of the network. The network achieves a balance between the amounts of parameters and the segmentation accuracy. Then, the details of components in these two paths are described. Finally, how we fuse features of different scales in the decoder path and restore the image resolution to obtain the final prediction result is demonstrated.

3.1. Encoder Path. For the insulator semantic segmentation task, ensuring a large receptive field is crucial for the final semantic segmentation result. Since the insulator is only in a small part of the aerial image and the pseudotarget in the background will interfere with the segmentation of the insulator, it is necessary to retain the largest receptive field to ensure the accuracy of insulator segmentation from a global perspective. At present, the mainstream methods of expanding the receptive field use the pyramid pooling module, Atrous Spatial Pyramid Pooling [20], or large kernel [17]. In this paper, attention mechanism and depth-wise separable convolution are introduced in the encoder stage to reduce the number of model parameters and expand the receptive field so that it can obtain more image context information. The encoder path consists of five stages, one of which is the initial module, and the other four stages are modules with the same structure. The details of Encoder path are shown in Figure 3, including IM, CA module, and CA-Bottleneck module. The initial module consists of two branches. One branch uses the depth-wise separable convolution of 3×3 and stride equal to 2 to downsample the original image; the other is divided into max-pooling to downsample the original image and finally fuse and input to the next stage in Figure 3(a). The next four stages consist of stacking different numbers of CA-Bottleneck modules, and only the first CA-Bottleneck module in each stage uses 1×1 conv for input-output feature map scale matching. The rest of the CA-Bottleneck modules have the same structure, as shown in Figure 3(c). It consists of the following four parts: (1) 1×1 convolution layer for dimension decline. (2) Depth-wise separable convolution is used to extract its features. The significance of depth-wise separable convolution layer is to reduce the amount of model parameters. (3) Adding

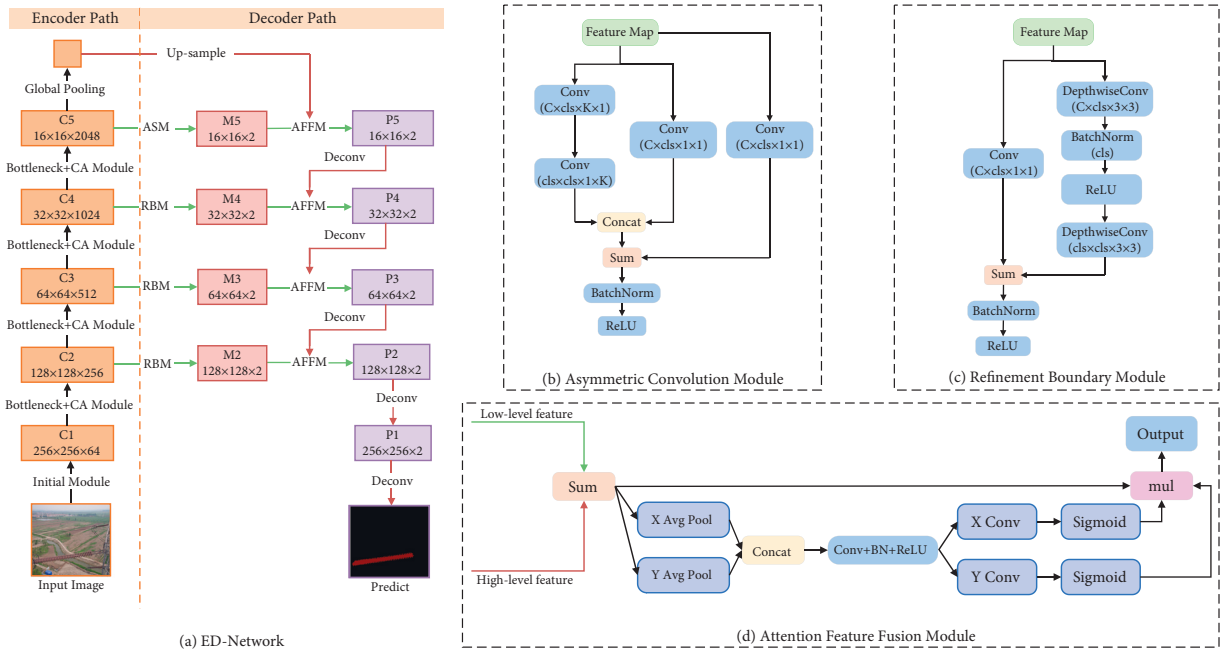

FIGURE 2: Overview of proposed ED-Net architecture (a). It consists of two parts: Encoder path and Decoder path. The feature maps of C1, C2, C3, C4, and C5 are obtained by the Initial Module (IM) and Bottleneck + CA Module. M2, M3, M4, and M5 are the feature maps of the encoder path obtained through Asymmetric Convolution Module (ASM) or Refinement Boundary Module (RBM). P1–P5 are obtained by the Attention Feature Fusion Module (AFFM), and P1 is used for insulator segmentation. The details of ASM, RBM, and AFFM are illustrated in (b), (c), and (d), respectively. The red and black lines represent the upsample and downsample operations, respectively. The green line does not change the size of the feature map, only the number of channels.

Coordinate Attention Mechanism and residual connection to weight the feature map to make the model pay more attention to the region of interest. (4) 1×1 convolution layer is used to improve the dimension and fuse with the input feature map to obtain the final output. The Batch Normalization [31] and ReLU are placed in the between of whole convolution operation.

3.2. Decoder Path. In the semantic segmentation task, the final segmentation result of the network is determined by the quality of feature fusion, since the features at different stages have different recognition capabilities. In the shallow stage of the encoder path, the network pays more attention to some low-level features, such as point, line, or edge information. At this time, the feature map has a large resolution, so it contains a lot of spatial information. However, in the high-level stage of the encoder, the features extracted from the network contain more semantic information, but the resolution of the feature map is low at this time, and the spatial information of the image is lost. Therefore, the Decoder path proposed in this paper integrates the high-level semantic information extracted from the network into the low-level features so as to better combine the semantic information and spatial information, thus improving the segmentation result of the network.

In this paper, RBM is proposed to optimize edge details of feature maps. The module is a residual structure composed of depth-wise separable convolution, Batch normalization, and nonlinear activation function, as shown in Figure 2(c). It is worth noting that only the feature maps from stage 2 to stage 4 of the Encoder path need to go through RBM. Second, inspired by the structure of InceptionV3, on $m \times m$ feature maps, where m ranges between 12 and 20, using asymmetric convolutions can improve the classification performance of the network [32]. Therefore, this paper proposes ASM for the feature map of stage 5 output in the Encoder path, as shown in Figure 2(b). ASM uses asymmetric convolution. Compared with the traditional 3×3 convolution, it requires less resource consumption and parameter amount, which is more effective for large kernel sizes. Finally, due to the difference between low-level features and high-level features, these features cannot be simply added together. In the early stage of the network, the network encodes rich spatial information, and in the later stage of the network, it mainly encodes the context information of the image. In other words, the feature map output at the early stage of the network is of low level, and the feature map output at the later stage of the network is of high level. Therefore, the AFFM is proposed to fuse low-level and high-level features in Figure 2(d). This module first sums low-dimensional and high-dimensional features for different levels of features. Next, average pooling is performed on the x-direction and y-direction of the feature map, respectively. After concatenating the feature map, convolution, Batch normalization and ReLU are used to balance the feature map scale. Finally, the weight vectors in the x-direction and y-direction are obtained through the sigmoid activation function, respectively, and the original feature map is reweighted. This module uses high-level semantic

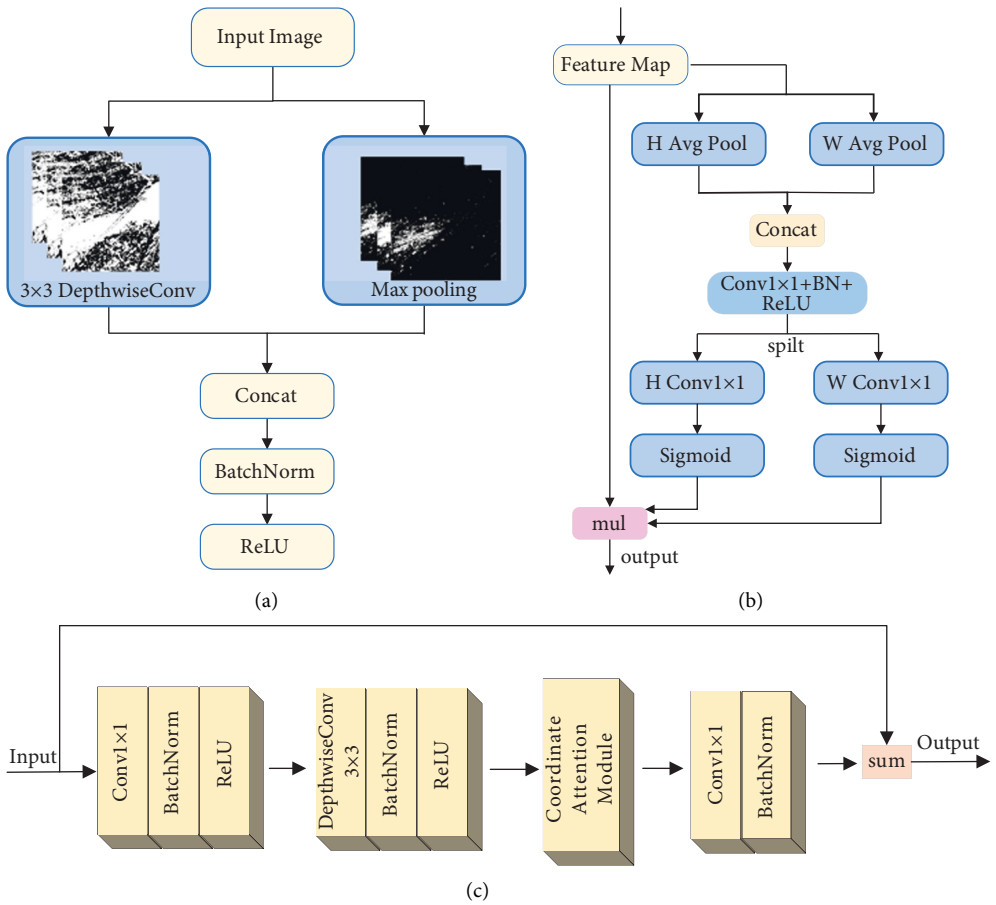

Figure 3: Encoder path components. (a) Components of the Initial Module. (b) Coordinate Attention Module. (c) Overall composition of CA-Bottleneck Module.

features to guide low-level detail features and refines feature maps so as to obtain improved segmentation result.

The proposed Encoder-Decoder Path Network did not use bias terms in any of the projections in order to reduce the number of kernel and overall memory operations, as cuDNN [33] uses separate kernels for convolution and bias addition. This choice did not have any impact on the accuracy. It is noted that each convolution operation make network better for gradient return accompanied by normalization and activation function, reducing the phenomenon of gradient disappearance and gradient explosion.

3.3. Network Architecture. With the Encoder path and Decoder path, a semantic segmentation network based on Encoder-Decoder structure is proposed to segment insulator images, called ED-Net. The overall flow of the network in this paper is shown in Figure 4. The multiscale feature map that is extracted from different stages of the Encoder path is used in the decoder path to generate finally predicted result.

In the Encoder path, the IM and stacked CA-Bottleneck module are used as the backbone network. CA-Bottleneck module adds coordinate attention mechanism with depth-wise separable convolution. The coordinate attention mechanism is effectively applied to semantic segmentation tasks, which enables the convolutional kernel to capture channel, direction, and position information and enables the model to locate the target more accurately. Depth-wise separable convolution is used to reduce the number of model parameters and improve the efficiency of model calculation. Then, the GP is added in the tail of backbone network to get the strongest consistency feature.

In the Decoder path, the output feature maps of Encoder path C2 to C4 are passed through RBM module, and the output of C5 is passed through ASM module to further enhance the consistency of feature. The feature maps of GP are $2\times$ upsampling and the feature maps of C5 are fused by AFFM. The fused feature map is deconvolved and the output feature map of the previous stage of RBM is fused by AFFM. Through this operation, high-level features and low-level features are fused together to reduce the gap between feature maps so that feature maps contain rich semantic information and spatial information. Finally, the image size is restored through deconvolution to achieve end-to-end training of the network. It is worth noting that the attention mechanism is only performed on the current feature map in the last AFFM.

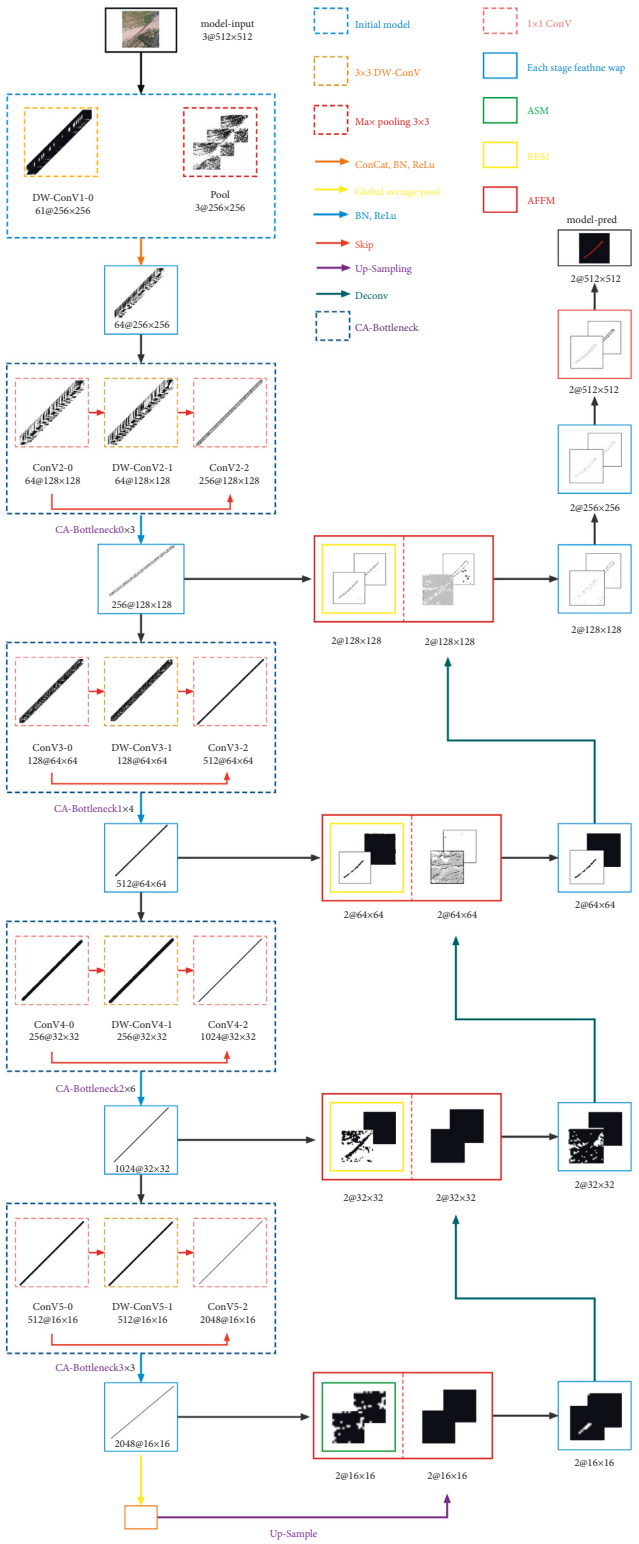

FIGURE 4: Inference process of the Encoder-Decoder Network.

4. Experiment Results

In this section, the proposed ED-Net network model is evaluated to verify the segmentation effect of the model on insulators in different environments. Firstly, the insulator dataset, implementation, and evaluation metrics used in the experiments are introduced. Then, the impact of each module in the proposed method on the overall model is analyzed. Next, the amounts of parameters, GFLOPs of the network, and the results that are generated by our algorithm on the insulator test dataset are shown, respectively. Finally, comparison with the current mainstream semantic segmentation models is carried out.

4.1. Insulator Dataset and Implementation

4.1.1. Insulator Dataset. Figure 5 shows the acquisition equipment of the aerial insulator image data used in this paper. The data acquisition system is composed of a FC300S camera of CASIO and a DJI Phantom 3 advanced UAV. The camera captures insulator images of transmission lines located in different environments, and the captured images are used as the insulator dataset in this paper. The insulator dataset used in this paper contains 100 training images and 20 testing images, which are resized to 512×512. Examples of train sample and label data are shown in Figure 6. The images contain 2 semantic categories, namely, insulator and background.

4.1.2. Training details. During the training time, a batch size of 16 is applied. The standard Adaptive Moment Estimation (Adam) optimizer is used to update the model weight parameters, where β_1 and β_2 are set to 0.9 and 0.99, respectively, weight decay $1e^{-3}$, initial learning rate $1e^{-4}$, and the learn rate is multiplied by 0.1 for every 40 iterations. All experiments are implemented in Python and trained using the PyTorch deep learning framework. All the experiments have been conducted on a Nvidia GeForce GTX 3090 GPU under Ubuntu 16.04.

4.1.3. Evaluation Metrics. In order to better understand the results of the insulator semantic segmentation network, this paper summarizes the different evaluation metrics [9] as follows:

(i) Pixel Accuracy: $(\sum_i n_{ii}/(\sum_i \sum_i n_{ij}))$

(ii) Class Accuracy: $((\sum_i n_{ii} + \sum_j n_{jj})/(\sum_i n_{ij} + \sum_j n_{ji} + \sum_i n_{ii} + \sum_j n_{jj}))$

(iii) Mean Intersection over Union (mean IOU): $(1/n_c(\sum_i n_{ii}/(\sum_i n_{ij} + \sum_j n_{ji} - n_{ii})))$

(iv) Frequency weighted Intersection over Union (f.w. IOU): $((1/\sum_i \sum_j n_{ij}) \sum_i n_{ii}/(\sum_i n_{ij} + \sum_j n_{ji} - n_{ii}))$

where n_c represents the number of categories in the dataset, n_{ii} represents the number of pixels whose real pixel class is i predicted to belong to class i, n_{ji} represents the number of pixels whose real category j predicted to belong to class i, and n_{ij} represents the number of pixels whose real category is i predicted to belong to class j.

In the following sections, a series of ablation experiments is to evaluate the effectiveness of proposed method. Then, the full results on Insulator test dataset are reported.

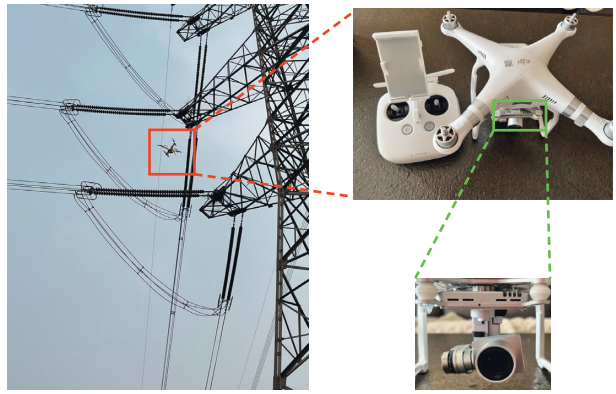

Figure 5: Data acquisition system.

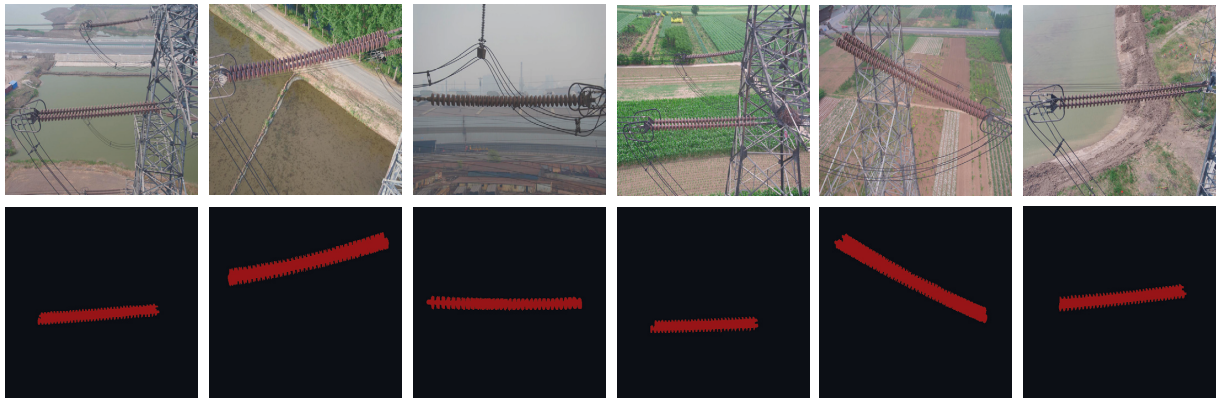

Figure 6: Example of train sample and label data.

4.2. Ablation Study. In this section, the proposed method is broken down step by step to reveal the effect produced by each module. The effectiveness of our method on the insulator dataset is verified using the Base Model as the base network.

Base Model. ResNet-50 is used as the feature extraction module of the Base Model, which is the Encoder Path. The Decoder Path directly deconvolution and fuses the feature maps to obtain the final prediction result, as shown in Figure 7. The Conv-1 in the Base Model uses the convolution of kernel size equal to 7, stride equal to 2 to downsample the image, and then stacks different numbers of Bottlenecks Module to obtain feature maps Res-2, Res-3, Res-4m and Res-5. The pooling operation is not used in the network, and the convolution with stride equal to 2 is used for downsampling instead. Considering the amounts of parameter in the network, all 3×3 convolution operations in the network are replaced by depth-wise separable convolutions. The depth-wise separable convolution can greatly reduce the amount of network parameters, reducing the complexity of the model and making it possible to run on devices with limited computing resources, as shown in Table 1. The output feature map of each stage first needs to go through the Trans Module (composed of 1×1 convolution), and after reducing the number of channels, deconvolution is performed and the feature map of the previous stage is fused. It is worth noting that the Conv-1 feature map does not participate in the fusion. After obtaining the P2 feature map, the image size is restored by two deconvolutions to obtain the final prediction result. The network prediction results are shown in the second column of Figure 8.

CA-Bottleneck Module. The Encoder part of the ED-Net proposed in this paper uses the CA-Bottleneck module for stacking, and adding an attention mechanism to the Bottleneck makes the network better focus on the global information of the image. The key parameter reduction ratio γ is gradually increased, but the performance of the model decreases when γ is increased to 512, as shown in Table 2. This shows that choosing a suitable reduction ratio γ in the early stage of the model is crucial to improve the performance of the model. Note that only multiples of two are used in the experiments because there is a twofold relationship between feature map size reduction and channel count improvement. In particular, when γ equals to 2, the model outperforms the Base Model by 6.05%. In the Base Model, the size of the feature map at each stage needs to be reduced by 1/2, and the number of corresponding channels needs to be doubled. According to this idea, the corresponding reduction ratio γ in the CA module of Res-3, Res-4, and Res-5 should also be reduced by two times to increase the number of channels. Using the CA-Bottleneck

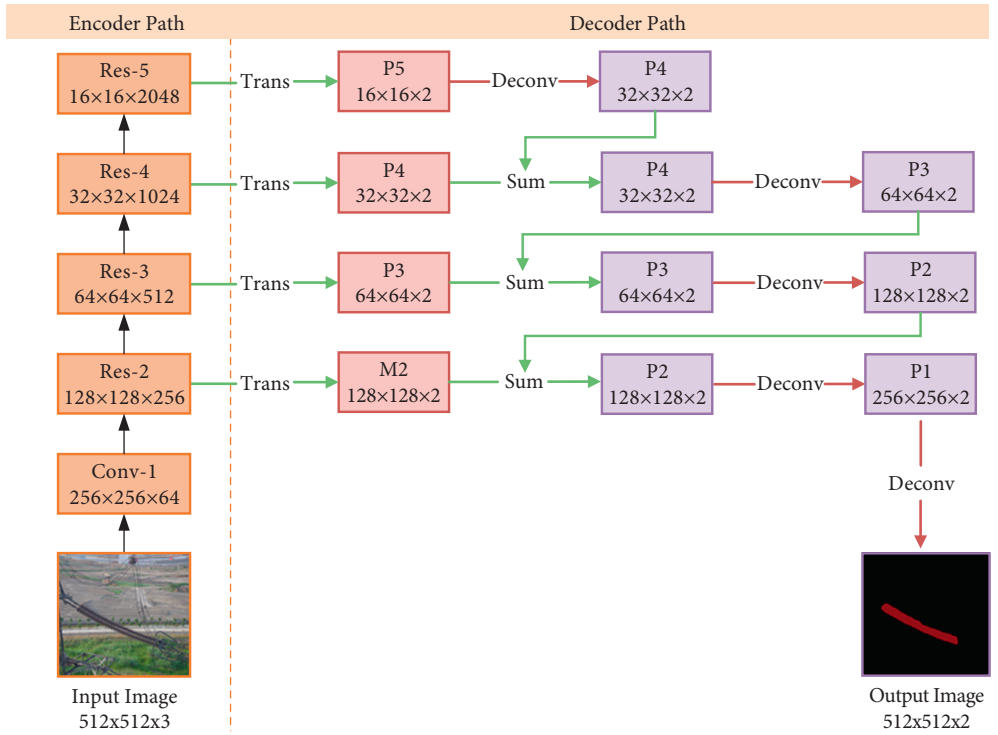

Figure 7: Base Model. Trans is to use 1 ∗ 1 convolution to change the number of channels. Sum is the addition of the corresponding elements of the feature map. Deconv uses the deconvolution of kernel size equal to 4, stride equal to 2, and padding equal to 2 to expand the feature map size.

Table 1: Accuracy and parameter analysis of Base Model on the insulator dataset. ResNet-50 and depth-wise separable convolution (DW)—ResNet-50 refers to the replacement of all 3×3 convolution in the network with depth-wise separable convolutions. GFLOPs estimated model complexity for $3 \times 512 \times 512$ input image.

	Parameter (M)	GFLOPs	mIOU (%)
Base	25.56	21.71	72.57
DW-base	13.48	13.18	72.50

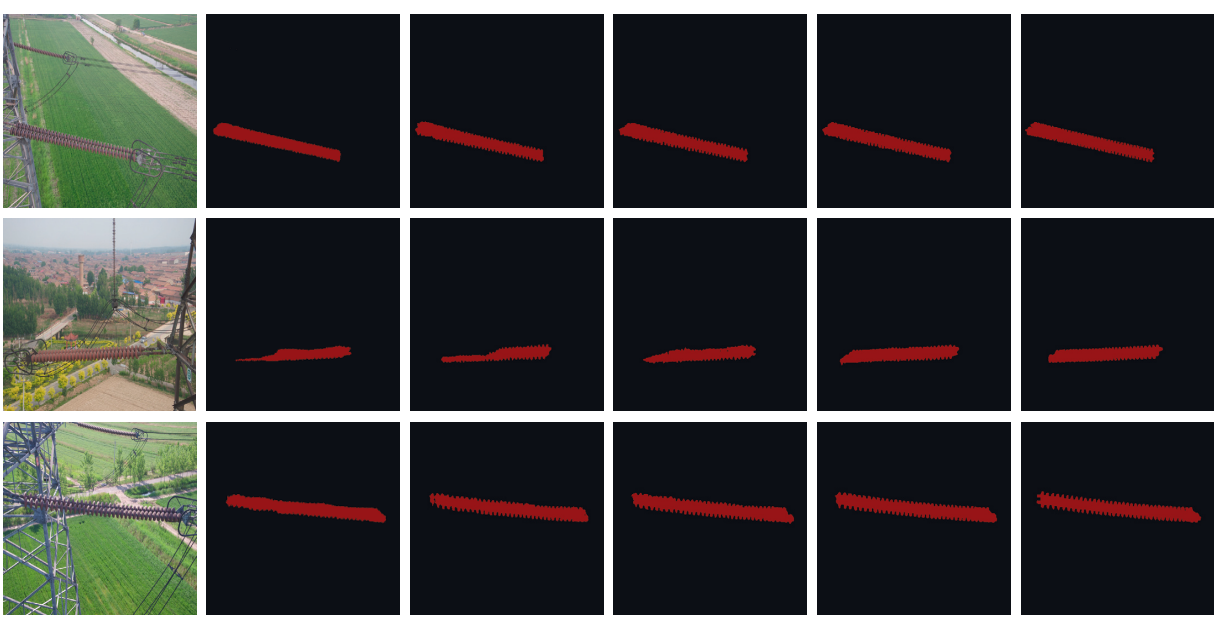

Figure 8: Examples of semantic segmentation results on insulator test dataset. (a) Original input image; (b) the predicted image of Base Module; (c) the predicted image of the former combined with CAM; (d) the predicted image of the former combined with RBM; (e) the predicted image of the former combined with AFFM; and (f) Ground truth.

Table 2: Experimental results of setting different reduction ratios γ using the CA-Bottleneck module in Res-2. The score is evaluated by standard mean IOU (%) on insulator test dataset.

γ	Base	8	16	32	64	128	256	512
mIOU	72.50	73.91	74.88	75.14	75.58	76.89	78.55	77.65

module in ResNet-50, the model mIOU = 81.08%. After adding CA Module, the network prediction results are shown in the third column of Figure 8.

Initial Module. As described in Section 3, the module is proposed which consists of depth-wise separable convolution and max-pooling to reduce model parameters and spatial information loss. The module subjects the input image to 3×3 depth-wise separable convolution with stride equal to 2 and overlapping max-pooling, respectively. The two outputs are concatenated in the channel dimension through Batch Normalization and ReLU. This module replaces the convolution of kernel size equal to 7, and the network performance is improved from 81.08% to 82.29%, as shown in Table 3.

4.2.1. Global average Pooling. The layer is used to make the Encoder path provide a larger receptive field. Although the original ResNet-50 network can theoretically cover most of the input image, it is necessary to use GP to further expand the receptive field. In this paper, the GP is added to the tail of the Encoder Path, then the output upsampling of the GP is fused with the feature map of Res-5 in the Encoder path in an additive manner. Model performance ranges from 82.29% to 83.93%, validating the effectiveness of GP, as shown in Table 3.

4.2.2. Refinement Boundary Module. To further improve the performance of the network, the RBM is designed in the Decoder Path. This module contains convolution, Batch normalization, and ReLU unit. Compared with Trans Module, RBM improves the model ability to optimize the target boundary, as shown in Table 3. After adding RBM, the network results are shown in the fourth column of Figure 8.

4.2.3. Asymmetric Convolution Module. Based on the RBM in the Decoder Path, the ASM is proposed to be applied in the stage with the smallest feature map size. ASM uses large convolution kernels to densely connect feature maps. The model performance ranges from 88.51% to 89.57%, which verifies the improvement of the overall performance of the model by ASM, as shown in Table 3.

4.2.4. Attention Feature Fusion Module. Considering the different levels of feature maps generated in different stages of the network, the low-level features generated when the network is shallow, and the high-level features generated by the deep network, the AFFM is proposed to effectively fuse these features. The evaluation of the results that is generated by summing these features directly and proposed AFFM is shown in Table 3. The network prediction results after using AFFM are shown in the fifth column of Figure 8.

Table 3: Detailed performance comparison of each component in our proposed ED-Net.

Module	mIOU (%)
CAM	81.08
CAM + IM	82.29
CAM + IM + GP	83.95
CAM + IM + GP + RBM	88.51
CAM + IM + GP + RBM (ASM)	89.57
CAM + IM + GP + RBM (ASM) + AFFM	95.12

Table 4: Parameter comparison of our method against other state-of-the-art methods on the Insulator test dataset. GFLOPs are estimated for input of $3 \times 512 \times 512$.

Model	Backbone	GFLOPs	Parameters (M)
FCN-8s	VGG16	80.63	20.1
SegNet	VGG16	286.0	29.43
U-Net	\	184.64	34.53
DeepLabV3	Xception	57.06	29.4
GCN	ResNet152	67.96	58.38
Ours	CA-Bottleneck	12.62	13.61

4.3. Comparison of Different Semantic Segmentation Algorithm. In this section, the complexity and parameter quantity of the model in this paper are firstly analyzed, and a comparative analysis is made with the current mainstream semantic segmentation networks, as shown in Table 4. Secondly, the segmentation results of the proposed algorithm and the mainstream algorithm in the insulator test set are compared, as shown in Table 5. Finally, some visual examples of the method in this paper and the mainstream semantic segmentation models are also given, as shown in Figure 9.

As shown in Table 4, the comparison between our proposed method and other methods between GFLOPs and parameter quantities is shown. GFLOPs represent the complexity of the model, and the amounts of parameter represents the number of operations when processing the image. In this paper, the unified input image resolution is 512×512. Table 5 shows the accuracy and speed comparison between the different methods in the insulator test dataset. Figure 10 shows the ROC curves generated by ED-Net and mainstream semantic segmentation models on the insulator test dataset. Compared with other mainstream

Table 5: Experimental results of our method against other state-of-the-art methods on the Insulator test dataset comparison of our method against other state-of-the-art methods on the Insulator test dataset.

Model	Pixel Acc	Class Acc	mIOU	f.w. IOU	Time (ms)
FCN-8s	98.85	88.50	86.66	97.75	157
SegNet	99.07	93.01	89.64	98.22	167
U-Net	99.20	93.28	90.67	98.46	181
DeepLabV3	98.90	91.10	87.40	97.89	176
GCN	99.06	92.11	89.07	98.18	348
Ours	99.61	97.44	95.12	99.24	67

Figure 9: In the insulator test dataset, the ROC curves are generated by ED-Net and mainstream segmentation models.

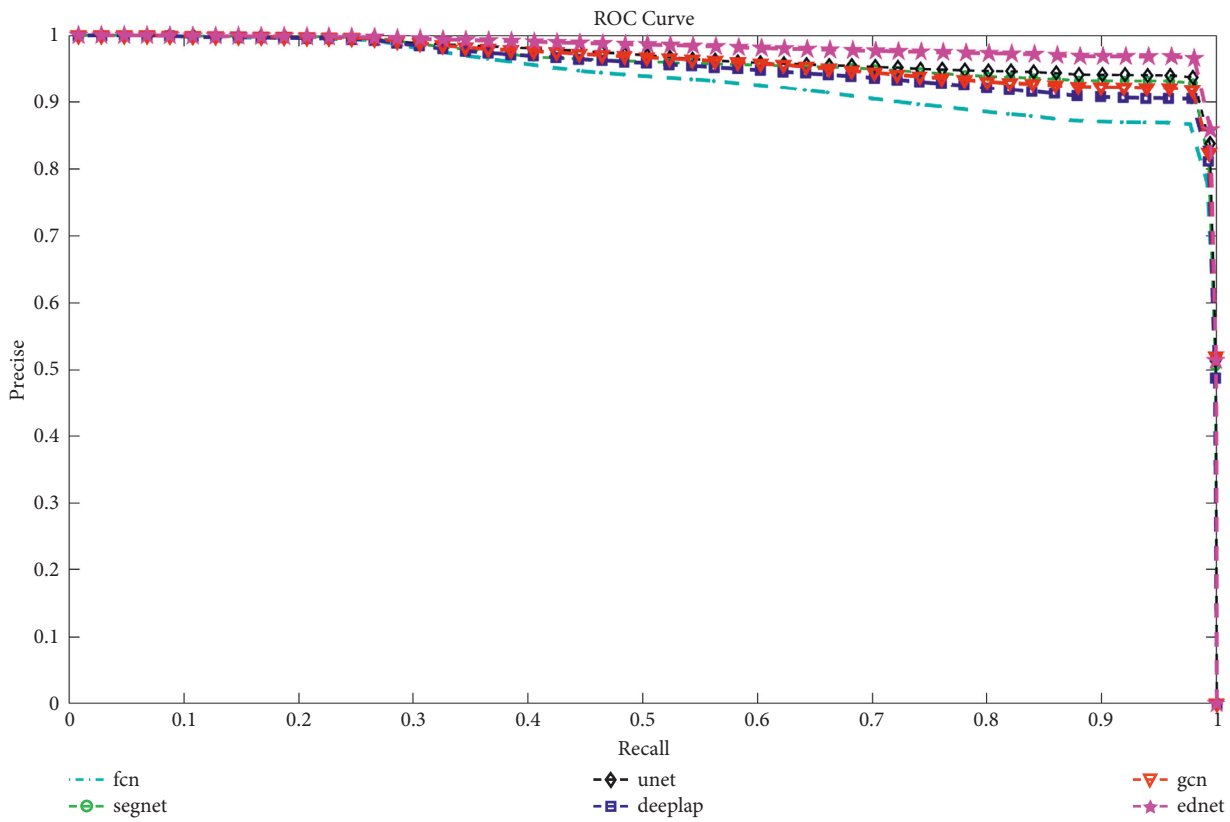

Figure 10: Semantic segmentation results of our method and other state-of-the-art methods on the insulator test set. The figure is the original image and the prediction results of each algorithm. From top to bottom are the original image, Ground Truth, FCN-8s, SegNet-VGG16, U-Net, DeepLabV3+, and GCN-ResNet152 and the last row is the prediction result of the network in this paper. The yellow box shows the details of the segmentation.

semantic segmentation models, our method has achieved great progress in both speed and accuracy.

Figure 9 shows the segmentation results of the proposed segmentation method and other state-of-the-art segmentation methods on the insulator test dataset. This set of images is representative because these images include insulators that are in different shapes, viewing angle, environments, and so on. As shown in Figure 9, semantic segmentation results of insulators can be achieved in most networks, but misclassification and missing segmentation will occur when there is too much background and insulator interference, such as the fourth and sixth images. The robustness of the proposed method is proved.

5. Conclusion

In this paper, an insulator semantic segmentation network is designed to achieve accurate and efficient segmentation insulators in different environments, which is based on Encoder-Decoder structure, called ED-Net. The network architecture consists of two paths: Encoder path and Decoder path. In the Encoder path, in order to improve the feature extraction ability of encoder, the CA Module is added into original Bottleneck to make the network focus on the insulator region. The amount of model parameters is reduced by initial module and depth-wise separable convolution to improve the efficiency of feature extraction. Moreover, GP is used to achieve more semantic information. In the Decoder Path, the RBM optimizes the edge details of the feature map generated by Encoder path. ASM uses large kernel size to obtain rich contexture information and reduce the number of parameters. Attention feature fusion model are proposed to reduce the difference between high-level features and low-level features and improve the accuracy of the model. For aerial images under different environments and lighting conditions, 95.12% mean IOU is obtained in the insulator test dataset and the amount of model parameters is only 13.61 M. In the future work, the insulator dataset needs to be further extended to ensure that the model can obtain accurate insulators in more complex environments. In addition, we will pay more attention to lightweight convolution neural network to obtain real-time segmentation results.

Data Availability

The data used to support the findings of the study are available from the corresponding author upon request.

Conflicts of Interest

The authors declare that they have no conflicts of interest regarding the publication of this paper.

Acknowledgments

This work was supported by the National Natural Science Foundation of China (Grant no. 62063011) and partially supported by Yunnan Fundamental Research Project (Grant no. 202001AV070001).

References

[1] W. Tong, J. Yuan, and B. Li, "Application of image processing in patrol inspection of overhead transmission line by helicopter," *Power System Technology*, vol. 34, no. 12, pp. 204–208, 2010.

[2] G. Qiang, Y. Wu, and L. Qian, "Research on deep belief network layer tendency and its application into identifying fault images of aerial images," *Chinese Journal of Scientific Instrument*, vol. 36, no. 6, pp. 1267–1274, 2015.

[3] W. Chang, G. Yang, J. Yu, and Z. Liang, "Real-time segmentation of various insulators using generative adversarial networks," *IET Computer Vision*, vol. 12, no. 5, pp. 596–602, 2018.

[4] M. J. B. Reddy, B. K. Chandra, and D. K. Mohanta, "A DOST based approach for the condition monitoring of 11 kV distribution line insulators," *IEEE Transactions on Dielectrics and Electrical Insulation*, vol. 18, no. 2, pp. 588–595, 2011.

[5] V. Murthy, K. Tarakanath, D. Mohanta, and S. Gupta, "Insulator condition analysis for overhead distribution lines using combined wavelet support vector machine (SVM)," *IEEE Transactions on Dielectrics and Electrical Insulation*, vol. 17, no. 1, pp. 89–99, 2010.

[6] Z. Zhao, N. Liu, and L. Wang, "Localization of multiple insulators by orientation angle detection and binary shape prior knowledge," *IEEE Transactions on Dielectrics and Electrical Insulation*, vol. 22, no. 6, pp. 3421–3428, 2015.

[7] W. Wang, Y. Wang, J. Han, and Y. Liu, "Recognition and drop-off detection of insulator based on aerial image," in *Proceedings of the International Symposium on Computational Intelligence and Design (ISCID)*, vol. 1, pp. 162–167, Hangzhou, China, December 2016.

[8] Y. Zhai, D. Wang, M. Zhang, J. Wang, and F. Guo, "Fault detection of insulator based on saliency and adaptive morphology," *Multimedia Tools and Applications*, vol. 76, no. 9, Article ID 12051, 2017.

[9] J. Long, E. Shelhamer, and T. Darrell, "Fully convolutional networks for semantic segmentation," *IEEE conference on computer vision and pattern recognition*, vol. 39, pp. 3431–3440, 2015.

[10] V. Badrinarayanan, A. Kendall, and R. Cipolla, "SegNet: a deep convolutional encoder-decoder architecture for image segmentation," *IEEE Transactions on Pattern Analysis and Machine Intelligence*, vol. 39, no. 12, pp. 2481–2495, 2017.

[11] O. Ronneberger, P. Fischer, and T. Brox, "U-net: convolutional networks for biomedical image segmentation," in *International Conference on Medical Image Computing and Computer-Assisted Intervention*, Springer, Cham, Switzerland, Europe, 2015.

[12] F. Gao, J. Wang, Z. Kong et al., "Recognition of Insulator Explosion Based on Deep learning," in *Proceedings of the International Computer Conference on Wavelet Active Media Technology and Information Processing (ICCWAMTIP)*, pp. 79–82, Chengdu, China, December 2017.

[13] Z. Ling, R. C. Qiu, Z. Jin et al., "An accurate and real-time self-blast glass insulator location method based on faster R-CNN and U-net with aerial images," 2018, https://arxiv.org/abs/1801.05143.

[14] C. Sampedro, J. Rodriguez-Vazquez, A. Rodriguez-Ramos, and A. P. Carrio, "Deep learning-based system for automatic recognition and diagnosis of electrical insulator strings," *IEEE Access*, vol. 7, Article ID 101283, 2019.

[15] A. Alahyari, A. Hinneck, R. Tariverdizadeh, and P. David, "Segmentation and defect classification of the power line insulators: a deep learning-based approach," *International Conference on Smart Grids and Energy Systems (SGES)*, pp. 476–481, Perth, Australia, 2020.

[16] Q. Hou, D. Zhou, and J. Feng, "Coordinate attention for efficient mobile network design," in *Proceedings of the IEEE/CVF Conference on Computer Vision and Pattern Recognition*, Article ID 13713, Nashville, TN, USA, June 2021.

[17] C. Peng, X. Zhang, G. Yu, and J. Sun, "Large kernel matters--improve semantic segmentation by global convolutional network," in *Proceedings of the IEEE conference on computer vision and pattern recognition*, pp. 4353–4361, Honolulu, HI, USA, July 2017.

[18] C. Wei, Y. Zhao, Y. Zheng, L. Xie, and K. M. Smedley, "Analysis and design of a non-isolated high step-down converter with coupled inductor and ZVS operation," *IEEE Transactions on Industrial Electronics*, vol. 69, pp. 9007–9018, 2021.

[19] L. C. Chen, G. Papandreou, I. Kokkinos, M. Kevin, and L. Y. Alan, "Semantic Image Segmentation with Deep Convolutional Nets and Fully Connected CRFs," 2014, https://arxiv.org/abs/1412.7062.

[20] L.-C. Chen, G. Papandreou, I. Kokkinos, K. Murphy, and A. L. Yuille, "DeepLab: semantic image segmentation with deep convolutional nets, atrous convolution, and fully connected CRFs," *IEEE Transactions on Pattern Analysis and Machine Intelligence*, vol. 40, no. 4, pp. 834–848, 2018.

[21] L. C. Chen, G. Papandreou, F. Schroff, and A. Hartwig, "Rethinking atrous convolution for semantic image segmentation," 2017, https://arxiv.org/abs/1706.05587.

[22] L. C. Chen, Y. Zhu, G. Papandreou, F. Schroff, and A. Hartwig, "Encoder-decoder with atrous separable convolution for semantic image segmentation," *Proceedings of the European conference on computer vision (ECCV)*, Springer, Cham, Switzerland, Europe, 2018.

[23] H. Zhao, J. Shi, X. Qi, X. Wang, and J. Jia, "Pyramid scene parsing network," in *Proceedings of the IEEE conference on computer vision and pattern recognition*, pp. 2881–2890, Honolulu, HI, USA, July 2017.

[24] W. Liu, A. Rabinovich, and A. C. Berg, "Parsenet: Looking wider to see better," 2015, https://arxiv.org/abs/1506.04579.

[25] D. Xiao, H. Chen, C. Wei, and B. Xiaoqing, "Statistical measure for risk-seeking stochastic wind power offering strategies in electricity markets," *Journal of Modern Power Systems and Clean Energy*, pp. 1–6, 2021.

[26] Z. Niu, G. Zhong, and H. Yu, "A review on the attention mechanism of deep learning," *Neurocomputing*, vol. 452, pp. 48–62, 2021.

[27] J. Hu, L. Shen, and G. Sun, "Squeeze-and-excitation networks," in *Proceedings of the IEEE conference on computer vision and pattern recognition*, pp. 7132–7141, Salt Lake City, UT, USA, June 2018.

[28] S. Woo, J. Park, J.-Y. Lee, and I. S. Kweon, "Cbam: convolutional block attention module," *Proceedings of the European conference on computer vision (ECCV)*, Springer, Cham, Switzerland, Europe, 2018.

[29] C. Szegedy, W. Liu, Y. Jia, P. Sermanet, S. Reed, and D. Anguelov, "Going deeper with convolutions," in *Proceedings of the IEEE conference on computer vision and pattern recognition*, pp. 1–9, Boston, MA, USA, June 2015.

[30] K. He, X. Zhang, S. Ren, and J. Sun, "Deep residual learning for image recognition," in *Proceedings of the IEEE conference on computer vision and pattern recognition*, pp. 770–778, Las Vegas, NV, USA, June 2016.

[31] S. Ioffe and C. Szegedy, "Batch normalization: accelerating deep network training by reducing internal covariate shift," pp. 448–456, 2015, https://arxiv.org/pdf/1502.03167.pdf.

[32] C. Szegedy, V. Vanhoucke, S. Ioffe, J. Shlens, and Z. Wojna, "Rethinking the inception architecture for computer vision," *Proceedings of the IEEE conference on computer vision and pattern recognition*, pp. 2818–2826, Las Vegas, NV, USA, June 2016.

[33] S. Chetlur, C. Woolley, P. Vandermersch et al., "Cudnn: Efficient Primitives for Deep learning," 2014, https://arxiv.org/abs/1410.0759.

Hindawi
Complexity
Volume 2022, Article ID 3304796, 21 pages
https://doi.org/10.1155/2022/3304796

Review Article

Advancements and Future Prospects of Electric Vehicle Technologies: A Comprehensive Review

M. S. Hossain,[1,2] **Laveet Kumar**,[3] **Mamdouh El Haj Assad**,[4] **and Reza Alayi**[5]

[1]*College of Environmental Science and Engineering, Peking University, Beijing 100871, China*
[2]*Institute for Energy Research, Jiangsu University, Zhenjiang 212013, China*
[3]*Department of Mechanical Engineering, Mehran University of Engineering and Technology, Jamshoro 76090, Sindh, Pakistan*
[4]*Sustainable and Renewable Energy Engineering Department, University of Sharjah, P.O. Box 27272, Sharjah, UAE*
[5]*Department of Mechanics, Germi Branch, Islamic Azad University, Germi, Iran*

Correspondence should be addressed to M. S. Hossain; m.shossein@yahoo.com and Reza Alayi; reza.alayi@yahoo.com

Received 19 March 2022; Revised 25 May 2022; Accepted 2 June 2022; Published 1 July 2022

Academic Editor: Xiaoqing Bai

Greenhouse gas (GHG) emissions are one of the major problems that the world is facing nowadays. The transportation sector, where vehicles run on oil, contributes a large amount of GHG. The development of electric vehicles to meet the allowed GHG limits has recently been the main focus of research worldwide. Research in electric vehicles (EVs) has observed a tremendous upsurge in recent years. However, reviews that analyze and present the demand and development of EVs comprehensively are still inadequate, and this integrative review is an effort to fill that gap. This study has revealed many thought-provoking understandings related to specific developments, specifically global demand and growth of EVs along with electricity and battery demand, current technological developments in EVs, energy storage technologies, and charging strategies. It also details the next generation of EVs and their technological advancements, such as wireless power transfer. The development of a smart city concept by EV implementation added a new aspect to this review. The summary would be advantageous to both scholars and policymakers, as there has been a lack of integrative reviews that assessed EVs' global demand and development simultaneously and collectively. This review concludes the intuitions for investors and policymakers to envisage electric mobility.

1. Introduction

Electric vehicle (EV) adoption rates have been growing around the world due to various favorable environments, such as no pollution, dependence on fossil fuel energy, efficiency, and less noise [1]. The current research into EVs is concerned with the means and productivity of expanding transportation, reducing costs, and planning effective charging strategies. Regardless of whether it is a hybrid, a modular crossover, or one of a multitude of functional EVs, people's interest will increase with falling costs. Moreover, the development of EVs is based on current and future global demand, which is interconnected to electricity and battery demand. Besides that, the productive development of EVs depends on the improvement of global values, EV policies, comprehensive frameworks, related peripherals, and easy-to-use programming [2]. However, the primary energy source of fossil fuel still commands the world's road transportation, but it is only a matter of time before EVs are adopted; in the next decade, people will begin to rely on electric vehicles.

Although there is virtually no scope for greenhouse gas emissions in EVs, the benefits of transport electrification in mitigating environmental changes become more apparent when the organization of EVs matches the DE (distributed energies) carbonization of the intensity structure. Strategies continue to improve electrical flexibility. The use of EVs usually begins with the formulation of many goals, followed by specifications for receiving and charging vehicles. Electric vehicle approval plans typically include acquisition programs to arouse interest in EVs and stand out from the public charging infrastructure system. On the other hand, the technological development of showcases for EVs has led to the creation of countless charging stations for EVs, with

which the electric vehicle network (EV-grid integration) can be connected. Newer charging stations can be divided into private and nonprivate charging stations, which can stimulate medium charging (levels 1 and (2) and fast charging (levels 3 and DC) [3]. The high tolls for EVs are private in moderately charged ports. However, future charging stations are to be developed at commercial locations to make them petrol stations for electric cars with extensive charging ports [4]. Wireless innovation is at the center of the future versatility of electrical equipment. These progressive developments cover the entire value chain of the project and the whole circular economy: research of managers, production and processing of crude oil, battery design, as well as the production, use, and disposal (sorting, reuse, and reuse) of the battery and the solution to overall savings and maintainability [5]. Most of the current progress of the battery depends on lithium particles, polymers of lithium particles, or nickel-cadmium, nickel-metal hydride [6]. Naumanen et al. and their team reported on the method of solid lithium-ion battery cars in China, the European Union, Japan, and the United States. They summarized the bulk of the use of the national battery improvement system at the point of an electric vehicle. China and the United States are the leading licensors and countries that monitor batteries [7]. However, the developing countries can lean on them to maintain the EV-related development and manufacturing R&D sectors. Despite the advancement of battery-based innovations, the battery testing phase, the construction of measuring instruments, the disposal and reuse of batteries, and the conduct of assessments are significant [8]. There will be a change in the amount of CO_2 emitted from the EV fleet's well-to-wheel (WTW) greenhouse gas emissions as energy use and electricity generation carbon intensity both decrease [9]. Thus, EVs could lead the decarbonization of the transportation sector towards carbon neutrality.

Besides that, smart cities are looking for new solutions to address some of the urban dilemmas (environmental, social, and financial) caused by the grid network, development, and the operation of underlying conditions (such as vehicles, waste, energy). However, this cooperation is not always recognizable and should be tested for the most considerable advantage [10, 11]. The use of petroleum products in the transport system causes atmospheric pollution due to the formation of particles and unnatural meteorological changes caused by carbon dioxide and primary air pollutant emissions. There are many mineral-filled vehicles in the world that can carry substances that deplete the ozone layer, which is one of the significant challenges facing the world [12, 13]. Consider that the benefit of answering the request is to improve the charge coordination of using low-carbon or low-carbon energy. Another essential aspect of EVs is the charging of batteries. The charging speed of the battery depends on the type of EV and the main battery charge. In most cases, the charger is divided into four levels, from level 1 to level 4. To complete the checkpoint, an accurate assessment of the relevant conditions for the electric vehicle must be made. Coordination between energy and land use and issues related to changes in global temperature and air pollution are fundamental prerequisites for the transportation sector. Therefore, car manufacturers only need to establish more apparent incentives to see increasingly effective results. In this particular case, there has recently been a concentration of vehicles with selective fuel and EVs. The International Energy Agency (IEA) is taking measures to reduce the similar outflow of carbon dioxide (CO_{2eq}), and many countries have made the introduction of EVs on the market an important goal [14, 15].

To overcome those difficulties, this study presents an innovative approach to EV development to provide an appropriate guideline for developing and nondeveloping countries. EVs coordinate various types of individual achievements and divide the overall field of EVs into several key areas, which can give increasingly important point-by-point data. Consider the benefit of answering the request: to improve the charge coordination of using low-carbon or low-carbon energy. It is assumed that the strength structure representation of the use of DG (distributed generation) assets will be further enhanced and combined with sustainable energy. The following article summarizes EV status, policies, future demand, and EV-related technology, specifically delving into next-generation EVs and their approaches. Nowadays, smart city development and maintenance are hot topics, and electric vehicles are playing an essential role in renewable energy growth. In this regard, this study went through an impact-related discussion. Lastly, the study summarizes and explores some different methods and their advantages and disadvantages. These discussions will give a general framework for increasing EV growth in the world.

However, it is important to see EV growth in the world. Figure 1 shows a summary of the global EV stock and EV sales market. The market share report shows that 3% of the total newly sold vehicles are EVs. As indicated in the Navigant Research report, this number may exceed 7%, or 6.6 million a year worldwide by 2020 [9]. The transportation of EVs has developed rapidly in the last ten years; in 2018, the worldwide transportation volume of EVs was more than 5 million. This is an increase of 63% over the previous year. In 2018, around 45% of EVs were produced in China, where the total number of EVs was 2.3 million, an increase of 39% over the previous year. In any case, 24% of the world's fleet is in Europe, while the United States has 22%. On the other hand, Norway is still a worldwide pioneer in the production of electric cars. About 49.10% of new electric car transactions in 2018 were almost twice as much as Iceland, an increase of 17.50%, and six times as much as Iceland as Sweden, an increase of 7.20% [16]. Most of the existing EVs have been manufactured in recent years, and more than 300 million vehicles will be manufactured by the end of 2018. Of course, most of them are in China. In contrast, two-wheeler electric vehicle sales are hundreds of times larger than anywhere in the world. Transactions with EVs are also increasing. In 2018, more than 460,000 cars are already on the world's roads. In addition, 5 million passenger cars and slow EVs were sold in 2018. All low-speed electric vehicles (EVs) are in China. Shared electric foot scooters, often known as "free-floating" scooters, became extremely popular in major cities throughout the world in 2018 and early 2019. These foot

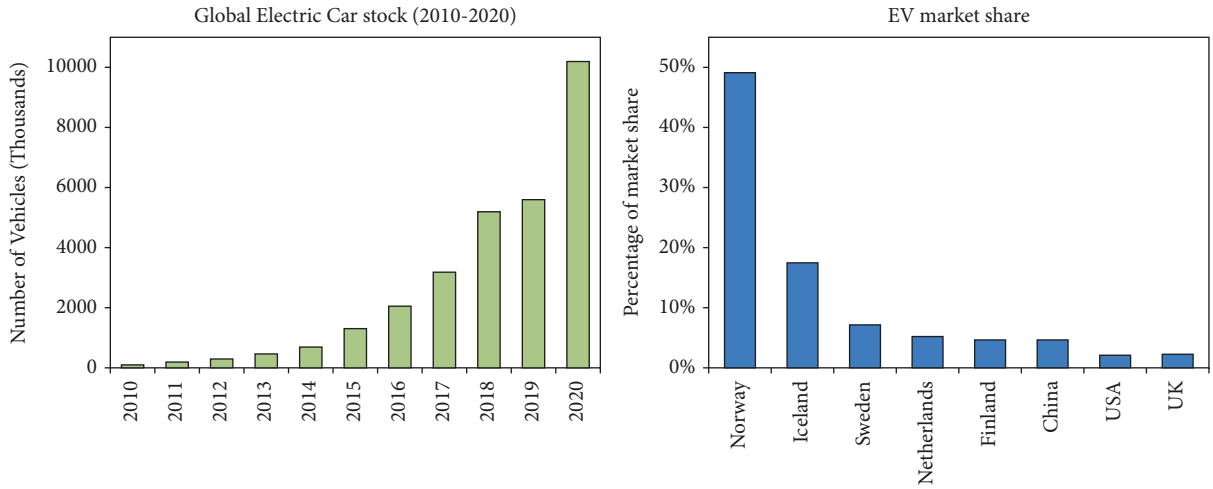

Figure 1: Global EV stock and EV sales market share in 2020. Redrawn and taken permission from Elsevier [17].

scooter conspiracies are currently active in approximately 129 urban areas in the United States; 30 in Europe; 7 in Asia; and 6 in Australia and New Zealand.

Moreover, the structure and configuration of EVs can be found in the next section. The development of EVs is based on current and future global demand, which is interconnected to electricity and battery demand. Besides that, the productive development of EVs depends on the improvement of global values, comprehensive frameworks, related peripherals, and easy-to-use programming [2]. There are several challenges to making EVs inexpensive in the market, such as efficient charging to the battery, battery price, flexibility in charging stations, EV technology innovation systems, EV sharing, and impacts related to EV and policy development. Thus, this review will provide significant approaches to EV growth in the world, which are based on technological advancement, identifying problems, and smart solutions. The following section summarizes the EV status, future EV material demand, and EV-related technology. We can see next-generation EVs and their approaches. Nowadays, smart city development and maintenance are some of the hot topics, and electric vehicles are playing an essential role in renewable energy growth. In this regard, the review went through an impact-related discussion. These discussions will give an overall dimension to resolving EV growth and development in the world.

2. Electric Vehicles (EVs) Status

EVs can be divided into two categories: hybrid EVs (HEV) and each type of all-electric vehicle (AEV) [18, 19]. An AEV is only equipped with a motor controlled by the power supply. AEV can also be divided into battery EV (BEV) and EV fuel cells (FCEV). A BEV is contained within an energy storage system (ESS) and a power control unit (PCU). The difference between BEV and FCEV is that the PCU is connected to a hydrogen tank (HT) and fuel cells (FCs). Thus, the FCEV does not require an external charging system. However, BEV only relies on the external power supply of the network to load a storage unit. A plug-in hybrid EV (PHEV) is a type of HEV that can be powered by a grid. The difference between a PHEV and a mild hybrid electric vehicle (MHEV) is that a PHEV has a smaller fuel engine and can be powered exclusively by a large battery pack. An MHEV blends traditional internal combustion (ICE) with electric power. All BEVs and PHEVs are called EVs. Figure 2 illustrates the classification of EVs and power sources for their wheels [17].

Figure 3 provides specific information about affordable EVs produced by different manufacturers [20–33]. The figure also shows the estimated charging time required to charge the car from 0% to 80% based on various charging principles. Here, the charging voltage in the first stage is equivalent to 110–120 V, the charging voltage in the second stage is 220–240 V, and the charging voltage in the third stage or DC fast charging (DCFC) is 200–800 V. It can be seen that the range of an electric vehicle is based on the battery charge. However, at about 100 kilometers, in some vehicle models and some other models, the battery runs for 200 to 400 kilometers. On the other hand, most of the current EV models run over 400 kilometers in China [34].

3. The Demand of EVs

3.1. Future Global Demand for EVs. To determine the base metals in future energy-based transportation, the first step is to create a situation where the number of EVs and future demand for subsequent metals can be estimated. Figure 4 shows an annual growth of three different types of EVs (BEV, PHEV, and HEV) with historical (2010), and future (2050) year scenarios, such as baseline (BS), Moderate (MS), and Stringent (SS) outcomes. The information used to improve the situation is taken from the integrated model to assess greenhouse effects (IMAGE), which was developed for the database of the shared socioeconomics pathways (SSP). An SSP is a long-term situation that enters the network due to changes in the environment. They depend on five different accounts, which translate into quantitative forecasts of three major financial factors, namely population, currency flows, and urbanization [35].

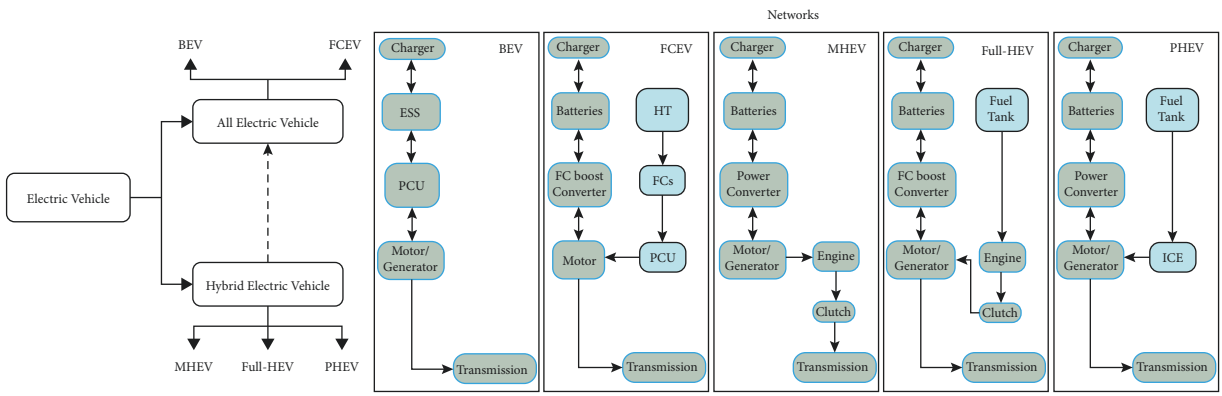

Figure 2: Classifications of EVs.

According to the outcomes of improving the situation, the absolute number of drivers in the basic situation is estimated to go from 1.13 billion in 2011 to 2.6 billion in 2050. Under moderate conditions, the number of station wagons is likely to increase to 2.55 billion by 2050, and to 2.25 billion. In difficult conditions, Figure 4 shows that in these three cases, the supply of three EVs increased from year to year.

3.2. Electricity Demand for EVs. The demand for EVs in the new political scenario is expected to reach only about 640 terawatt-hours (TWh), and the light-duty vehicle (LDV) is the largest pantograph of all EVs in 2030. Facts have proved that EVs are increasingly suitable for power supply systems, so make sure that management does not prevent their use through mandatory electrical structures. It is estimated that by 2030 globally, slow chargers that can be used to provide flexibility services to power systems will account for more than 60% of all electrical energy consumption. Meanwhile, fast charging demand periods such as at night will seriously affect the pile shape in the power structure [16].

3.3. Battery Demand for Electric Cars. The consumption of EVs and the relevant prerequisites for the production of batteries indicate that the automotive sector is more interested in new materials. Overall, by 2030, interest in cobalt and lithium should increase in both cases. Generally, cathode science influences the ability to control investment in metals, especially cobalt. It is necessary to increase the reserves of cobalt and lithium to ensure the expected EV absorption rate [35]. The scale of raw material interest adjustment for EVs also indicates the increase in raw material supply. Difficulties related to raw materials are mainly associated with the growth of creativity, natural impact, and social issues. The identification and directness of raw materials are essential tools to deal with some of these criticisms by maintaining the actual harvesting of minerals [6, 16].

4. EV-Related Technology

4.1. Current EV Technology. The innovation of EVs has aroused great interest from experts, organizations, and strategic developers in many countries. EVs coordinate various types of individual achievements and divide the overall field of EVs into several key areas, which can provide increasingly important point-by-point data [36]. Due to the positive aspects of use and low pollution levels, EVs can promote the decarbonization of transportation, and the growth of low-carbon emission urban areas has thus become one of the models to increase the enthusiasm of the automobile industry [37–39]. In any case, the future success of the electric vehicle business depends to a great extent on innovation [40, 41]. Politicians in many countries, such as Sweden, China, Malaysia, and South Korea, are serious about change in the field of EVs and are developing strategies to support the technological innovation of EVs [42, 43]. However, technological innovation in the field of EVs is an incredibly exciting topic. Figure 5 shows the analysis of the estimated improvement rate, where PE is the power electronics and EM is the electric motor. The figure also shows the estimation steps to improve the domains (power electronics, battery, electric motor as well as charging and discharging subdomains), which is the estimated density of the technological improvement of each domain or subdomain in the EV field.

An improved version of the HNS model (Human, System, and Nature) is offered for the mechanical navigation of EVs. They considered the need for angles (H, N, and S), although they were balanced as another base for support. The model is converted to NHS to show versatility from N to H, then switched to H to S. An increasingly accurate idea of the relationship between people, nature, and systems is that, in practice, the frame within the circle of people is floating around, and two of them fall into the sphere of nature, as shown in Figure 6. As shown in Figure 6, according to the previous model, each of the three representations has been similarly adjusted, but according to their proposed model (NHS), case (a) is more supportable than (b), and (b) more practical and therefore is better than (c). In the proposed model, we need to consider nature, humans, and systems separately. Unlike humans, nature depends on us and will remain without people as long as the structure depends on both humans and nature. As a rule, support implies a reasonable approach, which can limit negative environmental impacts, trying to maintain harmony between all three "columns." The opinions of people and structures should be determined from a natural point of view [44].

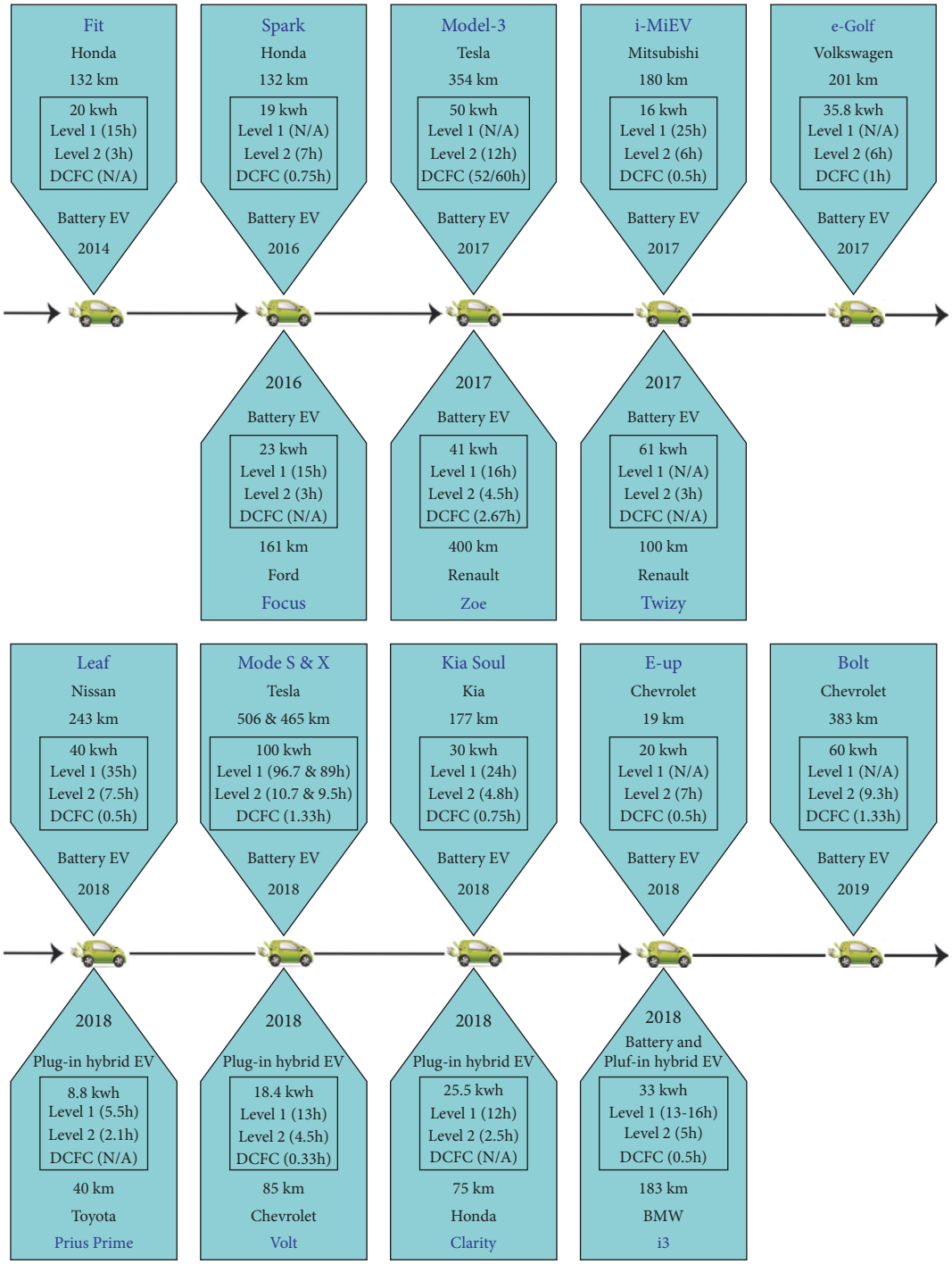

Figure 3: The most popular electric vehicle currency positions are listed.

Human and financial factors are critical factors in making progress. Countless people around the world have increased traffic. There are three types of EVs: HEV, FCEV, and EV. According to [45], all PHEVs in a municipal fleet can be divided into six categories:

(1) electric bicycles and bicycles,

(2) street electric cars,

(3) high-speed urban EVs,

(4) low-speed electric cars,

(5) supercars, and

(6) electric bus and electric truck.

We are talking about EVs in highway road cars (level 2). These types of vehicles are modular EVs that are driven by at least one electric motor and that use the energy that is regularly stored in battery-powered batteries. The use of petroleum products in the transport system causes atmospheric pollution due to the formation of particles and unnatural meteorological changes caused by carbon dioxide

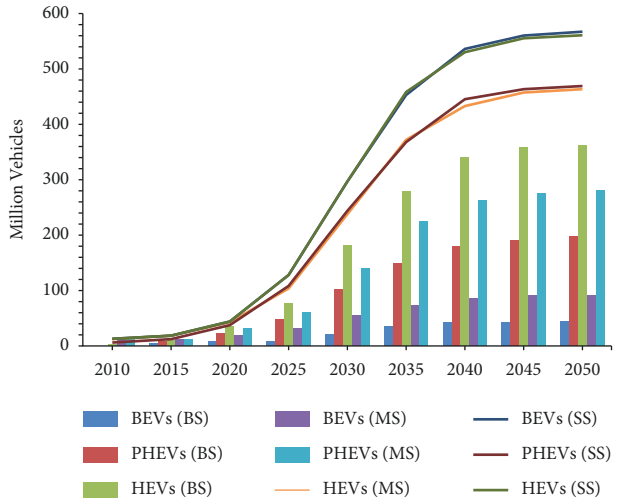

Figure 4: Annual growth of three different types of EVs stocks from 2010 to 2050 in three scenarios. Redrawn and taken permission from Elsevier [35].

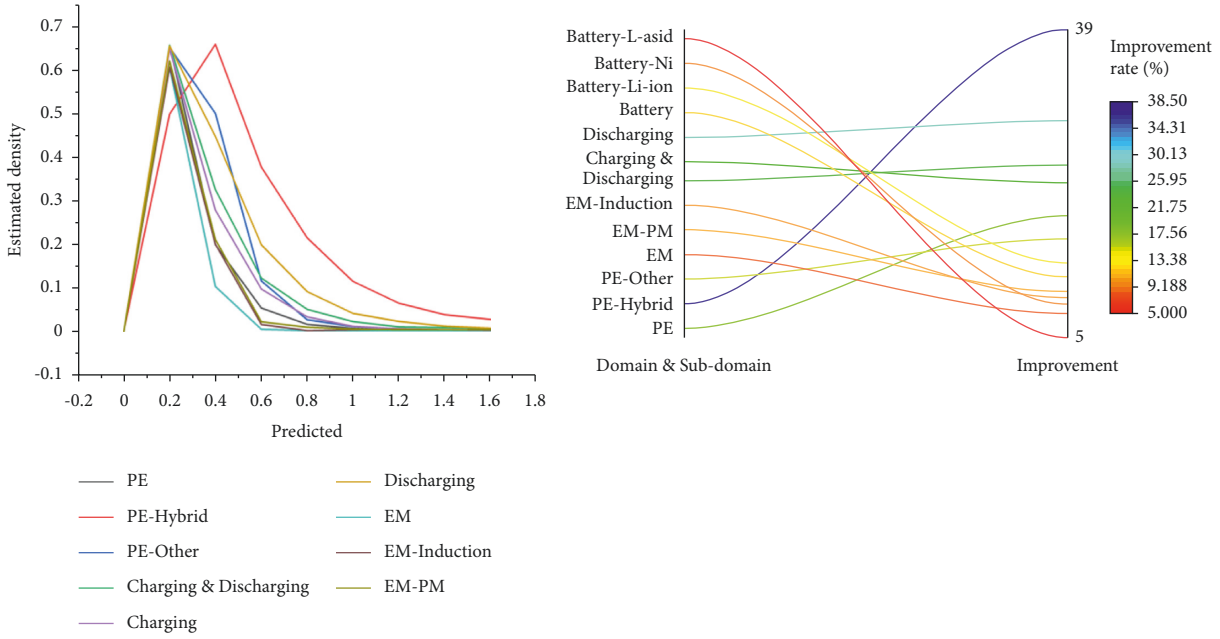

Figure 5: The estimated technological improvement rates of domains and subdomains. Redrawn and taken permission from Elsevier [36].

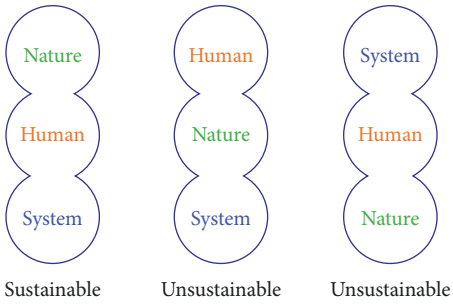

Figure 6: Models for humans, structures, and nature (HNS): (a) Sustainable and (b and c) Unsustainable. Redrawn and taken permission from Elsevier [44].

and primary air pollutant emissions. Conventional vehicles on transport chassis have the most significant influence on dangerous atmospheric forms. There are many mineral-filled vehicles in the world that can carry substances that deplete the ozone layer.

Human progress has resulted in present atmospheric changes and ozone-depleting chemical emissions, which are the world's major challenges [12, 13]. According to the announcement issued by the European Commission, transportation is the second most crucial factor in the release of ozone-depleting substances. This is equivalent to a quarter of the ozone layer in the European Union (EU). One of the primary ozone-depleting materials is CO_2 gas, and about 15% of the ozone-depleting elements (i.e., CO_2) are emitted by light vehicles such as pickup trucks and automobiles [46]. In recent years, some research projects involving the integration of electric vehicles into low-voltage grids have been carried out in Denmark, Norway, and Sweden. Figure 7 depicts a model of a grid-connected vehicle. The solar energy is connected to the home power supply for EV charging (during the daytime), which is called a solar to a vehicle (S2V) power supply. This charging process will reverse in the evening when the EV will discharge to home power by way of the vehicle-to-home (V2H) and vehicle-to-grid (V2G) processes. The issue of local area network constraints for locating electric vehicles with sufficient power in low-voltage residential area networks has been researched [13, 47].

4.1.1. Flexible and Innovative System in the Car. The advantages of EVs connected to the network include two-way dynamics. Therefore, this application (Dynamic Mobility between EVs and PHEV) will become an important choice for the smart grid area [48]. In addition, it is often used as the source of an energy crisis. An energy management mechanism is needed to promote the link between household business taxes and fast car charging. The power control mechanism is fractioning in two directions. For example, it works with an inverter to convert the direct current discharged by the battery into alternating current for home use and works with a rectifier (for example, when the current direction is opposite) to charge the battery. However, electric vehicles can be the best option to supply the various utilities because of their facilities and advantages [13, 49], such as the following:

(1) The charging station has large-scale loads compared to residential loads.

(2) In this situation, the transmission capacity has better response speeds.

(3) The charging points are available and have high flexibility.

4.1.2. Future Development Model of Electric Vehicle Network (EVGI). EVs can be used not only for transportation but also as electrical loads (grid-to-vehicle (G2V)), the corresponding energy stock of the grid (vehicle-to-grid (V2G)), the energy stock of various EVs (vehicle-to-vehicle (V2V)), and the energy stock of buildings (vehicle-to-building (V2B)) function system compliance center [17, 50]. In the field of vehicles, some new results are proposed, which can improve the availability and applicability of EVs in the most modern power grids. The latest innovations include proprietary wireless power transfer (WPT), connected mobility (CM), autonomous or autonomous EVs, and EVs' economic saving, and life-saving power network. By using these innovations, the fate of the transportation sector is reversed. Besides, how the future electrical transportation unit is firmly connected to the grid will affect the strength and energy of the automotive industry's innovation in creating these titles. Figure 8 shows a classification, and Figure 9 shows a proposed model for the future development of the EV network.

4.1.3. Renewable Energy Sources. While researching the impact of EV grid integration, it is difficult to overlook the work of environmentally friendly energy sources and the significant impact of the combination of EVs and systems. This section studies the effects of sustainable energy. In Knezovic et al. [52], the analysts considered the possibility and difficulty of coordinating inexhaustible energy sources (for example, based on wind and sun) to provide energy for battery charging, and then started again from the perspective of limiting greenhouse gas emissions. When adaptable loads are used, the problem of reducing the stability of the power structure due to the abuse of sustainable energy has not yet been significantly resolved. PEVs can charge EVs in peak-off hours or when renewable energy is available. Consider that the benefit of answering the request is to improve the charge coordination of using low-carbon or low-carbon energy. It is assumed that the strength structure representation of the use of DE (distributed energies) assets will be further improved and combined with sustainable energy. There is a lack of coordination between the host and the distributed generation energy system (DESS) with sustainable energy, which can be completed under the basic and maximum loads. At the optimal time, additional energy is fed into the grid. From what is written, the work in this field basically meets the broader prospects, which represents the study of the entire future interesting grid system and network [13].

4.1.4. Smart Grid Structure. Currently, the construction of the power grid does not meet the required flexibility. The smart grid is a complex system that is connected to all grid networks. To exhibit all system screen characters for this application, various networks need to be effectively copied, connected, and approved. However, the architect did not pay much attention to the plan of the grid network. The following are the main components of planning a keen system [13, 17].

(1) The substructure of the system must be adaptable and its components must be considered.

(2) The structured grid model should be able to support future expansion.

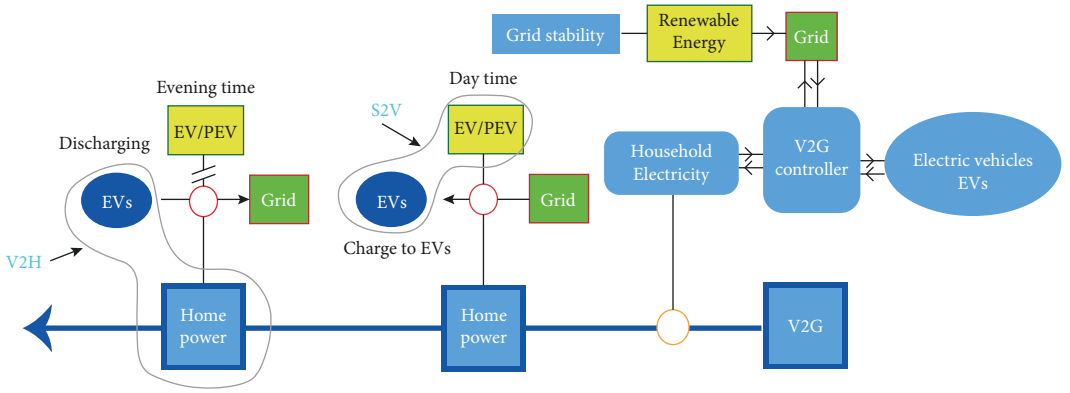

Figure 7: The relationship between EVs and the grid.

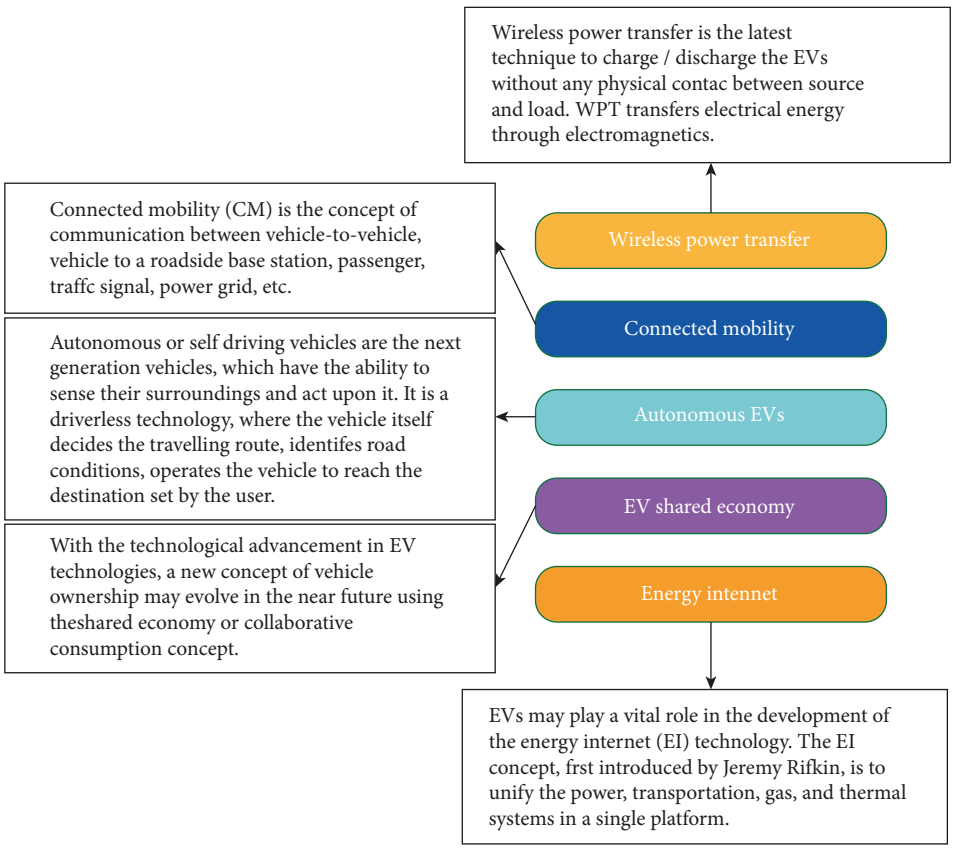

Figure 8: Classification of EV network.

(3) When planning the structure, the structure and points of the programming/device/grid structures should be considered.

(4) If the system update program is activated, it should be executed automatically.

4.2. Energy Storage Technology. Battery innovation is the so-called hot topic related to electric cars. The junction point is the anode, and the electrons move toward the cathode. At the same time, there is no electrical prevoltage during the movement of particles in the electrolyte. Lithium particles (Li particles) and nickel-metal hydride (NiMH) are two types of batteries used in EVs. Cars like the Nissan LeFeng and Mitsubishi iMiev use lithium batteries as an indispensable source of energy. On the other hand, in half of the EVs, such as the Toyota Prius, nickel-metal hydride batteries are used as primary resources [53]. The only source of energy that is remembered in EVs is batteries. It should be measured satisfactorily in order to promote energy transfer continuously. Before the battery is completely discharged, it can now confirm the additional charge generated by the regeneration process, for example, decelerating. Experts note that the safe zone is about 20%, which means that the emission zone should not exceed 80%, although it is possible to determine the state of a slow regenerative charge.

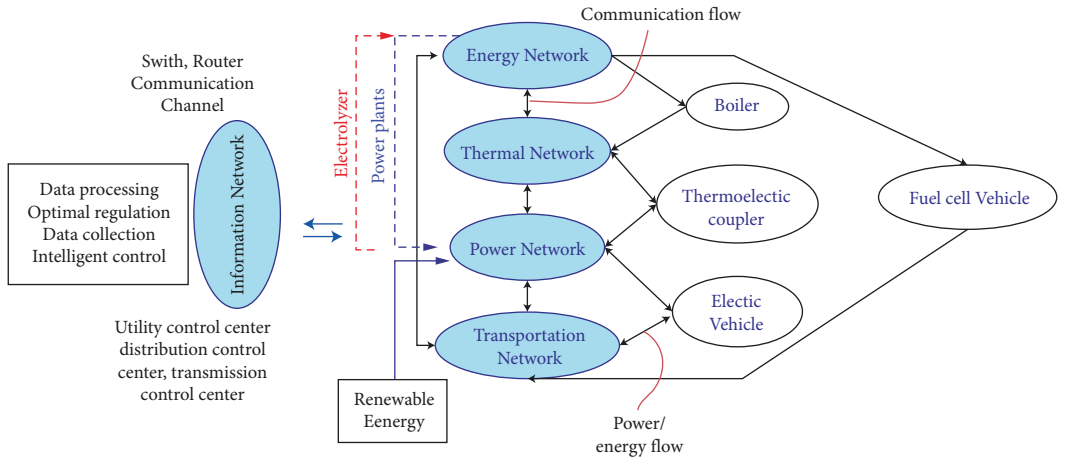

Figure 9: Structure of energy internet. Redrawn and taken permission from Elsevier [51].

Figure 10 shows an example of the EV battery charging capacity.

For this reason, during the hour of charging the battery [54], the stock increases by about 5%. If the highest state of charge (SOC) is 95% of the first SOC and the highest release rate is 20% of the first SOC, the battery size must be determined so that the required limit is correctly reached. The charge state is the current battery charge limit (upper limit), and deep discharge is the battery level released as the upper limit. Although the vehicle battery at the intersection is the primary source of energy for the traction, the goal is that, as with the device being measured, the limit of the required battery should be a series of hybrid organized vehicles [13]. Due to the fact that the internal combustion engine of a plug-in hybrid vehicle of this design distributes the required energy for the pedaling force, the required limit for the battery is small. In addition, batteries used in plug-in hybrid vehicles must flexibly meet the activity requirements. When the car stops at a low speed, it behaves like an electric car battery. In this sense, it is necessary to improve the battery to limit its highest point, freeing its depth to a higher level. To know the energy storage device, energy generation system, and energy sources for PEVs, the details of the approach can be found in Figure 11.

The energy storage (ES) system is a rapidly growing technology. ES gives attention to a solid-state storage system. This is indicative of the fast pace of development in the car battery area, whereas technical performance has a vital role in economic development. A comparative study evaluates the capital costs of different energy storage technologies [54]. The literature report shows that the energy storage capital cost depends on several facts, such as cost per kilowatt, per kilowatt-hour, and kilowatt-hour per cycle. For example, the supercapacitors, li-ion, flywheels, and sodium sulfate storage costs are calculated by kilowatt, kilowatt-hour, and fuel cell, and flow batteries costs are measured by kilowatt-hour per period.

4.2.1. Battery Charging Methods. Several structures can be used to charge EVs. The power level (kW), the electricity used, the accessories, and the battery types are factors that

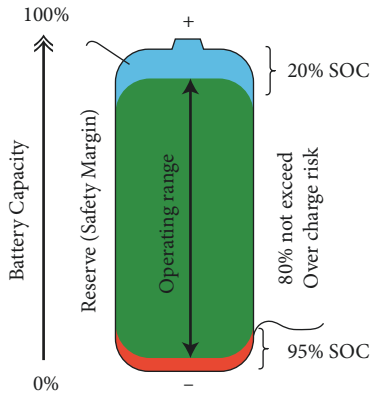

Figure 10: EV battery capacity.

determine the charging of EVs. The power for moderate charging is approximately 3.3 kW and the power for fast DC charging is approximately 50 kW [55].

At the simplest level, it is necessary to use chargers to power the battery from a conventional single-phase power source or a level two AC charging station or to connect a plug-in hybrid electric vehicle that is an integral part of the innovation of the complete vehicle. This innovation means that, for example, in Europe, people can connect electricity from a conventional single-phase 230 V AC socket via external vehicle accessories and then convert internal devices to DC to charge the battery. Charging is usually possible at these locations with low voltage frames. On the other hand, more and more people were demanding that the power of the DC station be quickly charged to 50 kW, while the power organized for the Tesla compressor was 120 kW.

4.2.2. Charging Cage for Electric Cars. Another essential aspect of EVs is the charging of batteries. The charging speed of the battery depends on the type of charger used and the main battery charge. In most cases, the charger is divided into four levels, from level 1 to level 4. In many EVs that use power supplies from home devices, level 1 chargers are EVSE (Electric Vehicle Maintenance) devices compared to implicit chargers that can be used in electric cars to charge fully for

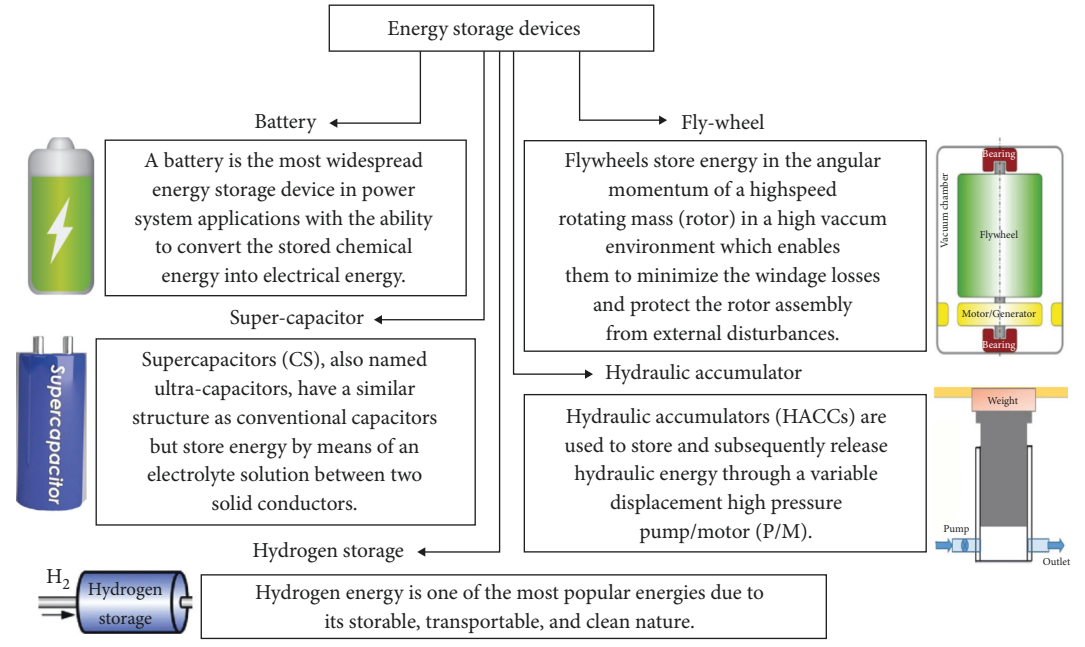

(a)

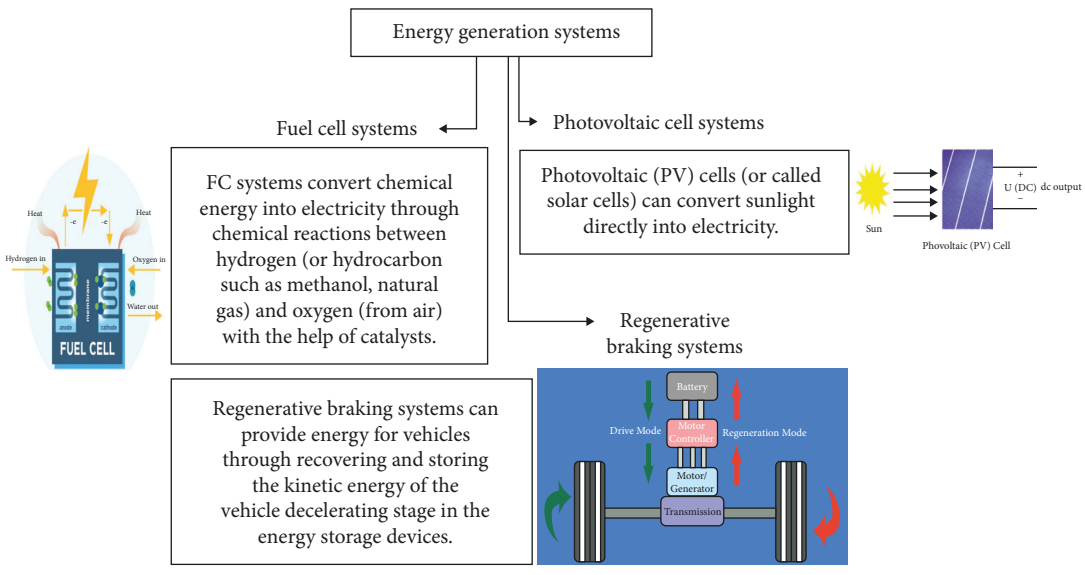

(b)

Figure 11: Continued.

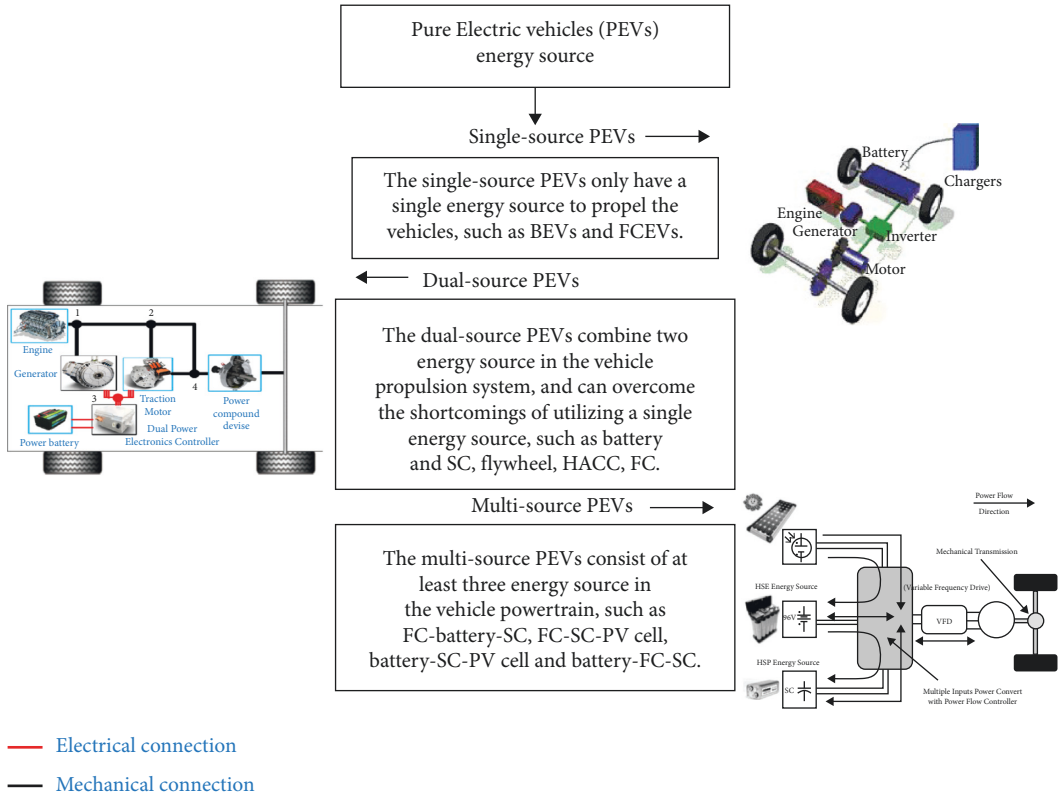

(c)

Figure 11: Classification of (a) energy storage devices, (b) energy generation systems, and (c) PEVs energy sources.

7–9 hours. Tier 3 and Tier 4 chargers are chargers that use advanced DC charging methods to charge EV batteries legitimately. This kind of configuration is mostly used in Singapore [56].

4.2.3. Approximate Time to Charge the Battery. The Independent State of Charging: In this state, 55% of the battery charge is completed during a period of low use (from 10 : 00 p.m. to 7 : 00 a.m.), and additionally, 45% is supplied from 7 : 00 a.m. to 10 : 00 a.m. In the subsequent express delivery, 75% of the battery charge of the electric vehicle ends when used less (from 10 : 00 p.m. to 7 : 00 a.m.), and the remaining 25% is made available between 7 : 00 a.m. and 10 : 00 p.m. In this example, synchronous loading or first loading is considered one of the most effective strategies. The transaction costs for energy, a measure of the energy consumption of a battery in the state of charge (SOC), are regarded as the parameters of this technology. In an uncontrolled state of charge, 55% of the charging time of the battery is used during periods of low usage (from 10 : 00 p.m. to 7 : 00 a.m.) and the remaining 45% at 7 : 00 a.m. (10 : 00 p.m.) provided between them [12].

To complete the checkpoint, an accurate assessment of the relevant conditions for the electric vehicle must be characterized. The proposed charging time is shown in Figure 12. It should be noted that one of the primary problems with this strategy is that the charging of connected EVs should be limited during periods of maximum energy consumption. The following mode (controlled state of charge) is considered as follows.

From the beginning, the battery pack and the bend of the battery pack were chosen according to the type of day. If it is possible to restore the possibility that the battery can hardly be fully charged at night the next night, the total load at night should be less than the estimated shutdown time, which depends on the peak load the next day. The updated lithium battery is suitable for charging EVs with a range of 170 kilometers. The maximum battery charge of EVs is around 20 to 30 kWh. EV FC batteries can charge 80% of EVs in less than 30 minutes.

4.3. EVs Next-Generation

4.3.1. EV and HEV Unit Design and Advanced Unit Development Guide. Therefore, the main models of EVs that compete with vehicles with an internal combustion engine (ICE) are battery EVs (BEV), hybrid EVs (HEV), fuel cell vehicles (FC), fuel cell hybrid EVs (FCHEV), and hybrid solar EVs (HSEV). Figure 13 shows the architectures, and the related inspections of ICE vehicles and charging vehicles are summarized. The development of environmentally friendly advanced vehicles based on advanced electric driving technologies should focus on the following aspects: reduction of costs, an increase in productivity, and the

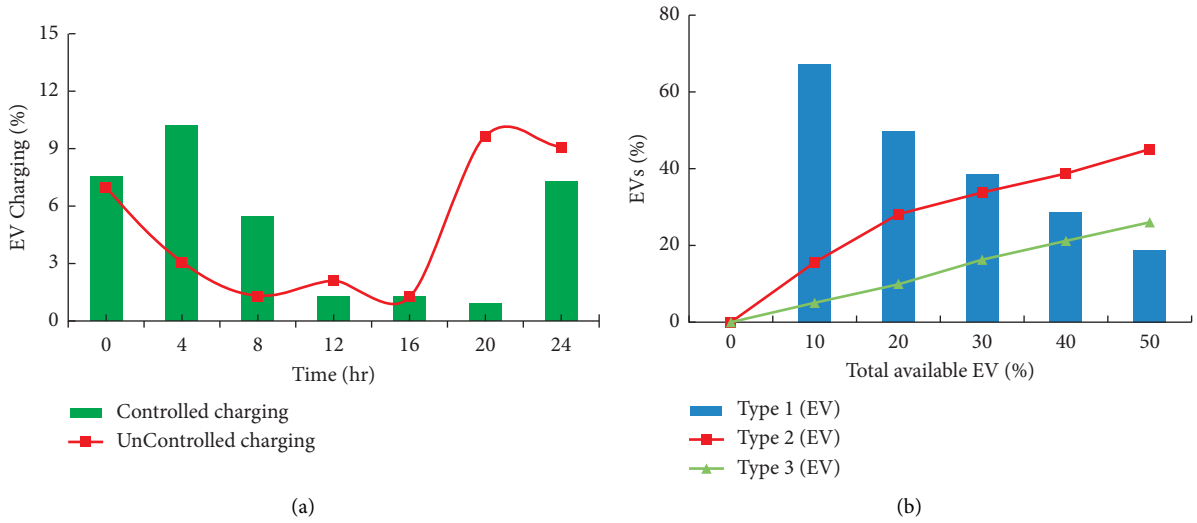

Figure 12: Charging schedule of EVs. Redrawn and taken permission from Elsevier [13]. (a) Charging is limited during peak times. (b) Charging process is completed before 6 a.m.

implementation of high power density [57]. The progress of the key authorizations that can improve the aforementioned engine performance can be summarized as [58–60]:

It is impossible to determine the absolute superiority of one technology over another, and a technological decision must be made after analyzing a number of factors for a particular application. In this context, after protecting the essential requirements for a specific EV or HEV vehicle (torque, power, speed, transmission specifications, etc.), the key features that need to be compared to choose the right technology can be summarized as follows [58, 61]:

(a) space required for installation and allowable weight of the machine (or specific power);
(b) special reliability requirements;
(c) overall efficiency over the entire operating range;
(d) the normal speed of the torque;
(e) overload capacity of the unit; and
(f) the total cost includes material and production.

4.3.2. Technological Approach from WPT. The world has started to discover the wireless power transfer (WPT) system for various applications such as electric cars, home appliances, mobile phones, laptops, home appliances, medical devices, and electric vehicles. Figure 14 shows a classification scheme for various wireless energy transmission technologies. WPT technology can be divided into four main categories: far-field, near-field transmission [51, 62], mechanical force like magnetic gear, and acoustic gear [63–65]. Magnetic transmission technology uses mechanical forces to convert energy. It was initially introduced to replace conventional connected devices and has proven itself for various applications, e.g., for the fixed charging of EVs, driving electric cars, wind energy, and low-performance medical devices [66].

The inductive power transfer (IPT) and EV framework are shown in Figure 15. The frame has two electrically separated sides: ground (transmitter, grid, or basic) and vehicle (beneficiary or optional). The transmitter side is installed on the street to get low repetitive power from the network, convert it to high frequency (HF), and control the transmitter circuit. The EMF generated by the transmitter is combined with the receiver's fluctuations (in the vehicle) to excite the HF voltage and flux in the auxiliary circuit. The optional HF power supply has been recertified to charge the vehicle's energy storage structure (such as a battery). Figure 15 also shows the close relationship between various innovations in terms of performance level, driving separation, and repetitive work [51].

4.4. EV Smart City Development. The idea of a smart city dates back to 2009, proposed by IBM in the United States [67]. The general definition emphasizes the use of information and communication technology (ICT) in vehicles, energy supply, and management personnel, open funds, urban assets of management personnel, and administrative departments in a new era to improve and change the ecological productivity of cities [10]. Besides, this study also plays a significant role, as the so-called "understanding" also implies updating the management structure, in which the monitoring, recovery, investment, and improvement modules are combined to provide a structured strategy [68, 69].

Smart cities are looking for new solutions to address some of the urban dilemmas (environmental, social, and financial) caused by the network, development, and the operation of underlying conditions (such as vehicles, waste, energy). However, this cooperation is not always recognizable and should be tested for the most considerable advantage [10, 11].

Due to the enormous demand for energy and the significant impact on air pollution and other related external influences (such as social security costs), fast, competent, and clean energy and transport structures are one of the main problems that community governments usually face [70]. For example, with regard to a cleaner and more efficient framework, transport policies have been adopted in many

Feature	ICE vehicle
Propulsion System	ICE based
Energy storage	Fuel tank
Energy source	Petrol
Energy source infrastructure	Refueling station
Well-to-tank	88.0%
Tank-to-wheel	12.1%
Well-to-wheel	10.6%
Commercialized	Yes
Smooth operation	No
Emissions	Very high
System complexity	Very low
Bulky	Yes

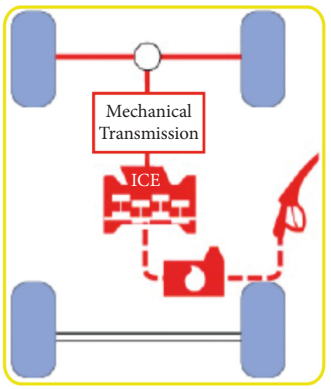

Feature	EV
Propulsion System	ED based
Energy storage	Battery Ultra capacitor Flywheel
Energy source	Electric
Energy source infrastructure	Charging station
Well-to-tank	37.0%
Tank-to-wheel	83%
Well-to-wheel	31.3%
Commercialized	Yes
Smooth operation	Yes
Emissions	No
System complexity	low
Bulky	No

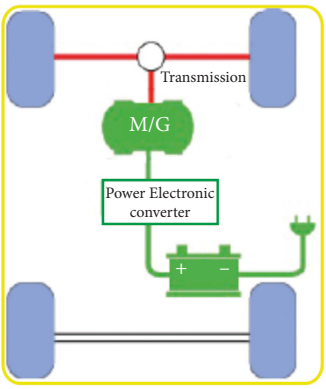

(a)

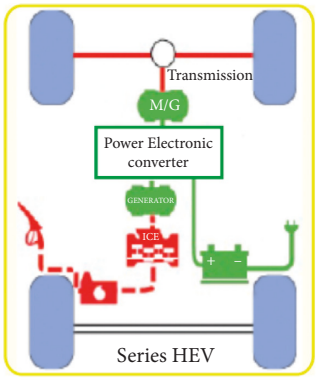

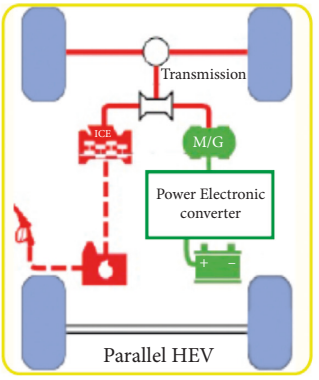

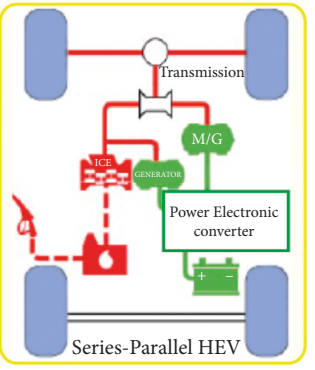

Feature	Complex HEV	Plug-in HEV
Propulsion System		ICE & ED based
Energy storage		Fuel tank Battery Ultra capacitor Flywheel
Energy source		Petrol & electric
Energy source infrastructure		Charging station & refueling station
Well-to-tank		Depend on the specifc vehicle
Tank-to-wheel		Depend on the specifc vehicle
Well-to-wheel		Depend on the specifc vehicle
Commercialized		Partially
Smooth operation		Yes
Emissions		Low
System complexity		High
Bulky		Yes

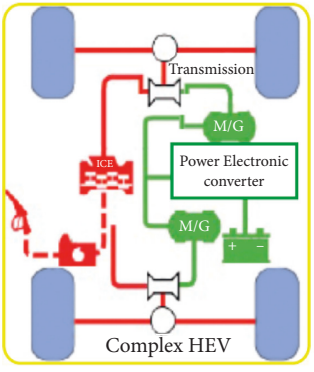

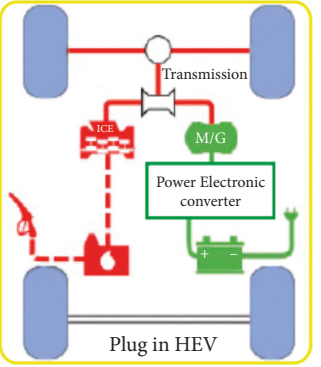

(b)

Figure 13: Continued.

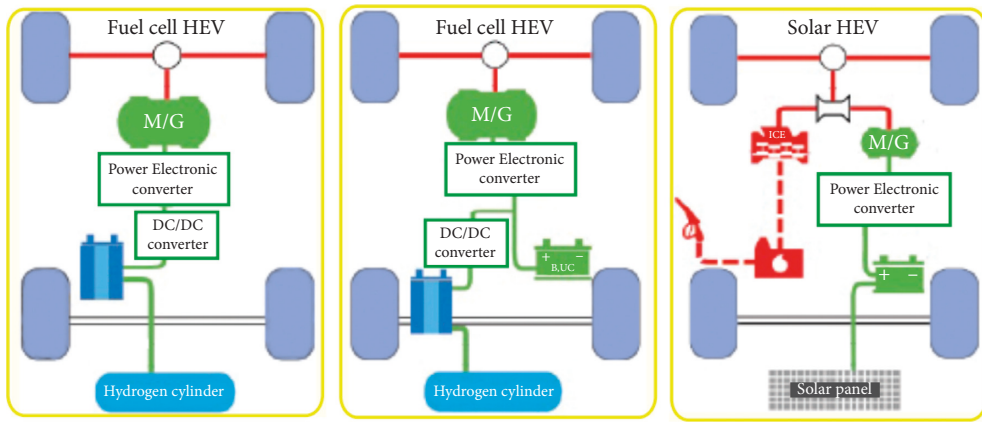

Feature	FC
Propulsion System	ED based
Energy storage	Fuel tank Battery Ultra capacitor Flywheel
Energy source	Hydrogen
Energy source infrastructure	Hydrogen refner & refueling station
Well-to-tank	58.4%
Tank-to-wheel	46.6%
Well-to-wheel	27.2%
Commercialized	No
Smooth operation	Yes
Emissions	Ultra low
System complexity	Very high
Bulky	No

(c)

Figure 13: ICE, EV, EC, and HEV architecture and characteristics. Redrawn and taken permission from Elsevier [58]. (a) ICV vs. EV architecture, (b) HEV architecture, (c) FC and HSVE architecture.

urban areas to reduce pollution [71], and research and development differ from the traditional structure. Among these other options, electric cars are some of the most famous vehicles and deserve a lot of research. For example, the link already includes a method of charging EVs. When presenting an overview of the smart tariff system, reference [50] discusses the use of EVs as a capacity. Fernandez et al. [72] and Beer et al. [73] or its effect on the grid and its use as a representative tool for maintaining sustainable energy in references Baloglu and Demir [74] and Villar et al. [75].

4.4.1. General SEMS Management Scheme. Given these points, Figure 16 shows the overall design of the proposed sustainable energy management system (SEMS) control system. To ensure reliable mobility, the level with the least control level (excitation level) follows the usual method, which depends on the PID (proportional integral derivative) and the rule-based controller. On this floor, there are thermostatic radiator valves (TRV) in each flat, siphons, and valves that feed the thermosiphons, boilers, and storage, as well as switches connected to all other electrical resources [76].

A technical basis of a smart city pilot project in China shows in Figure 17. Government, business, and citizens are the main actors. Based on the infrastructure of information and communication technologies, intelligent management, smart economy, smart citizens, and service are highlighted in detail [69].

As smart cities, smart infrastructure, and ICT-based management are also core components of smart industrial parks. Figure 17 also shows the overall technical structure of smart industrial parks, including smart infrastructure and technologies that support efficient resource management in industrial parks, smart decision support tools that support the evaluation and optimization of smart industrial parks. The stylish design of urban industrial symbols, supporting resources, and the optimal use of energy parks, as well as smooth business models and design software packages ION, support the implementation of smart industrial parks [69].

4.4.2. Overview of V2G, S2V, and V2I Structure

(1) Vehicle to Grid. V2G provides intelligent network operations through DR (Demand Response) services between EVs and the electricity grid. V2G here refers to the transmission of electricity and related data between transport and network systems, which implements the synergy between the two needed to achieve an intelligent city. Figure 18 shows a possible block diagram of a V2G structure [77].

(2) Sun to Vehicle. EVs currently in use worldwide require charging stations similar to those required for fuel-based vehicles. The use of a charging station powered by photovoltaic cells to charge solar energy is called S2V or EV-PV charging [78–80]. Figure 18 shows the smart grid concept

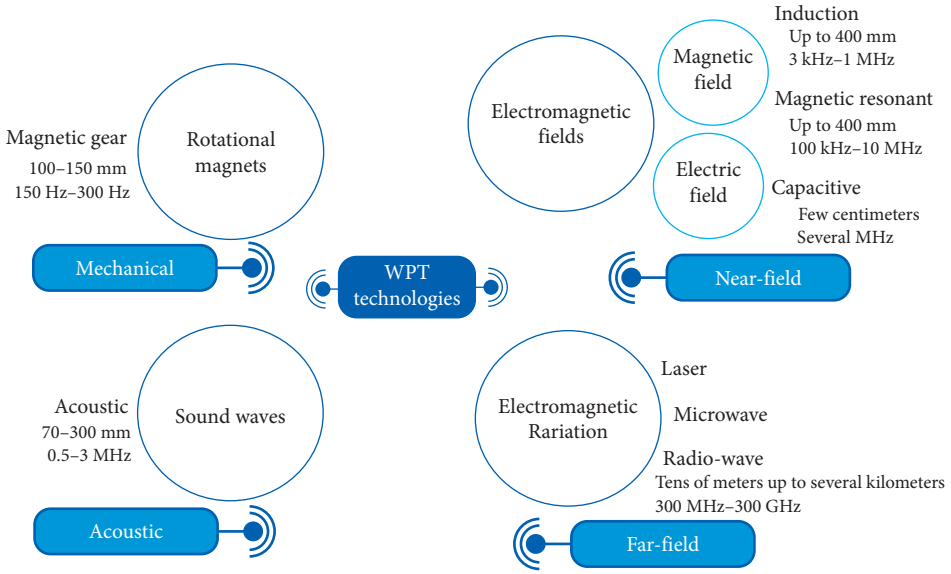

Figure 14: Wireless power transfer (WPT) technology. Redrawn and taken permission from Elsevier [51].

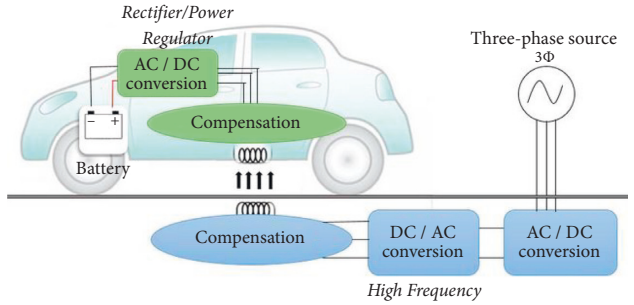

Figure 15: Inductive power transfer (IPT) system for EV charging.

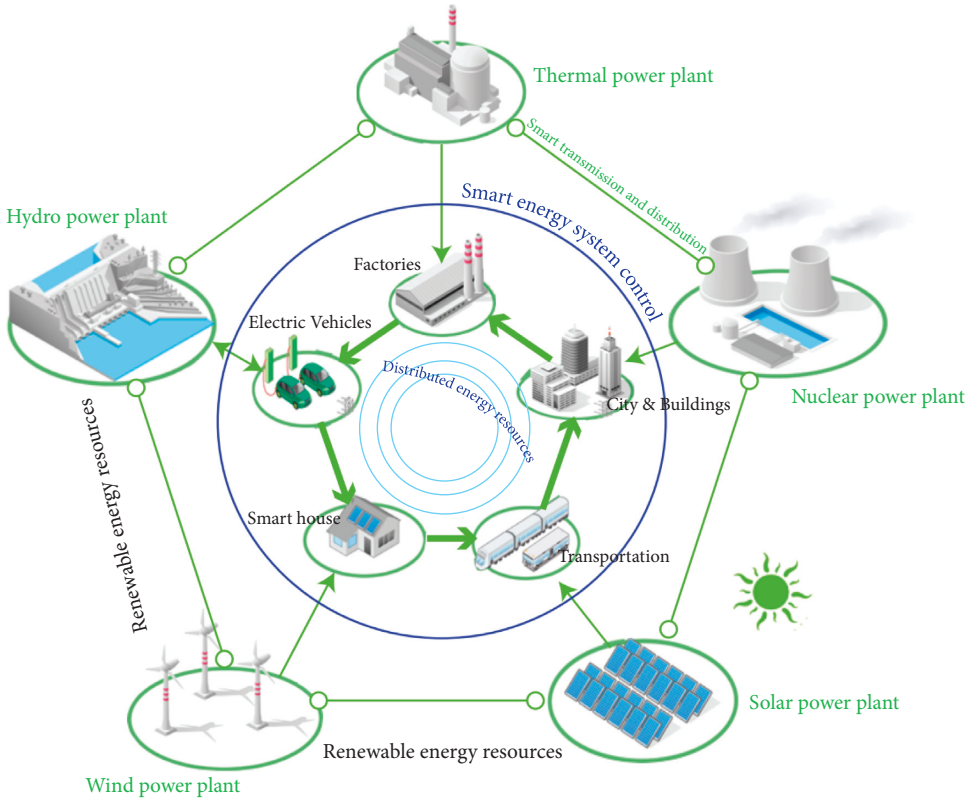

Figure 16: Overall energy management system.

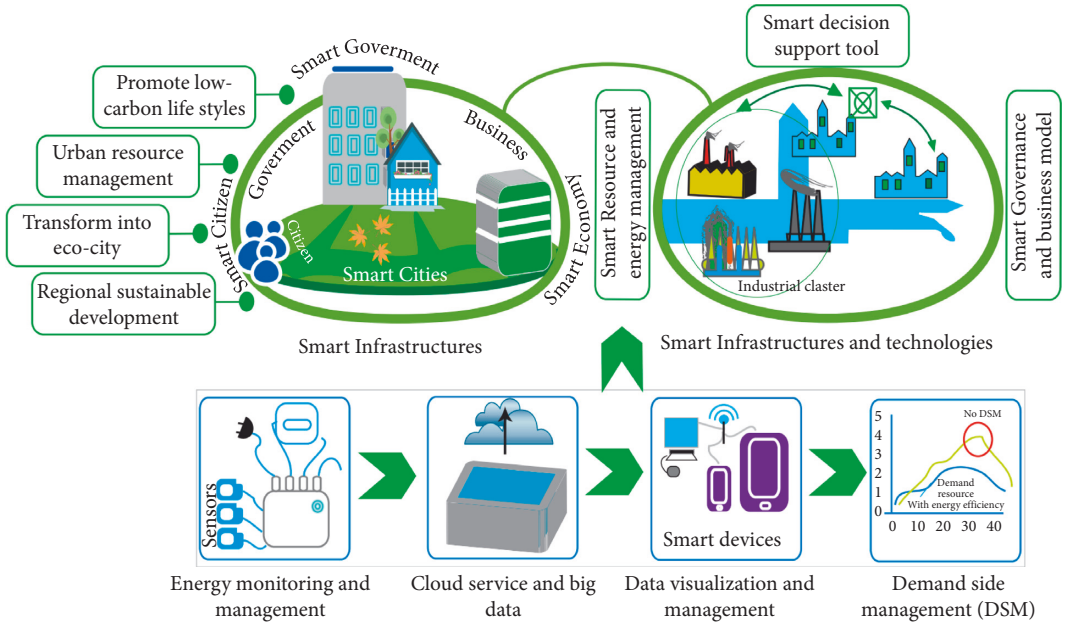

Figure 17: Example of smart infrastructures and smart technologies.

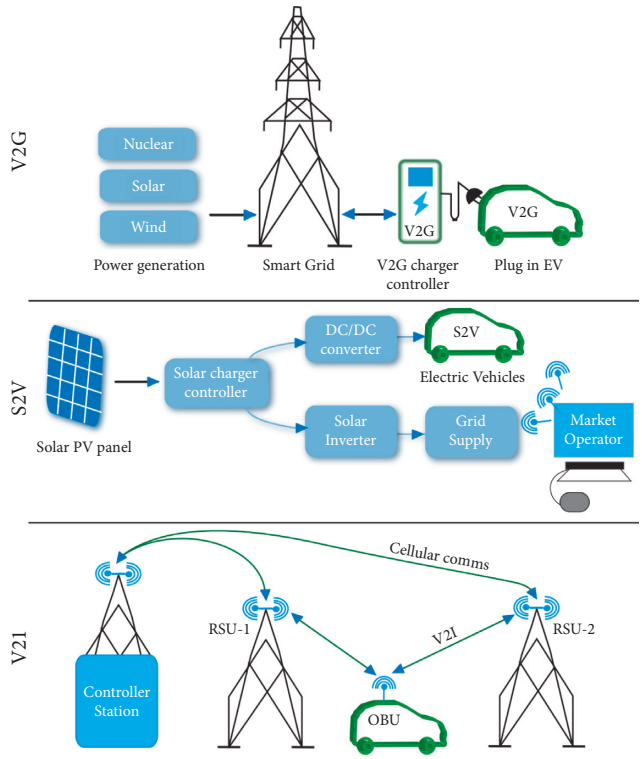

Figure 18: Example of V2G, S2V, and V2I structure.

implemented by S2V. Although the concept and implementation of solar machines are quite old, Birnie mainly uses the term S2V in his work [81]. He suggests that during the day, passengers who use electric cars every day can be charged by solar panels in the parking lot. These solar systems, used as charging stations for EVs, can help balance the current and reduce dependence on fossil fuels, thereby reducing carbon emissions.

(3) From Vehicles to Infrastructure. Communication V2I is one of the latest technologies in the fields of communications and automotive technology. In V2I, cars establish communication with the road unit for the exchange of information. Because of the different vehicle speeds, this architecture tends to create a dynamic performance. Some of the main problems solved with V2I technology are the increase in workload and road safety while reducing the environmental impact [77].

Table 1: Leading countries' national EV battery improvement technology and GHG emission.

Country	Development topic	Main aspect (finding)			
		Economical	Technological	Social	Environmental
China	Operating of EV	Low price, improved efficiency	Improve stability, acceleration sensor, fault detection, wireless communication, wireless transmission, intelligent control; older: Forklift truck, electric scooter	Ensure safety, display panel, intelligent electric vehicle, liquid crystal display, stable operation, USB interface, alarm module, easy use; older: Improve safety	China greenhouse gas emissions 10% by transportation sector in 2019 [82]
	Controlling of EV	Braking energy recovery, vehicle weight	Charge and discharge control; older: Battery service life, supercapacitor, electric braking, remote monitoring	Cruise/drive control, acceleration performance, driving safety, speed control; older: Travel distance	
	The battery module of the EV	—	Stability of battery, anti-collision, replacement battery, battery balancing, battery protection; older: Anti-theft, anti-explosion	—	
	Charging of EV	—	Inductive charging, charging condition, maximum load, charging efficiency, energy transmission, charging pile, charged control; older: Mobile charging, charging power, noncontact	Touch screen, charging schedule, parking lots/spaces	
USA	Operating of EV	Extend battery life, data collection	—	Self-locking	Transportation sector accounted for 29% of total U.S. greenhouse gas emissions in 2019 [83]. Contribution of GHG emission reduction of approx. 0.15% from 2005 to 2019, respectively. [83]
	Controlling of EV	—	Smaller battery	—	
	The battery module of the EV	—	—	—	
	Charging of EV	—	—	Older departure time	
Europe	Operating of EV	—	—	Safety device, reliable operation; older: easy maintenance	Transport accounted for 27% EU-28 greenhouse gas emissions in 2017 [84]. Contribution of GHG emission reduction of approx. 0.035% from 2005 to 2017, respectively [84]
	Controlling of EV	Development cost	Regenerative power generation, integrated control; older: Battery power consumption	Driving experience, user experience	
	The battery module of the EV	Older: Service lifetime	Battery balancing	—	
	Charging of EV	—	Battery condition; older: RFID tag	Vehicle network, mobile device; older: Mobile communication	
Japan	Operating of EV	—	—	—	Japan's transportation sector emitted 12.44% of the country's CO2 in FY2018 [85]. Transport sector: 4.5 million tons (2.1%) decrease in FY2018 [86]
	Controlling of EV	Distance travel, cost reduced battery life, data collection	—		
	The battery module of the EV	—	Housing battery	Quick change	
	Charging of EV	—	—	—	

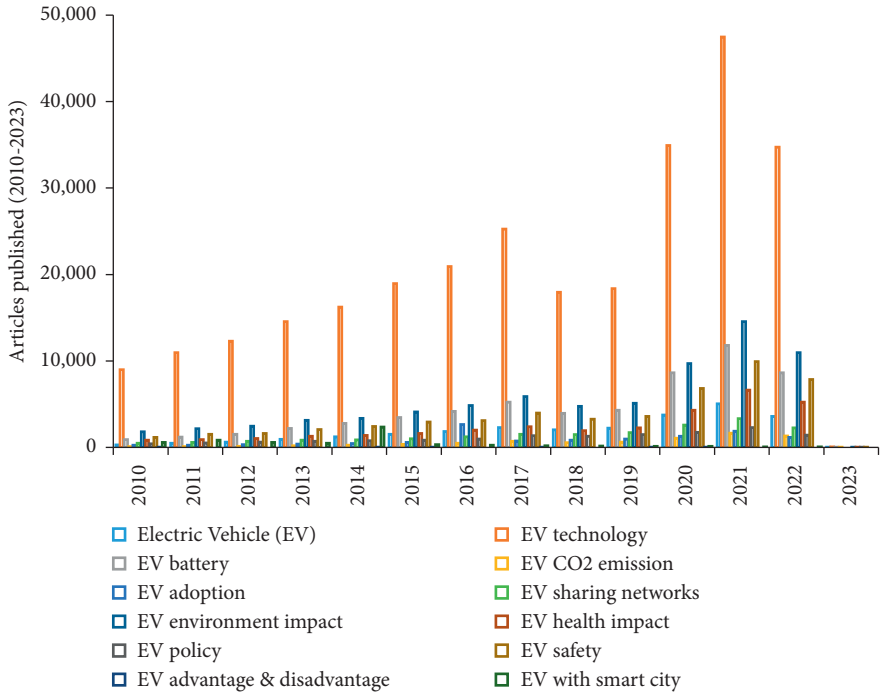

Figure 19: Number of published articles in EV technology, battery, CO_2 emission, adoption, sharing network, environmental and health impact, policy, safety, smart city development, advantage and disadvantage (the data source taken from ScienceDirect).

Figure 18 shows the block diagram of the overall installation of V2I. In this structure, only servers around the domain need the Internet, where information can be prepared and distributed as required. A global server with an Internet office can be used in conjunction with all competent authorities and contains a database for storing all data recorded by vehicles in motion. The car is suitable for continuously separating data about environmental and vehicle conditions, which must be systematically returned to the domain server. These can be completed through the onboard unit (OBU), equipped with a camera, and installing the sensor inside or inside the vehicle. The remote standard IEEE 802.11p (orthogonal frequency division multiplexing (OFDM)) is used to implement the physical V2I layer (PHY) with multichannel ambiguity. OBU can display 2G, 3G, 4G, or Wi-Fi to provide better usability in areas with little traffic.

5. Contribution of EV Technology Improvement and GHG Emission Reduction

Table 1 shows the leading countries' national EV battery technology improvement systems and their contribution of GHG emissions. China and the United States are the leading countries in the area of improving control over EVs.

6. Conclusions, Current Research Trends, and Future Recommendation

6.1. Conclusion. It is expected that progress in the development of EVs and contributions to the overall resources and facilities of renewable energy will improve the global reputation of electric cars. In this sense, additional technology improvements such as appropriate and reasonable charging rules, smart cities, robust adaptive frameworks, and business structures, policy, CO_2 emission reduction, and reduction to measure the impact on the environment, health, and power grid are fundamental to ensuring the most significant advantages from EVs with circulated benefit. Besides, Energy Internet will become an innovative network in the future and will use the latest energy frame panel to compute the energy framework fully. This study introduces all parts of the development structure of electric cars. After incorporating the principles of EVs and their adoption globally, electric vehicles must be widely known in the market. We carefully analyze the known electric car approach guidelines and many components so that future professionals can understand the solutions that will be implemented. Also, the various parts of the current framework used to load the communication and EV sharing networks have been carefully examined and improved, for example, strengths, consistency, control, and coordination strength, including their benefits and drawbacks. This study also suggests future research recommendations to overcome the tide. A letter on the future possibilities for electric cars shows that the exploration area needs to be reviewed.

6.2. Current Research Trends. Figure 19 shows the current research article trends and the number of published papers between 2010 and 2023 on EV-related topics. It can be observed that the current research trends follow the study topic, whereas EV technology is the top hot topic in these research areas. There are 47498 plus articles published in 2021, and the current year's published amount is about 34737. The second position is the EV environmental impact topic. There are 4844 additional articles published between

2020 and 2021, and till this year, 2022, about 10973 materials are already online. However, in the current year, publication topics such as EV battery, EV safety, EV health impact, and EV sharing networks are 8621, 7838, 5219, and 2251 higher than EV policy, EV CO_2 emission, EV adoption, and EV with smart city 1429, 1300, 1150, and 50, respectively. On the other hand, the EV advantage and disadvantage number of articles are significantly low. It is concluded that in the recent years from 2010 ahead, there has been significant progress in electric vehicle technology, which gives this subject the conviction area of exploration.

6.3. Future Recommendation. After reviewing the current research on electric vehicles (EVs) status, it is felt that the novel approaches can be useful to overcome the obstacles to EV development. Besides that, it is unbearable to discuss all the importance in one study. For further improvement, the research needs some future recommendations for enlightening its value, as given below.

(i) The energy storage battery technology needs to be improved for EV adoption, as well as the need to enhance the standard charging ports to user friendly.

(ii) The materials used in EV batteries are challenging to recycle. So, there is a need to find a new energy storage technology.

(iii) EV battery charging with grid connection still has adverse effects. These effects may need time to be reduced, which will increase a great chance to integrate EVs with renewable energy sources.

(iv) Reduce the EV battery temperature; an air-cooled medium technology can be applied, such as water or PCM (Phase Change Material). For more details, go to Akinlabi and Solyali [87].

(v) Develop new EV business and policy plans for customer's products and services about EVs.

(vi) Globally, EV acceptance still needs time. EV implementation can be improved by following some EV-accepted countries.

(vii) The information and communication should be more advance in EV smart cities with renewable energy development. To take the right plan, we need to collect more literature or online survey data, and the idea can generate from EV-developed countries.

Data Availability

All data used to support the findings of this study are included in the article.

Conflicts of Interest

The authors declared no potential conflicts of interest with respect to the research, authorship, and/or publication of this article.

References

[1] M. Rebecca, "The history of the electric car," 2014, https://www.energy.gov/articles/history-electric-car.

[2] A. Arancibia and K. Strunz, "Modeling of an electric vehicle charging station for fast DC charging," in *Proceedings of the Electric Vehicle Conference (IEVC) IEEE International*, Greenville, SC, USA, March 2012.

[3] N. Karali et al., *Vehicle-grid Integration*, Lawrence Berkeley National Laboratory, Califonia, CL, USA, 2017.

[4] W. Su, *Smart Grid Operations Integrated with Plug-In Electric Vehicles and Renewable Energy Resources*, North Carolina State University, Raleigh, NC, USA, 2013.

[5] N. Lebedeva, F. Di Persio, and L. Boon-Brett, *Lithium Ion Battery Value Chain and Related Opportunities for Europe*, 2017.

[6] S. Manzetti and F. Mariasiu, "Electric vehicle Battery technologies: from present State to future systems," *Renewable and Sustainable Energy Reviews*, vol. 51, pp. 1004–1012, 2015.

[7] M. Naumanen, T. Uusitalo, E. Huttunen-Saarivirta, and R. van der Have, "Development strategies for heavy duty electric battery vehicles: comparison between China, EU, Japan and USA. Resources," *Conservation & Recycling*, vol. 151, Article ID 104413, 2019.

[8] J. Du and D. Ouyang, "Progress of Chinese electric vehicles industrialization in 2015: a review," *Applied Energy*, vol. 188, pp. 529–546, 2017.

[9] Iea, "Global Ev Outlook," 2019, https://www.iea.org/reports/global-ev-outlook-2019.

[10] C. F. Calvillo, A. Sánchez-Miralles, and J. Villar, "Energy management and planning in smart cities," *Renewable and Sustainable Energy Reviews*, vol. 55, pp. 273–287, 2016.

[11] C. F. Calvillo, A. Sánchez-Miralles, J. Villar, and F. Martín, "Impact of EV penetration in the interconnected urban environment of a smart city," *Energy*, vol. 141, pp. 2218–2233, 2017.

[12] R. A. Walling, R. Saint, R. C. Dugan, J. Burke, and L. A. Kojovic, "Summary of distributed resources impact on power delivery systems," *IEEE Transactions on Power Delivery*, vol. 23, no. 3, pp. 1636–1644, 2008.

[13] Y. Zou, J. Zhao, X. Gao, Y. Chen, and A. Tohidi, "Experimental results of electric vehicles effects on low voltage grids," *Journal of Cleaner Production*, vol. 255, Article ID 120270, 2020.

[14] E. A. M. Falcão, A. C. R. Teixeira, and J. R. Sodré, "Analysis of CO2 emissions and techno-economic feasibility of an electric commercial vehicle," *Applied Energy*, vol. 193, pp. 297–307, 2017.

[15] Iea, *Electric and Hybrid Electric Vehicles*, p. 154, Tracking Clean Energy Progress International Energy Agency, 2013.

[16] Global EV, "Global EV Outlook," 2019, https://www.iea.org/reports/global-ev-outlook-2019.

[17] H. S. Das, M. M. Rahman, S. Li, and C. W. Tan, "Electric vehicles standards, charging infrastructure, and impact on grid integration: a technological review," *Renewable and Sustainable Energy Reviews*, vol. 120, Article ID 109618, 2020.

[18] D. Knutsen and O. Willen, *A Study of Electric Vehicle Charging Patterns and Range Anxiety*, Uppsala, Sweden, 2013.

[19] A. Purwadi, J. Dozeno, and N. Heryana, "Simulation and testing of a typical on-board charger for ITB electric vehicle prototype Application," *Procedia Technology*, vol. 11, pp. 974–979, 2013.

[20] Bmw i3, "Sacramento Electric Vehicle Association," 2018, https://www.bmwusa.com/vehicles/bmwi/bmw-i3.html.
[21] Chevrolet, "Chevrolet spark," 2016, https://www.chevrolet.com/cars/spark-subcompact-car/build-and-price/features/trims/?styleOne¼399827.
[22] Chevrolet, "Chevrolet volt," 2018, https://www.chevrolet.com/electric/volt-plug-in-hybrid.
[23] A. Heydari and A. Askarzadeh, "Techno-economic analysis of a PV/biomass/fuel cell energy system considering different fuel cell system initial capital costs," *Solar Energy*, vol. 133, pp. 409–420, 2016.
[24] Honda, "Honda clarity electric," 2018, https://automobiles.honda.com/clarity-electric.
[25] ft E. V. Honda, "Electric machines and energy storage technologies in EVs," 2014, https://automobiles.honda.com/images/2013/fit-ev/downloads/Automobile_Magazine.pdf.
[26] "Kia soul," 2018, https://www.kiamedia.com/us/en/models/soul-ev/2018/specifcations.
[27] F. Nazari, A. K. Mohammadian, and T. Stephens, "Modeling electric vehicle adoption considering a latent travel pattern construct and charging infrastructure," *Transportation Research Part D: Transport and Environment*, vol. 72, pp. 65–82, 2019.
[28] twizy, "Renault twizy," 2017, https://www.guideautoweb.com/en/makes/renault/twizy/2017/specifcations/40/.
[29] R. zoe, 2017, https://insideevs.com/new-2017-renault-zoe-ze-40-400-km-range-41-kwh-battery/.
[30] "Tesla model 3," 2018, https://www.tesla.com/model3.
[31] "Tesla model X," 2018, https://www.tesla.com/modelx.
[32] "Toyota prius prime," 2018, https://www.toyota.com/priusprime/faq.
[33] "Volkswagen E-Up," 2018, http://www.volkswagen.co.uk/new/up-pa/which-model-compare/details/2800.
[34] Bloomberg, "Tesla Nears Debut of New 400-mile China-made Model 3," 2020, https://fortune.com/2020/04/07/tesla-debut-new-400-mile-china-model-3/.
[35] K. Habib, S. T. Hansdóttir, and H. Habib, "Critical metals for electromobility: global demand scenarios for passenger vehicles, 2015–2050," *Resources, Conservation and Recycling*, vol. 154, Article ID 104603, 2020.
[36] S. Feng and C. L. Magee, "Technological development of key domains in electric vehicles: improvement rates, technology trajectories and key assignees," *Applied Energy*, vol. 260, Article ID 114264, 2020.
[37] M. H. Amini, M. P. Moghaddam, and O. Karabasoglu, "Simultaneous allocation of electric vehicles' parking lots and distributed renewable resources in smart power distribution networks," *Sustainable Cities and Society*, vol. 28, pp. 332–342, 2017.
[38] O. Veneri, *Technologies and Applications for Smart Charging of Electric and Plug-In Hybrid Vehicles Book*, 2017.
[39] X. Zhao, O. C. Doering, and W. E. Tyner, "The economic competitiveness and emissions of battery electric vehicles in China," *Applied Energy*, vol. 156, pp. 666–675, 2015.
[40] G. Correa, P. Muñoz, T. Falaguerra, and C. R. Rodriguez, "Performance comparison of conventional, hybrid, hydrogen and electric urban buses using well to wheel analysis," *Energy*, vol. 141, pp. 537–549, 2017.
[41] W. Hong, Y. Huang, H. He, L. Chen, L. Wei, and A. Khajepour, "Chapter 5 – energy management of hybrid electric vehicles," *Modeling Dynamics & Control of Electrifed Vehicles*, 2018.
[42] J. Brady and M. O'Mahony, "Travel to work in Dublin. The potential impacts of electric vehicles on climate change and urban air quality," *Transportation Research Part D: Transport and Environment*, vol. 16, no. 2, pp. 188–193, 2011.
[43] W. Sierzchula and G. Nemet, "Using patents and prototypes for preliminary evaluation of technology-forcing policies: lessons from California's Zero Emission Vehicle regulations," *Technological Forecasting and Social Change*, vol. 100, pp. 213–224, 2015.
[44] F. Samaie, H. Meyar-Naimi, S. Javadi, and H. Feshki-Farahani, "Comparison of sustainability models in development of electric vehicles in Tehran using fuzzy TOPSIS method," *Sustainable Cities and Society*, vol. 53, Article ID 101912, 2020.
[45] S. W. Hadley and A. A. Tsvetkova, "Potential impacts of plug-in hybrid electric vehicles on regional power generation," *The Electricity Journal*, vol. 22, no. 10, pp. 56–68, 2009.
[46] K. Clement-Nyns, E. Haesen, and J. Driesen, "The impact of vehicle-to-grid on the distribution grid," *Electric Power Systems Research*, vol. 81, no. 1, pp. 185–192, 2011.
[47] F. Marra, M. M. Jensen, R. Garcia-Valle, C. Træholt, and E. Larsen, "Power quality issues into a danish low-voltage grid with electric vehicles," in *Proceedings of the 11th International Conference on Electrical Power Quality and Utilisation*, pp. 1–6, Lisbon, Portugal, October 2011.
[48] S. Seyyedeh Barhagh, B. Mohammadi-Ivatloo, A. Anvari-Moghaddam, and S. Asadi, "Risk-involved participation of electric vehicle aggregator in energy markets with robust decision-making approach," *Journal of Cleaner Production*, vol. 239, Article ID 118076, 2019.
[49] C. Farkas, K. I. Szabó, and L. Prikler, "Impact assessment of electric vehicle charging on a LV distribution system," in *Proceedings of the 2011 3rd International Youth Conference on Energetics (IYCE)*, pp. 1–8, Leiria, Portugal, July 2011.
[50] J. García-Villalobos, I. Zamora, J. I. San Martín, F. J. Asensio, and V. Aperribay, "Plug-in electric vehicles in electric distribution networks: a review of smart charging approaches," *Renewable and Sustainable Energy Reviews*, vol. 38, pp. 717–731, 2014.
[51] A. Ahmad, M. S. Alam, and R. Chabaan, "A comprehensive review of wireless charging technologies for electric vehicles," *IEEE Transactions on Transportation Electrification*, vol. 4, no. 1, pp. 38–63, 2018.
[52] K. Knezović, S. Martinenas, P. B. Andersen, A. Zecchino, and M. Marinelli, "Enhancing the role of electric vehicles in the power grid: field validation of multiple ancillary services," *IEEE Transactions on Transportation Electrification*, vol. 3, no. 1, pp. 201–209, 2017.
[53] C. Jiang, R. Torquato, D. Salles, and W. Xu, "Method to assess the power-quality impact of plug-in electric vehicles," *IEEE Transactions on Power Delivery*, vol. 29, no. 2, pp. 958–965, 2014.
[54] Z. Li, A. Khajepour, and J. Song, "A comprehensive review of the key technologies for pure electric vehicles," *Energy*, vol. 182, pp. 824–839, 2019.
[55] Z. Wang and S. Wang, "Grid power peak shaving and valley filling using vehicle-to-grid systems," *IEEE Transactions on Power Delivery*, vol. 28, no. 3, pp. 1822–1829, 2013.
[56] S. Lefeng, L. Shengnan, L. Chunxiu, Z. Yue, L. Cipcigan, and T. L. Acker, "A framework for electric vehicle power supply chain development," *Utilities Policy*, vol. 64, Article ID 101042, 2020.
[57] U Drive, *Driving Research and Innovation for Vehicle Efficiency and Energy Sustainability Hydrogen Delivery Technical Team Roadmap*, Illinois, BP, USA, 2013.
[58] I. López, E. Ibarra, A. Matallana, J. Andreu, and I. Kortabarria, "Next generation electric drives for HEV/EV propulsion

systems: technology, trends and challenges," *Renewable and Sustainable Energy Reviews*, vol. 114, Article ID 109336, 2019.

[59] S. Rogers and S. Boyd, *Overview of the DOE VTO Electric Drive Technologies R&D Program*, US Department of Energy Vehicle Technologies Office, Argonne, IL, USA, 2016.

[60] B. Ozpineci, *Annual Progress Report for the Electric Drive Technologies Program*, Oak Ridge National Laboratory, Oak Ridge, TN, USA, 2016.

[61] T. Finken, M. Felden, and K. Hameyer, "Comparison and design of different electrical machine types regarding their applicability in hybrid electrical vehicles," in *Proceedings of the International Conference on Electrical Machines*, pp. 1–5, Vilamoura, Portugal, September 2008.

[62] C. Qiu, K. T. Chau, T. W. Ching, and C. Liu, "Overview of wireless charging technologies for electric vehicles," *Journal of Asian Electric Vehicles*, vol. 12, no. 1, pp. 1679–1685, 2014.

[63] W. Li, "High efficiency wireless power transmission at low frequency using permanent magnetic coupling," Thesis, The University of British Columbia, Vancouver, Canada, 2009.

[64] M. G. L. Roes, J. L. Duarte, M. A. M. Hendrix, and E. A. Lomonova, "Acoustic energy transfer: a review," *IEEE Transactions on Industrial Electronics*, vol. 60, no. 1, pp. 242–248, 2013.

[65] F. G. T. Victor, S. B. Sarah, and L. Nathan, "Acoustic Wireless Power Transfer with Receiver Array for Enhanced Performance," in *Proceedings of the 2017 IEEE Wireless Power Transfer Conference (WPTC)*, pp. 1–4, Taipei, Taiwan, May2017.

[66] S. n. Suzuki, M. Ishihara, and Y. Kobayashi, "The improvement of the noninvasive power-supply system using magnetic coupling for medical implants," *IEEE Transactions on Magnetics*, vol. 47, no. 10, pp. 2811–2814, 2011.

[67] G. C. Lazaroiu and M. Roscia, "Definition methodology for the smart cities model," *Energy*, vol. 47, no. 1, pp. 326–332, 2012.

[68] M. de Jong, S. Joss, D. Schraven, C. Zhan, and M. Weijnen, "Sustainable–smart–resilient–low carbon–eco–knowledge cities; making sense of a multitude of concepts promoting sustainable urbanization," *Journal of Cleaner Production*, vol. 109, pp. 25–38, 2015.

[69] Y. Wang, H. Ren, L. Dong, H.-S. Park, Y. Zhang, and Y. Xu, "Smart solutions shape for sustainable low-carbon future: a review on smart cities and industrial parks in China," *Technological Forecasting and Social Change*, vol. 144, pp. 103–117, 2019.

[70] J. Villar, I. Trigo, C. Diaz, and P. Gonzalez, "Cost-benefit analysis of plug-in electric vehicles penetration," in *Proceedings of the European Energy Market (EEM). 10th international conference*, pp. 1–8, Stockholm, Sweden, May 2013.

[71] D. J. Sun, Y. Zhang, R. Xue, and Y. Zhang, "Modeling carbon emissions from urban traffic system using mobile monitoring," *The Science of the Total Environment*, vol. 599-600, pp. 944–951, 2017.

[72] I. J. Fernández, C. F. Calvillo, A. Sánchez-Miralles, and J. Boal, "Capacity fade and aging models for electric batteries and optimal charging strategy for electric vehicles," *Energy*, vol. 60, pp. 35–43, 2013.

[73] S. Beer, T. Gomez, D. Dallinger et al., "An economic analysis of used electric vehicle batteries integrated into commercial building microgrids," *IEEE Transactions on Smart Grid*, vol. 3, no. 1, pp. 517–525, 2012.

[74] U. Baloglu and Y. Demir, *Economic Analysis of Hybrid Renewable Energy Systems with V2G Integration Considering Battery Life*, pp. 242–247, Energy Procedia, Turkey, 2017.

[75] J. Villar, C. Diaz, P. Gonzalez, and F. Campos, "Wind and solar integration with plug-in electric vehicles smart charging strategies," in *Proceedings of the European Energy Market (EEM), 11th International Conference*, pp. 1–6, Krakow, Poland, May 2014.

[76] E. O'Dwyer, I. Pan, S. Acha, and N. Shah, "Smart energy systems for sustainable smart cities: current developments, trends and future directions," *Applied Energy*, vol. 237, pp. 581–597, 2019.

[77] M. S. Adnan Khan, K. M. Kadir, K. S. Mahmood, M. I. Ibne Alam, A. Kamal, and M. M. Al Bashir, "Technical investigation on V2G, S2V, and V2I for next generation smart city planning," *Journal of Electronic Science and Technology*, vol. 17, no. 4, Article ID 100010, 2019.

[78] A. Schuller, C. M. Flath, and S. Gottwalt, "Quantifying load flexibility of electric vehicles for renewable energy integration," *Applied Energy*, vol. 151, pp. 335–344, 2015.

[79] X. Hu, Y. Zou, and Y. Yang, "Greener plug-in hybrid electric vehicles incorporating renewable energy and rapid system optimization," *Energy*, vol. 111, pp. 971–980, 2016.

[80] G. R. Chandra Mouli, P. Bauer, and M. Zeman, "System design for a solar powered electric vehicle charging station for workplaces," *Applied Energy*, vol. 168, pp. 434–443, 2016.

[81] D. P. Birnie, "Solar-to-vehicle (S2V) systems for powering commuters of the future," *Journal of Power Sources*, vol. 186, no. 2, pp. 539–542, 2009.

[82] W. Samantha, "Share of energy related carbon dioxide emissions in China in 2019," 2021, https://www.statista.com/statistics/1088662/china-share-of-energy-related-carbon-dioxide-emissions-by-sector/.

[83] Epa, "Sources of greenhouse gas emissions," 2021, https://www.epa.gov/ghgemissions/sources-greenhouse-gas-emissions.

[84] Eea, "Greenhouse gas emissions from transport in Europe," European Environment Agency, 2021, https://www.eea.europa.eu/data-and-maps/indicators/transport-emissions-of-greenhouse-gases/transport-emissions-of-greenhouse-gases-12.

[85] NIESJ, "Japan's National Greenhouse Gas Emissions," 2020, https://www.env.go.jp/press/814.pdf.

[86] NIESJ, "Japan's National Greenhouse Gas Emissions," in *Fiscal Year 2019 (Final Figures), nies.Go.jp/whatsnew/20210413/20210413-e.html,* National Institute for Environmental Studies, Japan, 2021.

[87] A. H. Akinlabi and D. Solyali, "Configuration, design, and optimization of air-cooled battery thermal management system for electric vehicles: a review," *Renewable and Sustainable Energy Reviews*, vol. 125, Article ID 109815, 2020.

Hindawi
Complexity
Volume 2022, Article ID 3258549, 9 pages
https://doi.org/10.1155/2022/3258549

Research Article

Location Optimization Model of a Greenhouse Sensor Based on Multisource Data Fusion

DianJu Qiao,[1] **ZhenWei Zhang**,[2] **FangHao Liu**,[3] **and Bo Sun**[1]

[1]*College of Intelligent Equipment, Shandong University of Science and Technology, Tai'an, Shandong 271000, China*
[2]*College of Electronic and Information Engineering, Shandong University of Science and Technology, Qingdao, Shandong 266590, China*
[3]*Shandong North Chuangxin Waterproof Science and Technology Group Co Ltd, Binzhou, Shandong 251900, China*

Correspondence should be addressed to Bo Sun; bo_sun@sdust.edu.cn

Received 8 February 2022; Accepted 29 March 2022; Published 27 April 2022

Academic Editor: Jing Na

In the traditional case, the uncertainty of the ambient temperature measured by the experiential distributed sensor is considered. In this paper, a model based on the moving least square method in the fusion algorithm is proposed to study the optimal monitoring point of the sensor in the greenhouse and determine the most suitable installation position of the sensor in the greenhouse to improve the control effect of the temperature control device of the system. MATLAB simulation software is used to simulate each working condition of the greenhouse. Temperature data measured at 15 locations in the greenhouse were used to evaluate all possible combinations of monitoring locations and to estimate the optimal location for indoor temperature sensors. Compared with the traditional method, the error is reduced to 0.373, and the data are more accurate.

1. Introduction

At present, China has implemented greenhouse energy-saving planting projects and intelligent technology is applied to the modern greenhouse control system. Proper control of temperature, humidity, and carbon dioxide concentration in greenhouse can effectively improve the growth speed, quality, and yield of crops [1]. All biochemical reactions of crops in the whole growth cycle require appropriate temperature. Compared with other environmental factors, temperature is a decisive factor for crop growth and development. Therefore, the study is of great importance to the high efficiency, energy saving, and high yield under the premise of greenhouse temperature analysis.

During the temperature data measurement in a greenhouse, a limited number of sensors are usually installed to improve the overall cost performance. In general, sensor locations are determined by experience. However, according to the empirical distribution measurement results, the correct representation of the whole temperature environment in the greenhouse is uncertain. Therefore, it is necessary to select the best installation location for a limited number of sensors to accurately monitor the internal temperature of larger greenhouses.

Currently, the studies on the optimal sensor placement are mainly to measure the stability of the internal detection system in a specific environment and to determine the optimal sensor location in different measurement environments. The new technology based on truck GPS trajectory optimization deployment strategy in the California highway has been investigated: one is to establish a flow measurement based on the intercepting model flow weighting factor with emphasis on different body position and another is to set up the truck and choose different relative position recognition model to determine the best position of identification of heavy truck movement [2].

A unified TWLS framework was proposed for the joint location estimation of multiple disconnected sources and sensors based on a more general measurement model, which can be applied to many different localization scenarios [3]. A sensor network design strategy for monitoring nonlinear dynamic chemical processes using UKF was proposed to

approximate the true mean and covariance of a nonlinearly transformed random variable, till the third order was correctly performed with a low computational workload [4]. A four-stage program for a practical solution was developed to predict seismic displacement responses on all building floors using accelerometer measurements in optimized sensor positions. A recursive neural network based on multiscale attention was proposed [5]. Based on the response mode analysis, the position optimization scheme of monitoring sensor for a deep-water drilling riser was proposed to predict the optimal position according to the principle of maximum response acceleration amplitude by selecting main excitation modes and considering the tilt angle of riser [6]. Wang Xiaoping et al. established a two standard model for the optimal sensor placement, by which gas concentration could reach the given value and the maximum in the shortest time [7]. Bowen et al. selected the position and number of measuring points of a scramjet combustion chamber with a genetic algorithm and obtained the best sensor position and number by using the global optimal search and large-scale parallel computing capability of the genetic algorithm [8]. A probabilistic scheme for sensor monitoring in a discrete nonlinear state space was proposed to estimate the probability density function of the state and the measurement noise covariance, which is considered as a random variable. With the variable decibel Bayesian method, a quantitative index characterizing the measurement quality and satisfactory state estimation was obtained [9].

However, the existing studies in sensor placement method enhances unceasingly perfectness, but the precision control is largely limited by the accuracy of the model and the complexity of measurement environment conditions. Due to the crop growth models, greenhouse temperature, forecast model, and so on, there is a certain distance from the actual production requirement of greenhouse.

Based on the crop growth model and performance index function, the Pontryagin's maximum principle (PMP) was used to calculate the optimal set value of greenhouse daytime temperature at different temperature and light levels [10]. The computer optimization system of greenhouse heating control target based on energy consumption prediction model was established [11], which can optimize and calculate the greenhouse temperature setting points during the day and night. A SVM prediction model for the photosynthetic rate was established to realize the increase of CO2 application on demand [12]. All possible combinations of monitoring positions were evaluated in [13] and the best sensor position was selected by many sensors. Two methods were used for the optimization: sensor placement based on error and sensor placement based on entropy. By the former method, the sensor locations can be selected where the monitoring data are close to the reference value, i.e., the average data of all measured positions. By the latter method, sensor locations that are subject to poor environmental control due to external weather conditions can be selected.

In view of the disadvantages of reference setting as the average value and the demand objectives of crop growth characteristics, energy consumption, economic benefit, etc., the simulation temperature of indoor environment was calculated by the moving least square (MLS) method, which was proposed systematically by P. Lancaster and K. Salkauskas in the early 1980s [14]. The MLS has two major improvements [15]: (1) it is more convenient to establish the fitting functions instead of the traditional polynomials or other functions and (2) it introduces the concept of compact support, i.e., the value y at point x is regarded as only affected by nodes in the subdomain near point x, which is called the support domain of point x, while nodes outside the support domain have no influence on the value of x. In the process of fitting, different basis functions can be used to obtain different precision, and the same weight function can be used to change the smoothness of the fitting curve.

The mobile least squares method is developed based on the traditional least squares method with the high numerical accuracy for good mathematical theory support. This is also unmatched by other meshless methods, such as smooth particle method, unit decomposition method, reconstructed kernel particle method, and radial basis function method [16].

Therefore, by the moving least square method, the present study aims to investigate the best monitoring point of the sensor in the greenhouse, determine the most suitable installation position of the sensor in the greenhouse, and improve the control effect of the system temperature control device and the temperature environment quality in the greenhouse.

2. Materials and Methods

2.1. Multisensor Distribution Model Based on Data Fusion. Multisensor data fusion refers to the fusion of data collected by different knowledge sources and sensors to achieve a better understanding of observed phenomena. The moving least square method selected in this paper belongs to data layer fusion, as shown in Figure 1. First, the observation data of all sensors are fused, and then feature vectors are taken from the fused data for judgment and recognition. Data layer fusion does not have the problem of data loss, and the result is the most accurate, but it has a high requirement on system communication bandwidth [17].

2.2. Moving Least Squares

2.2.1. Establishment of Fitting Function. In the local region of a fitting function selected, the fitting function is [18–23]:

$$f(x) = \sum_{i=1}^{m} h_i(x)\beta_i(x) = h^T(x)\beta(x). \quad (1)$$

In formula (1), $f(x) = \sum_{i=1}^{m} h_i(x)\beta_i(x) = h^T(x)\beta(x)$, $h(x) = [h_1(x), h_2(x), \ldots, h_m(x)]^T$ is called the basis function vector, which is a complete polynomial of order k, and m is the number of terms of the basis function. $\beta(x) = [\beta_1(x), \beta_2(x), \ldots, \beta_m(x)]^T$ is the undetermined coefficient of the fitting function, which is compared with the traditional least square method. $\beta(x) \neq C$, the undetermined coefficient is the spatial coordinate function of x.

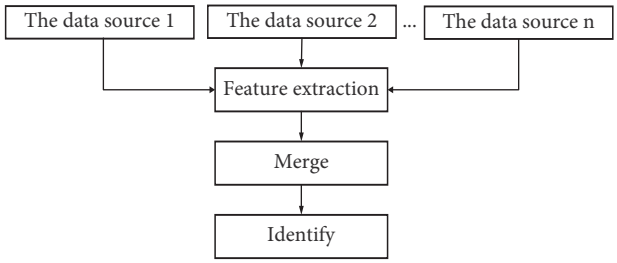

Figure 1: Flowchart of data layer fusion.

Consider the weighted discrete normal form of residuals below:

$$J = \sum_{I=1}^{n} \omega(x - x_I)\left[f(x) - y_I\right]^2 = \sum_{I=1}^{n} \omega(x - x_I)\left[h^T(x)\beta(x) - y_I\right]^2. \tag{2}$$

In formula (2), n is the number of nodes in the solution region, $f(x)$ is the fitting function, y_I is the node value at $x = x_I$, $y_I = y(x_I)$ and $\omega(x - x_I)$ is the weight function of the node x_I. In order to determine the coefficient $\beta(x)$, formula J should take a minimum value, so the partial derivative of its coefficient $\beta(x)$ should be calculated as follows:

$$\frac{\partial J}{\partial \beta} = A(x)\beta(x) - B(x)y = 0, \qquad \beta(x) = A^{-1}(x)B(x)y. \tag{3}$$

Substitute the following equations into formula (3)

$$A(x) = \sum_{I=1}^{n} \omega(x - x_I)h(x_I)h^T(x_I),$$
$$B(x) = [\omega(x - x_1)h(x_1), \omega(x - x_2)h(x_2), \ldots, \omega(x - x_n)h(x_n)],$$
$$y^T = [y_1, y_2, \ldots, y_n]. \tag{4}$$

By substituting the formula $\beta(x)$ into f(x), the moving least square function is obtained as follows:

$$f(x) = \sum_{I=1}^{n} \theta_I^k(x)y_I = \vartheta^k(x)y, \tag{5}$$

where $\vartheta^k(x)$ is called the form function and k represents the order of the basis function.

$$\vartheta^k(x) = \left[\theta_1^k(x), \theta_2^k(x), \ldots, \theta_n^k(x)\right] = p^T(x)A^{-1}(x)B(x). \tag{6}$$

2.2.2. Weight Function. Weight function plays an important role in moving least square method. The weight function $\omega(x - x_I)$ in the moving least squares method should be compactly supported, that is, the weight function is not equal to zero in a subdomain of x, but is zero outside this subdomain, which is called the support domain of the weight function (that is, the influence region of x). Generally, the circle is chosen as the supporting domain of the weight function (see Figure 2), and its radius is denoted as $R_{\max}$. Due to the compact support of the weight function, only these data points contained in the influence region have an effect on the value of point x.

The selection process of the influence radius is as follows:

(1) First, the overall characteristic line is obtained through linear fitting;

(2) Cycle each discrete point x again:

(2.1) Determine the support domain size of discrete point x;

(2.2) Determine the key nodes contained in the support domain of point x:

(2.2.1) Translate the overall feature line to point x;

(2.2.2) Calculate the distance between all nodes in x support domain and the overall feature line;

(2.2.3) Select several nodes closest to the overall feature line as key nodes and eliminate other nodes in the support domain;

(3) End the cycle of discrete points and use the moving least square method for curve fitting.

The weight function, $\omega(x - x_I)$, should be nonnegative and decreasing monotonically as $x - x_{I2}$ increases. The weight function should also have some smoothness because the fitting function inherits the continuity of the weight function. The commonly used weight function is spline function, $R = x - x_I$, $\overline{R} = R/R_{\max}$ then cubic spline weight function is shown in formula (10):

$$\omega(\overline{R}) = \begin{cases} \dfrac{2}{3} - 4\overline{R}^2 + 4\overline{R}^3, \left(0 \le \overline{R} \le \dfrac{1}{2}\right), \\ \dfrac{4}{3} - 4\overline{R} + 4\overline{R}^2 - \dfrac{4}{3}\overline{R}^3, \left(\dfrac{1}{2} < \overline{R} \le 1\right), \\ 0, \ (\overline{R} > 1). \end{cases} \tag{7}$$

Figure 3 shows the cubic spline function curve, where the independent variables are the values of $\overline{R}$, and the dependent variables are the values of the mapped spline function. The influence region should contain enough nodes to make $A(x)$ in (5) invertible.

Verified in the literature [15], in using the moving least-square method of curve fitting, the right to choose seven times spline function fitting curve effect is the best, but the large amount of calculation, and according to the example of this chapter, choose three to five times spline weight function was proposed to fit, take the high number of elected five or six times spline weight function. The fitting result is not as good as choosing cubic and quartic spline weight function. In general curve fitting, we can get better fitting results by using cubic spline weight function.

The derivation of the square matrix $A(x)$ invertibility condition of the weight function is as follows: Suppose there is a node $\{x_{i1}, x_{i2}, \ldots, x_{in}\}$ in the support domain of point x, and the total number of nodes is N. x_i is the i node. Due to

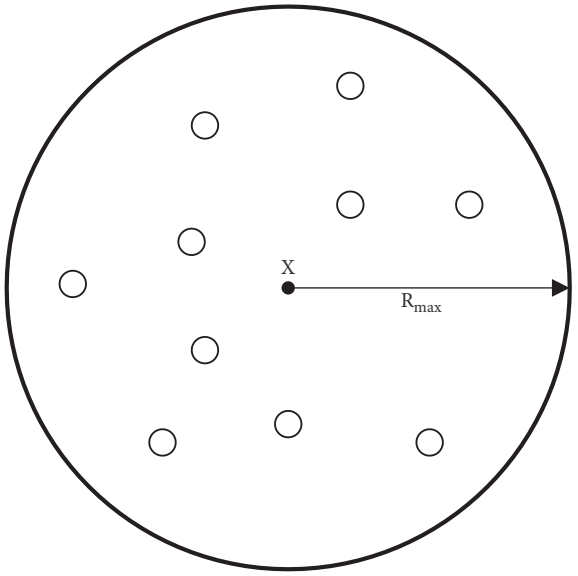

Figure 2: Weight function support domain.

$W(x) = diag(w_1(x), w_2(x), \ldots, w_n(x))$, when node x_i is in the support domain of x, there is $w_i > 0$, otherwise there is $w_i = 0$ $(1 \le i \le N)$, so there is a permutation matrix B, which makes $BWB^T = diag(w_{i1}w_{i2}, ..., w_{in}, 0, ..., 0)$, so there is $A = P^T WP = P^T(B^T B)W(B^T B)P = (BP)^T(BWB^T)(BP)$.

Moreover, the first n behavior of the matrix BP:

$$P_I = \begin{bmatrix} p_1(x_{i1}) \\ p_1(x_{i2}) \\ \vdots \\ p_1(x_{\text{in}}) \\ p_2(x_{i1}) \\ p_2(x_{i2}) \\ \vdots \\ p_2(x_{\text{in}}) \\ \cdots \\ \cdots \\ \ddots \\ \cdots \\ p_m(x_{i1}) \\ p_m(x_{i2}) \\ \vdots \\ p_m(x_{\text{in}}) \end{bmatrix}. \tag{8}$$

Write $W_{11}(x) = diag(\mathrm{w_{i1}(x)}, \mathrm{w_{i2}(x)}, \ldots, \mathrm{w_{in}(x)})$, P_2 as the matrix formed by the last $(N - n)$ lines of BP, then

$$A = (BP)^T\left(BWB^T\right)(BP) = \begin{pmatrix} P_1^T & P_2^T \end{pmatrix} \begin{pmatrix} W_{11} & 0 \\ 0 & 0 \end{pmatrix}\begin{pmatrix} P_1 \\ P_2 \end{pmatrix} = P_1^T W_{11} P_1. \tag{9}$$

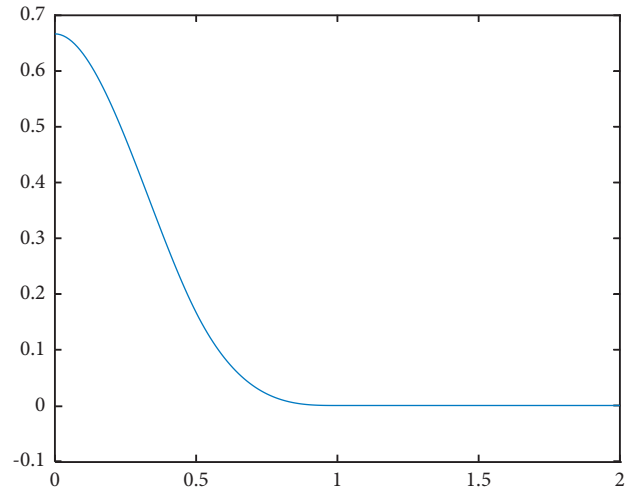

Figure 3: Cubic spline function curve.

Because W_{11} is positive definite, so $rank(A) = rank(P_1^T W_{11} P_1) = rank(P_1)$.

If and only if the column vector P_I is linearly independent, p(x) is linearly independent with respect to this node $\{x_{i1}, x_{i2}, \ldots, x_{in}\}$, rank$(P_1) = m$, so $A(x)$ is invertible if and only if our basis vector $p(x)$ is linearly independent with respect to these n nodes. In this way, when $p(x)$ is a two-dimensional linear basis, the column vectors of P_1 are linearly independent if and only if there are at least three non-collinear points in the support domain. When $p(x)$ is a two-dimensional quadratic basis, the column vectors of P_1 are linearly independent if and only if there are at least six points in the support domain, and these points are not on any one of the conics.

2.2.3. Optimal Sensor Position Model. The method based on moving least squares is used to select sensor locations that best represent the overall greenhouse environment. In addition, statistical indicators such as root mean square error (RMSE) and mean absolute percentage error (MAPE) are calculated to verify the accuracy of the measured data at the location selected by the moving least squares method.

RMSE is a measure of the difference between a composite trend and a reference trend. MAPE is a measure of predictive accuracy as a percentage of errors. Therefore, MAPE is used to assess the accuracy of the composite trend relative to the reference trend.

The comparison between RMSE and standard deviation is needed: Standard deviation is used to measure the dispersion degree of a set of numbers, while root mean square error is used to measure the deviation between the observed value and the true value. Their research objects and purposes are different, but the calculation process is similar. MAPE is expressed as a percentage, independent of proportion and can be used to compare predictions of different proportions.

Using these two statistics, the difference between the reference trend and the combined trend based on the number of sensors installed can be assessed. RMSE and

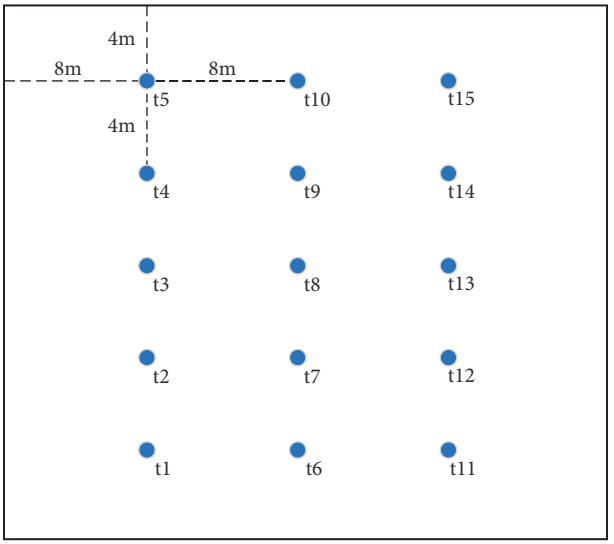

Figure 4: Sensor position.

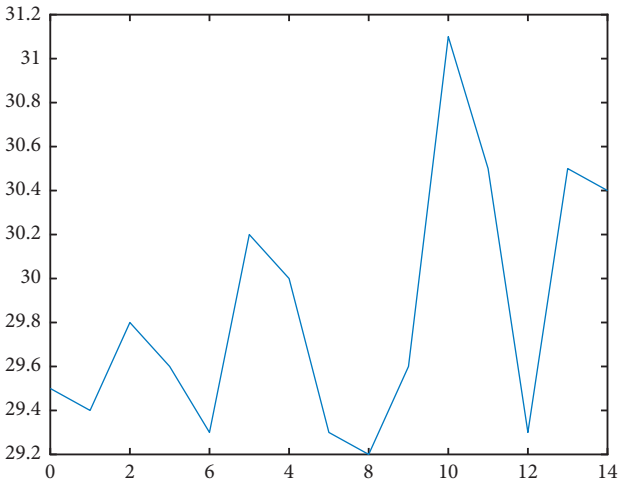

Figure 5: Measured temperature data.

Table 1: Specific measurement data.

Location	Temperature measurement data (°C)
t1	29.5
t2	29.4
t3	29.8
t4	29.6
t5	29.3
t6	30.2
t7	30.0
t8	29.3
t9	29.2
t10	29.6
t11	31.1
t12	30.5
t13	29.3
t14	30.5
t15	30.4
The minimum value (°C)	29.20
The maximum value (°C)	31.10
The average (°C)	29.85
The standard deviation	0.57
The range	1.90

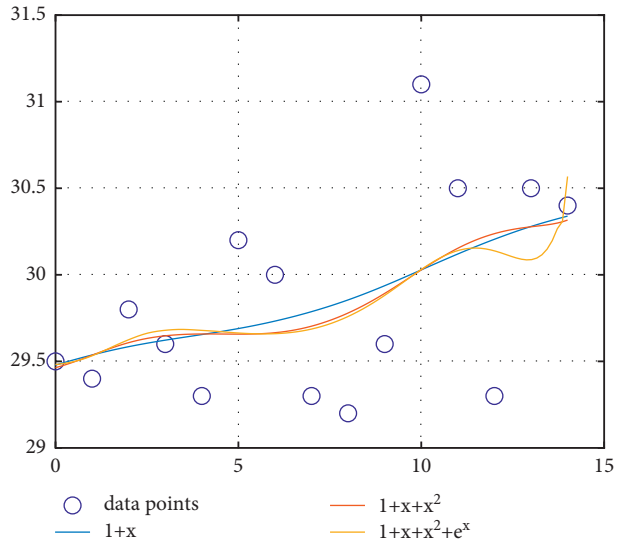

Figure 6: Moving least square simulation curve.

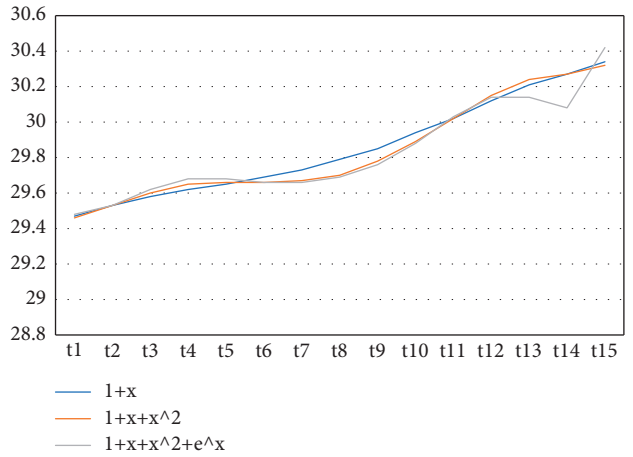

Figure 7: Error method to simulate the curve.

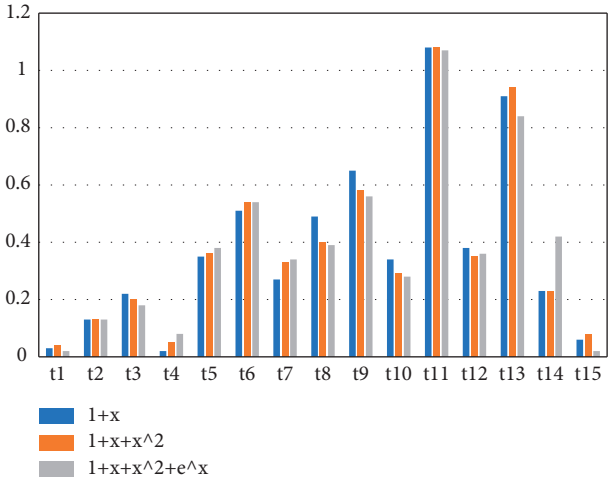

Figure 8: Relative error.

Table 2: Specific error data.

Location	The relative error		
	$1 + x$	$1 + x + x^2$	$1 + x + x^2 + e^x$
t1	0.03	0.04	0.02
t2	−0.13	−0.13	−0.13
t3	0.22	0.20	0.18
t4	−0.02	−0.05	−0.08
t5	−0.35	−0.36	−0.38
t6	0.51	0.54	0.54
t7	0.27	0.33	0.34
t8	−0.49	−0.40	−0.39
t9	−0.65	−0.58	−0.56
t10	−0.34	−0.29	−0.28
t11	1.08	1.08	1.07
t12	0.38	0.35	0.36
t13	−0.91	−0.94	−0.84
t14	0.23	0.23	0.42
t15	0.06	0.08	−0.02
The minimum value (°C)	1.08	1.08	1.07
The maximum value (°C)	−0.91	−0.94	−0.84
The average (°C)	0.378	0.373	0.374

Table 3: Statistical index.

Location	Statistical index					
	$1 + x$		$1 + x + x^2$		$1 + x + x^2 + e^x$	
	RMSE	MAPE	RMSE	MAPE	RMSE	MAPE
t1	0.03	0.006	0.04	0.009	0.02	0.004
t2	0.09	0.03	0.09	0.03	0.09	0.03
t3	0.14	0.08	0.13	0.08	0.12	0.07
t4	0.12	0.08	0.12	0.09	0.11	0.09
t5	0.19	0.16	0.19	0.17	0.20	0.17
t6	0.27	0.28	0.28	0.29	0.28	0.29
t7	0.27	0.34	0.29	0.36	0.29	0.37
t8	0.30	0.45	0.30	0.45	0.30	0.46
t9	0.36	0.60	0.34	0.59	0.34	0.59
t10	0.36	0.67	0.34	0.65	0.33	0.65
t11	0.47	0.91	0.46	0.88	0.45	0.88
t12	0.46	0.99	0.45	0.96	0.44	0.96
t13	0.51	1.20	0.50	1.17	0.49	1.15
t14	0.49	1.25	0.49	1.22	0.48	1.24
t15	0.48	1.26	0.47	1.24	0.46	1.24

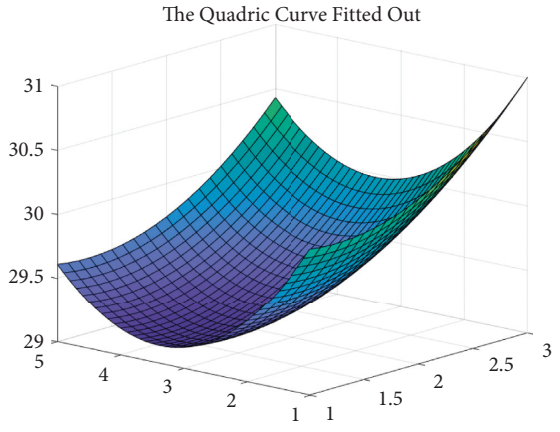

Figure 9: Quadric curve fitted out.

MAPE are calculated using equations, and detailed calculations are shown in formulas (10) and (11).

$$RMSE = \sqrt{\frac{\sum_{i=1}^{Z}(S_i - C_i)^2}{Z}}, \tag{10}$$

$$MAPE = \frac{100}{Z} \cdot \sum_{i=1}^{Z}\left|\frac{S_i - C_i}{S_i}\right|. \tag{11}$$

Here, RMSE is expressed in ℃, MAPE is expressed in percentage %, Z is the total amount of data, S_i is the value of the reference trend at a particular time, and C_i is the combined value of the trend at a particular time.

Compared with the traditional error method, the method based on the lower basis function is adopted to obtain the shape function with higher continuity and

compatibility by selecting appropriate weight function, and the numerical error after fitting is smaller. Substitute formulas (10) and (11) into A(x) and B(x) to obtain formulas (12) and (13).

$$A(x) = \sum_{\mathrm{I}=1}^{n} \frac{\mathrm{RMSE}}{\mathrm{MAPE}} \times \mathrm{h}(x_I) h^T(x_I), \tag{12}$$

$$B(x) = \left[\frac{\mathrm{RMSE}}{\mathrm{MAPE}_1} \cdot h(x_1), \frac{\mathrm{RMSE}}{\mathrm{MAPE}_2} \cdot h(x_2), \ldots, \frac{\mathrm{RMSE}}{\mathrm{MAPE}_n} \cdot \cdot h(x_n) \right]. \tag{13}$$

3. Results and Discussion

3.1. Descriptive Analysis of Environmental Data. The internal environment of the experimental greenhouse was monitored, and temperature sensors were installed at 15 positions in the greenhouse [24], SHT 71, Sensirion, a Switzerland sensor, error range ±0.1 ˚C, as shown in Figure 4. The measured data were obtained by experimental temperature collection in summer (May-June), and the broken line graph of temperature data relative to position coordinates was drawn, as shown in Figure 5. After excluding missing data and rough error, the data were substituted into the moving least square model for verification experiment. Specific data are shown in Table 1.

In order to verify the effectiveness of the moving least square method, this paper selects different weight functions for comparison simulation under the condition of using the same bar function and quadratic basis respectively. Suppose that during the simulation, the range of influence area is 0.3 m, and samples are taken every 10 minutes. Under the same conditions, three different weight functions are simulated and compared, and the simulation results are output as simulated temperature curves. The results are shown in Figure 6, which is a simulated data graph by the moving least square method. Figure 7 is the actual measurement data connection diagram. The error function is analyzed, and the results are shown in Figure 8 and Table 2. The ordinate of Figures 6 and 7 is temperature in ˚C.

As can be seen from Figure 8, when the system model is established and the weight function characteristics are known, the moving least squares method has a good curve fitting accuracy and memory stability. However, when the weight function changes, its error characteristics will change. It can be seen from Figure 7 that the weight function with higher order has better fitting effect. When the system adopts the moving least square method, the error data of T11 and T13 are excluded due to the fact that there are also sensors in the vent. During the whole simulation process, according to the analysis and calculation of the error and combined with the data in Table 2, the optimal sensor can be located at the T10 sensor with the error closest to the fitting value, namely, the central sensor.

3.2. Validation of Experimental Data. In order to further verify the practicability of the proposed algorithm and consider the feasibility of the experiment, root mean square error (RMSE) and mean absolute percentage error (MEAN absolute percentage error) of statistical indicators are used for experimental verification. The results are shown in Table 3 and Figure 9.

As shown in Table 3, the error variation trend of the data of statistical indicators and is basically the same as that of the moving least squares method, that is, the position prediction model based on the moving least squares method is verified. At the same time, it can be seen from the temperature simulation surface shown in Figure 9 that the temperature measurement error of the sensor in the center of the greenhouse is consistent with the trend of the simulation error [25, 26].

4. Conclusion

In this paper, a simulation system based on the moving least square method is proposed, which overcomes the divergence problem of traditional error analysis under different weight functions. Based on the moving least square method, the optimal sensor position algorithm selects the corresponding weight function by judging the statistical index. When the error appears divergence, the corresponding position can be eliminated in time to avoid mismeasurement. The shortcoming of the algorithm is that the error stability of the moving least square method needs to be further improved when the weight function of low order is adopted. Therefore, in this paper, the moving least square method is used to study the best monitoring point of the sensor in the greenhouse, and determine the most suitable installation position of the sensor in the greenhouse, and improve the control effect of the system temperature control device and the temperature environment quality in the greenhouse.

An adaptive control model can be added to improve the control accuracy of greenhouse parameters. In order to further reduce static errors, a genetic factor proposed in [27] is used to summarize the historical errors, thus effectively improving the system stability. We can take advantage of the adaptive control system for the later research of the estimation error [28] and minimize the cost function of the fixed time by adaptive control scheme, in order to shorten the time of the system state to reach sliding mode surface [29] and the use of the finite time adaptive algorithm based on parameter estimation error [30], make more accurate measurement scheme, etc. In order to improve the stability of temperature measurement system, the Lyapunov stability theoretical analysis method proposed by [31] can be used.

Data Availability

The data used to support the findings of this study are available from the corresponding author upon request.

Conflicts of Interest

The authors declare that they have no conflicts of interest.

Acknowledgments

This research was funded by the following projects: the Key Research and Development Project in Shandong Province (2019GGX101008) and College Students Innovation and Entrepreneurship Training Program (X202110424179).

References

[1] D. Cafuta, "Developing a modern greenhouse scientific research facility—a case study," *Sensors*, vol. 21, no. 8, p. 2575, 2021.

[2] J. Jung, A. Tok, and S. G. Ritchie, "Determining optimal sensor locations under uncertainty for a truck activity monitoring system on California freeways," *Journal of Intelligent Transportation Systems*, vol. 25, no. 3, 2019.

[3] D. Wang, J. Yin, T. Tang, R. Liu, and Z. Wu, "A two-step weighted least-squares method for joint estimation of source and sensor locations: a general framework," *Chinese Journal of Aeronautics*, vol. 32, no. 2, 2018.

[4] L. P. F. Rodriguez, J. A. Tupaz, and M. C. Sánchez, "Sensor location for nonlinear state estimation," *Journal of Process Control*, vol. 100, 2021.

[5] L. Teng, Y. Pan, K. Tong, C. E. Ventura, and C. W. de Silva, "A multi-scale attention neural network for sensor location selection and nonlinear structural seismic response prediction," *Computers & Structures*, vol. 248, 2021.

[6] P. Peng and G. Chen, "Method for optimizing the VIV monitoring sensor locations on deepwater drilling riser," *China off Shores Oil and Gas*, vol. 21, no. 3, pp. 204–206, 2009.

[7] X. Wang and H. Qi, "Study on optimal location of sensor placed in airtight container," *Huazhong Univ. of Sci. & Tech (Nature Science Edition)*, vol. 6, pp. 55-56, 2004.

[8] W. Bao, L. Guo, T. Cui, M. Lin, and J. Niu, "Optimal sensor location of scramjet combustor," *Journal of Aerospace Power*, vol. 3, pp. 475–479, 2007.

[9] S. Zhao, S. S. Yuriy, K. A. Choon, and C. Zhao, "Probabilistic monitoring of correlated sensors for nonlinear processes in state-space," *IEEE Transactions on Industrial Electronics*, vol. 67, no. 3, pp. 2294–2303, 2020.

[10] I. Seginer, G. Shina, L. D. Albright, and L. S. Marsh, "Optimal temperature setpoints for greenhouse lettuce," *Journal of Agricultural Engineering Research*, vol. 49, pp. 209–226, 1991.

[11] J. Dai, W. Luo, X. Qiao, and C. Wang, "Model-based decision support system for greenhouse heating temperature set point optimization," *Transactions of the CSAE*, vol. 11, pp. 187–191, 2006.

[12] Y. Ji, T. Li, M. Zhang, and S. Sha, "Design of CO2 fertilizer optimizing control system on WSN," *Transactions of the Chinese Society for Agricultural Machinery*, vol. 46, no. S1, pp. 201–207, 2015.

[13] S. Lee, I. Lee, U. Yeo, R. Kim, and J. Kim, "Optimal sensor placement for monitoring and controlling greenhouse internal environments," *Biosystems Engineering*, vol. 188, 2019.

[14] J. Liu, *Fitting and Interpolation Foe Curve and Surface from Scattered Data Using Moving Least Squares Method*, Zhejiang University, Zhejiang, China, 2011.

[15] H. Ni, *Research on Some Problems of Moving Least Square Method*, Zhejiang Sci-Tech University, Zhejiang, China, 2011.

[16] Y. Cheng, "Research progress and review of moving least square method," *Computer Aided Engineering*, vol. 18, no. 2, pp. 5–11, 2009.

[17] X. Nie, *Preliminary Study on Data Fusion Algorithm and its Application in Data Acquisition System*, Zhejiang University, Zhejiang, China, 2006.

[18] C. Zhong, L. Zhang, S. Yang, and Z. Li, "A weighted fusion algorithm of multi-sensor based on the Principle of Least Squares," *Chinese Journal of Scientific Instrument*, vol. 4, pp. 427–430, 2003.

[19] F. Mirzaee, E. Solhi, and S. Naserifar, "Approximate solution of stochastic Volterra integro-differential equations by using moving least squares scheme and spectral collocation method," *Applied Mathematics and Computation*, vol. 410, 2021.

[20] M. Hosseininia, M. H. Heydari, F. M. Maalek Ghaini, and Z. Avazzadeh, "A meshless technique based on the moving least squares shape functions for nonlinear fractal-fractional advection-diffusion equation," *Engineering Analysis with Boundary Elements*, vol. 127, 2021.

[21] M. Mohammad Javad, "Numerical analysis of the Volterra differential equations via a combination of evolutionary algorithms with moving least squares and finite difference methods," *Journal of Engineering*, vol. 3, 2021.

[22] H. Jiang, Y. Chen, X. Zheng, S. Jin, Q. Ma, and M. Shaat, "A study on stable regularized moving least-squares interpolation and coupled with SPH method," *Mathematical Problems in Engineering*, vol. 2020, Article ID 9042615, 28 pages, 2020.

[23] M. Arehpanahi and H. R. Jamalifard, "Time-varying magnetic field analysis using an improved meshless method based on interpolating moving least squares," *IET Science, Measurement & Technology*, vol. 12, no. 6, 2018.

[24] S. Lee, I. Lee, S. Lee et al., "Dynamic energy exchange modelling for a plastic-covered multi-span greenhouse utilizing a thermal effluent from power plant," *Agronomy*, vol. 11, no. 8, 2021.

[25] P. Shi, Q. Guo, and C. Xu, "Temperature field analysis of greenhouse based on moving least square method," *Agricultural Research and Application*, no. 2, pp. 37–41, 2015.

[26] Q. Zeng and D. Lu, "Curve and surface fitting based on moving least-squares methods," *Journal of Engineering Graphics*, vol. 1, pp. 84–89, 2004.

[27] B. Sun, Y. You, Z. Zhang, C. Li, and K. Liu, "Modelling and simulation of an intelligent photovoltaic controller based on variable step algorithm of versoria," *Complexity*, vol. 2020, 2020.

[28] S. Wang, J. Na, and Y. Xing, "Adaptive optimal parameter estimation and control of servo mechanisms: theory and experiment," *IEEE Transactions on Industrial Electronics*, vol. 68, 2019.

[29] S. Xie and Q. Chen, "Adaptive nonsingular predefined-time control for attitude stabilization of rigid spacecrafts," *IEEE Transactions on Circuits and Systems--II: Express Briefs*, vol. 69, no. 1, pp. 189–193, 2022.

[30] J. Na, Y. Huang, X. Wu, S. Su, and G. Li, "Adaptive finite-time fuzzy control of nonlinear active suspension systems with input delay," *IEEE Transactions on Cybernetics*, vol. 50, 2019.

[31] S. Wang, S. Li, Q. Chen, X. Ren, and H. Yu, "Funnel tracking control for nonlinear servo drive systems with unknown disturbances," *ISA Transactions*, 2021.

Hindawi
Complexity
Volume 2022, Article ID 2847785, 19 pages
https://doi.org/10.1155/2022/2847785

WILEY | Hindawi

Research Article

Incremental Adaptive Control of a Class of Nonlinear Nonaffine Systems

Yizhao Zhan, Shengxiang Zou, Xiongxiong He, and Mingxuan Sun

Data-driven Intelligent Systems Laboratory, College of Information Engineering, Zhejiang University of Technology, Hangzhou 310023, China

Correspondence should be addressed to Mingxuan Sun; mxsun@zjut.edu.cn

Received 21 January 2022; Accepted 15 March 2022; Published 7 April 2022

Academic Editor: Chih-Chiang Chen

As a class of familiar nonlinear systems, nonaffine systems are frequently encountered in practical applications. Currently, in the context of learning control, there is a lack of research results about such general class of nonlinear systems, especially for the case of performing infinite interval tasks. This article focuses on the incremental adaptive control for nonlinear systems in nonaffine form, without requiring periodicity or repeatability. Instead of using the integral adaptation, incremental adaptive mechanisms are developed and the corresponding control schemes are presented, by which the numerical integration for implementation can be avoided. With the proposed incremental adaptation, the implicit function theorem is introduced to solve the intractability problem of the nonaffine structure. The robustness (robust convergence) of the tracking error is characterized, with the aid of a proposed key lemma, while the boundedness of all the variables is examined. Numerical results are presented to verify the effectiveness of the proposed control design.

1. Introduction

In recent years, with the acceleration of energy transition, complex energy systems have become a fascinating research area. In particular, more and more attention has been paid to its complex nonlinear dynamic analysis and advanced control method design. Many complex systems in the real world can be described by nonaffine systems, such as wind turbine systems, chemical reactions, and flight control systems. Due to its important theoretical and practical significance, plenty of research effort has been paid on the topic over the years. Research works devoted in this topic can be found in many publications (see [1–6] and references therein).

In comparison with affine systems, the challenge for nonaffine systems is that the control input couples with the system state and acts on the system dynamics in a nonlinear implicit way. Therefore, there is usually no concept of control gain or control direction, which in fact increases the difficulty of controller design. By utilizing Taylor series expansion [2, 5], median value theorem [3], and Hadamard theorem [4], the system model subjected to nonaffine characteristics can be simplified before analysis and design. With these mathematical approximations, nonaffine systems can be expressed as an affine-like system or an exact affine form within a neighborhood of the equilibrium. In [2], by introducing the implicit function theorem, the existence of an ideal controller for nonaffine system stabilization was demonstrated. To deal with nonaffine problems, the dynamic inversion technology via time-scale separation was proposed for the system dynamics that are exactly or partially known [6]. Using the singular perturbation theory, this dynamic approach has been shown to be effective in obtaining equivalent controllers that satisfy the control requirements. In order to further reduce the dependence on the knowledge of system dynamics, the approximation technology [7], represented by the neural network (NN) and the fuzzy logic system (FLS), is widely used in nonaffine systems [8–14], by applying the well approximation ability on compact sets. In existing work, many efficient adaptive neural/fuzzy control schemes have been developed. In [8], the proposed neural control synthesis method avoids the

fixed-point problem brought by nonaffine structures. Exploiting input-to-state stability and the small gain theorem, the adaptive neural control design was proposed in [14] for the nonaffine systems with a mild assumption, which not only can overcome the problem of intractability when controlling nonaffine nonlinear systems, but also has the characteristics of dynamic learning. Regarding the NN approximation errors, [12] merged it with the external disturbance as a compounded disturbance and designed the disturbance observer for disturbance compensation. With the stochastic generalized Takagi–Sugeno fuzzy approximation models, an approach to a stabilization controller design was developed [13]. These results were generalized to MIMO nonaffine nonlinear systems [9, 10]. More recently, interesting results have been ever-increasing and reported in [15–23], wherein various adaptive NN/FLS-based control schemes have been shown to efficiently tackle challenges such as input saturation [15], nonlinear faults [17, 19], state/output constraints [23], and the consensus tracking control problem for multiagent systems [20].

In the above methods, a variety of effective adaptive mechanisms were proposed, in order to ensure the stability and convergence of the closed-loop system. Taking from the perspective of construction, these adaptive laws are integral adaptation, which are conducted in the time domain. As an alternative and supplement, the parameter adaptive learning mechanisms in the iteration domain are provided, in the context of learning control. As a control method that can significantly improve the control performance of systems that perform repeating tasks, learning control has been well established and comprehended theoretically and technically during the past several decades [24–35]. In the context of adaptive control, the theoretical frameworks of adaptive iterative learning control [28, 29, 32, 33] and adaptive repetitive control [25, 30, 31] are gradually developed and formed. Both are important research topics in the field of adaptive control and learning control, and different from traditional learning control with *input learning* features [24, 26], they emphasize *parameter learning*. Systematic methodologies were proposed in [25, 28], where [25] explored the Lyapunov-like approach for a repetitive controller design, while [28] developed the composite-energy-function approach for iterative learning control schemes. The effectiveness of the Lyapunov-like synthesis method in learning control performance analysis was further systematically demonstrated in [29]. In addition to the parameter adaptation in the iteration domain, adaptive learning control also provides the time-domain parameter adaptation [27], which can still perform well as the conventional adaptive control. In [32, 33], the composite learning algorithm was proposed, by combining the time- and iteration-domain parameter adaptations. Moreover, in [34], the projection modification was suggested, through which the parameter estimates can be guaranteed vary within a prespecified region. Similar correction ideas were also reflected in [30, 31], in which the properties of saturated functions [25] have been mainly applied, and the partially [30] and fully saturated [31] learning algorithms were developed. In [35], the Barbalat-like lemma was proposed to further address the problem of uniform convergence of learning control systems. The superiority and efficiency of learning control depend largely on the repeatability of system operation. However, there are often potential implementation problems for such strict requirements, which limit the practical application of learning control. To relax some fundamental constraints encountered, a great deal of efforts have been put into related research topics in recent years, and the main results are concentrated on the initial condition issue [36–38], the nonequal task problem [39–42], and so on. For the arbitrary initial condition, various effective techniques have been proposed to solve this problem, including the boundary layer method [36], the trajectory rectifying strategy [37], and the error tracking approach [38]. In addition, the identical trial length assumption was removed in the framework of adaptive learning control, and for the parameter learning, the reference signals are permitted to vary with iteration, and the controller design can be easily conducted [39–42]. With the rapid development of adaptive learning control theory, numerous results of the above control methods have been successfully applied in various practical systems [43–46].

It should be pointed out that most of the above-mentioned studies on learning control focus on the tracking problem on a finite time interval or that of tracking a periodic reference signal. In addition, the existing learning control theories mainly concern with the convergence analysis. At present, there is still a lack of relevant research for the learning systems performing the task over an infinite interval, without involving repositioning and repeatability [47–49]. Furthermore, few results on adaptive control have been available to tackle such nonlinear systems with nonaffine form based on learning control.

In this article, novel incremental adaptive control design methods are presented for nonaffine systems performing infinite-duration tasks, where the incremental adaptive mechanisms are exploited, instead of using the conventional integral adaptation. Drawing on existing learning control strategies, numerous incremental adaptations are developed and the corresponding performances are characterized, including the so-called closed-loop, open-loop, and fully saturated learning mechanisms. With the proposed incremental adaptation, the numerical integration required by the implementation for an integral adaptive algorithm is avoided. What's more, systems allow arbitrary bounded reference signals and there is no periodicity or repeatability requirements. Moreover, the implicit function theorem is applied to deal with the nonaffine-in-control problem, based on the incremental adaptation. Furthermore, a key lemma is provided as a technical tool, which can be used for the robust convergence analysis of incremental adaptive control (IAC) systems.

This article is organized as follows. The problem formulation is provided in Section 2, and preliminaries are given, which are helpful for the performance analysis of the IAC algorithms. In Section 3, the IAC problem for a simple class of uncertain nonaffine systems is addressed, in which the basic forms of the incremental adaptation with the corresponding system synthesis are described. In Section 4, the learning control design methods are introduced to the

high-order nonlinear nonaffine systems, and both the IAC control design and performance analysis are presented. In Section 5, the control performance is verified by the numerical examples. The conclusion is finally drawn in Section 6.

2. Problem Formulation and Preliminaries

Let us begin with the following systems with unknown parameters:

$$\dot{x} = \theta^T \varphi(x) + u, \tag{1}$$

where x and u are the scalar system state and the control input, respectively, $\theta \in R^n$ denotes a vector of unknown parameters, and $\varphi(x) \in R^n$ represents a known state-dependent vector-valued function, satisfying that φ is bounded as the state is bounded.

The control goal is to design an adaptive controller for system (1) such that the system state x converges to 0, that is, $\lim_{t\longrightarrow\infty} x(t) = 0$, while the boundedness of all signals in the closed-loop system are guaranteed.

For the adaptive system consisting of system (1), the controller can be designed as follows:

$$u = -\widehat{\theta}^T \varphi(x) - \beta x, \tag{2}$$

and the adaptation law

$$\dot{\widehat{\theta}} = \gamma \varphi(x) x, \tag{3}$$

where $\beta, \gamma > 0$ are adjustable parameters, and $\widehat{\theta}$ is the estimate of θ. Let us denote by $\widetilde{\theta} = \theta - \widehat{\theta}$ the estimation error. With control law (2), (1) can be expressed as

$$\dot{x} = \widetilde{\theta}^T \varphi(x) - \beta x. \tag{4}$$

To ensure the convergence of the adaptive system, the Lyapunov function $V = x^2/2 + (2\gamma)^{-1}\widetilde{\theta}^T\widetilde{\theta}$. is chosen. By applying (3), the derivative of V along (4) can be rewritten as $\dot{V} = -\beta x^2$, which implies that $\dot{V}$ is negative semidefinite; that is, $V(t)$ is bounded, as $V(0)$ is bounded. Because of the boundedness of V, the boundedness of x and $\widehat{\theta}$ is obvious, and then, we can say that $\dot{x}$ and u are bounded, as well as $\int_0^t x^2(s)\mathrm{d}s < +\infty$, as $t \longrightarrow \infty$. Invoking Barbalat's lemma shows that $\lim_{t\longrightarrow\infty} x(t) = 0$.

Now let us look into (3), which is usually referred to as the integral adaptive law, because it can be rewritten as

$$\widehat{\theta}(t) = \widehat{\theta}(0) + \gamma \int_0^t \varphi(x(s)) x(s) \mathrm{d}s, \tag{5}$$

which implies that, for $t > T$, where T is a positive constant,

$$\widehat{\theta}(t - T) = \widehat{\theta}(0) + \gamma \int_0^{t-T} \varphi(x(s)) x(s) \mathrm{d}s. \tag{6}$$

From the above two equations, we obtain

$$\widehat{\theta}(t) = \widehat{\theta}(t - T) + \gamma \int_{t-T}^{t} \varphi(x(s)) x(s) \mathrm{d}s. \tag{7}$$

Furthermore, by the integral mean value theorem, an incremental form of (3) can be given as

$$\widehat{\theta}(t) = \widehat{\theta}(t - T) + T\gamma\varphi(x(\tau)) x(\tau), \tag{8}$$

with τ being a certain moment located between $t - T$ and t.

Looking into the second item of the right-hand side of (8), $T\gamma\varphi(x(\tau))x(\tau)$, both the values of $\varphi(x(\tau))$ and $x(\tau)$ depend on τ, which should be given *a priori*. However, as time varies, τ also changes that the values of these items cannot be determined in advance at different moments. Due to the application of digital control technology, the integral adaptive law (3) can only be approximated in the implementation; that is, $\varphi(x(\tau))x(\tau)$ can be replaced by $\varphi(x(t))x(t)$ or $\varphi(x(t - T))x(t - T)$. Obviously, such these approximations have a deviation from the integral adaptive law (3) itself. In fact, no matter what kind of interpolation is used, the long-term drifting phenomenon may occur, since the small but unavoidable error at each numerical integration step accumulates.

Instead of using the integral adaptation, we intend to explore the incremental adaptive control method and present the corresponding performance analysis of the closed-loop system in detail, aiming at avoiding the numerical integration problems encountered when implementing the integral adaptation.

The following lemmas are useful for the control design and the performance analysis to be presented:

Lemma 1 (mean Value Theorem). *Function f: $[a, b] \longrightarrow R$ is continuous on the closed interval $[a, b]$ and differentiable on the open interval (a, b). Then, there exists $c \in (a, b)$ such that $f'(c) = f(b) - f(a)/b - a$.*

Lemma 2 (implicit Function theorem [2]). *Assume that function f: $R^n \times R \longrightarrow R$ is continuously differentiable, and there is a positive constant d such that for all $(x, u) \in R^n \times R$, $|\partial f(x, u)/\partial u| > d > 0$ holds. Then, there exists only a continuous function g: $R^n \longrightarrow R$ that makes $f(x, g(x)) = 0$.*

Lemma 3 *Let $\{d_k\}$ be a sequence of real numbers (need not be positive). Assume that both sequences of positive numbers $\{f_k\}$ and $\{g_k\}$ satisfy*

$$f_k \le f_{k-1} - g_k + d_k, \tag{9}$$

where f_0 is given and bounded. Then,

(i) if for all k, $|d_k| \le \overline{d}$, then $\lim_{k\longrightarrow\infty} sup g_k \le \overline{d}$;
(ii) As $d_k = 0$, $lim_{k\longrightarrow\infty} g_k = 0$.

Lemma 4 (see [31]) *For $a, b \in R^m$, if a satisfies $b_{i\min} \le a \le b_{i\max}$, then*

$$[(\zeta + 1)a - (\zeta b + \mathrm{sat}(b))]^T \Lambda [(b - \mathrm{sat}(b))] \le 0, \tag{10}$$

where $\zeta \ge 0$ is a constant and $\Lambda > 0$ is a diagonal matrix of appropriate dimensions. In particular, when $\zeta = 0$ and Λ is the identity matrix, $(a - sat(b))^T (b - sat(b)) \le 0$ holds.

Throughout this article, radial basis function neural network (RBFNN) will be used to model nonlinear functions. As an efficient approximation tool, RBFNN is widely used in the adaptive controller design. It has been shown that, by selecting enough neurons, RBFNN can approximate any smooth function on a given compact set with the expected approximation accuracy.

For smooth nonlinear function $f(Z)$: $\Omega_Z \subset R^q \longrightarrow R$, using RBF network $\theta^{*T}\varphi(Z)$, $f(Z)$ can be approximated as

$$f(Z) = \theta^{*T}\varphi(Z) + \varepsilon(Z), \quad \forall Z \in \Omega_Z, \tag{11}$$

where θ^* is an N-dimensional ideal constant weight vector, defined as

$$\theta^* = \arg\min_{\theta \in R^N} \left\{ \sup_{Z \in \Omega_Z} |f(Z)| - \theta^T \varphi(Z) \right\}, \tag{12}$$

where $\theta = [\theta_1, \theta_2, \ldots \theta_N]^T$ is an N-dimensional weight vector, N is the number of neural network nodes, $\varphi(Z) = [\varphi_1(Z), \varphi_2(Z), \ldots \varphi_N(Z)]^T \in R^N$ is the basis vector consisting of a series of basis functions $\varphi_i(Z)$, $i = 1, \ldots, N$, and $\varepsilon(Z)$ is the approximation error that satisfies $\overline{\varepsilon} \geq |\varepsilon(Z)| > 0$, $\forall Z \in \Omega_Z$.

A commonly used basis function is the Gauss function, which has the following form:

$$\varphi_i(Z) = e^{-\|Z - c_i\|^2 / 2b_i^2}, \quad i = 1, 2, \ldots, N, \tag{13}$$

where Z is the network input, $c_i, i = 1, 2, \ldots, N$ are the receptive field centers, and b_i is the width of the Gaussian function. For Gauss RBF networks, the following lemma provides an upper bound on $\varphi(Z)$, which is useful for the convergence analysis to be presented.

Lemma 5. *[7] For Gauss RBF network, let* $\rho = 1/2 \min_{i \neq j} \|\mu_i - \mu_j\|$*, the upper bound of* $\varphi(Z)$ *can be presented as*

$$\|\varphi(Z)\| \leq \sum_{i=0}^{\infty} 3q(i+1)^{q-1} e^{-2\rho^2 i^2 / \zeta^2} = \chi. \tag{14}$$

3. Incremental Adaptive Control Algorithm

For simplify the presentation, we address the problem of trajectory tracking of a simple class of uncertain nonaffine systems as an illustrative example. The proposed IAC strategies are shown to be able to deal with the difficulty in controlling nonaffine nonlinear systems, and the control design will be extended to the higher-order systems.

Let us consider the first-order nonaffine systems:

$$\dot{x} = f(x, u), \tag{15}$$

where $x \in R$ is the system state, $u \in R$ is the control input, and $f(x, u)$: $R \times R \longrightarrow R$ is a smooth unknown nonlinear function.

Define $f_u = (\partial f(x, u))/(\partial u)$, for which the following assumptions are made:

Assumption 1. The sign of f_u *is known, and* $|f_u| > 0$, $\forall (x, u) \in R \times R$.

Assumption 2. There exists a continuous function $\beta(x) > 0$, $\forall x \in R$, *such that* $|\dot{f}_u / f_u| \leq \beta(x)$.

Remark 1. Assumption 1 *means that* $\partial f(x, u)/\partial u$ *is strictly either positive or negative. Without loss of generality, suppose that there is a positive constant* b_f *such that* $f_u \geq b_f > 0$. *It should be noted that in the controller design to be presented, only* Assumptions 1 and 2 *are required, and there is no need to know the true value of* b_f *and the exact expression of* $\beta(x)$.

Here, the control goal is to design the controller u for system (15) to guarantee that the system state x tracks the given desired trajectory x_d with acceptable accuracy, while all closed-loop system signals are ensured to be bounded. For the given desired trajectory $x_d(t)$, both itself and the first derivative with respect to time are bounded. To achieve this control objective, this article proposes IAC approaches for the adaptive control design, with incremental adaptive mechanisms, instead of using the conventional integral adaptation.

3.1. Controller Design. Let us define the tracking error of the system undertaken as $e = x - x_d$. Its derivative can be written as follows, by adding and subtracting $\beta(x)e$:

$$\begin{aligned} \dot{e} &= f(x, u) - \dot{x}_d - \beta(x)e + \beta(x)e, \\ &= -\beta(x)e + f(x, u) + v(x, x_d, \dot{x}_d), \end{aligned} \tag{16}$$

where $v(x, x_d, \dot{x}_d) = -\dot{x}_d + \beta(x)(x - x_d)$. According to Lemma 2, for the given desired trajectory x_d and the system state x, there always exists a smooth function $\alpha(x, x_d, \dot{x}_d)$ such that

$$f(x, u)|_{u=\alpha(x, x_d, \dot{x}_d)} + v(x, x_d, \dot{x}_d) = 0. \tag{17}$$

Therefore, if the controller is taken as $u = \alpha(x, x_d, \dot{x}_d)$, the error system (16) can be rewritten as

$$\begin{aligned} \dot{e} &= -\beta(x)e + f(x, \alpha(x, x_d, \dot{x}_d)) + v(x, x_d, \dot{x}_d), \\ &= -\beta(x)e. \end{aligned} \tag{18}$$

Since $\beta(x) > 0$, according to assumption 2, the error system $\dot{e} = -\beta(x)e$ is asymptotically stable, and e converges to zero asymptotically, that is, $\lim_{t \longrightarrow \infty} e(t) = 0$.

To proceed, we apply RBF network to approximate the unknown smooth nonlinear function $\alpha(x, x_d, \dot{x}_d)$, that is,

$$\alpha(x, x_d, \dot{x}_d) = \theta^T \varphi(z) + \varepsilon(z), \quad z = [x, x_d, \dot{x}_d]^T, \tag{19}$$

where θ represents the weight vector, φ indicates the vector of basis functions, and $\varepsilon(z)$ is the approximation error bounded by $|\varepsilon(z)| \leq \overline{\varepsilon}$, with $\overline{\varepsilon}$ being a positive constant.

Now, the following controller can be designed as

$$u = -\kappa e + \widehat{\theta}^T \varphi(z), \tag{20}$$

where $\kappa > 0$ is the adjustable gain, and $\widehat{\theta}$ is the estimated value of θ, for which the adaptation law is to be presented.

Moreover, by applying Lemma 1, there is a constant $0 < \lambda < 1$ that satisfies

$$f(x,u) - f\left(x, \alpha\left(x, x_d, \dot{x}_d\right)\right) = f_{u_\lambda}\left(u - \alpha\left(x, x_d, \dot{x}_d\right)\right), \quad (21)$$

where $f_{u_\lambda} = \partial f(x,\overline{u})/\partial f(x,\overline{u})|_{\overline{u}=u_\lambda}$, and $u_\lambda = \lambda u + (1-\lambda)\alpha(x, x_d, \dot{x}_d)$. Apparently, $f_{u_\lambda} \geq b_f > 0$ according to Assumption 1.

According to (19) and (21), and using controller (20), then the error dynamics (16) can be rewritten as follows:

$$\begin{aligned} \dot{e} &= -\beta(x)e + f\left(x, \alpha\left(x, x_d, \dot{x}_d\right)\right) + f_{u_\lambda}\left(u - \alpha\left(x, x_d, \dot{x}_d\right)\right) + \upsilon\left(x, x_d, \dot{x}_d\right), \\ &= -\beta(x)e + f_{u_\lambda}\left(-\kappa e - \widetilde{\theta}^T\varphi(z) - \varepsilon(z)\right), \end{aligned} \quad (22)$$

where $\widetilde{\theta} = \theta - \widehat{\theta}$ is the weight estimation error.

3.2. Performance Analysis. For the parameter adaptation, we first consider the following incremental adaptive law:

$$\widehat{\theta}(t) = \begin{cases} \widehat{\theta}(t-T) - \gamma\varphi(z(t))e(t), & t \geq 0, \\ \widehat{\theta}_0, & t \in [-T, 0), \end{cases} \quad (23)$$

where the constant $\widehat{\theta}_0 > 0$ is the initial value of $\widehat{\theta}(t)$, $T > 0$ is the learning cycle, and $\gamma > 0$ is the adjustable parameter. By applying the incremental adaptation (23), we summarize the theoretical results including the boundedness of variables in the closed-loop system and the convergence of the tracking error in the following theorem.

Theorem 1. *Considering the learning control system consisting of system (15) and controller (20), and the learning law (23), under assumptions 1-2. For any bounded initial condition, e, $\int_{t-T}^{t} \|\widehat{\theta}(s)\|^2 ds$ and $\int_{t-T}^{t} u^2(s) ds$ are bounded, and e converges to a neighborhood to the origin whose radius is proportional to $\overline{\varepsilon}$.*

Proof. Let us choose the Lyapunov-like function: $L = (2f_{u_\lambda})^{-1}e^2 + (2\gamma)^{-1}\int_{t-T}^{t} \widetilde{\theta}^T(s)\widetilde{\theta}(s)ds$. Its derivative along (12) can be calculated as

$$\begin{aligned} \dot{L} &= \frac{1}{f_{u_\lambda}} e\left(-\beta(x)e + f_{u_\lambda}\left(-\kappa e - \widetilde{\theta}^T\varphi(z) - \varepsilon(z)\right)\right) - \frac{\dot{f}_{u_\lambda}}{2f_{u_\lambda}^2}e^2 + \frac{1}{2\gamma}\left(\widetilde{\theta}^T(t)\widetilde{\theta}(t) - \widetilde{\theta}^T(t-T)\widetilde{\theta}(t-T)\right), \\ &\leq -\kappa e^2 - \widetilde{\theta}^T(t)\varphi(z)e - \frac{\beta(x)}{f_{u_\lambda}}e^2 - \frac{\dot{f}_{u_\lambda}}{2f_{u_\lambda}^2}e^2 - e\varepsilon(z) - \frac{1}{\gamma}\widetilde{\theta}^T(t)\left(\widehat{\theta}(t) - \widehat{\theta}(t-T)\right), \end{aligned} \quad (24)$$

where

$$\begin{aligned} \widetilde{\theta}^T(t)\widetilde{\theta}(t) - \widetilde{\theta}^T(t-T)\widetilde{\theta}(t-T) &= -2\left(\widehat{\theta}(t) - \widehat{\theta}(t-T)\right)^T\widetilde{\theta}(t) - \left(\widehat{\theta}(t) - \widehat{\theta}(t-T)\right)^T\left(\widehat{\theta}(t) - \widehat{\theta}(t-T)\right) \\ &\leq -2\left(\widehat{\theta}(t) - \widehat{\theta}(t-T)\right)^T\widetilde{\theta}(t), \end{aligned} \quad (25)$$

Employing the learning law (23) gives rise to

$$\dot{L} \leq -\kappa e^2 - \frac{\beta(x)}{f_{u_\lambda}}e^2 - \frac{\dot{f}_{u_\lambda}}{2f_{u_\lambda}^2}e^2 - e\varepsilon(z). \quad (26)$$

According to Assumptions 1 and 2, we have the following relationship:

$$\frac{\dot{f}_{u_\lambda}}{2f_{u_\lambda}^2} \leq \frac{\left|\dot{f}_{u_\lambda}\right|}{2f_{u_\lambda}^2} \leq \frac{\beta(x)}{2f_{u_\lambda}} < \frac{\beta(x)}{f_{u_\lambda}}. \quad (27)$$

In addition, using Young's inequality yields

$$-e\varepsilon(z) \leq \frac{1}{4\eta}e^2 + \eta\varepsilon^2(z) \leq \frac{1}{4\eta}e^2 + \eta\overline{\varepsilon}^2, \quad (28)$$

where $\eta > 0$ is a constant. Substituting (27) and (28) into (26) gives rise to

$$\dot{L} \leq -\left(\kappa - \frac{1}{4\eta}\right)e^2 + \eta\overline{\varepsilon}^2. \quad (29)$$

In this way, when $\kappa > (4\eta)^{-1}$ and $|e| > (2\eta\overline{\varepsilon})/(\sqrt{4\eta\kappa - 1})$, $\dot{L} < 0$, ensuring that e is uniformly ultimately bounded, which means that there exists $T_1 > 0$ such that $|e(t)| \leq (2\eta\overline{\varepsilon})/(\sqrt{4\eta\kappa - 1})$, for $t \geq T_1$. Then, integrating both sides of (29) over $[0, t]$, we have

$$L(t) \le L(0) - \left(\kappa - \frac{1}{4\eta}\right)\int_0^t \left(e^2 - \frac{4\eta^2\bar{\varepsilon}^2}{4\eta\kappa - 1}\right)\mathrm{d}s. \tag{30}$$

For any bounded initial condition, $L(0)$ is bounded. Due to the positive definiteness of $L(t)$, for any finite time t, $\int_0^t e^2(s)\mathrm{d}s$ is bounded; otherwise, the right side of (30) tends to negative infinity, which contradicts the positive definiteness of $L(t)$. Therefore, for any finite time, $L(t)$ is bounded, and according to the definition of $L(t)$, the boundedness of $\int_{t-T}^t \|\widehat{\theta}\|^2\mathrm{d}s$ can be guaranteed.

By the inequality $(a+b)^2 \le 2a^2 + 2b^2$, it follows from (20) that

$$u^2 \le 2\kappa^2 e^2 + 2\left(\widetilde{\theta}^T\varphi\right)^2 \le d_1 + d_2\|\widehat{\theta}\|^2, \tag{31}$$

where $d_1 = 2\kappa^2 \sup_{t\in[0,+\infty)} e^2$ and $d_2 = 2\sup_{t\in[0,+\infty)}\|\varphi\|^2$. Furthermore,

$$\begin{aligned}\int_{t-T}^t u^2(s)\mathrm{d}s &\le \int_{t-T}^t \mathrm{d}_1 + \mathrm{d}_2\|\widehat{\theta}(s)\|^2\mathrm{d}s\\ &\le d_1 T + \mathrm{d}_2\int_{t-T}^t \|\widehat{\theta}(s)\|^2\mathrm{d}s\\ &< +\infty,\end{aligned} \tag{32}$$

which implies that $\int_{t-T}^t u^2(s)\mathrm{d}s$ is bounded..

Remark 2. As for the incremental adaptation law (23)*, the main feature is that the correction item, $\gamma\varphi(z(t))e(t)$, depends entirely on the information at the current moment. We may call it the closed-loop incremental adaptive learning law. As an alternative, an open-loop learning law,*

$$\widehat{\theta}(t+T) = \begin{cases}\widehat{\theta}(t) - \gamma\varphi(z(t))e(t), & t \ge T,\\ \widehat{\theta}_0, \quad t \in [0,T),\end{cases} \tag{33}$$

is also valid for system (15).

The following theorem illustrates the flexibility of choice of incremental adaptive learning mechanisms.

Theorem 2. *Let the control laws*

$$u = -\kappa e + \widehat{\theta}^T\varphi + u_1, \tag{34}$$

$$u_1 = -\frac{1}{2}\gamma\varphi^T\varphi e. \tag{35}$$

Together with the learning law (33) be applied to system (15), then the same results as in Theorem 1 hold.

Proof. We choose the Lyapunov–Krasovskii function candidate, $L(t) = V(t) + (2\gamma)^{-1}\int_t^{t+T}\widetilde{\theta}^T(s)\widetilde{\theta}(s)\mathrm{d}s$, where $V = 1/2 f_{u_\lambda} e^2$. By applying the control law (34), the error dynamics (16) can be rewritten as

$$\dot{e} = -\beta(x)e + f_{u_\lambda}\left(-\kappa e - \widetilde{\theta}^T\varphi - \varepsilon(z) + u_1\right). \tag{36}$$

Further using the control law (35), the derivative of V can be expressed as

$$\dot{V} = -\kappa e^2 - \widetilde{\theta}^T\varphi(z)e - \frac{\beta(x)}{f_{u_\lambda}}e^2 - \frac{\dot{f}_{u_\lambda}}{2f_{u_\lambda}^2}e^2 - e\varepsilon(z) - \frac{1}{2}\gamma\varphi^T\varphi e^2. \tag{37}$$

According to (36) and (37), the derivative of L is

$$\dot{L} = -\kappa e^2 - \widetilde{\theta}^T\varphi(z)e - \frac{\beta(x)}{f_{u_\lambda}}e^2 - \frac{\dot{f}_{u_\lambda}}{2f_{u_\lambda}^2}e^2 - \varepsilon e - \frac{1}{2}\gamma\varphi^T\varphi e^2 + \frac{1}{2\gamma}\left(\widetilde{\theta}^T(t+T)\widetilde{\theta}(t+T) - \widetilde{\theta}^T(t)\widetilde{\theta}(t)\right). \tag{38}$$

For the item $\widetilde{\theta}^T(t+T)\widetilde{\theta}(t+T)$ in the right side of (38), we have

$$\widetilde{\theta}^T(t+T)\widetilde{\theta}(t+T) = -2\left(\widehat{\theta}(t+T) - \widehat{\theta}(t)\right)^T\widetilde{\theta}(t) + \widetilde{\theta}^T(t)\widetilde{\theta}(t) + \left(\widehat{\theta}(t+T) - \widehat{\theta}(t)\right)^T\left(\widehat{\theta}(t+T) - \widehat{\theta}(t)\right). \tag{39}$$

Substituting (33) into (38), $\dot{L}$ can be rewritten as

$$\dot{L} = -\kappa e^2 - e\varepsilon(z) - \frac{\beta(x)}{f_{u_\lambda}}e^2 - \frac{\dot{f}_{u_\lambda}}{2f_{u_\lambda}^2}e^2 - \widetilde{\theta}^T\varphi e - \frac{1}{2}\gamma\varphi^T(z)\varphi(z)e^2 + \widetilde{\theta}^T\varphi e + \frac{1}{2}\gamma\varphi^T(z)\varphi(z)e^2 \le -\kappa e^2 - e\varepsilon(z), \tag{40}$$

where $-(\beta(x)/f_{u_\lambda})e^2 - ((\dot{f}_{u_\lambda})/(2f_{u_\lambda}^2))e^2 \le 0$, according to (27). Then, the proof can be carried out with similar lines to those of the proof for Theorem 1.

Remark 3. In (34)*, an additional component* u_1 *is added into* (20)*, for cancelling the extra term appeared when applying* (33).

Remark 4. By Theorems 1 and 2*, both the proposed incremental adaptive mechanisms* (23) *and* (33) *are applicable to the aforementioned system* (15)*. In comparison with* (8)*, no* τ *appears in the correction item of the adaptation laws* (23) *and* (33)*. Furthermore, taking the learning cycle* T *as the sampling period or an integer multiple of the sampling period, both the incremental adaptive learning laws* (23) *and* (33) *can be applied to the actual digital computer control system directly.*

Remark 5. With incremental adaptation (23) *or* (33)*, the tracking error* e*,* $\int_{t-T}^{t} \|\widehat{\theta}\|^2 \mathrm{d}s$ *and* $\int_{t-T}^{t} u^2(s)\mathrm{d}s$ *are assured to be bounded, while* e *converges to a neighborhood to the origin with the radius being proportional to* $\overline{\varepsilon}$*. It is worth noting that the boundedness of the parameter estimates and control input themselves are not guaranteed. In the following, we will provide more incremental adaptive learning mechanisms to achieve better control performance.*

4. Extension to High-Order Nonaffine Nonlinear Systems

In this section, the proposed design methods are extended to the following class of n th-order nonaffine nonlinear systems:

$$y^{(n)} = f\left(y, y^{(1)}, \ldots, y^{(n-1)}, u\right), \tag{41}$$

where y is the measurement output, u is the control input, $y^{(i)}$, $(i = 1, \ldots, n)$ is the i th time derivative of y, and the unknown smooth nonlinearity $f(\cdot)$: $R^{n+1} \longrightarrow R$ is an implicit function with respect to u.

Defining the state vector $x = [x_1, x_2, \ldots, x_n]^T = [y, y^{(1)}, \ldots, y^{(n-1)}]^T$, system (41) can be rewritten in a state space model:

$$\begin{cases} \dot{x}_1 = x_2, \\ \dot{x}_2 = x_3, \\ \vdots \\ \dot{x}_n = f(x, u), \\ y = x_1. \end{cases} \tag{42}$$

Let $f_u = ((\partial f(x,u))/(\partial u))$, and the following assumption is used for system (42).

Assumption 3. Without loss of generality, we shall assume that $f_u > 0$*, and there are positive constants* $\underline{f}_u$ *and* $\overline{f}_u$ *that satisfies* $0 < \underline{f}_u \le |f_u| \le \overline{f}_u < \infty, \quad \forall (x,u) \in \overline{R}^{n+1}$.

The control goal of this section is to design an incremental-adaptation-based IAC controller for system (42) such that the system output follows the given smooth desired trajectory y_d with acceptable accuracy, while all the signals in the closed-loop system are bounded. The given desired trajectory y_d is continuous and differentiable, and $y_d(t), y_d^{(1)}(t), \ldots, y_d^{(n)}(t)$ are all bounded for all $t \ge 0$.

4.1. IAC Design and Analysis. To design an IAC controller for the high-order nonaffine system (42), let us define the state error $e = x - x_d = [e_1, e_2, \ldots, e_n]^T$, with $x_d = [y_d(t), y_d^{(1)}(t), \ldots y_d^{(n-1)}(t)]^T$, and the filtered error is defined as

$$e_f = \left[\Lambda^T 1\right] e, \tag{43}$$

with $\Lambda = [\lambda_1, \lambda_2, \ldots \lambda_{n-1}]^T$ that is chosen to guarantee the polynomial $s^{n-1} + \lambda_{n-1}s^{n-2} + \cdots + \lambda_1$ is a Hurwitz. Obviously, e will converge to zero, as e_f approaches zero. At the same time, the output error $(e_1 = y - y_d)$ converges to zero too. Then, the e_f-dynamics can be given as

$$\begin{aligned} \dot{e}_f &= \left[0\Lambda^T\right] e + f(x,u) - y_d^{(n)} \\ &= F(x, v, u), \end{aligned} \tag{44}$$

where $F(x, v, u) = f(x, u) + v$, and $v = [0\Lambda^T]e - y_d^{(n)}$ with $(\partial v)/(\partial u) = 0$.

By applying Lemma 2, there is a continuous smooth function $\alpha(x, v)$ that assures

$$\begin{aligned} &F(x, v, u)|_{u=\alpha(x,v)} \\ &= f(x, \alpha(x, v)) + v = 0. \end{aligned} \tag{45}$$

RBFNN is used for approximating the unknown smooth nonlinear function $\alpha(x, v)$, in the manner of

$$\alpha(x, v) = \theta^T \varphi(z) + \varepsilon(z), \quad z \in [x, v]^T, \tag{46}$$

where $\varepsilon(z)$ is the approximation error that satisfies $|\varepsilon(z)| < \overline{\varepsilon}$, and $\overline{\varepsilon}$ is a positive constant.

To proceed, applying Lemma 1 again, we obtain that

$$F(x, v, u) = F(x, v, \alpha(x, v)) + F_{u_\lambda}(u - \alpha(x, v)), \tag{47}$$

where $F_{u_\lambda} = ((\partial F(x, v, \overline{u}))/(\partial \overline{u}))|_{\overline{u}=u_\lambda}$, and $u_\lambda = \lambda u + (1-\lambda)\alpha(x, v)$, with $\lambda \in (0, 1)$. According to Assumption 3 and the fact that $(\partial v)/(\partial u) = 0$, it is obvious that

$$\begin{aligned} \underline{f}_u \le F_{u_\lambda} &= \frac{\partial F(x, v, u_\lambda)}{\partial u_\lambda}, \\ &= \frac{\partial (f(x, u_\lambda) + v)}{\partial u_\lambda} \le \overline{f}_u. \end{aligned} \tag{48}$$

Then, the adaptive neural controller can be designed as

$$u = -\kappa e_f + \widehat{\theta}^T \varphi(z), \tag{49}$$

where $\kappa > 0$ is the adjustable control gain, and $\widehat{\theta}$ is the estimate of the ideal weight θ.

According to (45)–(49), the error system (44) can be rewritten as

$$\dot{e}_f = F_{u_\lambda}\left(-\kappa e_f - \widetilde{\theta}^T\varphi(z) - \varepsilon(z)\right), \tag{50}$$

where $\widetilde{\theta} = \theta - \widehat{\theta}$ is the weight estimation error.

Given $\overline{\varepsilon}$, let $\theta \in R^N$ be such that (46) hold. The results about the closed-loop stability and the error convergence of the proposed IAC scheme are summarized in the following theorem.

Theorem 3. *Consider the IAC system described by system (42), adaptive controller (49), and the following incremental adaptive learning law:*

$$(1+\gamma\sigma)\widehat{\theta}(t) = \widehat{\theta}(t-T) + \gamma\varphi(z(t))e_f(t), \tag{51}$$

and $\widehat{\theta}(t) = 0$ *for* $t \le 0$, *where* γ *and* σ *are the adjustable parameters, under the assumption 3. Then, for bounded initial conditions, by selecting the parameters appropriately, all the signals in the closed-loop system are bounded, and the state* x *remains in* $\Omega_x = \left\{x(t) \| e_f(t)| \le \sigma^{1/2}\kappa_f^{-1/2}\sqrt{\overline{\varepsilon}^2 + \|\theta\|^2/2}\right\}$, $t \ge T_1$, *where the positive constant* κ_f *satisfies* $\kappa_f \le \kappa \underline{f}_u - (2\underline{f}_u^2\chi^2 + \overline{f}_u^2/4 + 2\chi^2)/\sigma$. *Moreover, the filtered error satisfies* $lim_{t\longrightarrow\infty} sup \int_{t-T}^{t} e_f^2(s)ds \le \kappa_f^{-1}\sigma T(\overline{\varepsilon}^2 + \|\theta\|^2/2)$.

Proof. Let us consider the Lyapunov function candidate, $L(t) = 1/2e_f^2 + 1/2\gamma\int_{t-T}^{t}\widetilde{\theta}^T(s)\widetilde{\theta}(s)ds$.Then, the derivative of $L(t)$ along (50) is

$$\begin{aligned}\dot{L}(t) &= F_{u_\lambda}\left(-\kappa e_f^2(t) - \widetilde{\theta}^T(t)\varphi(z)e_f(t) - e_f(t)\varepsilon(z)\right) + \frac{1}{2\gamma}\left(\widetilde{\theta}^T(t)\widetilde{\theta}(t) - \widetilde{\theta}^T(t-T)\widetilde{\theta}(t-T)\right)\\ &\le F_{u_\lambda}\left(-\kappa e_f^2(t) - \widetilde{\theta}^T(t)\varphi(z)e_f(t) - e_f(t)\varepsilon(z)\right) - \frac{1}{\gamma}\widetilde{\theta}^T(t)\left(\widehat{\theta}(t) - \widehat{\theta}(t-T)\right),\end{aligned} \tag{52}$$

where the algebraic equation $(a-b)^T(a-b) - (a-c)^T(a-c) = (c-b)^T[2(a-b) + (b-c)]$ is used.

Using the fact that $|\varepsilon(z)| \le \overline{\varepsilon}$, and applying Young's inequality yields

$$\begin{aligned}-F_{u_\lambda}\widetilde{\theta}^T(t)\varphi(z)e_f(t) &\le \frac{2F_{u_\lambda}^2}{\sigma}e_f^2(t)\varphi^T(z)\varphi(z) + \frac{\sigma}{8}\widetilde{\theta}^T(t)\widetilde{\theta}(t)\\ &\le \frac{2F_{u_\lambda}^2\chi^2}{\sigma}e_f^2(t) + \frac{\sigma}{8}\widetilde{\theta}^T(t)\widetilde{\theta}(t),\end{aligned} \tag{53}$$

$$-F_{u_\lambda}e_f\varepsilon(z) \le \frac{F_{u_\lambda}^2}{4\sigma}e_f^2 + \sigma\varepsilon^2(z) \le \frac{F_{u_\lambda}^2}{4\sigma}e_f^2 + \sigma\overline{\varepsilon}^2, \tag{54}$$

where $\|\varphi(z)\| \le \chi$, according to Lemma 5.

Substituting (53) and (54) and the learning law (51) into (52) implies

$$\begin{aligned}\dot{L}(t) &\le -\kappa F_{u_\lambda}e_f^2(t) + \frac{2F_{u_\lambda}^2\chi^2}{\sigma}e_f^2(t) + \frac{\sigma}{8}\widetilde{\theta}^T(t)\widetilde{\theta}(t) + \frac{F_{u_\lambda}^2}{4\sigma}e_f^2(t) + \sigma\overline{\varepsilon}^2 - \frac{1}{\gamma}\widetilde{\theta}^T(t)\left(\widehat{\theta}(t) - \widehat{\theta}(t-T)\right)\\ &= -\left(\kappa F_{u_\lambda} - \frac{2F_{u_\lambda}^2\chi^2}{\sigma} - \frac{F_{u_\lambda}^2}{4\sigma}\right)e_f^2(t) + \frac{\sigma}{8}\widetilde{\theta}^T(t)\widetilde{\theta}(t) + \sigma\overline{\varepsilon}^2 - \widetilde{\theta}^T(t)\varphi(z)e_f(t) + \sigma\widetilde{\theta}^T(t)\widehat{\theta}(t)\\ &\le -\left(\kappa F_{u_\lambda} - \frac{2F_{u_\lambda}^2\chi^2}{\sigma} - \frac{F_{u_\lambda}^2}{4\sigma} - \frac{2\chi^2}{\sigma}\right)e_f^2(t) + \frac{\sigma}{4}\widetilde{\theta}^T(t)\widetilde{\theta}(t) + \sigma\overline{\varepsilon}^2 + \sigma\widetilde{\theta}^T(t)\widehat{\theta}(t),\end{aligned} \tag{55}$$

where $-\widetilde{\theta}^T(t)\varphi(z)e_f(t) \le 2/\sigma e_f^2(t)\|\varphi(z)\|^2 + \sigma/8\widetilde{\theta}^T(t)\widetilde{\theta}(t) \le 2\chi^2/\sigma e_f^2(t) + \sigma/8\widetilde{\theta}^T(t)\widetilde{\theta}(t)$ with $\|\varphi(z)\| \le \chi$, by using Young's inequality. Subsequently, the following inequality can be derived by completing the square:

$$\begin{aligned}\sigma\widetilde{\theta}^T(t)\widehat{\theta}(t) &= \sigma\widetilde{\theta}^T(t)\theta - \sigma\widetilde{\theta}^T(t)\widetilde{\theta}(t)\\ &\le \frac{\sigma}{2}\widetilde{\theta}^T(t)\widetilde{\theta}(t) + \frac{\sigma}{2}\|\theta\|^2 - \sigma\widetilde{\theta}^T(t)\widetilde{\theta}(t)\\ &= -\frac{\sigma}{2}\widetilde{\theta}^T(t)\widetilde{\theta}(t) + \frac{\sigma}{2}\|\theta\|^2,\end{aligned} \tag{56}$$

implying that

$$\begin{aligned}\dot{L}(t) &\le -\left(\kappa F_{u_\lambda} - \frac{2F_{u_\lambda}^2\chi^2}{\sigma} - \frac{F_{u_\lambda}^2}{4\sigma} - \frac{2\chi^2}{\sigma}\right)e_f^2(t)\\ &\quad - \frac{\sigma}{4}\widetilde{\theta}^T(t)\widetilde{\theta}(t) + \sigma\left(\overline{\varepsilon}^2 + \frac{\|\theta\|^2}{2}\right)\\ &\le -\left(\kappa \underline{f}_u - \frac{2\overline{f}_u^2\chi^2}{\sigma} - \frac{\overline{f}_u^2}{4\sigma} - \frac{2\chi^2}{\sigma}\right)e_f^2(t)\\ &\quad - \frac{\sigma}{4}\widetilde{\theta}^T(t)\widetilde{\theta}(t) + \sigma\left(\overline{\varepsilon}^2 + \frac{\|\theta\|^2}{2}\right).\end{aligned} \tag{57}$$

The control parameter is selected appropriately so as to satisfy

$$\kappa > \frac{2\overline{f}_u^2\chi^2 + \overline{f}_u^2/4 + 2\chi^2}{\sigma \underline{f}_u}. \tag{58}$$

Then, it follows that

$$\dot{L}(t) \le -\kappa_f e_f^2(t) - \frac{\sigma}{4}\widetilde{\theta}^T(t)\widetilde{\theta}(t) + \sigma\left(\overline{\varepsilon}^2 + \frac{\|\theta\|^2}{2}\right), \tag{59}$$

which is ensured to be negative on condition that

$$e_f^2(t) \ge \frac{\sigma}{\kappa_f}\left(\overline{\varepsilon}^2 + \frac{\|\theta\|^2}{2}\right). \tag{60}$$

As such, if $|e_f| > \sigma^{1/2}\kappa_f^{-1/2}\sqrt{\overline{\varepsilon}^2 + \|\theta\|^2}/2$, $\dot{L}(t)$ will be negative and L will decrease. Therefore, outside this region, $|e_f|$ decreases and finally converges within the bound. This ensures the uniformly ultimate boundedness of e_f, implying that there exists T_1 such that the system state $x(t)$ remains in Ω_x, for $t \ge T_1$. Similarly, from (59), the UUB property of $\widehat{\theta}(t)$ can also be guaranteed. Due to boundedness of x, $\widehat{\theta}$, and y_d, it is easy from (49) to establish the boundedness of u.

Now, integrating (59) over $[t-T, t]$ results in

$$\begin{aligned}L(t) &\le L(t-T) - \kappa_f\int_{t-T}^{t} e_f^2(s)\mathrm{d}s - \frac{\sigma}{4}\int_{t-T}^{t}\|\widetilde{\theta}(s)\|^2\mathrm{d}s + \sigma\int_{t-T}^{t}\left(\overline{\varepsilon}^2 + \frac{\|\theta\|^2}{2}\right)\mathrm{d}s\\ &\le L(t-T) - \kappa_f\int_{t-T}^{t} e_f^2(s)\mathrm{d}s + \sigma\left(\overline{\varepsilon}^2 + \frac{\|\theta\|^2}{2}\right)T.\end{aligned} \tag{61}$$

Considering (59) with $t = t_0 \in [0, T]$, it follows that $\dot{L}(t_0) \le -\kappa_f e_f^2(t_0) + \sigma(\overline{\varepsilon}^2 + \|\theta\|^2/2) \le \sigma(\overline{\varepsilon}^2 + \|\theta\|^2/2)$, which illustrates that $L(t_0)$ is finite, due to the boundedness of θ. Furthermore, with the aid of Lemma 3, the error variable $\int_{t-T}^{t} e_f^2(s)\mathrm{d}s$ could enter the specified bound $\sigma\kappa_f^{-1}T(\overline{\varepsilon}^2 + \|\theta\|^2/2)$, that is,

$$\lim_{t\longrightarrow\infty}\sup\int_{t-T}^{t} e_f^2(s)\mathrm{d}s \le \frac{\sigma T}{\kappa_f}\left(\overline{\varepsilon}^2 + \frac{\|\theta\|^2}{2}\right). \tag{62}$$

This completes the proof.

Remark 6. As for the learning algorithm (51)*, the modification is suggested by introducing the parameter σ, by which the finiteness of estimates is assured.*

4.2. Saturated Learning. In order to assure the finiteness of estimates within a prespecified bound, the fully/partially saturate learning algorithms are applicable. Taking advantage of the fully saturated learning, the weight estimate $\widehat{\theta}$ defined in (49) can be updated as follows:

$$\begin{cases}\widehat{\theta}(t) = \mathrm{sat}\left(\widehat{\theta}^*(t)\right),\\ \dot{\widehat{\theta}}^*(t) = \mathrm{sat}\left(\widehat{\theta}^*(t-T)\right) + \gamma\varphi(z(t))e_f(t).\end{cases} \tag{63}$$

Then, the results of boundedness and convergence are summarized as Theorem 4.

Theorem 4. *If the control law given by (49) with the fully saturation incremental adaptive learning law (63) is applied to system (42), then, by selecting the parameters appropriately, all the signals in the closed-loop system are bounded, and the state x remains in $\Omega_x = \{x(t)\|e_f(t)| \le \kappa_f^{-1/2}\eta^{1/2}(2B_\theta^2 + \overline{\varepsilon}^2)^{1/2}\}$, $t \ge T_1$, where the positive constant κ_f satisfies $\kappa_f \le \kappa \underline{f}_u - (\overline{f}_u{}^2\chi^2 + \overline{f}_u{}^2 + \chi^2)/(4\eta)$, and B_θ is to be specified. Moreover, the filtered error satisfies $\lim_{t\longrightarrow\infty}\sup\int_{t-T}^{t} e_f^2(s)ds \le \kappa_f^{-1}\eta T(2B_\theta^2 + \overline{\varepsilon}^2)$.*

Proof. Let us consider the same Lyapunov-like function candidate as given in the proof for Theorem 3. Similarly, by following the same line used in (52), and applying (63), the time derivative of L can be obtained:

$$\begin{aligned}\dot{L}(t) &\le F_{u_\lambda}\left(-\kappa e_f^2(t) - \widetilde{\theta}^T(t)\varphi(z)e_f(t) - e_f(t)\varepsilon(z)\right) - \frac{1}{\gamma}\widetilde{\theta}^T(t)\left(\widehat{\theta}(t) - \widehat{\theta}(t-T)\right)\\ &= F_{u_\lambda}\left(-\kappa e_f^2(t) - \widetilde{\theta}^T(t)\varphi(z)e_f(t) - e_f(t)\varepsilon(z)\right) - \frac{1}{\gamma}\widetilde{\theta}^T(t)\left(\widehat{\theta}(t) - \widehat{\theta}^*(t)\right) - \widetilde{\theta}^T(t)\varphi(z)e_f(t).\end{aligned} \tag{64}$$

By invoking Lemma 4, and we have the following inequality:

$$\begin{aligned}&-\frac{1}{\gamma}\widetilde{\theta}^T(t)\left(\widehat{\theta}(t) - \widehat{\theta}^*(t)\right)\\ &= \frac{1}{\gamma}\left(\theta - \mathrm{sat}\left(\widehat{\theta}^*(t)\right)\right)^T\left(\widehat{\theta}^*(t) - \mathrm{sat}\left(\widehat{\theta}^*(t)\right)\right) \le 0,\end{aligned} \tag{65}$$

implying that

$$\begin{aligned}\dot{L}(t) \le\ &-\kappa F_{u_\lambda} e_f^2(t) - F_{u_\lambda}\widetilde{\theta}^T(t)\varphi(z)e_f(t) - F_{u_\lambda}e_f(t)\varepsilon(z)\\ &- \widetilde{\theta}^T(t)\varphi(z)e_f(t).\end{aligned} \tag{66}$$

By Young's inequality, we obtain the following relationships:

$$-F_{u_\lambda}\widetilde{\theta}^T(t)\varphi(z)e_f(t) \le \frac{F_{u_\lambda}^2}{4\eta}\|\varphi(z)\|^2 e_f^2(t) + \eta\widetilde{\theta}^T(t)\widetilde{\theta}(t) \le \frac{F_{u_\lambda}^2\chi^2}{4\eta}e_f^2(t) + \eta\widetilde{\theta}^T(t)\widetilde{\theta}(t), \tag{67}$$

$$-\varepsilon F_{u_\lambda}e_f(t) \le \frac{F_{u_\lambda}^2}{4\eta}e_f^2(t) + \eta\varepsilon^2 \le \frac{F_{u_\lambda}^2}{4\eta}e_f^2(t) + \eta\bar{\varepsilon}^2, \tag{68}$$

$$-\widetilde{\theta}^T(t)\varphi(z)e_f(t) \le \frac{1}{4\eta}\|\varphi(z)\|^2 e_f^2(t) + \eta\widetilde{\theta}^T(t)\widetilde{\theta}(t) \le \frac{\chi^2}{4\eta}e_f^2(t) + \eta\widetilde{\theta}^T(t)\widetilde{\theta}(t), \tag{69}$$

where $\|\varphi(z)\| \le \chi$, by using Lemma 5, and the constant $\eta > 0$, which can be arbitrarily small. It follows that

$$\begin{aligned}\dot{L}(t) &\le -\left(\kappa F_{u_\lambda} - \frac{F_{u_\lambda}^2\chi^2}{4\eta} - \frac{F_{u_\lambda}^2}{4\eta} - \frac{\chi^2}{4\eta}\right)e_f^2(t) + 2\eta\widetilde{\theta}^T(t)\widetilde{\theta}(t) + \eta\bar{\varepsilon}^2\\ &\le -\left(\kappa\underline{f}_u - \frac{\overline{f}_u^{\,2}\chi^2}{4\eta} - \frac{\overline{f}_u^{\,2}}{4\eta} - \frac{\chi^2}{4\eta}\right)e_f^2(t) + \eta\left(2\|\widetilde{\theta}(t)\|^2 + \bar{\varepsilon}^2\right).\end{aligned} \tag{70}$$

By setting

$$\kappa > \frac{\overline{f}_u^{\,2}\chi^2 + \overline{f}_u^{\,2} + \chi^2}{4\eta\underline{f}_u}, \tag{71}$$

we have

$$\dot{L}(t) \le -\kappa_f e_f^2(t) + \eta\left(2\|\widetilde{\theta}(t)\|^2 + \bar{\varepsilon}^2\right). \tag{72}$$

There exists a positive constant B_θ such that $\|\widetilde{\theta}(t)\| \le B_\theta$, for $t \ge 0$, due to the properties of fully saturated learning algorithm (63). Thus, as long as $|e_f| > \kappa_f^{-1/2}\eta^{1/2}(2B_\theta^2 + \bar{\varepsilon}^2)^{1/2}$, L will decrease, and we conclude the UUB of e_f. Then, $x(t)$ will remain in Ω_x, for $t \in [T_1, +\infty)$. The conclusions follow with similar lines to those in the proof for Theorem 3.

Remark 7. By Theorems 3 *and* 4, *the robustness of the proposed IAC schemes is established, with the aid of Lemma* 3. *This lemma plays a key role to finalize the robust convergence analysis.*

Remark 8. Both the incremental adaptive control schemes proposed in Theorems 3 *and* 4 *are applicable for performing infinite-duration tasks. The presented theoretical results hold, as long as* $y_d(t)$ *and its derivatives are bounded, whereas the*

periodicity that $y_d(t) = y_d(t-T)$ *is not required, where* $T > 0$ *is the period.*

Remark 9. Similarly, taking advantage of the partially saturated learning algorithms developed in [30]*, we can also propose a partially saturated incremental adaptive learning mechanism:*

$$\widehat{\theta}(t) = \mathrm{sat}(\widehat{\theta}(t-T)) + \gamma\varphi(z(t))e_f(t). \tag{73}$$

However, *in the case of using incremental adaptation* (73)*, a dilemma arises in the corresponding stability and convergence analysis. Below, we briefly explain this difficulty. Consider the IAC system described by the system* (42)*, the adaptive controller* (33)*, and the learning law* (73)*, under* Assumption 3. *In the case, a Lyapunov–Krasovskii function candidate,* $L(t) = e_f^2(t)/2 + (2\gamma)^{-1}\int_{t-T}^{t}(\theta - \mathrm{sat}(\widehat{\theta}(s)))^T(\theta - \mathrm{sat}(\widehat{\theta}(s)))\mathrm{d}s$*, is suggested. Differentiating the function* $L(t)$*,*

$$\begin{aligned}\Delta L(t) &= L(t) - L(t-T)\\ &= \frac{1}{2}e_f^2(t) - \frac{1}{2}e_f^2(t-T) + \frac{1}{2\gamma}\int_{t-T}^{t}(\theta - \mathrm{sat}(\widehat{\theta}(s)))^T(\theta - \mathrm{sat}(\widehat{\theta}(s))) - (\theta - \mathrm{sat}(\widehat{\theta}(s-T)))^T(\theta - \mathrm{sat}(\widehat{\theta}(s-T)))\mathrm{d}s.\end{aligned} \tag{74}$$

where $(e_f^2(t) - e_f^2(t-T))/2 = \int_{t-T}^{t}F_{u_\lambda}(-\kappa e_f^2(s) - \widetilde{\theta}^T(s)\varphi(z)e_f(s) - \varepsilon e_f(s)\mathrm{d}s$*, according to* (50)*. Using Young's inequality for* $-F_{u_\lambda}\widetilde{\theta}^T(s)\varphi(z)e_f(s)$ *and* $-\varepsilon F_{u_\lambda}e_f(s)$ *same as* (67) *and* (68)*, we have* $-F_{u_\lambda}\widetilde{\theta}^T(s)\varphi(z)e_f(s) \le ((F_{u_\lambda}^2\chi^2)/(4\eta))e_f^2(s) + \eta\|\widetilde{\theta}(s)\|^2$*, and* $-\varepsilon F_{u_\lambda}e_f(s) \le ((F_{u_\lambda}^2)/(4\eta))e_f^2(s) + \eta\varepsilon^2$*. Furthermore, the following inequality can be derived by utilizing the incremental adaptation law* (73)*:*

$$\begin{aligned}&(\theta - \mathrm{sat}(\widehat{\theta}(s-T)))^T(\theta - \mathrm{sat}(\widehat{\theta}(s-T)))\\ &= \left(\theta - \widehat{\theta}(s) + \gamma\varphi(z)e_f(s)\right)^T\left(\theta - \widehat{\theta}(s) + \gamma\varphi(z)e_f(s)\right),\\ &= \widetilde{\theta}(s)^T\widetilde{\theta}(s) + 2\gamma\widetilde{\theta}^T(s)\varphi(z)e_f(s) + \gamma^2\|\varphi(z)\|^2e_f^2(s).\end{aligned} \tag{75}$$

It follows that

$$\begin{aligned}\Delta L(t) &= \int_{t-T}^{t} -\kappa F_{u_\lambda}e_f^2(s) - F_{u_\lambda}\widetilde{\theta}^T(s)\varphi(z)e_f(s) - \varepsilon F_{u_\lambda}e_f(s)\mathrm{d}s\\ &\quad + \frac{1}{2\gamma}\int_{t-T}^{t}(\theta - \mathrm{sat}(\widehat{\theta}(s)))^T(\theta - \mathrm{sat}(\widehat{\theta}(s))) - \widetilde{\theta}(s)^T\widetilde{\theta}(s) - 2\gamma\widetilde{\theta}^T(s)\varphi(z)e_f(s) - \gamma^2\|\varphi(s)\|^2e_f^2(s)\mathrm{d}s\\ &\le \int_{t-T}^{t} -\left(\kappa F_{u_\lambda} - \frac{F_{u_\lambda}^2\chi^2}{4\eta} - \frac{F_{u_\lambda}^2}{4\eta}\right)e_f^2(s) + \eta\left(\|\widetilde{\theta}(s)\|^2 + \overline{\varepsilon}^2\right)\mathrm{d}s\\ &\quad + \frac{1}{2\gamma}\int_{t-T}^{t}\Big((\theta - \mathrm{sat}(\widehat{\theta}(s)))^T(\theta - \mathrm{sat}(\widehat{\theta}(s))) - \widetilde{\theta}(s)^T\widetilde{\theta}(s) - 2\gamma\widetilde{\theta}^T(s)\varphi(z)e_f(s) - \gamma^2\|\varphi(z)\|^2e_f^2(s)\Big)\mathrm{d}s\\ &\le \int_{t-T}^{t} -\left(\kappa F_{u_\lambda} - \frac{F_{u_\lambda}^2\chi^2}{4\eta} - \frac{F_{u_\lambda}^2}{4\eta} - \frac{\gamma^2\chi^2}{\eta}\right)e_f^2(s) + \eta\left(2\|\widetilde{\theta}(s)\|^2 + \overline{\varepsilon}^2\right)\mathrm{d}s\\ &\quad + \frac{1}{2\gamma}\int_{t-T}^{t}\Big((\theta - \mathrm{sat}(\widehat{\theta}(s)))^T(\theta - \mathrm{sat}(\widehat{\theta}(s))) - \widetilde{\theta}(s)^T\widetilde{\theta}(s)\Big)\mathrm{d}s.\end{aligned} \tag{76}$$

where $-2\gamma\widetilde{\theta}^T(s)\varphi(z)e_f(s) \le \gamma^2\chi^2/\eta e_f^2(s) + \eta\|\widetilde{\theta}(s)\|^2$*, upon using Young's inequality. Besides, according to* [30]*,* $(\theta - \mathrm{sat}(\widehat{\theta}(s)))^T(\theta - \mathrm{sat}(\widehat{\theta}(s))) - \widetilde{\theta}(s)^T\widetilde{\theta}(s) \le 0$*, then*

$$\Delta L(t) \le \int_{t-T}^{t} -\left(\kappa F_{u_\lambda} - \frac{F_{u_\lambda}^2\chi^2}{4\eta} - \frac{F_{u_\lambda}^2}{4\eta} - \frac{4\gamma^2\chi^2}{4\eta}\right)e_f^2(s) + \eta\left(2\|\widetilde{\theta}(s)\|^2 + \overline{\varepsilon}^2\right)\mathrm{d}s. \tag{77}$$

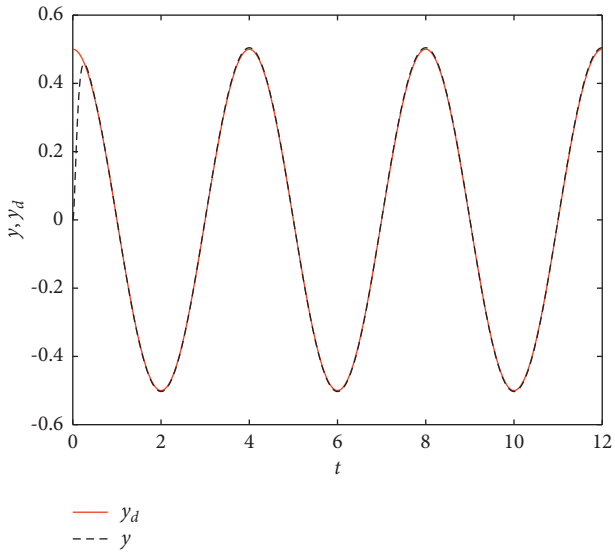

FIGURE 1: The reference signal y_d and output signal y for Example 1.

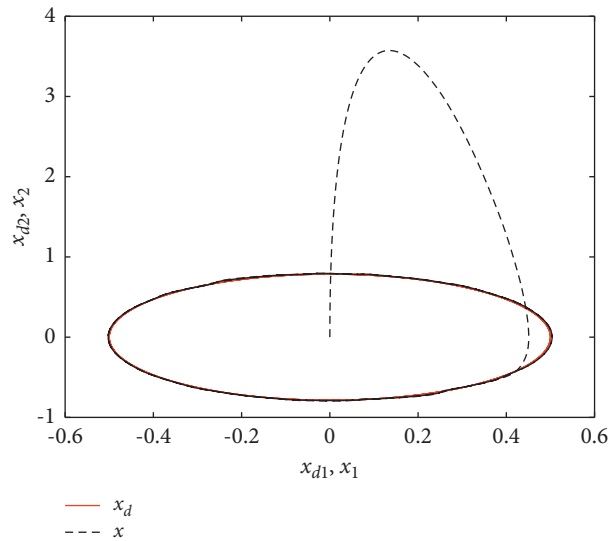

FIGURE 2: Convergence behavior ($x \longrightarrow x_d$) for Example 1.

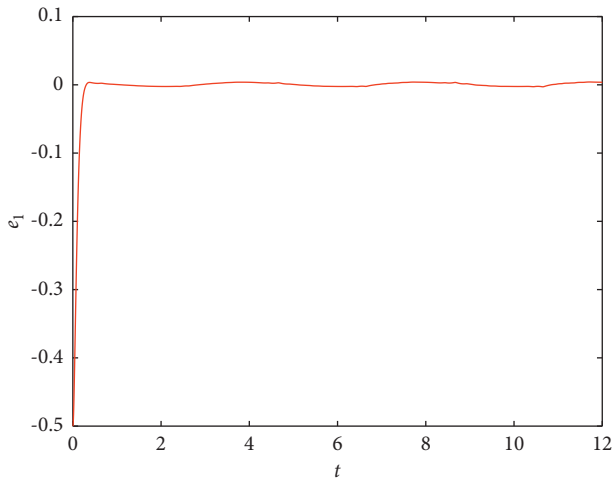

FIGURE 3: State error e_1 for Example 1.

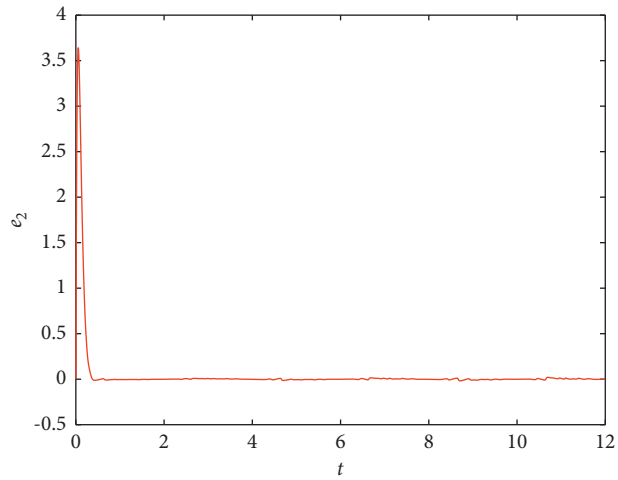

Figure 4: State error e_2 for Example 1.

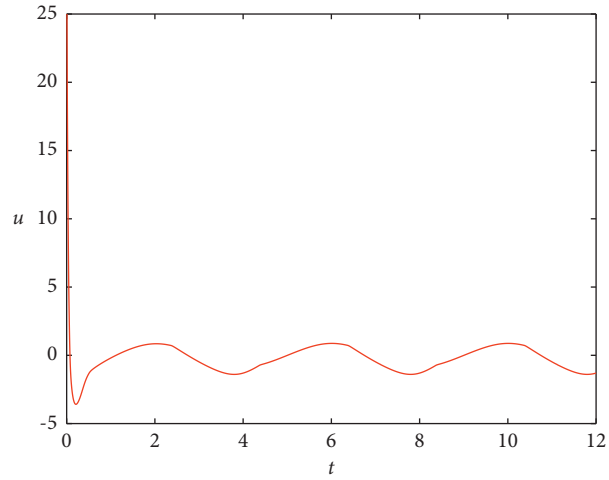

Figure 5: Control input u for Example 1.

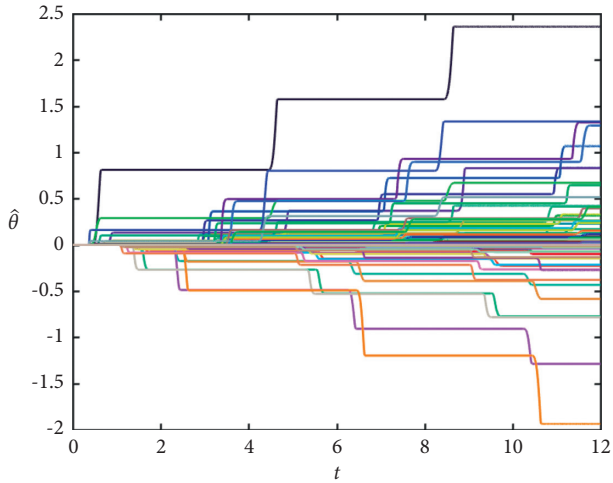

Figure 6: Weights estimates $\hat{\theta}$ for Example 1.

Obviously, for the above inequality, the weight estimation error $\widetilde{\theta}$ is not guaranteed to be bounded, because the learning law (73) *cannot ensure that the parameter estimate $\widehat{\theta}$ is bounded in advance. Therefore, it is difficult to continue the performance analysis. Compared with partially saturated incremental adaptation* (73)*, by the property of the saturation function, the entire right-hand side of the learning algorithm* (63) *is saturated, and the estimate for each parameter is guaranteed to be constrained in a prespecified region.*

5. Numerical Simulation

In this section, two examples are used to test the effectiveness of the presented incremental-adaptation-based IAC control schemes. The approach proposed in Theorem 4 will be utilized to construct controllers to control the systems under consideration.

Example 1. Consider the following second-order nonaffine system [11]:

$$\begin{cases} \dot{x}_1 = x_2, \\ \dot{x}_2 = f(x,u), \\ y = x_1, \end{cases} \tag{78}$$

where $x = [x_1, x_2]^T$ stands for the system state, and the nonlinear function $f(x,u)$ satisfies

$$f(x,u) = \begin{cases} u + 0.5\sin(u), & \text{if } x_1 + x_2 < 0, \\ \sin(x_1 + x_2) + u + 0.5\sin(u), & \text{otherwise.} \end{cases} \tag{79}$$

From the system descriptions above, we can achieve $f_u = (\partial f(x,u)/\partial u) > 0$ such that Assumption 3 holds. In addition, we assume that there is no a priori of uncertain nonlinearities in the abovementioned nonaffine systems. The reference trajectory is selected as $y_d(t) = 0.5\cos(0.5\pi t)$.

The controller given by (49) is applied, and the weight adaptation law (63) is adopted in this simulation, with the following parameter settings: $\kappa = 30, \lambda_1 = 12, \gamma = 2, T = 0.005, \widehat{\theta}_{i\min} = -10, \widehat{\theta}_{i\max} = 10, i = 1, 2, \ldots, 1089$. In addition, the centers of Gaussian RBFNN, $c_i, i = 1, 2, \ldots, 1089$, are evenly spaced on $[-1,1] \times [-4,4] \times [-10,10]$, with the width $b_i = 0.06$. In the simulation, we set the initial state as $x(0) = [0,0]^T$, and the initial weight estimate is $\widehat{\theta}(0) = 0$.

The simulation results are shown in Figures 1–6. Figures 1–4 depict the tracking performance of the IAC system, where Figure 1 shows the output tracking of the system, Figure 2 describes the convergence behavior of the system state, and Figures 3 and 4 give the corresponding state errors e_1 and e_2, respectively. Adopting the proposed IAC scheme, the output error converges to a neighborhood of the origin and remains there; that is, e_1 converges to $[-2.0, 4.0] \times 10^{-3}$. The resultant input is shown in Figure 5. In addition, Figure 6 shows the boundedness and convergence of weight estimates $\widehat{\theta}$. The presented numerical results demonstrate that the boundedness of all variables of the closed-loop system and the convergence of the tracking error are achieved by the proposed IAC scheme.

Example 2. To further illustrate the effectiveness of the proposed algorithm for higher-order and more complex nonaffine nonlinear systems, we consider the following system:

$$\begin{cases} \dot{x}_1 = x_2, \\ \dot{x}_2 = x_3, \\ \dot{x}_3 = x_1 - 0.35\sin\left(x_2^2\right) + \dfrac{x_1^2 + \left(2 + 0.5\sin\left(x_1 x_2\right)\right)u + 0.34\cos(u)}{2 - \cos(x_3) + 0.57 x_1^2 x_2^2}, \\ y = x_1, \end{cases} \tag{80}$$

where $x = [x_1, x_2, x_3]^T$ is the system state. For the nonlinear function $f(x,u) = x_1 - 0.35\sin(x_2^2) + x_1^2 + (2 + 0.5\sin(x_1 x_2))u + 0.34\cos(u)/2 - \cos(x_3) + 0.57 x_1^2 x_2^2$, we have $f_u = \partial f(x,u)/\partial u > 0$ that Assumption 3 is also holds. The reference trajectory is selected as $y_d(t) = 0.5\cos(0.5\pi t)$.

The same controller, together with the same adaptation laws is applied, and the control parameters are chosen as $\kappa = 30, \lambda_1 = 10, \lambda_2 = 5, \gamma = 0.5, T = 0.005, \widehat{\theta}_{i\min} = -10$, and $\widehat{\theta}_{i\max} = 10, i = 1, 2, \ldots, 3025$. In addition, the centers $c_i, i = 1, 2, \ldots, 3025$ are evenly spaced in $[-0.6, 0.6] \times [-1.0, 1.0] \times [-2, 3] \times [-15, 15]$, and the width $b_i = 0.1$. In this simulation, the initial state is $x(0) = [0,0,0]^T$.

The simulation results are shown in Figures 7–13. Similarly, the results about the boundedness and the error convergence of the proposed IAC control scheme are obtained. The state tracking performance is shown in Figures 7–11, and it is observed from Figure 9 that the boundary range of the ultimate output error is

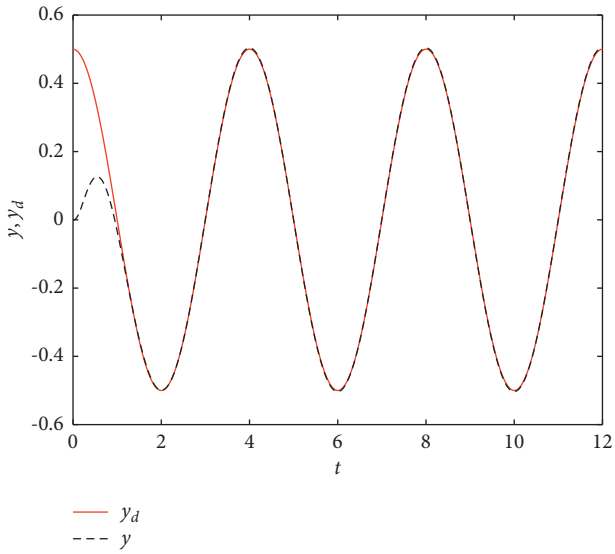

FIGURE 7: The reference signal y_d and output signal y for Example 2.

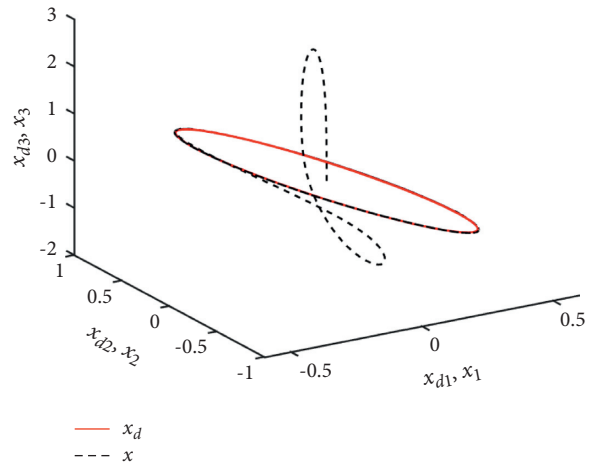

FIGURE 8: Convergence behavior ($x \longrightarrow x_d$) for Example 2.

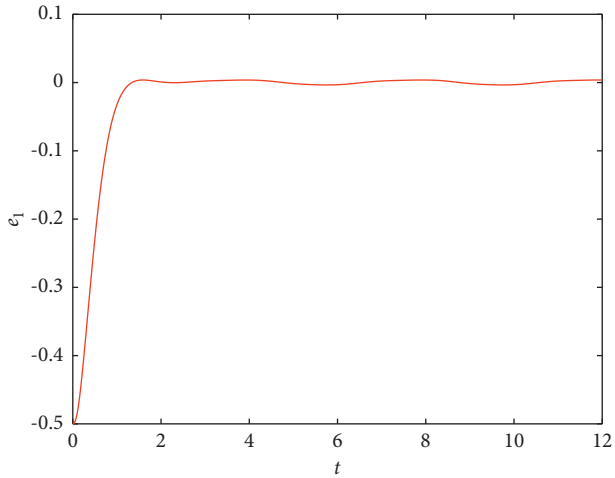

FIGURE 9: State error e_1 for Example 2.

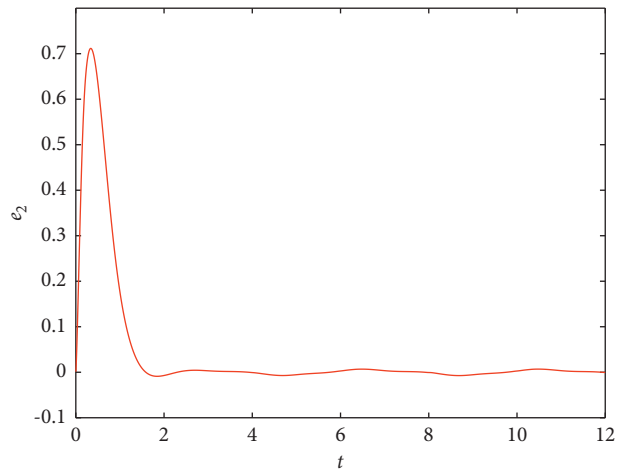

Figure 10: State error e_2 for Example 2.

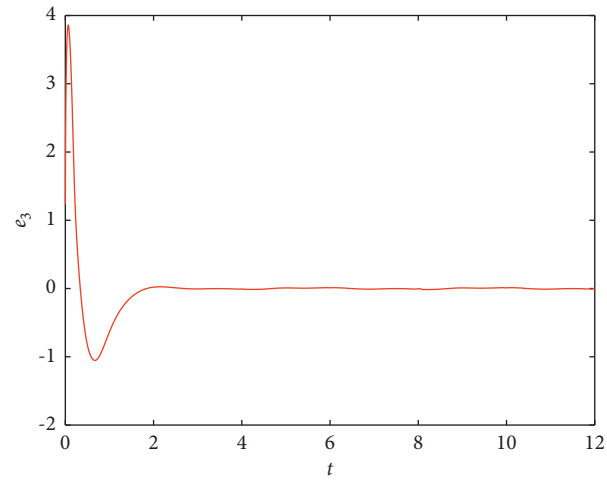

Figure 11: State error e_3 for Example 2.

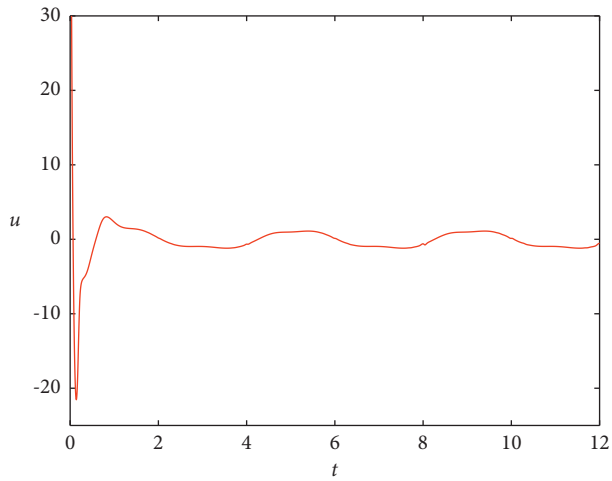

Figure 12: Control input u for Example 2.

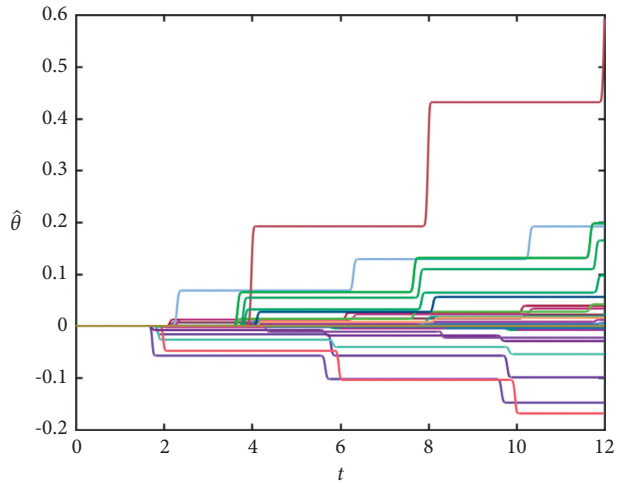

Figure 13: Weights estimates $\widehat{\theta}$ for Example 2.

$[-3.4, 3.6] \times 10^{-3}$. Figure 12 shows the corresponding control input. In Figure 13, the convergence of the weight estimates is given.

6. Conclusion

The incremental adaptation mechanisms are suggested in this article, including the so-called closed-loop, open-loop, and fully saturated learning mechanisms, and based on them, IAC schemes using neural network for nonaffine systems with infinite interval tracking are developed. With the proposed incremental-adaptation-based IAC schemes, there is no periodicity or repeatability requirements, while the numerical integration for implementation can be effectively avoid. Additionally, the robust convergence of the proposed learning control schemes is established, with the use of a key lemma. Theoretical results of establishing convergence performance of the tracking error and the numerical results have been presented, which demonstrate the effectiveness of the IAC schemes.

Data Availability

The data used to support the findings of this study are available from the corresponding author upon request.

Conflicts of Interest

The authors declare that they have no conflicts of interest.

Acknowledgments

This work was supported by the National Natural Science Foundation of China under Grant 62073291 and Grant 61873239.

References

[1] S. S. Ge, C. C. Hang, T. H. Lee, and T. Zhang, *Stable Adaptive Neural Network Control*, Kluwer, Boston, MA, 2001.

[2] S. S. Ge and C. C. Hang, "Adaptive neural network control of nonlinear systems by state and output feedback," *IEEE Transactions on Systems, Man and Cybernetics, Part B (Cybernetics)*, vol. 29, no. 6, pp. 818–828, 1999.

[3] J. Zhang, "Neural-network control of nonaffine nonlinear system with zero dynamics by state and output feedback," *IEEE Transactions on Neural Networks*, vol. 14, no. 4, pp. 900–918, 2003.

[4] A. S. Shiriaev and A. L. Fradkov, "Stabilization of invariant sets for nonlinear non-affine systems," *Automatica*, vol. 36, no. 11, pp. 1709–1715, 2000.

[5] J.-H. Park and G.-T. Park, "Robust adaptive fuzzy controller for non-affine nonlinear systems with dynamic rule activation," *International Journal of Robust and Nonlinear Control*, vol. 13, no. 2, pp. 117–139, 2003.

[6] N. Hovakimyan, E. Lavretsky, and A. Sasane, "Dynamic inversion for nonaffine-in-control systems via time-scale separation. part I," *Journal of Dynamical and Control Systems*, vol. 13, no. 4, pp. 451–465, 2007.

[7] A. J. Kurdila, F. J. Narcowich, and J. D. Ward, "Persistency of excitation in identification using radial basis function approximants," *SIAM Journal on Control and Optimization*, vol. 33, no. 2, pp. 625–642, 1995.

[8] B.-J. Yang and A. J. Calise, "Adaptive control of a class of nonaffine systems using neural networks," *IEEE Transactions on Neural Networks*, vol. 18, no. 4, pp. 1149–1159, 2007.

[9] "Robust adaptive controller design for a class of uncertain nonlinear systems using online T-S fuzzy-neural modeling approach," *IEEE Transactions on Systems, Man, and Cybernetics, Part B (Cybernetics)*, vol. 41, no. 2, pp. 542–552, 2011.

[10] Y. Wang, H. Chien, and T. Lee, "Observer-based T-S fuzzy control for a class of general nonaffine nonlinear systems using generalized projection-update laws," *IEEE Transactions on Fuzzy Systems*, vol. 19, no. 3, pp. 493–504, 2011.

[11] J. A. Farrell, "Tracking control for nonaffine systems: a self-organizing approximation approach," *IEEE Transactions on Neural Networks and Learning Systems*, vol. 23, no. 2, pp. 223–235, 2012.

[12] M. Chen and S. S. Ge, "Direct adaptive neural control for a class of uncertain nonaffine nonlinear systems based on disturbance observer," *IEEE Transactions on Cybernetics*, vol. 43, no. 4, pp. 1213–1225, 2013.

[13] Q. Gao, G. Feng, Y. Wang, and J. Qiu, "Universal fuzzy models and universal fuzzy controllers for stochastic nonaffine nonlinear systems," *IEEE Transactions on Fuzzy Systems*, vol. 21, no. 2, pp. 328–341, 2013.

[14] "Dynamic learning from adaptive neural network control of a class of nonaffine nonlinear systems," *IEEE Transactions on Neural Networks and Learning Systems*, vol. 25, no. 1, pp. 111–123, 2014.

[15] K. Esfandiari, F. Abdollahi, and H. A. Talebi, "Adaptive control of uncertain nonaffine nonlinear systems with input saturation using neural networks," *IEEE Transactions on Neural Networks and Learning Systems*, vol. 26, no. 10, pp. 2311–2322, 2015.

[16] H. Han, W. Zhou, J. Qiao, and G. Feng, "A direct self-constructing neural controller design for a class of nonlinear systems," *IEEE Transactions on Neural Networks and Learning Systems*, vol. 26, no. 6, pp. 1312–1322, 2015.

[17] Y.-X. Li and G.-H. Yang, "Fuzzy adaptive output feedback fault-tolerant tracking control of a class of uncertain nonlinear systems with nonaffine nonlinear faults," *IEEE Transactions on Fuzzy Systems*, vol. 24, no. 1, pp. 223–234, 2016.

[18] J. Jia and D. Song, "Barrier function-based neural adaptive control with locally weighted learning and finite neuron self-growing strategy," *IEEE Transactions on Neural Networks and Learning Systems*, vol. 28, no. 6, pp. 1439–1451, 2017.

[19] Y. Li, K. Sun, and S. Tong, "Observer-based adaptive fuzzy fault-tolerant optimal control for SISO nonlinear systems," *IEEE Transactions on Cybernetics*, vol. 49, no. 2, pp. 649–661, 2019.

[20] J. Qin, G. Zhang, W. X. Zheng, and Y. Kang, "Neural network-based adaptive consensus control for a class of nonaffine nonlinear multiagent systems with actuator faults," *IEEE Transactions on Neural Networks and Learning Systems*, vol. 30, no. 12, pp. 3633–3644, 2019.

[21] X. Bu, Y. Xiao, and H. Lei, "An adaptive critic design-based fuzzy neural controller for hypersonic vehicles: predefined behavioral nonaffine control," *IEEE*, vol. 24, no. 4, pp. 1871–1881, 2019.

[22] B. Wu and J. H. Park, "Adaptive fault-tolerant control of uncertain switched nonaffine nonlinear systems with actuator faults and time delays," *IEEE Transactions on Systems, Man, and Cybernetics: Systems*, vol. 50, no. 9, pp. 3470–3480, 2020.

[23] B. Wu, J. H. Park, X. P. Xie, C. Gao, and N. N. Zhao, "Fuzzy adaptive event-triggered control for a class of uncertain nonaffine nonlinear systems with full state constraints," *IEEE Transactions on Fuzzy Systems*, vol. 29, no. 4, pp. 904–916, 2021.

[24] S. Arimoto, "Learning control theory for robotic motion," *International Journal of Adaptive Control and Signal Processing*, vol. 4, no. 6, pp. 543–564, 1990.

[25] N. Sadegh, R. Horowitz, W. Kao, and M. Tomizuka, "A unified approach to the design of adaptive and repetitive controllers for robotic manipulators," *Journal of Dynamic Systems, Measurement, and Control*, vol. 112, no. 4, pp. 618–629, 1990.

[26] S. S. Saab, W. G. Vogt, and M. H. Mickle, "Learning control algorithms for tracking "slowly" varying trajectories," *IEEE Transactions on Systems, Man, and Cybernetics, Part B (Cybernetics)*, vol. 27, no. 4, pp. 657–670, 1997.

[27] M. French and E. Rogers, "Non-linear iterative learning by an adaptive Lyapunov technique," *International Journal of Control*, vol. 73, no. 10, pp. 840–850, 2000.

[28] "A composite energy function-based learning control approach for nonlinear systems with time-varying parametric uncertainties," *IEEE Transactions on Automatic Control*, vol. 47, no. 11, pp. 1940–1945, 2002.

[29] Z. Qu and J. X. Xu, "Model-based learning controls and their comparisons using Lyapunov direct method," *Asian Journal of Control*, vol. 4, no. 1, pp. 99–110, 2002.

[30] W. E. Dixon, E. Zergeroglu, D. M. Dawson, and B. T. Costic, "Repetitive learning control: a Lyapunov-based approach"," *IEEE Transactions on Systems, Man, and Cybernetics - Part B: Cybernetics*, vol. 32, no. 4, pp. 538–545, 2002.

[31] M. Sun and S. S. Ge, "Adaptive repetitive control for a class of nonlinearly parametrized systems," *IEEE Transactions on Automatic Control*, vol. 51, no. 10, pp. 1684–1688, 2006.

[32] C. J. Chien, "A combined adaptive law for fuzzy iterative learning control of nonlinear systems with varying control tasks," *IEEE Transactions on Fuzzy Systems*, vol. 16, no. 1, pp. 40–51, 2008.

[33] A. Tayebi and C. J. Chien, "A unified adaptive iterative learning control framework for uncertain nonlinear systems," *IEEE Transactions on Automatic Control*, vol. 52, no. 10, pp. 1907–1913, 2007.

[34] R. Marino and P. Tomei, "An iterative learning control for a class of partially feedback linearizable systems," *IEEE Transactions on Automatic Control*, vol. 54, no. 8, pp. 1991–1996, 2009.

[35] M. Sun, "A Barbalat-like lemma with its application to learning control," *IEEE Transactions on Automatic Control*, vol. 54, no. 9, pp. 2222–2225, 2009.

[36] C. J. Chien, C. T. Hsu, and C. Y. Yao, "Fuzzy system-based adaptive iterative learning control for nonlinear plants with initial state errors," *IEEE Transactions on Fuzzy Systems*, vol. 12, no. 5, pp. 724–732, 2004.

[37] J. X. Xu and R. Yan, "On initial conditions in iterative learning control," *IEEE Transactions on Automatic Control*, vol. 50, no. 9, pp. 1349–1354, 2005.

[38] M. Sun, T. Wu, L. Chen, and G. Zhang, "Neural AILC for error tracking against arbitrary initial shifts," *IEEE Transactions on Neural Networks and Learning Systems*, vol. 29, no. 7, pp. 2705–2716, 2018.

[39] X. Li, D. Shen, and J. X. Xu, "Adaptive iterative learning control for MIMO nonlinear systems performing iteration-varying tasks," *Journal of the Franklin Institute*, vol. 356, no. 16, pp. 9206–9231, 2019.

[40] D. Shen and J. X. Xu, "Adaptive learning control for nonlinear systems with randomly varying iteration lengths," *IEEE Transactions on Neural Networks and Learning Systems*, vol. 30, no. 4, pp. 1119–1132, 2019.

[41] D. Meng and J. Zhang, "Deterministic convergence for learning control systems over iteration-dependent tracking intervals," *IEEE Transactions on Neural Networks and Learning Systems*, vol. 29, no. 8, pp. 3885–3892, 2018.

[42] X. Jin, "Iterative learning control for MIMO nonlinear systems with iteration-varying trial lengths using modified composite energy function analysis," *IEEE Transactions on Cybernetics*, vol. 51, no. 12, pp. 6080–6090, 2021.

[43] J. S. Li and J. M. Li, "Adaptive iterative learning control for consensus of multi-agent systems," *IET Control Theory & Applications*, vol. 7, no. 1, pp. 136–142, 2013.

[44] H. Ji, Z. Hou, and R. Zhang, "Adaptive iterative learning control for high-speed trains with unknown speed delays and input saturations," *IEEE Transactions on Automation Science and Engineering*, vol. 13, no. 1, pp. 260–273, 2016.

[45] X. Bu and Z. Hou, "Adaptive iterative learning control for linear systems with binary-valued observations," *IEEE Transactions on Neural Networks and Learning Systems*, vol. 29, no. 1, pp. 232–237, 2018.

[46] W. He, T. Meng, D. Huang, and X. Li, "Adaptive boundary iterative learning control for an Euler-Bernoulli beam system with input constraint," *IEEE Transactions on Neural Networks and Learning Systems*, vol. 29, no. 5, pp. 1539–1549, 2018.

[47] M. Sun, "On incremental adaptive strategies," in *Proceedings of the 9th International Conference on Intelligent Computing Theories and Technology*, pp. 343–352, Nanning, China, July 2013.

[48] M. Sun, "Convergence of Incremental Adaptive Systems," 2014, https://arxiv.org/abs/1310.0975.

[49] M. Sun, C. Xu, and S. Zou, "An incremental adaptive learning algorithms," *High Technology Letters*, vol. 30, no. 7, pp. 666–675, 2020, in Chinese.